Nanomaterials for the Life Sciences

Edited by Challa Kumar

WILEY-VCH

Mixed Metal Nanomaterials

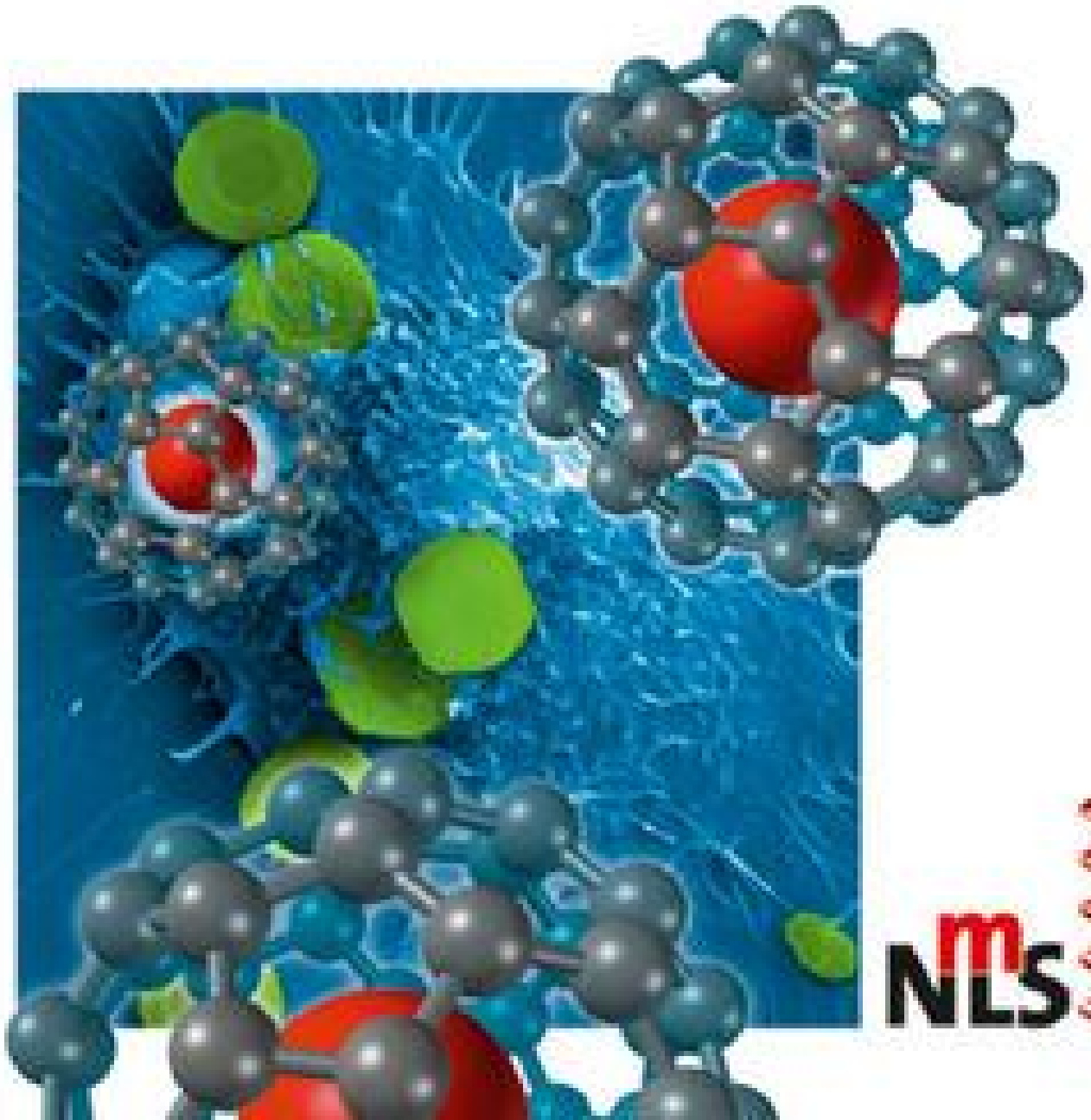

NLS

Contents

Preface *XIII*
List of Contributors *XVII*

1 Gold Nanoshells in Biomedical Applications *1*
Tim A. Erickson and James W. Tunnell
1.1 Introduction *1*
1.2 Physical Properties of Gold Nanoshells *2*
1.2.1 Overview of General Optical Properties *2*
1.2.2 The Physics of Gold Nanoshells *5*
1.2.2.1 The Dielectric Function of Gold *6*
1.2.2.2 The Quasi-Static Approximation and Conditions for Surface Plasmon Resonance *7*
1.2.2.3 Mie Theory *13*
1.2.2.4 Near-Field Enhancement *13*
1.2.2.5 Photoluminescence *14*
1.2.3 Photo-Thermal Material Characteristics *14*
1.3 Synthesis and Bioconjugation *16*
1.3.1 Synthesis *16*
1.3.2 Bioconjugation: Smarter Nanoshells *18*
1.4 Biodistribution, Toxicity Profile and Transport *19*
1.4.1 Biodistribution Studies *20*
1.4.2 Transport Mechanisms *22*
1.4.3 Toxicity *25*
1.5 Biomedical Applications *26*
1.5.1 *In Vitro* Cancer Detection and Imaging *26*
1.5.2 *In Vivo* Detection and Imaging *28*
1.5.3 Integrated Cancer Imaging and Therapy Agents *29*
1.5.4 *In Vitro* Studies *29*
1.5.5 *In Vivo* Photothermal Therapy *31*
1.5.6 Drug Delivery *34*
1.5.7 Tissue Welding *35*
1.5.8 Biosensors *35*
1.5.8.1 Absorbance-Based Biosensing *37*

Nanomaterials for the Life Sciences Vol. 3: Mixed Metal Nanomaterials. Edited by Challa S. S. R. Kumar

ISBN: 978-3-527-32153-7

1.5.8.2 SERS Biosensing *37*
1.6 Concluding Remarks *38*
References *39*

2 Anisotropic Bimetallic/Oxide Nanomaterials for The Life Sciences *45*
Jessica B. Graham, Megan E. Pearce and Aliasger K. Salem
2.1 Introduction *45*
2.2 Synthesis and Functionalization of Anisotropic Bimetallic Nanoparticles *45*
2.2.1 Nanorods *45*
2.2.2 Nanowires *47*
2.3 Applications in the Life Sciences *48*
2.3.1 Biosensing *48*
2.3.2 Imaging *49*
2.3.3 Gene Delivery *49*
2.3.4 Vaccine Applications *52*
2.4 Conclusions *54*
References *54*

3 Au—Pt Nanomaterials and Enzymatic Catalysts for Biofuel Cell Applications *57*
Aurélien Habrioux, Karine Servat, Boniface Kokoh and Nicolas Alonso-Vante
3.1 Introduction *57*
3.2 Oxygen Reduction Reaction (ORR) *58*
3.2.1 ORR Metal Catalysts *60*
3.2.2 ORR Enzymatic Catalysts *61*
3.2.2.1 Techniques Used for Enzyme Immobilization *61*
3.2.2.2 Enzymatic Reduction of Oxygen to Water *63*
3.3 Glucose Oxidation *70*
3.3.1 Process on Metal Electrodes *70*
3.3.1.1 Synthesis and Structural Properties of Gold–Platinum Nanoparticles *71*
3.3.1.2 Electrocatalytic Oxidation of D-(+)-Glucose on Gold–Platinum Catalysts *73*
3.3.2 Glucose Oxidation via Enzymes *77*
3.3.2.1 Glucose Oxidation Catalyzed by GDH *78*
3.3.2.2 Glucose Oxidation Catalyzed by GOx *79*
3.4 Application to Fuel Cell Systems *85*
3.4.1 Glucose/Oxygen Biofuel Cells *85*
3.4.2 Glucose/Oxygen Biofuel Cells with Au—Pt Nanoparticles as Anode Catalysts *90*
3.5 Summary and Outlook *91*
Acknowledgments *92*
Abbreviations *93*
References *93*

4 Spherical and Anisotropic Metallic Nanomaterials-Based NSET Biosensors *103*
Paresh Chandra Ray, Jelani Griffin, Wentong Lu, Oleg Tovmachenko, Anant K. Singh, Dulal Senapati and Gabriel A. Kolawole
4.1 Introduction *103*
4.1.1 Nanotechnology Promises on Biological Detection *105*
4.2 Size- and Shape-Dependent Super Quenching Properties of Nanomaterials *106*
4.3 Nanomaterial Surface Energy Transfer (NSET) *109*
4.3.1 Portable NSET Probes *111*
4.3.2 NSET Probe for DNA/RNA Hybridization Detection *112*
4.3.2.1 Size-Dependence Sensitivity *114*
4.3.3 Distance-Dependent NSET *115*
4.3.4 Multiplex DNA Detection *119*
4.3.5 NSET for Monitoring Mg^{2+}-Dependent RNA Folding *121*
4.3.6 NSET for DNA Cleavage Detection *125*
4.3.7 NSET for Cancer Cell Detection *128*
4.4 Gold Nanoshell-Based Biosensors *129*
4.5 Problems and Challenges *131*
4.6 Summary *131*
Acknowledgments *132*
References *132*

5 Mixed-Metal Oxide Nanomaterials for Environmental Remediation *139*
Dambar B. Hamal, Kennedy K. Kalebaila and Kenneth J. Klabunde
5.1 Introduction *139*
5.2 TiO_2 Heterogeneous Photocatalysis for Environmental Remediation *141*
5.2.1 Metal-Doped TiO_2 Mixed-Metal Oxides as UV-Light-Sensitive Photocatalysts *141*
5.2.2 Metal-Doped TiO_2 Mixed-metal Oxides as Visible-Light-Sensitive Photocatalysts *146*
5.3 Other Mixed-metal Oxide Photocatalysts *150*
5.4 Conclusions *156*
References *157*

6 Building Nonmagnetic Metal@Oxide and Bimetallic Nanostructures: Potential Applications in the Life Sciences *161*
Mao-Song Mo and Xu-Sheng Du
6.1 Introduction *161*
6.2 Building Nonmagnetic Metal@Oxide and Bimetallic Nanostructures *162*
6.2.1 Core-Shell Nanostructures and Building Strategy *162*
6.2.2 Metal@Oxide Core-Shell Nanostructures *163*
6.2.3 Bimetallic Nanostructures *164*
6.2.3.1 Bimetallic Core-Shell Nanostructures *164*

6.2.3.2 1-D Bimetallic Heteronanostructures *174*
6.2.3.3 Bimetallic Alloy Nanostructures *179*
6.2.4 3-D Mesoscale Bimetallic Patterning *185*
6.3 Current and Future Applications in the Life Sciences *188*
6.4 Summary and Outlook *191*
Acknowledgments *192*
References *192*

7 Biofunctionalization of Spherical and Anisotropic Bimetallic Nanomaterials *197*
Davide Prosperi, Laura Polito, Carlo Morasso and Diego Monti
7.1 Introduction *197*
7.2 Spherical Core-Shell Bimetallic Nanoparticles *198*
7.2.1 Ag_{Core}/Au_{shell} Nanoparticles *198*
7.2.2 Au_{Core}/Ag_{shell} Nanoparticles *201*
7.2.3 Silver Enhancement of Gold Nanoparticles *204*
7.2.4 DNA-Assisted Synthesis of Core-Shell Nanoparticles *205*
7.2.5 Biofunctionalization for the Construction of Core-Shell Bimetallic Nanostructures *206*
7.3 Anisotropically Shaped Nanoparticles: Nanorods and Nanowires *209*
7.3.1 Surface Modifications *210*
7.3.2 NW/NR Functionalization with Protein Molecules *212*
7.3.3 NW/NR Functionalization by DNA *218*
7.3.4 Detection and Sensing *220*
7.4 Profunctional Bimetallic Alloys *224*
7.4.1 Dendrimer-Encapsulated Bimetal Nanoparticles *225*
7.4.2 Surface Stabilization by Ligand Exchange *228*
7.4.3 DNA Metallization *228*
7.4.4 Miscellaneous *229*
7.5 Outlook *234*
References *234*

8 Multielemental Nanorods (Nanowires): Synthesis, Characterization and Analytical Applications *241*
Yang-Wei Lin, Zong-Hong Lin, Chih-Ching Huang and Huan-Tsung Chang
8.1 Introduction *241*
8.2 Synthetic Strategies *243*
8.2.1 Organic-Phase Synthesis *243*
8.2.1.1 Bimetallic NRs *243*
8.2.1.2 Semiconductor NRs *245*
8.2.2 Aqueous-Phase Synthesis *248*
8.2.2.1 Bimetallic NRs *248*
8.2.2.2 Multisegmented NRs *250*
8.2.2.3 Bimetallic/Trimetallic Oxide NRs *252*
8.2.2.4 Semiconductor NRs *254*

8.3 Properties *255*
8.3.1 Absorption *256*
8.3.2 Emission *258*
8.3.3 Surface-Enhanced Raman Scattering *260*
8.3.4 Catalytic Properties *262*
8.3.5 Magnetism *263*
8.4 Analytical Applications *264*
8.4.1 Detection of Gaseous Molecules *265*
8.4.2 Detection of Metal Ions *265*
8.4.3 Separation and Sensing of Proteins *267*
8.4.4 DNA Detection *269*
8.4.5 Detection of Pathogens and Bacteria *271*
8.5 Conclusions *271*
Abbreviations *272*
References *273*

9 Spherical and Anisotropic Nonmagnetic Core-Shell Nanomaterials: Synthesis and Characterization *281*
Tewodros Asefa, Abhishek Anan, Cole Duncan and Youwei Xie
9.1 Introduction: Core-Shell Nanomaterials and Their Biological/Medical Applications *281*
9.2 Nonmagnetic Core-Shell Nanomaterials *287*
9.3 Synthesis of Cores in Core-Shell Nanostructures *288*
9.3.1 Metal Cores *288*
9.3.2 Metal Oxide Cores *289*
9.3.3 Polymeric Cores *290*
9.3.4 Semiconductor Cores *290*
9.4 Deposition of Shells over the Core Nanomaterials *290*
9.5 Types of Core-Shell Nanomaterial *291*
9.5.1 Metal–Insulator Core-Shell Nanomaterials *291*
9.5.1.1 Metal-Dense Metal Oxide Core-Shell Nanomaterials *292*
9.5.1.2 Metal-Functionalized Metal Oxide Core-Shell Nanoparticles *294*
9.5.1.3 Metal–Porous Metal Oxide Core-Shell *294*
9.5.1.4 Metal–Polymer Core-Shell Nanoparticles *295*
9.5.1.5 Hollow Metal–Metal Oxide Shells by Controlled Core-Dissolution *298*
9.5.1.6 Metal Core–Dendrimer Core-Shell Nanoparticles *300*
9.5.1.7 Metal Core–Semiconducting Metal Oxide Shell Nanoparticles *300*
9.5.2 Insulator–Metal Core-Shell Nanomaterials *301*
9.5.2.1 Metal Oxide–Metal Core-Shell Nanostructures *301*
9.5.2.2 Polymer–Metal Core-Shell Nanostructures *301*
9.5.3 Insulator–Insulator Core-Shell Nanoparticles *302*
9.5.3.1 Polymer–Metal Oxide Core-Shell Nanomaterials *302*
9.5.3.2 Polymer–Polymer Core-Shell Nanomaterials *303*
9.5.3.3 Biomolecule (Protein) Core–Polymer Shell Core-Shell Nanoparticles *304*
9.5.3.4 Metal Oxide–Metal Oxide Core-Shell Nanomaterials *305*

9.5.3.5 Metal Oxide–Dye-Doped Silica and Dye-Doped Silica–Metal Oxide Core-Shell Nanostructures *305*
9.5.3.6 Metal Oxide–Polymer Core-Shell Nanoparticles *305*
9.5.3.7 Other Inorganic Materials Cores: Metal Oxide Shells *306*
9.5.4 Semiconductor–Insulator Core-Shell Nanomaterials *307*
9.5.5 Semiconductor–Semiconductor Core-Shell Nanomaterials *308*
9.5.6 Semiconductor–Semiconductor–Dendrimer Core-Shell-Shell Nanoparticles *308*
9.5.7 Insulator–Semiconductor Core-Shell Nanomaterials *309*
9.5.8 Metal–Metal Core-Shell *310*
9.5.9 Insulator–Metal Core-Shell Nanoparticles *313*
9.5.10 Carbon-Containing Core-Shell Nanomaterials *313*
9.5.10.1 Metal Oxide–Carbon Core-Shell Nanoparticles *313*
9.5.11 Other Carbon-Containing Core-Shell Nanomaterials *313*
9.5.12 Synthetic Methods to Create Core-Shell Nanomaterials, and their Characterizations *316*
9.6 Applications *317*
9.6.1 Applications in Biology and Medicine *317*
9.6.1.1 Bioimaging and Immunoassay *318*
9.6.1.2 Drug or Biomolecular Delivery Vehicles *319*
9.6.2 Core-Shell Nanomaterials for Catalysis *319*
9.7 Conclusions and Future Prospects *320*
Acknowledgments *321*
References *321*

10 Spherical and Anisotropic Silica Shell Nanomaterials *331*
Chih-Wei Lai, Jong-Kai Hsiao, Yu-Chun Chen and Pi-Tai Chou
10.1 Introduction *331*
10.2 Silica-Coated Metal Nanoparticles *332*
10.2.1 Noble Metal Nanoparticles: An Overview *332*
10.2.1.1 Sol–Gel method for Silica Coating *334*
10.2.2 Silica Shell for Biofunctionalization *338*
10.2.3 Application of Silica-Coated Metal Nanoparticles *338*
10.2.3.1 Silica Shell Modified with Oligonucleotides *338*
10.2.3.2 Surface-Enhanced Raman Scattering Effect *339*
10.2.3.3 Enhanced Luminescence Intensity *342*
10.2.4 Coating Silica Gold Nanorods *344*
10.2.5 Silica-Encapsulated Platinum *345*
10.3 Silica-Coated Quantum Dots *345*
10.3.1 The Advantages of Coating QDs with Silica *346*
10.3.2 Different Types of Silica-Coated QDs *347*
10.3.2.1 Hydrophobic QDs *347*
10.3.2.2 Hydrophilic QDs *349*
10.4 Silica-Encapsulated Magnetic Nanoparticles *351*
10.4.1 Silica-Coated Alloy Metal Nanoparticles *354*
10.4.2 Silica-Coated Magnetic Metal Oxide Nanoparticles *356*

10.4.3 Applications of Silica-Coated Magnetic Nanoparticles *359*
10.4.3.1 Forming Hybrid Materials with Optic Materials Dopant *359*
10.5 Hollow Silica Spherical Structures *363*
10.5.1 Au and Pt Nanoparticles in Hollow Spheres *363*
10.6 Conclusions *367*
References *368*

11 Spherical and Anisotropic Core-Shell and Alloy Nanomaterials: Characterization Using X-Ray Absorption Spectroscopy *377*
Loka Subramanyam Sarma, Hung-Lung Chou, Ming-Yao Cheng, Fadlilatul Taufany, Feng-Ju Lai, Meng-Che Tsai, Shih-Hong Chang and Bing-Joe Hwang
11.1 Introduction *377*
11.2 Nanoparticle Systems for Biomedical Applications *381*
11.2.1 Bioimaging (Magnetic Resonance Imaging) *381*
11.2.2 Drug Delivery *382*
11.3 Characterization of Spherical and Anisotropic Core-Shell and Alloy Nanomaterials using X-Ray Absorption Spectroscopy (XAS) *383*
11.3.1 XAS Fundamentals *384*
11.3.2 XAS Data Collection and Analysis *386*
11.3.3 Structural Characterization: XAS Methodologies *387*
11.3.3.1 Particle Size, Shape and Aspect Ratio of Nanoparticles *387*
11.3.3.2 Alloy Versus Core-Shell Structure, Atomic Distribution and Degree of Alloying of Nanomaterials: An XAS Methodology *389*
11.3.3.3 Surface and Core Composition in Bimetallic Nanoparticles: An XAS Methodology *391*
11.3.4 Review of XAS Characterization Methodologies for Nanomaterials *392*
11.3.5 XAS Characterization of Surface Interactions *399*
11.4 Conclusions *400*
Acknowledgments *401*
References *401*

12 Anisotropic Hexagonal Boron Nitride Nanomaterials: Synthesis and Applications *411*
Wei-Qiang Han
12.1 Introduction *411*
12.2 Synthesis of BN Nanotubes *412*
12.2.1 Introduction *412*
12.2.2 Arc Discharge *413*
12.2.3 Laser Ablation *416*
12.2.4 Carbon Nanotubes-Substitution Reaction *420*
12.2.5 Chemical Vapor Deposition *426*
12.2.6 Solid–Gas Reaction *429*
12.2.7 Low-Temperature Autoclaving *430*
12.2.8 Pore-Template *430*
12.2.9 Arc-Jet Plasma *432*

12.3 BNNT-Based Nano-Objects *433*
12.3.1 Filled BNNTs *433*
12.3.2 Functionalized BNNTs *436*
12.4 Porous BN and BN Mesh *439*
12.4.1 Direct Pyrolyzing Borazinic Precursors *439*
12.4.2 Use of Mesoporous Molds *440*
12.4.3 Carbon Template-Substitution Reaction *441*
12.5 BN Mono- or Few-Layer Sheets *443*
12.6 Physical Properties of h-BN *446*
12.7 Applications *447*
12.7.1 Pharmaceutical Table Lubricant *447*
12.7.2 Cosmetic Materials *448*
12.7.3 ^{10}BNNTs for Cancer Therapy and Diagnostics *449*
12.7.4 BNNT Composites *449*
12.7.5 Gas Adsorption *450*
12.7.6 Electrical Nanoinsulators *452*
12.7.7 Ultraviolet Lasers and LEDs *452*
12.7.8 BN as Support for Catalysts *452*
12.8 Concluding Remarks *453*
Acknowledgments *453*
References *453*

13 Spherical and Anisotropic Boron Nitride Nanomaterials: Synthesis and Characterization *463*
Chengchun Tang and Yangxian Li
13.1 Introduction *463*
13.2 BN Nanomaterials Synthesis *464*
13.2.1 Spherical BN Particles *464*
13.2.2 Anisotropic BN Nanostructures *470*
13.2.2.1 Multiwalled Nanotubes *470*
13.2.2.2 Single-Walled Nanotubes *476*
13.2.2.3 Collapsed BN Nanotubes *478*
13.2.2.4 Nanowires *480*
13.3 Remarks on Properties and Applications *483*
13.3.1 High-Temperature Chemical Inertness *484*
13.3.2 Electrical Properties *484*
13.3.3 High Thermal Conductivity *485*
13.3.4 Mechanical Properties *486*
13.3.5 Hydrogen Storage *487*
13.3.6 Life Sciences *487*
13.4 Concluding Remarks *489*
Acknowledgments *491*
References *491*

Index *499*

1
Gold Nanoshells in Biomedical Applications

Tim A. Erickson and James W. Tunnell

1.1
Introduction

Gold nanoshells are spherical particles with diameters typically ranging in size from 10 to 200 nm (Figure 1.1). They are composed of a dielectric core covered by a thin gold shell. As novel nanostructures, they possess a remarkable set of optical, chemical and physical properties, which make them ideal candidates for enhancing cancer detection, cancer treatment, cellular imaging and medical biosensing.

Gold nanoshells are unique in that they combine many ideal features in a single particle. As a direct result of nanoscale resonance phenomena, gold nanoshells have very large optical absorption and scattering cross-sections, which render them highly suitable as contrast agents for imaging. They can be tuned to preferentially absorb or scatter light at specific wavelengths in the visible and near-infrared (NIR) regions of the spectrum. In the NIR 'tissue window', light penetration into tissue is optimal. Nanoshells tuned to absorb NIR radiation are particularly useful as mediators of photothermal cancer therapy because they efficiently convert absorbed radiation into heat, and are thermally stable at therapeutic temperatures. Furthermore, nanoshells preferentially accumulate at tumor sites due to their nanoscale dimensions. The inert gold surface of nanoshells provides several advantages, including biocompatibility, noncytotoxicity, and it also facilitates conjugation to monoclonal antibodies or other biomolecules for both active tumor targeting and biosensing applications.

The first Stage I clinical trials using nanoshells as therapeutic agents to treat head and neck cancers are set to commence in 2008 [2]. Over the past few years, the pace of research in this field has accelerated rapidly, as have the number of potential biomedical applications for nanoshells. It has been the present authors' best attempt to keep abreast of new developments in the field but, given the pace of progress, this chapter will be partially outdated by the time it hits the press – which is good news! The chapter is designed with two distinct audiences in mind: researchers already in the field who may use it as a quick reference; and 'early-stage' researchers, who can use it as a first read to gain a broader understanding

Nanomaterials for the Life Sciences Vol. 3: Mixed Metal Nanomaterials. Edited by Challa S. S. R. Kumar

ISBN: 978-3-527-32153-7

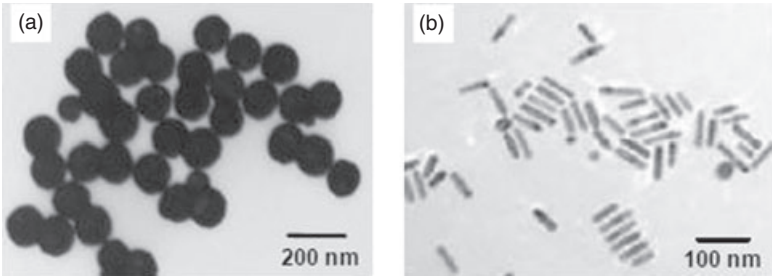

Figure 1.1 Transmission electron microscopy images of (a) gold nanoshells and their gold nanoparticle counterparts (b) gold nanorods. The size distribution typically has a standard deviation from the mean of 10–20% [1].

of the field. It is organized in the following manner. The first section highlights the unique optical and material properties of nanoshells and explores the physics underlying the associated phenomena. The second section we describe the synthesis of nanoshells. The third section describes the transport, biodistribution and benign toxicity profile of nanoshells *in vivo*, while the fourth section concludes with an extensive discussion on the various biomedical applications of nanoshells. Although the focus of the chapter is on gold nanoshells, their nanoparticle counterparts – gold nanorods, gold nanospheres and quantum dots – will also be discussed, in order to provide relevant comparisons and contrasts.

1.2 Physical Properties of Gold Nanoshells

1.2.1 Overview of General Optical Properties

Before delving into a comprehensive analysis of the physics behind nanoshells, it is worthwhile to highlight their novel optical properties. Nanoshells function as useful and versatile imaging agents because of their large extinction cross-sections, immunity to photobleaching, spectral tunability, absorption/scattering ratio tunability, electromagnetic near-field enhancement, and enhanced luminescence. These optical phenomena are in large part due to a resonance phenomenon, known as surface plasmon resonance, which is discussed in the next subsection.

The optical cross-sections and luminescent properties of gold nanoshells compare favorably with those of conventional fluorophores and quantum dots. Wu *et al*. found the absorption of a single 20 nm-diameter nanoshell to correspond to the absorption of 40 000 molecules of indocyanine green, a dye used as a photosensitizer in photodynamic therapy [3]. For nanoshells with a diameter of 130 nm, the optical extinction cross-section ($3.8 \times 10^{-14}\,m^2$) is more than one million times greater than the cross-section of an indocyanine green molecule ($1.66 \times 10^{-20}\,m^2$)

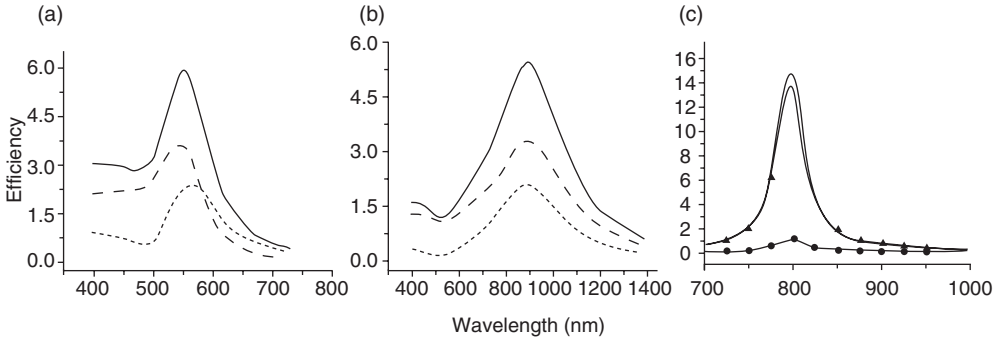

Figure 1.2 Calculated extinction (top curve), absorption (middle curve) and scattering (bottom curve) efficiencies for: (a) a 80 nm-diameter gold nanosphere; (b) a 70 nm-radius gold nanoshell with a 60 nm silica core; and (c) a 59.6 × 15.3 nm gold nanorod [6].

[4], and almost twice as great as the cross-section of a CdSe quantum dot ($1.5 \times 10^{14}\,m^2$) with the same radius [5]. The dimensionless extinction coefficient Q_{ext} of a gold nanoshells typically ranges from ~3 to 7, depending on nanoshell geometry, which is comparable to gold nanospheres, but less than half the *maximum* extinction coefficient of gold nanorods (~12–21) (Figure 1.2). In photoluminescence studies, Park *et al.* found both 120 nm gold nanoshells and 50 nm (long axis) gold nanorods to be 140 times brighter than 100 nm fluoresceinated polystyrene beads, which are commonly used in biological imaging applications [1]. This is similar to the results obtained by Wang *et al.*, who found the two-photon induced luminescence from a single gold nanorod to be almost 60-fold brighter than a single rhodamine 6G molecule [7].

An additional advantage of nanoshells and other gold nanoparticles is their photostability. In photoluminescence studies, they have not been found to photobleach [8]; conventional fluorophores are highly susceptible to photobleaching [9, 10]. Quantum dots, while being generally more resistant to photobleaching [11], suffer from intrinsic, intermittent emission or 'blinking' [12], which complicates sensitive imaging techniques.

Perhaps the most novel characteristic of gold nanoshells is their tunability. The position of the extinction (plasmon resonance) peak and the relative contributions of absorption and scattering to total extinction can be selected by configuring two parameters: the radii of the inner core (r_1); and the outer shell (r_2) (see Figure 1.7). For a given r_2, the position of the extinction peak is determined by the core to shell ratio (r_1/r_2) [13]. For greater core to shell ratios (thinner gold shells), the peak becomes shifted to longer wavelengths. For gold nanoshells, the position of the resonant extinction peak can be selectively tuned from 600 nm to greater than 1000 nm (Figure 1.3). This wavelength range is especially significant because it includes the 'NIR tissue window' from 700 to 900 nm, where tissue is most transparent to light. In the NIR region, effective (1/e) penetration depths vary from a

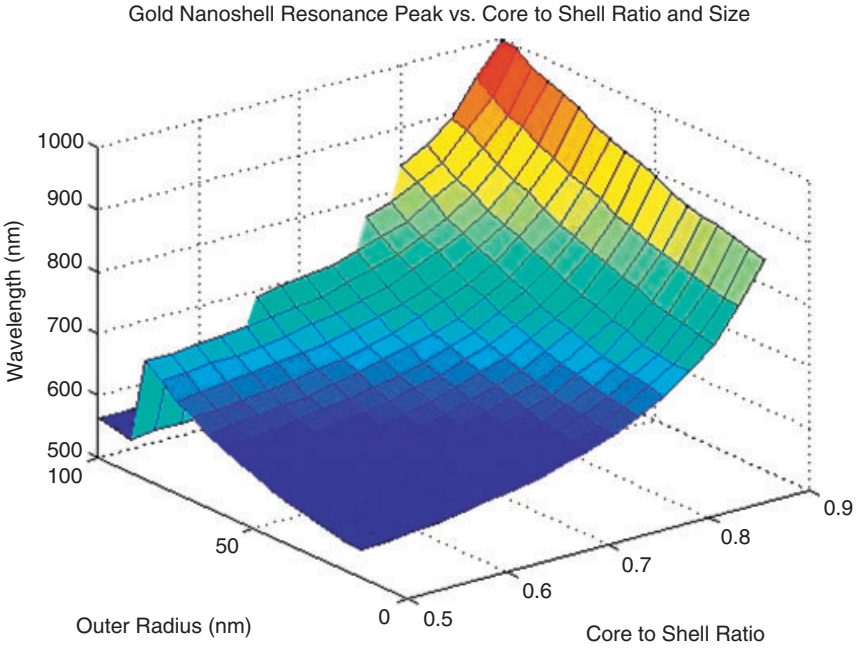

Figure 1.3 Gold nanoshell resonance peak versus core to shell ratio and size. Mie theory calculations of the plasmon resonance peak position as a function of nanoshell geometry from 500 to 1000 nm. Two trends are apparent. For a given nanoparticle size, the resonance peak can be selected by changing the core-to-shell ratio. Larger particles correspond to longer resonance peak wavelengths. The sharp drop-off for large nanoshells with smaller core-to-shell ratios is explained in Section 1.1.2.3.

few millimeters to several centimeters, depending on tissue type [14, 15]. The ability of nanoshells to be tuned to the NIR is central to their functionality for *in vivo* applications. Gold nanorods also exhibit spectral tunability across a broad range of wavelengths, including the NIR [6]; however, gold nanospheres may have limited use for certain applications because their resonance peak lies outside the NIR window at ~520 nm and their spectral tunability is very limited.

In addition to spectral tunability, the absorption to scattering ratio of nanoshells can also be tuned by changing the nanoshell's outer radius (r_2). For smaller nanoshells, absorption dominates scattering, whereas for larger nanoshells scattering dominates absorption. In between the two extremes, the contributions of absorption and scattering to total extinction can be made approximately equal (Figure 1.4). It is therefore possible to design nanoshells for dual imaging and photothermal therapy applications, where high scattering efficiencies facilitate scatter-based imaging and high absorption efficiencies facilitate photothermal therapy. By appropriately choosing the dimensions of r_1 and r_2, the position of the extinction peak and the relative amounts of absorption and scattering can be selected across a wide range of wavelengths, as demonstrated in Figures 1.3 and 1.4. This is a truly remarkable optical property, given that untold numbers of

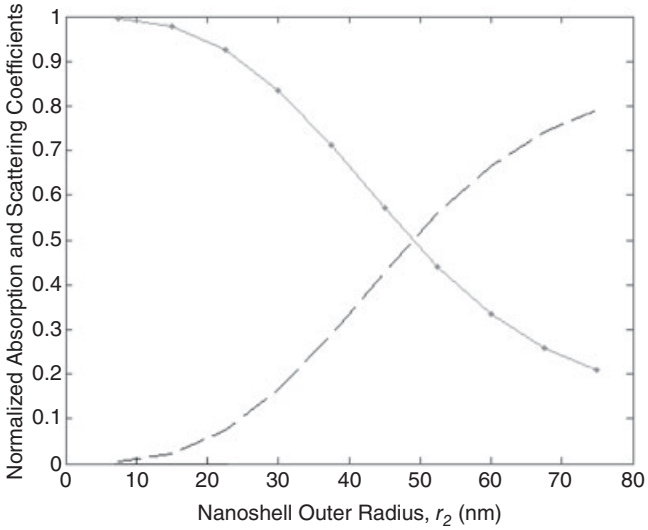

Figure 1.4 Absorption (solid line) and scattering (dashed line) coefficients calculated using Mie theory for a nanoshell with a fixed core-to-shell ratio of 0.8. For a nanoshell with an outer radius of 50 nm, the absorption and scattering efficiencies are almost equal. The normalized efficiencies were calculated by integrating the efficiencies between 500–1000 nm, and are thus indicative of the response to a broadband source.

conventional organic dyes would be required to cover the same spectral domain as geometrically tuned gold nanoshells.

Gold nanoshells and nanospheres exhibit another unique property, which is distinct from anything seen in conventional fluorophores. Metallic nanoparticles act as nanolenses, which efficiently focus incident electromagnetic radiation into the near-field region close to their surfaces with subwavelength precision [16, 17]. Jackson *et al.* have predicted near-field enhancements ($E_{enhancement} = E_{local}/E_{incident}$) of ~25 for silver nanoshells [18], while Averitt *et al.* have predicted local field enhancements of ~3 for gold nanoshells with outer radii of 12–15 nm [13]. Chien *et al.* have calculated enhancements of ~450 for assemblies of gold nanospheres (Figure 1.5), which can be thought of rows of nanolenses. Since the intensity scales as the electric field squared, these near-field enhancements produce intensity enhancements of many orders of magnitude. For the nanosphere assembly, the localized surface intensity would increase by a factor of over 200 000. Such enhancements have important applications in single molecule detection (see Section 1.5) [18].

1.2.2
The Physics of Gold Nanoshells

Nanoshells exhibit unique optical properties because their interaction with the electromagnetic field is greatly intensified by a phenomenon known as localized

Figure 1.5 Gold nanosphere assemblies used in theoretical calculations by Chien *et al.* The length of each chain is fixed to equal 167.5 nm [16].

surface plasmon resonance (LSPR). This resonance effect arises from the collective oscillation of the conduction electrons in the gold shell, which efficiently couple to the incident electromagnetic field, and propagate along the surface [13, 19]. The quanta of these surface charge density oscillations is referred to as a surface plasmon polariton.

The LSPR of gold nanoshells at visible and NIR wavelengths is a physical possibility because of two key factors: (i) the dielectric function of gold at optical wavelengths; and (ii) their nanoscale dimensions. Several distinct phenomena must be 'connected' in order to provide a theoretical framework for understanding the interaction between gold nanoshells and optical electromagnetic fields. First, the dielectric function of gold at optical wavelengths will be introduced, after which the dielectric function of gold will be related to the resonant interaction of gold nanoshells with optical electromagnetic fields. The absorption and scattering properties of nanoshells will then be elucidated by using the quasi-static approximation. Lastly, Mie theory [20] and plasmon hybridization [21] will be introduced as rigorous analytical methods for calculating and understanding their optical phenomena.

1.2.2.1 **The Dielectric Function of Gold**

The most recent experimental data for the dielectric function of gold comes from measurements published by Johnson and Christy in 1972 [22]. Unfortunately, there are significant gaps in the data at visible/NIR wavelengths. However, theoretical models have been formulated to fit the data and provide good estimates across the visible and NIR spectra (Figure 1.6). The optimized Drude–Lorentz model of gold's dispersion described by Vial *et al.* provides an analytical fit to the data at optical frequencies [23]. It modifies the standard Drude dielectric approximation, by adding a single frequency-dependent Drude–Lorentz oscillator term (L), in order to account for interband transitions of bound electrons, which are excited by wavelengths shorter than ~550 nm. Mathematically, the Drude–Lorentz dielectric function is given by

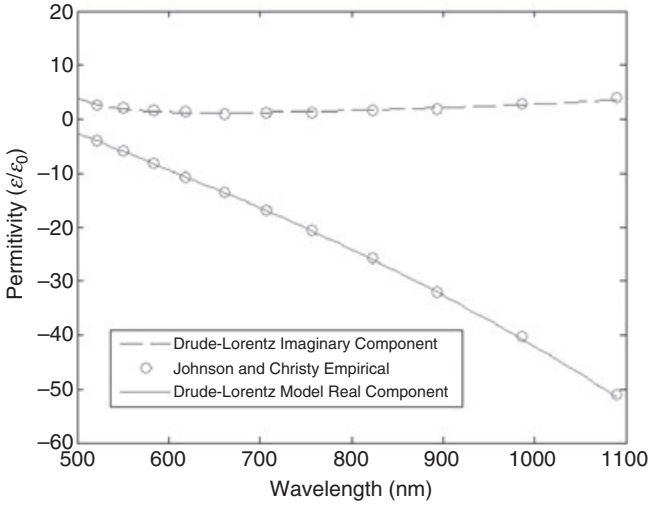

Figure 1.6 Complex dielectric function of gold consisting of both real and imaginary components. There is good agreement between the Johnson and Christy data points and the Drude–Lorentz model.

$$\varepsilon_{Drude-Lorentz}(\omega) = 1 - \frac{\omega_p^2}{\omega^2 + i\Gamma\omega} + L(\omega)$$

where ω_p is the volume plasma frequency of bulk gold, ω is the angular frequency of the electromagnetic field, and Γ is the damping coefficient or bulk collision frequency. The performance of the model in predicting the complex dielectric function of gold is depicted in Figure 1.6. The complex dielectric function of gold has a large, negative real component accounting for the reflectivity of bulk gold, and a smaller, positive imaginary component, which is associated with absorption. In the following section, we will show how gold's dielectric function is related to LSPR in gold nanoshells.

1.2.2.2 The Quasi-Static Approximation and Conditions for Surface Plasmon Resonance

In the following analysis, the nanoshell is modeled as shown in Figure 1.7, with inner radius r_1, outer radius r_2 and dielectric constants ε_1 (silica core = 2.13), ε_3 (surrounding aqueous medium = 1.78), and *dielectric function*, $\varepsilon_2(\omega)$, for the gold shell.

The quasi-static (dipole) approximation is a first-order approach, which describes the interaction between a gold nanoshell and electromagnetic radiation at optical frequencies [13]. In the quasi-static approximation, the incident electric field, $\boldsymbol{E(r,t)}$, is assumed not to vary spatially over the dimensions of the nanoshell, while maintaining its time-dependence so that $\boldsymbol{E(r,t)} = \boldsymbol{E}_o e^{-i\omega t}$. The quasi-static

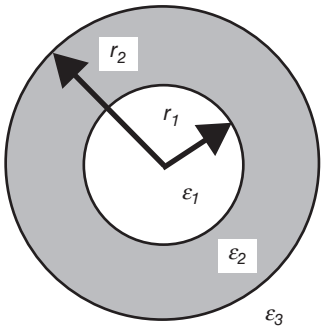

Figure 1.7 Schematic of gold nanoshell with indicated radii and three dielectric functions corresponding to the core, shell and ambient medium.

approximation is valid in the limit where the wavelength of incident light λ is much greater than the diameter d of the nanoshell ($\lambda >> d$). This is particularly accurate for nanoshells with radii of less than 40 nm [13]. Despite lacking rigor, the quasi-static approximation has several inherent advantages. As will be shown, it dramatically simplifies the mathematical analysis describing the nanoshell's interaction with the electric field and, more importantly, it provides a valuable physical interpretation of LSPR in gold nanoshells.

The solution for the electric field in the regions corresponding to the core (ε_1), shell (ε_2) and ambient medium (ε_3) is determined by solving Laplace's equation for the potential V in each region, then taking the gradient to determine the electric field $\boldsymbol{E}_i$ in each of the three regions, and finally adding the time-dependence ($e^{-i\omega t}$) [13]. The general solution for the potential in each region ($i = 1, 2, 3$) is

$$V_i = \left[A_i r + \left(B_i / r^2\right)\right]\cos(\theta)$$

with radius r, polar angle θ and coefficients A_i and B_i, which are determined by satisfying boundary conditions for continuity of the tangential component of the electric field and continuity of the normal component of the displacement field. After solving for V_i, the electric fields ($E_i = -\nabla V_i$) are calculated to be:

$$\boldsymbol{E}_1 = \frac{9\varepsilon_2\varepsilon_3}{\varepsilon_2\varepsilon_a + 2\varepsilon_3\varepsilon_b} E_o\left(\cos\theta\hat{r} - \sin\theta\hat{\theta}\right)$$

$$\boldsymbol{E}_2 = \frac{3\varepsilon_3}{\varepsilon_2\varepsilon_a + 2\varepsilon_3\varepsilon_b}\left[(\varepsilon_1 + 2\varepsilon_2) + 2(\varepsilon_1 - \varepsilon_2)\times(r_1/r)^3\right]E_o\cos\theta\hat{r} - \left[(\varepsilon_1 + 2\varepsilon_2) - (\varepsilon_1 - \varepsilon_2)(r_1/r)^3\right]E_o\sin\theta\hat{\theta}$$

$$\boldsymbol{E}_3 = \left(2\frac{\varepsilon_2\varepsilon_a - \varepsilon_3\varepsilon_b}{\varepsilon_2\varepsilon_a + 2\varepsilon_3\varepsilon_b}\frac{r_2^3}{r^3} + 1\right)E_o\cos(\theta)\hat{r} + \left(2\frac{\varepsilon_2\varepsilon_a - \varepsilon_3\varepsilon_b}{\varepsilon_2\varepsilon_a + 2\varepsilon_3\varepsilon_b}\frac{r_2^3}{r^3} - 1\right)E_o\sin(\theta)\hat{\theta}$$

where

$$\varepsilon_a = \varepsilon_1(3-2P) + 2\varepsilon_2 P$$

$$\varepsilon_b = \varepsilon_1 P + \varepsilon_2(3-P)$$

$$P = 1-(r_1/r_2)^3.$$

The induced field in the region outside the shell is the same as that of a *dipole* ($\boldsymbol{p} = \varepsilon_3\ \alpha\ \boldsymbol{E}_{\text{induced}}$) located at the center of the shell with polarizability,

$$\alpha(\omega) = 4\pi\varepsilon_o r_2^3 \left| \frac{\varepsilon_2\varepsilon_a - \varepsilon_3\varepsilon_b}{\varepsilon_2\varepsilon_a + 2\varepsilon_3\varepsilon_b} \right|, \text{ where } \varepsilon_o = 8.85\times10^{-12}\,\text{Fm}^{-1}.$$

When the temporal oscillation of the electric field is taken into account, we arrive at a classical physical interpretation of surface plasmon resonance in a nanoshell. In the quasi-static limit, the dominant behavior of a gold nanoshell in an electric field at optical frequencies is that of an oscillating dipole. In this classical picture, resonance occurs when the polarizability α is maximized, or when the denominator in the above equation goes to zero. The condition for resonance is thus:

$$\varepsilon_2\varepsilon_a + 2\varepsilon_3\varepsilon_b = 0$$

In this simplified analysis, the polarizability goes to infinity when the resonance condition is satisfied because damping effects due to reaction radiation have been neglected [19]. When effects from reaction radiation are incorporated the effective polarizability becomes

$$\alpha_{effective}(\omega) = \frac{\alpha(\omega)}{1 - i\dfrac{k^3}{6\pi\varepsilon_o}\alpha(\omega)}$$

It is instructive to observe how the resonance condition can be met for a generic nanoshell with a silica core and unknown shell dielectric function (ε_2). Figure 1.8 is a plot of $\varepsilon_2\varepsilon_a + 2\varepsilon_3\varepsilon_b$ versus the shell dielectric function (ε_2) for a $r_1 = 60\,\text{nm}$, $r_2 = 75\,\text{nm}$ nanoshell. As shown in Figure 1.8, this condition can only be satisfied if the dielectric function of the nanoshell has a negative real component at optical frequencies (as a material with a dielectric function of zero is not physically realizable). From Figure 1.6, it is apparent that gold satisfies this condition – which explains why gold nanoshells exhibit LSPR at optical frequencies. Notably, these conditions also hold for other metal nanoparticles at different frequencies, such as silver and copper nanospheres, which have been synthesized [24]. The behavior of gold nanoshells cannot be reproduced for macroscopic gold shells at longer wavelengths by simply invoking the scale-invariance of Maxwell's equations. This is because of the frequency-dependence of gold's dielectric function [19].

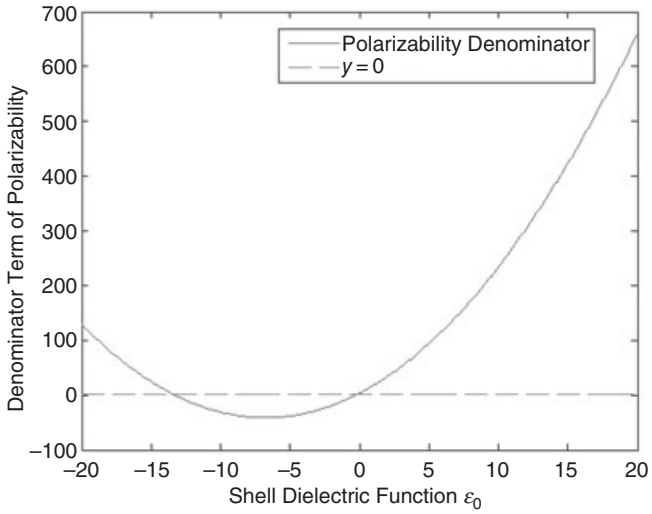

Figure 1.8 Resonance occurs for two dielectric function values. Only the negative value is physically realizable.

The value of the dipole approximation resides in its ability to produce good estimates for the absorption and scattering properties of nanoshells, including the position of the resonant extinction peak. From Mie scattering theory, the absorption σ_{abs} and scattering σ_{sca} cross-sections are given by [25]:

$$\sigma_{abs} = \frac{2\pi}{\lambda\varepsilon_o}\mathrm{Im}(\alpha) \quad \text{and} \quad \sigma_{sca} = \frac{8\pi^3}{3\varepsilon_o^2\lambda^4}|\alpha|^2,$$

so the absorption and scattering cross-sections are both functions of ω and λ. It is thus possible to plot the extinction cross-section $\sigma_{ext} = \sigma_{abs} + \sigma_{sca}$ to determine the position of the plasmon resonance peak (Figure 1.9).

Although the quasi-static approximation provides a relatively good estimate for the position of the resonant extinction peak, it drastically underestimates the plasmon linewidth of the observed extinction peak. Whereas, the full-width, half-maximum of the observed peak is ~300 nm, the linewidth of the approximated peak is less than 100 nm, giving an artificially sharp resonance. The broadness of the plasmon linewidth comes from three major sources [26]: (i) unavoidable polydispersivity; (ii) deviations between the *true* dielectric function of the gold shell and the bulk dielectric function of gold; and (iii) contributions from quadrapole and higher-order multipole resonances. It will be shown here how the first two can easily be incorporated into the quasi-static approximation.

Due to the nature of their synthesis in solution, nanoshells are not perfectly uniform spheres; rather, they generally exhibit size distributions of ±5–20% (standard deviation) [13, 17, 26–28]. As a result, the resonance peak becomes a weighted average of the contributions from the resonance peaks' individual nanoshells. The

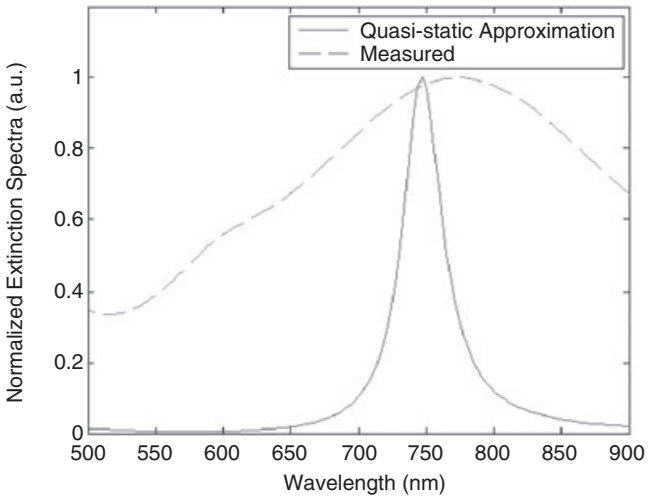

Figure 1.9 Comparison between the quasi-static approximated and measured resonant extinction peaks for gold nanoshells with nominal core radius of 58 nm and shell radius of 75 nm. The extinction peak was measured from nanoshells in deionized water with a Beckman Coulter DU 720 spectrophotometer.

second broadening mechanism arises from the nature of the dielectric function of the gold shell. The mean free electron scattering path in gold is ~42 nm, which is typically greater than the thickness of the thin shell, so the bulk gold dielectric function must be modified to account for electron scattering at the gold interface. Electron scattering reduces electron phase coherence, leading to broadening [13]. The effect of electron scattering is accounted for in the dielectric function by using the modified bulk collision frequency

$$\Gamma_{gold\ shell} = \Gamma_{bulk} + A\nu_f / a$$

with Fermi velocity $\nu_f = 1.4 \times 10^6\ \mathrm{m\,s^{-1}}$, shell thickness a and geometric parameter A, which is generally between 1–5 for nanoshells, depending on their exact dimensions. When these corrections are implemented into the approximation, there is a much better agreement (Figure 1.10). The electron-scattering correction also explains the origin of the absorption/scattering ratio tunability. As shown in Figure 1.11, the increased energy dissipation (absorption) in a small nanoshell is accounted for classically by an increase in the imaginary component of the shell's dielectric function.

In order to account for the third source of error, which exists because the electric field varies over the spatial extent of the nanoshell, the quasi-static approximation must be abandoned in favor of more rigorous analytical approaches.

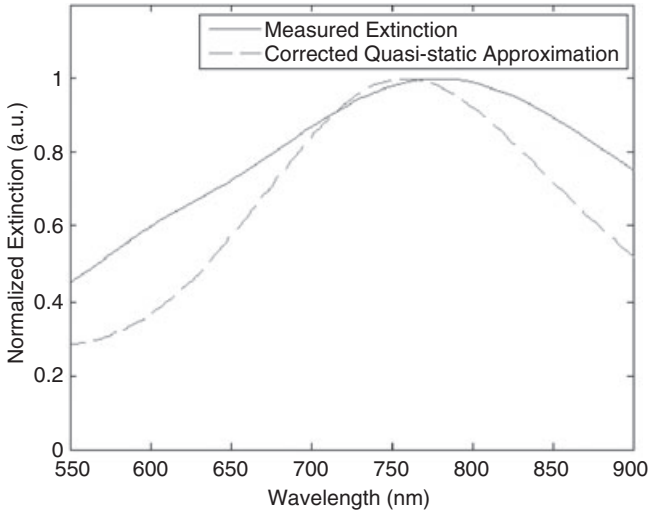

Figure 1.10 By implementing corrections for electron scattering and polydispersivity (normal distribution with standard deviation of ±15%), there is much better agreement between the approximation and experimental extinction spectra for nanoshells with inner radius of 58 nm and outer radius of 75 nm.

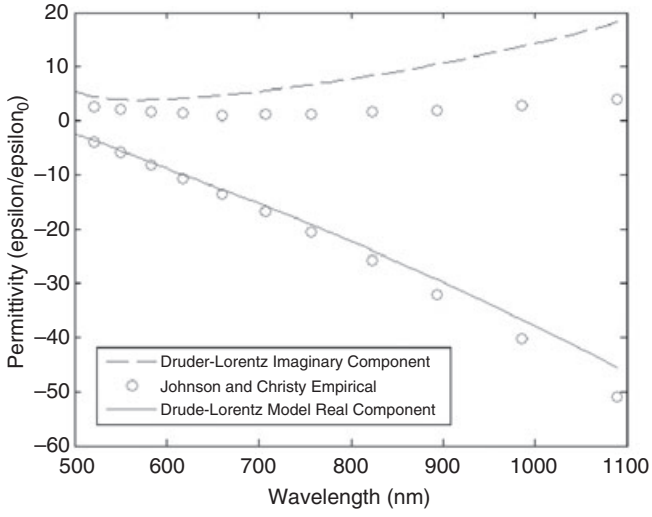

Figure 1.11 Corrected dielectric function for a small gold nanoshell with an inner radius of 20 nm and outer radius 25 nm. For thin nanoshells, the imaginary component of the dielectric function increases significantly, leading to greater absorption.

1.2.2.3 Mie Theory

Mie scattering theory [29, 30] provides complete analytical solutions of Maxwell's equations for the scattering of electromagnetic radiation by particles with spherical or cylindrical symmetry. A full treatment of scattering from concentric spherical shells was published by Aden and Kerker in 1951 [30]. In Mie theory, the harmonically oscillating electromagnetic fields are expressed in terms of a set of spherical vector basis functions, so that each term in the expansion represents one of the resonances. The first term in the expansion is the dipole term, as represented by the quasi-static approximation. Mie theory is a versatile technique for determining the optical properties of nanoshells or any other spherical particles of any dimension. Mie codes for Matlab and other mathematical software are available online. Christian Matzler's code (available online at: http://www.iwt-bremen.de/vt/laser/wriedt/Mie_Type_Codes/body_mie_type_codes.html) is particularly easy to use as it calculates scattering, absorption and phase functions for solid spheres and spherical shells. In general, Mie theory does an excellent job of predicting the far-field optical properties of gold nanoshells [27].

1.2.2.3.1 **The Plasmon Resonance Hybridization Picture** Although the plasmon resonance tunability of nanoshells is predicted from Mie theory calculations (see Figure 1.3), Mie theory does not intuitively explain why the position of the plasmon resonance peak can be selected by adjusting the core/shell ratio. In order to account for the nanoscopic origin of their tunability, the plasmon hybridization picture must be invoked [21]. It must be noted that the analysis is restricted to the dipole limit, as defined previously. A more rigorous hybridization analysis, which takes higher-order multipoles into account has not been published. In the hybridization picture, the geometry-dependent nature of plasmon resonance in a nanoshell results from the interaction of individual sphere and cavity plasmons. The strength of interaction depends on the thickness of the gold shell, and hence the core/shell ratio. The frequencies of the bonding (ω_-) and anti-bonding (ω_+) plasmon modes decomposed as spherical harmonics of order l are given by

$$\omega_{l\pm}^2 = \frac{\omega_B^2}{2}\left[1 \pm \frac{1}{2l+1}\sqrt{1+4l(l+1)\left(\frac{r_1}{r_2}\right)^{2l+1}}\right]$$

where ω_B is the bulk plasmon frequency. For bonding plasmon modes, an increased core/shell ratio produces lower-frequency plasmon modes, corresponding to plasmon resonance at longer wavelengths, which is consistent with Mie theory calculations.

1.2.2.4 Near-Field Enhancement

Near-field enhancement occurs because large amounts of charge temporarily build up on the surface of a gold nanoshell exposed to light at resonant wavelengths. A physically intuitive way to understand the phenomenon of local near-field enhancement is to imagine a plane wave incident upon a nanoshell [31]. Because of the nanoshell's high extinction cross-section, light from a large swath of area interacts

with the nanoshell. As predicted by the quasi-static approximation, the electric field surrounding the nanoshell then appears as an enhanced or 'concentrated' dipole field, which oscillates at the driving frequency of the incident electromagnetic field. In this framework, the nanoshell can also be viewed as a nano-antenna [17].

1.2.2.5 **Photoluminescence**

The enhanced photoluminescent properties of gold nanoshells and gold nanorods are mediated by LSPR [32]. Quantum mechanically, luminescence arises from radiative recombination of electron-hole pairs at selected symmetry points in the Brillouin zone [33]. Visible photoluminescence results from radiative recombination of electron-hole pairs formed by *interband* transitions in which electrons are excited from the d-band to the sp-conduction band. On the other hand, NIR luminescence results from the radiative recombination of electron-hole pairs formed by lower-energy *intraband* transitions within conduction states below the Fermi surface [32]. Whereas, Mooradian [34] reported luminescence from smooth gold films with small quantum efficiencies of ~10^{-10}, quantum efficiencies over a million times greater (10^{-3}–10^{-4}) have been observed in gold nanorods [35], and similar increases have been observed in gold nanoshells [1].

This enhanced luminescence results from localized surface plasmons [32, 33]. Surface plasmons produce transient, high charge densities near the surface of gold nanoshells and nanorods, leading to localized strong electric fields and, in turn, strong field gradients. The presence of strong field gradients enables transitions which would, ordinarily, be dipole-forbidden. Additionally, such fields have large associated wavenumbers, which carry enough momentum to allow direct intraband transitions within the conduction band. Localized surface plasmons enable the energy from these transitions to radiatively decay into the far field [32].

1.2.3
Photo-Thermal Material Characteristics

The highly efficient coupling of nanoshells to incident electromagnetic energy at surface plasmon frequencies leads to intense absorption and, in turn, heating of the nanoshells. Clarke *et al*. have monitored the thermal profile of individual nanoshells embedded in a dried lipid layer placed in an aqueous medium [36]. Under NIR excitation, the nanoshells triggered a lipid phase transition (24 °C), which induced local liposome budding. In general, nanoshells exhibit excellent thermal stability, in that their structure remains intact when exposed to light intensities required for applications in imaging and photothermal therapy. However, nanoshells are susceptible to photo-thermal damage (deformation and destruction) when exposed to very high incident intensities (fluence rates). A review of the literature reveals wide variations in the measured damage thresholds dependent on experimental conditions.

Park *et al*. investigated the damage threshold of gold nanoshells (800 nm resonance) in the context of two photon imaging studies [1]. Nanoshells in solution

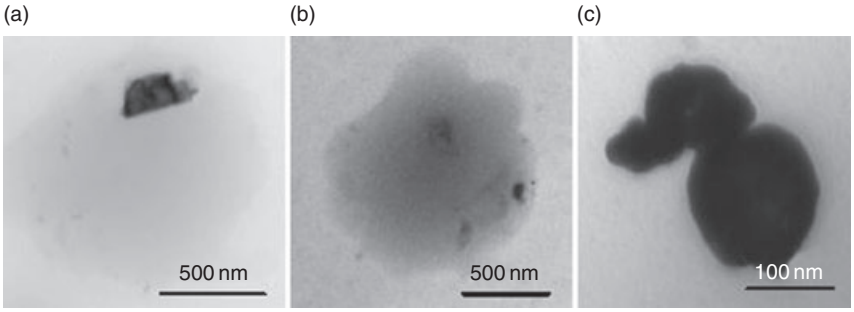

Figure 1.12 Images of nanoshells destroyed by laser irradiation. Gold (panels a and c) from the outer shell and silica from the core (panel b) [1].

remained intact when exposed to multiple Ti:sapphire 300 fs laser pulses at an average fluence rate of $9.06 \times 10^5\,W\,cm^{-2}$. However, when the fluence rate was increased by a factor of three to $2.71 \times 10^6\,W\,cm^{-2}$, the nanoshells were damaged, as observed in TEM images (Figure 1.12). Importantly, the laser fluence rates required for two photon imaging ($0.8–5 \times 10^5\,W\,cm^{-2}$) were significantly below the damage threshold.

Aguirre *et al.* performed damage threshold experiments on two sets of nanoshells for single pulses, providing insight into the mechanisms responsible for nanoshell damage [37]. Nanoshells resonant at 800 nm were placed in a rotating quartz cell and irradiated with a Ti:sapphire laser at a repetition rate of 250 kHz and pulse duration of 300 fs. Under these conditions, each nanoshell is exposed to one pulse on average. A separate group of nanoshells resonant at 1064 nm were placed in a small cuvette and irradiated with a single 9 ns pulse from a Nd:Yag laser. The damage mechanism and threshold were found to depend on the energy and pulse duration.

For the 9 ns pulse, complete destruction resulted primarily from photofragmentation and was only observed for energies of at least 0.005 mJ (average pulse fluence rate = $7.86 \times 10^3\,W\,cm^{-2}$). It has been posited that photofragmentation arises from an extreme photoelectric effect [38]. Energetic laser pulses cause electrons to be ejected from the gold shell, leaving excess positive charge, which causes the shell to explode due to coulombic repulsion.

For the 300 fs pulse, energies greater than 1.2 μJ (average pulse fluence rate = $9.52 \times 10^{10}\,W\,cm^{-2}$) resulted in the melting of nanoshells. The amount of energy absorbed from a 1.2 μJ pulse correlates with a lattice temperature of 1064 °C, which is the melting point of bulk gold. Much lower energies are required to destroy nanoshells under femtosecond pulses than nanosecond pulses because heat diffusion to the surroundings is limited in the femtosecond time regime. Single-pulse energies below 1.2 μJ did not produce melting; however, similar to Park *et al.*, multiple pulses were found to produce a slow reshaping and eventual degradation of the nanoshell structure, which is explained by large temperature rises near defects in the polycrystalline structure of the gold shell.

Of critical importance is the fact that the radiant intensities required to damage gold nanoshells are many orders of magnitude greater than those encountered in most applications. For instance, when nanoshells are used to mediate photothermal therapy, incident intensities are only in the $10\,W\,cm^{-2}$ range [4, 39].

1.3 Synthesis and Bioconjugation

1.3.1 Synthesis

Silica-core gold nanoshells, 'a new frequency-agile nanoparticle', were first fabricated by Oldenburg, Averitt, Westcott and Halas of Rice University, as described in their 1998 publication, *Nanoengineering of Optical Resonances* [40]. The theory predicting the plasmon resonance-derived optical properties of gold nanoshells had been laid out by Neeves and Birnboim [41] of the Rensselaer Polytechnic Institute in 1989, and further explored by Haus *et al.* in 1992 [28]. Members of the Halas group now hold several patents related to their pioneering work with nanoshells [42–45]. In this section we describe the synthesis of gold nanoshells employed by Oldenburg *et al.*, along with various techniques for functionalizing their surfaces. A detailed step-by-step synthesis protocol has been provided by Pham *et al.* [46]. The dimensions of the nanoshells (core radius and shell thickness) are controlled by varying the reactant concentrations.

The original synthesis is a four-step process [40] in which first, monodisperse silica nanoparticles are grown using the Stober method to produce the spherical dielectric cores [47]. The Stober method produces spherical silica particles by means of hydrolysis of alkyl silicates and subsequent condensation of silicic acid in alcoholic solution with an ammonia catalyst. In the second step, the surface of the silica nanoparticles is functionalized by the adsorption of an organosilane (3-aminopropyltriethoxysilane), with its amine tails protruding from the surface. In the third step a solution of gold colloid (~1–2 nm in diameter) is added to the solution. The gold colloid is produced separately from reduction of $HAuCl_4$ by alkaline tetrakis(hydroxymethyl)-phosphonium chloride, according to the method of Duff [48]. The gold particles bond to the organosilane linker via the amine group, producing silica nanoparticles with a smattered, uneven gold coating [49]. A final reduction process is used to produce silica nanoparticles with a uniform layer of gold – that is, a gold nanoshell. In the reduction process, the 'seeded' gold particles which are covalently bonded to the silica core serve as nucleation sites where an aged mixture of chloroauric acid and potassium carbonate is reduced in solution in the presence of sodium borohydride. This process forms a highly crystallized gold shell through Oswald ripening [50]. Transmission electron microscopy (TEM) images of the nanoshells during different phases of growth are shown in Figure 1.13.

UV-visible spectroscopy is used to monitor reaction kinetics, whereby complete nanoshell growth is confirmed by the appearance of characteristic plasmon extinc-

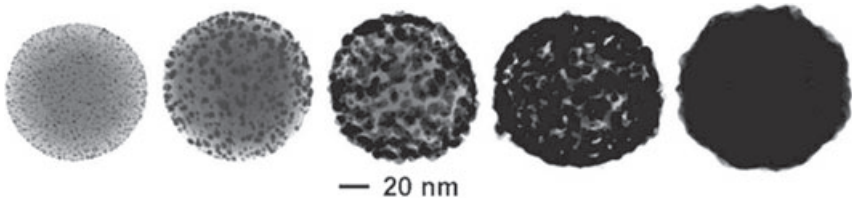

Figure 1.13 Transmission electron microscopy images of nanoshell growth phases from silica core (left) to gold-covered nanoshell (right) [39].

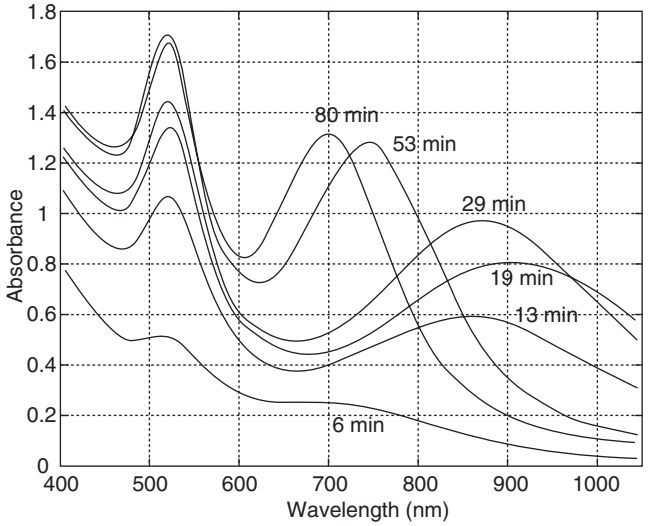

Figure 1.14 Ultra-violet/visible absorption spectrum for Au/Au_2S gold nanoshells as growth proceeds [40].

tion peaks (Figure 1.14). When using this method, the polydispersity (standard deviation) of nanoshells is generally close to 10% [40]. Recently, Phonthammachai *et al.* have published an alternative method for nanoshell synthesis, which employs the deposition–precipitation method [51]. The ideal reaction conditions are detailed thoroughly, including optimal pH, reaction temperature, reaction time and reactant concentrations. This method appears to be equally robust and more cost-effective than the original synthesis.

When the nanoshells have been fabricated it is possible to alter their surface topography through chemical postfabrication texturing. Wang *et al.* have reported site-selective chemical etching of nanoshells by exposing them in solution to the alkanethiol molecule, cystamine [52]. Such etching dramatically increases the roughness of the nanoshell surface, and leads to the production of 'hot spots' [32] where the near-field is predicted to be enhanced by a factor of 30 or more. Wang

et al. confirmed some degree of near-field enhancement by performing surface-enhanced Raman scattering (SERS) experiments, where increased signal intensities were observed for chemically etched nanoshells [52].

1.3.2 Bioconjugation: Smarter Nanoshells

The biologically inert gold surface of nanoshells [53] facilitates bioconjugation with antibodies and other biomarkers, rendering nanoshells capable of selectively binding to *in vivo* targets [54, 55]. The following examples of successful bioconjugation schemes should provide a general idea of the chemistry involved in the production of bioconjugated nanoparticles.

Sokolov *et al*. have synthesized bioconjugates of gold nanospheres with monoclonal antibodies against epidermal growth factor receptor (EGFR), a transmembrane glycoprotein (M_r 170 000) which is overexpressed in cancers originating from epithelial cells [55]. Colloidal gold of various sizes is prepared using a citrate reduction of $HAuCl_4$ (a detailed description of the protocol can be found in Ref. [56]). To prepare the bioconjugates, the gold colloid is diluted with 20 m*M* HEPES buffer, and anti-EGFR monoclonal antibodies are reconstituted in the same buffer at 100 μg ml^{-1} and mixed at a 1:1 volume ratio and allowed to interact for 20 min at room temperature. In this environment, gold nanospheres bind noncovalently with anti-EGFR antibodies at their isoelectric point to form stable bioconjugates. Polyethylene glycol (PEG) is added to the solution up to a final concentration of 0.2 mg ml^{-1}, after which the solution is centrifuged to remove any unbound antibody. After a second wash, the anti-EGFR gold nanoparticle pellet is resuspended in phosphate-buffered saline (PBS).

Human epidermal growth factor receptor 2 (HER2) is a frequently used breast cancer biomarker, and Loo *et al*. have successfully bioconjugated gold nanoshells with HER2 antibodies to target human mammary adenocarcinoma cells *in vitro* [54]. In the synthesis, *ortho*-pyridyl-disulfide-*n*-hydroxysuccinimide–PEG polymer (OPSS) is used to tether the antibodies on the surface after which, using $NaHCO_3$ (100 m*M*, pH 8.5), the OPSS is resuspended in a volume equal to that of the HER2 antibodies. The reaction bonding OPSS to anti-HER2 proceeds on ice for about 12 h, after which any excess OPSS is removed via membrane dialysis. The antibody complex (0.67 mg ml^{-1}) is then allowed to interact with added gold nanoshells (~10^9 nanoshells ml^{-1}) for 1 h, and any unbound antibody is then removed by centrifugation. The functionalized gold nanoshells pellet is then resuspended in potassium carbonate solution (2 m*M*). Following antibody conjugation, the nanoshell surfaces are further modified with PEG-thiol to prevent any nonspecific adsorption and improve biocompatibility.

Recently, Kumar *et al*. published a complete protocol for conjugating antibodies onto the surface of gold nanoparticles in a highly efficient manner [57]. This novel conjugation strategy employs a heterofunctional linker, hydrazide–PEG–dithiol, to directionally attach the nonbinding (Fc) region of the antibody to the gold surface. This technique enjoys several significant advantages over standard adsorption

techniques; mainly that the binding orientation of the antibodies is controlled to ensure maximum functionality and, due to the binding specificity, less antibody is required.

Bioconjugation dramatically enhances the clinical prospects of gold nanoshells by rendering them capable of targeting specific tissues through molecular recognition. Undoubtedly, innovative conjugation strategies will play an increasingly important role in the development of gold nanoshells for targeted therapeutics and diagnostics. In the next section, the connection between bioconjugation and biodistribution will be explored.

1.4 Biodistribution, Toxicity Profile and Transport

The dynamic biodistribution of nanoshells *in vivo* is of considerable clinical interest. Optimal imaging and treatment strategies require achievement of the highest concentration of nanoshells in the target tissue (i.e., a solid tumor), while minimizing concentrations in surrounding healthy tissues. Knowledge of the quantity of nanoshells reaching the target volume is needed to ensure optimal dosing.

Ultimately, the *in vivo* transport of nanoshells arises from a complex milieu of physical (pressure gradients, passage through vascular perforations, diffusion), chemical (antibody binding, transient binding) and cellular (endocytosis, vacuolar transport) processes [58]. A number of *in vivo* studies have been carried out to examine the net effect of transport, the differential and time-dependent distribution of nanoshells in various physiological compartments, namely the targeted tumor, blood, muscle tissue and major organs [59–62]. To date, the vast majority of *in vivo* studies have employed a murine model, whereby nanoshells are delivered intravenously through the tail vein and enter the systemic circulation. The biodistribution in human patients can likely be predicted based on existing pharmacokinetic modeling techniques, which use well-defined scale-up laws to estimate transport parameters [63].

In general, the distribution of nanoshells depends strongly on whether passive or active targeting methods are employed. Passive targeting relies exclusively on the nanoshell's size and a tumor's inherently 'leaky' vasculature to produce accumulation at tumor sites through an enhanced permeability and retention (EPR) effect [64]. In active targeting, the nanoshell's surface is functionalized with antibodies or other biomolecules, which bind to surface receptors on malignant cells to produce an enhanced accumulation at the tumor site [65]. Both targeting mechanisms are hindered by intrinsic host immune mechanisms, which clear nanoshells from circulation [66]. In both cases, the total circulation time is believed to correlate strongly with accumulation at the tumor site, independent of other anatomical and physiological factors [67]. The surface of gold nanoparticles is now routinely functionalized with PEG (PEGylation) to 'stealth' the nanoparticles from immune surveillance, and this has led to a dramatic increase in circulation times [68].

The following discussion is divided into three parts. First, an overview is provided of the techniques used to quantify the dynamic biodistribution of nanoshells, and the corresponding results. Second, the individual transport mechanisms responsible for the observed biodistribution are explored, based on information obtained from studies examining the transport mechanisms of similar-sized particles. Third, an overview is provided of the benign toxicity profile of nanoshells.

1.4.1 Biodistribution Studies

The current 'gold standard' for quantifying nanoshell concentrations in tissue is neutron activation analysis (NAA) [59]. This method requires the tissue excision, dehydration and bombardment of the sample of interest with neutrons in a nuclear reactor. Gold nanoshells absorb the neutrons, undergo a nuclear transition, and emit gamma rays with energies that are characteristic of gold. These gamma rays are then detected and related to the quantity of nanoshells present in the sample. James *et al*. employed this method to measure the concentration of nanoshells (~120 nm diameter) in different organs in mice at various time points [59]. Female albino mice with subcutaneous tumors (~5 mm) were injected with 100 µl of an isotonic saline solution of PEGylated nanoshells (2.4×10^{11} nanoshells ml^{-1}, passive targeting) and sacrificed at 1, 4, 24 and 48 h. Blood, liver, lung, spleen, muscle, kidney, bone and brain tissues were then analyzed using NAA. The study yielded several key findings; namely that tumor concentrations peaked at 24 h after injection, and the total tumor accumulation represented approximately 1% of the administered dose. Tumor concentrations were elevated relative to the blood, lungs, brain, bone and kidneys. (Figure 1.15) However, the highest accumulations were found in the liver and spleen, due to involvement of the reticuloendothelial system (RES).

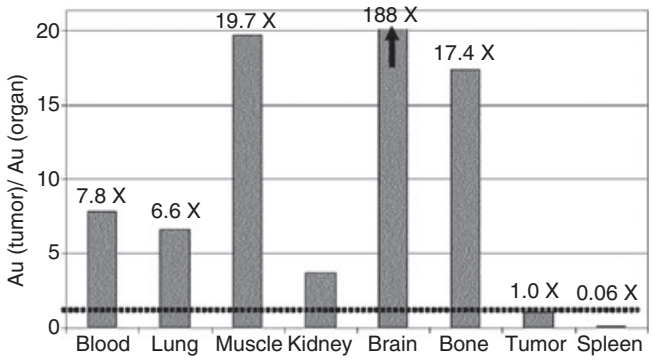

Figure 1.15 Ratio of tumor to organ concentrations at 24 h after dosing. Very high concentrations are observed in the spleen due to the action of the reticuloendothelial system [59].

Although this study provides valuable information regarding the biodistribution of nanoshells in mice, it does not address the question of how nanoshell size might affect biodistribution. Recently, De Jong *et al.* demonstrated the size-dependent nature of gold nanosphere organ distribution in normal, tumor-free rats using inductively coupled plasma mass spectrometry (ICP-MS) [69]. Rats were injected intravenously with nanospheres with diameters of 10, 50, 100 and 250 nm, respectively, and then sacrificed 24 h after injection. For all sizes of nanospheres, the highest concentrations were found in the blood, liver and spleen. However, there was a clear difference between the smaller (10 nm) and the larger nanospheres, with the smaller particles exhibiting a more pervasive organ distribution and being the only particles with detectable accumulations in the brain. Of particular interest was the fact that the NAA data for 120 nm gold nanoshells and the ICP-MS data for 100 nm nanospheres were not in good agreement. After 24 h, James *et al.* found the concentration of nanoshells in the spleen to be about fivefold greater than in the liver (1890 versus 311 $\mu g\,g^{-1}$), whereas De Jong *et al.* found higher concentrations of nanospheres in the liver than the spleen (3268 versus 1793 $ng\,g^{-1}$). This very significant discrepancy warrants further investigation, since it does not eliminate the possibility that there might be substantial differences in the biodistribution of gold nanospheres and nanoshells.

While generally providing excellent accuracy, NAA and ICP-MS have several drawbacks. Both techniques are labor-intensive, take significant time to acquire results, and are incapable of *in vivo* quantification because the organism must be sacrificed. In contrast, diffuse optical spectroscopy (DOS) and dynamic light scattering (DLS) provide a rapid means for determining *in vivo* nanoshell concentrations noninvasively. In DOS, a probe containing both optical source and detector fibers is placed in direct contact with the tissue [60], and the diffusely reflected light is then collected and spectrally analyzed. The concentration of nanoshells can be measured by fitting the diffusely reflected spectrum to a diffusion model through nonlinear regression. Zaman *et al.* used DOS to quantify nanoshell concentrations in live mice, yielding values within 12.6% of the known concentrations. DOS provides reliable average concentration measurements in the volume sampled, but can only be used to sample regions accessible by the probe.

Xie *et al.* have used DLS to quantify nanoshell concentrations in whole blood [61]. Blood samples (15 µl) were taken from mice at fixed times after nanoshell injection to study the circulation times and clearance in blood. DLS estimates particle concentrations by comparing the relative scattering from particles of a given size to particles of a known concentration and different size. In this study (where the comparative scatterer was Triton X-100 micelles), the measured whole-blood values were in good agreement with NAA measurements, showing an exponential decay of blood concentrations with a half-life of 5 h.

For malignancies located in close proximity to the surface of the epithelium, optimal biodistribution may be achieved through topical delivery rather than systemic administration. Although the results of *in vivo* studies have yet to be published, *in vitro* studies have yielded promising results. Using engineered tissue

constructs, Sokolov *et al*. showed that gold nanospheres (~12 nm diameter) can be delivered throughout the epithelium by using the penetration enhancers polyvinylpyrollidone (PVP) and dimethyl sulfoxide (DMSO), both which have been approved by the FDA for use in humans [55]. Confocal reflectance microscopy measurements revealed a uniform distribution of nanoshells up to a depth of 400 μm, which is significant because precancers of the squamous epithelium typically originate at a depth of 300–500 μm below the surface.

A study comparing the effects of active and passive targeting on the biodistribution of gold nanoshells has not been carried out to date. However, Qian *et al*. have conducted a similar study using gold nanospheres (~80 nm diameter), which demonstrated the advantage of employing active targeting mechanisms [65]. Nanoparticle concentrations were measured in sacrificed mice with xenografted human squamous carcinoma tumors, using ICP-MS. For active targeting, the nanoparticles were conjugated to anti-EGFR antibodies that bind to the EGFR, which is normally overexpressed on the surface of tumor cells. The targeted gold nanoparticles were found to accumulate in the tumor 10-fold more efficiently than the nontargeted particles, which represented a substantial difference. It is therefore likely that enhanced accumulations would be observed with targeted nanoshells.

The effects of active targeting have also been studied on the cellular level. For example, Fu *et al*. used polarized light scattering to quantify the number of antibody-conjugated nanoshells bound to a targeted cancer cell [70]. Here, SK-BR-3 breast cancer cells were incubated with anti-HER2/nanoshell bioconjugates in a cell culture, with approximately 800–1600 nanoshells being bound to the HER2 receptors on each cell. Cell-specific anti-HER2 conjugates were shown to exhibit binding efficiencies more than 10-fold greater than those of nonspecific anti-IgG conjugates. Clearly, active targeting mechanisms will play an increasingly important role in determining the maximum therapeutic efficacy of nanoshells for the treatment of various cancers.

1.4.2 Transport Mechanisms

The transport of molecules and particles in solid tumors is a vast and active area of research because if its potential to illuminate new methods for achieving optimal delivery of therapeutic agents to the tumor site. The following discussion is intended only as an overview of the subject area, outlining the basic characteristics and underlying mechanisms of nanoparticle transport in solid tumors, which can be generalized to nanoshells.

Upon introduction into the host's vasculature, the fate of a typical nanoshell is predictable if the host is tumor-free and the nanoshell surface is not modified by antibodies or other protein-binding ligands. As normal blood vessels are highly impermeable to particles the size of nanoshells [58, 62], the nanoshells will remain in circulation until they reach the spleen and liver, where they are scavenged by macrophages, such as Kupffer cells, in the host's RES (this accounts for the high

concentrations observed in the liver and spleen). Large numbers of nanoshells remain in the RES tissues for many weeks and perhaps longer [59]. However, conflicting data exist with regards to the eventual clearance of nanoshells. Whereas, gold nanoparticles smaller than 10 nm are slowly eliminated from the host's system via renal excretion [66], the case may be different for larger gold nanoparticles. In magnetic resonance imaging (MRI) studies, Choyke *et al.* found that 'virtually no' contrast agents (gadolinium dendrimers) larger than 11 nm were eliminated through renal excretion [71]; hence, it stands to reason that whole gold nanoshells (~100 nm) would also be excluded from renal clearance. However, significant amounts of gold and copper have been found in the urine of mice injected with gold-copper nanoshells, which suggests partial renal clearance [72]. Nanoshells are also likely excreted in the feces, similar to quantum dots [73].

If a tumor is present, then the transport and biodistribution of nanoshells changes significantly. The tumor vasculature is physiologically distinct from normal vasculature, as it lacks a functional lymphatic system [74], exhibits spatial and temporal heterogeneity [58], structural irregularity, abnormal fluid flow, and hyperpermeability to particles with diameters up to 1.2 μm [75]. The overall result is a series of peculiar transport properties that vary across the tumor type, stage of development and the surrounding microenvironment [67].

One prominent feature of vascular transport in tumors is the EPR effect [64], whereby particles with diameters of tens to hundreds of nanometers extravasate through the 'leaky' microvasculature and accumulate in the tumor interstitium. For example, a 400–600 nm cut-off has been found for the extravasation of liposomes [76]. Multiple causes of associated tumor 'leakiness' have been identified, including physical openings, cytokine-influenced permeability changes and various cellular transport mechanisms. Hashizume *et al.* showed that, in highly leaky MCa-IV mouse mammary tumors, 14% of the vessel surface was lined with poorly connected, overlapping endothelial cells. Transcellular holes were also present, but these were only 8% as numerous as intercellular openings [75]. An electron microscopy image showing an open endothelial gap in a tumor blood vessel in a liposome-injected mouse is shown in Figure 1.16, where the liposomes can be seen migrating through the open junction.

Dvorak *et al.* investigated extravasation with fluorescence and electron microscopy by injecting tumor-bearing mice and guinea pigs with fluoresceinated dextrans (diameters of 2.4, 11.6 and 17.4 nm) and colloidal carbon (~50 nm) [62]. (Note: it very worthwhile viewing the images produced in this study because they provide an excellent visual description of tumor vessel architecture and morphology.) The 11.6 nm and 17.4 nm tracers did not perfuse into normal tissues, but leaked extensively at tumor sites, thus setting a rough limit on the minimum size needed for nanoparticles to achieve preferential tumor accumulation. Additionally, colloidal carbon was found in vacuoles of individual tumor endothelial cells, thus implicating transcytosis as a mechanism for vascular transport and corroborating previous findings [77]. Cytokines also play an important role in extravasation. One peptide which is commonly secreted by human and animal tumors, namely vascular permeability factor (VPF), greatly enhances the permeability of nanoparticles

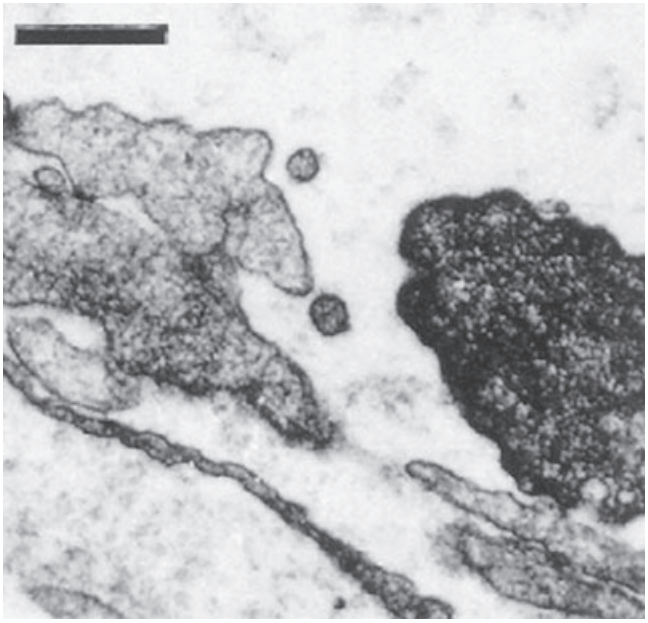

Figure 1.16 Endothelial gap with migrating liposomes. Two circular liposomes are seen crossing the gap.

[62]. For example, Monsky *et al*. demonstrated that low doses of vascular endothelial growth factor (VEGF) (10 ng ml^{-1}) doubled the pore sizes and increased the frequency of 400 nm pores in human colon xenografts [78].

After extravasation into the interstitial space, the transport of particles occurs via two mechanisms – diffusion and convection – which in turn presents a challenge to nanoparticle delivery because both processes produce very slow particle migrations. This is evidenced by the fact that extravasated particles remain largely confined to the perivascular region of the interstitium. By using two-photon microscopy, Park *et al*. showed that extravasated nanoshells remained in close proximity to the tumor microvasculature in subcutaneous mouse colon carcinoma xenografts, as can be seen in the three-dimensional (3-D) visualization in Figure 1.17. Similar transport behaviors of nanoshells have been demonstrated in other studies [58, 74, 79, 80].

Li *et al*. used photoacoustic microscopy to image the passive accumulation of nanoshells in murine colon carcinoma tumors grown in BALB/c mice [79]. Nanoshells were found to accumulate heterogeneously in the tumor, characterized by high concentrations in the vascular-rich cortex and very low concentrations in the tumor core. These results correlated well with previous studies, which have shown drug delivery to tumor cores to be minimal because of several inherent tumor mechanisms [80].

The high interstitial pressure in the center of a tumor that inhibits the convectional flow of extravasated particles in the vascular-rich periphery is a consequence

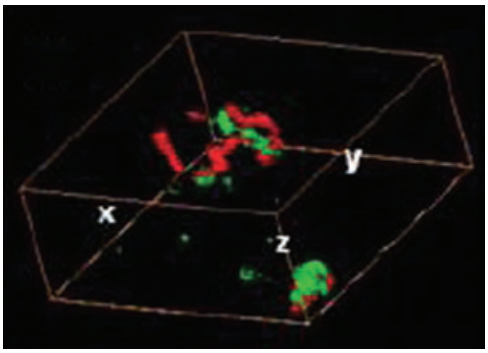

Figure 1.17 Nanoshells (green) in close proximity to tumor vasculature (red) [1].

of leakage from blood vessels, coupled with an impaired fluid clearance through dysfunctional lymphatic drainage [74]. Characteristically low diffusion coefficients hinder significant diffusion; for example, it has been estimated that it would take immunoglubulin G (IgG) several days to move 1 mm within a solid tumor, by the process of diffusion [58].

Transport also varies across tumor type, microenvironment and stage of development. For example, Hobbs *et al.* showed delivery to be less efficient in cranial tumors than in subcutaneous tumors, and that delivery was reduced during regression in hormone-dependent tumors during hormonal ablation [67].

Future research aimed at a better understanding of the mechanisms of transport, and how transport varies by tumor type, microenvironment and stage of development, will provide the valuable information required to optimize the therapeutic efficacy of gold nanoshells, gold nanoparticles and other cancer treatments.

1.4.3 Toxicity

Although no comprehensive studies evaluating the long-term (years) toxicity of gold nanoshells have yet been reported, all available evidence indicates that – at physiological doses – gold nanoshells are not cytotoxic and pose no short-term health risks. In fact, the favorable toxicity profile of nanoshells results from the nontoxicity of the shell components.

Gold has been used to treat rheumatoid arthritis since the 1930s [81], and is universally recognized as the most biologically inert of metals [81]. Likewise, silica nanospheres have been shown to be nontoxic in a murine mouse model [82]. The safety of gold nanospheres has been well documented; in experiments performed *in vitro*, gold nanospheres incubated with macrophages were found to be both noncytotoxic and nonimmunogenic [83]. Nanospheres were also found to reduce the production of both reactive oxygen species (ROS) and nitrite radicals, and did not stimulate the secretion of inflammatory cytokines.

Numerous *in vivo* studies conducted in mice have provided the best evidence that nanoshells are not only nontoxic but also safe. In all instances, mice treated with nanoshells exhibited no clinical abnormalities or side effects at months after treatment [4, 84, 85]. It should be noted that, although a prolonged respiratory exposure to high doses of crystalline silica has been linked to lung cancer in epidemiological studies [86], the carcinogenic potential of gold nanoshells is minimal for the following reasons. The silica used in nanoshells is completely obscured from the host by the gold shell, which is not carcinogenic. Likewise, comparatively lower doses of nanoshells would be necessary for clinical applications, and the intravenous route of administration prevents high concentrations from ever reaching the lungs. Although gold nanoshells can generally be considered 'safe', their long-term effects on human health will need to be closely monitored.

Significantly, gold nanoshells appear to be much safer than both quantum dots and gold nanorods. Quantum dots are, presumably, cytotoxic because the toxic heavy metals found in their cores (i.e., cadmium and lead) can leach into the surrounding environment [87]. The available evidence regarding the cytotoxicity of nanorods renders a split verdict, however, with some studies suggesting that nanorods have no effect on cell viability while others have demonstrated cytotoxicity. It should be noted that the cytotoxicity of nanorods appears to be solely related to the presence of cetyltrimethylammonium bromide (CTAB), a chemical used in their synthesis [72].

1.5 Biomedical Applications

Due to their unique physical characteristics and benign toxicity profile, gold nanoshells have been at the forefront of a growing number of biomedical applications. They have shown potential as integrated cancer targeting, imaging and therapy agents. As contrast agents, nanoshell bioconjugates have been used to detect and image individual cancer cells *in vitro* and in solid tumors *in vivo*. As photothermal agents, nanoshells have successfully been used in animal studies to induce thermal necrosis of tumors. On the laboratory bench, they have been used to potentiate thermal drug delivery in temperature-sensitive hydrogels. Outside the realm of cancer treatment, nanoshells have proven their worth in a number of novel applications; for example, as biosensors they have been used for the sensitive detection of biomarkers at the $ng\,ml^{-1}$ level.

1.5.1 *In Vitro* Cancer Detection and Imaging

Detecting cancer in its earliest stages is strongly associated with positive patient outcomes, including reduced morbidity and improved five-year survival rates [88]. As many cancers originate from a small number of malignant epithelial cells [89], the ability to detect low numbers of malignant or precancerous epithelial cells

in vivo would represent a giant leap forward in the fight against cancer. Notably, it would facilitate the detection of cancer in its earliest stages, before any significant pathogenesis, tumor formation and metastasis. A number of groups have successfully demonstrated *in vitro* single cancer cell detection, with exceptional contrast and specificity, using bioconjugated gold nanoparticles as molecular-specific contrast agents. Here, the general detection scheme relies on conjugating nanoparticles to antibodies that target epithelial cell-surface receptors (e.g., EGFR and HER2) which are commonly overexpressed in cancer cells. The resultant high concentrations of nanoparticles found on the surface of targeted cancer cells, combined with their high scattering cross-sections, greatly facilitates imaging on the cellular level.

Loo *et al.* have used anti-HER2-conjugated nanoshells to detect and image HER2-positive SKBr3 breast adenocarcinoma cells using dark-field microscopy *in vitro* (Figure 1.18) [54, 90]. In this experiment, both SKBr3 and MCF7 (HER2-negative) cancer cells were incubated with nanoshells at a concentration of $8\,\mu g\,ml^{-1}$ for 1 h. Consequently, the SKBr3 cells targeted with molecular-specific anti-HER2 showed a marked (300%) increase in contrast over the nonspecific anti-IgG control group, whereas no appreciable differences in contrast were noted between HER2-negative control cell groups, indicating that nanoshells targeted the HER2 receptor on SKBr3 cells with high specificity.

Other types of gold nanoparticle, such as nanospheres and nanorods, have also been successfully employed to detect and image cancer cells *in vitro*. Durr *et al.* have used anti-EGFR-conjugated nanorods to detect and image A431 skin cancer cells embedded in a 3-D tissue scaffold using two-photon luminescence (TPL) microscopy [91]. The nanorods produced a TPL signal enhancement of more than three orders of magnitude over the intrinsic fluorescence of unlabeled cancer cells, which enabled the imaging of cancer cells up to a depth of 75 µm. El-Sayed *et al.* have used anti-EGFR gold nanorods to detect and image two oral squamous carcinoma cell lines, HSC 313 and HOC 3 [92, 93]. The nanorods were found to bind specifically and homogeneously to the surface of cancer cells with 600% greater

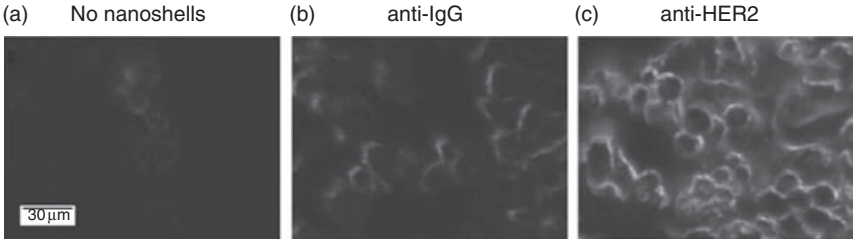

Figure 1.18 Dark-field images of SKBr3 cancer cells exposed to (a) no nanoshells, (b) anti-IgG-conjugated nanoshells and (c) anti-HER2 nanoshells. Note the significant difference in contrast between the anti-HER2 nanoshells designed to target breast cancer cells, and the control and anti-IgG nanoshells [54].

affinity than to nonmalignant cells. Dark-field microscopy revealed an intense resonant scattering from the labeled oral cancer cells, whereas scattering from a normal cell line (HaCaT) was minimal.

Sokolov *et al.* have used anti-EGFR-conjugated nanospheres and reflectance confocal microscopy to detect and image SiHa cervical cancer cells in 3-D tissue constructs [55], while Mallidi *et al.* used optoacoustic imaging in conjunction with anti-EGFR nanospheres to detect and image A431 skin cancer cells to depths of up 1 mm in tissue phantoms [94]. Optoacoustic imaging using nanoshells has been studied to a lesser extent [95]. Aaron *et al.* have used anti-EGFR gold nanospheres as molecular-specific probes to distinguish between normal and malignant cervical biopsies [89], with confocal reflectance images showing an up to a 21-fold difference in signal intensity between normal and abnormal biopsies. As an additional detection feature, a ~100 nm red shift in the reflectance spectra was observed in malignant biopsies; this was due to plasmon resonant coupling of aggregated nanospheres on the cell surface, where EGFR is densely expressed [96]. This feature also has a significant diagnostic value, as it provides a reliable quantitative assessment of tissue status. As a consequence of these findings, the use of gold nanoparticles for *in vitro* cancer detection and imaging is now well established.

1.5.2
In Vivo Detection and Imaging

Recently, progress in the detection and imaging of malignant cells *in vitro* has been followed up by *in vivo* studies, where bioconjugated gold nanoparticles have been used successfully to target and detect tumors in mice. Qian *et al.* have created specialized gold nanospheres for SERS imaging [65] that are first stabilized with PEG-thiol and then conjugated to a Raman reporter (malachite green) and to anti-EGFR antibodies for active tumor targeting. In the experiment, nude mice with xenografted human head and neck cancer tumors (Tu686) were injected with specialized nanospheres through the tail vein. The tumors were approximately 3 mm in diameter. After 5 h, NIR SERS spectra were obtained using a 785 nm excitation laser on a hand-held Raman system. The SERS spectra measured from an intramuscular tumor located ~1 cm below the surface were distinct from the background spectra, demonstrating the effective detection of small tumors at depths of at least 1 cm. However, based on a favorable signal-to-noise ratio, the authors concluded that the maximum achievable penetration depth for SERS detection was likely in the 1–2 cm range.

Aaron *et al.* have used anti-EGFR-conjugated nanospheres to monitor carcinogenesis *in vivo* in a hamster cheek pouch model [89]. A carcinogen, dimethylbenzanthracene (DMBA), was repeatedly applied to the hamster's inner cheek to induce carcinogenesis over the course of weeks. After anesthetizing the hamster, the inner cheek was then imaged with a portable confocal reflectance microscope before and after the topical application of gold nanospheres. The inner cheek was rinsed shortly after nanosphere application to eliminate any nonspecific binding.

Images were subsequently taken over the span of many weeks to detect and monitor dysplasia. At week zero, images taken before and after application were almost the same, but by week 3 there was a marked difference in the two images, indicating cancer progression and specific binding to cancer cells overexpressing EGFR. Although the results of this study highlighted the potential of gold nanoparticles for the localized optical detection of cancer cells *in vivo*, it should be noted that favorable results were not always repeatable. The authors of the study attributed such poor reproducibility to the thick keratin layer present in the buccal mucosa of hamsters, which inhibits nanosphere delivery.

Gobin *et al.* have demonstrated the role of nanoshells as contrast agents for *in vivo* optical coherence tomography (OCT) imaging [97]. BALBc mice with subcutaneous murine colon carcinoma tumors were injected with PEGylated nanoshells at 20 h before OCT imaging, which was carried out using a commercially available OCT system. Due to their large resonant scattering cross-sections and ability to accumulate at tumor site, the nanoshells were found to significantly enhance the optical contrast of the tumor compared to normal tissue. Thus, in nanoshell-treated mice the integrated scattering intensity was 56% greater in tumor tissue than normal tissue, whereas in control mice the difference was only 16%. It appears that gold nanoshells represent excellent contrast agents, and are suitable for a wide range of imaging techniques.

1.5.3
Integrated Cancer Imaging and Therapy Agents

Gold nanoshells and nanorods are not merely ideal agents for detecting and imaging cancer – the same nanoparticles can be used as therapeutic agents to treat cancer with photothermal therapy. Unlike nanospheres, nanoshells and nanorods can be engineered either to scatter NIR radiation for imaging, or to absorb it and efficiently convert it to heat for the selective destruction of targeted tumor cells. Nanoshells and nanorods are integrated multifunctional nanoparticles, useful for both imaging and therapy [90, 97]. Although the ability of both nanorods and nanoshells to mediate the photothermal destruction of targeted cancer cells *in vitro* has been established, until now only nanoshells have been shown to treat tumors effectively *in vivo*. However, the details of *in vivo* studies carried out with nanorods have not yet been reported.

1.5.4
In Vitro Studies

In an *in vitro* study, Hirsch *et al.* incubated breast carcinoma (SKBr3) cells with unconjugated nanoshells for 1 h, after which the cells were rinsed to remove unbound nanoshells and then exposed to 820 nm laser light with an intensity of $35\,W\,cm^{-2}$ for 7 min. After treatment, all nanoshell-treated cells within the laser spot were dead, whereas those cells in the control groups remained viable [4]. Others have carried out similar *in vitro* experiments. For example, Stern used

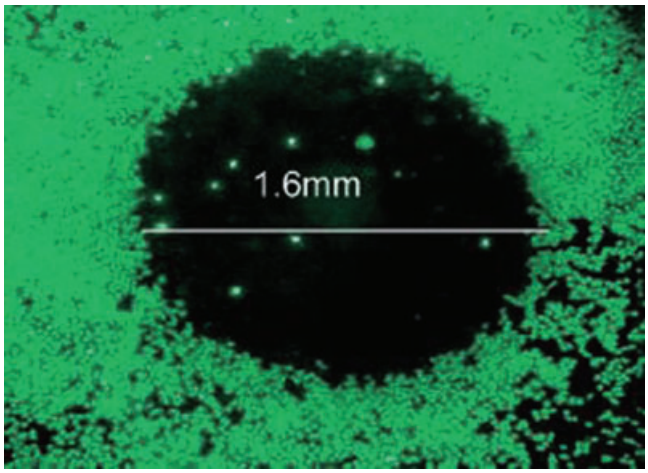

Figure 1.19 PC-3 prostatic cancer cells treated with gold nanoshells and exposed to NIR laser light focused to a spot size of 1.6 mm. Calcein viability staining reveals selective destruction of cells within the laser spot [98].

unconjugated nanoshells as mediators to photothermally ablate two types (PC-3 and C4-2) of human prostate cancer cell (Figure 1.19) [98], while Loo *et al.* used anti-HER2-conjugated nanoshells to target and ablate SKBr3 breast carcinoma cells [90]. In another study, El-Sayed *et al.* used anti-EGFR-conjugated gold nanorods to treat two human oral cancer cells types (HSC 313 and HOC 3) and a benign control, human epithelial keratinocytes (HaCat). After having exposed the cells to various intensities of 800 nm laser light for 4 min, irreversible photothermal injury of nanorod-treated cells was observed for intensities as low as 19 W cm^{-2}. More significantly, photothermal destruction was observed in malignant cells at less than half the laser power needed to induce destruction in healthy cells, thus permitting the selective destruction of cancer cells. Of particular interest here was the lower laser intensities needed to induce the destruction of malignant cells using nanorods compared to nanoshells. This presumably occurred because nanorods have a larger size-normalized absorption cross-section than do nanoshells [6]. An authoritative study evaluating the effectiveness of both types of nanoparticle under identical experimental conditions is yet to be published, however.

Everts *et al.* have conjugated gold nanospheres to adenovirus vectors to investigate their potential for combined photothermal and gene cancer therapy applications [99]. Adenovirus vectors, which normally do not infect cancer cells, were re-targeted to infect cancer cells expressing the tumor-associated oncoprotein carcinoembryonic antigen (CAE) *in vitro*, thus providing a method for introducing gold nanoparticles into the nuclei of targeted cancer cells. For *in vivo* applications, nanoshells or nanorods tuned to absorb in the NIR could be used to induce selective hyperthermia in particular segments in the genome of a tumor cell. However, more simple targeting mechanisms have been shown to be highly effective.

1.5.5 *In Vivo* Photothermal Therapy

Multiple *in vivo* studies have demonstrated the efficacy of nanoshells for the non-invasive treatment of tumors through targeted photothermal destruction [4, 84, 85]. Here, the overall concept is straightforward; nanoshells with absorption peaks in the NIR region of the spectrum (~800 nm) accumulate at the tumor site through passive and/or active mechanisms. The 800 nm absorption peak is in the NIR 'optical window' region of the spectrum where tissue absorption is minimal, permitting optimal penetration [15, 100]. When the tumor site is exposed to NIR radiation (which the nanoshells absorb intensely because of plasmon resonance), the absorbed energy is efficiently converted into heat, leading to thermal destruction of the tumor.

O'Neal *et al.* have successfully treated mice inoculated with tumors using this technique [84]. In the experiment, albino mice were inoculated subcutaneously with CT26.WT murine colon carcinoma cells in the right dorsal flank, and selected for treatment when the tumors had reached diameters of 3–5.5 mm. An aliquot (100 μl) of PEGylated nanoshell solution (2.4×10^{11} nanoshells ml^{-1}) was then injected via a tail vein. After allowing a 6 h period for the nanoshells to accumulate, the laser treatment was commenced, with the tumors being exposed to NIR light at 808 nm at 4 W cm^{-2} for 3 min. Measurements revealed a marked increase in surface temperature at the tumor site, to ~50 °C, and both tumor size and animal survival was monitored for up to 90 days after treatment. In the nanoshell treatment group, a complete resorption of tumors was observed within 10 days, and all mice were healthy and free of tumors at 90 days. By contrast, in the control groups the tumors continued to grow after sham treatment, with a mean survival time of 10.1 days (Figure 1.20). This dramatic difference in results highlighted the therapeutic potential of nanoshells.

In a separate study, Hirsch *et al.* studied the temperature distribution in tumors during thermal therapy, and highlighted the merits of injecting nanoshells directly into the tumor interstitium rather than administering them intravenously [4]. Female nonobese diabetic mice were inoculated with transmissible venereal tumor (TVT) cells in the hind leg, and the tumors allowed to grow until they reached a diameter of ~1 cm. Nanoshells were then injected interstitially to a depth of ~5 mm into the tumor volume. At only minutes (rather than hours) after injection, the tumor sites were exposed to NIR radiation (4 W cm^{-2}, spot diameter ~5 mm) for 6 min, during which the tumor volume temperatures were monitored using magnetic resonance temperature imaging. The mean change in temperature for the nanoshell group (37.4 ± 6.6 °C) was high enough to cause irreversible thermal damage, whereas the more modest temperature increase in the nanoshell-free control group (9.1 ± 4.7 °C) was insufficient to cause any permanent damage (Figure 1.21). Interestingly, the heating profile was approximately homogeneous, which indicated that the tumor volume contained a near-uniform distribution of nanoshells. The maximum temperatures were found approximately 1 mm below the surface, and not at the site of injection. Such behavior was most likely the

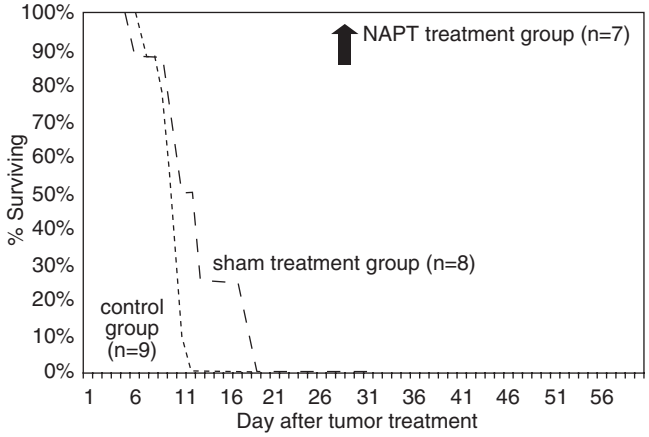

Figure 1.20 Survival rates of control, sham and treatment groups of mice undergoing nanoshell-assisted photothermal therapy (NAPT) of cancer [84]

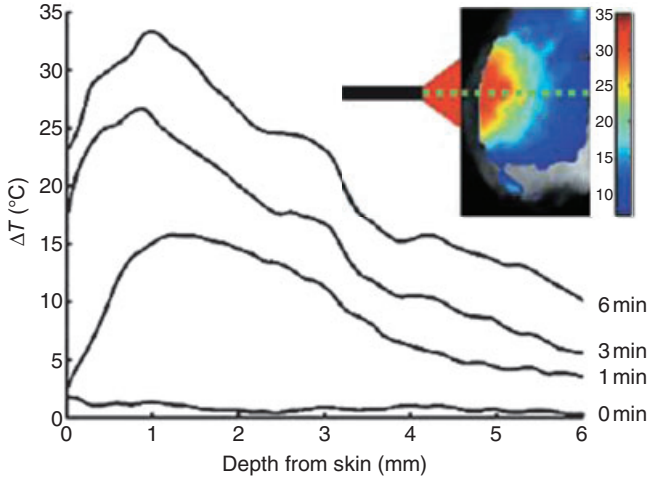

Figure 1.21 Net temperature change (°C) as a function of skin depth for various NIR exposure times [4].

result of higher photon fluence rates, which are known to peak slightly below the surface in highly scattering mediums, such as tissue [101]. An histological analysis performed after the procedure confirmed a diffuse distribution of nanoshells over a large volume within the tumor, and suggested that nanoshells might have a maximal therapeutic efficacy when administered directly to the tumor site.

Diagaradjane *et al.* have demonstrated that nanoshell-induced hyperthermia significantly enhances radiation therapy in mice [102]. In this study, mice with

xenografted tumors were injected with gold nanoshells via the tail vein and, at 24 h after injection, a NIR laser was used to induce hyperthermia at the tumor site for 3–5 min. Immediately hyperthermia induction, the mice received a single 10 Gy dose of radiation therapy. At 20 days after irradiation, the average tumor volume had more than doubled in the radiation cohort, but remained approximately constant in the combined hyperthermia/radiation cohort. The two mechanisms thought to account for the additional therapeutic benefit of hyperthermia are increased perfusion (which reduces the fraction of cells that contribute to radiation resistance) and a subsequent induction of vascular disruption, which causes extensive necrosis.

Stern *et al*. examined the dose-dependent nature of nanoshell therapy for treating prostatic cancer in a murine mouse model [85]. Surprisingly, a mere 20% modification in the administered dose was the difference between successful tumor ablation and continued tumor presence. In this study, male athymic nude mice were inoculated subcutaneously with PC-3 prostate cells in the hind flanks, and the tumors then grown until they attained a volume of approximately 40 mm^3. Nanoshells were then injected intravenously and NIR laser treatment commenced at 8 h after injection, so as to allow the nanoshells time to circulate and accumulate. An initial dosage of 7.0 $\mu l\, g^{-1}$ body weight (based on the successful treatment dosage of O'Neal's experiment; see above) failed to produce tumor necrosis, but did halt further tumor growth. In contrast, tumors in the control groups showed a dramatic threefold increase in volume. In a second treatment group, where the dose was raised to 8.5 $\mu l\, g^{-1}$, the results were much more favorable, with 93% of the high-dose-treated tumors being thermally ablated and exhibiting total resorption at 21 days, while the control groups experienced the same threefold volume increase as before (Figure 1.22). While the maximum surface temperatures reached

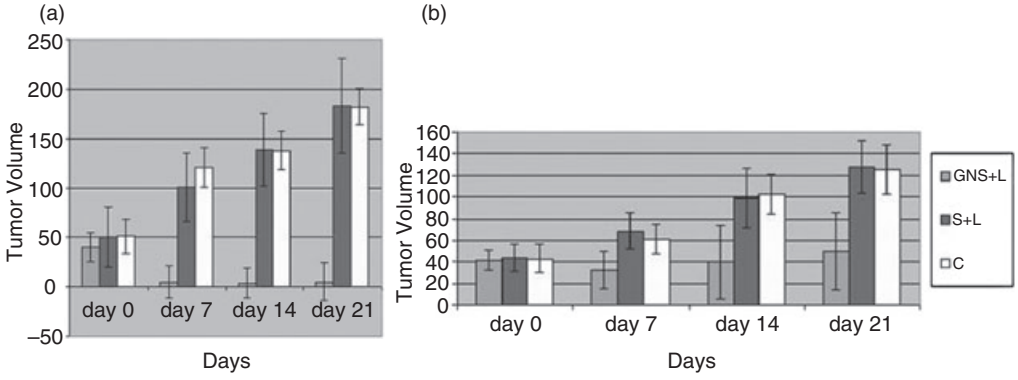

Figure 1.22 (a) High-dose and (b) low-dose treatment groups of gold nanoshells plus laser (GNS+L), saline plus laser (S+L) and negative control (C). A 20% increases in dose leads to a significant different in outcome [85].

65 °C in the nanoshell-rich tumor region, those of the irradiated normal skin areas did not exceed 45 °C. It has been shown that temperatures in excess of 55 °C are required to achieve hyperthermia of prostate cancer cells [103].

The study authors could only speculate as to why one tumor among the 15 treated with the higher dose failed to necrotize, compared to a 100% cure rate in the study of O'Neal. The suggestion was made that an insufficient number of nanoshells had reached the tumor site and, indeed, in a previous *in vitro* study Stern and colleagues had shown that a ratio of 5000 nanoshells per cell was needed to induce thermal necrosis at a fixed intensity [98]. Nonetheless, the results of this study underscore the need for future research to determine optimal dosing schemes.

Elliot *et al*. have modeled nanoshell-mediated photothermal therapy using the diffusion approximation to predict spatiotemporal temperature fluctuations in tissue undergoing therapy [104]. The model was validated using results from tissue phantom experiments, and predicted measured temperature values with reasonable accuracy. However, it did not account for those factors present under *in vivo* conditions, such as blood perfusion. However, in looking to the future, a quantitative *in vivo* model of nanoshell-mediated photothermal therapy will surely be very helpful in tailoring individual treatment regimens to human patients.

1.5.6 Drug Delivery

Nanoshells have long shown promise for increasing drug delivery to tumors. Shetty *et al*. have demonstrated enhanced tumor perfusion in mice with xenografted prostate tumors, the perfusion being increased by nanoshell-mediated heating [105]. Mice were injected with nanoshells at 24 h before laser treatment, and perfusion was monitored using MRI. Whereas, heating with low (0.8 W cm^{-2}) and high (4 W cm^{-2}) laser intensities decreased contrast uptake, heating with an intensity of 2 W cm^{-2} almost doubled the uptake, thus highlighting the potential of nanoshells for improving drug delivery.

Nanoshells have also been demonstrated to modulate drug delivery. For example, Sershen *et al*. incorporated nanoshells with an 832 nm resonance into a thermally responsive polymer, *N*-isopropylacrylamide-*co*-acrylamide (NIPAAm), to create a photomediated drug delivery hydrogel composite [106, 107]. Hydrogels based on NIPAAm exhibit a lower critical solution temperature above which the hydrogel undergoes a reversible volume phase change transition. The nanoshells used in the experiment were engineered to have a core radius of 50 nm and shell thickness of 7 nm, in order to maximize absorption. When the composite is illuminated with a diode laser at 832 nm, the nanoshells convert light into heat, inducing a reversible and repeatable light-driven collapse of the composite hydrogel matrix. After 40 min of irradiation at 1.8 W cm^{-2}, the hydrogel composite had shrunk to 10% of its initial weight (Figure 1.23).

Recently, Bikram *et al*. demonstrated the potential value of nanoshell composites as drug delivery vehicles in specific applications [108]. In this case, hydrogels

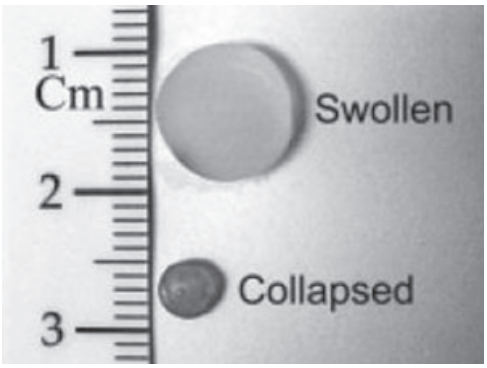

Figure 1.23 Swollen and collapsed nanoshell–polymer hydrogels. The change in volume is induced by heating [107].

containing 10^9 nanoshells ml^{-1} were swollen in solutions containing 10 mg ml^{-1} insulin, lysozyme and methylene blue, which was used as a model drug. When the release of each compound was monitored before and after laser irradiation, the release profiles of the embedded drugs upon irradiation were found to depend on their molecular weights. The release of methylene blue (14.1 mg g^{-1} polymer) and insulin (12.9 mg g^{-1}) occurred spontaneously, but the release of lysozyme occurred only upon laser irradiation. Moreover, the amounts of insulin and methylene blue released were approximately doubled on irradiation. Taken together, these results indicate that nanoshell-composite hydrogels have great potential for future drug delivery applications.

1.5.7
Tissue Welding

Nanoshells may represent a rapid means of treating lacerations in an emergency room setting. As an example, Gobin *et al*. have used nanoshells as an exogenous NIR absorber for welding deep tissue wounds [109]. In this study, a nanoshell-based solder (nanoshells + bovine serum albumin (BSA)) was applied to full-thickness incisions made on rats, after which the incisions were irradiated with NIR laser light for several minutes to initiate tissue welding. Notably, the healing results were similar to the suture–treat control group until day 5, after which healing was shown to be better in the suture group.

1.5.8
Biosensors

Nanoshells have several unique properties that are ideal for biosensing applications. The position of the plasmon resonance peak and absorbance depended heavily on the refractive index (dielectric constant) of the surrounding medium,

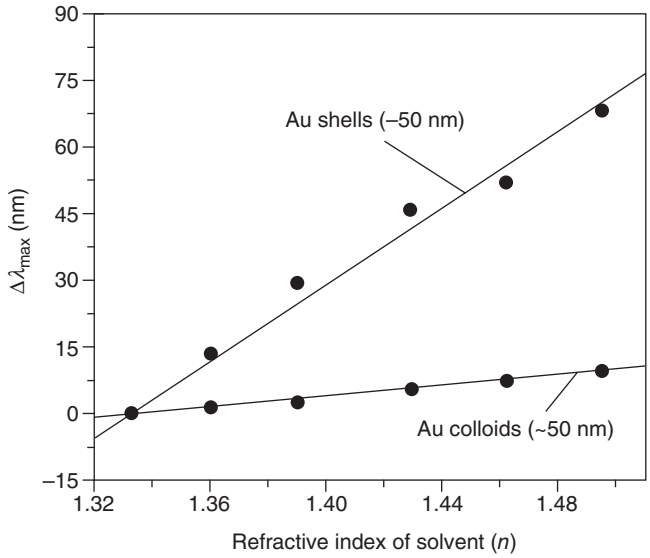

Figure 1.24 Linear relationship between shift in resonance peak and change in the index of refraction (n) of the surrounding environment. Nanoshells show greater sensitivity than nanospheres [70].

which is predicted by Mie theory [13]. As an example, Sun *et al.* have shown that gold nanoshells are more sensitive than nanospheres to changes in the refractive index (n) of the surrounding environment, and that the observed peak shift varies linearly with n [110] (Figure 1.24). In an aqueous medium, a 10% change in n corresponds to a substantial peak shift of approximately 50 nm – a finding which is consistent with the results of Tam *et al.*, who measured sensitivities of up to $\Delta\lambda/\Delta n = 555.4$ [111]. Thus, nanoshells exhibit optical sensitivity to the surrounding environment, a property which may be exploited to detect biomarkers in simple absorbance assays [112, 113].

Nanoshells can also be used to render conventional fluorophores sensitive to the surrounding environment, while protecting them from degradation. Recently, Chen *et al.* observed a fivefold enhancement of the fluorescence efficiency of a tetramethyl rhodamine dye molecule embedded within the silica core of a nanoshell [114]. The peak wavelength of the fluorophore was shifted by over 50 nm when the refractive index of the surrounding medium changed from 1.3 to 1.6.

Nanoshells are also capable of immensely amplifying SERS signals [31, 115] by many orders of magnitude (10^{12}–10^{15}) through strong electromagnetic near-field enhancement [13, 18], thus enabling exquisite detection in the picomolar range [116]. Typically, Raman signal strength scales as the electric field to the fourth power (E^4). The following examples serve to highlight the two primary methods for using nanoshells in biosensing schemes, namely absorbance and SERS measurements.

1.5.8.1 Absorbance-Based Biosensing

Several groups have demonstrated the use of biosensors for quantifying protein concentrations in diluted human whole blood, using bioconjugated nanoshells. Neither of the following applications requires any sample preparation, which represents a major advantage over other immunoassay techniques, such as enzyme-linked immunosorbent assay (ELISA). Wang *et al.* have developed a biosensor based on self-assembled gold nanoshell monolayers to optically transduce interactions between the vitamin biotin and streptavidin (a tetrameric bacterial protein) in a 20% blood solution [113]. The monolayer was grown on an APTES (amine-functionalized) glass slide, immersed in a cystamine solution, and then reacted with biotin–*N*-hydroxysuccinimide in a DMSO solution. After blocking with BSA to prevent nonspecific adsorption, the sensor was exposed to 20% whole blood with different concentrations of streptavidin for 1 h. Absorbance changes at 730 nm were measured with a UV/visible spectrophotometer in transmission mode. In this way, the sensor proved capable of the accurate and reproducible detection of streptavidin at concentrations ranging from 3 to 50 $\mu g\,ml^{-1}$.

Hirsch *et al.* have developed a nanoshell absorbance-based sensor, capable of detecting very low ($ng\,ml^{-1}$) concentrations of multivalent antigens in whole blood within 10–30 min [112]. This detection scheme is based on monitoring changes in the UV/visible spectrum as the analyte binding proceeds. Such binding results in nanoshell aggregation, which leads in turn to a decrease in extinction and a red-shifted broadening of the plasmon resonance peak [96]. In this experiment, PEGylated nanoshells were functionalized with rabbit anti-IgG, and the immunoassay was carried out to detect rabbit IgG successfully in 20% human whole blood, with a detection limit of 4.4 $ng\,ml^{-1}$ and good reproducibility.

Recently, Shuford *et al.* have developed and characterized a new variety of nanoshell, namely 'gold pyramidal shells' which, unlike their spherical brethren, are larger (~300 nm diameter), exhibit orientation-dependent spectra, and possess a unique TE-like plasmon mode in addition to the standard dipole and quadrapole resonances [117]. As the TE-like plasmon mode disappears when the pyramid's apex is altered, the authors speculated that pyramidal shells could be used in a 'sandwich' assay, in which the analyte binds to the tip and base of the pyramid.

1.5.8.2 SERS Biosensing

Qian *et al.* have demonstrated intense SERS signal enhancements using nanoshells for cancer cell detection [65]. PEGylated nanospheres with Raman reporter 3,3′-diethylthiatricarbocyanine iodide (DTTC), a NIR dye, were conjugated with EGFR antibody and incubated with head and neck Tu686 carcinoma cells. The PEGylated nanospheres enhanced the SERS signal enough to permit Raman molecular profiling studies of single cancer cells. For comparison, the nanoshells were found to be three times brighter than NIR-emitting quantum dots on a per volume basis, and more than 200 times brighter on a per particle basis, thus demonstrating the utility of nanoshells in sensitive detection schemes.

Beier *et al.* have investigated the use of gold nanoshell-based SERS as a novel platform for diagnosing Alzheimer's disease in its earliest stages, by detecting structure-specific forms of β-amyloid peptide, a biomolecule thought to be present

in the cerebrospinal fluid in miniscule, but pathologically distinguishable, concentrations [116]. β-Amyloid, which is a signature biomarker of the disease, aggregates to form senile plaques in the brains of Alzheimer's patients. At present, there is no method available for the definitive diagnosis of Alzheimer's disease pre-mortem, as any probable diagnosis is based on MRI imaging of the brain and cognitive function tests [118]. In this experiment, nanoshells were deposited uniformly onto a glass slide to form a monolayer, and then functionalized with cystamine bound to sialic acid, which has a high affinity for β-amyloid. The nanoshell slide was then immersed in solutions containing known amounts of β-amyloid for 30–45 min to permit binding. After rinsing, the slides were exposed to Congo Red, a SERS-active NIR dye which binds specifically to β-amyloid. After another round of rinsing, SERS measurements were performed, producing signal intensities sufficient for the detection of β-amyloid at concentrations as low as 1 p*M*. However, the signal contrast was not high enough to permit a definitive determination of concentration, which would certainly be valuable from a diagnostic standpoint.

In recent years, nanoshells and other gold nanoparticles have shown great promise as biosensors for quantifying very low concentrations of biomarkers, although many more investigations are required in order to refine this nascent technology for specific clinical applications.

1.6 Concluding Remarks

Because of their unique features and vast potential for a variety of biomedical applications, gold nanoshells and other gold nanoparticles represent a major achievement in nanotechnology. The synergy of ideal chemical, physical and optical properties in a single particle is a resounding affirmation of the promise of nanotechnology in general.

Gold nanoshells have opened new frontiers in medicine. Because they are biocompatible, optically tunable, strongly photoluminescent and bind to antibodies, nanoshells are highly suitable for *in vivo* imaging studies. Likewise, because they accumulate within tumors due to passive and active mechanisms, they hold great promise for revolutionizing cancer detection. Their success in multiple animal studies has confirmed a great potential as agents for photothermal cancer therapy, with the added benefit of serving as contrast agents for cancer detection. Clinical trials, which are currently under way, will most likely establish their efficacy for the treatment of human forms of cancer.

However, there are several pressing research problems, which are yet to be investigated. For example, what is the largest size tumor that nanoshells can effectively treat? And, can patient-specific antibodies be targeted to enhance their efficacy? It is hoped that, in the near future, these questions will be addressed and the novel properties of nanoshells will continue to be exploited in a growing number of applications. Clearly, it will be very exciting to see many existing applications make the successful transition from the laboratory bench to the clinic.

References

1 Park, J., Estrada, A., Sharp, K., Sang, K., Schwartz, J.A., Smith, D.K., Coleman, C., Payne, J.D., Korgel, B.A., Dunn, A.K. and Tunnell, J.W. (2008) Two-photon-induced photoluminescence imaging of tumors using near-infrared excited gold nanoshells. *Optics Express*, **16**, 1590–9.

2 Nanospectra Biosciences Inc. (2008) www.nanospectra.com (last accessed 26 June 2008)

3 Wu, C., Liang, X. and Jiang, H. (2005) Metal nanoshells as a contrast agent in near-infrared diffuse optical tomography. *Optics Communications*, **253**, 214–21.

4 Hirsch, L.R., Stafford, R.J., Bankson, J.A., Sershen, S.R., Rivera, B., Price, R.E., Hazle, J.D., Halas, N.J. and West, J.L. (2003) Nanoshell-mediated near-infrared thermal therapy of Tumors under magnetic resonance guidance. *Proceedings of the National Academy of Sciences of the United States of America*, **100**, 13549–54.

5 Leatherdale, C.A., Woo, W.K., Mikulec, F.V. and Bawendi, M.G. (2002) On the absorption cross section of CdSe nanocrystal quantum dots. *The Journal of Physical Chemistry B*, **106**, 7619–22.

6 Jain, P.K., Lee, K.S., El-Sayed, I.H. and El-Sayed, M.A. (2006) Calculated absorption and scattering properties of gold nanoparticles of different size, shape, and composition: applications in biological imaging and biomedicine. *The Journal of Physical Chemistry B*, **110**, 7238–48.

7 Wang, H., Huff, T.B., Zweifel, D.A., He, W., Low, P.S., Wei, A. and Cheng, J.X. (2005) In vitro and in vivo two-photon luminescence imaging of single gold nanorods. *Proceedings of the National Academy of Sciences of the United States of America*, **102**, 15752–6.

8 Yguerabide, J. and Yguerabide, E.E. (2001) Resonance light scattering particles as ultrasensitive labels for detection of analytes in a wide range of applications. *Journal of Cellular Biochemistry*, **84**, 71–81.

9 Eggeling, C., Widengren, J., Rigler, R. and Seidel, C.A.M. (1998) Photobleaching of fluorescent dyes under conditions used for single-molecule detection: evidence of two-step photolysis. *Analytical Chemistry*, **70**, 2651–9.

10 Widengren, J. and Rigler, R. (1996) Mechanisms of photobleaching investigated by fluorescence correlation spectroscopy. *Bioimaging*, **4**, 149–57.

11 Chan, W.C.W. and Nie, S. (1998) Quantum dot bioconjugates for ultrasensitive nonisotopic detection. *Science*, **281**, 2016.

12 Hohng, S. and Ha, T. (2004) Near-complete suppression of quantum dot blinking in ambient conditions. *Journal of the American Chemical Society*, **126**, 1324–5.

13 Averitt, R.D., Westcott, S.L. and Halas, N.J. (1999) Linear optical properties of gold nanoshells. *Journal of the Optical Society of America B*, **16**, 1824–32.

14 Stolik, S., Delgado, J.A., Pérez, A. and Anasagasti, L. (2000) Measurement of the penetration depths of red and near infrared light in human 'ex vivo' tissues. *Journal of Photochemistry & Photobiology B: Biology*, **57**, 90–3.

15 Ntziachristos, V., Ripoll, J., Wang, L.V. and Weissleder, R. (2005) Looking and listening to light: the evolution of whole-body photonic imaging. *Nature Biotechnology*, **23**, 313–20.

16 Chien, W.Y. and Szkopek, T. (2008) Multiple-multipole simulation of optical nearfields in discrete metal nanosphere assemblies. *Optics Express*, **16**, 1820–35.

17 Oldenburg, S.J., Hale, G.D., Jackson, J.B. and Halas, N.J. (1999) Light scattering from dipole and quadrupole nanoshell antennas. *Applied Physics Letters*, **75**, 1063.

18 Jackson, J.B., Westcott, S.L., Hirsch, L.R., West, J.L. and Halas, N.J. (2003) Controlling the surface enhanced Raman effect via the nanoshell geometry. *Applied Physics Letters*, **82**, 257.

19 Novotny, L. and Hecht, B. (2006) *Principles of Nano-Optics*, Cambridge University Press, Cambridge.

20 Mie, G. (1908) Beiträge zur Optik trüber Medien, speziell kolloidaler Metallösungen. *Annalen der Physik*, **330**, 377–445.

21 Prodan, E., Radloff, C., Halas, N.J. and Nordlander, P. (2003) *A Hybridization Model for the Plasmon Response of Complex Nanostructures*, American Association for the Advancement of Science, pp. 419–22.

22 Johnson, P.B. and Christy, R.W. (1972) Optical constants of the noble metals. *Physical Review B*, **6**, 4370–9.

23 Vial, A., Grimault, A.S., Macías, D., Barchiesi, D. and de la Chapelle, M.L. (2005) Improved analytical fit of gold dispersion: application to the modeling of extinction spectra with a finite-difference time-domain method. *Physical Review B*, **71**, 85416.

24 Jensen, T.R., Malinsky, M.D., Haynes, C.L. and Van Duyne, R.P. (2000) Nanosphere lithography: tunable localized surface plasmon resonance spectra of silver nanoparticles. *The Journal of Physical Chemistry B*, **104**, 10549–56.

25 Ishimaru, A. (1978) *Wave Propagation and Scattering in Random Media*, Academic Press, New York.

26 Westcott, S.L., Jackson, J.B., Radloff, C. and Halas, N.J. (2002) Relative contributions to the plasmon line shape of metal nanoshells. *Physical Review B*, **66**, 155431.

27 Nehl, C.L., Grady, N.K., Goodrich, G.P., Tam, F., Halas, N.J. and Hafner, J.H. (2004) Scattering spectra of single gold nanoshells. *Nano Letters*, **4**, 2355–9.

28 Haus, J.W., Zhou, H.S., Takami, S., Hirasawa, M., Honma, I. and Komiyama, H. (1993) Enhanced optical properties of metal-coated nanoparticles. *Journal of Applied Physics*, **73**, 1043.

29 van de Hulst, H.C. (1957) *Light Scattering by Small Particles. Light Scattering by Small Particles*, John Wiley & Sons, Inc., New York.

30 Aden, A.L. and Kerker, M. (2004) Scattering of electromagnetic waves from two concentric spheres. *Journal of Applied Physics*, **22**, 1242.

31 Campion, A. and Kambhampati, P. (1998) Surface-enhanced Raman scattering. *Chemical Society Reviews*, **27**, 241–50.

32 Beversluis, M.R., Bouhelier, A. and Novotny, L. (2003) Continuum generation from single gold nanostructures through near-field mediated intraband transitions. *Physical Review B*, **68**, 115433.

33 Boyd, G.T., Yu, Z.H. and Shen, Y.R. (1986) Photoinduced luminescence from the noble metals and its enhancement on roughened surfaces. *Physical Review B*, **33**, 7923–36.

34 Mooradian, A. (1969) Photoluminescence of metals. *Physical Review Letters*, **22**, 185–7.

35 Mohamed, M.B., Volkov, V., Link, S. and El-Sayed, M.A. (2000) The lightning rod effect in gold nanorods: fluorescence enhancement of over a million compared to the gold metal. *Chemical Physics Letters*, **317**, 517–23.

36 Clarke, M.., Kang, H., Yim, P., Kishore, R., Helmerson, K. and Hwang, J. (2008) Thermal properties of gold nanoshells in lipid vesicles studied by single particle tracking measurements. *Proceedings of SPIE*, **6849**, 68490H/1–68490H/9.

37 Aguirre, C.M., Moran, C.E., Young, J.F. and Halas, N.J. (2004) Laser-induced reshaping of metallodielectric nanoshells under femtosecond and nanosecond plasmon resonant illumination. *Journal of Physical Chemistry B*, **108**, 7040–5.

38 Kamat, P.V., Flumiani, M. and Hartland, G.V. (1998) Picosecond dynamics of silver nanoclusters. Photoejection of electrons and fragmentation. *The Journal of Physical Chemistry B*, **102**, 3123–8.

39 Lin, A., Hirsch, L., Lee, M.H., Barton, J., Halas, N., West, J. and Drezek, R. (2004) Nanoshell-enabled photonics-based imaging and therapy of cancer. *Technology in Cancer Research & Treatment*, **3**,

40 Oldenburg, S.J., Averitt, R.D., Westcott, S.L. and Halas, N.J. (1998) Nanoengineering of optical resonances. *Chemical Physics Letters*, **288**, 243–7.

41 Neeves, A.E. and Birnboim, M.H. (1989) Composite structures for the enhancement of nonlinear-optical susceptibility. *Journal of the Optical Society of America B: Optical Physics*, **6**, 787–96.

42 Averitt, R.D., Oldenburg, S.J., Halas, N.J., Sershen, S.R. and West, J.L. (2002) Temperature-sensitive polymer/nanoshell composites for photothermally. US Patent 6,428,811.

43 Oldenburg, S.J., Averitt, R.D. and Halas, N.J. (2004) Metal nanoshells. US Patent 6344272.

44 West, J.L., Halas, N.J., Oldenburg, S.J. and Averitt, R.D. (2004) Metal nanoshells for biosensing applications. US Patent 6699724.

45 West, J.L., Drezek, R., Sershen, S. and Halas, N.J. (2004) Optically-absorbing nanoparticles for enhanced tissue repair. US Patent 6685730.

46 Pham, T., Jackson, J.B., Halas, N.J. and Lee, T.R. (1998) Preparation and characterization of gold nanoshells coated with self-assembled monolayers. *Physics Letters*, **288**, 243.

47 Stober, W., Fink, A. and Bohn, E. (1968) Controlled growth of monodisperse silica spheres in the micron size range. *Journal of Colloid and Interface Science*, **26**, 62–9.

48 Duff, D.G., Baiker, A. and Edwards, P.P. (1993) A new hydrosol of gold clusters. 1. Formation and particle size variation. *Langmuir*, **9**, 2301–9.

49 Leff, D.V., Brandt, L. and Heath, J.R. (1996) Synthesis and characterization of hydrophobic, organically-soluble gold nanocrystals functionalized with primary amines. *Langmuir*, **12**, 4723–30.

50 Roosen, A.R. and Carter, W.C. (1998) Simulations of microstructural evolution: anisotropic growth and coarsening. *Physica A*, **261**, 232–47.

51 Phonthammachai, N., Kah, J., Jun, G., Sheppard, C., Olivo, M., Mhaisalkar, S., White, T. (2008) Synthesis of contiguous silica-gold core-shell structures: critical parameters and processes. *Langmuir*, **24** (9), 5109–12.

52 Wang, H., Goodrich, G., Tam, F., Oubre, C., Nordlander, P. and Halas, N.J. (2005) Controlled texturing modifies the surface topography and plasmonic properties of Au nanoshells. *Journal of Physical Chemistry B*, **109**, 11083–7.

53 Tang, L., Liu, L. and Elwing, H.B. (1998) Complement activation and inflammation triggered by model biomaterial surfaces. *Journal of Biomedical Materials Research*, **41**, 333–40.

54 Loo, C., Hirsch, L., Lee, M.H., Chang, E., West, J., Halas, N. and Drezek, R. (2005) Gold nanoshell bioconjugates for molecular imaging in living cells. *Optics Letters*, **30**, 1012–14.

55 Sokolov, K., Follen, M., Aaron, J., Pavlova, I., Malpica, A., Lotan, R. and Richards-Kortum, R. (2003) Real-time vital optical imaging of precancer using anti-epidermal growth factor receptor antibodies conjugated to gold nanoparticles 1. *Cancer Research*, **63**, 1999–2004.

56 Burns, R. (2005) *Immunochemical Protocols; Methods in Microbiology*, Humana Press.

57 Kumar, S., Aaron, J. and Sokolov, K. (2008) Directional conjugation of antibodies to nanoparticles for synthesis of multiplexed optical contrast agents with both delivery and targeting moieties. *Nature Protocols*, **3**, 314–20.

58 Jain, R.K. (1999) Transport of molecules, particles, and cells in solid tumors. *Annual Review of Biomedical Engineering*, **1**, 241–63.

59 James, W.D., Hirsch, L.R., West, J.L., O'Neal, P.D. and Payne, J.D. (2007) Application of INAA to the build-up and clearance of gold nanoshells in clinical studies in mice. *Journal of Radioanalytical and Nuclear Chemistry*, **271**, 455–9.

60 Zaman, R.T., Diagaradjane, P., Wang, J.C., Schwartz, J., Rajaram, N., Gill-Sharp, K.L., Cho, S.H., Rylander, H.G., III, Payne, J.D., Krishnan, S. and Tunnell, J.W. (2007) In vivo detection of gold nanoshells in tumors using diffuse optical spectroscopy. *IEEE Journal*, **13**, 1715–20.

61 Xie, H., Gill-Sharp, K.L. and O'Neal, D.P. (2007) Quantitative estimation of gold nanoshell concentrations in whole blood using dynamic light scattering. *Nanomedicine: Nanotechnology, Biology, and Medicine*, **3**, 89–94.

62 Dvorak, H.F., Nagy, J.A., Dvorak, J.T. and Dvorak, A.M. (1988) Identification and characterization of the blood vessels of solid tumors that are leaky to circulating macromolecules. *American Journal of Pathology*, **133**, 95–109.

63 Dedrick, R.L. (1973) Animal scale-up. *Journal of Pharmacokinetics and Pharmacodynamics*, **1**, 435–61.

64 Iyer, A.K., Khaled, G., Fang, J. and Maeda, H. (2006) Exploiting the enhanced permeability and retention effect for tumor targeting. *Drug Discovery Today*, **11**, 812–18.

65 Qian, X., Peng, X.H., Ansari, D.O., Yin-Goen, Q., Chen, G.Z., Shin, D.M., Yang, L., Young, A.N., Wang, M.D. and Nie, S. (2008) In vivo tumor targeting and spectroscopic detection with surface-enhanced Raman nanoparticle tags. *Nature Biotechnology*, **26**, 83–90.

66 Hainfeld, J.F., Slatkin, D.N., Focella, T.M. and Smilowitz, H.M. (2006) Gold nanoparticles: a new X-ray contrast agent. *British Journal of Radiology*, **79**, 248.

67 Hobbs, S.K., Monsky, W.L., Yuan, F., Roberts, W.G., Griffith, L., Torchilin, V.P. and Jain, R.K. (1998) Regulation of transport pathways in tumor vessels: role of tumor type and microenvironment. *Proceedings of the National Academy of Sciences*, **95**, 4607.

68 Niidome, T., Yamagata, M., Okamoto, Y., Akiyama, Y., Takahashi, H., Kawano, T., Katayama, Y. and Niidome, Y. (2006) PEG-modified gold nanorods with a stealth character for in vivo applications. *Journal of Controlled Release*, **114**, 343–7.

69 De Jong, W.H., Hagens, W.I., Krystek, P., Burger, M.C., Sips, A. and Geertsma, R.E. (2008) Particle size-dependent organ distribution of gold nanoparticles after intravenous administration. *Biomaterials*, **29** (12), 1912–19.

70 Fu, K., Sun, J., Bickford, L.R., Lin, A.W.H., Halas, N.J., Yu, T.K. and Drezek, R.A. (2008) Measurement of immunotargeted plasmonic nanoparticles' cellular binding: a key factor in optimizing diagnostic efficacy. *Nanotechnology*, **19**, 45103–9.

71 Choyke, P.L. and Kobayashi, H. (2006) Functional magnetic resonance imaging of the kidney using macromolecular contrast agents. *Abdominal Imaging*, **31**, 224–31.

72 Lewinski, N., Colvin, V. and Drezek, R. (2008) Cytotoxicity of nanoparticles. *Small*, **4**, 26–49.

73 Cai, W., Hsu, A.R., Li, Z.B. and Chen, X. (2007) Are quantum dots ready for in vivo imaging in human subjects? *Nanoscale Research Letters*, **2**, 265–81.

74 McDonald, D.M. and Baluk, P. (2002) Significance of blood vessel leakiness in cancer 1. *Cancer Research*, **62**, 5381–5.

75 Hashizume, H., Baluk, P., Morikawa, S., McLean, J.W., Thurston, G., Roberge, S., Jain, R.K. and McDonald, D.M. (2000) Openings between defective endothelial cells explain tumor vessel leakiness. *American Journal of Pathology*, **156**, 1363–80.

76 Yuan, F. (1995) Vascular permeability in a human tumor xenograft: molecular size dependence and cutoff size. *Cancer Research*, **55**, 3752–6.

77 Jain, R.K. (1987) Transport of molecules across tumor vasculature. *Cancer and Metastasis Reviews*, **6**, 559–93.

78 Monsky, W.L., Fukumura, D., Gohongi, T., Ancukiewcz, M., Weich, H.A., Torchilin, V.P., Yuan, F. and Jain, R.K. (1999) Augmentation of transvascular transport of macromolecules and nanoparticles in tumors using vascular endothelial growth factor 1. *Cancer Research*, **59**, 4129–35.

79 Li, M.L., Schwartz, J.A., Wang, J., Stoica, G. and Wang, L.V. (2007) In-vivo imaging of nanoshell extravasation from solid tumor vasculature by photoacoustic microscopy. *Proceedings of SPIE*, **6437**, 64370B.

80 Padera, T.P., Stoll, B.R., Tooredman, J.B., Capen, D., di Tomaso, E. and Jain, R.K. (2004) Pathology: cancer cells compress intratumour vessels. *Nature*, **427**, 695.

81 Merchant, B. (1998) Gold, the noble metal and the paradoxes of its toxicology. *Biologicals*, **26**, 49–59.

82 Choi, J., Burns, A.A., Williams, R.M., Zhou, Z., Flesken-Nikitin, A., Zipfel, W.R., Wiesner, U. and Nikitin, A.Y. (2007) Core-shell silica nanoparticles as fluorescent labels for nanomedicine. *Journal of Biomedical Optics*, **12**, 064007.

83 Shukla, R., Bansal, V., Chaudhary, M., Basu, A., Bhonde, R.R. and Sastry, M. (2005) Biocompatibility of gold

nanoparticles and their endocytotic fate inside the cellular compartment: a microscopic overview. *Langmuir*, **21**, 10644–54.

84 O'Neal, D.P., Hirsch, L.R., Halas, N.J., Payne, J.D. and West, J.L. (2004) Photo-thermal tumor ablation in mice using near infrared-absorbing nanoparticles. *Cancer Letters*, **209**, 171–6.

85 Stern, J.M., Stanfield, J., Kabbani, W., Hsieh, J.T. and Cadeddu, J.A. (2008) Selective prostate cancer thermal ablation with laser activated gold nanoshells. *The Journal of Urology*, **179**, 748–53.

86 Balduzzi, M., Diociaiuti, M., De Berardis, B., Paradisi, S. and Paoletti, L. (2004) In vitro effects on macrophages induced by noncytotoxic doses of silica particles possibly relevant to ambient exposure. *Environmental Research*, **96**, 62–71.

87 Shiohara, A., Hoshino, A., Hanaki, K., Suzuki, K. and Yamamoto, K. (2004) On the cyto-toxicity caused by quantum dots. *Microbiology and Immunology*, **48**, 669–75.

88 Etzioni, R., Urban, N., Ramsey, S., McIntosh, M., Schwartz, S., Reid, B., Radich, J., Anderson, G. and Hartwell, L. (2003) The case for early detection. *Nature Reviews Cancer*, **3**, 243–52.

89 Aaron, J., Nitin, N., Travis, K., Kumar, S., Collier, T., Park, S.Y., José-Yacamán, M., Coghlan, L., Follen, M. and Richards-Kortum, R. (2007) Plasmon resonance coupling of metal nanoparticles for molecular imaging of carcinogenesis in vivo. *Journal of Biomedical Optics*, **12**, 034007.

90 Loo, C., Lowery, A., Halas, N., West, J. and Drezek, R. (2005) Immunotargeted nanoshells for integrated cancer imaging and therapy. *Nano Letters*, **5**, 709–11.

91 Durr, N.J., Larson, T., Smith, D.K., Korgel, B.A., Sokolov, K. and Ben-Yakar, A. (2007) Two-photon luminescence imaging of cancer cells using molecularly targeted gold nanorods. *Nano Letters*, **7**, 941–5.

92 El-Sayed, I.H., Huang, X. and El-Sayed, M.A. (2006) Selective laser photo-thermal therapy of epithelial carcinoma using anti-EGFR antibody conjugated gold nanoparticles. *Cancer Letters*, **239**, 129–35.

93 El-Sayed, I.H., Huang, X. and El-Sayed, M.A. (2005) Surface plasmon resonance scattering and absorption of anti-EGFR antibody conjugated gold nanoparticles in cancer diagnostics: applications in oral cancer. *Nano Letters*, **5**, 829–34.

94 Mallidi, S., Larson, T., Aaron, J., Sokolov, K. and Emelianov, S. (2007) Molecular specific optoacoustic imaging with plasmonic nanoparticles. *Optics Express*, **15**, 6583–8.

95 Fournelle, M., Maass, K., Fonfara, H., Welsch, H.J., Hewener, H., Gunther, C. and Lemor, R.M. (2007) P6A-5 real-time optoacoustic imaging using near infrared absorbing gold nanoshells for contrast enhancement, Ultrasonics Symposium, IEEE, pp. 2417–20.

96 Rechberger, W., Hohenau, A., Leitner, A., Krenn, J.R., Lamprecht, B. and Aussenegg, F.R. (2003) Optical properties of two interacting gold nanoparticles. *Optics Communications*, **220**, 137–41.

97 Gobin, A.M., Lee, M.H., Halas, N.J., James, W.D., Drezek, R.A. and West, J.L. (2007) Near-infrared resonant nanoshells for combined optical imaging and photothermal cancer therapy. *Nano Letters*, **7**, 1929–34.

98 Stern, J.M. and Cadeddu, J.A. (2008) Emerging use of nanoparticles for the therapeutic ablation of urologic malignancies. *Urologic Oncology: Seminars and Original Investigations*, **26**, 93–6.

99 Everts, M., Saini, V., Leddon, J.L., Kok, R.J., Stoff-Khalili, M., Preuss, M.A., Millican, C.L., Perkins, G., Brown, J.M. and Bagaria, H. (2006) Covalently linked Au nanoparticles to a viral vector: potential for combined photothermal and gene cancer therapy. *Nano Letters*, **6**, 587–91.

100 Chance, B. (1991) Optical method. *Annual Review of Biophysics and Biophysical Chemistry*, **20**, 1–30.

101 Welch, A.J. and van Gemert, M.J.C. (1995) *Optical-thermal Response of Laser-irradiated Tissue*, Plenum Publishing Corp.

102 Diagaradjane, P, Shetty, A., Wang, J., Elliot, A., Schwartz, J., Shentu, S., Park,

C., Deorukhkar, A., Stafford, J., Cho, S., Tunnell, J.W., Hazle, J. and Krishnan, S. (2008) Gold nanoshell mediated hyperthermia enhances the efficacy of radiation therapy. *Proceedings of the SPIE*, **6895**, 68650N.

103 Patriarca, C., Bergamaschi, F., Gazzano, G., Corrada, P., Ordesi, G., Zanitzer, L., Di Pasquale, M., Giunta, P. and Campo, B. (2006) Histopathological findings after radiofrequency (RITA) treatment for prostate cancer. *Prostate Cancer and Prostatic Diseases*, **9**, 266–9.

104 Elliott, A.M., Stafford, R.J., Schwartz, J., Wang, J., Shetty, A.M., Bourgoyne, C., O'Neal, P. and Hazle, J.D. (2007) Laser-induced thermal response and characterization of nanoparticles for cancer treatment using magnetic resonance thermal imaging. *Medical Physics*, **34**, 3102.

105 Shetty, A., Elliott, A.M., Schwartz, J.A., Wang, J., Esparza-Coss, E., Klumpp, S., Taylor, B., Hazle, J.D. and Stafford, R.J. (2008) Use of gold nanoshells to mediate heating induced perfusion changes in prostate tumors. *Proceedings of SPIE*, **6842**, 68420S.

106 Sershen, S.R., Westcott, S.L., Halas, N.J. and West, J.L. (2002) Independent optically addressable nanoparticle-polymer optomechanical composites. *Applied Physics Letters*, **80**, 4609.

107 Sershen, S.R., Westcott, S.L., West, J.L. and Halas, N.J. (2001) An opto-mechanical nanoshell-polymer composite. *Applied Physics B: Lasers and Optics*, **73**, 379–81.

108 Bikram, M., Gobin, A.M., Whitmire, R.E. and West, J.L. (2007) Temperature-sensitive hydrogels with SiO_2–Au nanoshells for controlled drug delivery. *Journal of Controlled Release*, **123**, 219–27.

109 Gobin, A.M., O'Neal, D.P., Halas, N.J., Drezek, R. and West, J.L. (2005) near infrared laser tissue welding using nanoshells as an exogenous absorber. *Lasers in Surgery and Medicine*, **37**, 123–9.

110 Sun, Y. and Xia, Y. (2003) Synthesis of Gold Nanoshells and Their Use in Sensing Applications. Unconventional Approaches to Nanostructures with Applications in Electronics, Photonics, Information Storage and Sensing, as held at the 2003 MRS Spring Meeting, pp. 31–6.

111 Tam, F., Moran, C. and Halas, N. (2004) Geometrical parameters controlling sensitivity of nanoshell plasmon resonances to changes in dielectric environment. *The Journal of Physical Chemistry B*, **108**, 17290–4.

112 Hirsch, L.R., Jackson, J.B., Lee, A., Halas, N.J. and West, J.L. (2003) A whole blood immunoassay using gold nanoshells. *Analytical Chemistry*, **75**, 2377–81.

113 Wang, Y., Qian, W., Tan, Y. and Ding, S. (2008) A label-free biosensor based on gold nanoshell monolayers for monitoring biomolecular interactions in diluted whole blood. *Biosensors and Bioelectronics*, **23** (7), 1166–70.

114 Chen, X., He, S. and Choy, W. (2008) Highly efficient and tunable fluorescence of a nanofluorophore in silica/metal dual shells with plasmonic resonance. *Journal of Applied Physics*, **103** (2), 024301/1–024301/5.

115 Oldenburg, S.J., Westcott, S.L., Averitt, R.D. and Halas, N.J. (1999) Surface enhanced Raman scattering in the near infrared using metal nanoshell substrates. *The Journal of Chemical Physics*, **111**, 4729.

116 Cowan, C., Theresa, A., Beier, H.T., Cote, G. and Jackson, J.B. (2007) Application of surface enhanced Raman spectroscopy for detection of beta amyloid mediated by sialic acid, The 2007 Annual Meeting.

117 Shuford, K.L.; Lee, J.; Odom, T.W.; Schatz, G.C. (2008) Optical properties of gold pyramidal shells. *Journal of Physical Chemistry C*, **112** (17), 6662–6.

118 McKhann, G. (1984) Clinical diagnosis of Alzheimer's disease: report of the NINCDS-ADRDA Work Group under the auspices of Department of Health and Human Services Task Force on Alzheimer's Disease. *Neurology*, **34**, 939–44.

Keywords

gold nanoparticles; gold nanoshells; photothermal therapy; contrast agents; targeted cancer therapy; biosensors; cellular imaging.

2
Anisotropic Bimetallic/Oxide Nanomaterials for The Life Sciences

Jessica B. Graham, Megan E. Pearce and Aliasger K. Salem

2.1
Introduction

Anisotropic bimetallic/oxide nanomaterials, such as nanoparticles and nanorods, have been used in a variety of applications in the life sciences, ranging from sensing applications to vaccine and gene delivery systems. The development of new methods of nanoparticle preparation and nanoparticle surface modification have resulted in increased specific targeting capabilities, and has opened up this emergent technology to an even greater range of applications [1, 2]. Bimetallic nanoparticles show unique catalytic, electronic and optical properties in comparison to their individual metallic components [3]. Additionally, the large surface area-to-volume ratio of nanoparticles allows for different functionalities to be assigned to the separate segments of the nanorod, which greatly increases the flexibility of the system [4, 5]. In this chapter we introduce the development of the nanoparticle systems, followed by a description of the applications where they are beginning to show promise in the life sciences. Attention will be focused on the development of new imaging technologies, as well as on sensing, gene delivery and vaccination applications.

2.2
Synthesis and Functionalization of Anisotropic Bimetallic Nanoparticles

2.2.1
Nanorods

There are two main approaches to nanorod synthesis: (i) the 'top-down' approach, which utilizes hard template lithographic methods; and (ii) a 'bottom-up' approach, which uses seed mediation and has been developed to overcome some of the limitations to lithography [6]. A range of synthetic chemical methods have been used to construct metallic nanoparticles – most commonly using a mild chemical

Nanomaterials for the Life Sciences Vol. 3: Mixed Metal Nanomaterials. Edited by Challa S. S. R. Kumar

ISBN: 978-3-527-32153-7

reduction of metal salts in solution phase. Reducing agents such as sodium borohydride [4, 7–10], sodium citrate [11] and ascorbic acid [12] are added to the metal ion solutions containing metals such as Fe^{2+}, Ag^{+}, Cu^{2+} or Pd^{2+} [13]. In order to stabilize the particle, the metallic center can be combined with additional surfactants or polymers.

The development of a simple chemical synthetic method to produce multicomponent nanoparticles has been challenging. One-dimensional nanorod synthesis is dependent on allowing growth in only one direction while restricting growth in the other two directions. It is necessary to break the symmetry during the growth, in order to achieve these one-dimensional materials, and this becomes more difficult for multicomponent materials with distinct stoichiometries [14]. A few reports have been made of successful chemical synthetic approaches to produce multicomponent nanoparticles. For example, Jin *et al.* have prepared Ag–Au bimetallic colloids with hollow interiors and nanospikes by seeding with citrate-reduced silver nanoparticles [15]. The same method, but using gold nanorods as the seeds under alkaline conditions, led to the production of dumbbell-shaped Au–Ag core-shell nanorods (Figure 2.1) [4, 16]. Xiang *et al.* formed Au/Ag nanorods using Au nanorods as templates. Here, by using cetyltrimethylammonium bromide (CTAB) for surfactant-directed elongation, an anisotropic Ag coating was

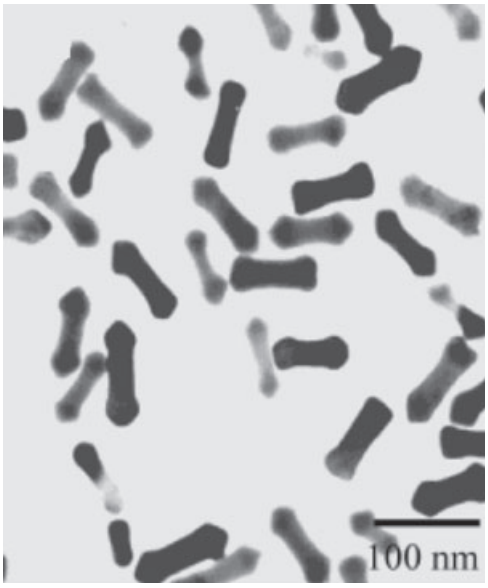

Figure 2.1 Transmission electron microscopy image of dumbbell-shaped Au/Ag nanoparticles. The contrast indicates the core-shell structure, with the bright segments indicating silver. Reprinted with permission from Ref. [4]; © 2004, American Chemical Society.

formed on the nanorods, yielding an orange segment-like shape for the Au/Ag nanorods [17].

2.2.2 Nanowires

More commonly, a template-directed synthesis involving either chemical or electrochemical deposition is used to create nanowires [16]. These methods can utilize either hard templates, such as block copolymers, carbon nanotubes and glass, or soft templates, including monolayers, vesicles, micelles and liquid crystals [18]. A monodisperse suspension of the individual particles occurs, such that the different segments of the nanowire can be functionalized [1]. In mechanical synthesis, multicomponent nanorods are often prepared by using a porous template, such as an alumina filtration membrane, and coating one side with a metal film to function as an electrode. The other side of the template is then submerged in the plating solution for electrodeposition. Depending on the strength and length of the current that is passed through, nanowires of different lengths can be formed. This method can be used to form large arrays of segmented wires with very complex striping patterns along the length of the wires. The reproducibility and monodispersity of rod samples has been improved over time, allowing the mass transport of ions and gases through the pores of the membrane. The most recent modifications include controlling the temperature with a recirculating temperature bath, and electroplating within an ultrasonication bath [19].

Walter *et al*. have prepared long bimetallic nanowires that are compositionally modulated along the axis of the nanowire, using a combination of electrochemical methods. By combining both the slow growth and nanowire growth forms of electrochemical deposition, the metals are 'wired' together using particles of one metal and nanowires of a second. This method allowed the creation of beaded bimetallic nanowires in parallel arrays, up to 1 mm in length [20].

The functionalization of nanoparticles allows for increased solubility, targeting properties, tracking and transportation [21–24]. The functionalization of multisegment nanorods can be localized to specific segments; this can be achieved by functionalizing using reactions that are specific to the surface chemistry of the individual metal segment. For example, nickel is usually functionalized with carboxylic acids that bind to the oxide layer on the metal, whereas gold nanorods are often functionalized with thiols [25]. Surface polymeric functionalization is another common approach that can also be integrated into the nanorod itself. For example, Mbindyo *et al*. have reported that an internal polymeric incorporation is possible for multifunctional arrangements. In between the metallic segments, these authors integrated 16-mercaptohexadecanoic acid polymer segments into striped nanowires. Then, by using a track-etched polycarbonate membrane that was coated with a 100 nm layer of gold, an electrodeposition method could be utilized, such that the monolayers of 16-mercaptohexadecanoic acid were gathered at the tip of the nanowires, and the electroless plating-added metal caps on top of the monolayer [26].

2.3 Applications in the Life Sciences

2.3.1 Biosensing

Nanosensors developed from nanorods and carbon nanotubes with semiconductor structures have garnered significant attention in the area of biosensing. Although specific protein-binding capabilities are necessary for the sensing of proteins or glucose, this is not without its own challenges, as protein binding is generally very nonspecific [27, 28].

Sheu *et al*. created a multicomponent system which comprised gold nanoparticles bound to *N*-(2-aminoethyl)-3-aminopropyl-trimethoxysilane (AEAPTMS)-pretreated silicon nanowires. The silicon nanowires were fabricated using scanning probe lithography and wet etching methods. A thiol-engineered enzyme, KSI-126C, was then bound to the gold nanoparticles on the surface of the wires. Following binding of the protein molecules and gold nanoparticles, shifts in the turn-on voltage were used to visibly demonstrate the system's efficacy [29]. Nanorods capable of sensing proteins at low concentrations with electrical detection may have many potential applications in the life sciences.

Meyer *et al*. have developed a multicomponent nanowire system for selective protein adsorption. In this study, gold–nickel nanowires which were approximately 10–35 μm long and 200 nm in diameter, were selectively functionalized with alkyl-terminated monolayers on nickel and hexa(ethylene glycol) (EG_6)-terminated monolayers on gold. In order to create a selective functionalization, metal-specific gold–thiol and nickel–carboxylic acid interactions were used. The (EG_6)-terminated monolayers were seen to reduce the protein adherence, while the immunoglobulin G (IgG) fluorescently tagged antibody proteins were adsorbed preferentially to the methyl-terminated nickel surfaces. The results of this study showed that a modification of nanostructures at the molecular level can lead to selective protein adsorption in localized specific regions [25, 30].

Another current area of research and development in the use of functionalized nanorods is that of glucose sensing. Today, over 18 million of the American population live with diabetes and must regularly monitor their blood glucose levels in order to know what foods they should eat, or if an insulin injection is necessary [31]. Because of the high demand for glucose monitoring, improved sensing methods are being sought. One type of recently developed composite electrode uses granular Teflon as a binder, mixed with carbon nanotubes that act as a conductor [32]. This combination allows for a low-potential detection of hydrogen peroxide (H_2O_2) and reduced nicotinamide adenine dinucleotide (NADH), it is feasible that, when combined with different oxidase and dehydrogenase enzymes, it might be used for glucose sensing. Glucose oxidase and alcohol dehydrogenase present in the complex transforms the bulk of the electrode complex into a reservoir for the enzyme, yielding signals of up to 2.4 μA. Detection is quite selective, and is not affected by the presence in the blood of acetaminophen (paracetamol)

or uric acid at voltages of 0.1–0.2 V. This combination of bulk electrodes, and the electronic properties of carbon nanotubes, provides the benefits of both components in a multifunctional structure [32].

One other rapidly developing application for nanorod components is in the area of pathogen sensing. Fu *et al*. have shown that Au/Si nanorods can be biofunctionalized with a fluorescent dye immobilized in the Si portion, with an anti-*Salmonella* antibody conjugated to the Au portion. In this way, a rapid and sensitive detection of the presence of *Salmonella* organisms can be measured due to the antigen–antibody reaction. Clearly, this application might be extended in the detection of other pathogens by substituting antibodies that would capture the detection microbe of interest [33].

2.3.2 Imaging

Nanorods can also be used for imaging applications, mainly because colloidal metal particles have a strong and broad absorption band that is absent from the bulk spectra. The surface modification of nanoparticles with protein and DNA molecules allows for sensing due to the size and shape-dependence of their optical properties. Nanowire optical labels can be formed from bimetallic nanowires that are adjusted along the axis of the nanowire. These multifunctional nanoparticles have significant potential for cancer-specific therapies and imaging agents. The sensitive spectral responses to the immediate environment of the nanoparticle surface provide strong scattering and absorption, allowing for a simple monitoring of the light signal [34–36]. The multicomponent nanorods can integrate different segments within a particle, to yield multiwavelength fluorescent tags. The use of ternary compounds (a–b–c) establishes band gap energies between a–b and b–c; then by altering the metallic composition of the nanorod the band gap of an active region can be designed.

Svensson *et al*. have developed a GaAsP segment with a direct band gap into a GaP nanowire [37]. As the GaP nanowire already has an indirect band gap, the segment functions as an optically active segment. The wires formed were approximately 2.8 μm in length and 60 μm wide, formed by metal organic vapor-phase epitaxy. The nanowires emitted light different wavelengths at room temperature when analyzed by a photoluminescence system. When the nanorods are grown with a PH_3 flow in parallel with AsH_3, the spectra are blue-shifted, depending on the PH_3 flow. These nanoparticle complexes have significant potential in biomedical analytical systems for optoelectronic tags.

2.3.3 Gene Delivery

In gene delivery, a major barrier to obtaining efficient gene transfection is delivering the plasmid DNA to the target cells. One way in which metallic nanoparticles have been applied to gene delivery techniques is through the coupling of gold

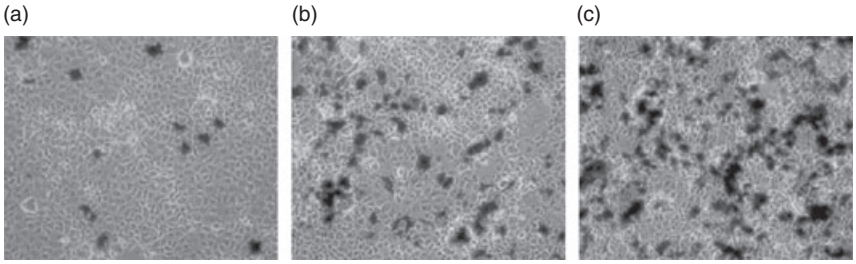

Figure 2.2 Histochemical staining with X-Gal of COS-7 cell cultures transfected in the presence of 10% serum with the β-gal gene mediated by polyethylenimine 2 (PEI2) and its derivatives. (a) PEI2 (N/P = 50); (b) PEI2–GNPII (N/P = 150); (c) PEI2–GNPII/dodecyl–PEI2 (N/P = 150 + 40). Reprinted with permission from Ref. [39]; © 2003, National Academy of Sciences.

nanoparticles (GNPs) to branched polyethylenimine (PEI), a nonviral polymeric delivery vehicle. Thomas and Klibanov used PEI chains with an average molecular weight of 2 kDa that were complexed with plasmid DNA and covalently attached to the GNPs [38]. The transfection efficiencies in COS-7 cells varied as a function of the molar ratio of PEI to gold in the complexes, with the most effective ratio being 12-fold more efficient than PEI alone. Additionally, linking PEI to the GNPs allowed transfection of 25% of the available cells, compared to just 4% with the unmodified PEI (Figure 2.2). To further enhance transfection, amphiphilic *N*-dodecyl-PEI was added during complex formation with the DNA, and provided transfection efficiencies that were an order of magnitude greater than with 25 kDa PEI, which is commonly used as a gene delivery vehicle. Transmission electron microscopy (TEM) imaging showed that the complexes had trafficked to the nucleus in less than 1 h after transfection.

Another approach to nanoparticle-mediated gene delivery is the application of photon irradiation to trigger biological activity [40]. These nanoparticle-based gene carriers have two functions: (i) delivery of the gene to the cell; and (ii) the switching on of the gene expression. The near-infrared (NIR) radiation used in this approach causes significantly less damage in comparison to UV-visible irradiation, and penetrates more deeply into the tissues for a better therapeutic potential [41, 42]. The enhanced green fluorescence protein (EGFP) gene has been conjugated to gold nanorods to track gene expression both *in vitro* and *in vivo*. Electrophoresis, UV-visible spectroscopy and TEM were each used to characterize the effects of NIR irradiation and discover the structural and optical properties of the nanorod complexes before and after laser treatment. When exposed to femtosecond NIR irradiation, the EGFP–gold nanorod complexes changed their sizes and shapes, releasing the DNA (Figure 2.3). Following transfection of the complexes into HeLa cells, and irradiation with the NIR sources as a low dose, GFP expressions was observed where the laser was applied. The adaptation of different cell targeting ligands can further enhance the nanorod gene delivery.

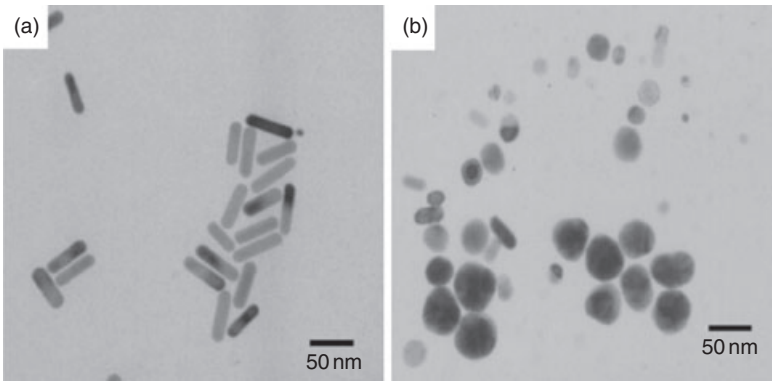

Figure 2.3 Typical TEM images of EGFP–gold nanorod conjugates (a) before and (b) after irradiation with laser beam (70 μJ per pulse for 60 s). Reprinted with permission from Ref. [40]; © 2006, Institute of Physics.

Rosi *et al.* have developed gene regulation agents for intracellular protein expression using gold nanoparticle–oligonucleotide complexes [43]. These modified nanoparticles resist degradation by nuclease activity, and also have higher affinity constants for their complementary nucleic acids than unmodified oligonucleotides. Antisense therapies have potential applications in cancer and AIDS therapy, by hybridizing with target messenger RNA (mRNA) sequences that downregulate specific protein expression. Because of transfection limitations of the oligonucleotides, and the increased transfection efficiency and stability of gold nanoparticles, the coupling of the two could be used as an antisense agent, scavenging intracellular RNA or DNA. By altering the DNA surface density on the gold nanoparticle, a high transfection efficiency with gene knockdown can be observed. Further development of this system could result in alternative therapies for gene regulation.

Recently, we have investigated the use of metallic nanorods for self-assembly and gene delivery applications, utilizing the ability to selectively functionalize different metal segments [44–47]. For example, two segment gold-nickel nanorods were selectively functionalized with the plasmid DNA on the nickel segment, and the cell targeting ligand transferrin on the gold segment. Transferrin is involved in receptor-mediated endocytosis, and can be used to promote cell uptake by this pathway. The nanorods were suspended in a 0.1 *M* solution of 3-[(2-aminoethyl)dithio] propionic acid (AEDP) to bind the DNA to the nickel electrostatically. Primary amine end groups spaced by a reducible disulfide linkage are established when the carboxylic acid terminus of the AEDP binds to the native oxide on the nickel segment. Rhodamine was also tagged to the transferrin to confirm the presence and location of the nanorods in the transfected cells. The transferrin and plasmid DNA did not interfere with each other due to spatial control over the binding. Figure 2.4 shows the cellular location and confirmation of transfection with

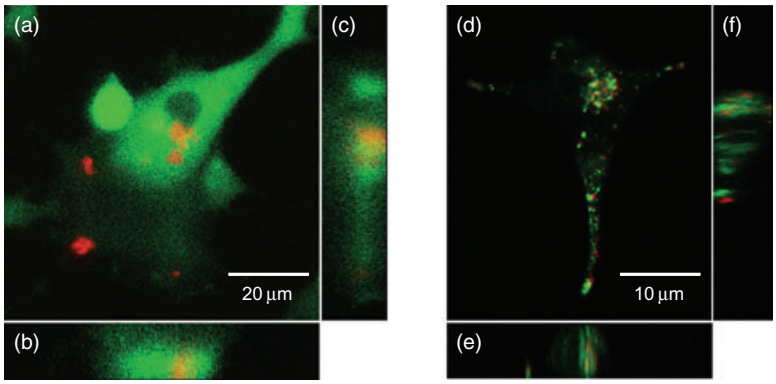

Figure 2.4 (a) A live HEK293 cell (red, 633 nm, green, 543 nm). Rhodamine (633 nm) identifies the subcellular location of the nanorods, while GFP expression (543 nm) provides confirmation of transfection; (b, c) Orthogonal sections confirm that the nanorods are located within the cell; (d) Confocal microscope stacked images of a live HEK 293 cell stained with Lysotracker Green identifying the location of the nanorods (rhodamine) in relation to acidic organelles in both orthogonal sections (e) and (f). Reprinted with permission from Ref. [44]; © 2003, Macmillan Publishers Ltd.

the GFP gene, while the scanning electron microscopy (SEM) and confocal microscopy images show cell internalization of the nanorods, and that they are located in acidic organelles or the cytoplasm. The addition of transferrin to the nanorods gave a fourfold increase in luciferase transgene expression when compared to nanorods with plasmid DNA alone in the human embryonic kidney (HEK293) cell line. The use of a gene gun for the ballistic delivery of the nanorods to the shallow subdermal layers of murine skin showed a strong and transient luciferase transgene expression. This approach has shown potential in genetic vaccination applications [44].

2.3.4 Vaccine Applications

As a follow-up to our study on multicomponent nanorods for nonviral gene delivery, we examined the nanorods' ability to enhance an antigen-specific immune response. The nickel–gold nanorods were engineered to include two additional molecules: ovalbumin (OVA), a model protein antigen, on the gold segments; and empty insert plasmids with immunostimulatory CpG sequences on the nickel segments. The body's immune system is activated when antigens are taken up by antigen-presenting cells (APCs), such as dendritic cells and macrophages. Antigens are processed in the APCs via class I or class II pathways. Typically, antigens alone are processed via the class II pathway; however, the class I pathway is critical to generating a strong CD8 T-cell response. CpG motifs can chaperone the antigen to be processed in the class I pathway, by binding to Toll receptor 9 [47–50]. For

this reason, the nanorods are critical for the codelivery of both the antigen and CpG to the same cell. The codelivery of CpG and OVA on the same nanorod gave a 10-fold increase in the CD8+ T-cell response compared to OVA delivery on the nanorods alone (Figure 2.5). Both, cellular and humoral antigen-specific immune responses can be generated by the nanorods to attack tumor cells and prevent recurrence [44, 51–53].

Polymeric materials such as chitosan and gold nanoparticles can be combined to produce DNA vaccine delivery systems. Chitosan, a natural cationic polysaccharide derived from crustacean shells, is nontoxic, and has good biocompatibility and a strong DNA-binding affinity, and is therefore an attractive polymer for DNA delivery. However, problems with low solubility at neutral pH and unstable polyplex formation with shorter chitosan monomer units have proven to be limitations in DNA delivery using chitosan alone. In a recent study, Zhou *et al.* investigated low-molecular-weight chitosans (6 kDa) that were attached covalently to gold nanoparticles for plasmid DNA delivery *in vivo* and *in vitro* [54]. Following intramuscular immunization in BALB/c mice, the complexes produced a serum antibody response that was 10-fold stronger than the DNA vaccine alone. The chitosan–gold nanoparticles also induced a 100-fold stronger cytotoxic T lymphocyte cellular response (even at low doses) than control groups. Although the modification of the chitosan delivery system with gold nanoparticles has provided an increased delivery efficiency, further studies are necessary to investigate the potential rate-limiting steps of the vaccine trafficking, such as the mechanism of DNA unpacking from the delivery device.

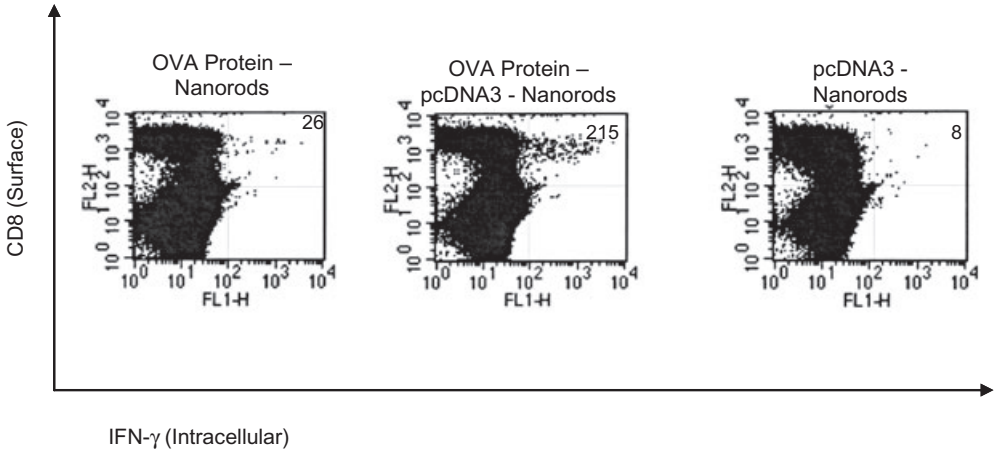

Figure 2.5 Ovalbumin-specific CD8 responses in C57BL/6 mice immunized with various antigen–nanorod particle formulations. C57BL/6 mice were immunized with control blank plasmid (CpG motif) bound to nanorods, ovalbumin antigen–nanorod formulation and an ovalbumin antigen/control blank pcDNA3 (CpG motif)–nanorod formulation via a gene gun. IFN-γ = interferon-γ. Reprinted with permission from Ref. [47]; © 2005, Institute of Physics.

2.4 Conclusions

In this chapter we have discussed some selected examples of anisotropic bimetallic/oxide nanomaterials in a variety of applications in the life sciences. The nanoparticles and nanorods can be used in protein and glucose sensing, DNA detection assays, targeted gene delivery and vaccine applications. By functionalizing the nanorod or nanoparticle, multiple functionalities can be introduced for targeting, imaging and delivery enhancement. Potential new applications and improvements to existing technologies continue to emerge in this dynamic field.

References

1 Wildt, B., Mali, P. and Searson, P.C. (2006) Electrochemical template synthesis of multisegment nanowires: fabrication and protein functionalization. *Langmuir*, **22** (25), 10528–34.

2 El-Sayed, M.A. (2001) Some interesting properties of metals confined in time and nanometer space of different shapes. *Accounts of chemical Research*, **34** (4), 257–64.

3 Hodak, J.H., Henglein, A. and Hartland, G.V. (2000) Coherent excitation of acoustic breathing modes in bimetallic core-shell nanoparticles. *Journal of Physical Chemistry*, **104** (21), 5053–5.

4 Huang, C.C., Yang, Z. and Chang, H.T. (2004) Synthesis of dumbbell-shaped Au-Ag core-shell nanorods by seed-mediated growth under alkaline conditions. *Langmuir*, **20**, 6089–92.

5 Henglein, A. (2000) Preparation and optical absorption spectra of AucorePtshell and PtcoreAushell colloidal nanoparticles in aqueous solution. *Journal of Physical Chemistry*, **104**, 2201–3.

6 Katz, E. and Willner, I. (2004) Integrated nanoparticle-biomolecule hybrid systems: synthesis, properties, and applications. *Chemical Informatics*, **43**, 6042–108.

7 Lu, L., H. Wang, Y. Zhou, S. Xi, H. Zhang, and B. Zhao (2002) Seed-mediated growth of large, monodisperse core-shell gold–silver nanoparticles with Ag-like optical properties. *Chemical Communications*, 144–5.

8 Wang, L., G. Wei, L.L. Sun, Z.G. Liu, Y.H. Song, T. Yang, Y.J. Sun, C.L. Guo and Z. Li (2006) Self-assembly of cinnamic acid-capped gold nanoparticles. *Nanotechnology*, **17** (12), 2907–12.

9 Gole, A. and Murphy, C.J. (2004) Seed-mediated synthesis of gold nanorods: role of the size and nature of the seed. *Chemistry of Materials*, **16** (19), 3633–40.

10 Lee, P.C. and Meisel, D. (1982) Adsorption and surface-enhanced Raman of dyes on silver and gold sols. *The Journal of Physical Chemistry*, **86**, 3391–5.

11 Pei, L.H., Mori, K. and Adachi, M. (2004) Formation process of two-dimensional networked gold nanowires by citrate reduction of $AuCl^{4-}$ and the shape stabilization. *Langmuir*, **20** (18), 7837–43.

12 Murphy, C.J., H. Wang, Y. Zhou, S. Xi, H. Zhang and B. Zhao (2005) Anisotropic metal nanoparticles: synthesis, assembly, and optical applications. *Journal of Physical Chemistry B*, **109** (29), 13857–70.

13 Glavee, G., K. Klabunde, C. Sorensen and G. Hadjipanayis (1995) Chemistry of borohydride reduction of Iron(II) and Iron(III) Ions in aqueous and nonaqueous media – formation of nanoscale Fe, Feb, and Fe2B powders. *Inorganic Chemistry*, **34** (1), 28–35.

14 Shankar, K.S. and Raychaudhuri, A.K. (2005) Fabrication of nanowires of multicomponent oxides: review of recent advances. *Materials Science and Engineering: C*, **25** (5-8), 738–51.

15 Jin, Y. and Dong, S. (2003) One-pot synthesis and characterization of novel

silver-gold bimetallic nanostructures with hollow interiors and bearing nanospikes. *Journal of Physical Chemistry B*, **107**, 12902–5.

16 Zou, X.Q., Ying, E.B. and Dong, S.J. (2007) Preparation of novel silver-gold bimetallic nanostructures by seeding with silver nanoplates and application in surface-enhanced Raman scattering. *Journal of Colloid and Interface Science*, **306** (2), 307–15.

17 Xiang, Y., X. Wu, D. Liu, Z. Li, W. Chu, L. Feng, K. Zhang, W. Zhou and S. Xie (2008) Gold nanorod-seeded growth of silver nanostructures: from Homogeneous coating to anisotropic coating. *Langmuir*, **24** (7), 3465–70.

18 Hurst, S.J., E.K. Payne, L.D. Qin and C.A. Mirkin (2006) Multisegmented one-dimensional nanorods prepared by hard-template synthetic methods. *Angewandte Chemie–International Edition in English*, **45** (17), 2672–92.

19 Martin, B.R., D.J. Dermody, B.D. Reiss, M. Fang, L.A. Lyon, M.J. Natan and T.E. Mallouk (1999) Orthogonal self-assembly on colloidal gold-platinum nanorods. *Advanced Materials*, **11**, 1021–5.

20 Walter, E.C., B.J. Murray, F. Favier and R.M. Penner (2003) 'Beaded' bimetallic nanowires: wiring nanoparticles of metal 1 using nanowires of metal 2. *Advanced Materials*, **15** (5), 396–9.

21 Wu, X.J., An, W. and Zeng, X.C. (2006) Chemical functionalization of boron-nitride nanotubes with NH_3 and amino functional groups. *Journal of the American Chemical Society*, **128** (36), 12001–6.

22 Nakanishi, M., H. Takatani, Y. Kobayashi, F. Hori, R. Taniguchi, A. Iwase and R. Oshima (2005) Characterization of binary gold/platinum nanoparticles prepared by sonochemistry technique. *Applied Surface Science*, **241** (1-2), 209–12.

23 Takatani, H., H. Kago, M. Nakanishi, Y. Kobayashi, F. Hori and R. Oshima (2003) Characterization of noble metal alloy nanoparticles prepared by ultrasound irradiation. *Reviews on Advanced Materials Science*, **5**, 232–8.

24 Mizukoshi, Y., T. Fujimoto, Y. Nagata, R. Oshima and Y. Maeda (2000) Characterization and catalytic activity of core-shell structured gold/palladium bimetallic nanoparticles synthesized by the sonochemical method. *Journal of Physical Chemistry B*, **104** (25), 6028–32.

25 Birenbaum, N.S., B.T. Lai, C.S. Chen, D.H. Reich and G.J. Meyer (2003) Selective noncovalent adsorption of protein to bifunctional metallic nanowire surfaces. *Langmuir*, **19** (23), 9580–2.

26 Mbindyo, J.K.N., T.E. Mallouk, J.B. Mattzela, I. Kratochvilova, B. Razavi, T.N. Jackson and T.S. Mayer (2002) Template synthesis of metal nanowires containing monolayer molecular junctions. *Journal of the American Chemical Society*, **124**, 4020–6.

27 Kong, J., N.R. Franklin, C. Zhou, M.G. Chapline, S. Peng, K. Cho and H. Dai (2000) Nanotube molecular wires as chemical sensors. *Science*, **287**, 622–5.

28 Alivisatos, P. (2004) The use of nanocrystals in biological detection. *Nature Biotechnology*, **22** (1), 47–52.

29 Sheu, J.T., C.C. Chen, P.C. Huang, Y.K. Lee and M.L. Hsu (2005) Selective deposition of gold nanoparticles on SiO_2 – Si nanowires for molecule detection. *Japanese Journal of Applied Physics Part 1 – Regular Papers Short Notes & Review Papers*, **44** (4B), 2864–7.

30 Fond, A.M., N.S. Birenbaum, E.J. Felton, D.H. Reich and G.J. Meyer (2007) Preferential noncovalent immunoglobulin G adsorption onto hydrophobic segments of multi-functional metallic nanowires. *Journal of Photochemistry and Photobiology A: Chemistry*, **186** (1), 57–64.

31 NIH (2005) Diabetes, in *NIH MedlinePlus Medical Encyclopedia*, U.S. National Library of Medicine and National Institutes of Health, Bethesda.

32 Wang, J. and Musameh, M. (2003) Carbon nanotube/teflon composite electrochemical sensors and biosensors. *Analytical Chemistry*, **75** (9), 2075–9.

33 Fu, J.E.A. (2008) An Au/Si hetero-nanorod-based biosensor for *Salmonella* detection. *Nanotechnology*, **19**, 155502.

34 Lee, K.S. and El-Sayed, M.A. (2006) Gold and silver nanoparticles in sensing and imaging: sensitivity of plasmon response to size, shape, and metal composition.

Journal of Physical Chemistry A, **110** (39), 19220–5.

35 Asaduzzaman, A.M. and Springborg, M. (2005) Structural and electronic properties of Au, Pt, and their bimetallic nanowires. *Physical Review B*, **72** (16), 165422–165429.

36 Nicewarner-Pena, S.R., R.G. Freeman, B.D. Reiss, L. He, D.J. Pena, I.D. Walton, R. Cromer, C.D. Keating and M.J. Natan (2001) Submicrometer metallic barcodes. *Science*, **294** (5540), 137–41.

37 Svensson, C.P.T., W. Seifert, M.W. Larsson, L.R. Wallenberg, J. Stangl, G. Bauer and L. Samuelson (2005) Epitaxially grown GaP/$GaAs_{1-x}Px$/GaP double heterostructure nanowires for optical applications. *Nanotechnology*, **16** (6), 936–9.

38 Thomas, M. and Klibanov, A.M. (2003) Conjugation to gold nanoparticles enhances polyethylenimine's transfer of plasmid DNA into mammalian cells. *Proceedings of the National Academy of Sciences of the United States of America*, **100** (16), 9138–43.

39 Thomas, M. and Klibanov, A.M. (2003) Conjugation to gold nanoparticles enhances polyethylenimine's transfer of plasmid DNA into mammalian cells. 100 (16), 9138–43.

40 Wang, A.A., J. Lee, G. Jenikova, A. Mulchandani, N.V. Myung and W. Chen (2006) Controlled assembly of multi-segment nanowires by histidine-tagged peptides. *Nanotechnology*, **17**, 3375–9.

41 Weissleder, R. (2001) A clearer vision for in vivo imaging. *Nature Biotechnology*, **19** (4), 316–17.

42 Vogel, A. and Venugopalan, V. (2003) Mechanisms of pulsed laser ablation of biological tissues. *Chemical Reviews*, **103** (5), 2079.

43 Rosi, N.L., D.A. Giljohann, C.S. Thaxton, A.K.R. Lytton-Jean, M.S. Han, C.A. Mirkin (2006) Oligonucleotide-modified gold nanoparticles for intracellular gene regulation. *Science*, **312** (5776), 1027–30.

44 Salem, A.K., Searson, P.C. and Leong, K.W. (2003) Multifunctional nanorods for gene delivery. *Nature Materials*, **2**, 668–71.

45 Salem, A.K., J. Chao, K.W. Leong, P.C. Searson (2004) Receptor-mediated self-assembly of multi-component magnetic nanowires. *Advanced Materials*, **16** (3): 268–271.

46 Salem, A.K., M. Chen, J. Hayden, K.W. Leong and P.C. Searson (2004) Directed assembly of multisegment Au/Pt/Au nanowires. *Nano Letters*, **4** (6), 1163–5.

47 Salem, A.K., C.F. Hung, T.W. Kim, T.C. Wu, P.C. Searson and K.W. Leong (2005) Multi-component nanorods for vaccination applications. *Nanotechnology*, **16** (4), 484–7.

48 Salem, A.K., A.D. Sandler, G.J. Weiner, X.Q. Zhang, N.K. Baman, X. Zhu and C.E. Dahle (2006) Immunostimulatory antigen loaded microparticles as cancer vaccines. *Molecular Therapy*, **13**, pS105.

49 Zhang, X.Q., C.E. Dahle, N.K. Baman, N. Rich, G.J. Weiner and A.K. Salem (2007) Potent antigen-specific immune responses stimulated by co-delivery of CpG ODN and antigens in degradable microparticles. *Journal of Immunotherapy*, **30** (5), 469–78.

50 Zhang, X.Q., C.E. Dahle, G.J. Weiner and A.K. Salem (2007) A comparative study of the antigen-specific immune response induced by co-delivery of CpG ODN and antigen using fusion molecules or biodegradable microparticles. *Journal of Pharmaceutical Sciences*, **96** (12), 3283–92.

51 Hung, C.F. and Wu, T.C. (2003) Improving DNA vaccine potency via modification of professional antigen presenting cells. *Current Opinion in Molecular Therapeutics*, **5** (1), 20–4.

52 Hung, C.F., W.F. Cheng, K.F. Hsu, C.Y. Chai, L.M. He, M. Ling and T.C. Wu (2001) Cancer immunotherapy using a DNA vaccine encoding the translocation domain of a bacterial toxin linked to a tumor antigen. *Cancer Research*, **61** (9), 3698–703.

53 Raychaudhuri, S. and Rock, K.L. (1998) Fully mobilizing host defense: building better vaccines. *Nature Biotechnology*, **16** (11), 1025–31.

54 Zhou, X.F., X. Zhang, X. Yu, X. Zha, Q. Fu, B. Liu, X. Wang, Y. Chen, Y. Shan, Y. Jin, Y. Wu, J. Liu, W. Kong, J. Shen (2008) The effect of conjugation to gold nanoparticles on the ability of low molecular weight chitosan to transfer DNA vaccine. *Biomaterials*, **29** (1), 111–17.

Abstract

Anisotropic bimetallic/oxide nanoparticles have shown significant potential in a variety of applications in the life sciences. Chemical and dimensional control can be achieved in the nanoparticles by incorporating multiple metallic segments. Functional biomolecules can be attached to the nanoparticles that correspond to the surface chemistry of the metallic segment. The high aspect ratio of the particles yields a large surface area for functionalization. These functionalized nanoparticles have applications that include imaging, protein and glucose sensing, gene regulation and delivery, and vaccinations.

Keywords

multifunctional nanorods; functionalization; imaging; gene delivery; vaccines.

3
Au—Pt Nanomaterials and Enzymatic Catalysts for Biofuel Cell Applications

Aurélien Habrioux, Karine Servat, Boniface Kokoh and Nicolas Alonso-Vante

3.1
Introduction

All systems which use a biocatalyst to transform chemical to electrical energy via electrochemical reactions involving biochemical pathways may be referred to as biofuel cells [1]. In order to facilitate kinetics improving the power density of biofuel cells, nanomaterials such as nanoparticles, nanofibers and mesoporous media, are used as hosts of enzyme immobilization [2]. Although the large surface area of these objects can increase the enzyme loading, the major requirement for a potential application of biofuel cells – as devices – is a high stability of the immobilized biological components. The main benefits of enzyme-based cathodes are their ability to reduce molecular oxygen without the formation of side products such as hydrogen peroxide. It has been reported that glucose oxidase (GOx) is an efficient anode at a pH value different from that of the main biocathodes (laccase) [3, 4]. In fact, its performance decreases when O_2 crosses over towards the anode, where this oxidant can be reduced to H_2O_2 that inhibits the anode enzyme. It has also been reported that glucose oxidation on GOx is a diffusion-controlled reaction process under steady-state conditions [1, 5]. Other fuels, such as ethanol, formic acid or lactic acid, are also utilized on the anodic side. In the process of seeking novel alternative energy sources, many research groups have shown a growing interest in biofuel cell systems because of environmental concerns. Such systems are, furthermore, attractive because of the cathode and bioelectrocatalytic improvements in the molecular oxygen reduction reaction. In parallel, recent advances in nanoscale science and technology continue to fuel a new wave of revitalization in the field of biocatalysts. In this sense, materials chemistry of various nanostructures have manifested their great potential in stabilizing and activating enzymes with performance well beyond the scope of traditional immobilization techniques [1, 2]. Therefore, in this chapter we explore the opportunities for developing the performance of enzymatic and metallic catalysts as a source of energy, taking into account the best of fuel cell systems and classical biofuel cell systems. For this reason, a description is provided of a new concentric design of biofuel cells based

Nanomaterials for the Life Sciences Vol. 3: Mixed Metal Nanomaterials. Edited by Challa S. S. R. Kumar

ISBN: 978-3-527-32153-7

on the use of tubular carbon tubes. Today, electrode nanomaterial synthesis with a controlled composition and a size distribution represents a major challenge; likewise, stability and durability are also major requirements for the development of stable, longlasting anodes for glucose oxidation. Alloys based on gold and platinum electrodes have been tested for their activity in several organic electro-oxidation reactions [6–8], and the use of Au–Pt materials as anodes in biofuel cells may permit the maintenance of cell biocompatibility in environmentally friendly applications. Indeed, these nanoalloys are currently being developed for biofuel cell systems as a source of renewable and sustainable power with a view to enhancing glucose oxidation. The use of gold–platinum nanoalloys also represents an innovation for the possible molecular oxidation of glucose at a lower potential. The gold–platinum nanocatalyst allows for a significant increase in biofuel cell performance, and it is indeed possible to envisage new applications for such a system. Unfortunately, this process is known to be sensitive to the metal electrode material and to the crystalline orientation of the electrode surface [9–11], and platinum electrodes may undergo self-poisoning during glucose oxidation in alkaline solution [12]. Nonetheless, gold electrodes continue to demonstrate interesting electrocatalytic activities for glucose oxidation, with no observable self-poisoning.

As shown schematically in Figure 3.1, within the electro-oxidation mechanism, glucose is transformed to α- and β-pyranose in aqueous solution via a chemical reaction between the aldehyde group and the secondary alcohol in the C5-position, such that these anomeric forms become electroactive species of glucose. Oxidation of the carbon (two- electron) at the C1-position on noble metals (Pt or Au) proceeds by dehydrogenation. Furthermore, the lactone undergoes hydrolysis in solution to form gluconic acid.

A second pathway consists of transforming the carbon in the C6-position on the noble metal electrode. Oxidation of the primary alcohol resembles the so-called methanol oxidation (four-electron). Moreover, the synthesis of glucaric acid occurs by the oxidation of either gluconic acid (4 e^-) or glucuronic acid (2 e^-).

3.2 Oxygen Reduction Reaction (ORR)

The oxygen reduction reaction (ORR) is relevant to both fundamental electrochemistry and materials science. This cathodic process occurs in a low-temperature fuel cell and is dependent on the nature of the catalysts, the reaction proceeding in two parallel reaction pathways: (i) the direct reduction of O_2 to H_2O (in acid solution) or OH^- ions (in alkaline solution); and (ii) an indirect pathway with H_2O_2 (in acid solution) or HO_2^- (in alkaline solution) as intermediates. The reactions in acid solution are as follows:

Direct reduction:

$$O_2 + 4\ H^+ + 4\ e^- \rightarrow 2\ H_2O \qquad E = 1.23\ V/NHE \tag{3.1}$$

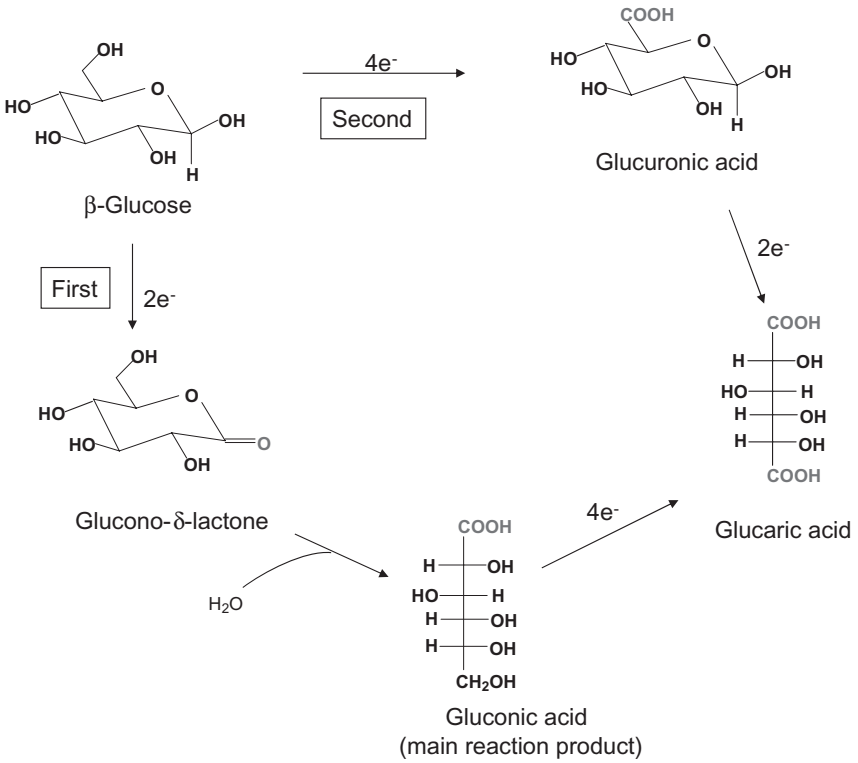

Figure 3.1 The mechanism of glucose electro-oxidation in an aqueous medium, showing the first or second electron charge transfer pathways.

Indirect reduction:

$$O_2 + 2\,H^+ + 2\,e^- \rightarrow H_2O_2 \qquad E = 0.682\ \text{V/NHE} \tag{3.2}$$

$$H_2O_2 + 2\,H^+ + 2\,e^- \rightarrow 2\,H_2O \quad E = 0.77\ \text{V/NHE} \tag{3.3}$$

Electrocatalysis of this multielectron charge-transfer reaction implies that the oxygen bond must be weakened at the electrode surface atoms. The adsorption of this molecule can take place in an *end-on* form. However, this is not a favorable geometry to weaken the O—O bond sufficiently, and the reaction in Equation 3.2 is favored, whereas bridged or bidentate bonding of the O_2 to a surface two metal atoms will favor the reaction in Equation 3.1. The experimental observations confirm that the direct reduction pathway is more labile to poisoning than the indirect pathway [13]. The technique that has proved ideal for the study of the ORR is the rotating ring disk electrode (RRDE), where the generated intermediate (H_2O_2) is itself electroactive and can be oxidized to molecular oxygen at the ring

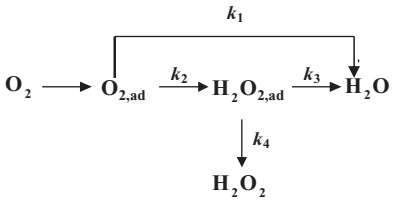

Figure 3.2 The kinetic model proposed by Damjanovic *et al.* [15] for molecular oxygen reduction.

(Pt) of the RRDE. The current of the process In Equation 3.2, j_{ind_red}, can be analyzed as the measured ring current: $j_R = N\, j_{ind\_red}$., where N is the collection efficiency of the RRDE system. Therefore, a ratio j_{ind_red}/j_{dir_red}, ≈0.01 indicates that a four-electron pathway dominates. This is the case for metals such as platinum, platinum-based compounds and ruthenium clusters [14], as the main channel is the four-electron charge-transfer process (96%), thus leading to the formation of water. A complete analysis of parallel processes can be performed following the scheme of Figure 3.2 [15].

3.2.1
ORR Metal Catalysts

It has long been recognized that platinum and platinum-group transition metals are the most active materials for the ORR process. Platinum and platinum-based materials are the main components for the anode and cathode of the technically most advanced fuel cells that exist to date [13, 16–19]. Although, perhaps the biggest concern is the high cost and rarity of platinum, the research groups are also confronted by issues that a cathode material must possess (at least):

- A high electrochemical activity
- Chemical stability
- A high selectivity
- Electrical conduction.

It must also be recalled that much insight into the ORR has been gained based on electrochemical measurements on well-defined (hkl) surfaces [13, 20–22].

Aside from the numerous studies reported on polycrystalline electrodes [23–25], the reactivity of Pt–M alloys (M = Fe, Pd, Ni, Cr, Mn, Co) has been addressed. Here, the focus is to enhance catalytic activity by modifying the electronic structure (d-band) of Pt. The increase in the d-band vacancy per atom, as a function of the electron affinity of the alloying element, has been probed using X-ray absorption spectroscopy (XAS) [26]. Furthermore, the d-band vacancy parameter is shown to decrease with the increasing size of the platinum nanodivided material (the 'particle size effect') [27]. These electronic and geometric factors are also modulated by the applied electrode potential and species present in the electrochemical cell.

Electronic and geometric factors are also responsible for electrocatalysis, and in this connection novel materials have been tailored within a cluster-like structure, and further developed in powder or colloidal forms [28].

3.2.2 ORR Enzymatic Catalysts

Although enzymatic catalysts are in general highly selective, it is only that portion of the enzyme located near the electrode surface that is really effective. Consequently, in an economically efficient process the enzymes must be confined strictly to the close vicinity of the electrode surface.

3.2.2.1 Techniques Used for Enzyme Immobilization

One key issue in the development of enzyme-based biofuel cells is to improve the immobilization methods, thereby increasing the performance and lifetime of the enzyme molecules. For this reason, it is necessary to be able to control not only the orientation of the immobilized biomolecule but also the distance between the active center of the enzyme and the substrate. Nondeformation of the protein structure during the immobilization step leads to a better stability of the enzyme molecule. During the past few years, many different methods to immobilize biomolecules have been developed, such that it is now possible to immobilize enzymes into an electropolymerized film, to entrap biocatalysts with a polymer membrane, or to bind the enzyme covalently at the electrode surface. The electropolymerization method involves applying an appropriate potential to the working electrode, which is soaked in an aqueous solution containing both enzyme and monomer molecules. As a result, those enzymes in the immediate vicinity of the electrode surface are thus incorporated into the growing polymer. Various reports have been made describing the use of different polymers such as polypyrrole [29], polyaniline [30] or polyphenol [31, 32]. The formed polymer may be either conductive or nonconductive, according to the electrochemical conditions used for electropolymerization and the nature of the monomer. The main interest in developing a conducting three-dimensional (3-D) polymer is the possibility of using polymer fibers for electron transfer between the enzyme and substrate molecules. In this way it is possible to proceed to an electrochemical growth of the polymer by a variety of methods, including chronoamperometry, potentiometry [5] or cyclic voltammetry [29]. Unfortunately, the chronoamperometric method leads to nonreproducible 3-D polymeric films due to variations in the current response from sample to sample [29]. Whichever method is used, however, the thickness of the polymer film can be controlled by employing the relationship of equivalence between current and matter [29]. Consequently, the voltammetric method of electropolymerization has been shown to lead to more homogeneous and compact films [33]. The immobilization of enzyme molecules into these types of film can be preceded by a single enzymatic adsorption step [34].

Another means of immobilizing enzymes involves entrapping the biomolecules into a polymer matrix, and for this a variety of polymers have recently been used,

including chitosan or Nafion. Chitosan is derived from chitin and is insoluble above pH 6.3 due to nonprotonation of the amino groups. As these two polymers possess both hydrophobic and hydrophilic moieties, it is possible to observe the formation of micellar structures which are more stable than surfactant micelles [35]. The enzymatic immobilization can occur into the pore structures of the polymer [36]. The structure and size of the pores can also be modified by chemical modification of polymers. In fact, it has been shown that the modification of Nafion with hydrophobic ammonium salts leads to an exchange of the ammonium cation for the proton on the sulfonic acid group, which in turn increases the hydrophobicity of the polymer [37]. It has also been clearly shown that the modification of chitosan by grafting alkyl chains allows the formation of a more hydrophobic polymer [38]. Nevertheless, when the size and hydrophobicity of the polymer are increased, the size of the micelles increases but the number of micellar structures decreases [39]. Moreover, the chitosan matrix presents good mechanical properties [40] (good adhesion, high permeability towards water) and offers the possibility to disperse carbon nanotubes [41] that can be used as a substrate to promote direct electron transfer in enzymatic reactions. On most occasions, the chitosan and enzymes are crosslinked using a glutaraldehyde solution that causes a not only loss of enzymatic activity but also of the control of polymer thickness. In order to overcome these problems, a new method of chitosan electrodeposition has been investigated in which chitosan (which is positively charged under acidic conditions) can be simply deposited on a negatively charged electrode in response to an applied voltage. In this process, control of the polymer thickness depends only on the deposition time [42].

Recently, Heller's group developed another method of enzyme immobilization that consisted of wiring the enzyme molecules to the electrode surface with a redox osmium-based polymer [43–45]. In all previous methods, the mediator was immobilized with the enzyme or was free in solution, but in the case of immobilization by entrapment into a polymeric matrix the problem of mediator leaching arises [3]. Such a problem may also cause a total loss in the electrochemical activity of the enzymatic electrode and, as a result, the polymer will bind the enzyme molecule to form a 3-D structure. The electrons are then transferred by the redox polymer, which is permeable to the substrate. The major interest in this type of immobilization is the nondiffusion of a mediator into a polymeric layer and a reduction of the distance between redox centers of enzymes and redox centers of the osmium polymer.

Antigen–antibody recognition is a method which has been used to produce glucose oxidase [46], laccase [47] and horseradish peroxidase electrodes [48]. This technique allows a step-by-step deposition of enzyme layers, for which the affinity between avidin and biotin is very often used. Most often, a *N*-hydroxysuccinimide function is grafted onto the electrode, and this allows a biotin derivative to be linked onto the surface [49]. Later, a monomolecular layer of enzyme conjugated avidin can be deposited. Anicet *et al*. found that it was possible to control the number of deposited enzymatic layers, and have explained the mediator diffusion limitation in such layers. The same group also showed the enzymatic activity to

be stable (only 10% loss for a glucose electrode over a period of 40 days), and to be initially the same as when in solution [46].

The final method of enzyme immobilization involves covalent binding of the enzyme molecule to the electrode surface, with a defined communication. The grafting of enzyme molecules has been achieved by functionalization of the electrode surface with amino groups and reticulation between the amino groups of the protein and those of the surface with a molecule such as glutaraldehyde. Such an immobilization procedure has been shown to provide great stability of laccase electrodes [47, 50]. Moreover, the performances obtained with a grafted laccase electrode have also been shown to be higher than those with a laccase electrode built by molecular recognition (avidin–biotin system) [47]. Recently, a new approach for enzyme immobilization was developed that involved direct binding the redox active center of the biomolecule to the electrode surface by a defined pathway. This type of immobilization requires the use of nanomaterials, such as carbon nanotubes or gold nanoparticles, as electrical connectors. Carbon nanotubes allow a favorable orientation of the surface [51] and interact directly with the redox active center to realize an electrical connection.

3.2.2.2 Enzymatic Reduction of Oxygen to Water

Different enzymatic pathways of O_2 reduction to water have been investigated. In general, the enzymes used are laccase and bilirubin oxidase, which are multicopper oxidases. The major interest of this type of catalyst is the ability to directly reduce oxygen to water at higher potentials than platinum catalysts [52], and without the formation of H_2O_2 during the process. These two enzymes contain four Cu^{2+}/Cu^{+} active centers which are classified as three types namely T_1, T_2 and T_3. The T_1 site is responsible for the electro-oxidation of the electron-donating substrate, while a trinuclear cluster composed of one T_2 site and two T_3 sites is responsible for the reduction of oxygen [53, 54]. The mechanism associated with the oxygen reduction reaction is shown in Figure 3.3. During the process, four electrons are provided by the T_1 site, and consequently the trinuclear center is in a fully reduced state. Subsequently, the T_2 and T_3 centers interact with the O_2

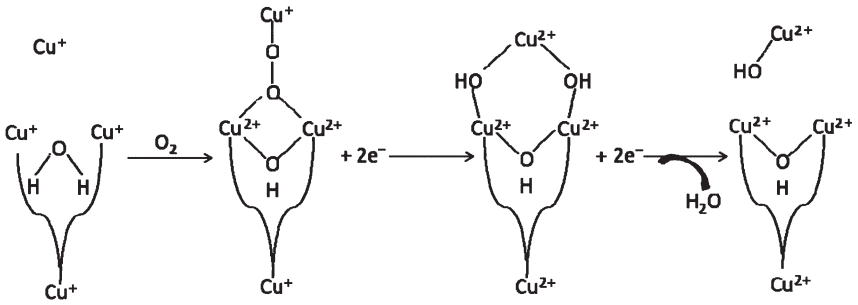

Figure 3.3 Schematic view of the molecular oxygen reduction reaction catalyzed by multicopper oxidases.

molecule to form a peroxide-level intermediate that is then reduced to a hydroxide ion.

3.2.2.2.1 **Oxygen Reduction Catalyzed by Laccase** Laccase is a multicopper oxidase that catalyzes the oxidation of several aromatic compounds and some inorganic compounds, with the concomitant reduction of oxygen to water. According to the microorganism from which it is extracted, laccase presents very different redox potential values ranging from 430 to 780 mV (versus NHE) for the T_1 site. In fact, the sequence of amino groups near the T_1 site explains the different potentials [55]. With regards to the mechanism of substrate oxidation, kinetic measurements performed with laccase have shown that reduction of the T_1 site occurs before that of the T_2 site, which is followed by an intramolecular electron transfer to the two T_3 sites [56]. From a thermodynamic point of view, laccase from *Trametes versicolor* is a very attractive enzyme in the field of biofuel cells. as the formal potential of the T_1 site of this enzyme is approximately 780 mV (versus NHE) [57] and is higher than most of the T_1 sites of other sources of laccase. In the case of mediated electron transfer, in order to minimize the loss of voltage at the cathode, it is necessary to use a mediator that has a formal potential close to that of the T_1 site. Two approaches are possible for mediated electron transfer.

The first approach is based on the use of classical small mediator molecules, among which can be included 2,2-azinobis-3-ethylbenzothiazoline-5-sulfonic acid (ABTS), ferrocene (0.405 V versus SCE at pH 4) [55], potassium ferricyanide (0.119 V versus SCE at pH 4) [55] or syringaldazine [58]. It has been reported that the optimal pH value for laccase electrodes depends on the substrate used. For example, Xu *et al*. have shown that the optimum range of pH value is between 5 and 8 when phenolic substrates are used as substrates, but lower than 7 for non-phenolic substrates [59]. Among these mediators, $ABTS^{\bullet-}$ presents the better formal potential and it exhibits two quasi-reversible systems the half-waves of which are 0.469 V and 0.870 V (versus Ag/AgCl in an acetate buffered solution, pH 5) [60]. The optimum pH of laccase-mediated ABTS electrodes was shown to be 3 in a citrate–phosphate-buffered solution [55]. The optimum working temperature was shown to be between 40 and 50 °C, while the activation energy associated to oxygen reduction was 52.5 kJ mol^{-1} and the turnover approximately 1400 s^{-1} [61]. Moreover, Palmore *et al*. [55] have shown that the rate of reduction of $ABTS^{-}$ at the cathode exceeds the rate at which $ABTS^{2-}$ is oxidized by O_2. Hence, it can be concluded that the rate-determining step at the cathode is the reduction of O_2 to water. The performances of this type of electrode are known to be higher than those of platinum electrodes. For example, in a pH 4 acetate-buffered solution, the open-circuit potential in an oxygenated solution are 0.34 V and 0.28 V (both versus SCE) for platinum and glassy carbon electrodes, respectively, compared to 0.5 V (versus SCE) for a laccase-ABTS electrode. The effect of pH on laccase-ABTS electrodes is shown in Figure 3.4.

The second approach to mediated electron transfer is based on entrapment of the enzyme into films of metalloporphyrins composed of osmium [62], ruthenium [63] and iron complex polymers [63]. Nevertheless, it has been shown that in a pH

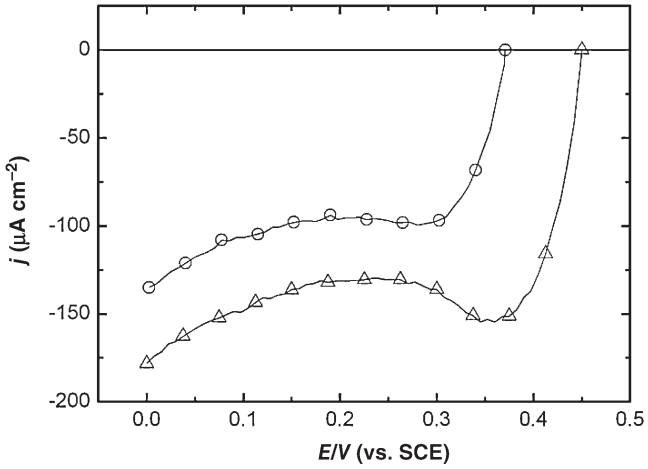

Figure 3.4 Effect of pH (3: △ and 5: ○) on the electrocatalytic behavior of laccase-ABTS electrode. Scan rate = 5 mV s^{-1}.

4.5 citrate-buffered solution, mediators such as $[Ru(CN)_6]^{4-/3-}$, [Fe(2,2′;-bypiridine)]$^{2+/3+}$ and [Fe(1,10-phenanthroline)$_3$]$^{2+/3+}$ are not efficient when they are associated with laccase. This phenomenon may be due to the fact that their redox potentials are high (0.68 V, 0.86 V and 0.9 V versus Ag/AgCl, respectively), as compared to the redox potential of the T_1 site of laccase [63].

When the redox potential of a mediator increases, then the rate of electron transfer will decrease; in fact, the latter rate becomes very low when the redox potential is close to or superior to the redox potential of the T_1 site of laccase. Consequently, osmium polymers only seem capable of providing good current densities when they mediate the electron charge transfer between the laccase and the electrode. Barrière *et al*. have shown that a laccase electrode modified with [Os(bipyridine)$_2$(poly(*N*-vinylimidazole)$_2$]Cl_2, which possesses a redox potential of 0.4 V (versus Ag/AgCl) delivers current densities of approximately 240 μA cm^{-2} at pH 5 [63].

At present, the wiring of laccase by osmium polymers introduced by Heller's group gives the best results for the oxygen reduction reaction. This consists of immobilizing laccase by crosslinking into the redox hydrogel containing a high density of $Os^{2+/3+}$ centers. This polymer possesses an eight atom-long flexible tether between the osmium centers, and a polymer backbone leading to a high electron diffusion coefficient of 7.6×10^{-7} cm^2 s^{-1}. This is most likely due to the flexibility of the eight-atom chain, allowing mobility of the osmium centers. The resultant laccase electrodes deliver an oxygen reduction current density of 860 μA cm^{-2} compared to 560 μA cm^{-2} when no spacer is used. Moreover, the overpotential observed for the oxygen reduction reaction is lower than on a platinum wire. In fact, laccase electrode reaches 90% of its limiting current density at only –0.07 V (versus O_2/H_2O at pH 5) against –0.4 V (versus O_2/H_2O) for the platinum wire [64]. Nevertheless, numerous studies have shown that, laccase electrodes

produce negligible current densities at neutral pH and/or in the presence of chloride ions. Barrière *et al*. reported that, at pH 7, only 7% of the activity determined at pH 5 was retained when the osmium polymer-modified laccase electrode was used for the oxygen reduction reaction [63]. This observation was confirmed by Barton *et al*., who showed that at pH 7 with a chloride concentration approaching 100 m*M*, most laccases are inactive [62]. However, this loss of activity might depend on the substrate and the source of laccase. One study which was conducted on several sources showed that laccase from *Coriolus hirsutus, Coriolopsis gallica* and *Pleurotus ostreatus* retained only 40% of their activity when the chloride concentration was near 100 m*M* in a 0.2 pH 5 citrate-buffered solution. In the same study, laccase from *C. hirsutus* and *C. gallica* was shown to be inactive at pH 7 while, under the same conditions, laccase from *P. ostraetus* seemed capable of retaining, at pH 7, 20% of its activity at pH 5 [62]. It should be noted here that this inactivity may also be a function of the substrate used. In fact, it has been shown that laccase from *P. ostreatus* and *C. gallica* retained, at pH 7, 70% of its activity at pH 5 for the oxidation of syringaldazine [65]. It has also been shown that laccase from *Trametes versicolor* has an optimum pH value of 4.7 when $Os(bpy)_2Cl_2^{2+/3+}$ was used as mediator [66].

In the case of a direct electron transfer (DET), the current densities obtained with a laccase electrode were improved with an enzyme immobilized on carbon nanocomposite, as shown by Tarasevich *et al*. [67]. Recently, an interesting DET was demonstrated between the enzyme and a glassy carbon-modified carbon nanotube electrode. In this study, an electrocatalytic current associated to oxygen reduction appeared at 530 mV (versus SCE) in a phosphate-buffered solution at pH 6.0 [68]. Such a pH value allows this type of electrode to be used in biofuel cells, while the DET eliminates problems linked to the use of a mediator. In most cases, however, the laccase electrodes studied in biofuel cells employed a mediated electron transfer (MET).

3.2.2.2.2 **Reduction of Oxygen Catalyzed by Bilirubin Oxidase** The major interest in using bilirubin oxidase as a catalyst for molecular oxygen reduction reactions is its ability not to be inhibited by the chloride anions present in physiological media over a concentration range from zero to 1 *M*, as demonstrated by Mano and coworkers [69]. At a higher concentration of chloride (>1.5 *M*), such inhibition is due to specific binding between cupric ions and chloride [70]. Hence, this enzyme offers the possibility to build electrodes with good efficiency at physiological pH [69, 71, 72]. Bilirubin oxidase naturally catalyzes the oxidation of bilirubin to biliverdin, with concomitant O_2 reduction [73]. The amino acid sequence of bilirubin oxidase is very close to that of other multicopper oxidases such as laccase. The enzyme contains one T_1 site, one T_2 site and two T_3 sites, exactly as does laccase. The T_1 site accepts electrons from organic substrates before relaying them to the dioxygen reduction site, which is composed of T_2 and T_3 sites [70]. It has been shown that the formal potential of the T_1 site depends on the nature of the axial ligand used [74]. Replacement of glutamine by methionine leads to a positive shift for the redox potential of T_1 site [75]. The most frequently used sources of bilirubin

oxidase are from *Myrothecium verrucaria* [73] and *Trachyderma tsunodae* [69]; both are monomeric proteins with approximate molecular weights of 66 [73] and 64 kDa, respectively [69]. The isoelectric point of bilirubin oxidase is approximately pH 4 [76], which means that under physiological conditions bilirubin oxidase exists as a polyanion. The redox potential of the T_1 site of bilirubin oxidase from *M. verrucaria* is close to 670 mV (versus NHE), while that of *T. tsunodae* is between 650 and 750 mV (versus NHE) [77]. The redox potential of the T_2 site is approximately 400 mV (versus NHE) [77]. In terms of thermal stability, the activity of bilirubin oxidase from *T. tsunodae* has been shown to increase up to 40 °C but to decline rapidly after 60 °C [69]. In the case of bilirubin oxidase from *M. verrucaria* the activity increased up to 60 °C [70]. It has also been shown that the oxidation of bilirubin to biliverdin, catalyzed by bilirubin oxidase, can involve the formation of H_2O_2 during O_2 reduction [78]. Hence, it can be concluded that the main product of oxygen reduction reaction depends on the nature of the oxidized substrate. It is also clear that the amount of H_2O_2 formed depends on the quantity of oxygen in the system [79]. Nevertheless, RRDE studies conducted using osmium polymers as electrochemical mediators for the reduction of oxygen catalyzed by bilirubin oxidase from *M. verrucaria* led to a negligibly low current on the ring, demonstrating a lack of H_2O_2 formation during the reduction process [70]. When $ABTS^{2-}$ is used as a substrate, indirect observations realized by estimating the decrease in oxygen concentration have shown the stoichiometric ratio of $ABTS^{2-}$: oxygen to be 4 : 1, and in agreement with the fact that no H_2O_2 hydrogen peroxide formation occurs during the process [71]. A second observation has been made regarding the duration of oxygen consumption by a bilirubin oxidase-$ABTS^{2-}$ electrode. In fact, such duration is unaffected by the addition of catalase, which is able to catalyze the dismutation of H_2O_2 [71]. The results of this experiment show, indirectly, that H_2O_2 is not formed during the reduction of oxygen by bilirubin oxidase when $ABTS^{2-}$ is used as an electron mediator, and hence the catalytic performance of bilirubin oxidase electrodes depend on the substrate. Rather, the potential at which the bioelectrocatalytic current appears is a function of the redox potential of the electron mediator; namely, the higher the redox potential of the electrochemical mediator, the higher the formal potential of the bioelectrode. However, if the thermodynamic gap between the redox potential of the electron mediator and that of the enzyme's T_1 site is not large enough, the reaction rate of the oxygen reduction will be low [80]. Different types of mediator, which may be classified into two groups, have been investigated. The first group comprises small molecules, while the second group comprises redox polymers, such as those of osmium. The first group of mediators, which may either be immobilized onto the electrode surface [72] or remain free in solution [71], included molecules such as $ABTS^{2-}$ (0.469 V versus Ag/AgCl in a pH 5 acetate-buffered solution [60]), $[W(CN)_8]^{3-/4-}$ (0.314 V versus Ag/AgCl at pH 5 [80]), $[Os(CN)_6]^{3-/4-}$ (0.444 V versus Ag/AgCl at pH 5 [80]) and $[Mo(CN)_8]^{3-/4-}$ (0.577 V versus Ag/AgCl at pH 5 [80]). Among these electrochemical mediators, only $ABTS^{2-}$ [71] and $[W(CN)_8]^{3-/4-}$ lead to relatively high current densities [80]. The use of bilirubin oxidase–$ABTS^{2-}$ electrodes for oxygen reduction reaction leads, for example, to the appearance of a bioelectrocatalytic

current at 430 mV (versus SCE) and a current density of $-350\,\mu A\,cm^{-2}$ at 0.1 V (versus SCE) in a phosphate-buffered solution at pH 7.4 under steady-state conditions [72]. The catalytic performances of a bilirubin oxidase–$ABTS^{2-}$ electrode, where the enzyme and mediator are adsorbed chemically onto the carbon electrode surface before immobilization in an electropolymerized polypyrrole film, are shown in Figure 3.5. In this figure, it can be seen clearly that polymer thickness is an important parameter in order for the electrode to acquire a high efficiency. In fact, a thin film leads to the problem of mediator loss, while a thicker polypyrrole film leads to the formation of a more crosslinked matrix, implying a difficult access to the active site of the enzyme. Electron transfer between the substrate and enzyme also becomes more difficult under these conditions.

In the case of bilirubin oxidase–$ABTS^{2-}$ electrodes, it has been reported that the oxidation of $ABTS^{2-}$ occurs at an optimum pH value of 4.0 [81]. Moreover, the Michaelis constant for $ABTS^{2-}$ is $11\,\mu mol\,l^{-1}$, while that for oxygen has been calculated as $51\,\mu mol\,l^{-1}$ [71]. It has been shown that the catalytic performance of these electrodes can depend on the ionic strength of the solution [71]. Hence, when Tsujimura *et al.* studied the influence of ionic strength by adjusting it with potassium chloride, they found that an increase in ionic strength from 0.1 *M* to 0.2 *M* led to a 45% decrease in the catalytic current [71]. The second method of rendering bilirubin oxidase electrodes capable of reducing molecular oxygen efficiently is based on the use of redox polymers such as osmium polymers [69]. When bilirubin oxidase is adsorbed solely onto the electrode surface, only those active centers located near the surface will be electroactive. In the case of entrapment in a redox

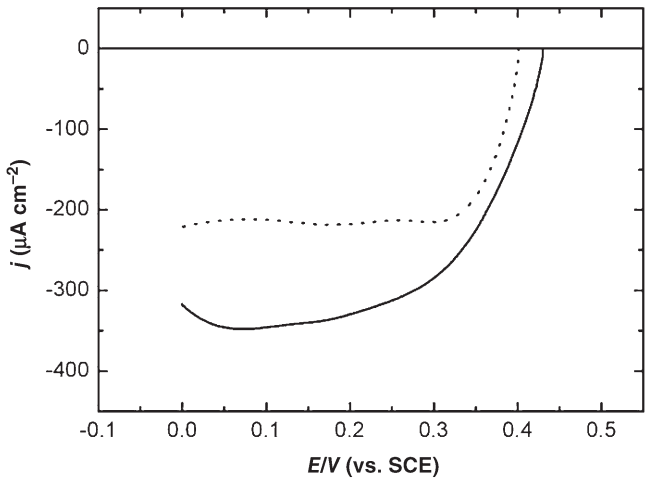

Figure 3.5 Polarization curves displaying catalytic performances of bilirubin oxidase–$ABTS^{2-}$ electrodes with species immobilized into an electropolymerized polypyrrole film with thickness of 1.4 μm (solid line) and 2.8 μm (dotted line). Results were obtained in a 0.2 *M* phosphate-buffered solution (pH 7.4). Scan rate = $5\,mV\,s^{-1}$.

polymer, the electrons can be transferred in the hydrogel, thus increasing the number of active centers. The composition of the film is an important parameter in this approach, however. For example, by using bilirubin oxidase from *T. tsunodae*, the optimized catalyst has been estimated to contain 44.6 wt% of enzyme, 6.9 wt% of PEGDGE, and 48.5 wt% of osmium-based redox polymer which has a redox potential at 350 mV (versus Ag/AgCl) for a total loading of 0.6 mg cm^{-2} [69]. It is important to note here that, in the presence of oxygen, these catalysts present an open-circuit potential of 530 mV (versus Ag/AgCl at pH 7.4), which represents an overpotential of only 26 mV for the oxygen reduction reaction [69]. Oxygen electroreduction to water, catalyzed by a bilirubin oxidase from *M. verrucaria* wired with an osmium polymer, delivers a current density of 0.73 mA cm^{-2} at 0.25 V (versus Ag/AgCl) [70] in a physiological phosphate-based buffer. A degree of improvement in this catalytic performance has been achieved by using an alternative source of enzyme. In fact, the use of bilirubin oxidase from *T. tsunodae* involves a catalytic current density of 0.88 mA cm^{-2} at only 0.3 V (versus Ag/AgCl) [69]. This improvement was due to a difference in the amino acid sequence near the T_1 site, which led to an increase in the redox potential of the T_1 site. Moreover, the electrode exhibited a wide range of optimum pH values between 7.5 and 10.5 [69], and an excellent stability under running conditions. Following six days of continuous working, the wired electrode with bilirubin oxidase from *T. tsunodae* as catalyst lost only 5% of its activity per day [69] (compared to a 10% loss when bilirubin oxidase from *M. verrucaria* was used as catalyst [70]). Following a three-week storage period, the activity of the electrode was approximately 95% of the initial activity [69]. Such excellent stability of this type of electrode might be explained by the electrostatic bonding that exists between the enzyme and the polymer wire, although in serum-wired bilirubin oxidase the cathode loses its activity within only a few hours [70]. Such loss of activity occurs in the presence of oxygen, and has been attributed to the binding of one or several cupric ions, and with a product derived from the oxidation of urate catalyzed by bilirubin oxidase [82]. This loss of activity can be reduced, however, by adding chloride ions or by the application of a Nafion film to the catalyst [82]. It has also been shown that wired bilirubin oxidase electrodes may be stored in deoxygenated serum in the presence of urate, as this allows the Cu centers to be maintained in their reduced state [4]. A high stability of bilirubin oxidase electrodes can also be achieved by creating a covalent attachment of enzymes on a functionalized electrode surface. In order to obtain such stability, it is also possible to entrap the bilirubin oxidase in a quaternary ammonium salt-treated Nafion polymer, as this provides a good environment for stabilization of the enzyme [83]. With regard to mediator-free studies, a direct electron transfer has been demonstrated between *M. verrucaria* bilirubin oxidase and a graphite electrode [84]. Likewise, Weigel *et al.* have shown that a direct electron transfer may occur when bilirubin oxidase is linked covalently to multiwall carbon nanotubes. Here, the half-wave potential for the oxygen reduction reaction was 350 mV (versus Ag/AgCl) at pH 7 [85], with higher current densities being expected when bilirubin oxidase was immobilized by electrostatic interaction in multiple layers with a poly-L-lysine film. This type of

electrode delivers a current density of $-845\,\mu A\,cm^{-2}$ at 1400 rpm in an oxygen-saturated solution at pH 7 [76], the half-wave potential of the reduction wave being 0.33 V (versus Ag/AgCl).

3.3 Glucose Oxidation

3.3.1 Process on Metal Electrodes

The electrocatalytic oxidation of glucose on metals has been widely reported [12, 86–95], with platinum being the most extensively studied electrode material [96–98]. The initial target when using platinum as the anode catalyst in a biofuel cell is to reduce the overpotential with regards to glucose oxidation. Indeed, it is well known that platinum activates the dehydrogenation of organic molecules at potentials below 0.5 V (versus RHE). It is also known that platinum-based materials are more stable than enzymes, and highly sensitive to self-poisoning in glucose electro-oxidation [90, 91], as their surface becomes rapidly blocked by chemisorbed intermediates. In order to solve this problem, a range of studies were conducted on bimetallic electrodes. Subsequently, it was reported that platinum surfaces modified by heavy metals such as Tl, Pb, Bi or W, showed a catalytic activity for glucose oxidation [99] that increased in line with the pH of the electrolytic solution. However, the dissolution and toxicity of these heavy metal elements have prevented such systems from being further developed. As an example, Mallouk *et al.* [96] investigated the glucose electro-oxidation on Pt alloys constituted by Pb, Au, Pd and Rh, and concluded that Pt–Pb alloys exhibited the highest electrocatalytic activity. This observation was confirmed by Becerik and coworkers [100], who showed that Pt–Bi and Pt–Pb materials, when incorporated into a polypyrrole matrix, were the most active catalysts for the oxidation of glucose in a physiological, phosphate-buffered solution. In attempting to improve the glucose oxidation, other bimetallic compositions were investigated, initially via the synthesis of gold and platinum nanoparticles. It is well known that gold–platinum alloys cause an increase in the oxidation current densities of organic molecules when compared to pure platinum [101], with such increase being attributed to the presence of gold in the alloy. Later, Jin and coworkers [95] examined glucose oxidation catalyzed by Pt–Au prepared by a coreduction method from metallic salts, and showed the oxidation peak of glucose to occur at a much lower potential than on the gold electrode alone. These authors also showed that both metals favored the dehydrogenation of the glucose molecule, but concluded that the presence of gold led to a much weaker adsorption of the phosphate species onto the platinum surface. The biocompatibility of, and interest in, these gold–platinum nanocomposites for the oxidation of glucose have led to a scrutinizing of their properties, the aim being to better understand any link between the physical structure of the materials and their activity towards glucose oxidation.

3.3.1.1 Synthesis and Structural Properties of Gold–Platinum Nanoparticles

3.3.1.1.1 Synthesis A wide variety of gold–platinum nanoparticle synthetic processes have been explored, including Polyol [102], sol–gel [103], water-in-oil microemulsion [104], electrodeposition [105] and Bönnemann [106]. The structural properties of the nanoparticles are highly dependent on the synthetic method used and which, for most of the time, is based on the coreduction of chloroauric acid and chloroplatinic acid. In this process, the nanoparticles are either entrapped in a matrix [103] or supported on carbon black (Vulcan XC-72, Vulcan XC-72 R) [106, 107]. In the following section, only those results relating to the synthesis of gold–platinum nanoparticles via the water-in-oil microemulsion method will be described. The term microemulsion defines a fine emulsion obtained by stirring two immiscible liquids, of which the thermodynamic stability is assured by an emulsifier molecule. According to Capek *et al.*, when the emulsifier concentration exceeds the critical micelle concentration (CMC), the emulsifier molecules form micelles that are responsible for the solubilization of hydrophilic compounds in the oil phase [108]. A stabilization of nanodroplets of water into the oil phase then occurs. The mixing of a microemulsion containing a reducing agent in the aqueous phase with a microemulsion containing one or several metal precursors in the aqueous phase, allows metallic nanoparticles to be obtained following the collision of water droplets. The nanoparticles produced can then be cleaned and dispersed onto a carbon support. In the system described here, *n*-heptane is used as the oil phase, a nonionic polyethyleneglycol-dodecylether serves as the emulsifier molecule, and sodium borohydride as the reducing agent. This choice is one among various, but the emulsifier molecule determines the flexibility and interfacial tension of the surfactant film, and consequently the properties of the micelles. Two other important parameters – namely the choice of reducing agent and the water-to-surfactant molar ratio – determine the size of the micelles and of the nanoparticles obtained [109]. The most commonly used reducing agents include hydrazine [110] and sodium borohydride [111]. Many groups have noted that the key problem when using nanoparticles synthesized via microemulsion methods for electrocatalytic reactions is the removal of any surfactant shell that might block the active sites of the catalyst. Chemical treatments to overcome this problem have included washing the catalyst with organic solvents [112], while thermal treatments have been shown to lead to a sintering of the particles and a consequent reduction in the catalyst's active surface area [113].

3.3.1.1.2 Structural Properties Wide-angle X-ray scattering (WAXS) analysis, performed on a 40 wt% metal loading of Pt, $Au_{70}Pt_{30}$ and Au catalysts, allows acquisition of the corrected pattern and fitted profile (solid line), as shown in Figure 3.6.

The fit with five Pearson VII functions provides two important parameters, namely the accurate peak positions, *br*, and the integral line width *db* in reciprocal b-space. These are plotted in Figure 3.7 (black circles) and, as a result of the best fit (open circles), it is possible to obtain three parameters – the mean crystallite

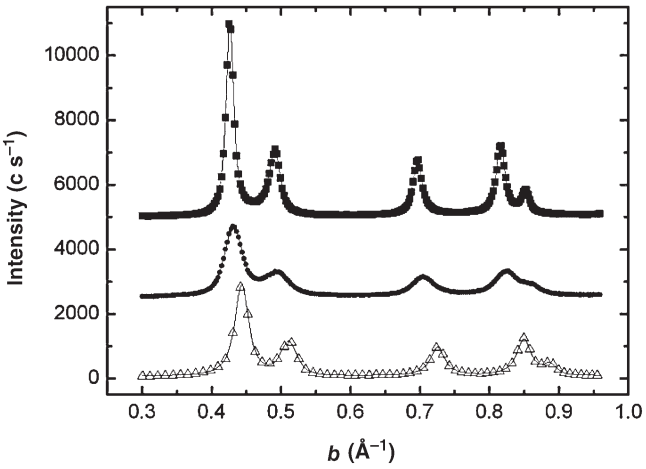

Figure 3.6 Diffraction patterns of Pt, $Au_{70}Pt_{30}$ and Au samples (from bottom). Experimental points are shown as symbols, and fitted profiles as a continuous line. The curves are shifted upwards.

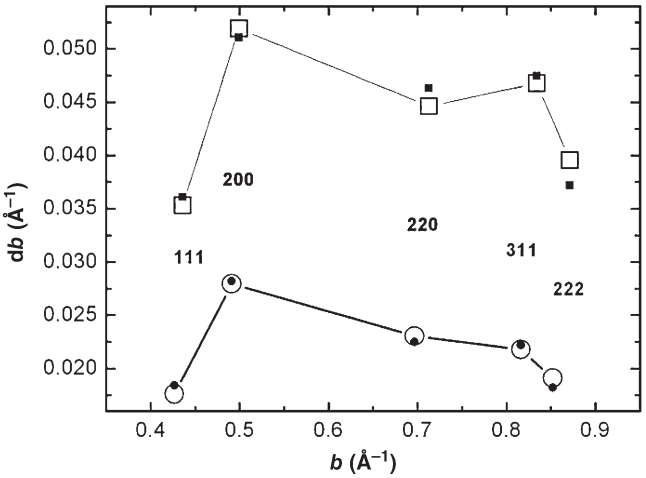

Figure 3.7 Williamson–Hall plots obtained with Au and $Au_{30}Pt_{70}$ samples. ●, experimental data; ○, fitted data.

size, mean strain, and mean stacking fault probability. Wide variations of the integral line width exist that are not expected for simple size broadening. Metal nanoparticles may have large internal strains that vary with the lattice direction, as represented by the *hkl*-indices according to the elastic anisotropy. The values of the internal strains are very high for bimetallic particles compared to those obtained for monometallic particles. In fact, for the $Au_{70}Pt_{30}$ sample a mean strain

of 490 N mm^{-2} is reached, compared to a value of only 170 N mm^{-2} for Pt nanoparticles. These internal strains might be due to high dislocation densities or epitaxial phenomena; moreover, they are frequently faulted by departing from the regular stacking periodicity ABCABC, described by a high stacking fault probability for samples such as $Au_{70}Pt_{30}$ and $Au_{80}Pt_{20}$ for which stacking fault probabilities are 7.4 and 8.2%, respectively. It has been shown that the line fluctuations shown in Figure 3.7 can be ascribed to these defects [114, 115]; likewise, the mean crystal size increases systematically with the gold content and ranges between 3.5 nm for Pt samples and 9.6 nm for Au samples.

The lattice parameters of different samples are presented, plotted against the proportion of gold (atom %) in Figure 3.8. It can be seen that, for nanoparticles containing 70–80% gold, the calculated lattice parameter is in fair agreement with Vegard's law, which is symbolized by the fitted line drawn by taking into account the bulk data from Darling *et al*. [116]. In fact, previous studies carried using X-ray diffraction (XRD) methods have shown that gold–platinum nanoparticles exhibit alloy phase properties [102] for compositions containing more than 50% gold [104]. For the sample containing less gold (i.e., $Au_{30}Pt_{70}$), the stoichiometric deviation observed from the fitted line is attributed to phase segregation.

3.3.1.2 Electrocatalytic Oxidation of D-(+)-Glucose on Gold–Platinum Catalysts

In this section, the aim is to demonstrate the correlation between structural properties, the surface composition of catalysts, and their electrocatalytic activities towards glucose oxidation. Unlike the classical X-ray photoelectron (XPS) technique, which is used to quantify the surface compositions of gold–platinum bimetallic structures in vacuum and demonstrate the presence of gold and platinum at

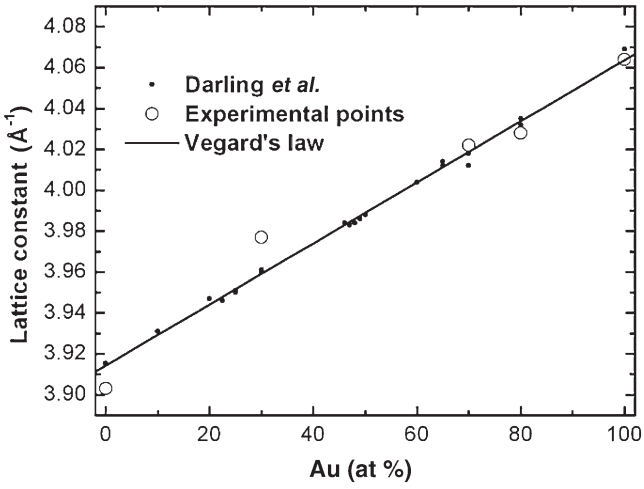

Figure 3.8 Lattice constant parameter of Au—Pt samples plotted versus the atomic percentage of gold.

the alloy surface of a bimetallic sample [117, 118], electrochemistry allows an estimation to be made of the surface composition of those bimetallic nanoparticles in contact with other species in an electrolyte.

3.3.1.2.1 **Surface Characterization of Catalysts** The surface compositions of different gold–platinum nanocatalysts can be determined from voltammetric measurements made in an alkaline medium (0.1 *M* NaOH), using the charge associated with the reduction peak of the oxide species [104, 119]. The charge calculated for pure metals is 493 μC cm^{-2} and 543 μC cm^{-2} for Au and Pt, respectively, for an upper potential value of 250 mV (versus MSE). The atomic ratio of platinum and gold can be deduced from Equations 3.4 and 3.5:

$$\%\mathrm{Au} = \frac{S_{\mathrm{Au}}}{S_{\mathrm{Au}} + S_{\mathrm{Pt}}} \times 100 \tag{3.4}$$

$$\%\mathrm{Pt} = \frac{S_{\mathrm{Pt}}}{S_{\mathrm{Au}} + S_{\mathrm{Pt}}} \times 100 \tag{3.5}$$

where S_{Au} and S_{Pt} are the calculated active surface areas for gold and platinum, respectively. This method for determining the surface composition of gold–platinum alloys was used previously by Woods and coworkers [120, 121]. Figure 3.9 shows the voltammograms of Au, $Au_{80}Pt_{20}$, $Au_{20}Pt_{80}$ and Pt nanoparticles synthesized using a water-in-oil microemulsion method. In this figure, the chemisorption of oxygen can be seen to start at –0.2 V (versus SCE) on pure platinum and

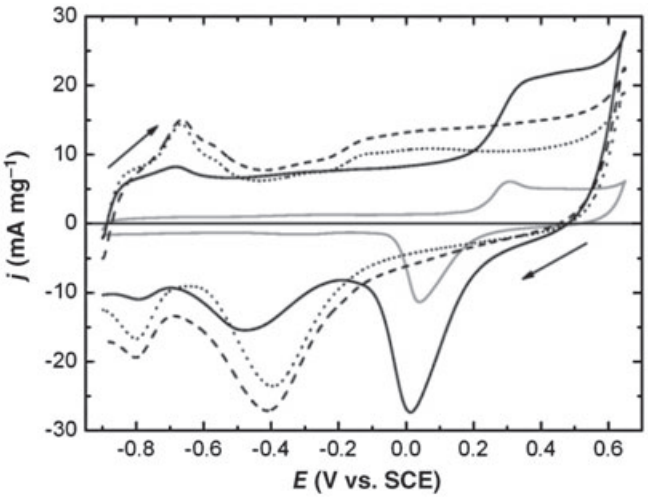

Figure 3.9 Voltammograms (after 19 cycles) of Pt (dotted line), $Au_{20}Pt_{80}$ (dashed line), $Au_{80}Pt_{20}$ (solid line) and Au (gray line) nanoparticles recorded at 25 °C in alkaline media (0.1 *M* NaOH). Scan rate = 20 mV s^{-1}.

Table 3.1 Surface compositions of some Au–Pt nanocatalysts.

	$Au_{20}Pt_{80}$	$Au_{40}Pt_{60}$	$Au_{70}Pt_{30}$	$Au_{80}Pt_{20}$
% Au	0	10	56	71
% Pt	100	90	44	29

at +0.2 V (versus SCE) on pure gold. For all compositions, desorption of oxygen species is seen to occur in two consecutive peaks. Reduction of the gold surface takes place at 0 V (versus SCE), whereas the potential for which the platinum surface is reduced depends on the amount of gold in the alloy. In fact, for pure platinum nanoparticles this potential is approximately –0.4 V (versus SCE), but the potential of the oxygen species desorption shifts to a lower value when the atomic ratio of gold is increased in the alloys. Moreover, the deformation of this peak increases with the amount of gold, most likely due to the formation of more complex platinum oxides.

The different surface compositions of gold–platinum nanocatalysts are listed in Table 3.1. Here, gold appears at the surface of the catalyst for samples containing <40% platinum, this confirming the results of the WAXS analysis. There is probably also a surface segregation of platinum [119], though this effect seems to decrease concomitantly as the amount of gold increases in the catalyst. In conclusion, when the nanocatalyst has a low gold content, a Au core Pt shell structure is observed; however, when the composition contains >50% gold, both metals are present on the catalyst surface.

3.3.1.2.2 **Correlation of Catalyst Efficiency with Glucose Oxidation** In order to determine how glucose oxidation is catalyzed by nanoalloys, voltammograms on different gold–platinum nanocatalysts were recorded in the presence of D-(+)-glucose in an alkaline medium (see Figure 3.10). Here, different oxidation peaks are visible according to the potential range considered. In fact, peak A – which is controlled by adsorption [8] – has been attributed by many authors to dehydrogenation of the anomeric carbon of the glucose molecule [6, 7, 122] on platinum. Peaks B and C, which occur in the hydroxides region, are thought to be at the origin of the direct oxidation of glucose [8, 104]. In the case of $Au_{70}Pt_{30}$ the different oxidation peaks are not well defined, with the oxidation of glucose starting earlier on the Pt–Au alloy than on Au alone, and continuing (as indicated by a broad shoulder) to have a high current density representing oxidation on both platinum and gold hydroxides. The formation of Pt–OH and Au–OH species contributes to enhance the reaction by a synergistic effect of the alloyed materials [104]. The oxidation of glucose on gold nanoparticles is clearly depicted in Figure 3.10, and the activity of Au–OH sites has been identified [123, 124]. In the case of $Au_{70}Pt_{30}$, two new oxidation peaks (E, F) are visible during the negative-direction scan. When the potential becomes negative enough to reduce gold oxide surface species, active hydroxyl ions are released in the vicinity of the surface, and these are responsible

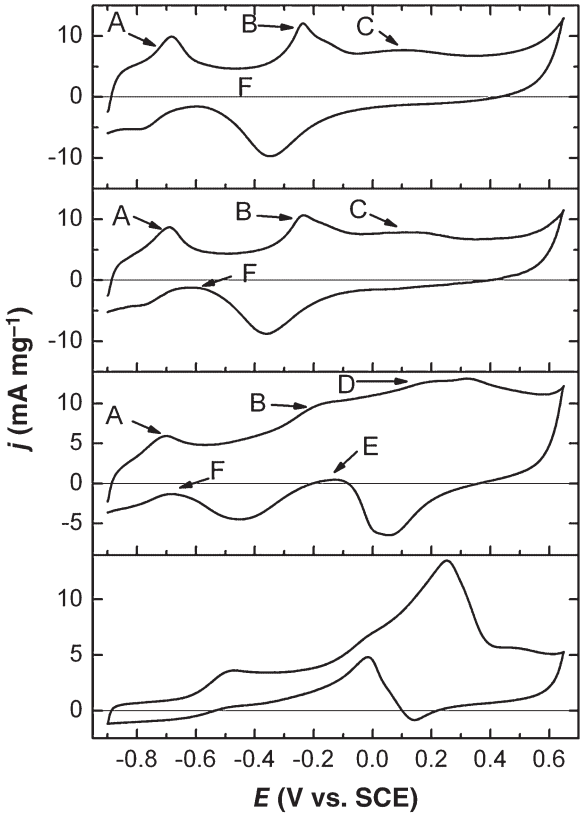

Figure 3.10 Low-temperature (3 °C) voltammograms (after 19 cycles) registered in alkaline media (0.1 *M* NaOH) in the presence of 10 m*M* D-(+)-glucose on Pt, $Au_{20}Pt_{80}$, $Au_{70}Pt_{30}$ and Au (from top to bottom). Scan rate = 20 mV s^{-1}.

for oxidation of the lactone which is adsorbed onto the catalyst surface (peak E). The same phenomenon can be observed during the reduction of a platinum surface [125]. Moreover, Figure 3.10 shows an increasing shift of the cathodic peak towards lower potentials when the gold content is increased in the alloyed nanoparticles. This shift causes of a lower potential oxidation of adsorbed lactone (peak F) when the reduction of platinum hydroxide species occurs (Figure 3.10). This phenomenon represents another interesting point for the use of these gold–platinum nanocatalysts in glucose oxidation.

3.3.1.2.3 **Electro-Oxidation of Glucose in Neutral Media** In this section we take into account the oxidation of glucose in neutral media, catalyzed by platinum and gold based nanoparticles. In fact, the presence of chloride and phosphate ions in a neutral medium triggers a competitive adsorption between glucose and these ions, and is responsible for an inhibition of catalytic sites at the surface of platinum

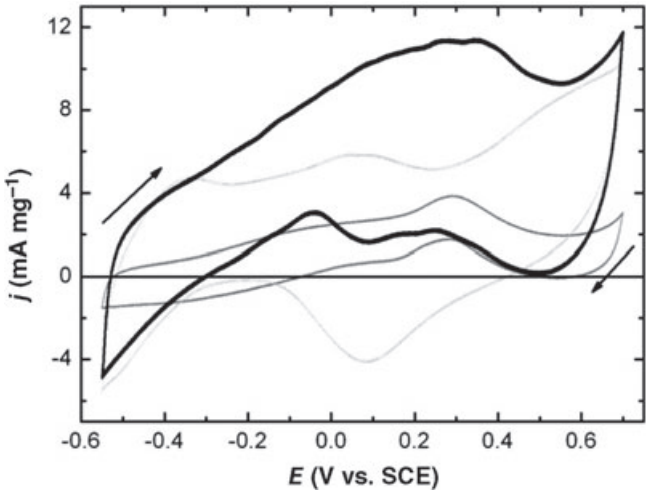

Figure 3.11 Voltammograms (after 19 cycles) recorded on Au (light gray solid line), Pt (gray solid line) and $Au_{70}Pt_{30}$ (black thick line) in a phosphate-buffered solution containing 10 m*M* glucose at 20 mV s^{-1} and 37 °C.

electrodes [86, 126]. Typical voltammograms obtained for a glucose-containing, phosphate-buffered solution with a pH value fixed at 7.4 are shown in Figure 3.11.

The data in Figure 3.11 demonstrate the value of using gold–platinum nanoparticles for glucose electro-oxidation in physiological media. For $Au_{70}Pt_{30}$, the oxidation current is increased very quickly after dehydrogenation of the glucose molecule, compared to currents obtained with gold or platinum nanocatalysts. The fact that the current density associated with glucose dehydrogenation is higher for $Au_{70}Pt_{30}$ than for pure Pt is due to a weaker sensitivity of the gold–platinum alloy towards the adsorption of phosphate ions.

All of these phenomena are caused by the synergistic effect displayed in Figure 3.10. It should be noted that glucose electro-oxidation begins at a remarkably low potential compared to that obtained with Pt—Ru [100] Pt—Sn [100] Pt—Bi [100] or Pt_2—Pb [96] electrodes. Moreover, chronoamperometry (Figure 3.12) measurements performed at –0.38V (versus SCE) revealed a higher current density for $Au_{80}Pt_{20}$ nanoparticles. The rise in current was approximately 20% higher on $Au_{80}Pt_{20}$ than Pt nanoparticles, due to the ability of gold to regenerate platinum catalytic sites from chemisorbed poison [95].

3.3.2
Glucose Oxidation via Enzymes

The major part of developments relating to the anodic compartments of biofuel cells is dedicated to the elaboration of successful enzymatic electrodes. Hence,

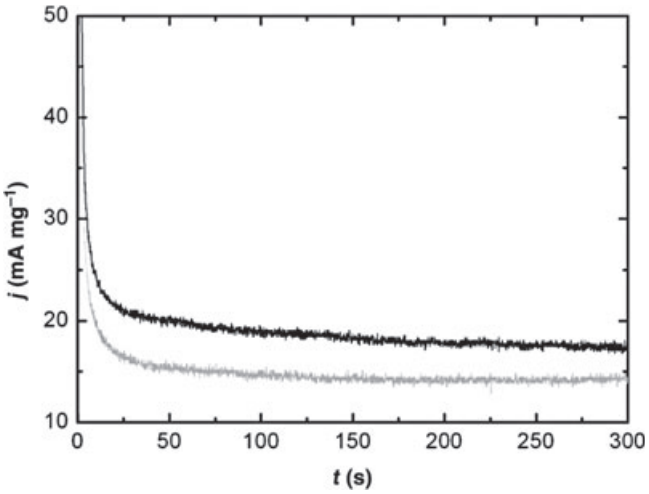

Figure 3.12 Chronoamperograms of $Au_{80}Pt_{20}$ (dark line) and Pt (gray line) recorded at –0.38 V (versus SCE) in a physiological buffered solution containing 0.1 *M* glucose at 25 °C.

glucose oxidase (GOx) and glucose dehydrogenase (GDH) are the enzymes under scrutiny here. The aim of all such studies has been to produce a stable electrode capable of oxidizing glucose under physiological conditions, ultimately to envisage the development of implantable, micro-scale devices. The properties and performances of GOx and GDH are detailed in the following two sections.

3.3.2.1 Glucose Oxidation Catalyzed by GDH

The lack of sensitivity of GDH to dioxygen [127] is of major interest with regards to its use as a glucose oxidation catalyst. Like most dehydrogenases, GDH is an NAD-dependent enzyme, with the enzymatic reaction requiring the presence of an NAD^+ source, which is a very expensive compound. Immobilization of the enzyme and the pyridine cofactor (NAD^+) is key to promoting an economically efficient process, such that the cofactor is allowed to access the enzyme. It is well known that the potential for the oxidation of biofuels catalyzed by dehydrogenases is limited by the kinetics of the direct oxidation of NADH to NAD^+, of which the redox potential is –0.560 V (versus SCE) at pH 7.0 [128]. Surface-modified electrodes have been proposed in order to improve the rate of the reaction [129]. Likewise, a variety of mediators have been used to oxidize NADH, including (most often) methylviologen, meldola blue, methylene blue and polybrilliant cresyl blue. It has been shown that the oxidation of NADH catalyzed by meldola blue adsorbed on a graphite electrode occurs at approximately –0.14 V (versus SCE) in a phosphate-buffered solution (pH 7.0) [129]. Gao *et al.* [130] have used organic compounds presenting π-conjugative structures capable of interacting with carbon nanotubes containing π-stacking interactions. The electropolymerization of these

compounds led to the formation of a nanocomposite on which GDH could be immobilized, using a crosslinking method. The bioanode thus obtained exhibited a high electrochemical activity as the onset potential of oxidation of glucose was approximately –0.25 V (versus Ag/AgCl), and the maximum current density 310 $\mu A\,cm^{-2}$ for a scan rate of 1 $mV\,s^{-1}$ in a phosphate-buffered solution (pH 7.0) containing glucose (100 m*M*)–NADH (20 m*M*). Another procedure involved the association of a second enzyme-catalyzed reaction to achieve cofactor regeneration. For this, Sato *et al.* [131] proposed the use of diaphorase immobilized in a poly(ethylene-glycol) diglycidyl ether (PEGDGE) film containing a polyallylamine–vitamin K_3 mediator as catalyst to oxidize the NADH. The system exhibited a reversible wave with a half-peak potential of approximately –0.25 V (versus Ag/AgCl). The bioanode was then prepared by the deposition of GDH immobilized in a mixture consisting of a cationic biopolymer and PEGDGE [131]. An alternative solution has been proposed which uses a quinoprotein–GDH connected to a pyrroloquinoline quinone cofactor. This system does not require NAD^+ as cofactor as the stability of the pyrroloquinoline quinone–glucose dehydrogenase (PQQGDH) is limited. Yuhashi *et al.* [132] examined the continuous performance of a glucose/oxygen biofuel cell using (PQQGDH) to catalyze the oxidation of glucose to gluconic acid. The maximum power density was 17.6 $\mu W\,cm^{-2}$ and, after working for 24 h, the PQQGDH electrode retained only 40% of its initial activity. Along these lines, when the authors proposed the use of a Ser415Cys mutant, a major improvement in stability was observed and the electrode retained 80% of its initial response after a 24 h working period. Hence, the loss of activity was attributed to inactivation of the mediator.

3.3.2.2 Glucose Oxidation Catalyzed by GOx

3.3.2.2.1 Properties of the Enzyme Most studies involving the elaboration of a bioanode aimed at oxidizing glucose to gluconic acid under physiological conditions are based on the use of GOx as an anode catalyst. The most commonly used GOx, which is extracted from *Aspergillus niger*, has a high molecular weight (155 kDa), a size of $60 \times 52 \times 77$ Å [133], and consists of two identical subunits [134]. GOx contains two tightly bound flavin adenine dinucleotide (FAD) cofactors that are only accessible through an opening of 10×10 Å [133]. In Nature, the enzyme catalyzes the oxidation of β-(D)-glucose to gluconolactone, in which reaction molecular oxygen is the natural electron acceptor and there is a consequent formation of H_2O_2. The corresponding reactions are described by Equations 3.6 and 3.7:

$$\beta\text{-(D)-glucose} + \text{GOx}-\text{FAD} \rightarrow \text{gluconolactone} + \text{GOx}-\text{FADH}_2 \tag{3.6}$$

$$\text{GOx}-\text{FADH}_2 + \text{O}_2 \rightarrow \text{H}_2\text{O}_2 + \text{GOx}-\text{FAD} \tag{3.7}$$

The redox potential of the enzyme is –0.36 V (versus Ag/AgCl) at pH 7.2 [135]. It is well known that H_2O_2 has an inhibitory effect on GOx performance, with

inhibition of the enzyme being due to a modification of the amino group residue near the active site [136]. The pH for which the activity of a GOx electrode is optimum depends on the electron acceptor used, and has been estimated as between 5.5 and 6 [137] for oxygen, pH 7.5 for methylene blue [138] and pH 3 for potassium ferricyanide [138]. The activity of GOx is also known to decrease dramatically when the temperature exceeds 40 °C [137]. The isoelectric point of the enzyme is approximately 4; consequently, under physiological conditions GOx is a highly anionic enzyme [139]. It is of interest to note that the Michaelis constant of GOx for β-(D)-glucose has been reported as between 11 and 41.8 m*M* [140].

3.3.2.2.2 **Oxidation of β-(D)-Glucose Catalyzed by Glucose Oxidase** Glucose oxidase cannot transfer electrons directly to conventional electrodes, because the distance between its redox centers and the electrode surface exceeds the distance across which electrons are transferred at sufficient rates [141]. During the past decade, two electron-transfer designs have been developed, based on the method of electrical connection between the enzyme and the conducting support:

- In a DET system the enzyme and current collector are in direct contact, and electrons pass from the electrode surface to the reducing substrate center of the enzyme. This design allows electrons to be shuttled directly from the active site of the enzyme to the electrode surface (Figure 3.13). This is possible when the distance between the FAD redox centers of GOx and the electrode surface is in the range of a tunneling distance [53, 141].
- In a MET system a redox-active molecule is used to act as a reducing substrate and carry electrons from the electrode surface to the enzyme. MET generally offers a higher current density than DET if the system has been well optimized and the appropriate mediator employed. However, the MET design introduces an additional level of complexity, such that electrode performance becomes a matter of mediator integrity and stability, as well as stability of the enzyme itself [142]. In MET, the redox mediator must be reduced by GOx; moreover, this molecule must be reversibly reoxidized at the electrode surface at a low overpotential (Figure 3.14).

3.3.2.2.2.1 *Direct Electron Transfer* The major interest in shuttling electrons from a glucose molecule via DET is to reduce the overpotential due to regenera-

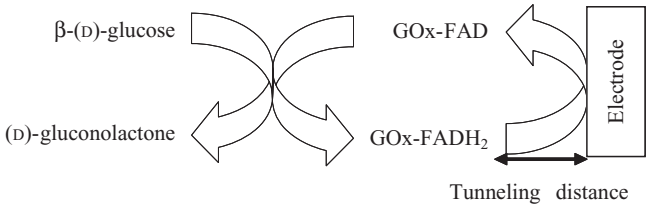

Figure 3.13 Schematic representation of a direct electron charge transfer.

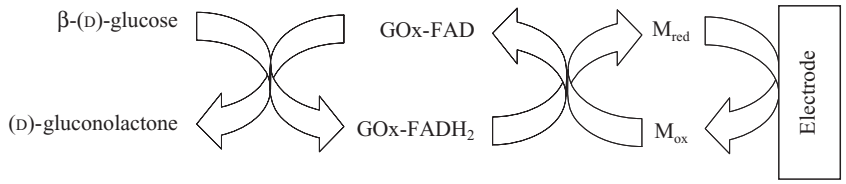

Figure 3.14 The mechanism of mediated electron transfer.

tion of the mediator at the electrode surface, as occurs in MET. Heller's group [141] has shown that it is possible to chemically modify GOx by including electron relays into the protein, which are closer to both the electrode surface and the FAD centers. The key issue of the DET method is to reduce the distance between FAD centers and relays, between the relays themselves, and between the relays and the electrode surface. However, glucose is oxidized at relatively high potentials (0.440 V versus SHE at pH 7.2) due to the use of a ferrocene molecule as a relay. Ianello *et al.* [143] have also demonstrated the possibility of DET between a cyanuric chloride-modified graphite electrode and glucose oxidase. More recently, it was shown possible to link the FAD center with the electrode surface by a spacer arm, and then to reconstitute GOx from an apoenzyme [144]. The recorded voltammograms exhibited a quasi-reversible system, showing the possibility of a DET.

Another method explored has involved the use of carbon nanotubes. Since their discovery in 1991, a variety of investigations have demonstrated the unique mechanical and electronic properties of carbon nanotubes, which involve a rapid electron transfer rate in electrochemical reactions [145]. Carbon nanotubes have been used extensively to couple their properties with enzymes in order to prepare bioelectrodes capable of providing DET. Therefore, the immobilization of GOx on carbon nanotubes, previously dispersed into a cetyltrimethylammonium bromide (CTAB) solution, led to a highly reversible electrochemical system with a mid-point potential at −466 mV (versus SCE) in a phosphate-buffered solution at pH 6.9 [146]. Notably, the activity of GOx was not affected by such immobilization. Ivnitski *et al.* [147] also investigated the possibility of elaborating an anode for a glucose/oxygen biofuel cell based on DET between multiwall carbon nanotubes and the FAD centers of glucose oxidase. Here, a carbon Toray felt was modified by the growth of carbon nanotubes prepared by a chemical vapor deposition (CVD) technique. The process was catalyzed by the presence of cobalt nanoparticles, and the GOx entrapped in a positively charged polyethylenimine (PEI) film that allowed an electrostatic attraction between the negatively charged GOx and the electrode surface. The electrode was finally covered by a tetrabutylammonium bromide (TBAB) salt treated with a Nafion solution to obtain an ion exchange. It has been shown previously that the entrapment of enzymes in such modified Nafion films leads to a less acidic environment that increases the lifetime and activity of the immobilized enzyme [148]. Voltammograms recorded with this electrode showed a highly reversible electrochemical system at −0.460 V (versus Ag/AgCl) at pH 7.9

and indicating the existence of a DET process, probably due to the presence of carbon nanotubes at a distance of significantly less than 13 Å (the distance between the FAD centers and the GOx surface). This calculation indicated an electron transfer rate of 2.3 s^{-1}, which was in agreement with data reported elsewhere [149]. The oxidation of glucose on these electrodes begins at a very low potential of approximately –0.4 V (versus Ag/AgCl) in a physiological buffered solution (pH 6.9); in contrast, in the presence of 20 m*M* glucose the current densities are close to 500 μA cm^{-2}.

3.3.2.2.2.2 *Mediated Electron Transfer* The use of a mediator to transfer electrons from the active site of GOx to the electrode surface allows the rate of transfer to be increased, and thus to increase the current densities delivered by an enzymatic electrode. However, this process often leads to high overpotentials during the oxidation of glucose. The presence of a mediator may also limit the parasitic reaction between glucose and oxygen that produces H_2O_2. In this case, it is necessary that the rate of electron transfer between GOx and the mediator be superior to the rate of electron transfer between GOx and oxygen. The coupling of GOx with different electrochemical mediators has been investigated. Among the complexes most commonly used are those of osmium [139, 150], ferrocene compounds [151] and 8-hydroxyquinoline-5-sulfonic acid (HQS) [5], all of which have interesting properties as redox mediators in glucose/oxygen biofuel cells. The high redox potentials of ferrocene derivatives [151] do not support their possible use as electrochemical mediators for the anode of a biofuel cell. HQS exhibits a redox potential of approximately 28 mV (versus SCE) in a phosphate-buffered solution (pH 7.4), which again does not exclude its use in biofuel cells. This value involves a great overpotential with regards to glucose oxidation, as the redox potential of the FAD centers is –0.360 V (versus Ag/AgCl) at pH 7.2. Currently, the most efficient mediator has been synthesized by Mano *et al.* [139], the redox potential of this osmium polymer being approximately –0.195 V (versus Ag/AgCl) at pH 7.2. The 13 atom-long flexible tethers allow connections to be made between the redox centers and the backbone, and also causes an increase in the statistical collisions between oxidized and reduced osmium centers. As a consequence, the diffusion coefficient of electrons into the polymer reaches a remarkably high value of 5.8×10^{-6} $cm^2 s^{-1}$ [45]. Furthermore, the polycationic nature of the polymer provokes an electrostatic interaction between the redox polymer and GOx, which is a polyanion at physiological pH, and this interaction facilitates contact between the two entities. Crosslinking of the osmium polymer with PEGDGE allows the formation of a redox hydrogel in which GOx is bonded. The whole system constitutes a three-dimensional (3-D) matrix connected to the surface, while the swelled hydrogel is permeable to the substrate. The crosslinking must not be so great as to allow swelling of the polymer in water [139]. The optimized electrode is composed of 1% PEGDGE, 45% GOx and 54% osmium polymer. The oxidation of glucose begins at –0.360 V (versus Ag/AgCl) and reaches a limiting current at 1.3 mA cm^{-2} from –0.100 V (versus Ag/AgCl) in a physiological buffered solution (pH 7.2) containing 15 m*M* glucose at a scan rate of 1 mV s^{-1} [152]. Another possibility of elaborating an anode,

based on the use of glucose oxidase as anodic catalyst, has been brought to light by Willner's group, who proposed the reconstitution of an apo glucose oxidase enzyme on a PQQ–FAD monolayer connected to a gold electrode [153, 154]. Here, PQQ acts as an electron mediator and allows the connection between the FAD redox centers and the electrode surface previously covered by a cystamine base. Willner's group also showed that such an electrode leads to an electron transfer rate higher than that observed between GOx and oxygen, the natural electron acceptor between the enzyme and the electrode surface. This implies a lack of sensitivity of the electrode towards the presence of oxygen. The oxidation of glucose on this type of electrode involves the appearance of an anodic current at –0.125 V (versus SCE), which represents the redox potential of PQQ mediator. Such electrode architecture, with connections between the enzyme redox centers and the mediator, clearly allows the avoidance of diffusion phenomena of the mediator in some enzymatic films.

3.3.2.2.3 **Oxidation of Glucose Catalyzed by GOx Immobilized in a Polypyrrole Film** In this section, attention is focused on the oxidation of β-(D)-glucose catalyzed by a GOx–HQS-mediated system entrapped in a polypyrrole film. Parameters such as the coulometry of the film, reticulation by glutaraldehyde treatment after electropolymerization and immobilization methods are described. In contrast to the above-described systems, no connection between the redox centers of the enzyme and the mediator takes place. Two methods of immobilization have been used to elaborate a GOx anode. The first ('classical') method is based on entrapment of the adsorbed enzyme and mediator into a polypyrrole film obtained by electropolymerization of a pyrrole monomer at 0.9 V (versus Ag/AgCl) in a 0.2 *M* phosphate-buffered solution at pH 7.0 [5]. Such immobilization of GOx has been widely investigated [155]. It has been shown that, for an immersion time of 1 min in the enzyme solution, the major part of the amperometric response (90%) was due to an enzyme confined into the 3-D polypyrrole matrix [156]. In the method described here, the immersion times were longer (12 h), and involved the enzyme being located mainly on the surface of the carbon electrode. In the described system, the polymer acts as a conducting matrix to avoid enzyme linkage and the loss of mediator. The second immobilization method is based on grafting the GOx enzyme, and has already been described in the case in where the laccase electrode was built [47].

Figure 3.15 shows the polarization curves of bioanodes in an unstirred phosphate buffer (pH 7.4) containing 10 m*M* glucose; here, the two polarization curves 4 and 6 clearly show the same electrochemical behavior.

The catalytic oxidation of glucose begins at approximately –50 mV (versus SCE), and reaches a semi-plateau; this indicates that the reaction mechanism is controlled by mass transport. Without stirring the solution, and in order to operate under the conditions of a biofuel cell, the mass transport limitation is hidden at potentials higher than 0.1 V (versus SCE) by a quasi-linear increase of the current density due to the resistive behavior of the polypyrrole film. To improve electrochemical performances of the system, the influences of chemical treatment with

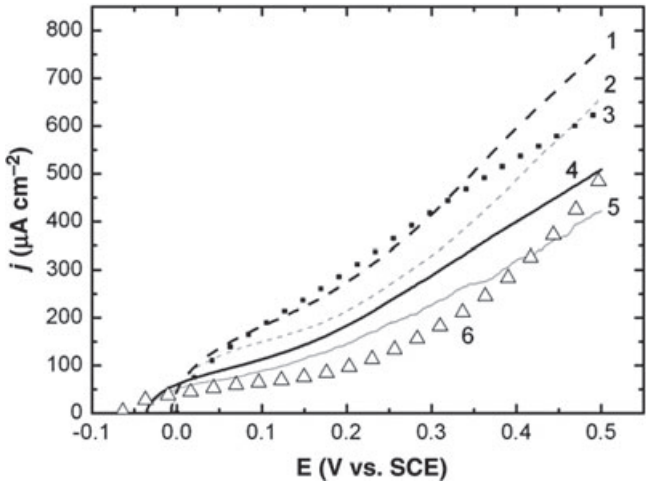

Figure 3.15 Polarization curves of entrapped enzyme and grafted enzyme recorded in a phosphate-buffered (0.2 *M* pH 7.4) solution containing 10 m*M* glucose at 37 °C. Curve 1, GOx electrode with a 2 μm polypyrrole film and treated with glutaraldehyde; curve 2, GOx electrode with a 1 μm polypyrrole film and treated with glutaraldehyde; curve 3, GOx electrode with a 0.5 μm polypyrrole film and treated with glutaraldehyde; curve 4, GOx electrode with a 2 μm polypyrrole film; curve 5, GOx electrode with a 1 μm polypyrrole film; curve 6, grafted GOx electrode.

glutaraldehyde and of the thickness of the polypyrrole film were examined. The current–potential characteristics that can be generated by varying these two parameters are also shown in Figure 3.15 (see curves 1 to 5).

As the polypyrrole polymer is responsible for diffusion resistance of the substrates, its thickness was varied by limiting the total charge involved during the electropolymerization for 2 C and 4 C. However, no real effect was observed on the catalytic electro-oxidation of glucose at the anode. This confirms that only a small amount of GOx was confined in the polymer matrix. In the case of the bioanode, the electropolymerization charges of 2 C and 4 C provide polymer thicknesses of ~1 and 2 μm, respectively, as estimated using Faraday's law. For both thickness values, the diffusion barrier is still important for the glucose in the polymer, and the reaction mechanism is still controlled by mass transport. Figure 3.15 also shows the influence of chemical reticulation of the enzymes in the polymer on the electrochemical activity of the bioelectrodes. The applied reticulation time is fixed at 30 min, and the reticulation solution contains 1% glutaraldehyde. Crosslinking of the enzymes with a bifunctional group such as glutaraldehyde has been widely used to prevent enzyme leaching and to improve enzyme stability. Chaubey *et al*. [157] have shown an improvement in the stability of the lactate dehydrogenase microenvironment during the reaction after such treatment. Moreover, Gaikwad *et al*. have pointed out that such treatment might lead to a better access to the active sites of GOx [158]. The data in Figure 3.15 also clearly show that crosslinking induces higher current densities and a higher formal potential, this

behavior perhaps being due to retention of the enzymes and mediators in the polymer. Another explanation might be a prevention of the chemical reaction between hydroquinone moieties and amino acid residues from GOx [34], which favors electron transfer from GOx to electrodes. It is also possible that the increase in current density is due to a favored access of the reactive species to the active site of the enzyme.

3.4 Application to Fuel Cell Systems

3.4.1 Glucose/Oxygen Biofuel Cells

The first biofuel cell, which was described by Yahiro *et al.* in 1964, consisted of a two-compartment anionic membrane cell in which two platinum foils were used as conducting supports. The electrolyte was a phosphate-buffered solution at pH 6.7, and GOx was dissolved in the anodic compartment, which contained glucose [159]. Over the past few decades, the development of biofuel cells has focused on power sources for an artificial heart, while current investigations concern implantable microscale devices. These features simply use glucose and oxygen as fuel and oxidant, respectively, from organic tissues. The development of such devices requires the miniaturization of all components, and the associated difficulties have been reported by Heller [160]. Many systems that operate under physiological conditions have been described, all of which require separation of the anodic and cathodic compartments in order to prevent any interference. When GOx is used as an anode catalyst, for example, oxygen can be used as the electron acceptor, but this may involve a side reaction producing H_2O_2. However, some methods to immobilize GOx allow the oxygen reduction reaction to be avoided during the oxidation of glucose [161]. In this case, the construction of noncompartmentalized glucose/O_2 biofuel cell is possible, using bilirubin oxidase cathodes that operate under physiological conditions, without any loss of activity. In contrast to laccase, which is highly sensitive to the presence of chloride ions, the properties of bilirubin oxidase provide the possibility of creating implantable microscale devices, the best known of which has been developed by Mano *et al.* This comprised two small carbon fibers about 2 cm long and 7 μm in diameter, onto which was deposited a hydrogel composed of the enzyme, osmium polymer and PEGDGE. This noncompartmentalized system had a performance that was relatively high, delivering a power density of 430 μW cm^{-2} at an operating potential of 0.52 V in the presence of 15 m*M* glucose and under physiological conditions [131]. It was also a very stable system, with the power density falling less than 5% per day. When the device was implanted into a grape (a glucose-rich fruit), it was able to deliver a power of 2.3 μW at 25 °C [160], although this had fallen to only half of the initial value after only 20 h of functioning. The obtained power density was also seen to depend on the penetration distance of the fibers into the grape [162].

The use of GDH as an anode catalyst in glucose/oxygen biofuel cells was also investigated. Although GDH does not catalyze O_2 reduction reaction (in contrast to GOx), all systems containing this enzyme commonly exhibit weak power densities and stability. Sato *et al.* have described a glucose/oxygen biofuel cell which delivered 14.5 $\mu W\,cm^{-2}$ at a cell voltage of 0.36 V. Under physiological operating conditions (37 °C, pH 7) the resulting system was not very stable after 4 days, retaining only 25% of the initial power density [131].

Other systems based on laccase and glucose oxidase have also been designed. For example, Barrière *et al.* developed a membrane-less biofuel cell using osmium polymers as electrochemical mediators. The enzyme and redox polymer were crosslinked with polyoxyethylene bis(glycidyl ether) on graphite electrodes, and the system delivered 16 $\mu W\,cm^{-2}$ at a cell voltage of 0.25 V in a phosphate-buffered solution (pH 7.4) containing 0.1 *M* sodium chloride. When the effect of medium pH on power density was reported, the optimal medium was considered to be a pH 5.5, phosphate-buffered solution containing 10 m*M* glucose. In fact, in such a medium the system delivered a power density of 40 $\mu W\,cm^{-2}$ at 0.4 V [150]. It is important to note that the use of laccase often leads to weak performances under physiological conditions. Recently, an alternative system based on concentric tubular tubes as electrodes and operating at physiological pH was developed. In this device, an oxygen-saturated phosphate-buffered solution (pH 7.4) is circulated inside an internal tubular electrode composed of porous carbon and providing oxygen diffusion. The concentric system is immersed in a phosphate-buffered solution (pH 7.4) containing 10 m*M* glucose (Figure 3.16).

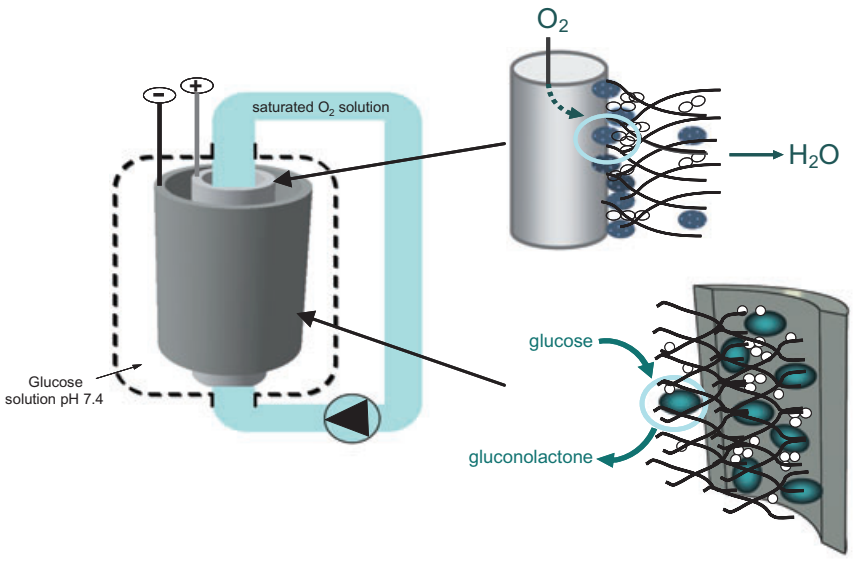

Figure 3.16 Schematic view of the glucose/oxygen biofuel cell system.

Oxygen consumption occurs at the cathode, such that no oxygen diffuses towards the anode; this avoids the formation of H_2O_2 during the electro-oxidation of glucose. Glucose oxidation is catalyzed by GOx immobilized with the redox mediator HQS at the anode, while oxygen is reduced by bilirubin oxidase coimmobilized with $ABTS^{2-}$ at the cathode. The enzymes and redox mediators were entrapped at the electrode surfaces by a polypyrrole film. The surfaces of the cathode and anode were 3.14 cm^2 and 4.40 cm^2, respectively. The performance of the biofuel cell was investigated in terms of power density and lifetime, with expressed power densities being normalized using the geometric surface of the anodic conducting support. The polarization curves of the two electrodes used are shown in Figure 3.17.

A catalytic electroreduction current corresponding to the indirect reduction of oxygen to water appeared at 0.42 V (versus SCE) and reached a plateau at –237 $\mu A\,cm^{-2}$, indicating that the reduction is controlled by diffusion. The shape of the polarization curve presented a peak at approximately 0.3 V, which could be explained by the direct reduction of $ABTS^{\bullet-}$. (It is important to note here that the current density of oxygen reduction is higher than the current density of glucose electro-oxidation.) Consequently, it can be stated that the power output is limited by the catalytic electro-oxidation of glucose, probably due to several factors including: (i) mass transfer to and throughout the polypyrrole polymer; (ii) the low enzymatic activity; and/or (iii) by the leaching of the species out of the polymer. Another reason may be the chemical reaction of hydroquinone moieties, which have a certain level of reactivity and may react with the amino acid residues derived

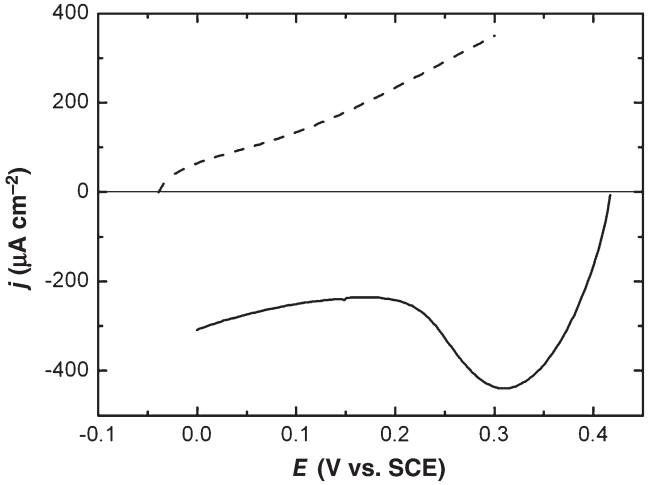

Figure 3.17 Polarization curves obtained for the bioanode GOx/HQS in a 10 m*M* glucose solution (dashed line) and for the biocathode bilirubin oxidase/ABTS with a circulating saturated O_2 solution in the inner electrode surface (solid line), at 37 °C in a phosphate-buffered solution (pH 7.4). Scan rate = 5 $mV\,s^{-1}$.

from the glucose oxidase [163]. The decrease in the mobility of the hydroquinone moieties may cause an electron transfer from glucose oxidase to the electrodes. Figure 3.18 shows the performances of the biofuel cell determined in a phosphate-buffered solution (pH 7.4) containing 10 m*M* glucose at 37 °C, and where the initial maximum power density was 33 $\mu W\,cm^{-2}$ at a cell voltage of 0.32 V.

It is important to note that, after a running period of 3 h, the system retained 94% of its initial power density, whereas after a two-day storage at 4 °C in phosphate buffer (pH 7) only 72% was retained. This loss of efficiency during storage can be associated with the deactivation of Cu centers of bilirubin oxidase [4]. In order to improve the performance of the biofuel cell, the anode was entrapped in a glutaraldehyde matrix, as described previously. The anode used was modified by a thin polypyrrole film (2 µm), followed by enzyme crosslinking, while the cathode was modified by a thinner film (1.4 µm), but without enzyme crosslinking. As this treatment did not have any effect on the activity of the cathode, it was not carried out on the conducting support [72]. The maximum power density of the resultant biofuel cell is shown graphically in Figure 3.18.

The maximum power density was 42 $\mu W\,cm^{-2}$ at 0.32 V, with increases in performance from 33 $\mu W\,cm^{-2}$ to 42 $\mu W\,cm^{-2}$ demonstrating the improvements in bioanode efficiency. Although a concentric biofuel cell using tubular electrodes represents a promising architecture, one of the greatest problems encountered is the weak stability of the performances achieved. Thus, in order to improve system stability the enzymes have been grafted onto the electrode surface with an alkyl

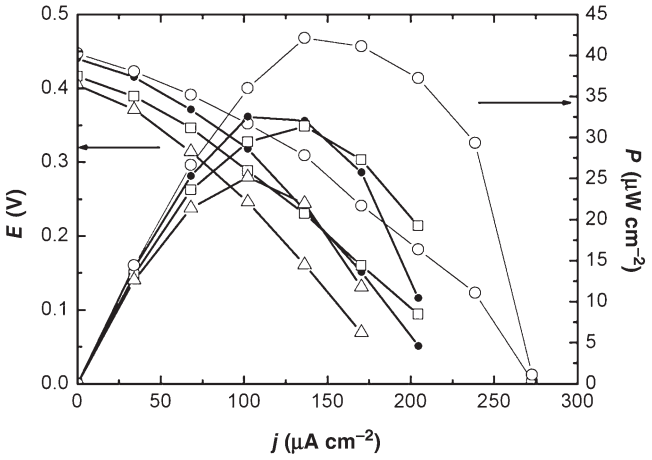

Figure 3.18 Fuel cell performances obtained with the biocathode and bioanode in a phosphate-buffered solution (pH 7.4) containing 10 m*M* glucose at 37 °C. ●, Initial performance; □, after operating for 3 h; △, after operating for 3 h and 2 days storage at 4 °C. The open-circle curves show the fuel cell performance carried out with a bioanode treated with glutaraldehyde after electropolymerization (total charge of electropolymerization = 4 C) and a biocathode (total charge of electropolymerization = 2 C) in phosphate-buffered solution (0.2 *M*, pH 7.4) containing 10 m*M* glucose at 37 °C. A saturated O_2 solution is circulated in the inner surface of the cathode.

chain. In fact, the enzymes were grafted by chemical fixation through spacers with various lengths to a poly(aminopropylpyrrole) film which was electrogenerated initially at the electrode surface. The amino groups of the polymer were then coupled to those of the enzyme with aldehyde functions. For bilirubin oxidase, it has been shown that a long spacer arm exhibits the higher electroactivity, with a current density of 85 $\mu A\,cm^{-2}$ and a formal potential of 0.4 V (versus SCE) in an O_2-saturated pH 7.4, phosphate-buffered solution. In the case of GOx, the range of lengths explored does not involve any modification to the performances, as the catalytic current resulting from glucose electro-oxidation reached a plateau at 50 $\mu A\,cm^{-2}$ and a formal potential of –60 mV (versus SCE) in a phosphate-buffered solution (0.2 *M* pH 7.4) containing 10 m*M* glucose. The performances of the resultant electrodes are shown in Figure 3.19.

Figure 3.20 displays the power density curves of the biofuel cell assembled from the biocathode synthesized with bilirubin oxidase through the larger spacer, and the bioanode synthesized with GOx through the shorter spacer to the poly(amino propylpyrrole). The mediators ($ABTS^{2-}$, HQS) were entrapped in a PEGDGE film. The maximum power density was measured after intermittent use over a 45-day period, with the bioelectrodes being stored at 4 °C in a phosphate-buffered solution between each use. The initial power density of 20 $\mu W\,cm^{-2}$ at 0.3 V remained stable with time. Indeed, such operational stability constituted a remarkable improvement compared to the stability of the previous devices. However, the initial performances of the grafted bioelectrode were weaker than those observed when the enzymes were entrapped on the electrode surfaces.

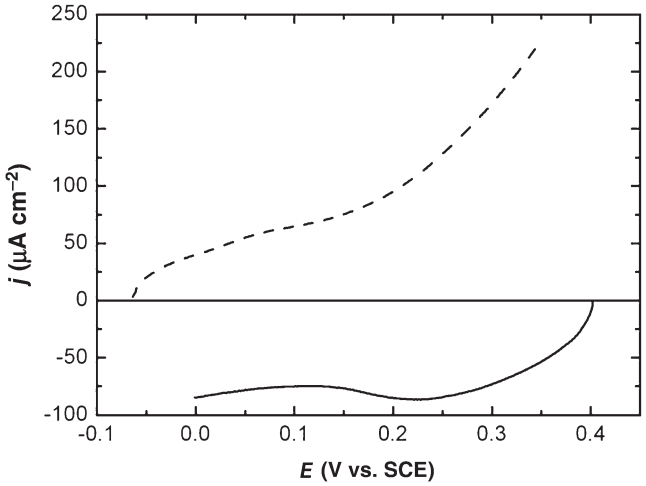

Figure 3.19 Polarization curves of grafted glucose oxidase (dashed line) and bilirubin oxidase (solid line) electrodes with a short and a long spacer arm, respectively, obtained in a phosphate-buffered solution (0.2 *M*, pH 7.4) at 37 °C containing 10 m*M* glucose in the case of glucose oxidase electrode. The solution circulating in the inner surface of the cathodic tube is saturated with oxygen in the case of bilirubin oxidase electrode. Scanning rate = 5 $mV\,s^{-1}$.

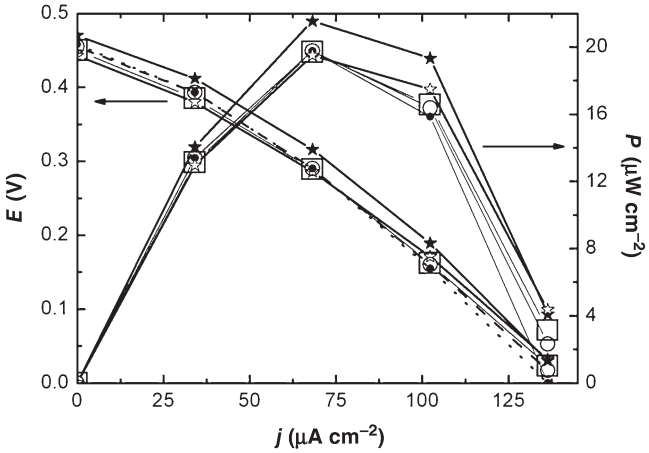

Figure 3.20 Power densities obtained after different times of electrodes storage in a phosphate-buffered solution (0.2 *M*, pH 7.4) containing 10 m*M* glucose at 37 °C with glucose oxidase grafted with a short spacer arm and bilirubin oxidase grafted with a long spacer arm as anodic and cathode catalysts. Filled circles indicate initial performance; subsequent performances are indicated following storage of the electrode in the phosphate-buffered solution for 6 days (full stars), 16 days (open squares), 34 days (open stars) and 45 days (open circles).

3.4.2
Glucose/Oxygen Biofuel Cells with Au—Pt Nanoparticles as Anode Catalysts

In order to improve the performances of the anode in this biofuel cell system, the decision was taken to replace GOx with gold–platinum nanoparticles (the properties of which have already been discussed). It is, in fact, difficult to build an implantable microscale device with Au—Pt as the anodic catalyst, mainly because the specificity of the nanoparticles is poor and many organic molecules may undergo oxidation on such catalysts. Nonetheless, the use of this type of catalyst should lead to the development of new nonimplantable applications. The unique properties of Au—Pt catalysts for glucose oxidation allow for the development of renewable and sustainable power sources, and indeed a number of fuel cell tests have recently been conducted using different compositions of Au—Pt catalysts. The system used is similar to that described in Figure 3.18, but with the Au—Pt catalyst being immobilized on the internal surface of the external tube with a Nafion polymer. The cathode catalyst, composed of a Nafion film containing bilirubin oxidase and $ABTS^{2-}$, is immobilized on the internal surface of the inner tube to avoid depolarization of the anode catalyst with oxygen. Proton transfer between the anodic and cathodic compartments then occurs via the pore of the inner porous tube.

The results of some fuel cell tests using different compositions of Au—Pt catalyst are shown in Figure 3.21, where it is clear that the best power density is obtained with $Au_{70}Pt_{30}$ as the anodic catalyst. In fact, the maximum power density obtained was approximately 90 μW cm^{-2} with a cell voltage of 0.68 V. It is important

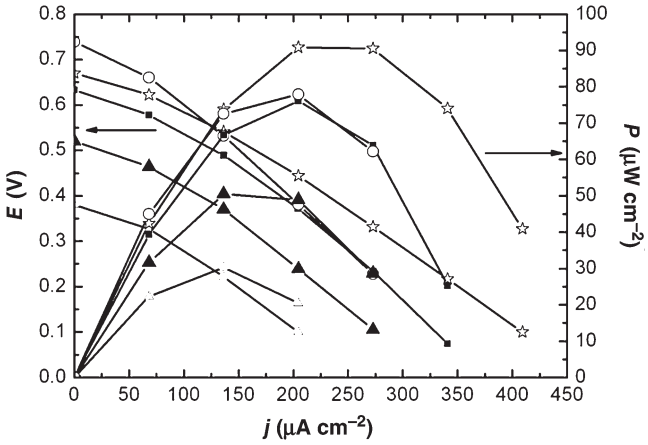

Figure 3.21 Fuel cell performances obtained with Au (▲, $Au_{80}Pt_{20}$ (■), $Au_{70}Pt_{30}$ (✡), $Au_{50}Pt_{50}$ (○) and Pt (△) nanoparticles as anode catalysts. Power densities were obtained in phosphate-buffered solution (0.2 *M*, pH 7.4) containing 10 m*M* glucose at 37 °C. A saturated O_2 solution was circulating in the inner surface of the cathode.

to note that, with $Au_{50}Pt_{50}$, a cell voltage of 0.74 V could be obtained. Although the presence of only 25% gold at the surface produced a rapid poisoning of the catalytic surface, this was not the case for the $Au_{70}Pt_{30}$ catalyst, which presents 56% gold at the interface such that the performance obtained was only 75 μW cm^{-2}. In the case of platinum, this low cell voltage can be explained on the basis of the competition between phosphate ions and glucose for the catalytic sites of platinum. Such competition also occurs on other Au—Pt catalysts, despite the presence of gold allowing a weaker interaction between phosphate ions and the metallic surface. Subsequently, higher concentrations of glucose were used in this system. The data in Figure 3.22 show a clear but strong increase in cell voltage with glucose concentration. Such an increase, observed between 0.1 and 0.3 *M* glucose, can be attributed to the slow adsorption of phosphate ions due to the presence of higher glucose concentrations. Moreover, the maximum power density was also increased from 90 μW cm^{-2} (for a glucose concentration of 10 m*M*) up to 190 μW cm^{-2} (for a glucose concentration of 0.7 *M*). The weak increase in power density between 0.3 *M* and 0.7 *M* glucose may be the result of saturation of the anodic surface, and/or a limitation due to too-weak cathodic performances.

3.5 Summary and Outlook

In this chapter we have provided evidence that the power output of biofuel cell systems can be enhanced by the judicious choice not only of the nanostructure

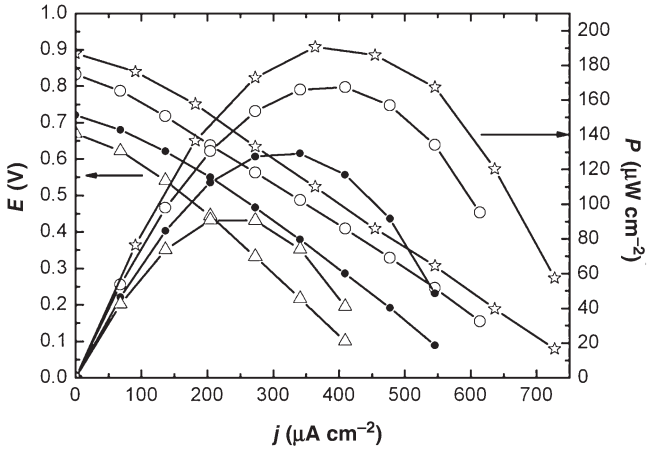

Figure 3.22 Fuel cell performances obtained with 10 m*M* glucose (△), 100 m*M* glucose (●), 300 m*M* glucose (○) and 700 m*M* glucose (✡), with $Au_{70}Pt_{30}$ nanoparticles as anode catalysts. Power densities were obtained in phosphate-buffered solution (0.2 *M*, pH 7.4) containing 10 m*M* glucose at 37 °C. A saturated O_2 solution was circulating in the inner surface of the cathode.

materials but also of the methods used to graft enzyme molecules at the cathode and anode sites. Indeed, these are the main issues addressed by the biofuel cell community at present, and may in time make such systems attractive for energy conversion, as they operate at temperatures ranging between ambient and body temperature. The most interesting aspect here was to put into play the physicochemical properties of the alloy nanomaterials generated, based on Pt and Au, using water-in-oil microemulsion techniques. As these materials displayed electrocatalytic activity with respect to glucose oxidation, as evidenced using cyclic voltammetry, it is clear that an optimum of platinum versus gold sites, as compared to the bulk, should promote bifunctional mechanisms in glucose dehydrogenation. This approach should considerably enhance the electrical performance when compared to the use of GOx as the anode in biofuel cells. Undoubtedly, since the first recognition by Palmore and Whitesides in 1994 of the potential of biofuel cells [164], progress in this area will continue to be made.

Acknowledgments

The authors acknowledge 'le Conseil Regional de Poitou-Charentes' for financial support, Dr Sophie Tingry of the Institut Européen des Membranes, Montpellier, France, for helpful discussions, and Dr Walter Vogel from the Chemistry Department, National Center University Taiwan for technical assistance with the X-ray diffraction measurements.

Abbreviations

ABTS	2,2-azinobis-3-ethylbenzothiazoline-5-sulfonic acid
DET	Direct electron transfer
FAD	Flavin adenine dinucleotide
GDH	Glucose dehydrogenase
GOx	Glucose oxidase
HQS	8-Hydroxyquinoline-5-sulfonic acid
MET	Mediated electron transfer
MSE	Mercurous sulfate electrode
NAD	Nicotinamide adenine dinucleotide
NHE	Normal hydrogen electrode
ORR	Oxygen reduction reaction
PEGDGE	Poly(ethylene-glycol) diglycidyl ether
PQQ	Pyrroloquinoline quinone
PQQGDH	Pyrroloquinoline quinone glucose dehydrogenase
RHE	Reference hydrogen electrode
RRDE	Rotating ring disk electrode
SCE	Saturated calomel electrode
SHE	Standard hydrogen electrode
WAXS	Wide-angle X-ray scattering
XAS	X-ray absorption spectroscopy
XPS	X-ray photoelectron spectroscopy

References

1 Bullen, R.A., Arnot, T.C., Lakeman, J.B. and Walsh, F.C. (2006) Biofuel cells and their development. *Biosensors and Bioelectronics*, **21**, 2015–45.

2 Kim, J., Jia, H. and Wang, P. (2006) Challenges in biocatalysis for enzyme-based biofuel cells. *Biotechnology Advances*, **24**, 296–308.

3 Farneth, W.E. and D'Amore, M.B. (2005) Encapsulated laccase electrodes for fuel cell cathodes. *Journal of Electroanalytical Chemistry*, **581**, 197–205.

4 Kang, C., Shin, H. and Heller, A. (2005) On the stability of the 'wired' bilirubin oxidase oxygen cathode in serum. *Bioelectrochemistry*, **68**, 22–6.

5 Brunel, L., Denele, J., Servat, K., Kokoh, K.B., Jolivalt, C., Innocent, C., Cretin, M., Rolland, M. and Tingry, S. (2007) Oxygen transport through laccase biocathodes for a membrane-less glucose/O_2 biofuel cell. *Electrochemistry Communications*, **9**, 331–6.

6 Ernst, S., Heitbaum, J. and Hamann, C.H.J.E. (1979) The electrooxidation of glucose in phosphate buffer solutions: part I reactivity and kinetics below 350 mV/RHE. *Journal of Electroanalytical Chemistry*, **100**, 173–183.

7 Essis Yei, L.H., Beden, B. and Lamy, C. (1988) Electrocatalytic oxidation of glucose at platinum in alkaline medium: on the role of temperature. *Journal of Electroanalytical Chemistry*, **246**, 349–362.

8 Largeaud, F., Kokoh, K.B., Beden, B. and Lamy, C. (1995) On the electrochemical reactivity of anomers: electrocatalytic oxidation of alpha- and beta-glucose on platinum electrodes in acid and basic media. *Journal of Electroanalytical Chemistry*, **397**, 261–9.

9 Vassilyev, Y.B., Khazova, O.A. and Nikolaeva, N.N. (1985) Kinetics and mechanism of glucose electrooxidation on different electrode-catalysts: Part I. Adsorption and oxidation on platinum. *Journal of Electroanalytical Chemistry*, **196**, 105–25.

10 Nikolaeva, N.N., Khazova, O.A. and Vassilyev, Y.B. (1982) Effect of electrode nature on the electrooxidation of glucose. *Elektrokhimiya*, **18**, 1120–2.

11 Adzic, R.R., Hsiao, M.W. and Yeager, E.B. (1989) Electrochemical oxidation of glucose on single crystal gold surfaces. *Journal of Electroanalytical Chemistry*, **260**, 475–85.

12 Lei, H.-W., Wu, B., Cha, C.-S. and Kita, H. (1995) Electro-oxidation of glucose on platinum in alkaline solution and selective oxidation in the presence of additives. *Journal of Electroanalytical Chemistry*, **382**, 103–10.

13 Markovic, N.M., Schmidt, T.J., Stamenkovic, V. and Ross, P.N. (2001) Oxygen reduction reaction on Pt and Pt bimetallic surfaces: a selective review. *Fuel Cells*, **1**, 105–16.

14 Alonso-Vante, N. (2003) Chevrel phase and cluster-like chalcogenide materials, in *Handbook of Fuel Cells*, Vol. **2** (eds W. Vielstich, A. Lamm and H. Gasteiger), John Wiley & Sons, Ltd, Chichester, pp. 534–43.

15 Damjanovic, A., Genshaw, M.A. and O'M Bockris, J. (1966) Distinction between intermediates produced in main and side electrodic reactions. *The Journal of Chemical Physics*, **45**, 4057–9.

16 Wells, P.P., Qian, Y.D., King, C.R., Wiltshire, R.J.K., Crabb, E.M., Smart, L.E., Thompsett, D. and Russell, A.E. (2008) To alloy or not to alloy? Cr modified Pt/C cathode catalysts for PEM fuel cells. *Faraday Discussions*, **138**, 273–85.

17 Bezerra, C.W.B., Zhang, L., Liu, H., Lee, K., Marques, A.L.B., Marques, E.P., Wang, H. and Zhang, J. (2007) A review of heat-treatment effects on activity and stability of PEM fuel cell catalysts for oxygen reduction reaction. *Journal of Power Sources*, **173**, 891–908.

18 Adzic, R.R., Zhang, J., Sasaki, K., Vukmirovic, M.B., Shao, M., Wang, J.X., Nilekar, A.U., Mavrikakis, M., Valerio, J.A. and Uribe, F. (2007) Platinum monolayer fuel cell electrocatalysts. *Topics in Catalysis*, **46**, 249–62.

19 Alonso-Vante, N. (2006) Carbonyl tailored electrocatalysts. *Fuel Cells*, **6**, 182–9.

20 Markovic, N.M. and Ross, P.N. (2002) Surface science studies of model fuel cell electrocatalysts. *Surface Science Reports*, **45**, 121–229.

21 Maciá, M.D., Campiña, J.M., Herrero, E. and Feliu, J.M. (2004) On the kinetics of oxygen reduction on platinum stepped surfaces in acidic media. *Journal of Electroanalytical Chemistry*, **564**, 141–50.

22 Ross, Jr, P.N. (1979) Structure sensitivity in electrocatalytic properties of Pt–2. Oxygen reduction on low index single crystals and the role of steps. *Journal of the Electrochemical Society*, **126**, 78–82.

23 Haung, J.C., Sen, R.K. and Yeager, E. (1979) Oxygen reduction on platinum in 85% orthophosphoric acid. *Journal of the Electrochemical Society*, **126**, 786–92.

24 Hsueh, K.L., Chin, D.T. and Srinivasan, S. (1983) Electrode kinetics of oxygen reduction. A theoretical and experimental analysis of the rotating ring-disc electrode method. *Journal of Electroanalytical Chemistry*, **153**, 79–95.

25 Hsueh, K.L., Gonzalez, E.R. and Srinivasan, S. (1983) Electrolyte effects on oxygen reduction kinetics at platinum: A rotating ring-disc electrode analysis. *Electrochimica Acta*, **28**, 691–7.

26 Mukerjee, S., Srinivasan, S., Soriaga, M.P. and McBreen, J. (1995) Effect of preparation conditions of Pt alloys on their electronic, structural, and electrocatalytic activities for oxygen reduction - XRD, XAS, and electrochemical studies. *The Journal of Physical Chemistry*, **99**, 4577–89.

27 Mukerjee, S. and McBreen, J. (1998) Effect of particle size on the electrocatalysis by carbon-supported Pt electrocatalysts: an in situ XAS investigation. *Journal of Electroanalytical Chemistry*, **448**, 163–71.

28 Alonso-Vante, N. (2003) Novel nanostructured material based on transition metal compounds for electrocatalysis, in *Catalysis of Nanoparticles Surfaces* (eds A.

Wieckowski, E. Savinova and C. Vayenas), Marcel Dekker, Inc., New York, Basel, pp. 931–58.

29 Fei, J., Song, H.K. and Palmore, G.T.R. (2007) A biopolymer composite that catalyzes the reduction of oxygen to water. *Chemistry of Materials*, **19**, 1565–70.

30 Timur, S., Pazarl Ioglu, N., Pilloton, R. and Telefoncu, A. (2004) Thick film sensors based on laccases from different sources immobilized in polyaniline matrix. *Sensors and Actuators B*, **97**, 132–6.

31 Bartlett, P.N., Tebbutt, P. and Tyrrell, C.H. (1992) Electrochemical immobilization of enzymes. 3. Immobilization of glucose oxidase in thin films of electrochemically polymerized phenols. *Analytical Chemistry*, **64**, 138–42.

32 Bartlett, P.N. and Cooper, J.M. (1993) A review of the immobilization of enzymes in electropolymerized films. *Journal of Electroanalytical Chemistry*, **362**, 1–12.

33 Rosenthal, M.V., Skotheim, T.A. and Linkous, C.A. (1986) Polypyrrole-phthalocyanine. *Synthetic Metals*, **15**, 219–27.

34 Servat, K., Tingry, S., Brunel, L., Querelle, S., Cretin, M., Innocent, C., Jolivalt, C. and Rolland, M. (2007) Modification of porous carbon tubes with enzymes: application for biofuel cells. *Journal of Applied Electrochemistry*, **37**, 121–7.

35 Klotzbach, T., Watt, M., Ansari, Y. and Minteer, S.D. (2006) Effects of hydrophobic modification of chitosan and Nafion on transport properties, ion-exchange capacities, and enzyme immobilization. *Journal of Membrane Science*, **282**, 276–83.

36 Moore, C.M., Akers, N.L., Hill, A.D., Johnson, Z.C. and Minteer, S.D. (2004) Improving the environment for immobilized dehydrogenase enzymes by modifying Nafion with tetraalkylammonium bromides. *Biomacromolecules*, **5**, 1241–7.

37 Thomas, T.J., Ponnusamy, K.E., Chang, N.M., Galmore, K. and Minteer, S.D. (2003) Effects of annealing on mixture-cast membranes of Nafion® and quaternary ammonium bromide salts. *Journal of Membrane Science*, **213**, 55–66.

38 Klotzbach, T.L., Watt, M., Ansari, Y. and Minteer, S.D. (2008) Improving the microenvironment for enzyme immobilization at electrodes by hydrophobically modifying chitosan and Nafion(polymers. *Journal of Membrane Science*, **311**, 81–8.

39 Schrenk, M.J., Villigram, R.E., Torrence, N.J., Brancato, S.J. and Minteer, S.D. (2002) Effects of mixture casting Nafion® with quaternary ammonium bromide salts on the ion-exchange capacity and mass transport in the membranes. *Journal of Membrane Science*, **205**, 3–10.

40 Luo, X.L., Xu, J.J., Du, Y. and Chen, H.Y. (2004) A glucose biosensor based on chitosan-glucose oxidase-gold nanoparticles biocomposite formed by one-step electrodeposition. *Analytical Biochemistry*, **334**, 284–9.

41 Chu, X., Duan, D., Shen, G. and Yu, R. (2007) Amperometric glucose biosensor based on electrodeposition of platinum nanoparticles onto covalently immobilized carbon nanotube electrode. *Talanta*, **71**, 2040–7.

42 Wu, L.Q., Gadre, A.P., Yi, H., Kastantin, M.J., Rubloff, G.W., Bentley, W.E., Payne, G.F. and Ghodssi, R. (2002) Voltage-dependent assembly of the polysaccharide chitosan onto an electrode surface. *Langmuir*, **18**, 8620–5.

43 Lumley-Woodyear, T.D., Rocca, P., Lindsay, J., Dror, Y., Freeman, A. and Heller, A. (1995) Polyacrylamide-based redox polymer for connecting redox centers of enzymes to electrodes. *Analytical Chemistry*, **67**, 1332–8.

44 Forster, R.J., Walsh, D.A., Mano, N., Mao, F. and Heller, A. (2004) Modulating the redox properties of an osmium-containing metallopolymer through the supporting electrolyte and cross-linking. *Langmuir*, **20**, 862–8.

45 Mao, F., Mano, N. and Heller, A. (2003) Long tethers binding Redox centers to polymer backbones enhance electron transport in enzyme 'wiring' hydrogels. *Journal of the American Chemical Society*, **125**, 4951–7.

46 Anicet, N., Bourdillon, C., Moiroux, J. and Saveant, J.M. (1998) Electron transfer in organized assemblies of biomolecules. Step-by-step avidin/biotin construction and dynamic characteristics of a spatially ordered multilayer enzyme electrode. *The Journal of Physical Chemistry B*, **102**, 9844–9.

47 Merle, G., Brunel, L., Tingry, S., Cretin, M., Rolland, M., Servat, K., Jolivalt, C., Innocent, C. and Seta, P. (2008) Electrode biomaterials based on immobilized laccase. Application for enzymatic reduction of dioxygen. *Materials Science and Engineering C*, **28** (5-6), 932–8.

48 Limoges, B., Saveant, J.M. and Yazidi, D. (2003) Quantitative analysis of catalysis and inhibition at horseradish peroxidase monolayers immobilized on an electrode surface. *Journal of the American Chemical Society*, **125**, 9192–203.

49 Anne, A., Blanc, B., Moiroux, J. and Saveant, J.M. (1998) Facile derivatization of glassy carbon surfaces by *N*-hydroxysuccinimide esters in view of attaching biomolecules. *Langmuir*, **14**, 2368–71.

50 Zhu, Y., Kaskel, S., Shi, J., Wage, T. and Van Pée, K.-H. (2007) Immobilization of *Trametes versicolor* laccase on magnetically separable mesoporous silica spheres. *Chemistry of Materials*, **19**, 6408–13.

51 Wang, J. (2008) Electrochemical glucose biosensors. *Chemical Reviews*, **108**, 814–25.

52 Soukharev, V., Mano, N. and Heller, A. (2004) A four-electron O_2-electroreduction biocatalyst superior to platinum and a biofuel cell operating at 0.88 V. *Journal of the American Chemical Society*, **126**, 8368–9.

53 Barton, S.C., Gallaway, J. and Atanassov, P. (2004) Enzymatic biofuel cells for implantable and microscale devices. *Chemical Reviews*, **104**, 4867–86.

54 Palmer, A.E., Lee, S.K. and Solomon, E.I. (2001) Decay of the peroxide intermediate in laccase: reductive cleavage of the O—O bond. *Journal of the American Chemical Society*, **123**, 6591–9.

55 Tayhas, G., Palmore, R. and Kim, H.-H. (1999) Electro-enzymatic reduction of dioxygen to water in the cathode compartment of a biofuel cell. *Journal of Electroanalytical Chemistry*, **464**, 110–17.

56 Andreasson, L.-E. and Reinhammar, B. (1979) The mechanism of electron transfer in laccase-catalysed reactions. *Biochimica et Biophysica Acta*, **568**, 145–56.

57 Shleev, S., Tkac, J., Christenson, A., Ruzgas, T., Yaropolov, A.I., Whittaker, J.W. and Gorton, L. (2005) Direct electron transfer between copper-containing proteins and electrodes. *Biosensors and Bioelectronics*, **20**, 2517–54.

58 Liu, Y., Wang, M., Zhao, F., Liu, B. and Dong, S. (2005) A low-cost biofuel cell with pH-dependent power output based on porous carbon as matrix. *Chemistry – A European Journal*, **11**, 4970–4.

59 Xu, F. (1997) Effects of redox potential and hydroxide inhibition on the pH activity profile of fungal laccases. *The Journal of Biological Chemistry*, **272**, 924–8.

60 Solis-Oba, M., Ugalde-Saldivar, V.M., Gonzalez, I. and Viniegra-Gonzalez, G. (2005) An electrochemical-spectrophotometrical study of the oxidized forms of the mediator 2,20-azino-bis-(3-ethylbenzothiazoline-6-sulfonic acid) produced by immobilized laccase. *Journal of Electroanalytical Chemistry*, **579**, 59–66.

61 Zawisza, I., Rogalski, J. and Opallo, M. (2006) Electrocatalytic reduction of dioxygen by redox mediator and laccase immobilized in silicate thin film. *Journal of Electroanalytical Chemistry*, **588**, 244–52.

62 Barton, S.C., Pickard, M., Vazquez-Duhalt, R. and Heller, A. (2002) Electroreduction of O_2 to water at 0.6 V(SHE) at pH 7 on the 'wired' *Pleurotus ostreatus* laccase cathode. *Biosensors and Bioelectronics*, **17**, 1071–4.

63 Barrière, F., Ferry, Y., Rochefort, D. and Leech, D. (2004) Targetting redox polymers as mediators for laccase oxygen reduction in a membrane-less biofuel cell. *Electrochemistry Communications*, **10**, 237–41.

64 Mano, N., Soukharev, V. and Heller, A. (2006) A laccase-wiring redox hydrogel

for efficient catalysis of O_2 electroreduction. *The Journal of Physical Chemistry B*, **110**, 11180–7.

65 Tinoco, R., Pickard, M.A. and Vazquez-Duhalt, R. (2001) Kinetic differences of purified laccases from six *Pleurotus ostreatus* strains. *Letters in Applied Microbiology*, **32**, 331–5.

66 Trudeau, F., Daigle, F. and Leech, D. (1997) Reagentless mediated laccase electrode for the detection of enzyme modulators. *Analytical Chemistry*, **69**, 882–6.

67 Tarasevich, M.R., Bogdanovskaya, V.A. and Kapustin, A.V. (2003) Nanocomposite material laccase/dispersed carbon carrier for oxygen electrode. *Electrochemistry Communications*, **5**, 491–6.

68 Zheng, W., Zhou, H.M., Zheng, Y.F. and Wang, N. (2008) A comparative study on electrochemistry of laccase at two kinds of carbon nanotubes and its application for biofuel cell. *Chemical Physics Letters*, **457**, 381–5.

69 Mano, N., Kim, H.H. and Heller, A. (2002) On the relationship between the characteristics of bilirubin oxidases and O_2 cathodes based on their 'wiring'. *The Journal of Physical Chemistry B*, **106**, 8842–8.

70 Mano, N., Kim, H.H., Zhang, Y. and Heller, A. (2002) An oxygen cathode operating in a physiological solution. *Journal of the American Chemical Society*, **124**, 6480–6.

71 Tsujimura, S., Tatsumi, H., Ogawa, J., Shimizu, S., Kano, K. and Ikeda, T. (2001) Bioelectrocatalytic reduction of dioxygen to water at neutral pH using bilirubin oxidase as an enzyme and 2,2-azinobis (3-ethylbenzothiazolin-6-sulfonate) as an electron transfer mediator. *Journal of Electroanalytical Chemistry*, **496**, 69–75.

72 Habrioux, A., Merle, G., Servat, K., Kokoh, K.B., Innocent, C., Cretin, M. and Tingry, S. (2008) Concentric glucose/O_2 biofuel cell. *Journal of Electroanalytical Chemistry*, **622**, 97–102.

73 Shimizu, A., Kwon, J.H., Sasaki, T., Satoh, T., Sakurai, N., Sakurai, T., Yamaguchi, S. and Samejima, T. (1999) *Myrothecium verrucaria* bilirubin oxidase and its mutants for potential copper ligands. *Biochemistry*, **38**, 3034–42.

74 Li, H., Webb, S.P., Ivanic, J. and Jensen, J.H. (2004) Determinants of the relative reduction potentials of type-1 copper sites in proteins. *Journal of the American Chemical Society*, **126**, 8010–19.

75 Kataoka, K., Nakai, M., Yamaguchi, K. and Suzuki, S. (1998) Gene synthesis, expression, and mutagenesis of *Zucchini mavicyanin*: the fourth ligand of blue copper center is Gln. *Biochemical and Biophysical Research Communications*, **250**, 409–13.

76 Tsujimura, S., Kano, K. and Ikeda, T. (2005) Bilirubin oxidase in multiple layers catalyzes four-electron reduction of dioxygen to water without redox mediators. *Journal of Electroanalytical Chemistry*, **576**, 113–20.

77 Christenson, A., Shleev, S., Mano, N., Heller, A. and Gorton, L. (2006) Redox potentials of the blue copper sites of bilirubin oxidases. *Biochimica et Biophysica Acta – Bioenergetics*, **1757**, 1634–41.

78 Wang, J. and Ozsoz, M. (1990) A polishable amperometric biosensor for bilirubin. *Electroanalysis*, **2**, 647–50.

79 Shoham, B., Migron, Y., Riklin, A., Willner, I. and Tartakovsky, B. (1995) A bilirubin biosensor based on a multilayer network enzyme electrode. *Biosensors and Bioelectronics*, **10**, 341–52.

80 Tsujimura, S., Kawaharada, M., Nakagawa, T., Kano, K. and Ikeda, T. (2003) Mediated bioelectrocatalytic O_2 reduction to water at highly positive electrode potentials near neutral pH. *Electrochemistry Communications*, **5**, 138–41.

81 Xu, F., Shin, W., Brown, S.H., Wahleithner, J.A., Sundaram, U.M. and Solomon, E.I. (1996) A study of a series of recombinant fungal laccases and bilirubin oxidase that exhibit significant differences in redox potential, substrate specificity, and stability. *Biochimica et Biophysica Acta*, **1292**, 303–11.

82 Kang, C., Shin, H., Zhang, Y. and Heller, A. (2004) Deactivation of bilirubin oxidase by a product of the reaction of urate and O_2. *Bioelectrochemistry*, **65**, 83–8.

83 Topcagic, S. and Minteer, S.D. (2006) Development of a membraneless ethanol/oxygen biofuel cell. *Electrochimica Acta*, **51**, 2168–72.

84 Shleev, S., Kasmi, A.E., Ruzgas, T. and Gorton, L. (2004) Direct heterogeneous electron transfer reactions of bilirubin oxidase at a spectrographic graphite electrode. *Electrochemistry Communications*, **6**, 934–9.

85 Weigel, M.C., Tritscher, E. and Lisdat, F. (2007) Direct electrochemical conversion of bilirubin oxidase at carbon nanotube-modified glassy carbon electrodes. *Electrochemistry Communications*, **9**, 689–93.

86 Lerner, H., Giner, J., Soeldner, J.S. and Colton, C.K. (1979) electrochemical glucose oxidation on a platinized platinum electrode in Krebs-ringer solution. *Journal of the Electrochemical Society*, **126**, 237–42.

87 Giner, J., Marincic, L., Soeldner, J.S. and Colton, C.K. (1981) Electrochemical glucose oxidation on a platinum electrode in Krebs-Ringer solution. *Journal of the Electrochemical Society*, **128**, 2106–14.

88 Shao, M.-J., Xing, X.-K. and Liu, C.-C. (1987) Cyclic voltammetric study of glucose oxidation on an oxide-covered platinum electrode in the presence of an underpotential-deposited thallium layer. *Bioelectrochemistry and Bioenergetics*, **17**, 59–70.

89 Larew, A. and Johnson, D.C. (1989) Concentration dependence of the mechanism of glucose oxidation at gold electrodes in alkaline media. *Journal of Electroanalytical Chemistry*, **262**, 167–82.

90 Bae, I.T., Xing, X., Liu, C. and Yeager, E. (1990) In situ Fourier transform infrared reflection absorption spectroscopic studies of glucose oxidation on platinum in acid. *Journal of Electroanalytical Chemistry*, **284**, 335–49.

91 Bae, I.T., Yeager, E., Xing, X. and Liu, C.C. (1991) In situ infrared studies of glucose oxidation on platinum in an alkaline medium. *Journal of Electroanalytical Chemistry*, **309**, 131–45.

92 Hsiao, M.W., Adzic, R.R. and Yeager, E.B. (1992) The effects of adsorbed anions on the oxidation of D-glucose on gold single crystal electrodes. *Electrochimica Acta*, **37**, 357–63.

93 Wilde, C.P. and Zhang, M. (1993) The influence of lead upd on the oxidation of glucose at platinum electrodes an electrochemical quartz crystal microbalance study. *Electrochimica Acta*, **38**, 2725–32.

94 Hsiao, M.W., Adzic, R.R. and Yeager, E.B. (1996) Electrochemical oxidation of glucose on single crystal and polycrystalline gold surfaces in phosphate buffer. *Journal of the Electrochemical Society*, **143**, 759–67.

95 Jin, C. and Chen, Z. (2007) Electrocatalytic oxidation of glucose on gold-platinum nanocomposite electrodes and platinum-modified gold electrodes. *Synthetic Metals*, **157**, 592–6.

96 Sun, Y., Buck, H. and Mallouk, T.E. (2001) Combinatorial discovery of alloy electrocatalysts for amperometric glucose sensors. *Analytical Chemistry*, **73**, 1599–604.

97 Kokoh, K.B., Léger, J.-M., Beden, B., Huser, H. and Lamy, C. (1992) 'On line' chromatographic analysis of the products resulting from the electrocatalytic oxidation of D-glucose on pure and adatoms modified Pt and Au electrodes – Part II. Alkaline medium. *Electrochimica Acta*, **37**, 1909–18.

98 Kokoh, K.B., Léger, J.-M., Beden, B. and Lamy, C. (1992) 'On line' chromatographic analysis of the products resulting from the electrocatalytic oxidation of D-glucose on Pt, Au and adatoms modified Pt electrodes - Part I. Acid and neutral media. *Electrochimica Acta*, **37**, 1333–42.

99 Park, S., Boo, H. and Chung, T.D. (2006) Electrochemical non-enzymatic glucose sensors. *Analytica Chimica Acta*, **556**, 46–57.

100 Becerik, I. and Kadirgan, F. (2001) Glucose sensitivity of platinum-based alloys incorporated in polypyrrole films at neutral media. *Synthetic Metals*, **124**, 379–84.

101 Möller, H. and Pistorius, P.C. (2004) The electrochemistry of gold-platinum alloys. *Journal of Electroanalytical Chemistry*, **570**, 243–55.

102 Garcia-Gutierrez, D.I., Gutierrez-Wing, C.E., Giovanetti, L., Ramallo-Lopez, J.M., Requejo, F.G. and Jose-Yacaman, M. (2005) Temperature effect on the synthesis of Au-Pt bimetallic nanoparticles. *The Journal of Physical Chemistry B*, **109**, 3813–21.

103 Devarajan, S., Bera, P. and Sampath, S. (2005) Bimetallic nanoparticles: a single step synthesis, stabilization, and characterization of Au-Ag, Au-Pd, and Au-Pt in sol-gel derived silicates. *Journal of Colloid and Interface Science*, **290**, 117–29.

104 Habrioux, A., Sibert, E., Servat, K., Vogel, W., Kokoh, K.B. and Alonso-Vante, N. (2007) Activity of platinum-gold alloys for glucose electrooxidation in biofuel cells. *The Journal of Physical Chemistry B*, **111**, 10329–33.

105 Roustom, B.E., Siné, G., Fóti, G. and Comninellis, C. (2007) A novel method for the preparation of bi-metallic (Pt—Au) nanoparticles on boron doped diamond (BDD) substrate: application to the oxygen reduction reaction. *Journal of Applied Electrochemistry*, **37**, 1227–36.

106 Atwan, M.H., Macdonald, C.L.B., Northwood, D.O. and Gyenge, E.L. (2006) Colloidal Au and Au-alloy catalysts for direct borohydride fuel cells: electrocatalysis and fuel cell performance. *Journal of Power Sources*, **158**, 36–44.

107 Zeng, J., Yang, J., Lee, J.Y. and Zhou, W. (2006) Preparation of carbon-supported core-shell Au-Pt nanoparticles for methanol oxidation reaction: the promotional effect of the Au core. *The Journal of Physical Chemistry B*, **110**, 24606–11.

108 Capek, I. (2004) Preparation of metal nanoparticles in water-in-oil (w/o) microemulsions. *Advances in Colloid and Interface Science*, **110**, 49–74.

109 López-Quintela, M.A., Tojo, C., Blanco, M.C., Rio, L.G. and Leis, J.R. (2004) Microemulsion dynamics and reactions in microemulsions. *Current Opinion in Colloid and Interface Science*, **9**, 264–78.

110 Boutonnet, M., Kizling, J., Stenius, P. and Maire, G. (1982) The preparation of monodisperse colloidal metal particles from microemulsions. *Colloids and Surfaces*, **5**, 209–25.

111 Solla-Gullon, J., Vidal-Iglesias, F.J., Montiel, V. and Aldaz, A. (2004) Electrochemical characterization of platinum-ruthenium nanoparticles prepared by water-in-oil microemulsion. *Electrochimica Acta*, **49**, 5079–88.

112 Solla-Gullon, J., Rodes, A., Montiel, V., Aldaz, A. and Clavilier, J. (2003) Electrochemical characterisation of platinum-palladium nanoparticles prepared in a water-in-oil microemulsion. *Journal of Electroanalytical Chemistry*, **554-555**, 273–84.

113 Brimaud, S., Coutanceau, C., Garnier, E., Leger, J.M., Gerard, F., Pronier, S. and Leoni, M. (2007) Influence of surfactant removal by chemical or thermal methods on structure and electroactivity of Pt/C catalysts prepared by water-in-oil microemulsion. *Journal of Electroanalytical Chemistry*, **602**, 226–36.

114 Vogel, W., Tesche, B. and Schulze, W. (1983) X-ray structure and optical properties of silver films prepared by condensation of pre-formed Ag-clusters. *Chemical Physics*, **74**, 137–42.

115 Vogel, W., Bradley, J., Vollmer, O. and Abraham, I. (1998) Transition from five-fold symmetric to twinned FCC gold particles by thermally induced growth. *The Journal of Physical Chemistry B*, **102**, 10853–9.

116 Darling, A.S., Mintern, R.A. and Chaston, J.C. (1952) The gold-platinum system. *Journal Institute of Metals*, **81**, 1952–3.

117 Qian, L. and Yang, X. (2006) Polyamidoamine dendrimers-assisted electrodeposition of gold-platinum bimetallic nanoflowers. *The Journal of Physical Chemistry B*, **110**, 16672–8.

118 Cen, L., Neoh, K.G., Cai, Q. and Kang, E.T. (2006) Au-Pt bimetallic nanoparticles formation via viologen-mediated reduction on polymeric nanospheres. *Journal of Colloid and Interface Science*, **300**, 190–9.

119 Burke, L.D., Moran, J.M. and Nugent, P.F. (2003) Cyclic voltammetry responses of metastable gold electrodes in aqueous media. *Journal of Solid State Electrochemistry*, **7**, 529–38.

120 Woods, R. (1971) The surface composition of platinum-gold alloys. *Electrochimica Acta*, **16**, 655–9.
121 Woods, R. (1969) Electrocatalytically co-deposited platinum-gold electrodes and their electrocatalytic activity for acetate ion oxidation. *Electrochimica Acta*, **14**, 533–40.
122 Becerik, I., Suzer, S. and Kadirgan, F. (1999) Platinum-palladium loaded polypyrrole film electrodes for the electrooxidation of -glucose in neutral media. *Journal of Electroanalytical Chemistry*, **476**, 171–6.
123 Tominaga, M., Shimazoe, T., Nagashima, M. and Taniguchi, I. (2005) Electrocatalytic oxidation of glucose at gold nanoparticle-modified carbon electrodes in alkaline and neutral solutions. *Electrochemistry Communications*, **7**, 189–93.
124 Governo, A.T., Proença, L., Parpot, P., Lopes, M.I.S. and Fonseca, I.T.E. (2004) Electro-oxidation of D-xylose on platinum and gold electrodes in alkaline medium. *Electrochimica Acta*, **49**, 1535–45.
125 Beden, B., Largeaud, F., Kokoh, K.B. and Lamy, C. (1996) Fourier transform infrared reflectance spectroscopic investigation of the electrocatalytic oxidation of D-glucose: identification of reactive intermediates and reaction products. *Electrochimica Acta*, **41**, 701–9.
126 Rao, M.L.B. and Drake, R.F. (1969) Studies of electrooxidation of dextrose in neutral media. *Journal of the Electrochemical Society*, **116**, 334–7.
127 Zhang, M., Mullens, C. and Gorski, W. (2007) Coimmobilization of dehydrogenases and their cofactors in electrochemical biosensors. *Analytical Chemistry*, **79**, 2446–50.
128 Silber, A., Bräuchle, C. and Hampp, N. (1995) Electrocatalytic oxidation of reduced nicotinamide adenine dinucleotide (NADH) at thick-film gold electrodes. *Journal of Electroanalytical Chemistry*, **390**, 83–9.
129 Delecouls-Servat, K., Bergel, A. and Basseguy, R. (2001) Surface modified electrodes for NADH oxidation in oxidoreductase-catalyzed synthesis. *Journal of Applied Electrochemistry*, **31**, 1095–101.
130 Gao, F., Yan, Y., Su, L., Wang, L. and Mao, L. (2007) An enzymatic glucose/O_2 biofuel cell: preparation, characterization and performance in serum. *Electrochemistry Communications*, **9**, 989–96.
131 Sato, F., Togo, M., Islam, M.K., Matsue, T., Kosuge, J., Fukasaku, N., Kurosawa, S. and Nishizawa, M. (2005) Enzyme-based glucose fuel cell using vitamin K3-immobilized polymer as an electron mediator. *Electrochemistry Communications*, **7**, 643–7.
132 Yuhashi, N., Tomiyama, M., Okuda, J., Igarashi, S., Ikebukuro, K. and Sode, K. (2005) Development of a novel glucose enzyme fuel cell system employing protein engineered PQQ glucose dehydrogenase. *Biosensors and Bioelectronics*, **20**, 2145–50.
133 Alvarez-Icaza, M., Kalisz, H.M., Hecht, H.J., Aumann, K.D., Schomburg, D. and Schmid, R.D. (1995) The design of enzyme sensors based on the enzyme structure. *Biosensors and Bioelectronics*, **10**, 735–42.
134 Zhu, Z., Momeu, C., Zakhartsev, M. and Schwaneberg, U. (2006) Making glucose oxidase fit for biofuel cell applications by directed protein evolution. *Biosensors and Bioelectronics*, **21**, 2046–51.
135 Mano, N., Mao, F. and Heller, A. (2002) A miniature biofuel cell operating in a physiological buffer. *Journal of the American Chemical Society*, **124**, 12962–3.
136 Kleppe, K. (1966) The effect of hydrogen peroxide on glucose oxidase from *Aspergillus niger*. *Biochemistry*, **5**, 139–43.
137 Kenausis, G., Chen, Q. and Heller, A. (1997) Electrochemical glucose and lactate sensors based on 'wired' thermostable soybean peroxidase operating continuously and stably at 37 °C. *Analytical Chemistry*, **69**, 1054–60.
138 Wilson, R. and Turner, A.P.F. (1992) Glucose oxidase: an ideal enzyme. *Biosensors and Bioelectronics*, **7**, 165–85.
139 Mano, N., Mao, F. and Heller, A. (2005) On the parameters affecting the characteristics of the 'wired' glucose oxidase anode. *Journal of Electroanalytical Chemistry*, **574**, 347–57.

140 Bohmhammel, K., Huttl, R., Pritzkat, K. and Wolf, G. (1993) Thermokinetic investigations into enzyme-catalyzed glucose-oxidation. *Thermochimica Acta*, **217**, 9–18.

141 Degani, Y. and Heller, A. (1987) Direct electrical communication between chemically modified enzymes and metal electrodes. I Electron transfer from glucose oxidase to metal electrodes via electron relays, bound covalently to the enzyme. *The Journal of Physical Chemistry*, **91**, 1285–9.

142 Gallaway, J., Wheeldon, I., Rincon, R., Atanassov, P., Banta, S. and Barton, S.C. (2008) Oxygen-reducing enzyme cathodes produced from SLAC, a small laccase from *Streptomyces coelicolor*. *Biosensors and Bioelectronics*, **23**, 1229–35.

143 Ianniello, R.M., Lindsay, T.J. and Yacynych, A.M. (1982) Differential pulse voltammetric study of direct electron transfer in glucose oxidase chemically modified graphite electrodes. *Analytical Chemistry*, **54**, 1098–101.

144 Savitri, D. and Mitra, C.K. (1998) Electrochemistry of reconstituted glucose oxidase on carbon paste electrodes. *Bioelectrochemistry and Bioenergetics*, **47**, 67–73.

145 Luo, H., Shi, Z., Li, N., Gu, Z. and Zhuang, Q. (2001) Investigation of the electrochemical and electrocatalytic behavior of single-wall carbon nanotube film on a glassy carbon electrode. *Analytical Chemistry*, **73**, 915–20.

146 Cai, C. and Chen, J. (2004) Direct electron transfer of glucose oxidase promoted by carbon nanotubes. *Analytical Biochemistry*, **332**, 75–83.

147 Ivnitski, D., Branch, B., Atanassov, P. and Apblett, C. (2006) Glucose oxidase anode for biofuel cell based on direct electron transfer. *Electrochemistry Communications*, **8**, 1204–10.

148 Akers, N.L., Moore, C.M. and Minteer, S.D. (2005) Development of alcohol/O_2 biofuel cells using salt-extracted tetrabutylammonium bromide/Nafion membranes to immobilize dehydrogenase enzymes. *Electrochimica Acta*, **50**, 2521–5.

149 Zhao, Y.D., Zhang, W.D., Chen, H. and Luo, Q.M. (2002) Direct electron transfer of glucose oxidase molecule adsorbed onto carbon nanotubes powder microelectrode. *Analytical Sciences*, **18**, 939–41.

150 Barrière, F., Kavanagh, P. and Leech, D. (2006) A laccase-glucose oxidase biofuel cell prototype operating in a physiological buffer. *Electrochimica Acta*, **51**, 5187–92.

151 Cass, A.E.G., Davis, G., Francis, G.D., Hill, H.A.O., Aston, W.J., Higgins, I.J., Plotkin, E.V., Scott, L.D.L. and Turner, A.P.F. (1984) Ferrocene-mediated enzyme electrode for amperometric determination of glucose. *Analytical Chemistry*, **56**, 667–71.

152 Mano, N., Mao, F. and Heller, A. (2004) Electro-oxidation of glucose at an increased current density at a reducing potential. *Chemical Communications*, 2116–17.

153 Katz, E., Riklin, A., Heleg-Shabtai, V., Willner, I. and Bückmann, A.F. (1999) Glucose oxidase electrodes via reconstitution of the apo-enzyme: tailoring of novel glucose biosensors. *Analytica Chimica Acta*, **385**, 45–58.

154 Willner, I., Heleg-Shabtai, V., Blonder, R., Katz, E., Tao, G., Bückmann, A.F. and Heller, A. (1996) Electrical wiring of glucose oxidase by reconstitution of FAD-modified monolayers assembled onto Au-electrodes. *Journal of the American Chemical Society*, **118**, 10321–2.

155 Gros, P., Bergel, A. and Comtat, M. (1996) Electrochemically assisted catalyst for enzymatic glucose oxidation. *Chemical Engineering Science*, **51**, 2337–46.

156 Gros, P. and Bergel, A. (1995) Improved model of a polypyrrole glucose oxidase modified electrode. *Journal of Electroanalytical Chemistry*, **386**, 65–73.

157 Chaubey, A., Gerard, M., Singhal, R., Singh, V.S. and Malhotra, B.D. (2001) Immobilization of lactate dehydrogenase on electrochemically prepared polypyrrole-polyvinylsulphonate composite films for application to lactate biosensors. *Electrochimica Acta*, **46**, 723–9.

158 Gaikwad, P.D., Shirale, D.J., Savale, P.A., Datta, K., Ghosh, P., Pathan, A.J., Rabbani, G. and Shirsat, M.D. (2007)

Development of PANI-PVS-GOD electrode by potentiometric method for determination of glucose. *International Journal of Electrochemical Science*, **2**, 488–97.

159 Yahiro, A.T., Lee, S.M. and Kimble, D. O. (1964) Bioelectrochemistry I. Enzyme utilizing bio-fuel cell studies. *Biochimica et Biophysica Acta*, **88**, 375–83.

160 Heller, A. (2004) Miniature biofuel cells. *Physical Chemistry Chemical Physics*, **6**, 209–16.

161 Katz, E., Willner, I. and Kotlyar, A.B. (1999) A non-compartmentalized glucose O_2 biofuel cell by bioengineered electrode surfaces. *Journal of Electroanalytical Chemistry*, **479**, 64–8.

162 Mano, N., Mao, F. and Heller, A. (2003) Characteristics of a miniature compartment-less glucose-O_2 biofuel cell and its operation in a living plant. *Journal of the American Chemical Society*, **125**, 6588–94.

163 Tamaki, T., Ito, T. and Yamaguchi, T. (2007) Immobilization of hydroquinone through a spacer to polymer grafted on carbon black for a high-surface-area biofuel cell electrode. *The Journal of Physical Chemistry B*, **111**, 10312–19.

164 Palmore, G.T.R. and Whitesides, G.M. (1994) Microbial and enzymatic biofuel cells, in *Enzymatic Conversion of Biomass for Fuels Production*, Vol. **566** (ed. E. Himmel), American Chemical Society, pp. 271–90.

Keywords

biofuel cells; O_2 reduction; bilirubin oxidase; laccase; glucose oxidase; redox mediator; AuPt nanoparticles; nanoalloys.

4
Spherical and Anisotropic Metallic Nanomaterials-Based NSET Biosensors

Paresh Chandra Ray, Jelani Griffin, Wentong Lu, Oleg Tovmachenko, Anant K. Singh, Dulal Senapati and Gabriel A. Kolawole

4.1
Introduction

The fast-growing research fields related to genomics and proteomics have attracted much interest in the development of novel tools for the rapid, simple and specific electrical or optical detection of biomolecules [1–4]. Disease-causing mutations have been identified in an increasing number of genes in recent years using molecular genetic techniques [1–4]. As these newly identified genes are analyzed, it is clear that, except in a few genetic diseases where one mutation accounts for the majority of the cases, multiple mutant alleles are involved in each condition, and that mutations are often family- or population-specific. For each new patient of a genetic disorder, identifying the mutation in the candidate gene requires the scanning of a substantial portion of the gene, using laborious techniques such as DNA sequencing. Once the mutation is identified, however, other family members at risk can be screened for the specific disease-causing mutation alone to assess disease risk. Because the majority of mutations in genetic disorders are due to single base pair changes or to small insertions or deletions, it is highly desirable to develop a DNA diagnostic test that is highly sensitive, specific, cost-effective and easy to carry out for each mutation screened in the clinical laboratory. Such an approach would be useful for a variety of commercial and scientific applications, including the identification of genetic mutations or single-nucleotide polymorphisms (SNPs), medical diagnostics, gene delivery, assessment of gene expression and drug discovery. In order to continue these advances, as well as to exploit these opportunities and address the growing market needs of the twenty-first century, future devices must link high performance with speed, simplicity and low cost. In the coming decade, the ability to sense and detect the state of biological systems and living organisms, whether optically, electrically or magnetically, will be radically transformed by developments in material physics and chemistry. Moreover, the emerging ability to control the patterns of matter on a nanometer length scale can be expected to lead to entirely new types of biological sensor. These new

Nanomaterials for the Life Sciences Vol. 3: Mixed Metal Nanomaterials. Edited by Challa S. S. R. Kumar

ISBN: 978-3-527-32153-7

systems will be capable of sensing at the single-molecule level in living cells, and also capable of parallel integration for the detection of multiple signals, enabling a diversity of simultaneous experiments, as well as better crosschecks and controls.

During the past 15 years the field of biosensor using nanomaterials has witnessed a veritable explosion of interest in the use of nanomaterials in assays for DNA/RNA, protein and cell markers for many diseases. The intense research undertaken has been fueled by the need for practical, robust and highly sensitive and selective detection agents that can address the deficiencies of conventional technologies. Consequently, over the past decade, hundreds of research papers on nanomaterial-based biosensors have been published [1–111]. Nanomaterial-based biosensors, as one of the main optical biosensor technologies, have been extensively featured in both books [108–111] and reviews [5–7, 19, 87–94] describing biosensors. In this chapter, we will review recent advances in nanomaterials surface energy transfer (NSET) -based sensor technology, and its applications.

Noble metal nanostructures attract much interest on the basis of their unique properties, including large optical field enhancements resulting in the strong scattering and absorption of light [5–97]. Such enhancements in the optical and photothermal properties of noble metal nanoparticles arise from the resonant oscillation of their free electrons in the presence of light, also known as surface plasmon resonance (SPR). The nanoscience revolution that sprouted throughout the 1990s is today having a major impact on current and future biotechnology worldwide [5–111]. Thus, the increasing availability of nanostructures with highly controlled optical properties in the nanometer size range has created widespread interest in their use in biotechnological systems for diagnostic applications and biological imaging [5–111]. Recently, many reports have been made on the development of fluorescence-based assays for biodetection [1–4], these assays being based on Förster resonance energy transfer (FRET) [59] or non-FRET quenching mechanisms. FRET is a spectroscopic technique used for measuring distances in the 3–8 nm range. Although FRET technology is very convenient, and can be applied routinely at the single-molecule detection limit, the efficiency of FRET is very sensitive to the distance between the donor and an acceptor. The length scale for detection using FRET-based methods is limited by the nature of the dipole–dipole mechanism, which effectively constrains the length scales to distances on the order of <100 Å ($R_0 \approx 60$ Å). However, the limitations of FRET can be overcome by using a dynamic molecular ruler based on the distance-dependent plasmon coupling of metal nanoparticles. Recently, several groups – including that of the present authors [10–14, 25–35, 37–58] – have reported that NSET is a technique capable of measuring distances almost twice as far as FRET, in which energy transfer from a donor molecule to a nanoparticle surface follows a predictable distance dependence. In this chapter, we discuss the NSET properties of spherical and anisotropic metallic nanomaterials, and present examples of how these materials are being utilized for biodiagnostics, biophysical studies and biosensor devices. Particular emphasis is placed as to how the unique tunability of the plasmon resonance properties of metal nanoparticles, through variation of their

size, shape, composition and medium, allows chemists to design nanostructures geared for specific bioapplications.

4.1.1 Nanotechnology Promises on Biological Detection

The nanoscience revolution that sprouted throughout the 1990s is having a major impact on current and future sensor technologies worldwide [5–97]. Today, nanotechnology is an emerging technology that not only holds promises for society but also is capable of revolutionizing our approaches to common problems. Nanotechnology is poised to have a major impact on science, food systems, agriculture, medicine and the environment. Nanoparticles are particularly useful because of their extremely small size (1 to 100 nm), which enables them to access a variety of biological environments. Such small size also endows nanoparticles with valuable size-dependent properties that can be exploited in a number of applications. These benefits of nanotechnology make it ideal for sensor development, and also for environmental and biological monitoring. Finally, the large surface areas of nanoparticles may serve as platforms for the engineering of multifunctional systems. Many points of intersection occur between nanoscience and nanotechnology and the biological sciences; indeed, the elementary functional units of biological systems comprise complex nanoscale components. In terms of biological sensing, the use of nanotechnology has led to the production of numerous small-scale, rapid, sensitive multianalyte instruments that are useful not only in the laboratory but also as field-portable instruments. The merging of biotechnology with nanoscience will allow us not only to take advantage of the improved evolutionary biological components to generate new smart sensors, but also to apply today's advanced characterization and fabrication techniques to solve environmental and biological problems. Miniature sensors developed through nanotechnology could also be used to detect specific bioagents that have been accidentally or deliberately released into the environment. Cancer nanotechnology represents an interdisciplinary area of research in science, engineering and medicine, with broad applications for molecular imaging, molecular diagnosis and targeted therapy. Here, the basic rationale is that the nanometer-sized particles, such as semiconductor quantum dots and iron oxide nanocrystals, have optical, magnetic or structural properties that are not available from molecules or bulk solids. Yet, when linked with tumor-targeting ligands, such as monoclonal antibodies, peptides or small molecules, the nanoparticles can be used to target both tumor antigens and vasculatures, with high affinity and specificity. Within the mesoscopic size range of 5–100 nm diameter, nanoparticles also have large surface areas and functional groups for conjugating to multiple diagnostic and therapeutic agents. Recent advances have led to the development of bioaffinity nanoparticle probes for molecular and cellular imaging, of targeted nanoparticle drugs for cancer therapy, and of integrated nanodevices for early cancer detection and screening. Taken together, these developments raise exciting opportunities for personalized oncology in which genetic and protein biomarkers may be used to diagnose and treat cancer,

based on the molecular profiles of individual patients. In aiming to address issues concerning the potential effects of emerging nanotechnologies on biodetection, we discuss in this chapter the recent efforts made on the development of NSET probes for screening pathogens DNA/RNA and cancer cells.

4.2
Size- and Shape-Dependent Super Quenching Properties of Nanomaterials

The optical properties of a material are determined by the type of motion that its electrons are allowed to execute. Unbound electrons have a motion that is not quantized and can thus absorb any amount of energy. When an electron is bound in an atom or in a molecule, its motion becomes highly confined and quantization sets in. The permitted types of motion in atomic or molecular orbitals are found to have well-defined energies. In the hydrogen atom, the electron is confined to a length scale of ~50 pm, but what would happen if we were able to reduce the physical size of the material so that it became comparable to, or even smaller than, the Bohr radius? This would decrease the space in which the charge carriers moved, and thus an additional quantum confinement would be imposed on their motion. This would in turn lead to an increase in the band gap energy, the electron and hole kinetic energy, and the density of the charge carriers within and at the nanoparticle surface. For these reasons, as well as the fact that the surface-to-volume ratio greatly increases, new properties are observed. In noble metals, the decrease in size below the electron mean free path gives rise to intense absorption in the visible–near-ultraviolet (UV) range. This results from the coherent oscillation of the free electrons from one surface of the particle to the other, and is referred to as the surface plasmon absorption. Such strong absorption induces a strong coupling of the nanoparticles to the electromagnetic radiation of light, which in turn provides these metallic nanoparticles with the brilliant color in colloidal solution that first intrigued scientists in the seventeenth century. Due to strong surface plasmon absorption, the molar extinction coefficients at the wavelength of the maximum absorption of gold colloids are few orders of magnitudes higher than those of strong organic dyes, as reported recently [37–58] [$\varepsilon_{(15)\ 528nm} = 3.6 \times 10^8\,cm^{-1}\,M^{-1}$, $\varepsilon_{(30)\ 530nm} = 3.0 \times 10^9\,cm^{-1}\,M^{-1}$, $\varepsilon_{(40)\ 533nm} = 6.7 \times 10^9\,cm^{-1}\,M^{-1}$, $\varepsilon_{(50)\ 535nm} = 1.5 \times 10^{10}\,cm^{-1}\,M^{-1}$, $\varepsilon_{(60)\ 540nm} = 2.9 \times 10^{10}\,cm^{-1}\,M^{-1}$, and $\varepsilon_{(80)\ 550nm} = 6.9 \times 10^{10}\,cm^{-1}\,M^{-1}$]. Due to their large molar extinction coefficients (~$10^{10}\,cm^{-1}\,M^{-1}$ for 45 nm particles) and its nanomolar binding affinities for organic dyes, gold nanostructures have interesting and potentially useful effects on the photoluminescence of nearby emitters. Molecular chromophores situated in the vicinity of isolated colloidal metal particles in suspension usually experience a quenching of their fluorescence, whereas photoluminescence may be enhanced in more complex structures that arise from the deposition of aggregated metal particles onto surfaces. The local field enhancement leads to an increased excitation rate, whereas nonradiative energy transfer to the particle leads to a decrease in the quantum yield (quenching). Because of these competing effects, various experiments have shown either fluorescence enhancement or fluorescence quench-

ing, depending on the distance regime. At very close distances (<10 Å), a radiative rate enhancement is observed [37–58], while at intermediate distances (20–300 Å) energy transfer is the dominant process. Yet, at very large distances (>500 Å), fluorescence oscillations due to dipole–mirror effects take precedence.

Figure 4.1a shows the quenching behavior of 5′-Cy3-modified GTAACTTC-CATTTCTTTTGG-3′ DNA as a function of 45 nm gold nanoparticle concentration ($\approx 10^{-11}$ *M*). Figure 4.1b shows a linear plot, with the F_0/F intercept equal to 1, and a slope of $K_{SV} \approx 2.7 \times 10^{10}\, M^{-1}$, expressing the hyperquenching efficiency of the fluorophore-excited state. The results indicate that 45 nm gold nanoparticles are seven to eight orders of magnitude more efficient than typical small-molecule dye–quencher pairs [97]. This strong quenching ability of colloidal gold is related to its large molar extinction coefficients ($\sim 10^{10}\, cm^{-1}\, M^{-1}$ for 45 nm particles) and its nanomolar binding affinities for organic dyes [14, 37–58, 97]. Figure 4.1c shows

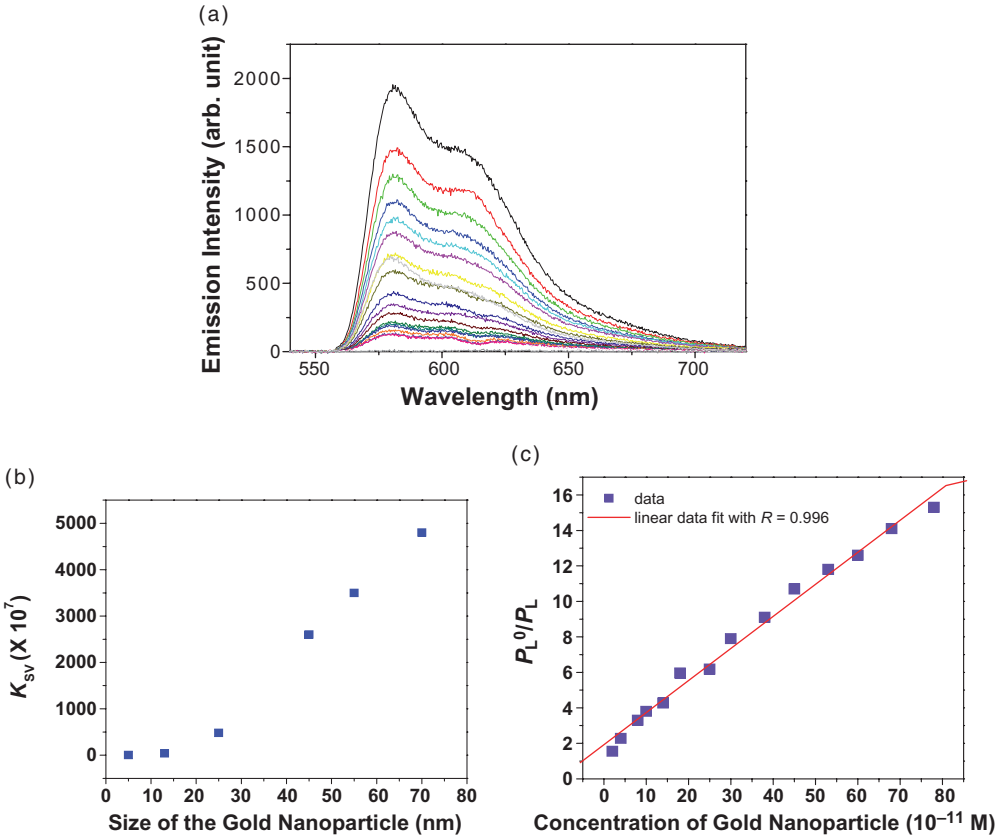

Figure 4.1 (a) Hyperefficient quenching by gold nanoparticles; (b) Stern–Volmer plots of emission intensity change due to photoluminescence quenching by 45 nm gold nanoparticles; (c) Variation of the Stern–Volmer quenching constant (K_{SV}) with gold nanoparticle size. Reprinted with permission from Ref. [97].

how the Stern–Volmer quenching constant (K_{sv}) varies with particle size. As noted from the figure, the quenching efficiency increases tremendously with the increase in particle diameter, rising by three orders of magnitude from 4×10^7 to 3.7×10^{10} as the particle size increased from 5 to 70 nm. This tremendous increment with particle size may be due to several factors, including:

- A reduced surface area in smaller nanoparticles, which will limit dye accommodation on the gold nanoparticles.
- An impressive difference in extinction coefficients (from 8×10^7 to 3.2×10^{10}) of the visible absorption spectra of 5 nm to 70 nm gold nanoparticles.
- An increased overlap between nanoparticle absorption with Cy3 emission with particle size.

Due to this extraordinarily high K_{SV}, quenching can be observed even at subpicomolar concentrations of nanoparticles, which suggests that a combination of Cy3-modified DNA with correctly sized gold nanoparticles may, potentially, lead to highly sensitive optical biosensors.

Recently, Kondon *et al.* [52] reported the photoluminescence quenching of a CdSe quantum dot (QD) by well-defined hexanethiolate monolayer-protected clusters (MPCs). The study results highlighted the fact that photoluminescence quenching by small MPCs occurs via a resonant electron transfer mechanism, with the electron transfer quenching efficiency increasing greatly in line with increasing MPC size. The reported correlation between the electron transfer quenching efficiency and the MPC core volume suggested that the quenching efficiency was governed by the absorption cross-section of the MPC quencher that scales as its core volume. Park *et al.* [53] demonstrated that the silica spacer effectively reduces photoluminescence quenching of the core by the gold nanostructure. Photoluminescence measurements at the single particle level showed that addition of the spacer layer effectively reduces the core photoluminescence quenching by the gold layer, rendering both constituents of the multicomponent nanostructure optically active. The study results demonstrated the utility of the novel nanomaterials, which simultaneously exhibit both bright photoluminescence and an available metal surface for biofunctionalization. Pons *et al.* [54] reported the quenching of luminescent CdSe–ZnS QDs due to interactions with proximal Au nanoparticles (NPs) conjugated to the nanocrystal surface by rigid, variable-length peptides. By using a combination of easy to implement self-assembly and rigid beta-sheet peptides, these authors were able to achieve two unique features: (i) to vary the ratio of Au–NP to QD in a given QD–YEHK$_m$-Au–NP conjugate sample; and (ii) to discretely span a broad range of separation distances by varying the number of repeat units m from one conjugate series to another. Dulkeith *et al.* [57] reported the radiative and nonradiative decay rates of lissamine dye molecules, chemically attached to differently sized gold nanoparticles, by using a time-resolved fluorescence technique. Here, a pronounced fluorescence quenching was demonstrated for the smallest nanoparticles of 1 nm radius. Moreover, the results indicated that the quenching was caused not only by an increased nonradiative rate but, equally importantly, by a drastic decrease in the dye's radiative rate. Fan *et al.*

[58] showed that gold nanoparticles would quench the fluorescence of cationic polyfluorene with Stern–Volmer constants (K_{SV}) approaching $10^{11}\,M^{-1}$ – several orders of magnitude larger than any previously reported conjugated polymer–quencher pair, and nine to ten orders larger than small molecule dye–quencher pairs. Fan's group also showed that K_{SV} depends on ionic strength, charge and conjugation length of the polymer, and the dimensions (and thus optical properties) of the nanoparticles. The study results confirmed that three factors accounted for this extraordinary efficiency: (i) an amplification of the quenching via rapid internal energy or electron transfer; (ii) electrostatic interactions between the cationic polymer and anionic nanoparticles; and (iii) the ability of gold nanoparticles to quench via efficient energy transfer.

4.3 Nanomaterial Surface Energy Transfer (NSET)

Fluorescence (or Förster) resonance energy transfer (FRET) [59] (see Figure 4.2a) involves nonradiative energy transfer from a photoexcited donor molecule, following the absorption of a higher energy photon, to an acceptor molecule of a different species (brought in close proximity), which may relax to its ground state by emitting a lower-energy photon. As this process results from dipole–dipole interactions, it is heavily dependent on the center-to-center separation distance, and also requires a nonzero integral of the spectral overlap between donor emission and acceptor absorption. The rate of energy transfer for an isolated single donor–acceptor (D-A) pair separated by distance r can be expressed using the Förster formalism as [59]

$$k_{D-A} = \frac{B \times Q_D^I}{\tau_{Dr^6}} = \left(\frac{1}{\tau_D}\right) \times \left(\frac{R_0}{r}\right)^6 \tag{4.1}$$

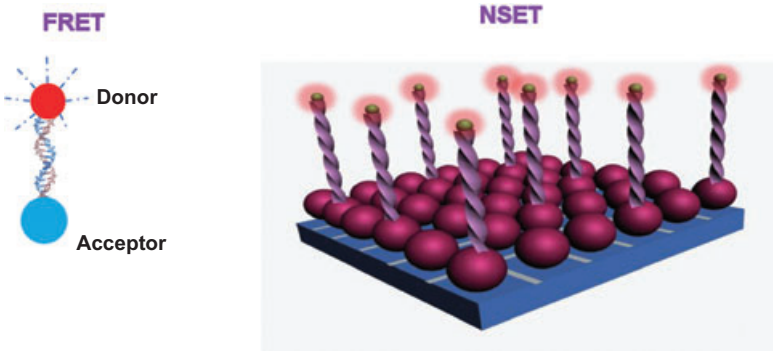

Figure 4.2 (a) Schematic representation of Föster resonance energy transfer (FRET); (b) Schematic representation of nanomaterials surface energy transfer (NSET).

where Q_D is the quantum yield of the donor and τ_D is the excited-state lifetime of the donor; the constant B can then be expressed as

$$B = \frac{[9000 \times (\ln 10)\kappa_p^2}{128\pi^5 n_D^4 N_A} \tag{4.2}$$

where B is a function of the refractive index of the medium n_D, Avogadro's number N_A, and a parameter, κ_p, that depends on the relative orientation of the donor and acceptor dipoles ($\kappa_p^2 = 2/3$ for randomly oriented dipoles) and varies between 0 and 4 for the cases of orthogonal and parallel dipoles, respectively. The Förster radius (or distance), R_0, is defined as

$$R_0 = (BQ_D I)^{1/6} = \left(\frac{9000(\ln 10)\kappa_p^2 Q_D}{N_A 128\pi^5 n_D^4} I \right)^{1/6} \tag{4.3}$$

and corresponds to a separation distance at which the rate of transfer matches the rate of exciton decay: $k_{D-A} = \tau_D^{-1}$.

The FRET efficiency, E, defined as

$$E = \frac{k_{D-A}}{k_{D-A} + \tau_D^{-1}} = \frac{R_0^6}{R_0^6 + r^6} \tag{4.4}$$

where R_0 is the distance at which 50% of the energy is transferred and is a function of the spectral overlap of the donor emission and acceptor absorption, the refractive index of the medium, the quantum yield of the donor, and a factor κ^2 that depends on the relative orientation in space between the transition dipoles for donor and acceptor. A small change in distance between the two sites of a biological molecule where donor and acceptor are attached can result in a sizable change in E. Therefore, structural changes of biological molecules, or a relative motion between two different molecules, can be detected via FRET changes. Although FRET technology is very convenient and can be applied routinely at the single-molecule detection limit, the length scale for detection using a FRET-based method is limited by the nature of the dipole–dipole mechanism, which effectively constrains the length scales to distances on the order of <100 Å ($R_0 \approx 60$ Å). FRET is observed even when the donor and acceptor are placed 20 bases apart on an oligonucleotide. However, the limitations of FRET can be overcome with a dynamic molecular ruler based on the distance-dependent plasmon coupling of metal nanoparticles.

Recently, several groups – including that of the present authors [37–58] – have shown NSET (see Figure 4.2b) to be capable of measuring distances almost twice those measured with FRET, in which energy transfer from a donor molecule to a nanoparticle surface follows a predictable distance dependence. The net luminescence may either decrease or increase, depending on how the gold particle affects the chromophore's excitation rate R_{exc}, and the radiative and nonradiative decay

rates of its excited state, R_{rad} and R_{nonrad}, which together determine the observed luminescence emission rate R_{emiss} [37–58]

$$R_{emiss} = R_{exe}\,\eta \tag{4.5}$$

Where,

$$\eta = \frac{R_{rad}}{R_{rad} + R_{nonrad}} \tag{4.6}$$

is the quantum efficiency of luminescence which is modified by Au-NPs. The relative orientation of a chromophore's molecular dipole moment with respect to the Au-NP surface determines whether the radiative rate is increased or decreased. For a tangentially oriented dipole, the radiative rate is diminished because the molecular dipole and the dipole induced on the Au-NP radiate out of phase. Additionally, the Au-NP increases the nonradiative rate due to energy transfer. Both effects likewise lead to luminescence quenching. Consequently, a full understanding of the chromophore–Au-NP interaction requires the detection of both R_{rad} and R_{nonrad}.

4.3.1 Portable NSET Probes

The general scheme of the miniaturized system components [14, 47] for NSET sensor configuration to detect pathogen DNA and Hg(II) is shown in Figure 4.3a. For fluorescence excitation, a continuous-wavelength Melles–Griot green laser pointer (18 Lab 181) operating at 532 nm was used as an excitation light source. The laser pointer can be maintained for 10~13 h using with two AAA-size batteries,

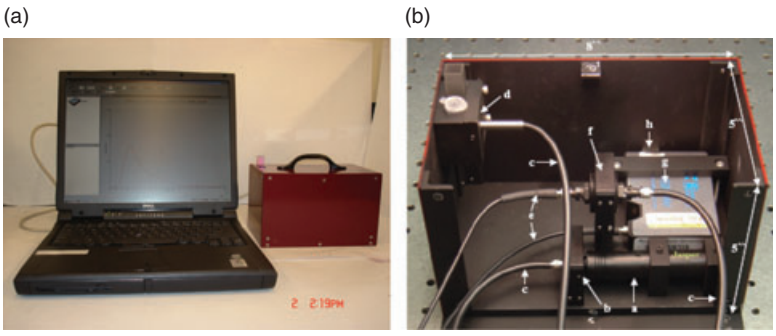

Figure 4.3 (a) The minimized NSET probe box, connected to a laptop computer for data acquisition; (b) The system components for the laser-induced fluorescence (LIF) sensor configuration. Reprinted with permission from Refs [14, 47].

with a maximum power output of ~5 mW. Such a light source has the capability to minimize the whole sensor configuration. The total size of the sensor configuration was $12 \times 20 \times 12$ cm, including the laser pointer, optical fiber and Ocean Optics Instruments (OOI) spectrometer in the aluminum box. The probe consisted in total of seven optical fibers, each with a 200 μm core diameter, one launching fiber, and six surrounding collecting fibers (see Figure 4.3b). The excitation light source was first attenuated using an appropriate neutral density (ND) filter which was coupled to the excitation arm of the Y-shaped reflection probe through a planoconvex lens ($f \sim 4.5$ mm) as shown in Figure 4.3b. A typical laser energy at the sample was adjusted to ~1.3 mW with a 0.3 ND (neutral density) filter.

The collected emission signal was transmitted through an online filter module to a 600 μm core diameter UV-grade fused silica auxiliary fiber, prior to its being fed to a spectrometer. A low-resolution OOI spectrometer with 600/1 mm grating (cover 200–850 nm) was used for these studies. The spectrometer was interfaced with a note book computer via a USB port, and the laser-induced fluorescence (LIF) spectrum collected using OOI data acquisition software. The On/Off (Push/Pull) switch of the laser pointer is located at the other end of laser pointer, and fixed in such a way that it can be operated from outside the aluminum box.

4.3.2
NSET Probe for DNA/RNA Hybridization Detection

The analysis of specific nucleic acid sequences by hybridization has a major impact in diverse areas, such as the molecular diagnosis of disease and the assessment of therapy, food, agriculture, forensic science and environmental testing. The Human Genome Project has provided a vast amount of sequence data and has consequently initiated a new era of nucleic acid-based tests. High-throughput DNA/RNA analysis techniques, however, are required in order to exploit the accumulated genetic information. The use of metal nanoparticles represents an alternative to the standard fluorescence labeling of DNA. A schematic diagram of the nanoparticle probes and their operating principles for a single DNA hybridization detection process is shown in Figure 4.4. Dye-tagged single-stranded DNA (ssDNA) is adsorbed onto the gold nanoparticle and, as a result, the fluorescence from the dye is completely quenched by the gold nanoparticle

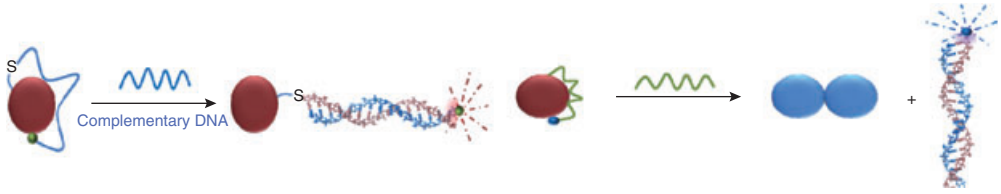

Figure 4.4 Schematic representation of the DNA hybridization process.

[10, 14, 35–51]. When a dye-labeled oligonucleotide molecule is adsorbed onto a nanoparticle, the fluorophore at the distal end may loop back and be adsorbed onto the same particle. The experimental data showed a quenching efficiency of almost 100% when the fluorophore was statically adsorbed onto the particle (static quenching). Further important insight was derived from recently reported [10] surface-enhanced Raman scattering (SERS) studies, the results of which showed that fluorescent dyes could adsorb reversibly onto the surface of colloidal silver and gold nanoparticles. In this way, a several orders of magnitude surface-enhanced resonant Raman scattering (SERRS) signal enhancement was observed (Figure 4.5) from rhodamine 6G-tagged ssDNA (Rh6G-5′-AGAAGATATTTG GAATAACATGACCTGGATGCA-3′) adsorbed onto gold nanorods. The Raman modes at 234, 253, 273 and 371 cm^{-1} are N–C–C bending modes of the ethyl-amine group of the Rh6G ring, while the strong Raman modes at 613, 777, 1182, 1347 and 1366 cm^{-1} are due to C–C–C ring in-plan bending, C–H out-of-plan bending, C–C stretching and C–N stretching. Details of SERS measurements have recently been reported [35].

Thus, when an oligonucleotide molecule is firmly tethered to a particle, the fluorophore at the distal end can loop back and adsorb onto the same particle. Because the backbone of ssDNA is conformationally flexible, a favorable conformation for the adsorbed oligonucleotides is an arch-like structure, in which both the 3′- and 5′-ends are attached to the particle, although the DNA chain does not contact the surface.

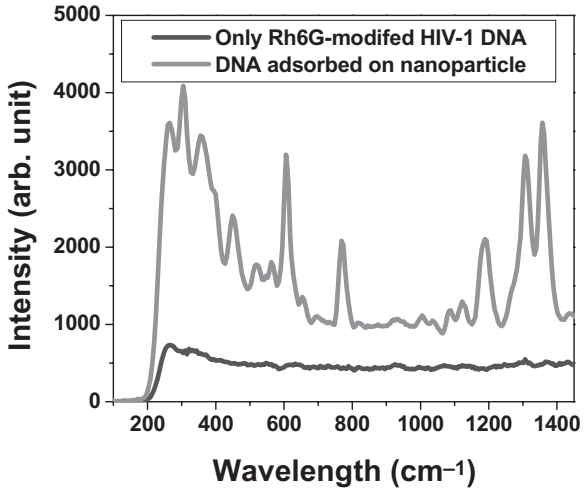

Figure 4.5 Surface-enhanced resonant Raman scattering (SERRS) from rhodamine 6G-tagged ssDNA (Rh6G-5′-AGAAGATATTTGGAATAACATGACCTGGATGCA-3′), with and without gold nanorods. Reprinted with permission from Ref. [10].

Upon target binding, due to the duplex structure, the double-stranded DNA (dsDNA) does not adsorb onto gold and the fluorescence persists (as shown in Figure 4.4).

This structural change generates a fluorescence signal that is highly sensitive and specific to the target DNA. As shown in Figure 4.6a, a very distinct LIF intensity change after hybridization was observed even at 120 p*M* concentration of probe fluorophore-tagged ssDNA [10, 14, 45–50, 97]. As the surface adsorption energies of organic dyes on gold are normally in the range of 8–16 kcal mol^{-1} (i.e., much smaller than energies involved in DNA hybridization, of 80–100 kcal mol^{-1}), after hybridization the constrained conformation is opened and the fluorophore was separated from the particle surface. This high fluorescence enhancement clearly shows that a nanoparticle-based LIF assay can be used as a highly sensitive probe for monitoring DNA hybridization. Figure 4.6a also illustrates single-mismatch detection capability, where the result indicates that the NSET probes are highly specific in discriminating against noncomplementary DNA sequences and single-base mismatches. The addition of noncomplementary nucleic acids had no effect on the fluorescence, while a single-base mismatch reduced the fluorescence intensity by 90% (compared to the fluorescence intensity of perfectly matched targets). Hence, the NSET probes would be applicable to the rapid detection of SNPs in genomic DNA. This is, indeed, an exciting prospect for eliminating the time-consuming and expensive gel sequencing procedures currently required in the standard protocol.

In order to evaluate whether the NSET probe was capable of measuring target DNA concentrations on a quantitative basis, a series of NSET intensity measurements was performed at different concentrations of the target DNA. As shown in Figure 4.6b, the NSET emission intensity is highly sensitive to the concentration of target DNA ions, with the intensity increasing linearly in line with concentration. In fact, a linear correlation was found between the emission intensity and concentration of target DNA over the range of 20 to 450 pM (see Figure 4.6c). Hence, the NSET probe is capable of providing quantitative measurements of the HIV-1 *geg gene* DNA concentration in a biological sample.

4.3.2.1 **Size-Dependence Sensitivity**

The way in which the NSET detection limit for DNA varies with particle size is shown in Figure 4.7. Such detection limits have been chosen when the NSET intensity change is 12, before and after hybridization. As can be seen in Figure 4.7, NSET sensitivity depends heavily on the particle diameter. Consequently, as the particle diameter increases the detection limit steadily improves; indeed, recently acquired data indicate that NSET can be used to detect DNA concentrations down to 300 f*M*, when the particle size is 110 nm. This variation of sensitivity efficiency with particle size may be due to several factors, including: (i) the reduced surface area of smaller nanoparticles will limit the dye-tagged DNA accommodation on the gold nanoparticles; and (ii) an increasing overlap between nanoparticle absorption with Cy3 emission and K_{SV} values with particle size. Thus, the experimental data suggest that a combination of Cy3-modified DNA and correctly

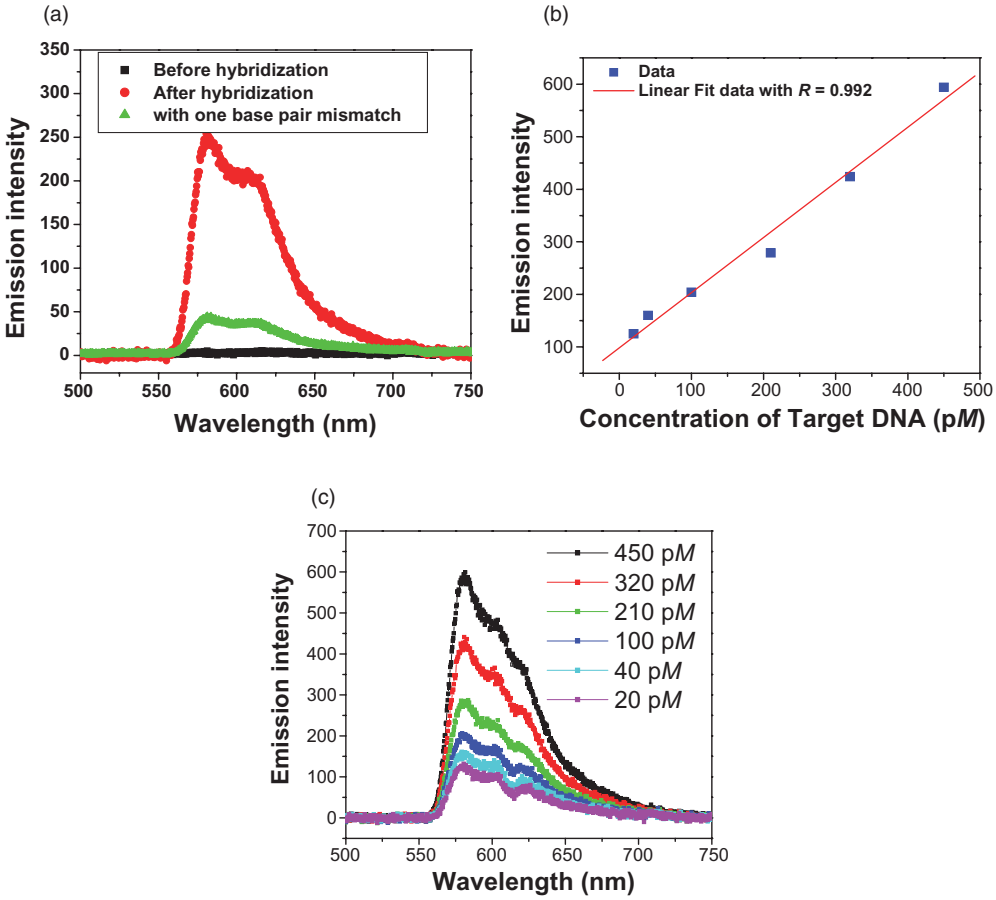

Figure 4.6 (a) Plot of fluorescence intensity versus wavelength for 5′-Cy3-modified GTAACTTCCATTTCTTTTGG-3′ oligonucleotides; (b) Fluorescence response upon addition of different concentrations of target DNA onto 150 nm probe DNA; (c) Plot of fluorescence intensity versus target concentration (p*M*). A linear correlation exists over the range of 20 to 450 p*M*, with $R = 0.992$. Reprinted with permission from Ref. [97].

sized gold nanoparticles may potentially lead to the creation of highly sensitive optical biosensors.

4.3.3 Distance-Dependent NSET

While FRET technology is very convenient and can be applied routinely at the single-molecule detection limit, the length scale for detection using Förster method is limited by the nature of the dipole–dipole mechanism. The quantum efficiency of energy transfer can be written as

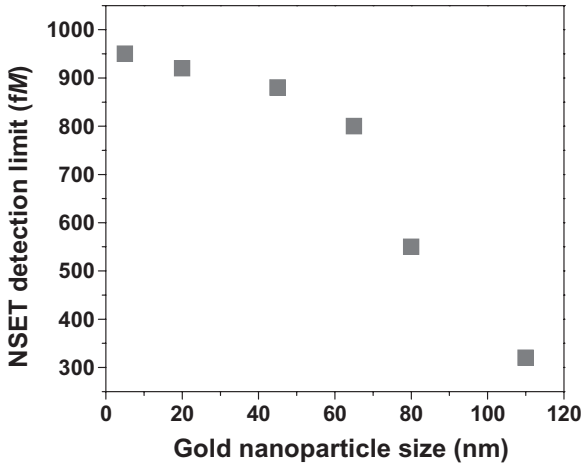

Figure 4.7 Variation NSET detection limit for DNA detection with particle size.

$$\Phi_{EnT} = \frac{1}{1+\left(\frac{r}{r_0}\right)^n} \tag{4.7}$$

where r is the distance between donor and acceptor, and r_0 is the distance between donor and acceptor at which the energy transfer efficiency is 50%. In the case of Förster or dipole–dipole energy transfer, $n = 6$ and $r_0 = R_0$, and is significant over a very short distance range of $r_0 \sim 4$–6 nm for typical fluorophores. In order to appreciate the limitations of the NSET probe in terms of RNA length and gold nanoparticle size, hepatitis C virus (HCV) genome RNA of different lengths was used. In this case, ssRNA of different lengths attached to gold nanoparticles of different sizes via thiol-gold chemistry were used, as shown in Figure 4.8. For this purpose, -SH-linked RNAs were gradually exposed to gold nanoparticle in a phosphate-buffered saline (PBS) buffer over a 16 h period, according to a procedure reported by Mirkin and coworkers. Unlike previous experiments, in this situation the RNA cannot disengage from the particles upon hybridization. Figure 4.8 shows, in diagrammatic form, the NSET probes and their operating principles for RNAs of different lengths. After hybridization, by varying the RNA lengths, the separation distance between the gold nanoparticle and the Cy3 dye can be systematically changed between 8 nm and 50 nm, by varying the number of base pairs. The distance from the center of the molecule to the metal surface is estimated by taking into account size of the fluorescent dye, 0.32 nm for each base pair, and 1.8 nm for the Au–S distance + base pair to dye distance. As a result, after hybridization the distance becomes 8.2 nm for 20 bp RNA, 14.6 nm for 40 bp RNA, 24.2 nm for 70 bp RNA and 40.2 nm for 120 bp RNA. Here, a linear dsRNA strand configuration has been assumed because dsRNA is known to be rigid and to have a persistence length of 90 nm [31].

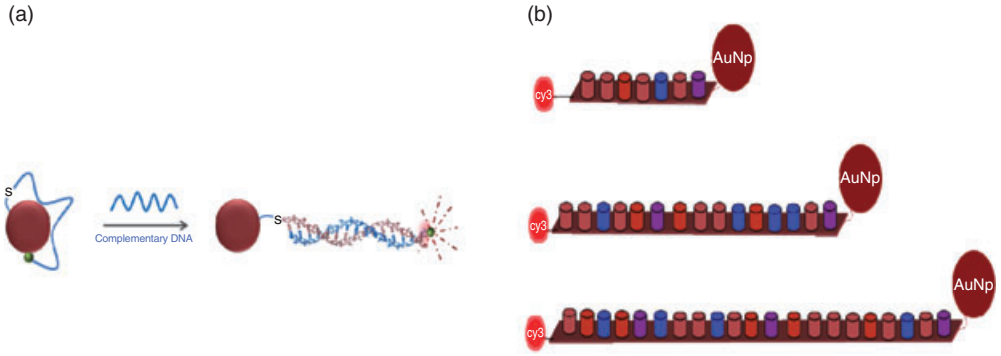

Figure 4.8 (a) Schematic representation of the RNA hybridization process, when one end of the RNA is covalently coupled via thiol–gold chemistry; (b) Schematic illustration of 5′-JOE- and 3′-SH- modified DNA of different lengths. (Reprinted from reference [97], with permission.)

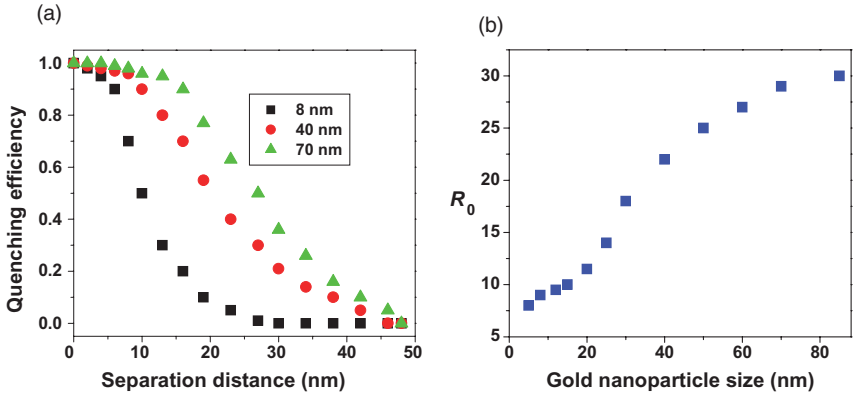

Figure 4.9 (a) Variation of the quenching efficiency with distance between gold nanoparticle and Cy3 dye; (b) Variation of R_0 with the size of gold nanoparticle. (Reprinted from reference [97], with permission.)

Figure 4.9 shows how the quenching efficiency varies with the increase in the distance between the gold nanoparticle and Cy3 dye for gold nanoparticles of different particle sizes. The results show that the distance-dependent quenching efficiency depends heavily on the particle size. In Figure 4.9b, it can be seen how R_0 (the distance at which the energy transfer efficiency is 50%) value varies with the gold nanoparticle size. The results also indicate that the ranging can be tuned all the way from 8 nm (which is very close to the accessible distance conventional FRET of 6 nm) to about 40 nm by choosing gold nanoparticles of different diameters.

Although, in general, the interaction between nanoparticle and dye is quite complex, taking into consideration all illumination polarizations, distance ranges and particle sizes, the situation can be understood as follows:

- As FRET physically originates from the weak electromagnetic coupling of two dipoles, it can be imagined that introducing additional dipoles – and thus providing more coupling interactions – can circumvent the FRET limit. Light induces oscillating dipole moments in each gold particle, and their instantaneous $(1/r)^3$ coupling results in a repulsive or attractive interaction, thus modifying the plasmon resonance of the system. The lesser dependence of interaction strength on particle separation (r) results in a much longer interaction range compared to FRET.
- The fluorescence quantum yield is determined by the radiative rate constant, k_r, and its nonradiative counterpart, k_{nr} : $\tau = (k_r + k_{nr})^{-1}$. At small distances (1–2 nm), the large fluorescence quenching efficiency of 99.8% is due to two effects: (i) gold nanoparticles increase the nonradiative rate R_{nonrad} of the molecules due to energy transfer; and (ii) the radiative rate R_{rad} of the molecules decreases because the molecular dipole and the dipole induced on the gold nanoparticles radiate out of phase if the molecules are oriented tangentially to the gold nanoparticle's surface. At a greater distance, the distance-dependent quantum efficiency is governed almost exclusively by the radiative rate, as reported recently.

Recently, Seelig *et al.* [55] reported that nanoparticle-induced lifetime modification can serve as a nanoscopic ruler for the distance range well beyond 10 nm, which is the upper limit of FRET. Their results showed that the life time (τ_r) depends heavily on the particle size, as well as on the distance between the nanoparticle and dye. In fact, Seelig *et al.*'s data indicated that, for larger sized nanoparticle (20–40 nm in diameter), τ_r is highly sensitive to small changes in the dye–particle distance, even if separated by up to 40 nm; this explains our observation of a high variation of R_0 with gold nanoparticle size. Our observations also point to the fact that, when selecting experimental parameters for optimizing NSET sensitivity, it is very important to take into account the effect of the gold nanoparticle size, which greatly affects the quenching efficiency and distance-dependent NSET. It must also be remembered that, due to the effect of surface charge, surface coverage and mutual strand interaction on the bending properties of individual RNA strands, the apparent length of the oligonucleotides may be less than the expected molecular length.

Jennings *et al.* [61] have reported quenching efficiency of the fluorophore at discrete distances by using three different lengths of dsDNA–dye, two dyes of different energies, and 1.5 nm-diameter gold nanoparticles. The steady-state and picosecond time-resolved spectroscopy measurements reported by these authors indicated that the NSET followed a $1/d^4$ distance-dependence. Pons *et al.* [54] reported that Au-nanoparticle-driven QD photoluminescence quenching extends over a large distance range – in fact, much larger than was predicted and measured for dye–dye and QD–dye pairs. Their results suggested that it might be possible

to extend the energy transfer rate and the utility of sensors based on this pair to separation distances of ~200 Å, far beyond the range allowed by 'classic' dye-to-dye FRET pairs. By using a close comparison of the predominant descriptive theories, Pons *et al.* found that cumulatively the QD photoluminescence quenching was due mainly to nonradiative energy dissipation by the Au-nanoparticle, without any significant modifications of the QD radiative rate. The long-distance quenching rate was better described with a slower, distance-dependence quenching rate than the classical $1/R^6$ characteristic of Förster energy transfer. It was also reported that the dipole to metal NSET model provides a better description of the distance-dependence of the quenching efficiencies, even though such agreement was only qualitative as the measured values were always larger than predicted. Sönnichsen *et al.* [62] showed that plasmon coupling could be used to monitor distances between single pairs of gold and silver nanoparticles, by following the directed assembly of gold and silver nanoparticle dimers in real time, and then studying the kinetics of single DNA hybridization events. Their results indicated that 'plasmon rulers' would be capable of continuously monitoring separations of up to 70 nm for more than 3000 s.

4.3.4 Multiplex DNA Detection

Among modern biosensing methodologies, the direct assessment of unique DNA sequences of targeted living organisms (i.e., bacteria, viruses) offers the best specificity for identification. The rapid and accurate detection of DNA markers in a straightforward, inexpensive and high-throughput format constitutes an effective and powerful screening tool that could ultimately be adapted in the early diagnosis of a variety of diseases. An efficient high-throughput scheme that can screen for multiple DNA targets in parallel is highly desirable. Hence, to demonstrate that the FRET probe can detect multiple DNA hybridization, both anthrax DNA and *Escherichia coli* DNA have been used [14, 50]. An oligonucleotide sequence associated with the anthrax lethal factor (5′-GGATTATTGTTAAATATTGATAAGGAT-3′) was chosen as an initial target; this sequence is important for bioterrorism and biowarfare applications, and consequently has been well studied. The sequence of the target *E. coli* DNA (positions 1027–1057 of the *E. coli* 23S rDNA) was 5′-AAACGATGTGGGAAGGCCCAGACAGCCAGG-3′.

Figure 4.10a shows, in diagrammatic fashion, the nanoparticle probes and their operating principles for a multiple DNA hybridization detection process. Following the hybridization of both DNAs, gold nanoparticles were seen to undergo aggregation due to the presence of NaCl, and as a result there was a color change from pink to blue (as shown in Figure 4.10a). Figure 4.10b shows that the gold nanoparticle-based FRET probe could be used to detect multiple DNA very easily. Thus, when both single-sized and mixed nanoparticles were used, the results indicate that FRET intensity became maximal when a 1 : 1 mixture of 13 nm and 60 nm gold nanoparticle was present. Following the hybridization of only one DNA, no color change was observed, although this may have been due to one of

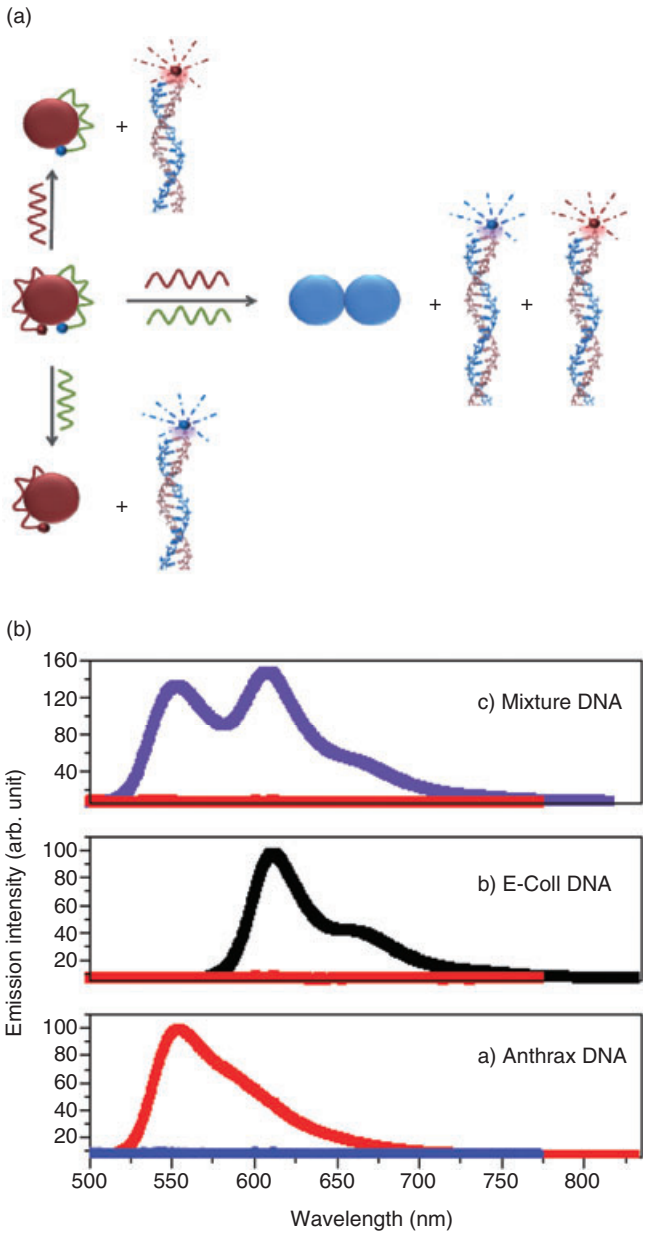

Figure 4.10 (a) Schematic representation of the multiple DNA hybridization process. The circular shapes represent the gold nanoparticles; (b) Plot of fluorescence intensity versus wavelength for (a) 5′-Texas Red-modified GGATTATTGTTAAATATTGATAAGGAT-3′oligonucleotides, (b) 5′-Cy3-modified AAACGATGTGGGAAGGCCCAGACAGCCAGG-3, and (c) a mixture of both. Reprinted with permission from Ref. [50].

the ssDNAs still being adsorbed onto the gold nanoparticle, such that the nanoparticles could not undergo aggregation.

Kim *et al.* [63] have developed multicolor hybrid DNA probes employing green, yellow and orange color QD-conjugated molecular beacons with a black hole quencher. Both, optical and electrophoretic characterization showed the presence of a fluorescent energy transfer that followed the FRET mechanism with single nucleotide discrimination. Target DNA identification was observed to be highly sensitive up to 8 ng in gel electrophoresis.

4.3.5
NSET for Monitoring Mg^{2+}-Dependent RNA Folding

RNA folding is a remarkably complex problem that involves ion-mediated electrostatic interaction, conformational entropy, base pairing and stacking, as well as noncanonical interactions. A fundamental understanding of RNA folding relies critically on the characterization of the associated folding transition states – that is, the highest energy states along the reaction coordinates that dictate the transition kinetics. However, characterization of the transition states of RNA folding lags far behind that of protein folding, in part because of a more rugged energy landscape for RNA that leads to multiple folding pathways and intermediate states, making it difficult to characterize elementary RNA folding transitions. Recently, it has been demonstrated [60] that gold nanoparticle-based FRET can be used to track the folding of RNA (as shown in Figure 4.11). As a model system, the conformational changes of two-helix junction RNA molecules induced by the binding of Mg^{2+} ions can be studied by measuring time-dependent fluorescence signals (as shown in Figure 4.11a). The transition from a folded to an open configuration changed the distance between the gold nanoparticles and the dye molecule attached

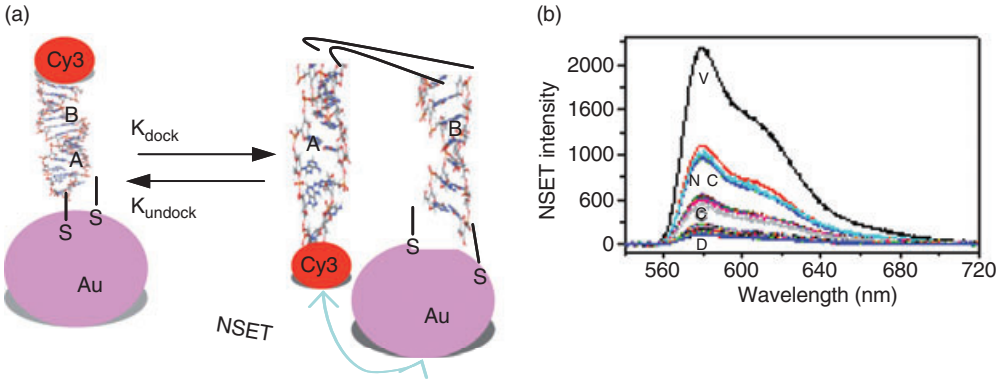

Figure 4.11 Schematic representation of NSET assay to track RNA folding; (b) Time-dependent NSET intensity in the presence of 15 m*M* Mg^{2+} at 25 °C. Reprinted with permission from Ref. [60].

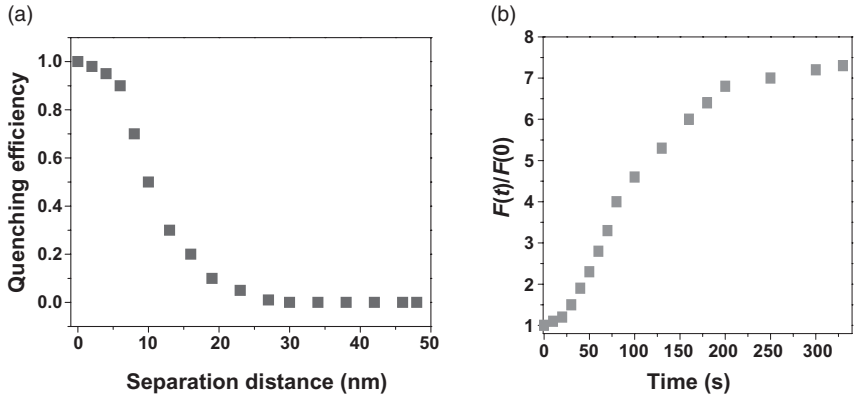

Figure 4.12 (a) Variation of quenching efficiency with distance between the gold nanoparticle and the Cy3 dye; (b) Fluorescence signal change with time for docked state after the addition of Mg^{2+} ions. Reprinted with permission from Ref. [60].

to the ends of two helices in the RNA junction, and as a result the unfolding process could be monitored via the change in fluorescence intensity.

In order to probe the transition states involved during transition, the unfolding of two-helix junction RNA molecules induced by Mg^{2+} was studied by measuring time-dependent NSET signal (as shown in Figure 4.11b). The experimental results showed clearly that there are four separate states involved during docking to undocking transition, with RNAs switching very slowly between the four states. The emission intensity changes with time for each state follow first-order kinetics, as shown in Figure 4.12, for the docked configuration. The lowest emission intensity configuration is the docked configuration (D), where the two domains are in contact and at a 70° angle, as reported in the crystal structure. In this configuration the Cy3 dye is very close to the gold nanoparticle, which almost completely quenches the fluorescence. The highest emission intensity configuration is an extended form that represents the undocked state (U), where the gold nanoparticle and Cy3 dye are about 43 nm apart. The distance from the center of the molecule to the metal surface is estimated by taking into account size of the fluorescent dye: 0.32 nm for each base pair, and 1.8 nm for the Au–S distance + base pair to dye distance (as shown in Figure 4.13). The other two states are transition states, through which RNA folding takes place from the D → U state. In order to understand the structure of these two transition states, the distance dependent NSET is measured.

For this purpose, we have used dsRNAs of different lengths attached to gold nanoparticles via thiol–gold chemistry at one end, while the other end is attached to the Cy3 dye (as shown in Figure 4.8a). Here, the distance has been varied from 3 nm to 50 nm by altering the number of base pairs in the RNA; for example, 3.08 nm for 4 bp RNA, 8.2 nm for 20 bp RNA, 14.6 nm for 40 bp RNA, 24.2 nm for

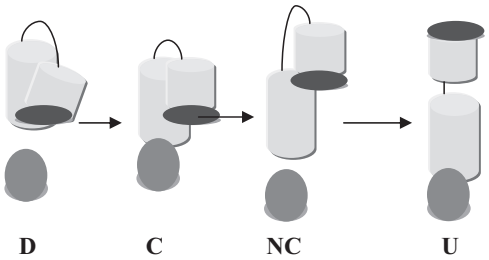

Figure 4.13 Schematic representation of possible transition states involved in the docked to undocked state. Reprinted with permission from Ref. [60].

70 bp RNA and 40.2 nm for 120 bp RNA. We have assumed a linear dsRNA strand configuration because dsRNA is known to be rigid and to have a persistence length of 90 nm. The data in Figure 4.12 show how the quenching efficiency varies with the gold nanoparticle–Cy3 dye distance. The results show a 10% quenching efficiency, even at a distance of 20 nm, which is twice that measured by FRET. The time-dependent experiments (as shown in Figure 4.11b) indicate that quenching efficiency is about 98% in the D state, 85% in the first transition state, 45% in the second transition state, and 0% in the U state. Based on the distance-dependence curve in Figure 4.3a, the distance between the gold nanoparticle and Cy3 was estimated as ~3 nm in the D state, 5 nm in the first transition state and 12 nm in the second transition state. The folding of RNA molecules occurs in the presence of positively charged ions, so as to allow close packing of the negatively charged phosphate backbone. Positively charged ions can interact with RNA in two ways: (i) through nonspecific electrostatic interactions; or (ii) through binding to specific sites that stabilize a particular folding motif. From the distance-dependence NSET and time-dependent RNA folding data, it was proposed that, during folding from the D → U state, the first transition state may be where the two domains are in direct contact at a parallel 0° angle, and start to allow the insertion of hydrated metal ions (C). Then, the second transition state is where the two domain surfaces are apart at a 0° angle (NC), allowing the insertion of a large amount of hydrated metal ions (as shown in Figure 4.13). A four-state RNA folding process has been proposed previously for smaller, two-way junction RNA by Zhuang *et al.* [95, 96]. By fitting the time-dependent fluorescence intensity change with first-order reaction kinetics, it was possible to measure the rate constant for each state. Thus, the rate constant for $K_C = 0.008\,s^{-1}$, for $K_{NC} = 0.18\,s^{-1}$, and for $K_U = 2\,s^{-1}$. The measured values of K_C and K_{NC} were lower than were reported for smaller, two-way junction RNA by Zhuang *et al.* [10, 11]. Moreover, it is due to the fact that for general FRET, the interaction between donor (Cy3 dye) and acceptor (Cy5 dye) is only dipole–dipole coupling, whereas in the case of NSET the gold nanoparticle and Cy3 are bound by a strong, electrostatic interaction.

The next stage was to probe directly the influence of metal ions on the unfolding process. The study results indicated that the unfolding process was independent of

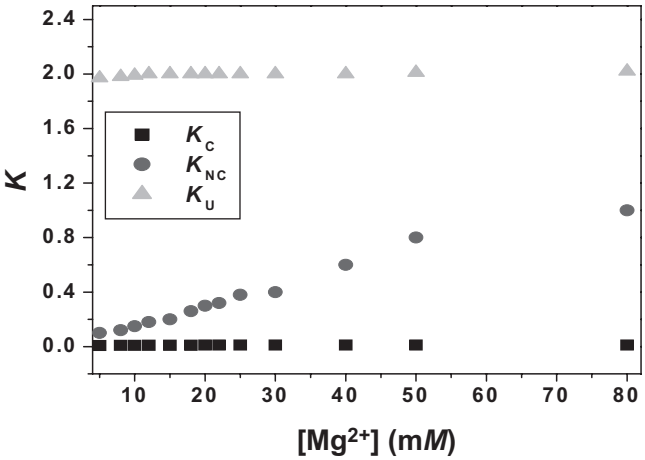

Figure 4.14 Effect of Mg^{2+} ion concentration on rate constants of undocking transition. Reprinted with permission from Ref. [60].

$[Mg^{2+}]$ over almost the entire concentration range (4–80 m*M*). At 25 °C, it was possible to follow all of the undocking transition state rate constants (as shown in Figure 4.14), and to show that K_C and K_U are independent of $[Mg^{2+}]$ between 4 and 80 m*M*. However, K_{NC} was seen to be heavily dependent on $[Mg^{2+}]$, with values increasing almost 10-fold with each increment of $[Mg^{2+}]$ over the range of 4 to 80 m*M*. As K_C is the slowest step or rate-determining state, the overall unfolding process must be independent of $[Mg^{2+}]$ over almost the entire range of 4 to 80 m*M*.

Seferos *et al*. [64] showed that oligonucleotide-modified gold nanoparticle probes hybridized to fluorophore-labeled complements could be used as both transfection agents and as cellular 'nanoflares' for detecting mRNA in living cells. The results of this group indicated that nanoflares exhibited a high-signaling, low-background signal and were sensitive to changes in the number of RNA transcripts present in the cell. Bates *et al*. [65] reported Mg^{2+}-mediated RNA–RNA loop–receptor interactions using self-assembled nanowires, while Jennings *et al*. [61] found that NSET could be used to measure Mg^{2+}-induced conformational changes for a hammerhead ribozyme, and subsequently confirmed their measurements using FRET. These results indicate that NSET was able to enhance our understanding of the different kinetic pathways for ribozymes. When Zhang *et al*. [66] reported the details of a QD-based nanosensor that could be used in FRET assays of Rev responsive element (RRE) IIB RNA–Rev peptide interactions, their results suggested that a QD-based nanosensor would offer the distinct advantage of not inhibiting the Rev–RRE interaction, as well as having high sensitivity, improved accuracy and simultaneous FRET-related two-parameter detection. This QD-based nanosensor provides a new approach for studying the effects of inhibitors on Rev–RRE interaction, and may have a wide applicability in the development of new drugs to treat HIV-1 infection.

4.3.6
NSET for DNA Cleavage Detection

Damage to DNA within its biological environment has been associated with alterations in DNA sequence, aberrant gene expression, increased mutation rates, cell transformation and the development of cancer. Interactions of DNA with chemical or physical agents occurring in the environment may result in changes in genetic information (mutations), and subsequently in serious health disorders [1–5]. The ultrasensitive detection of DNA cleavage species in the environment, water and food is therefore important for human health protection. In order to assay cleavage efficiency, several traditional methods such as gel electrophoresis, filter binding and high-performance liquid chromatography (HPLC) are commonly used. Unfortunately, however, each of these methods is discontinuous, time-consuming and laborious. Furthermore, the detection of cleavage at low substrate concentrations necessitates radiolabeling. In the recent past, many different routes have been taken to develop fluorescence assays for DNA cleavage, most of which are based on FRET or non-FRET quenching mechanisms. Usually, a fluorescence signal enhancement is observed after the cleavage reaction. Although these assays are continuous and convenient, the length scale for detection using a FRET-based method is limited by the nature of the dipole–dipole mechanism, which effectively constrains the length scales to distances on the order of <100 Å ($R_0 \approx 60$ Å). Recently, we have reported [45] a gold nanoparticle (Au-NP)-based FRET assay to monitor the cleavage of DNA by nucleases. A schematic diagram of the nanoparticle probes, together with their operating principles for the DNA cleavage process when the ssDNA is attached to a gold nanoparticle through a –S– linkage is shown in Figure 4.15.

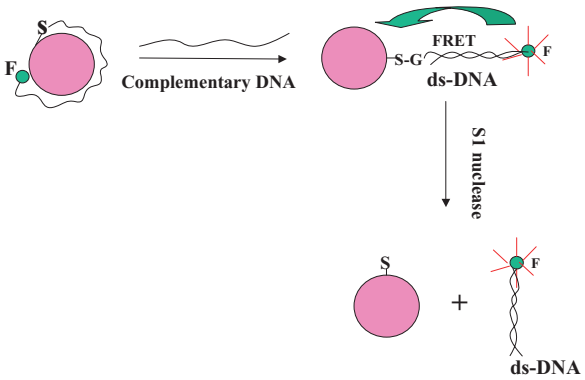

Figure 4.15 Schematic illustration of the DNA cleavage process, when DNA is attached to the gold nanoparticle through an –SH group. The circle represents the gold nanoparticle, and F the fluorophore. Reprinted with permission from Ref. [45].

The assay consists of two separate steps:

- The Cy3-labeled DNA-coated gold nanoparticles were hybridized with the complementary nucleic acid containing one nucleotide less. The hybridization was followed by fluorescence quenching of the dye by gold nanoparticles.
- The Au-NP–dye-DNA duplex was treated with S1 nuclease to cleave the DNA, and the kinetics of the cleavage process monitored for the recovery of dye fluorescence.

As shown in Figure 4.16, the fluorescence from Cy3-labeled nucleic acid is totally quenched by gold nanoparticles after hybridization, with recovery of the fluorescence signal being observed only after DNA cleavage. A very distinct LIF intensity change after cleavage was observed, even at a 250 *fM* concentration of fluorophore-tagged dsDNA.

A 120-fold enhancement of the fluorescence signal was observed following the cleavage reaction in the presence of S1 nuclease. The assay reported here permits an extremely high signal-to-background ratio of approximately 120. As a control experiment, Cy3-labeled, ssDNA-coated gold nanoparticles were treated with S1 nuclease to cleave the ssDNA. The addition of S1 nuclease had no effect on the fluorescence quenching, and only a weak and broad background was observed. This indicates that, although the S1 nuclease is able to cleave the ssDNA it can also affect the adsorbed fluorophore position, and consequently the fluorescence was quenched in total. In order to appreciate the limitations of this assay, ssDNAs of different lengths attached to gold nanoparticles via the –SH linkage of a 3′-thiol group, as well as a 5′-fluorophore containing ssDNAs of different lengths, were used. The data in Figure 4.17 indicate how the fluorescence intensity varies with

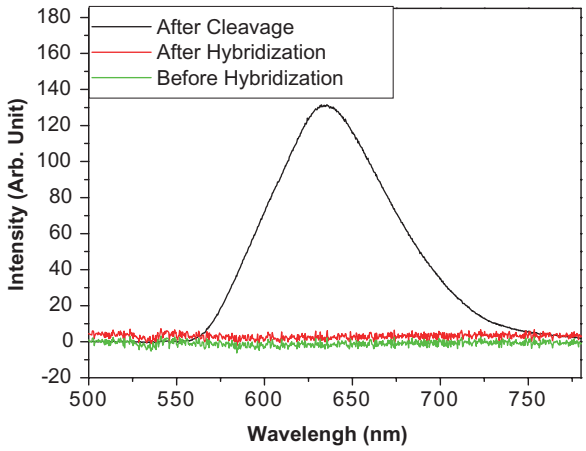

Figure 4.16 Plot of fluorescence intensity versus wavelength for 5′-Cy3-modified GAAAAACCCCTTTTTT-3′oligonucleotide. Reprinted with permission from Ref. [45].

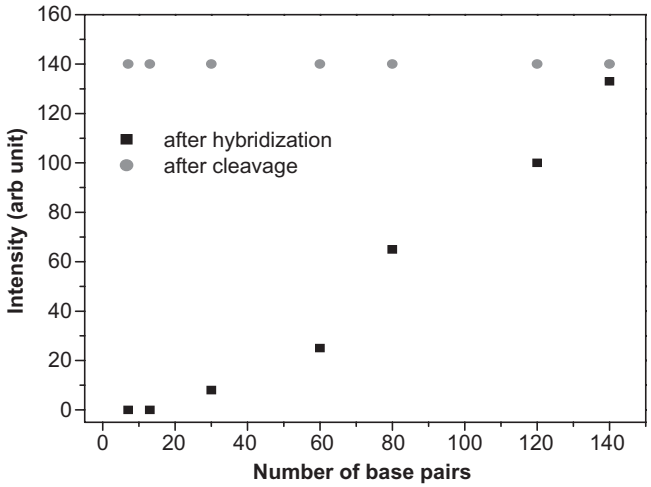

Figure 4.17 Variation of fluorescence intensity with increment of the number of base pairs in 3′-thiol (–SH) group- and 5′-Cy3-modified DNA. Reprinted with permission from Ref. [45].

the increase in the gold nanoparticle–dye distance. As the results indicate that no quenching occurs beyond 160 base pairs, the assay can be used conveniently for DNA lengths up to 120 base pairs. In addition to its high sensitivity and convenience, the method has several other advantages. First, it is several orders of magnitude more sensitive than gel electrophoresis or HPLC techniques, and a few orders of magnitude more sensitive than UV assays. Second, it can be used for multiple-target DNA damage detection. Third, it is much faster in operation than previously used assays, with an easier means of detection.

Itamar *et al.* [67] reported the details of nucleic acid-functionalized CdSe/ZnS QDs hybridized with a complementary Texas Red-functionalized nucleic acid, where the hybridization was monitored using FRET from the QDs to the dye units. Treatment of the QD–dye-DNA duplex structure with DNase I resulted in cleavage of the DNA and a recovery of the fluorescence properties of the CdSe/ZnS QDs. However, the results also indicated that the luminescence properties of the QDs were only partially recovered due to nonspecific adsorption of the dye onto the QDs. Skewis *et al* [68] reported the influence of spermidine on the cleavage kinetics of RNase A at the single molecule level, using pairs of RNA-tethered 40 nm gold nanoparticles. The study results highlighted the fact that, because of their high temporal resolution and ability to follow the cleavage of individual RNA molecules, the RNA plasmon rulers could provide information concerning the relative stabilities of a weakly stabilized subpopulation and their lifetimes. It was also shown that efficient RNA cleavage rates could be achieved for all of the concentrations investigated (1–5 m*M*). The results of additional time-resolved cleavage experiments (temporal resolution ~10 ms) indicated that, with increasing spermidine concentration, cleavage was delayed such that discrete subpopulations with longer

lifetimes emerged. The reduction in RNase A cleavage rates and appearance of subpopulations indicating transient structural RNA stabilization, confirmed that the RNA-binding enzyme activity was regulated through spermidine-induced changes in the charge and structure of the RNA substrate.

4.3.7
NSET for Cancer Cell Detection

Today, cancer has become the leading cause of death among Americans, it having been estimated that in 2006 alone over 500 000 people will die from this condition. Cancer is a highly complex disease to comprehend, because it entails multiple cellular physiological systems such as cell signaling and apoptosis. Thus, the most common cancer treatments are limited to chemotherapy, radiation and surgery. Limitations in cancer treatment are the result of challenges seen in the cancer therapies of today, including a lack of early disease detection, nonspecific systemic distribution, inadequate drug concentrations reaching the tumor, and an inability to monitor therapeutic responses. Poor drug delivery and residence at the target site lead to significant complications, such as multidrug resistance. Yet, nanotechnology has the potential to offer solutions to these current obstacles in cancer therapies, because of its properties of unique size (1–100 nm) and large surface-to-volume ratios. In creating a method to detect breast carcinoma cells, gold nanoparticles were conjugated to monoclonal antibodies specific to HER2-overexpressing breast carcinoma cells. Subsequently, a change in the NSET signal of about an order of magnitude was demonstrated from T47D breast carcinoma cells conjugated with gold nanoparticles, compared to normal cells (J. Griffin *et al.*, unpublished results) (Figure 4.18).

Zhang *et al.* [69] reported the details of a novel QD/aptamer (Apt)/doxorubicin (Dox) conjugate – QD-Apt(Dox) – as a targeted cancer imaging, therapy and sensing system. By functionalizing the surface of fluorescent QDs with the A10 RNA aptamer, which recognizes the extracellular domain of the prostate-specific membrane antigen (PSMA), it was possible to develop a targeted QD imaging system (QD-Apt) capable of differential uptake and imaging of prostate cancer cells expressing the PSMA protein. The results showed that FRET between QD and Dox, and between Dox and APt, occurred when Dox intercalated within the A10 aptamer. The specificity and sensitivity of this nanoparticle conjugate as a cancer imaging, therapy and sensing system was also demonstrated *in vitro*. Here, Cisell *et al.* [70] reported a hybridization assay to detect the microRNA, miR21, in cancer cells using the bioluminescent enzyme *Renilla* luciferase (Rluc) as a label. This involved the development of a competitive oligonucleotide hybridization assay for the detection of miR21, using the free miR21 and Rluc-labeled miR21 that compete to bind to an immobilized, miR21 complementary probe. The assay was used to detect miR21 in both human breast adenocarcinoma MCF-7 cells and nontumorigenic epithelial MCF-10A cells. Subsequently, the hybridization assay was developed in a microplate format with a total assay time of 1.5 h, without the need for sample amplification via the polymerase chain reaction (PCR).

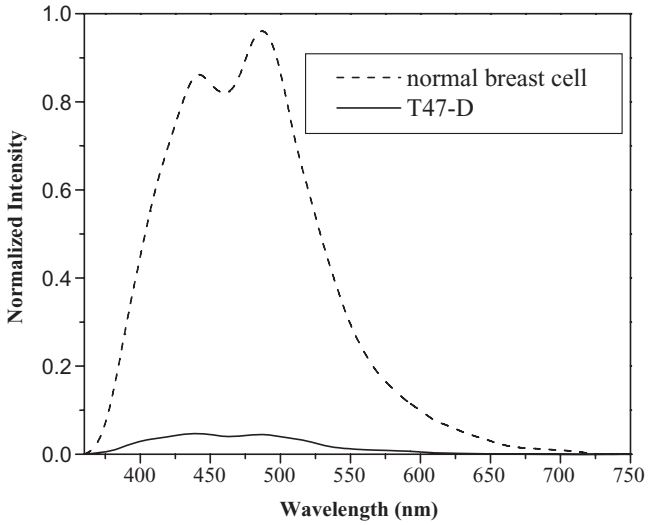

Figure 4.18 NSET spectra from T47-D breast carcinoma cells and normal breast cells when conjugated with nanoparticles.

4.4 Gold Nanoshell-Based Biosensors

Gold nanoshells, composed of a spherical dielectric core surrounded by a concentric metal shell, support plasmon resonances the energies of which are determined sensitively by the inner core and outer shell dimensions. Gold nanoshells are typically composed of a dielectric silica core and a thin metallic gold outer layer, and a wide range of sizes can easily be fabricated using currently available chemical techniques. The plasmon resonance of the nanoshells can be tuned by varying the ratio of the core/shell radius [98, 99]. An enhancement in the electromagnetic energy can be found, at resonance, in the region close to the nanoshell known as the 'near field'. It has been shown – both theoretically and experimentally – that if the evanescent near fields of a surface plasmon polariton and a particle plasmon overlap, then an efficient exchange of energy from the freely propagating electromagnetic waves into surface plasmons can be achieved. Gold nanoshells are a novel type of spherical concentric nanoparticle that possesses high optical efficiencies well into the near-infrared (NIR). Gold nanoshells can scatter and/or absorb light with optical cross-sections that often are several times larger than the geometric cross-section. As an NIR absorber, nanoshells are optically very robust; the nanoshell's rigid structure and noble metal surface make it far less susceptible to chemical/thermal denaturation and photobleaching effects than conventional NIR dyes, thus providing an extended performance *in situ*.

Tam *et al.* [100] reported the role of nanoparticle plasmon resonance energy and nanoparticle scattering cross-section on the fluorescence enhancement of adjacent indocyanine green (ICG) dye molecules. The study results indicated that

the enhancement of molecular fluorescence by more than a factor of 50 could be achieved for ICG next to a nanoparticle with a large scattering cross-section and a plasmon resonance frequency corresponding to the emission frequency of the molecule. Subsequently, Wang *et al.* [101] reported that gold nanoshells (GNSs) could be used as an effective signal transduction in whole blood. In these studies, after modifying the cation with cystamine and biotin–*N*-hydroxy succinimide, GNS self-assembled monolayers (SAMs) were used as a novel optical biosensor for the real-time detection of streptavidin–biotin interactions in diluted human whole blood within a short assay time, and without any sample purification/separation. Such an approach provides an opportunity to construct a localized surface plasmon resonance (LSPR) biosensor for protein sensing and cellular analysis in diluted whole blood. The ability to control both wavelength-dependent scattering and the absorption of nanoshells offers the opportunity to design nanoshells that which provide, in a single nanoparticle, both diagnostic and therapeutic capabilities. In a later study, Loo *et al.* [102] demonstrated a novel nanoshell-based, all-optical platform technology for integrating cancer imaging and therapy applications. Here, immunotargeted nanoshells were engineered not only to scatter light in the NIR, enabling optical molecular cancer imaging, but also to absorb light, allowing the selective destruction of targeted carcinoma cells through photothermal therapy. Gobin *et al.* [103] designed nanoshells to provide optical contrast for improved diagnostic imaging and, at higher light intensity, rapid heating for photothermal therapy. When using these nanoshells in a mouse model, a dramatic contrast enhancement was demonstrated in optical coherence tomography (OCT) and the effective photothermal ablation of tumors. Su *et al.* have [104] synthesized Au_3Cu_1 (gold and copper) nanoshells that showed a promising magnetic resonance (MR) contrast effect. The study results showed that, for *in vivo* MR imaging, the Au_3Cu_1 nanocontrast agents enhanced the contrast of blood vessels, while in a cytotoxicity and animal survival assay they showed a dose-dependent toxic effect.

Hirsch *et al.* [105] reported a rapid immunoassay capable of detecting analytes within complex biological media. These authors have demonstrated a simple rapid immunoassay capable of detecting $pg\,ml^{-1}$ quantities of various analytes in different media, using spectrophotometry – a simple, low-cost method of detection. The study results indicated that the simple thiol-mediated assembly of OPSS–PEG-antibodies onto nanoshells could be extended to any number of antibody/analyte immunoassay systems, thus creating a robust immunoassay capable of detecting a variety of clinically relevant blood-borne analytes. Park *et al.* [106] reported the luminescence brightness of nanoshells, compared to that of gold nanorods and fluorescent beads. The study results showed the nanoshells to be as bright as the nanorods, and 140-fold brighter than the fluorescent beads. In order to demonstrate the potential application of this bright two-photon-induced photoluminescence (TPIP) signal for biological imaging, Park's group reported the 3-D distribution of gold nanoshells targeted towards tumors. Wang *et al.* [107] also showed that nanoshells could be used *in vivo* as a new contrast-enhancing agent for photoacoustic tomography. The reported images, captured after three sequen-

tial administrations of nanoshells, demonstrated a gradual enhancement of the optical absorption in the brain vessels by up to 63%.

4.5
Problems and Challenges

The continued optimization of different parameters is necessary to determine the applicability of these assays in point-of-care settings. The ability of an assay to detect DNA in complex environments, with high background and competing targets, requires an exquisite selectivity and sensitivity, and will ultimately serve as a yardstick for the applicability of such assays in an environmental setting. The transition to such settings often results in added complexity, and affects the ultimate assay performance. Hence, these assays will need to be merged with simple and convenient sample handling systems in such a way that they do not become prohibitively complicated or costly. Since the possible hazards associated with nanomaterials can be significant, an understanding of biological response, and of environmental remediation, is necessary. Future advances will require continued innovations to be made by chemists, in close collaboration with experts in both medical and biological fields. Further challenges in this emerging field include the mimicking of other aspects of biology in creating biomaterials. For example, materials constructed in biology have highly ordered hierarchy structures, and respond to chemical stimuli both passively and progressively in such a way as to change the environment. An example of this is when an enzyme expression is turned on in response to the presence of a substrate, such that the latter may be digested. Clearly, it would be desirable if nanomaterials possessed similar properties so that they could be used not only for sensing but also for autonomous repair and renewal. Yet, no matter what methods were required to meet these challenges, biology would always remain the major inspiration.

4.6
Summary

In conclusion, in this chapter we have discussed our and other groups efforts to develop a nanomaterial-based NSET for the detection of DNA/RNA hybridization, RNA folding, DNA/RNA cleavage and carcinoma cells. Our experimental observations serve as a paradigm for the design of optical-based molecular ruler strategies at distances more than double of those achievable using traditional dipole–dipole columbic energy transfer-based methods. Such a long-range feature will lead to the development of biosensors and homogeneous bioassays not feasible when using general FRET process. So, if we look into the future we would expect these NSET sensor developments to have important implications in the development of better biosensors and bioassays that can be applied to pathogen detection, heavy metal ion detection in environmental samples, clinical analysis and biomedical

research. Our observations also point towards the exciting possibility of performing spatially confined detection on array formats of biological recognition, including RNA/DNA hybridization and/or antibody–antigen recognition. The examples of applications of noble metal nanostructures provided herein can be readily generalized to other areas of biology and medicine, simply because plasmonic nanomaterials exhibit a great range, versatility and systematic tunability of their optical attributes.

Acknowledgments

Dr. Ray would like to thank NSF-PREM grant # DMR-0611539, NSF-BIO grant # 0641455, ARO grant # W911NF-06-1-0512 and NIH-SCORE grant # S06GM 008047 for their generous funding. The authors also thank those reviewers whose valuable suggestions improved the quality of this chapter.

References

1 Tyers, M. and Mann, M. (2003) Overview From genomics to proteomics. *Nature*, **422**, 193–7.
2 Tarkkanen, M. (2006) The diagnostic use of cytogenetic and molecular genetic techniques in the assessment of small round cell tumours. *Current Diagnostic Pathology*, **8**, 338–48.
3 Syvanen, A.-C. (2001) Accessing genetic variation: genotyping single nucleotide polymorphisms. *Nature Reviews Genetics*, **2**, 930–42.
4 Wallance, D.C. (2005) A mitochondrial paradigm of metabolic and degenerative diseases, aging, and cancer: a dawn for evolutionary medicine. *Annual Review of Genetics*, **39**, 359–407.
5 Burda, C., Chen, X., Narayanan, R. and El-Sayed, M.A. (2005) Chemistry and properties of nanocrystals of different shapes. *Chemical Reviews*, **105**, 1025.
6 Christine, M. and Astruc, D. (2004) Gold nanoparticles: assembly, supramolecular chemistry, quantum-size-related properties, and applications toward biology, catalysis, and nanotechnology. *Chemical Reviews*, **104**, 293.
7 Kinbara, K. and Aida, T. (2005) Toward intelligent molecular machines: directed motions of biological and artificial molecules and assemblies. *Chemical Reviews*, **105**, 1377.
8 Alivisatos, A.P., Johnson, K.P., Peng, X., Wislon, T.E., Bruchez, M.P. and Schultz, P.G. (1996) Organization of 'nanocrystal molecules' using DNA. *Nature*, **382**, 609.
9 Mirkin, C.A., Letsinger, R.L., Mucic, R.C. and Storhoff, J.J. (1996) A DNA-based method for rationally assembling nanoparticles into macroscopic materials. *Nature*, **382**, 607.
10 Darbha, G.K., Rai, U.S., Singh, A.K. and Ray, P.C. (2008) Gold nanorod based sensing of sequence specific HIV-1 virus DNA using hyper Rayleigh scattering spectroscopy. *Chemistry - A European Journal*, **14**, 3896–903.
11 Darbha, G.K., Rai, U.S., Singh, A.K. and Ray, P.C. (2008) Highly selective detection of Hg^{2+} ion using NLO properties of gold nanomaterial. *Journal of the American Chemical Society*, **130**, 8038–42.
12 Wang, Z., Pan, S., Kraus, T.D., Du, H. and Rothberg, L.J. (2003) The structural basis for giant enhancement enabling single-molecule Raman scattering. *Proceedings of the National Academy of Sciences of the United States of America*, **100**, 8638.
13 Zhang, X., Young, M.A., Lyandres, O. and Van Duyne, R.P. (2005) Rapid

detection of an anthrax biomarker by surface-enhanced Raman spectroscopy. *Journal of the American Chemical Society*, **127**, 4484.

14 Darbha, G.K., Glenn, L.E., Anderson, E., Preston, Y.R., Mitchell, F., Ray, K. and P.C. (2008) Miniaturized NSET sensor for microbial pathogens DNA and chemical toxins. *IEEE Sensor Journal*, **8**, 693–701.

15 Cao, Y.W.C., Jin, R.C. and Mirkin, C.A. (2002) Nanoparticles with Raman spectroscopic fingerprints for DNA and RNA detection. *Science*, **297**, 1536–40.

16 Park, S.J., Taton, T.A. and Mirkin, C.A. (2002) Array-based electrical detection of DNA with nanoparticles probes. *Science*, **295**, 1503.

17 Nie, S. and Emory, S.R. (1997) Probing single molecules and single nanoparticles by surface-enhanced Raman scattering. *Science*, **275**, 1102–4.

18 Sato, K., Hosokawa, K. and Maeda, M. (2003) Rapid aggregation of gold nanoparticles induced by non-cross-linking DNA hybridization. *Journal of the American Chemical Society*, **125**, 8102.

19 Aslan, K., Lakowicz, J.R. and Geddes, C.D. (2005) Plasmon light scattering in biology and medicine: new sensing approaches, visions and perspectives. *Current Opinion in Chemical Biology*, **9**, 538–44.

20 Aslan, K. and Geddes, C.D. (2005) Metal-enhanced fluorescence: an emerging tool in biotechnology. *Current Opinion in Biotechnology*, **16**, 55–62.

21 Ryan, B.C., Kwong, G.A., Radu, C.G., Witte, O.N. and Heath, J.R. (2007) DNA-encoded antibody libraries: a unified platform for multiplexed cell sorting and detection of genes and proteins. *Journal of the American Chemical Society*, **129**, 1959–67.

22 Francisco, G., Viana, J., Jose, B.P. and R. (2007) Gold nanoparticle based systems in genetics. *Current Pharmacogenomics*, **5**, 39–47.

23 Rodrigo, M., Pedro, B., Leandro, R., Goncalo, D., Leonardo, S., Ricardo, F. and Elvira, F. (2007) Amorphous/nanocrystalline silicon biosensor for the specific identification of unamplified nucleic acid sequences using gold nanoparticle probes. *Applied Physics Letters*, **90**, 023903/1–023903/3.

24 Bao-An, D., Zheng-Ping, L. and Cheng-Hui, L. (2006) One-step homogeneous detection of DNA hybridization with gold nanoparticle probes by using a linear light-scattering technique. *Angewandte Chemie - International Edition*, **45**, 8022–5.

25 Hong, O.E., Lee, M.Y., Nam, D., Yoon, S.H. and Kim, H.C. (2005) Inhibition assay of biomolecules based on fluorescence resonance energy transfer (FRET) between quantum dots and gold nanoparticles. *Journal of the American Chemical Society*, **127**, 3270–1.

26 Reinhard, B.M., Siu, M., Agarwal, H., Alivisatos, A.P. and Liphardt, J. (2005) Calibration of dynamic molecular rulers based on plasmon coupling between gold nanoparticles. *Nano Letters*, **5**, 2246–52.

27 Yun, C.S., Javier, A., Jennings, T., Fisher, M., Hira, S., Peterson, B., Hopkins, N., Reich, O. and Strouse, G.F. (2005) Nanometal surface energy transfer in optical rulers, breaking the fret barrier. *Journal of the American Chemical Society*, **127**, 3115–19.

28 Benoit, D. (2005) Quantum dots: DNA detectives. *Nature Materials*, **4**, 797–8.

29 Zhang, C.-Y., Yeh, H.-C., Kuroki, M.T. and Wang, T.-H. (2005) Single-quantum-dot-based DNA nanosensor. *Nature Materials*, **4**, 826–31.

30 Dubertret, B., Calame, M. and Libchaber, A.J. (2001) Single-mismatch detection using gold-quenched fluorescent oligonucleotides. *Nature Biotechnology*, **19**, 365–70.

31 Nam, J.M., Thaxton, C.S. and Mirkin, C.A. (2003) Nanoparticle-based bio-bar codes for the ultrasensitive detection of proteins. *Science*, **301**, 1884–6.

32 Alivisatos, P. (2004) The use of nanocrystals in biological detection. *Nature Biotechnology*, **22**, 47–52.

33 Gaylord, B.S., Bazan, G.C. and Heeger, A.J. (2003) DNA hybridization detection with water-soluble conjugated polymers and chromophore-labeled single-stranded DNA. *Journal of the American Chemical Society*, **125**, 896–900.

34 Maxwell, D.J., Taylor, J.R. and Nie, S. (2002) Self-assembled nanoparticle

probes for recognition and detection of biomolecules. *Journal of the American Chemical Society*, **124**, 9606.

35 Li, H. and Rothberg, L.J. (2004) DNA sequence detection using selective fluorescence quenching of tagged oligonucleotide probes by gold nanoparticles. *Analytical Chemistry*, **76**, 5414.

36 Rosi, N.L. and Mirkin, C.A. (2005) Nanostructures in biodiagnostics. *Chemical Reviews*, **105**, 1547.

37 Fan, C., Wang, S., Hong, J.W., Bazan, G.C., Plaxco, K.W. and Heeger, A.J. (2003) Beyond superquenching: hyper-efficient energy transfer from conjugated polymers to gold nanoparticles. *Proceedings of the National Academy of Sciences of the United States of America*, **100**, 6297–301.

38 Aldaye, F.A. and Sleiman, H.F. (2007) Dynamic DNA templates for discrete gold nanoparticle assemblies: control of geometry, modularity, write/erase and structural switching. *Journal of the American Chemical Society*, **129**, 4130–1.

39 Seelig, J., Leslie, K., Renn, A., Kuhn, S., Jacobsen, V., van de Corput, M., Wyman, C. and Sandoghdar, V. (2007) Nanoparticle-induced fluorescence lifetime modification as nanoscopic ruler: demonstration at the single molecule level. *Nano Letter*, **7**, 685.

40 Jennings, T.L., Singh, M.P. and Strouse, G.F. (2006) Fluorescent lifetime quenching near d = 1.5 nm gold nanoparticles: probing NSET validity. *Journal of the American Chemical Society*, **128**, 5462.

41 Jain, P.K., Huang, W. and El-Sayed, M.A. (2007) On the universal scaling behavior of the distance decay of plasmon coupling in metal nanoparticle pairs: a plasmon ruler equation. *Nano Letter*, **7**, 2080.

42 Reinhard, B.M., Siu, M., Agarwal, H., Alivisatos, A.P. and Liphardt, J. (2007) Calibration of dynamic molecular rulers based on plasmon coupling between gold nanoparticles. *Nano Letter*, **5**, 2246.

43 Darbha, G.K., Ray, A. and Ray, P.C. (2007) Gold nanoparticle-based miniaturized NSET probe for rapid and ultra-sensitive detection of mercury in soil, water and fish. *ACS Nano*, **3**, 208–14.

44 Rex, M., Hernandez, F.E. and Campiglia, A.D. (2006) Pushing the limits of mercury sensors with gold nanorods. *Analytical Chemistry*, **78**, 445–4.

45 Ray, P.C., Fortner, A. and Darbha, G.K. (2006) Gold nanoparticle based FRET assay for the detection of DNA cleavage. *The Journal of Physical Chemistry B*, **110**, 20745–8.

46 Ray, P.C. (2006) Label-free diagnostics of single base-mismatch DNA hybridization on gold nanoparticles using hyper-Rayleigh scattering technique. *Angewandte Chemie*, **45**, 1151–4.

47 Kim, C.K., Kalluru, R.R., Singh, J.P., Fortner, A., Griffin, J., Darbha, G.K. and Ray, P.C. (2006) Gold nanoparticle based miniaturized laser induced fluorescence probe for specific DNA hybridization detection: studies on size dependent optical properties. *Nanotechnology*, **17**, 3085.

48 Tiwari, V.S., Tovmachenko, O., Darbha, G.K., Hardy, W., Singh, J.P. and Ray, P.C. (2007) Non-resonance SERS effects of silver colloids with different shapes. *Chemical Physics Letters*, **446**, 77–82.

49 Ray, P C, Darbha, G.K., Ray, A., Walker, J., Hardy, W. and Perryman, A. (2007) Gold nanoparticle based FRET for DNA detection. *Plasmonics*, **2**, 173–83.

50 Ray, P.C., Darbha, G.K., Ray, A., Hardy, W. and Walker, J. (2007) Gold nanoparticle based FRET probe for multiplexed hybridization detection: accurate identification of bio-agents DNA. *Nanotechnology*, **18**, 375504.

51 Ray, P.C., Darbha, G.K., Ray, A., Hardy, W. and Walker, J. (2007) Gold nanoparticle based FRET probe for multiplexed hybridization detection: accurate identification of bio-agents DNA. *Nanotechnology*, **18**, 375504–10.

52 Kondon, M., Kim, J., Udawatte, N. and Lee, D. (2008) Origin of size-dependent energy transfer from photoexcited CdSe quantum dots to gold nanoparticles. *The Journal of Physical Chemistry C*, **112**, 6695–9.

53 Park, S.-J., Duncan, T.V., Sanchez-Gaytan, B.L. and Park, S.-J. (2008) Bifunctional nanostructures composed of

fluorescent core and metal shell subdomains with controllable geometry. *The Journal of Physical Chemistry C*, **112** (30), 11205–10.

54 Pons, T., Medintz, I.L., Sapsford, K.E., Higashiya, S., Grimes, A.F., English, D.S. and Mattoussi, H. (2007) On the quenching of semiconductor quantum dot photoluminescence by proximal gold nanoparticles. *Nano Letters*, **7**, 3157–64.

55 Wang, L., Yan, R., Huo, Z., Wang, Z., Bao, J., Wang, J., Peng, S., Li, Q. and Y. (2005) fluorescence resonant energy transfer biosensor based on upconversion-luminescent nanoparticles. *Angewandte Chemie*, **117**, 6208–11.

56 Jain, P.K., Huang, W. and El-Sayed, M.A. (2007) On the universal scaling behavior of the distance decay of plasmon coupling in metal nanoparticle pairs: aplasmon ruler equation. *Nano Letters*, **7**, 2080.

57 Dulkeith, E., Morteani, A.C., Niedereichholz, T., Klaar, T.A., Feldmann, J., Levii, S.A. and Reinhoudt, D.N. (2002) Fluorescence quenching of dye molecules near gold nanoparticles: radiative and nonradiative effects. *Physical Review Letters*, **89**, 203202–5.

58 Wark, A.W., Lee, H.J., Qavi, A.J. and Corn, R.M. (2007) Nanoparticle-enhanced diffraction gratings for ultrasensitive surface plasmon biosensing. *Analytical Chemistry*, **79**, 6697–701.

59 Forster, T. (1948) Intermolecular energy transference and fluorescence. *Annalen der Physik*, **2**, 55–7.

60 Griffin, J. and Ray, P.C. (2008) Gold nanoparticle based NSET For monitoring Mg^{2+} dependent RNA folding. *The Journal of Physical Chemistry B*, **112** (36), 11198–201.

61 Jennings, T.L., Schlatterer, J.C., Singh, M.P., Greenbaum, N.L. and Strouse, G.F. (2006) NSET molecular beacon analysis of hammerhead RNA substrate binding and catalysis. *Nano Letters*, **6**, 1318–24.

62 Sönnichsen, C., Reinhard, B.M., Liphardt, J. and Alivisatos, P. (2005) A molecular ruler based on plasmon coupling of single gold and silver nanoparticles. *Nature Biotechnology*, **23**, 741–5.

63 Kim, J.H., Chaudhary, S. and Ozkan, M. (2007) Multicolour hybrid nanoprobes of molecular beacon conjugated quantum dots: FRET and gel electrophoresis assisted target DNA detection. *Nanotechnology*, **18**, 195105.

64 Seferos, D.S., Giljohann, D.A., Hill, H.D., Prigodich, A.E. and Mirkin, C.A. (2007) Nano-flares: probes for transfection and mRNA detection in living cells. *Journal of the American Chemical Society*, **129**, 15477–9.

65 Bates, A.D., Callen, B.P., Cooper, J.M., Cosstick, R., Geary, C., Glidle, A., Jaeger, L., Pearson, J.L., Proupin-Perez, M., Xu, C. and Cumming, D.R.S. (2006) Construction and Characterization of a gold nanoparticle wire assembled using Mg^{2+}-dependent RNA-RNA interactions. *Nano Letters*, **6**, 445–8.

66 Zhang, C.-Y. and Johnson, L.W. (2006) Quantum-dot-based nanosensor for RRE IIB RNA-Rev peptide interaction assay. *Journal of the American Chemical Society*, **128**, 5324–5.

67 Gill, R., Willner, I., Shweky, I. and Banin, U. (2005) Fluorescence resonance energy transfer in CdSe/ZnS-DNA conjugates: probing hybridization and DNA cleavage. *The Journal of Physical Chemistry B*, **109**, 23715–19.

68 Skewis, L.R. and Reinhard, B.M. (2008) Spermidine modulated ribonuclease activity probed by RNA plasmon rulers. *Nano Letters*, **8**, 214–20.

69 Bagalkot, V., Zhang, L., Levy-Nissenbaum, E., Jon, S., Kantoff, P.W., Langer, R. and Farokhzad, O.C. (2007) Quantum dot-aptamer conjugates for synchronous cancer imaging, therapy, and sensing of drug delivery based on Bi-fluorescence resonance energy transfer. *Nano Letters*, **7**, 3065–70.

70 Cissell, K.A., Rahimi, Y., Shrestha, S., Hunt, E.A. and Deo, S.K. (2008) Bioluminescence-based detection of MicroRNA, miR21 in breast cancer cells. *Analytical Chemistry*, **80**, 2319–25.

71 Medley, C.D., Smith, J.E., Tang, Z., Wu, Y., Bamrungsap, S. and Tan, W. (2008)

Gold nanoparticle-based colorimetric assay for the direct detection of cancerous cells. *Analytical Chemistry*, **80**, 1067–72.

72 Yu, C., Nakshatri, H. and Irudayaraj, J. (2007) Identity profiling of cell surface markers by multiplex gold nanorod probes. *Nano Letters*, **7**, 2300–6.

73 El-Sayed, I.H., Huang, X. and El-Sayed, M.A. (2005) Surface plasmon resonance scattering and absorption of anti-EGFR antibody conjugated gold nanoparticles in cancer diagnostics: applications in oral cancer. *Nano Letters*, **5**, 829–34.

74 Quarta, A., Corato, R.D., Manna, L., Argentiere, S., Cingolani, R., Barbarella, G. and Pellegrino, T. (2008) Multifunctional nanostructures based on inorganic nanoparticles and oligothiophenes and their exploitation for cellular studies. *Journal of the American Chemical Society*, **130** (32), 10545–55.

75 Aslan, K., Huang, J., Wilson, G.M. and Geddes, C.D. (2006) Metal-enhanced fluorescence-based RNA sensing. *Journal of the American Chemical Society*, **128**, 4206–7.

76 Loo, L., Guenther, R.H., Lommel, S.A. and Franzen, S. (2007) Encapsidation of nanoparticles by red clover necrotic mosaic virus. *Journal of the American Chemical Society*, **129**, 11111–17.

77 Koyfman, A.Y., Braun, G., Magonov, S., Chworos, A., Reich, N.O. and Jaeger, L. (2005) Controlled spacing of cationic gold nanoparticles by nanocrown RNA. *Journal of the American Chemical Society*, **127**, 11886–7.

78 Kumar, A. and Jakhmola, A. (2007) RNA-mediated fluorescent Q-PbS nanoparticles. *Langmuir*, **23**, 2915–18.

79 Li, H. and Rothberg, L. (2005) Detection of specific sequences in RNA using differential adsorption of single-stranded oligonucleotides on gold nanoparticles. *Analytical Chemistry*, **77**, 6229–33.

80 Dillenback, L.M., Goodrich, G.P. and Keating, C.D. (2008) Temperature-programmed assembly of DNA:Au nanoparticle bioconjugates. *Nano Letters*, **8**, 1556.

81 Wang, H., Tessmer, I., Croteau, D.L., Erie, D.A. and Van Houten, B. (2008) Functional characterization and atomic force microscopy of a DNA repair protein conjugated to a quantum dot. *Nano Letters*, **8**, 1631–7.

82 Medintz, I.L., Berti, L., Pons, T., Grimes, A.F., English, D.S., Alessandrini, A., Facci, P. and Mattoussi, H. (2007) A reactive peptidic linker for self-assembling hybrid quantum dot-DNA bioconjugates. *Nano Letters*, **7**, 1741–8.

83 Numnuam, A., Chumbimuni-Torres, K.Y., Xiang, Y., Bash, R., Thavarungkul, P., Kanatharana, P., Pretsch, E., Wang, J. and Bakker, E. (2008) Potentiometric detection of DNA hybridization. *Journal of the American Chemical Society*, **130**, 410–11.

84 Kumar, A. and Kumar, V. (2008) Self-assemblies from RNA-templated colloidal CdS nanostructures. *The Journal of Physical Chemistry C*, **112**, 3633–40.

85 Long, H., Kudlay, A. and Schatz, G.C. (2006) Molecular dynamics studies of ion distributions for DNA duplexes and DNA clusters: salt effects and connection to DNA melting. *The Journal of Physical Chemistry B*, **110**, 2918–26.

86 Liu, Y., Zhong, M., Shan, G., Li, Y., Huang, B. and Yang, G. (2008) Biocompatible ZnO/Au nanocomposites for ultrasensitive DNA detection using resonance Raman scattering. *The Journal of Physical Chemistry B*, **112**, 6484–9.

87 Ghosh, S.K. and Pal, T. (2007) Interparticle coupling effect on the surface plasmon resonance of gold nanoparticles: from theory to applications. *Chemical Reviews*, **107**, 4797–862.

88 Sassolas, A., Leca-Bouvier, B.D. and Blum, L.J. (2008) DNA biosensors and microarrays. *Chemical Reviews*, **108** (1), 109–39.

89 Hatchett, D.W. and Josowicz, M. (2008) Composites of intrinsically conducting polymers as sensing nanomaterials. *Chemical Reviews*, **108**, 746–69.

90 Famulok, M., Hartig, J.S. and Mayer, G. (2007) Functional aptamers and aptazymes in biotechnology, diagnostics, and therapy. *Chemical Reviews*, **107**, 3715–43.

91 Borisov, S.M. and Wolfbeis, O.S. (2008) Optical biosensors. *Chemical Reviews*, **108**, 423–61.

92 Jain, P.K., Huang, X., El-Sayed, I.H. and El-Sayed, M.A. (2008) Noble metals on the nanoscale: optical and photothermal properties and some applications in imaging, sensing, biology, and medicine. *Accounts of Chemical Research*, 2008, **41**, 1578–86.

93 Gordon, R., Sinton, D., Kavanagh, K.L. and Brolo, A.G. (2008) A new generation of sensors based on extraordinary optical transmission. *Accounts of Chemical Research*, **41**, 1049–57.

94 Lu, Y. and Liu, J. (2007) Smart nanomaterials inspired by biology: dynamic assembly of error-free nanomaterials in response to multiple chemical and biological stimuli. *Accounts of Chemical Research*, **40**, 315–23.

95 Zhuang, X., Bartley, L.E., Babcock, H.P., Russell, R., Ha, T. and Chu, S. (2000) A single-molecule study of RNA catalysis and folding. *Science*, **288**, 2048–51.

96 Bokinsky, G., Rudes, D., Mosra, V.K., Gordus, A., Rhodes, M.M., Barbock, H.P., Walter, N.G. and Zhuang, X. (2003) Single-molecule transition-state analysis of RNA folding. *Proceedings of the National Academy of Sciences of the United States of America*, **100**, 9302–8.

97 Griffin, J., Singh, A.K., Senapati, D., Rhodes, P., Mitchell, K., Robinson, B., Yu, E. and Ray, P.C. (2009) Size and Distance Dependence NSET Ruler for Selective Sensing of Hepatitis C virus RNA, *Chemistry European Journal*, **15**, 342.

98 Wang, H., Wu, Y., Lassiter, B., Nehl, C.L., Hafner, J.H., Nordlander, P. and Halas, N.J. (2006) Symmetry breaking in individual plasmonic nanoparticles. *Proceedings of the National Academy of Sciences of the United States of America*, **103**, 10856–60.

99 Lassiter, J.B., Aizpurua, J., Hernandez, L.I., Brandl, D.W., Romero, I., Lal, S., Hafner, J.H., Nordlander, P. and Halas, N.J. (2008) Close encounters between two nanoshells. *Nano Letters*, **8**, 1212–18.

100 Tam, F., Goodrich, G.P., Johnson, B.R. and Halas, N.J. (2007) Plasmonic enhancement of molecular fluorescence. *Nano Letters*, **7**, 496–501.

101 Wang, Y., Qian, W., Tan, Y. and Ding, S. (2008) A label-free biosensor based on gold nanoshell monolayers for monitoring biomolecular interactions in diluted whole blood. *Biosensors and Bioelectronics*, **28**, 1166–70.

102 Loo, C., Lowery, A., Halas, N., West, J. and Drezek, R. (2005) Immunotargeted nanoshells for integrated cancer imaging and therapy. *Nano Letters*, **5**, 709–11.

103 Gobin, A.M., Lee, M.H., Halas, N.J., James, W.D., Drezek, R.A. and West, J.L. (2007) Near-infrared resonant nanoshells for combined optical imaging and photothermal cancer therapy. *Nano Letters*, **7**, 1929–34.

104 Su, C.-H., Sheu, H.-S., Lin, C.-Y., Huang, C.-C., Lo, Y.-W., Pu, Y.-C., Weng, J.-C., Shieh, D.-B., Chen, J.-H. and Yeh, C.-S. (2007) Nanoshell magnetic resonance imaging contrast agents. *Journal of the American Chemical Society*, **129**, 2139–46.

105 Hirsch, L.R., Jackson, J.B., Lee, A., Halas, N.J. and West, J.L. (2003) A whole blood immunoassay using gold nanoshells. *Analytical Chemistry*, **75**, 2377–81.

106 Park, J., Estrada, A. Sharp, K. Sang, K Schwartz, J.A., Smith, D.K., Coleman, C., Payne, J.D. Korgel, B.A., Dunn, A.K. and Tunnell, J.W. (2008) Two-photon-induced photoluminescence imaging of tumors using near-infrared excited gold nanoshells. *Optics Express*, **16**, 1590–9.

107 Wang, Y., Xie, X., Wang, X., Ku, G., Gill, K.L., O'Neal, D.P., Stoica, G. and Wang, L. (2004) Photoacoustic tomography of a nanoshell contrast agent in the in vivo rat brain. *Nano Letters*, **4**, 1689–92.

108 Ligler, F.S. and Taitt, C.A.R. (2002) *Optical Biosensors: Present and Future*, Elsevier, Amsterdam, The Netherlands.

109 Malhotra, B.D. and Turner, A.P.F. (2003) *Perspectives in Biosensors*, JAI, Amsterdam, The Netherlands.

110 Gorton, L. (2005) *Biosensors and Modern Biospecific Analytical Techniques*, 1st edn, Elsevier, Amsterdam, The Netherlands.

111 Vo-Dinh, T. (2007) *Nanotechnology in Biology and Medicine: Methods, Devices, and Applications*, CRC Press, Boca Raton, FL.

Abstract

The ability to integrate metal nanoparticles into biological systems has had a major impact in biology and biomedicine. The development of nanobased biosensors has increased tremendously over the past few years, as demonstrated by the large number of scientific publications in this area. In this chapter we discuss recent efforts in the development of a nanomaterials surface energy transfer (NSET) probe for sensing biomolecules. Such a probe can improve the analytical figures of merit, such as detection limits, sensitivity, selectivity, and dynamic range, relative to currently available commercial systems.

Keywords

metallic nanomaterials; nanomaterials surface energy transfer; size-dependent; distance-dependent; biosensors; RNA folding; cancer detection.

5
Mixed-Metal Oxide Nanomaterials for Environmental Remediation

Dambar B. Hamal, Kennedy K. Kalebaila and Kenneth J. Klabunde

5.1
Introduction

Over the past few decades, much research effort has been focused on developing not only new methods but also new materials for the removal of toxic pollutants from water, soil and air. In order to address these issues, an environmental remediation campaign involving photocatalysis has emerged as a process that has attracted considerable interest. Photocatalysis involves the transformation of solar light energy into charged particles (electrons and holes) by the excitation of electrons in a semiconductor. The successful isolation of these charged particles can lead to their use as active species to bring about a chemical reaction.

First, inorganic semiconductors differ from metallic conductors and insulators based on their electronic band structure. Generally, in an isolated atom, the electrons occupy discrete energies (levels) that are very close, forming a continuous band in the solid state. The highest occupied band – the valence band – is separated from the lowest unoccupied band – the conduction band – by an energy difference; this is referred to as the band gap energy, E_g. When the energy of the incident photon is greater than the band gap of the semiconductor, an electron in the valence band is excited into the conduction band, leaving a vacancy called a hole (positively charged), in the valence band. The charges formed are free to move independently of each other, or the electron and hole may exist as a bound pair – called an exciton – due to the coulombic forces of attraction between the two opposite charges [1].

Semiconductor nanoparticles characteristically exhibit physical and chemical properties that are different from those of bulk materials, as a result of their having dimensions on the order of 1 to 100 nm. Semiconducting nanoparticles (quantum dots; QDs) exhibit size-dependent electronic and optical properties when the dimension of the particle is decreased relative to the bulk excitonic Bohr radius. These quantum confinement effects give rise to a blue-shift in the optical band gap energy. Because the size of the nanoparticles can be tuned to absorb or emit

Nanomaterials for the Life Sciences Vol. 3: Mixed Metal Nanomaterials. Edited by Challa S. S. R. Kumar

ISBN: 978-3-527-32153-7

light of a particular energy, it is possible to prepare nanoparticles with tailored properties for applications such as light-emitting diodes, gas sensing, photovoltaics, fluorescent medical labeling and photocatalysis. In photocatalysis, the generated electrons and holes can be utilized to reduce and oxidize organic molecules on the surface of the semiconductor. Among the various possible semiconductors, titania (TiO_2, $E_g = 3.2\,eV$) has attracted considerable interest as a photocatalyst in the decomposition of organic compounds. TiO_2 has several attractive features, including an inertness and resistant to corrosion, and requires little post-processing, which also makes it inexpensive. Most of the photoactivity of TiO_2 utilizes ultraviolet (UV) light, which constitutes about 4% of the solar energy; hence, the efficiency of TiO_2 as a photocatalyst is decreased. Consequently, there has been a growing trend towards sensitizing TiO_2 in the visible region (which constitutes 40–45% of solar energy) by the use of bandgap engineering. One way in which TiO_2 has been made visible light-active is by anchoring organic dyes (which absorb light in the visible region), and although the performance of such dye–TiO_2 composites has been greatly improved, the dyes are expensive and their long-term stability is poor [2, 3]. Visible light-active TiO_2 has also been prepared by doping cations or anions into the TiO_2 lattice, with the dopants modifying the bandgap structure of TiO_2 [4–6]. Because the amount and nature of the metal dopant can be widely varied, as per experimental needs, the doping of TiO_2 with metal cations has in recent years been the subject of extensive research interest. It can, therefore, be considered as an appealing avenue for the synthesis of highly active TiO_2 photocatalysts for numerous photocatalytic applications. These metal cation-doped TiO_2 photocatalysts are regarded as mixed-metal oxide photocatalysts with enhanced photoactivity.

In order to further increase the performance of the TiO_2 systems, a sol–gel synthetic approach has been used to prepare nanostructured gels (xerogels or aerogels) with appreciable surface area and porosity relative to bulk TiO_2. A high surface area is required to adsorb a large quantity of materials, while a porous system allows gaseous pollutants and byproducts to diffuse in and out of the photocatalyst. The sol–gel method also offers excellent control for synthesizing multicomponent oxides by varying the synthetic conditions. For example, when the rates of hydrolysis and condensation are similar, multicomponent metal oxides that are homogeneous at the molecular level can be prepared [7]. In addition, the preparation of TiO_2 on a nanoscale level increases the number of reactive sites on the surface of the catalyst [8].

In this chapter, attention will be focused on those reports where TiO_2 has been investigated as a nanomaterial for both UV and visible light photocatalysis for environmental remediation. Specifically, emphasis will be placed on the introduction of metal ions into the TiO_2 matrix to enhance not only UV activity but also visible-light photocatalysis. Finally, the details of other metal oxides that have been investigated for the degradation of organic pollutants are discussed. It is important to note that these systems are not based on a TiO_2 framework and are not necessarily nanostructured materials; rather, the results indicate the extent of research into materials used for environmental remediation.

5.2
TiO_2 Heterogeneous Photocatalysis for Environmental Remediation

Heterogeneous photocatalysis with TiO_2 in the form of anatase phase, as obtained at 500 °C, has shown greater photoactivity than the rutile phase, which is obtained by annealing at temperatures in excess of 550 °C. Compared to other single metal oxides (e.g., CeO_2, Cr_2O_3, CuO, Fe_2O_3, In_2O_3, SnO_2, V_2O_5 and WO_3, but excepting ZnO), TiO_2 has been shown to demonstrate an overall superior photocatalytic activity for the photodegradation of methylene blue (MB) under UV light irradiation [9]. Moreover, various toxic compounds such as CO [10], Cr(VI) [11], As(III) [12], organic aldehydes [13], amino acids [14], dimethyl methylphosphonate (DMMP) [15], sulfides [16], phenol [17], methyl orange [18] and rhodamine dyes [19] have been successfully photodegraded with TiO_2 photocatalysis under UV light illumination. There are, however, a number of avenues for enhancing the photoresponse and photocatalytic activity of pure TiO_2 both under UV and visible light.

5.2.1
Metal-Doped TiO_2 Mixed-Metal Oxides as UV-Light-Sensitive Photocatalysts

As mentioned above, several research groups have reported that the photocatalytic performance of TiO_2 may be enhanced by doping with an optimum amount of certain metal ions. For example, Bessekhouad *et al.* [20] investigated the effect of alkali metal ions (Li, Na, K) on doped TiO_2 nanoparticle photocatalysts for the photocatalytic degradation of Malachite green oxalate, 4-hydroxybenzoic acid and benzamide. Here, alkaline-doping was observed to increase the acidic sites at low alkaline levels (1 atom%), and the basic sites at higher levels of 3 and 5 atom%. Regardless of the type of alkaline used at low concentration, the experimental results showed that the efficiency of photocatalysts prepared using the impregnation technique was superior to that of pure TiO_2-P25 (Degussa P25, a commercial product containing 70% anatase and 30% rutile). Likewise, Li *et al.* [21] showed that doping TiO_2 with alkaline-earth metal ions (Be, Mg, Ca, Sr, Ba) caused an increase in photocatalytic activity of hydrogen production from an aqueous solution of C_2H_5OH, under UV light and using Pt as a cocatalyst. In fact, the activities of the doped TiO_2 photocatalysts were seen to depend on not only the size of the dopant ions but also the doping method used. In another study, Jin *et al.* [22] showed that doping with lanthanum ions (La^{3+}) enhanced the adsorption properties and photocatalytic activity of TiO_2 for MB and acetaldehyde degradation, again under UV light. Similarly, Galindo *et al.* [23] reported that nanocrystalline TiO_2–CeO_2 (5 wt%) mixed oxides of the smallest crystallite size and band gap prepared using the sol–gel method displayed the highest UV light photoactivity for 2-dichlorophenoxyacetic acid degradation.

Furthermore, Wang *et al.* [24] reported the details of three-dimensionally ordered macroporous mixed nanoparticle photocatalysts of ZrO_2–TiO_2 and Ta_2O_5–TiO_2, both of which exhibited homogeneous wall compositions; notably, either Zr or Ta

was uniformly dispersed into the TiO_2 framework, with loading levels of 5–20 mol% for Zr and 2.5–7.5 mol% for Ta. The estimated macropore diameter and wall thickness of these materials ranged from 280 to 290 nm, and from 30 to 50 nm, respectively. High-resolution transmission electron microscopy (TEM) (Figure 5.1) showed that the ZrO_2–TiO_2 and Ta_2O_5–TiO_2 particles aggregated on the material walls, with a homogeneous particle size distribution (10–12 nm) and a round shape. No phase segregation of ZrO_2 or Ta_2O_5 was observed, which implied that the dopants were dispersed homogeneously within the TiO_2 structure. The dark areas in the TEM images represented the composite particles. The UV-visible diffuse reflectance spectra (Figure 5.2) showed a red shift of the optical absorption

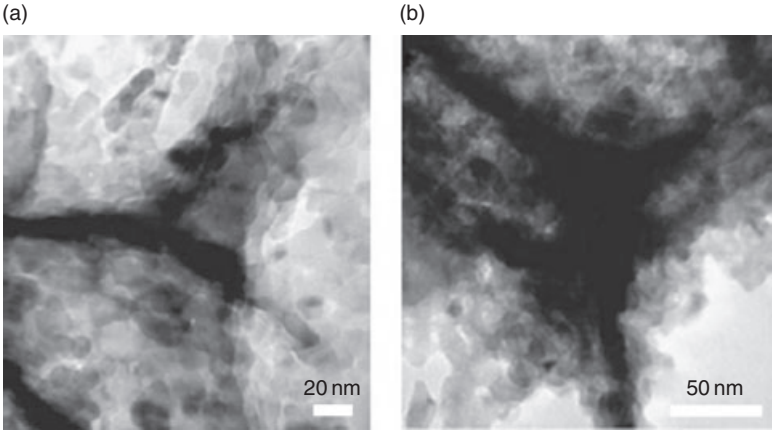

Figure 5.1 Transmission electron microscopy (TEM) images of as-prepared three-dimensionally ordered macroporous (3-DOM) TiO_2/Ta_2O_5 (a) and TiO_2/ZrO_2 (b) [24].

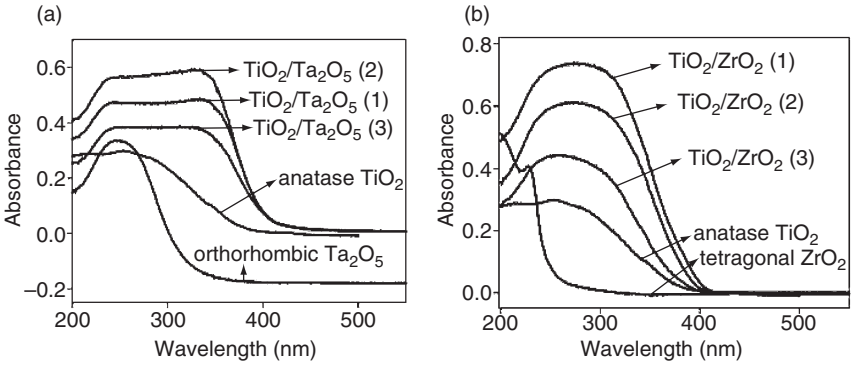

Figure 5.2 UV-visible diffuse reflectance spectra of 3-DOM materials. (a) TiO_2, Ta_2O_5 and TiO_2/Ta_2O_5 composites with different Ta_2O_5 loading levels; (b) TiO_2, ZrO_2 and TiO_2/ZrO_2 composites with different ZrO_2 loading levels [24].

edge of ZrO_2–TiO_2 and Ta_2O_5–TiO_2 mixed-metal oxide photocatalysts compared to individual metal oxides. The photocatalytic tests revealed that the ZrO_2–TiO_2 and Ta_2O_5–TiO_2 systems exhibited superior UV light photoactivities for 4-nitrophenol (4-NP) and rhodamine B (RhB) photodegradation compared to the corresponding single metal oxide photocatalysts (Figure 5.3). The enhanced photoactivities of the mixed-metal oxide nanoparticle photocatalysts were attributed to a decrease in the optical band gap of TiO_2, a better dispersion of Ta_2O_5 and ZrO_2 within the TiO_2 framework, and to the higher surface areas (66–78 $m^2 g^{-1}$) of the mixed-metal oxide photocatalysts compared to the individual metal oxides (31–34 $m^2 g^{-1}$). In addition, several other mixed-metal oxides nanoparticle photocatalysts of Mo [25], Zn [26], Ga [27] and In [28] -doped TiO_2 have been reported for methyl orange, phenol, benzoic acid and 2-chlorophenol photodegradation under UV light, respectively. Nevertheless, Yu *et al.* [29] reported that an anatase-phase, hollow microspherical solid-solution photocatalyst of Sn^{4+}-doped TiO_2 exhibited a better photocatalytic activity for the degradation of acetone in air and RhB in aqueous solution (Figure 5.4). A typical scanning electron microscopy (SEM) image (Figure 5.5a) indicated that the outer surfaces of the Sn^{4+}-doped TiO_2 microspheres, with an average size of 1 μm, were rough and composed of a large number of loosely packed nanoparticles. Consequently, such a mesoscopical structural organization might be beneficial to the enhancement of reagent adsorption and mass transportation, due to the higher surface area (66.9 $m^2 g^{-1}$) and presence of interconnected porous networks. A TEM image (Figure 5.5b) further confirmed that some of the broken microspheres appeared to have a hollow interior, suggesting the formation of hollow TiO_2 structures. An enlarged TEM image (Figure 5.5c) of the outer surface of the hollow microspheres showed them to consist of nanocrystals with a size range of 20–30 nm. Moon *et al.* [30] prepared a Sb-doped TiO_2 nanocrystalline photocatalyst

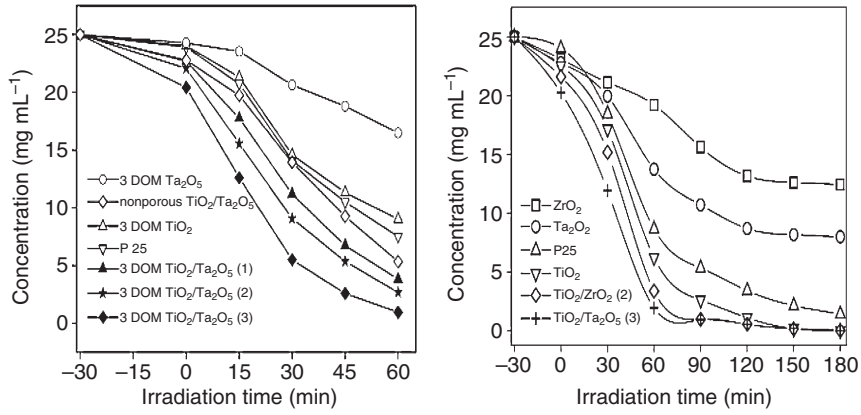

Figure 5.3 (a) Degradation profiles of 4-nitrophenol over the 3-DOM TiO_2/Ta_2O_5, P25 and pure 3-DOM metal oxides. $C_0 = 25\ mg\ l^{-1}$, catalyst 0.08 g; (b) Degradation profiles of RhB over different catalysts. $C_0 = 50\ mg\ l^{-1}$, catalyst 0.08 g [24].

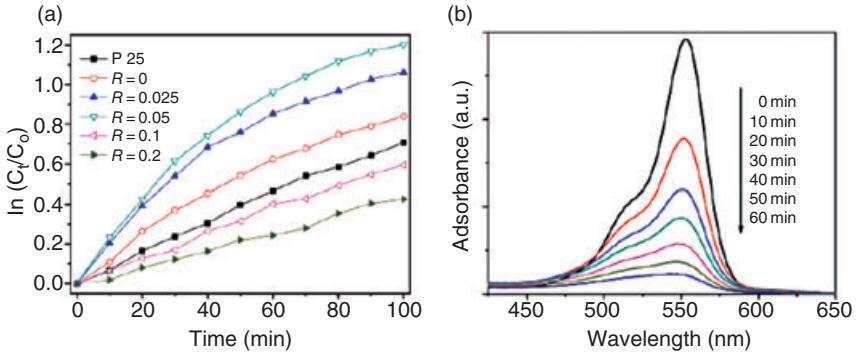

Figure 5.4 (a) Comparison of the photocatalytic activity of P25 and $Ti_{1-x}Sn_xO_2$ samples obtained with varying R for the degradation of acetone in air; (b) Adsorption changes of RhB aqueous solution under photocatalytic degradation using a typical $Ti_{1-x}Sn_xO_2$ sample obtained with $R = 0.05$ ($R = Sn^{4+}/Sn^{4+} + Ti^{4+}$) [29].

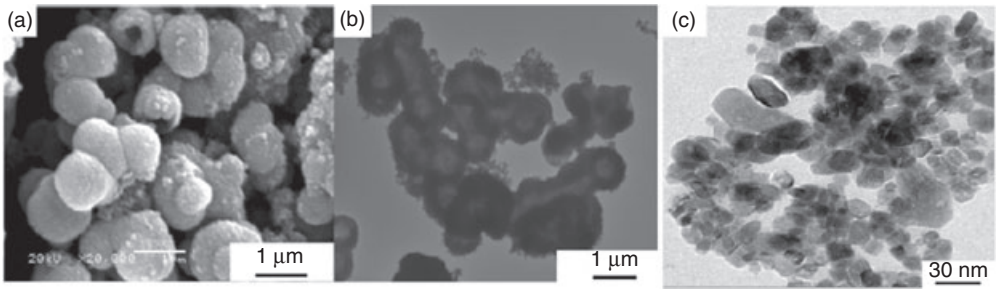

Figure 5.5 Scanning electron microscopy image (a) and transmission electron microscopy images (b, c) of a typical $Ti_{1-x}Sn_xO_2$ sample obtained with $R = 0.05$ [29].

by using a coprecipitation method, and showed that antimony doping significantly improved photocatalytic performance in the photodegradation of MB, as compared to the undoped TiO_2. Similarly, Zuo *et al.* [31] reported a prism-shaped Bi^{3+}-TiO_2 photocatalyst composed of crystallites of anatase with an average particle size of 6 nm, as determined from a TEM image (Figure 5.6). These authors showed that Bi^{3+} ion doping into TiO_2 resulted in a narrowing of the band gap of TiO_2, thereby improving the photoreactivities for the degradation of RhB in aqueous solution (Figure 5.7). Moreover, Kapoor *et al.* [32] reported that the aerogel processing of some nanocrystalline mixed-metal oxides of type MTi_2O_5 (M = Mg, Mn, Fe, Zn, Sn) showed only UV-light activity for CH_3CHO degradation (Table 5.1), except for $CoTi_2O_5$, which showed a dark catalytic activity for acetaldehyde degradation (Figure 5.8). The SEM image (Figure 5.9) showed clearly that the aerogel-processed $CoTi_2O_5$ catalysts comprised uniform crystallites of $CoTi_2O_5$. Overall, these

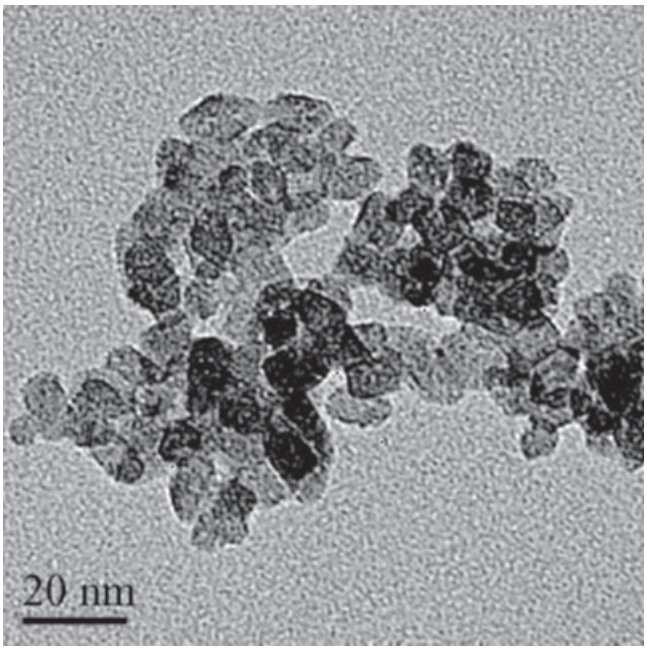

Figure 5.6 Transmission electron microscopy images of Bi^{3+}–TiO_2 [31].

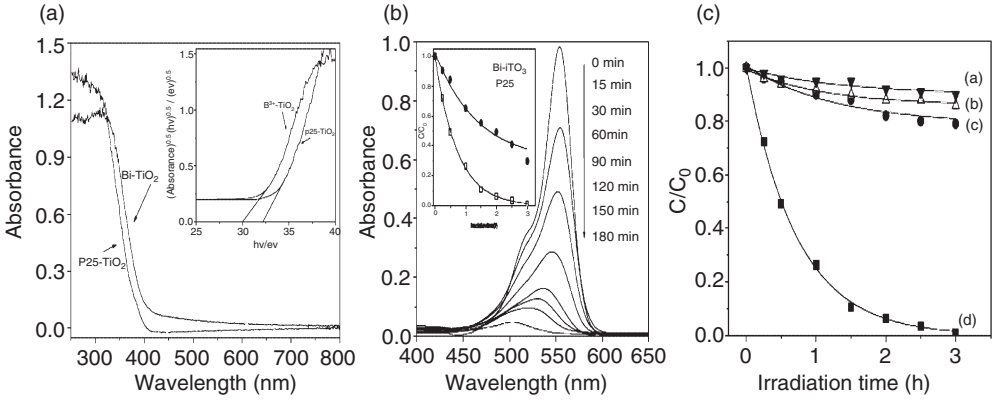

Figure 5.7 (a) UV-visible reflectance spectra of P25 TiO_2 and Bi^{3+}–TiO_2; (b) Spectral change of RhB in aqueous Bi^{3+}–TiO_2 dispersions as a function of irradiation time (The insert shows RhB concentration changes over Bi^{3+}–TiO_2 and P25–TiO_2); (c) Kinetics of degradation of RhB (10^{-4} *M*, pH 2.0) under different conditions: curve a, Bi^{3+}–TiO_2, air, dark; curve b, Bi^{3+}–TiO_2, N_2, UV light; curve c, without catalyst, air, UV light; curve d, Bi^{3+}–TiO_2, air, UV light. C_0 and C are the concentrations of RhB determined before and after irradiation [31].

Table 5.1 Pseudo-first-order rate constants[a] (k, min^{-1}) for the degradation of acetaldehyde by $MgTi_2O_5$ and the composites $MTiO_3/TiO_2$ (M = Fe, Zn) under UV irradiation (320 nm < λ < 400 nm).

Sample	Rate constant (k, min^{-1})
Degussa P25 TiO_2	0.010
$MgTi_2O_5$	0.004
$FeTiO_3/TiO_2$	0.001
$ZnTiO_3/TiO_2$	0.003

a Calculated from plots of $\ln(C_0/C)$ versus time (t), where C_0 and C denote the gas-phase concentrations of acetaldehyde at $t = 0$ and $t = t$, respectively [32].

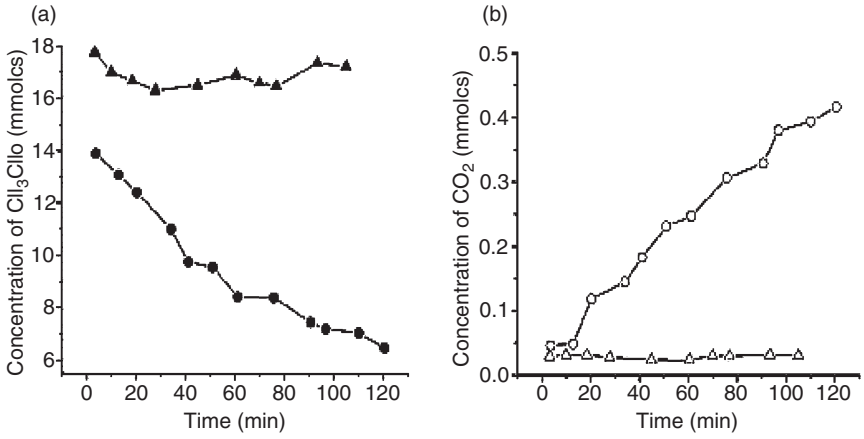

Figure 5.8 (a) ●, Rate of decomposition of acetaldehyde in the dark by $CoTiO_3/TiO_2$.▲, concentrations of acetaldehyde in the absence of any catalyst; (b) ○, Formation of CO_2 in the dark by $CoTiO_3/TiO_2$. △, concentrations of CO_2 in the absence of any catalyst [32].

findings suggested that metal-doped TiO_2 mixed-metal oxide photocatalysts exhibited a better catalytic performance than pure, undoped TiO_2.

5.2.2
Metal-Doped TiO_2 Mixed-metal Oxides as Visible-Light-Sensitive Photocatalysts

Since incident solar light contains an abundant amount of visible light (40–45%), the development of visible-light-sensitive photocatalysts would not only show more promise but also be more efficient for both gas-phase and liquid-phase environmental remediation of indoor and outdoor pollutants. In this context, Fan *et al.*

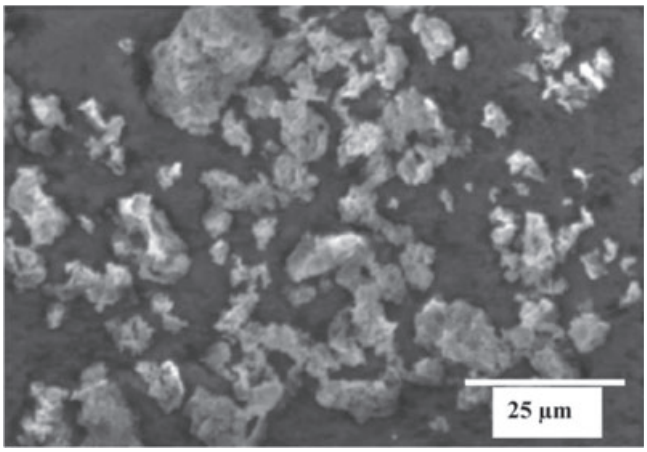

Figure 5.9 Scanning electron microscopy images of $CoTiO_3/TiO_2$ [32].

[33] identified a visible-light-active mesoporous Cr-doped TiO_2 photocatalyst with wormlike channels, and showed its photocatalytic activity to be higher than that of undoped TiO_2 for gaseous acetaldehyde photodecomposition under visible-light irradiation. Song *et al.* [34] synthesized nanocrystalline WO_x-doped TiO_2 powders by using a sol-mixing method, and showed a MB solution to be successfully degraded using the WO_x–TiO_2 photocatalyst under visible-light illumination, especially when the pH of the solution was higher than 6. Similarly, others have reported V [35], Fe [36], Ce [37] and Bi [38] -doped TiO_2 mixed-metal oxide photocatalytic systems for the photodegradation of MB, methyl orange, RhB and *p*-chlorophenol under visible light, respectively. These findings suggest that the electronic and optical properties of the TiO_2 photocatalyst could be modified by preparing nanocrystalline metal-doped TiO_2 mixed-metal oxide as visible-light-active photocatalysts for environmental applications. In 2004, however, Martyanov *et al.* [39] reported that structural defects were the main factors for the visible light absorption of TiO_2-based photocatalysts (Figure 5.10, left). In order to study these structural defects, commercial TiO_2 Degussa, TiN, TiC, TiO and Ti_2O_3 were annealed at 800 °C for 2 h in air, after which the resultant materials were found to have a TiO_2 rutile phase. The gas-phase acetaldehyde photodegradation results showed that the visible-light activities of these catalysts were dependent on the source of the initial precursor materials of TiO_2. It was also observed that TiO_2 rutile obtained from the annealing of commercial TiO showed the highest photoactivity (see Figure 5.10, right). Unfortunately, however, this high-temperature (800 °C) synthetic method resulted in rutile TiO_2 photocatalyst of very low surface area.

In order to increase the surface area, Wang [40] and Rodrigues *et al.* [41] have developed high-surface-area photocatalysts based on a composite mixture of TiO_2- and SiO_2-doped transition metal ions (TiO_2/SiO_2/metal oxide) for visible-light,

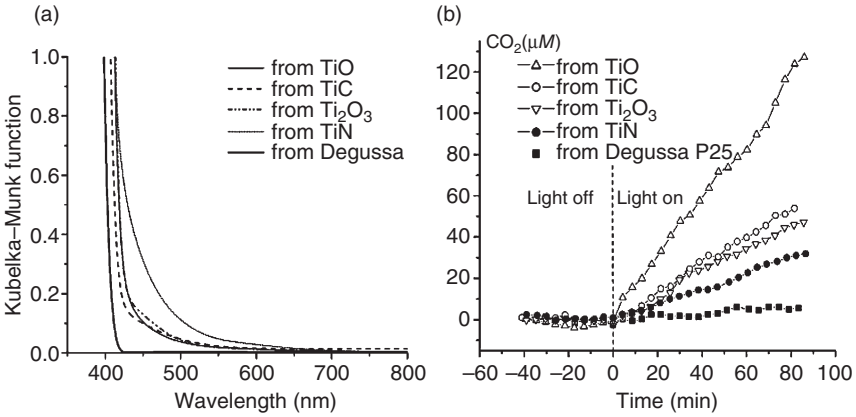

Figure 5.10 (a) Visible parts of the optical spectra of titanium dioxides prepared from different precursors; (b) Influence of the precursors on the photoactivity of TiO_2 in the reaction of acetaldehyde oxidation in air under visible light ($\lambda = 546$ nm, green to the eye; 7.4×10^{16} photon $s^{-1}cm^{-2}$) at 25 °C. The initial gas-phase acetaldehyde concentration was ca. 2 m*M*; the initial concentration of carbon dioxide fitted to zero. The corresponding consumption of acetaldehyde and production of acetic acid are not shown, for sake of clarity [39].

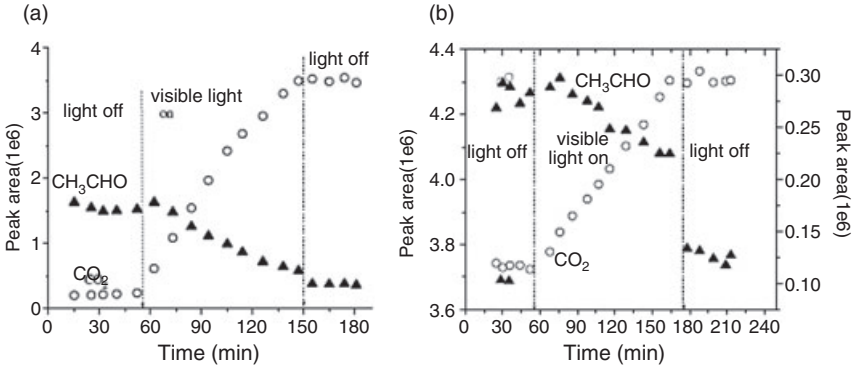

Figure 5.11 Photocatalytic properties of (a) Cr/SiO_2 and (b) V/SiO_2. CH_3CHO decomposition and CO_2 evolution are shown as a function of irradiation time during the photodegradation of CH_3CHO under visible light (>420 nm) [40].

gas-phase CH_3CHO photodegradation (Figures 5.11 and 5.12). When the same groups also prepared transition metal-only oxides in a SiO_2 matrix, the photoactivity was seen to be comparable with that of the TiO_2/SiO_2/metal oxide. Furthermore, when Rodrigues *et al.* [42] prepared a Cr–Al–MCM-41 photocatalyst for the photo-oxidation of trichloroethylene (TCE) (Figure 5.13), the results of this mechanistic study suggested that the photocatalysis process had occurred on isolated Cr^{6+}

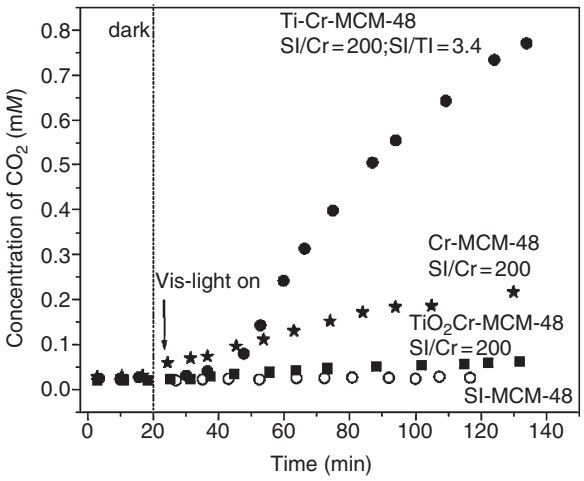

Figure 5.12 Photocatalytic activity of mesoporous materials for the degradation of acetaldehyde in air under visible light. The consumption of acetaldehyde is not shown for sake of clarity [41].

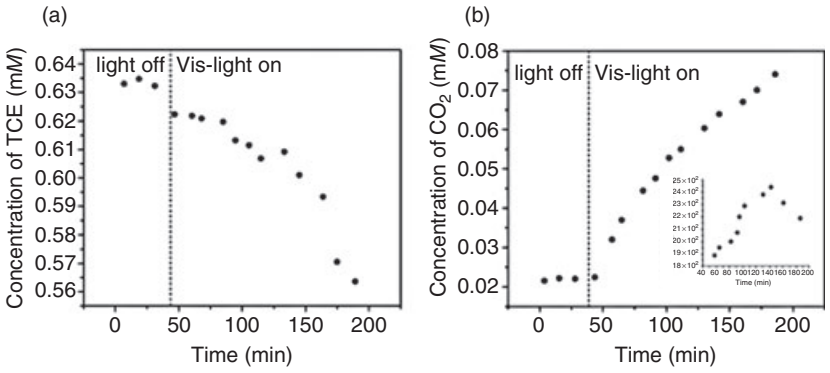

Figure 5.13 Plot of concentration versus time for (a) trichloroethylene (TCE) consumption and (b) CO_2 evolution using Cr–Al–MCM-41 (Si/Cr = 20) under visible-light irradiation. The insert in (b) shows the evolution of $COCl_2$ [42].

ions, supported on a predominantly SiO_2 framework. In contrast, the same group [43] also reported the details of a AgBr–Al–MCM-41 visible-light photocatalyst for the gas-phase decomposition of CH_3CHO (Figure 5.14). It was concluded that AgBr, together with Ag^0, was the photoactive species in CH_3CHO photodecomposition, while the high-surface-area Al-MCM-41 aided in the high dispersion of AgBr on the support.

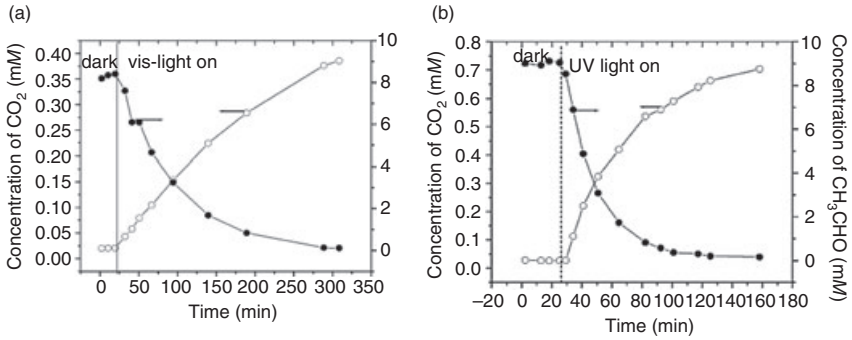

Figure 5.14 Plot of concentration versus time for evolution of CO_2 and decrease in concentration of CH_3CHO using AgBr/Al-MCM-41 under (a) visible light irradiation and (b) UV irradiation [43].

Apart from high-surface-area, visible-light photocatalysts based on a nonreactive SiO_2 support, it was envisioned that an appropriate combination of metal and nonmetal codoped TiO_2 mixed-metal oxide systems might be made even more efficient by using visible light for the heterogeneous photodegradation of volatile organic compounds. By doing so, it was also envisaged that the doped metal would help reduce the electron–hole recombination and that the doped nonmetal would result in band gap narrowing of TiO_2. Based on this new concept, a degree of success has been achieved in designing new nanoparticle mixed-metal oxide photocatalysts of V–C–TiO_2 [44] and Ag/(C,S)–TiO_2 [45] for gas-phase acetaldehyde photodecomposition (Figures 5.15 and 5.16) under visible-light illumination.

Very interestingly, these findings suggest that doped carbon and/or sulfur predominantly resulted in a band gap narrowing and a shift in the optical absorption edge of TiO_2, whereas the codoped silver present as Ag^+ and Ag^0 in TiO_2 seemed responsible for the separation of photoinduced charge carriers (Figure 5.17). Consequently, the rate of photodegradation of gaseous acetaldehyde with these new photocatalysts was enhanced under both visible- and UV-light irradiations (Table 5.2). These results strongly suggest that such new nanocrystalline metal and nonmetal-codoped TiO_2 mixed-metal oxide photocatalysts might have a great potential for environmental applications, notably the remediation of volatile and nonvolatile organic–inorganic pollutants.

5.3
Other Mixed-metal Oxide Photocatalysts

Apart from the wide interest in using TiO_2 as a major component in designing photocatalysts, several research groups have reported the details of ternary oxide

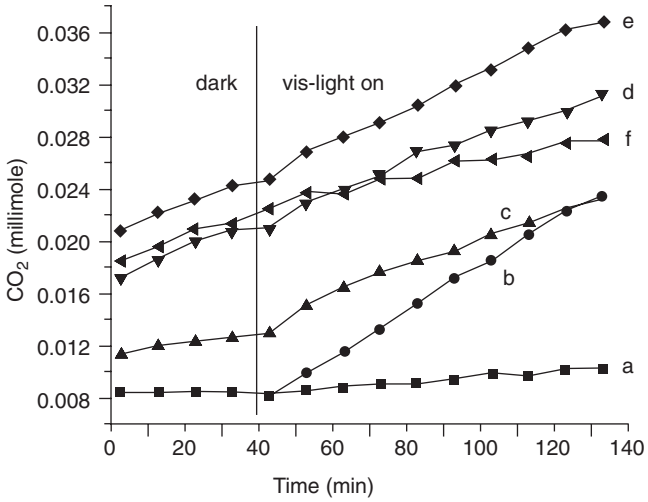

Figure 5.15 CO_2 evolution during CH_3CHO oxidation on P25-TiO_2 and doped TiO_2. Curve a = P25-TiO_2; curve b = C-doped TiO_2; curve c = C-, V-doped TiO_2 (0.5% V); curve d = C-, V-doped TiO_2 (1.0% V); curve e = C-, V-doped TiO_2 (2% V); curve f = C-, V-doped TiO_2 (3.0% V) [44].

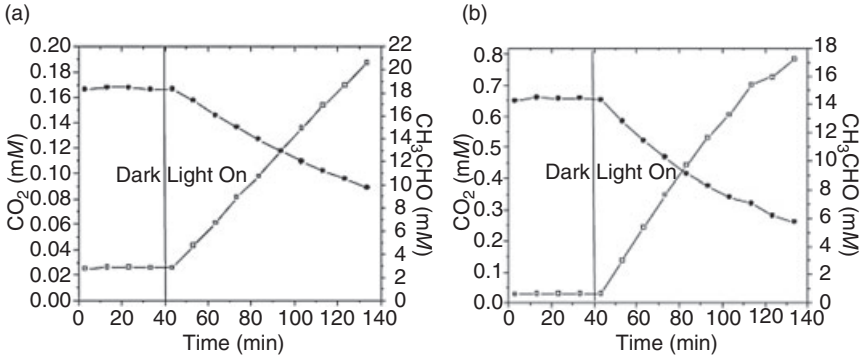

Figure 5.16 Degradation of gaseous acetaldehyde on Ag/(C, S)–TiO_2-01 catalyst under (a) visible and (b) UV light illumination [45].

systems that are both visible- and UV-light-active. Moreover, the materials are often prepared via solid-state routes, which undoubtedly lead to lower surface areas of the materials. Among such materials reported are $CaBi_2O_4$ [46], $PbBi_2Nb_2O_9$ [47] and $BiVO_4$ [48], all of which have appreciable absorption in the visible range, while their larger sizes usually leads to simple precipitation and hence an easy recovery from water purification. However, as noted by Long *et al.* [49], a combination of the lower surface areas, the long migration distances for the exciton, and the high

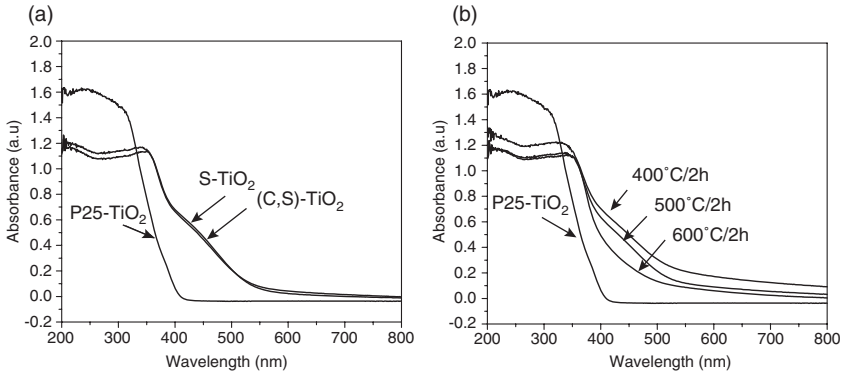

Figure 5.17 UV-visible absorption profiles of (a) C and/or S-doped TiO_2 and (b) Ag/(C, S)–TiO_2-01 catalysts at various temperatures, compared to P25-TiO_2 [45].

Table 5.2 Initial rates ($mM\,min^{-1}$) of production of CO_2 and degradation of CH_3CHO on various catalysts under visible and UV light [45].

Catalyst used	$(CO_2)_{vis}$ production	$(CH_3CHO)_{vis}$ degradation	$(CO_2)_{UV}$ production	$(CH_3CHO)_{UV}$ degradation
P25 (TiO_2)	0.0002	0.009	0.01	0.05
Ag/(C,S)-TiO_2-01	0.002	0.110	0.008	0.16
Ag/(C,S)-TiO_2-02	0.002	0.060	0.008	0.11
(C,S)-TiO_2-01	0.0007	0.053	0.009	0.20
S-TiO_2-02	0.0005	0.046	0.007	0.12

recombination rates of excitons lead to lower photocatalytic activities. Other reports have suggested that the performance of these materials was increased when small amounts of Pt, Ag or NiO were introduced, this effect being attributed to an altering of the energy band gap structures as well as of the electronic properties of the dopants [50–52]. Long and coworkers [49] exploited $BiVO_4$, which is known to split water and photodegrade organic pollutants under visible light, and also CoO_x, a well-known and efficient catalyst, to prepare a $CoO_x/BiVO_4$ composite material. The TEM image (Figure 5.18a) of a typical $Co_3O_4/BiVO_4$ composite particle revealed that the $BiVO_4$ particles were microparticles with sizes of several micrometers. From the TEM analysis, it became clear that small heteroparticles were dispersed over the edge of large $BiVO_4$ particles, forming $BiVO_4$ particles of an irregular shape. Furthermore, the magnified image (Figure 5.18b) showed the Co_3O_4 powder to be composed of nanoparticles with sizes ranging from 20 to 30 nm, deposited over the surface of $BiVO_4$, and constituting a type of composite heterojunction structure. When the same groups studied the degradation of phenol, they found

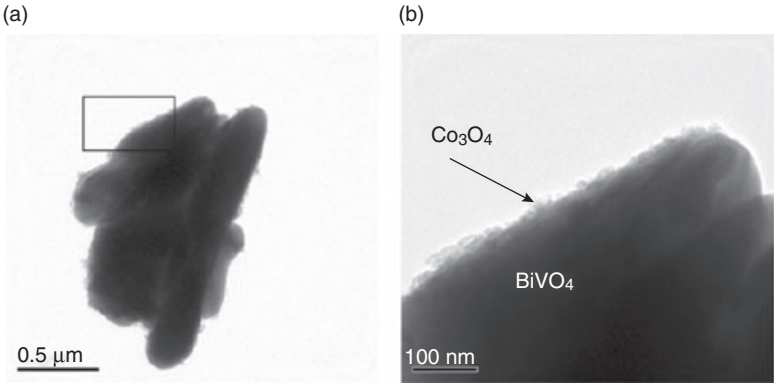

Figure 5.18 Transmission electron microscopy image of (a) the $Co_3O_4/BiVO_4$ composite; (b) magnified views of the composite heterojunction structure [49].

that a 0.8 wt% CoO_x loading into a $BiVO_4$ matrix gave the best results, as evidenced by the reduction of phenol by up to 96% (Figure 5.19). As reported elsewhere, although the adsorption of phenol onto bare TiO_2 or $BiVO_4$ from solution is very difficult [53], this $CoO_x/BiVO_4$ composite performed well for this purpose. It is believed that the p-type CoO_x and n-type $BiVO_4$ form a p–n heterojunction on which photogenerated charge carriers electrons move form the p-type to the n-type, while simultaneously the holes migrate from n-type to p-type (Figure 5.20). This migration of charge carriers reduces the recombination of the charges and leads to an enhancement of the photocatalysis. The authors concluded that optimal calcination temperatures and cobalt contents are important for the high crystallinity (this favors the migration of electrons and holes), leading to high activity.

Liu and Sun have reported the effect of impregnating CeO_2 on a $Fe_2O_3/\gamma\text{-}Al_2O_3$ composite catalyst on the catalytic activity of wet peroxide oxidation of azo dyes [54]. The rationale behind doping with CeO_2 is that it promotes oxygen storage and release, thus enhancing oxygen mobility; in addition, it forms surface and bulk vacancies, thus improving redox properties in conjunction with transition metal oxides. The authors also showed the catalytic activity of $Fe_2O_3–CeO_2/\gamma\text{-}Al_2O_3$ to be higher than that of $Fe_2O_3/\gamma\text{-}Al_2O_3$, this being attributed in part to the more adsorbed surface oxygen. X-ray photoelectron spectroscopy (XPS) data indicated a higher percentage of adsorbed oxygen in the CeO_2-doped catalyst. In order to show that the observed decomposition of the azo dyes was not merely adsorption but rather catalytic oxidation, a number of experiments were conducted without H_2O_2; consequently, only 30% of the azo dye color was removed compared to 90% when H_2O_2 was present. Zhong and coworkers have reported studies on the effect of doping $Ce_{0.5}Zr_{0.5}O_2$ with metal ions, and monitoring their UV photocatalytic activity in the decomposition of benzene, a common indoor and industrial air pollutant [55]. The $CeO_2–ZrO_2$ catalyst is used commercially on the basis of its high oxygen storage capacity, while the incorporation of Zr into the CeO_2 lattice creates a high

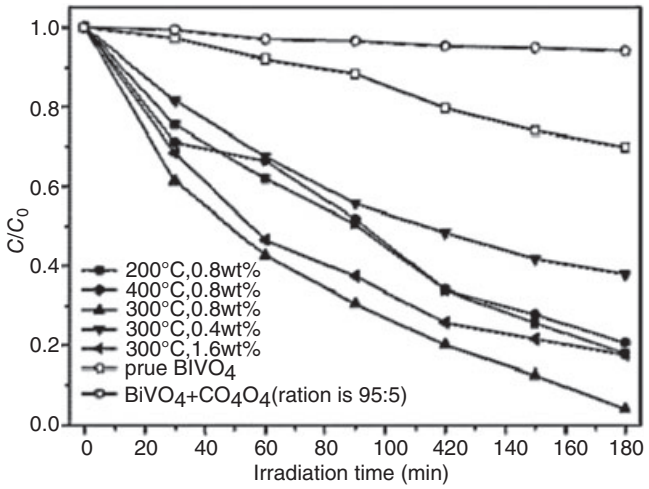

Figure 5.19 Degradation of phenol by different photocatalysts as a function of visible-light irradiation time. The photocatalysts used were $BiVO_4$, $BiVO_4$ and a Co_3O_4 mixture, and a $CoO_x/BiVO_4$ composite calcined at different temperatures for 2 h with different Co contents (photocatalyst loading 3 $g\,l^{-1}$; initial phenol concentration ca. 18 $mg\,l^{-1}$, without pH modulation) [49].

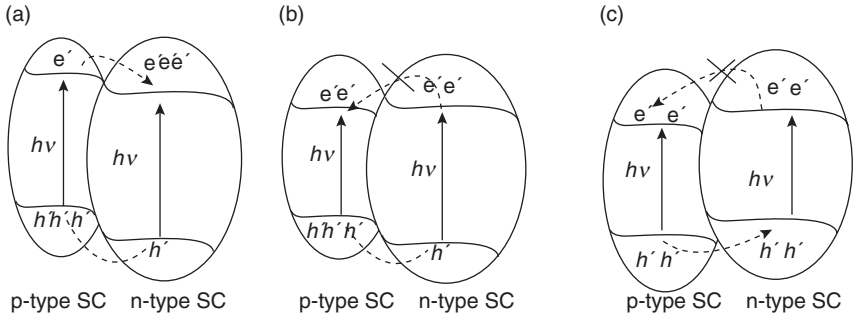

Figure 5.20 (a) Most favorable charge separation principle for a p–n heterojunction semiconductor photocatalyst under irradiation; (b) Favorable hole migration, but unfavorable electron transfer; (c) Neither electron nor hole transfer is favored [49].

concentration of defects, and thus oxygen mobility. When doping was achieved with various ions such as Y, La and Mn, using TiO_2 as a support matrix to form $TiO_2/Ce_{0.45}Zr_{0.45}M_{0.1}O_2$, the TiO_2-loaded CeO_2–ZrO_2 was found to be more photoactive in degrading benzene than was native CeO_2–ZrO_2. Moreover, this activity was further enhanced when metal ions where introduced into the TiO_2/CeO_2–ZrO_2 lattice, owing to the fact that ions increases crystal defects and oxygen cavities on

the surface of $TiO_2/Ce_{0.45}Zr_{0.45}M_{0.1}O_2$ than that of $TiO_2/Ce_{0.5}Zr_{0.5}O_2$. Hence, the increased oxygen cavities can capture electrons, thus impeding electron–hole recombination, and leading to more available holes.

Another interesting class mixed-metal oxide photocatalysts is that based on a cristoballite-related structure. This structure is characterized by networks of corner-connected tetrahedrals of anions that surround a central cation, forming a layered framework structure. Li and colleagues have prepared Ag_2ZnGeO_4 and tested its potential for the removal of dyes from water. The catalyst was exposed to aqueous solutions of RhB and Orange II, under visible-light irradiation [56]. In the absence of any catalyst, the photodecomposition of RhB was very slow, whereas Orange II did not show any changes, even after prolonged exposure to visible light. When the catalyst was present, however, and the system was exposed to visible light (>420 nm), there was a significant decrease in the concentrations of both dyes (100% decay for RhB, 69.2% for Orange II; see Figure 5.21). The authors tested the stability of the catalyst by comparing X-ray diffraction patterns of the catalysts before and after exposure to dyes under visible light, and noted that the crystal structure of the catalyst was maintained. The replacement of Na by Ag in the parent material Na_2ZnGeO_4 was also shown to lower the bandgap, to 2.29 eV from 4.89 eV, thus enabling visible light-activity of Ag_2ZnGeO_4. Density functional theory (DFT) calculations also revealed that the top of the valence band comprised Ag $4d^{10}$ and O $2p^6$ orbitals, whereas only O $2p^6$ were present in the parent Na_2ZnGeO_4 (Figure 5.22). The replacement of Na by Ag caused a significant lowering of the band gap, due to hybridization between Ag Ag $4d^{10}$ and O $2p^6$. Several other research groups have also reported that layered structured compounds such

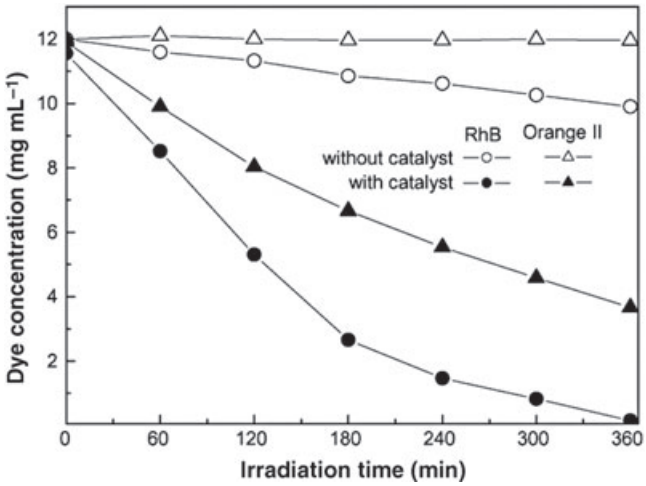

Figure 5.21 Photocatalytic degradation of Rhodamine B (RhB) and Orange II in the presence of Ag_2ZnGeO_4. Reaction conditions: dye solution, 100 ml, 12.0 mg l^{-1}; catalyst 0.3 g; 300 W Xe-lamp, $\lambda > 420$ nm, intensity 58.9 mW cm^{-2} [56].

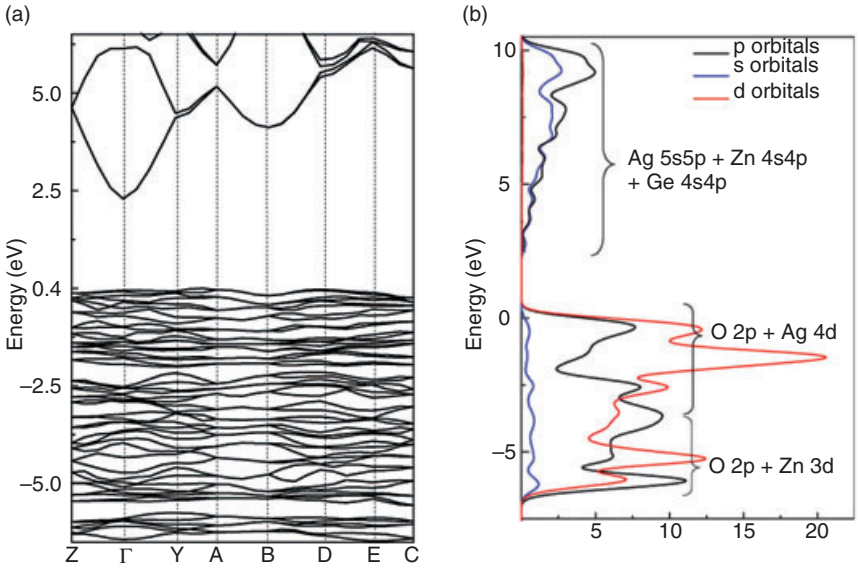

Figure 5.22 Calculated energy band (a) and density of states (b) of Ag_2ZnGeO_4 [56].

as $K_4NB_6O_{17}$ [57], $AgInW_2O_8$ [58] and KNb_3O_8 [59] have the ability to decompose organic compounds effectively, with the separation and transportation of the electron–holes believed to be facilitated by the layered structures.

5.4 Conclusions

Mixed-metal oxide nanomaterials have emerged as a class of new materials in the improved utilization of solar energy for the photodecomposition of both volatile and nonvolatile organic pollutants. In particular, mixed-metal oxide nanoparticle photocatalysts have demonstrated superior photocatalytic activities in air and water remediation processes when compared to the single metal oxide photocatalyst. More importantly, the success of these materials as photocatalysts in hazardous waste remediation is based on the synthetic abilities to engineer the band gap, to limit the electron–hole recombination, and to increase surface areas. Furthermore, in order to harvest visible solar light more efficiently in the future, heterogeneous photocatalysis with both metal(s) and nonmetal(s) codoped TiO_2 mixed-metal oxide photocatalysts appears to represent a promising technology in the remediation and detoxification of air and water, based on the photostability, nontoxicity and low cost of TiO_2. Moreover, photocatalytic degradation represents an alternative to other methods of remediation, such as catalytic combustion, which requires very high temperatures of up to 1200 °C. Photocatalysis also has the extraordinary capability of detoxifying environmental pollutants at ambient temperatures. Con-

sequently, the design and development of mixed-metal oxide photocatalysts for detoxification and environmental remediation processes must be pursued, with great emphasis placed on the fundamental scientific aspects and efforts to build and protect a healthy environment.

References

1 West, A.R. (1998) *Basic Solid State Chemistry*, 1st edn, John Wiley & Sons, Inc., New York.

2 Grätzel, M. and Hagfeldt, A. (2000) Molecular photovoltaics. *Accounts of Chemical Research*, **33**, 269–77.

3 Garcia, C.G., De Lima, J.F. and Iha, N.Y.M. (2000) Energy conversion: from the ligand field photochemistry to solar cells. *Coordination Chemistry Reviews*, **196**, 219–24.

4 Zou, Z., Ye, J., Sayama, K. and Arakawa, H. (2001) Direct splitting of water under visible light irradiation with an oxide semiconductor photocatalyst. *Nature*, **414**, 625–7.

5 Anpo, M. (2004) Preparation, characterization, and reactivities of highly functional titanium oxide-based photocatalysts able to operate under UV-visible light irradiation: approaches in realizing high efficiency in the use of visible light. *Bulletin of the Chemical Society of Japan*, **77**, 1427–42.

6 Asahi, R., Morikawa, T., Ohwaki, T., Aoki, K. and Taga, Y. (2001) Visible-light photocatalysis in nitrogen-doped titanium oxides. *Science*, **293**, 269–71.

7 Hüsing, N. and Schubert, U. (1998) Aerogels-airy materials: chemistry, structure, and properties. *Angewandte Chemie - International Edition*, **37**, 22–45.

8 Koper, O.B., Rajagopalan, S., Winecki, S. and Klabunde, K.J. (2007) *Environmental Applications of Nanomaterials: Synthesis, Sorbents and Sensors* (eds G.E. Fryxell and G. Cao), Imperial College Press, London, pp. 3–24.

9 Miyauchi, M., Nakajima, A., Watanabe, T. and Hashimoto, K. (2002) Photocatalysis and photoinduced hydrophilicity of various metal oxide thin films. *Chemistry of Materials*, **14**, 2812–16.

10 Vorontsov, A.V., Savinov, E.N., Kurkin, E.N., Torbova, O.D. and Parmon, V.N. (1997) Kinetic features of the steady state photocatalytic CO oxidation by air on TiO_2. *Reaction Kinetics and Catalysis Letters*, **62**, 83–8.

11 Sun, B., Reddy, E.P. and Smirniotis, P.G. (2005) Visible light Cr(VI) reduction and organic chemical oxidation by TiO_2 photocatalysis. *Environmental Science and Technology*, **39**, 6251–9.

12 Dutta, P.K., Pehkonen, S.O., Sharma, V.K. and Ray, A.K. (2005) Photocatalytic oxidation of arsenic (III): evidence of hydroxyl radicals. *Environmental Science and Technology*, **39**, 1827–34.

13 Ye, X., Chen, D., Gossage, J. and Li, K. (2006) Photocatalytic oxidation of aldehydes: byproduct identification and reaction pathway. *Journal of Photochemistry and Photobiology A: Chemistry*, **183**, 35–40.

14 Tran, T.H., Nosaka, A.Y. and Nosaka, Y. (2006) Adsorption and photocatalytic decomposition of amino acids in TiO_2 photocatalytic systems. *The Journal of Physical Chemistry B*, **110**, 25525–31.

15 Moss, J.A., Szczepankiewicz, S.H., Park, E. and Hoffmann, M.R. (2005) Adsorption and photodegradation of dimethyl methylphosphonate vapor at TiO_2 surfaces. *The Journal of Physical Chemistry B*, **109**, 19779–85.

16 Habibi, M.H. and Vosooghian, H. (2005) Photocatalytic degradation of some organic sulfides as environmental pollutants using titanium dioxide suspension. *Journal of Photochemistry and Photobiology A: Chemistry*, **174**, 45–52.

17 Colon, G., Sanchez-Espana, J.M., Hidalgo, M.C. and Navio, J.A. (2006) Effect of TiO_2 acidic pre-treatment on the photocatalytic properties for phenol degradation. *Journal of Photochemistry and Photobiology A: Chemistry*, **179**, 20–7.

18 Yan, M., Chen, F., Zhang, J. and Anpo, M. (2005) Preparation of controllable crystalline titania and study on the photocatalytic properties. *The Journal of Physical Chemistry B*, **109**, 8673–8.

19 Aarthi, T. and Madras, G. (2007) Photocatalytic degradation of rhodamine dyes with nano-TiO_2. *Industrial and Engineering Chemistry Research*, **46**, 7–14.

20 Bessekhouad, Y., Robert, D., Weber, J.-V. and Chaoui, N. (2004) Effect of alkaline-doped TiO_2 on photocatalytic efficiency. *Journal of Photochemistry and Photobiology A: Chemistry*, **167**, 49–57.

21 Li, Y., Peng, S., Jiang, F., Lu, G. and Li, S. (2007) Effect of doping TiO_2 with alkaline-earth metal ions on its photocatalytic activity. *Journal of the Serbian Chemical Society*, **72**, 393–402.

22 Jin, M., Nagaoka, Y., Nishi, K., Ogawa, K., Nagahata, S., Horikawa, T., Katoh, M., Tomida, T. and Hayashi, J. (2008) Adsorption properties and photocatalytic activity of TiO_2 and La-doped TiO_2. *Adsorption*, **14**, 257–63.

23 Galindo, F., Gomez, R. and Aguilar, M. (2008) Photodegradation of the herbicide, 2, 4- dichlorophenoxyacetic acid on nanocrystalline TiO_2-CeO_2 sol-gel catalysts. *Journal of Molecular Catalysis A-Chemical*, **281**, 119–25.

24 Wang, C., Geng, A., Guo, Y., Jiang, S., Qu, X. and Li, L. (2006) A novel preparation of three- dimensionally ordered macroporous M/Ti (M = Zr or Ta) mixed oxide nanoparticles with enhanced photocatalytic activity. *Journal of Colloid and Interface Science*, **301**, 236–47.

25 Yang, Y., Li, X.-J., Chen, J.-T. and Wang, L.-Y. (2004) Effect of doping mode on the photocatalytic activities of Mo/TiO_2. *Journal of Photochemistry and Photobiology A: Chemistry*, **163**, 517–22.

26 Jing, L., Xin, B., Yuan, F., Xue, L., Wang, B. and Fu, H. (2006) Effects of surface oxygen vacancies on photophysical and photochemical processes of Zn-doped TiO_2 nanoparticles and their relationships. *The Journal of Physical Chemistry B*, **110**, 17860–5.

27 Zhou, J., Zhang, Y., Zhao, X.S. and Ray, A.K. (2006) Photodegradation of benzoic acid over metal-doped TiO_2. *Industrial and Engineering Chemistry Research*, **45**, 3503–11.

28 Shchukin, D., Poznyak, S., Kulak, A. and Pichat, P. (2004) TiO_2-In_2O_3 photocatalysts: preparation, characterizations and activity for 2-chlorophenol degradation in water. *Journal of Photochemistry and Photobiology A: Chemistry*, **162**, 423–30.

29 Yu, J., Liu, S. and Zhou, M. (2008) Enhanced photocatalytic activity of hollow anatase microspheres by Sn^{4+} incorporation. *The Journal of Physical Chemistry*, **C** (112), 2050–7.

30 Moon, J., Takagi, H., Fujishiro, Y. and Awano, M. (2001) Preparation and characterization of the Sb-doped TiO_2 photocatalysts. *Journal of Materials Science*, **36**, 949–55.

31 Zuo, H., Sun, J., Deng, K., Su, R., Wei, F. and Wang, D. (2007) Preparation and characterization of Bi^{3+}-TiO_2 and its photocatalytic activity. *Chemical Engineering and Technology*, **30**, 577–82.

32 Kapoor, P.N., Uma, S., Rodriguez, S. and Klabunde, K.J. (2005) Aerogel processing of MTi_2O_5 (M = Mg, Mn, Fe, Co, Zn, Sn) compositions using single source precursors: synthesis, characterization and photocatalytic behavior. *Journal of Molecular Catalysis A-Chemical*, **229**, 145–50.

33 Fan, X., Chen, X., Zhu, S., Li, Z., Yu, T., Ye, J. and Zou, Z. (2008) The structural, physical and photocatalytic properties of the mesoporous Cr-doped TiO_2. *Journal of Molecular Catalysis A-Chemical*, **284**, 155–60.

34 Song, H., Jiang, H., Liu, X. and Meng, G. (2006) Efficient degradation of organic pollutant with WOx modified nano TiO_2 under visible irradiation. *Journal of Photochemistry and Photobiology A: Chemistry*, **181**, 421–8.

35 Wu, J.C.-S. and Chen, C.-H. (2004) A visible-light response of vanadium-doped titania nanocatalyst prepared by sol-gel method. *Journal of Photochemistry and Photobiology A: Chemistry*, **163**, 509–15.

36 Wang, X.H., Li, J.-G., Kamiyama, H., Moriyoshi, Y. and Ishigaki, T. (2006) Wavelength-sensitive photocatalytic degradation of methyl orange in aqueous suspension over iron(III)-doped TiO_2 nanopowders under UV and visible light

irradiation. *The Journal of Physical Chemistry B*, **110**, 6804–9.
37 Tong, T., Zhang, J., Tian, B., Chen, F., He, D. and Anpo, M. (2007) Preparation of Ce-TiO_2 catalysts by controlled hydrolysis of titanium alkoxide based on esterification reaction and study on its photocatalytic activity. *Journal of Colloid and Interface Science*, **315**, 382–8.
38 Bian, Z., Zhu, J., Wang, S., Cao, Y., Qian, X. and Li, H. (2008) Self-assembly of active Bi_2O_3/TiO_2 visible photocatalyst with ordered mesoporous structure and highly crystallized anatase. *The Journal of Physical Chemistry C*, **112**, 6258–62.
39 Martyanov, I.N., Uma, S., Rodrigues, S. and Klabunde, K.J. (2004) Structural defects cause TiO_2-based photocatalysts to be active in visible light. *Chemical Communications*, **21**, 2476–7.
40 Wang, J., Uma, S. and Klabunde, K.J. (2004) Visible light photocatalytic activities of transition metal oxide/silica aerogels. *Microporous and Mesoporous Materials*, **75**, 43–147.
41 Rodrigues, S., Ranjit, K.T., Uma, S., Martyanov, I.N. and Klabunde, K.J. (2005) Single-step synthesis of a highly active visible-light photocatalyst for oxidation of a common indoor air pollutant: acetaldehyde. *Advanced Materials*, **17**, 2467–71.
42 Rodrigues, S., Ranjit, K.T., Uma, S., Martyanov, I.N. and Klabunde, K.J. (2005) Visible-light photooxidation of trichloroethylene by Cr-Al-MCM-41. *Journal of Catalysis*, **230**, 158–65.
43 Rodrigues, S., Uma, S., Martyanov, I.N. and Klabunde, K.J. (2005) AgBr/Al-MCM-41 visible-light photocatalyst for gas-phase decomposition of CH_3CHO. *Journal of Catalysis*, **233**, 405–10.
44 Yang, X., Cao, C., Hohn, K., Erickson, L., Maghirang, R., Hamal, D.B. and Klabunde, K.J. (2007) Highly visible-light active C-doped and V-doped TiO_2 for degradation of acetaldehyde. *Journal of Catalysis*, **252**, 296–302.
45 Hamal, D.B. and Klabunde, K.J. (2007) Synthesis, characterization, and visible light activity of new nanoparticle photocatalysts based on silver, carbon, and sulfur-doped TiO_2. *Journal of Colloid and Interface Science*, **311**, 514–22.
46 Tang, J., Zou, Z. and Ye, J. (2004) Efficient photocatalytic decomposition of organic contaminants over $CaBi_2O_4$ under visible-light irradiation. *Angewandte Chemie - International Edition*, **43**, 4463–6.
47 Kim, H.G., Hwang, D.W. and Lee, J.S. (2004) An undoped, single-phase oxide photocatalyst working under visible light. *Journal of the American Chemical Society*, **126**, 8912–13.
48 Kudo, A., Ueda, K., Kato, H. and Mikami, I. (1998) Photocatalytic O_2 evolution under visible light irradiation on $BiVO_4$ in aqueous $AgNO_3$ solution. *Catalysis Letters*, **53**, 229–30.
49 Long, M., Cai, W., Cai, J., Zhou, B., Chai, X. and Wu, Y. (2006) Efficient photocatalytic degradation of phenol over Co_3O_4/$BiVO_4$ composite under visible light irradiation. *The Journal of Physical Chemistry B*, **110**, 20211–16.
50 Ishihara, T., Baik, N.S., Ono, N., Nishiguchi, H. and Takita, Y. (2004) Effects of crystal structure on photolysis of H_2O on K-Ta mixed oxide. *Journal of Photochemistry and Photobiology A: Chemistry*, **167**, 149–57.
51 Teramura, K., Maeda, K., Saito, T., Takata, T., Saito, N., Inoue, Y. and Domen, K. (2005) Characterization of ruthenium oxide nanocluster as a cocatalyst with (Ga_{1-x}Znx) ($N_{1-x}O_x$) for photocatalytic overall water splitting. *The Journal of Physical Chemistry B*, **109**, 21915–21.
52 Wang, J., Zou, Z. and Ye, J. (2005) Surface modification and photocatalytic activity of distorted pyrochlore-type Bi_2M (M = In, Ga and Fe) TaO_7 photocatalysts. *Journal of Physics and Chemistry of Solids*, **66**, 349–55.
53 Kohtani, S., Hiro, J., Yamamoto, N., Kudo, A., Tokumura, K. and Nakagaki, R. (2005) Adsorptive and photocatalytic properties of Ag-loaded $BiVO_4$ on the degradation of 4-n-alkylphenols under visible light irradiation. *Catalysis Communications*, **6**, 185–9.
54 Liu, Y. and Sun, D. (2007) Effect of CeO_2 doping on catalytic activity of Fe_2O_3/γ-Al_2O_3 catalyst for catalytic wet peroxide oxidation of azo dyes. *Journal of Hazardous Materials*, **143**, 448–54.
55 Zhong, J.B., Lintao, G.M., Wang, J.L., Liu, Z.M., Zhao, M. and Yaoqiang, C. (2007) Effect of metal doping into $Ce_{0.5}Zr_{0.5}O_2$ on

photocatalytic activity of TiO_2/$Ce_{0.45}Zr_{0.45}M_{0.1}O_x$ (M = Y, La, Mn). *Journal of Hazardous Materials*, **143**, 516–21.

56 Li, X., Ouyang, S., Kikugawa, N. and Ye, J. (2008) Novel Ag_2ZnGeO_4 photocatalyst for dye degradation under visible light irradiation. *Applied Catalysis A: General*, **334**, 51–8.

57 Kudo, A., Sayama, K., Tanaka, A., Asakura, K., Domen, K., Maruya, K. and Onishi, T. (1989) Nickel-loaded $K_4Nb_6O_{17}$ photocatalyst in the decomposition of H_2O into H_2 and O_2: structure and reaction mechanism. *Journal of Catalysis*, **120**, 337–52.

58 Tang, J., Zou, Z. and Ye, J. (2003) Photophysical and photocatalytic properties of $AgInW_2O_8$. *The Journal of Physical Chemistry B*, **107**, 14265–9.

59 Zhang, G., Gong, J., Zou, X., He, F., Zhang, H., Zhang, Q., Liu, Y., Yang, B. and Hu, B. (2006) Photocatalytic degradation of azo dye Acid red G by KNb_3O_8 and the role of potassium in the photocatalysis. *Chemical Engineering Journal*, **123**, 59–64.

Keywords

mixed-metal oxide; nanomaterials; photocatalysis; photodegradation; pollutants; remediation; UV-visible photocatalysts; environmental remediation.

6
Building Nonmagnetic Metal@Oxide and Bimetallic Nanostructures: Potential Applications in the Life Sciences

Mao-Song Mo and Xu-Sheng Du

6.1
Introduction

Nanomaterials exhibit unique optical, thermal, electronic, magnetic and surface properties, and potentially have very useful functions. These properties and functions depend sensitively on the size, composition and shape of building units on a nanoscale, and are fundamentally different from those of the same macroscale bulk solids or traditional single molecules. Extensive research on nanomaterials has been mainly directed towards their potential use in catalysts, composites, microelectronics, optoelectronics and high-density memory devices. Yet, recent progress has also demonstrated that nanostructured materials such as metallic or semiconductor nanoparticles/nanorods have important applications in molecular biology and medicine [1–5]. Cells and their constituent organelles lie on a submicron- to micron-sized scale. Further, the proteins and nucleic acids (DNA and RNA) that are found throughout the cell are on a nanometer-sized scale. Because of similar dimensions to those of biomacromolecules, nanostructures ranging from a few to a hundred nanometers in size become ideal as labels, probes and drug/gene carriers for incorporation into biological systems [6–8]. This integration of nanotechnology and molecular biology and medicine has led to the creation of a 'new frontier' in which 'smart' nanostructures can be engineered for disease detection, diagnosis and therapy [9–15]. In recognizing this huge potential, considerable efforts have been devoted to this area, and major improvements have resulted in the design and chemical synthesis of a variety of metallic and semiconductor nanostructures and their surface bioconjugation. This in turn has led to the production of large quantities of high-quality, biocompatible nanocrystal moieties for cancer cell targeting, imaging and therapy [10–18]. Furthermore, with rapid extension of biomedical applications of nanomaterials, a major significance has recently been recognized to develop a new class of multicomponent and multifunctional nanomaterials integrated with multiple functions in individual particles [19–21]. To this end, several reviews have been

Nanomaterials for the Life Sciences Vol. 3: Mixed Metal Nanomaterials. Edited by Challa S. S. R. Kumar

ISBN: 978-3-527-32153-7

prepared detailing such magnetic metallic/oxide nanostructures or semiconductor chalcogenide nanoparticles for biomedical applications [10–15]. In this chapter, attention is focused mainly on the chemical build-up of a large variety of nonmagnetic bimetallic nanostructures, and on their potential applications in the life sciences.

6.2
Building Nonmagnetic Metal@Oxide and Bimetallic Nanostructures

Metal nanoparticles have a unique surface plasmon resonance (SPR) in the visible range, and do not blink or bleach [22]. The surface plasmon oscillation of metal free electrons results in a strong enhancement of absorption and scattering of electromagnetic radiation in resonance with the SPR frequency of the metal nanoparticles, giving them not only intense colors but also interesting optical properties. Further, the SPR frequency is sensitively dependent on the size, shape and chemical compositions of metallic nanostructures. This makes the SPR features of metallic nanostructures tunable, and endows such nanostructures potentially with very useful functions. For example, noble metal nanoparticles can be employed as alternative probes to overcome the limitations of organic fluorophores [1, 2, 23–29]. Noble metal nanoparticles, especially Au particles (with their high stability, strong optical property, nontoxicity and facile surface chemistry), have immense potential for intracellular gene regulation as well as for cancer diagnosis and therapy, on account of their SPR-enhanced light scattering and absorption [14, 30, 31]. The conjugation of Au nanoparticles to ligands specifically targeted to biomarkers on cancer cells can allow molecular-specific imaging and detection of cancer cells [14]. Au and related multimetallic nanoparticles can efficiently convert the strongly absorbed light into localized heat, and this has been exploited for the selective laser photothermal therapy of cancer [5]. By changing the size, shape or composition of Au-based nanostructures, the SPR can be tuned to the near-infrared (NIR) region [5, 14], allowing deep-tissue *in vivo* molecular imaging and photothermal therapy of cancer [5, 14, 32]. During the past two decades, the main effort has been focused on the preparation of size-/shape-/composition-controllable multimetallic (especially Au-containing) nanostructures and their self-assemblies for *in vivo* applications [33–37]. Here, we summarize the latest experimental achievements on building noble metal (mainly bimetallic) nanostructures, including core-shell type, one-dimensional (1-D) type, alloy nanostructures and mesoscale self-assemblies.

6.2.1
Core-Shell Nanostructures and Building Strategy

Core-shell nanostructures are of both scientific and technical importance, because of their unique physical and surface-chemical properties as well as their biomedical applications [3, 38–42]. The core-shell nanostructure involves a nanocrystal core

uniformly encapsulated by a layer of another material shell, which usually reproduces the symmetry of the inner core. The physical/chemical properties and performances of the core-shell nanostructures depend heavily on their sizes, components and microstructures, including the structure of the core, the shell and their interface [38–42]. The interface is particularly important because its sharpness, the degree of lattice match/mismatch and chemical gradient are critical for electron transfer and coupling. An epitaxial orientation relationship between the core and the shell favors the formation of polyhedral core-shell structures, and epitaxial growth is determined by their crystal structures [42]. In general, the associations of various metals and/or oxides in core-shell configurations often exhibit distinct behavior as compared to that inherent to the individual components. These include tunable or tailorable optical properties and enhanced catalytic activity, depending on the specific chemical compositions and sizes of the core and the shell. The strategies for accessing core-shell nanostructures have proliferated during the past decade, and normally include: (i) the direct heterogeneous nucleation and growth of the shell material onto the preformed nanocrystal core; (ii) shell growth after chemical activation of the core surface; (iii) sacrificial conversion of the outermost exposed layers of the nanocrystal core into a different material by a redox replacement reaction; and (iv) one-pot approaches by self-controlled nucleation growth [43].

6.2.2
Metal@Oxide Core-Shell Nanostructures

Considerable efforts by many different groups have focused on building metal@oxide–typically metal@silica–core-shell nanostructures. The silica coating layer is both protective and hydrophilic, and contains functional groups for covalent bioconjugation. Usually, these types of nanostructured moieties have been obtained by selective heterogeneous nucleation and growth of a shell layer of second material on preformed nanocrystal seeds, with or without chemical surface activation of the seed. Recently, the groups of Gerritsen, Klimov and Ying have developed spherical Au@silica core-shell nanoparticles [44–46]. Figure 6.1 shows a transmission electron microscopy (TEM) image of the resultant particles [44]. The obvious light–dark contrast in the TEM image clearly shows the core-shell structure, with both the core and shell ~30 nm in size. The employed building approaches involve the synthesis of gold seed nanoparticles, gold-particle surface activation and silica-shell deposition. The silica shell thickness can also be finely tailored with nanometer precision. Song *et al*. fabricated Au@SiO_2 core-shell nanoparticles without any chemical surface activation of the seed [47], and showed that the size of the metal cores could be finely tuned on a nanoscale by using different amounts of etchants (Figure 6.2). In addition, Abe and coworkers built spherical Ag@TiO_2 core-shell nanoparticles by direct heterogeneous nucleation and growth of the shell material onto the preformed Ag nanocrystal core [48]. These metal@oxide core-shell nanomotifs provide fundamental model systems for both physical/chemical property studies and biomedical applications.

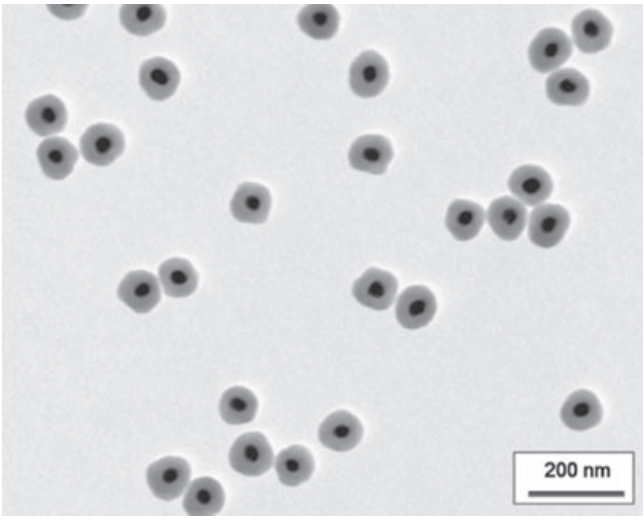

Figure 6.1 Transmission electron microscopy images of Au@silica core-shell nanoparticles. Reprinted with permission from Ref. [44]; © 2006, Wiley Interscience.

6.2.3 Bimetallic Nanostructures

Currently, bimetallic nanostructures continue to attract much interest due to their unique catalytic, electronic and optical properties, which differ widely from those of the corresponding monometallic components [49–51]. These coupling properties can vary dramatically both with size – as occurs in monometallic nanoclusters – and with chemical composition. Bimetallic nanosystems are generally based on noble metals, due to their stable chemical properties and multifunctional applications. In particular, core-shell nanostructured bimetallic colloids with a strained metal shell attain widespread applications including plasmonics, biological sensing and catalysis, which places them at the frontier of advanced materials chemistry [52–54].

6.2.3.1 Bimetallic Core-Shell Nanostructures

Intensive efforts have been made into the synthesis of bimetallic core-shell nanostructures with different shapes and sizes. Besides the conventional self-sacrificial template approach [55], several new strategies are currently being exploited for building bimetallic core-shell nanostructures. José-Yacamán and coworkers reported an unusual three-layer AuPt core-shell nanostructure which was composed of an evenly alloyed inner core, an Au-rich intermediate layer and a Pd-rich outer shell (Figure 6.3) [56]. Here, the building strategy involves the synthesis of polymer-protected AuPd nanoparticles by the successive polyol reduction of their corresponding metallic salts. Detailed structural characterizations enable

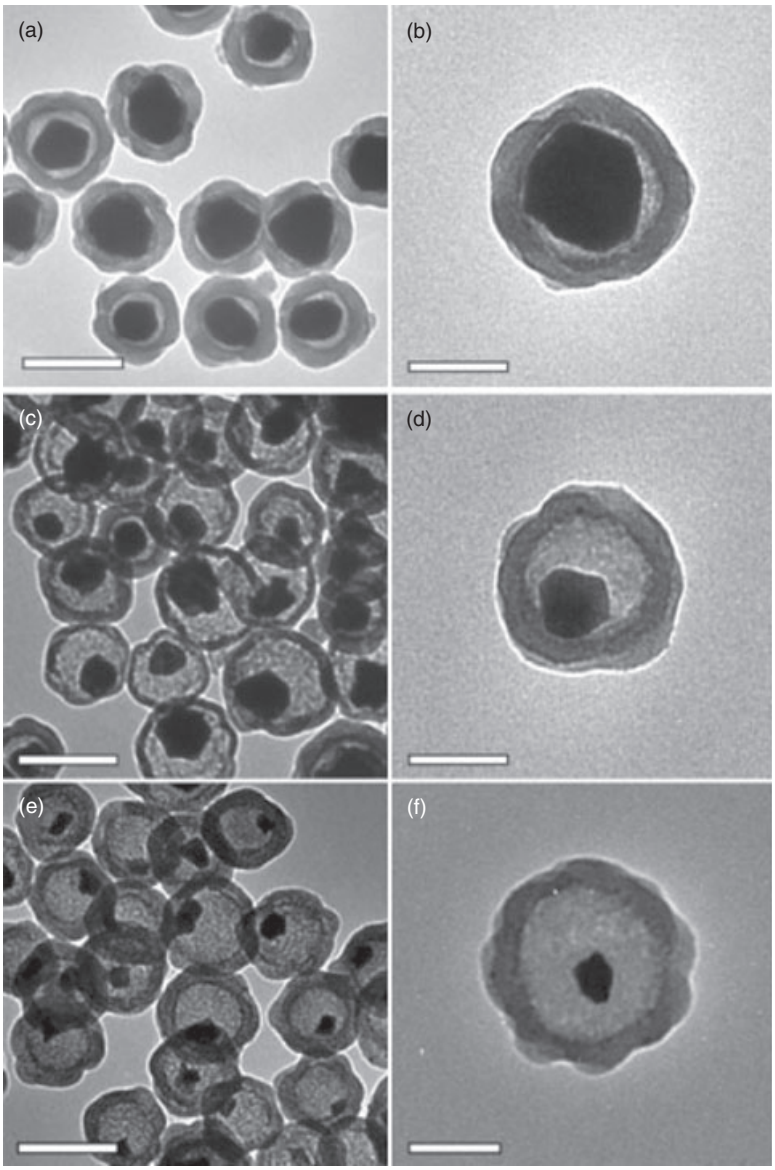

Figure 6.2 TEM images of Au@SiO_2 core-shell frameworks. Diameters of Au core are (104 ± 9) nm (a, b), 67 ± 8 nm (c, d) and (43 ± 7) nm (e, f), respectively. Scale bars: 200 nm in (a, c, e); 100 nm in (b, d, f). Reprinted with permission from Ref. [47]; © 2008, Wiley Interscience.

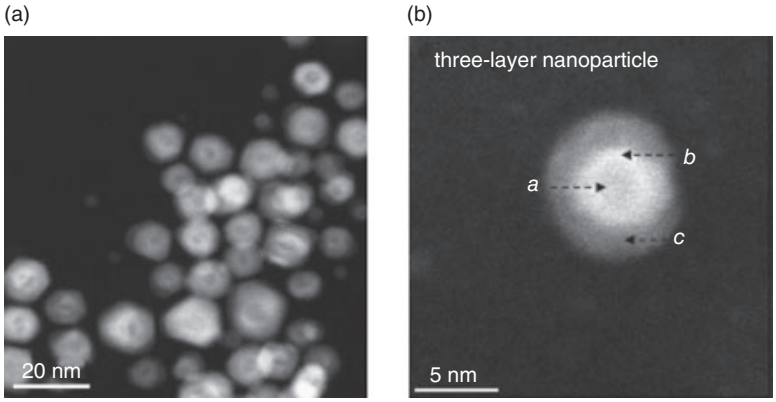

Figure 6.3 High-angle annular dark field-scanning transmission electron microscopy (HAADF-STEM) images of AuPt core-shell nanoparticles. (a) Overview; (b) View of individual particles. Reprinted with permission from Ref. [56]; © 2007, American Chemical Society.

recognition of the morphology of the resultant nanoparticles, together with an understanding of the formation process of nanoparticles in relation to potential practical applications. Several characterization techniques, including high-resolution TEM (HRTEM), scanning TEM (STEM), energy filtering TEM (EFTEM) and convergent-beam electron diffraction (CBED) are currently being exploited to determine the resultant core-shell structures and the influence of nanoparticle size on both the intimate alloying and chemical segregation of monometallic elements that form separate domains of gold and palladium. Figure 6.3 shows two high-angle annular dark field (HAADF) STEM images of the resultant particles. In Figure 6.3b, three distinct regions on the image can clearly be seen, namely the inner core at the center as a dark region (marked *a*), a light intermediate region surrounding this core (marked *b*), and a dark outer shell (designated *c*). The variations on the HAADF contrast strongly suggest a three-layer core-shell structure of the particles. The distribution of elements in the individual nanoparticles can be assessed by using a line scanning analysis employing STEM and energy dispersive X-ray spectroscopy (EDS). Figure 6.4 shows the STEM-EDS composition analysis spectra of each one of the observed three layers in individual particles, and also the HAAEF-STEM images of different individual particles. It can be seen that the Pd concentration peaks locate in the inner core, near the edges of the nanoparticles, whereas the intermediate layers signal Au and Pd peaks (Figure 6.4a). It can also be seen that the elemental signals are not symmetrical in the nanoparticles. Clearly, these peaks corroborate the presence of layers with different compositions in the nanoparticles. Further, it is found that elemental segregation and alloying possess a critical diameter dependence: the nanoparticles with diameters <5 nm present only alloying events, while those with >5 nm behave as chemically elemental segregation, leading to a core-shell structure [56]. As shown in Figure 6.4b, the

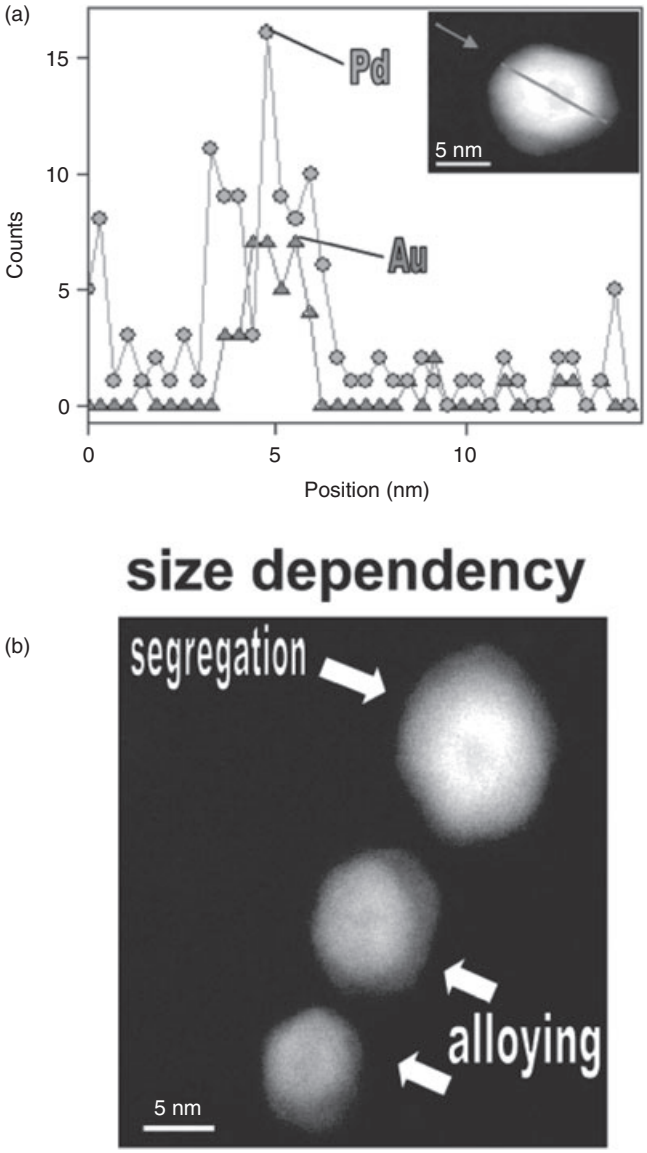

Figure 6.4 (a) Characterization of Au and Pd elemental distribution across the nanoparticle using a STEM-EDS line-scanning technique. The inset shows the analyzed area and direction of analysis; (b) STEM image revealing the influence of nanoparticle diameter on elemental segregation and alloying. Reprinted with permission from Ref. [56]; © 2007, American Chemical Society.

three-layer contrast does not appear for particles smaller than ~5 nm; rather, only two clear layers can be observed. This is clarified by obtaining a STEM-EDS spectrum of nanoparticles below and above the critical diameter of 5 nm. Thus, the small nanoparticles show an alloyed structure among the inner core and the intermediate layer and a weak outer shell, while in large nanoparticles the Pd tends to locate on the periphery, with Au in the center. A more quantitative EDS analysis has been performed to analyze the three layers observed in nanoparticles with diameters >5 nm. Such quantitative spectroscopic analysis shows that central layer *a* has a uniformly alloyed composition of gold and palladium, while the intermediate layer *b* is rich in gold. This is consistent with the fact that the STEM image shows the brightest region of the nanoparticle. The most external layer, *c*, has a large Pd content, which might explain the lower level of contrast observed. It is interesting to note that neither the core nor the shell is composed of a single element, thereby revealing elemental alloying events in the three detected layers. The size, shape and internal structure of nanoparticles can be further accessed using HRTEM. An HRTEM image of an AuPd nanoparticle is shown in Figure 6.5, confirming a three-layer core-shell structure of AuPt colloids. An immediate finding here is that the crystal structure of the nanoparticle is a face-centered cube (*fcc*), while the morphology delineates a nicely truncated octahedron. As shown in Figure 6.5, the edges of the particle are not smooth but rather form a 'zigzag' structure at the periphery, due to the atomic steps. The lattice spacing can be measured directly from the HRTEM image, with measurements of the lattice fringes showing different magnitudes in the three layers observed in the nanoparticles. The inner core (designated *a*) and external (designated *c*) layers have values of lattice spacing of 0.225 nm and 0.227 nm, respectively. On the other hand, the

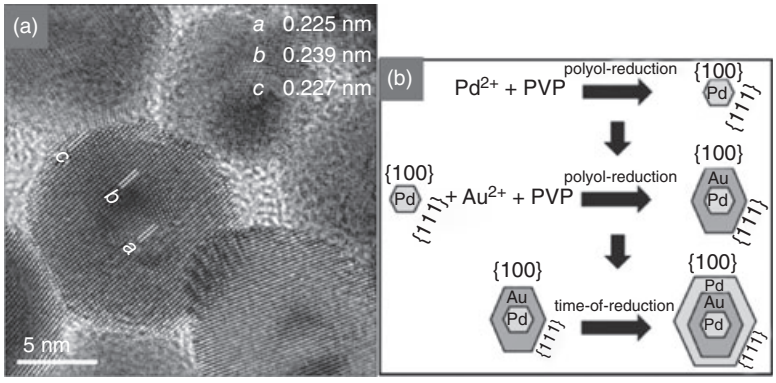

Figure 6.5 (a) HRTEM image displaying the lattice fringes of the Au—Pd nanoparticle obtained by successive reduction of monometallic ions; (b) Modeling for the formation of three-layer core-shell structure. Reprinted with permission from Ref. [56]; © 2007, American Chemical Society.

intermediate region (designated *b*) presents a lattice spacing of 0.239 nm. A very interesting fact here is that no Moiré fringes are observed in this HRTEM image [57], which suggests that there are no misorientations among the layers identified in the nanostructure. Furthermore, electron diffraction patterns collected from single nanoparticles demonstrate the single crystalline nature of nanoparticles. On the basis of such experimental procedure and characterizations, a model has been proposed for the formation of the observed three-layer structure in Figure 6.5b. That is, formation of the three-layer structure involves the early reduction of Pd in the presence of poly(*N*-vinyl-2-pyrrolidone (PVP), which serves as a suitable protective agent. When the palladium reaches the zerovalent state, Au is introduced to the medium, to envelop the first coagulating clusters. However, the remainder of the Pt ions in solution grow continuously in an epitaxial fashion that enables the formation of an external layer of palladium that envelops the intermediate gold and the first reduced Pd clusters.

Mirkin *et al.* reported a unique SPR-driven synthesis strategy for triangular Au@Ag core-shell nanoprisms from a mixture of Au particles and Ag particles with Au particles as seeds and Ag particles as an Ag^+ feedstock [58]. Figure 6.6 shows a TEM image of the Au@Ag core-shell nanoprisms synthesized by the irradiation of a mixture of ~10 nm Au particles and ~5 nm Ag particles with 550 nm light. It can be seen clearly that the resultant nanostructures consisted of relatively light triangular prism shells (average edge length 70 ± 6 nm) and dark spherical, single-particle cores. The core-shell nanostructures had a total thickness of 14 nm (Figure 6.6a, inset). Further examination using HR-TEM showed the triangular faces to be (111), with a lattice spacing of 1.448, indexed as {220} of fcc Ag (Figure

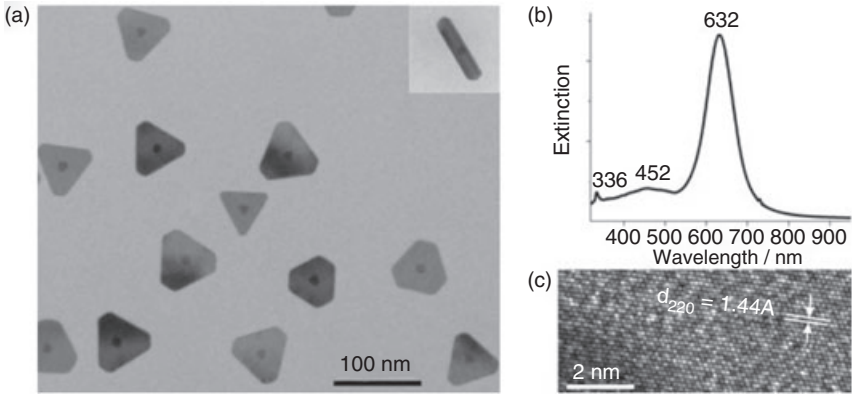

Figure 6.6 (a) TEM image of the Au@Ag core-shell nanoprisms. The inset shows the side view of a core-shell nanoprism; (b) Extinction spectrum of the Au@Ag core-shell colloidal nanoprisms after centrifugation; (c) HRTEM image of the (111) face of the Au@Ag core-shell nanoprisms. The hexagonal lattice shows a spacing of 1.442, indexed as {220} of *fcc* structured Ag. Reprinted with permission from Ref. [58]; © 2007, Wiley Interscience.

6.6c). The extinction bands at 632, 452 and 336 nm (measured using UV–visible spectroscopy) indicate that these core-shell nanoprisms have optical features similar to those of pure silver prisms, without gold cores. These results confirmed that the core was the Au nanoparticle, while the shell was formed from the Ag nanotriangle. The compositions of the Au core and Ag shell can be ascertained using EDS. For gold and silver nanoparticles, the dipolar SPR bands are located at 516 and 395 nm, respectively. The growth of these novel core-shell nanostructures is attributed to plasmon excitation, and can be considered as a two-step pathway [58]. In the first growth step, the incident light preferentially excites the dipolar plasmon resonance of the gold nanoparticles, which induces the deposition of silver layers (the silver ions in solution derive from the dissolution of small silver nanoparticles by oxidation of dissolved O_2 in the presence of light), because the SPR band of gold nanoparticles (516 nm) is closer to the excitation wavelength (550 nm) than that of the silver nanospheres (395 nm). Consistent with this hypothesis, the SPR band of the silver-coated gold nanoparticles blue-shifts from 516 to a lower wave band with increased band intensity [58]; this indicates that these nanoparticles exhibit hybrid optical features of gold and silver. The use of Ag particles as an Ag^+ feedstock is very significant here. The low redox potential of 5 nm Ag nanoparticles compared to the Au@Ag core-shell nanostructures allows the preferential oxidation and dissolution of the silver nanoparticles, which in turn keeps the Ag^+ concentration low, but consistent throughout the photochemically induced Ag^+ reduction and deposition onto the gold surfaces. This results in a final triangular shell shape in the second growth step. The growth of silver triangular shells does not show any specific dependence on the shape and symmetry of gold cores; rather, it is controlled simply by the excitation wavelength since, with longer excitation wavelengths, the triangular shells have larger average edge lengths. When 514 nm light (which almost coincides with the plasmon band of the gold nanoparticles) is used to excite the colloid, smaller triangular nanoprisms and more hexagonal plates are observed. Irradiation at wavelengths shorter than 514 nm leads to an increase in irregular anisotropic particles with a low yield of core-shell nanoprisms [58]. In each case, these prismatic shells continue to grow until the final structures no longer absorb the wavelength of irradiation. The average thickness of these core-shell nanoprisms does not depend on the excitation wavelength, however; rather, the thickness of the nanoprisms seems to be regulated by the diameter of the gold cores. For example, for 5 nm gold nanoparticles a triangular silver shell growth with a final prism thickness of 8 ± 1 nm can be observed. The contrast of the 5 nm gold cores in the silver prism shell is low, and hence the gold core cannot be distinguished from the side planes. For comparison, when larger gold particles (25 nm diameter) are used, a core-shell prism with a thickness of 30 ± 3 nm can be observed [58]. Such a plasmon-driven synthetic strategy can be exploited for building composite metallic nanostructures that may not be accessed by any other method.

Another interesting concept for building bimetallic core-shell heterostructures is the seeded growth of metal nanocrystals, thus exploiting the epitaxial relationship between the two different metals. Epitaxial growth of a secondary metal on

well-faceted seeds enables one to use the crystallographic orientation of the seed to control metal reduction and shaped growth of the secondary structure; this results in the production of anisotropic bimetallic core-shell nanorods and shaping nanopolyhedra, which differ from conventional core-shell nanostructured spheres. Wu and coworkers reported the formation of rectangularly shaped Pd@Au core-shell nanorods by competing epitaxial growth of a Pd shell on the {110} and {100} side surface facets of Au nanorod seeds [59]. The thickness of the Pd shell could be controlled by adjusting the amount of precursor $PdCl_4^{2-}$ added. The TEM and HR-TEM images of the resultant Au@Pd core-shell bimetallic nanorods are shown in Figure 6.7. The low-magnification TEM image (Figure 6.7a) highlights a distinct variation in contrast between the darker gold core and the lighter palladium shell, thus verifying the formation of a Pd shell around the Au core. The difference in morphology, especially at the rod ends, can also be seen clearly. In comparison with the cylindrical shapes of the Au nanorods, all Pd-coated nanorods exhibit a rectangular morphology with sharp edges. The HR-TEM images (Figure 6.7b and c) provide direct evidence for the crystal structure of the Pd shell: the Pd shell grows epitaxially around the Au nanorod and is structurally single-crystalline. Then, when the electron beam is aligned in the [001] direction, the distribution of the atoms on the {001} faces of the Pd shell is imaged. The lattice distance is measured as 2 Å, corresponding to a lattice distance of {002} surfaces of Pd. This is also confirmed by the corresponding fast Fourier transform (FFT) analysis (Figure 6.7b, inset): the FFT pattern corresponds to only one set of diffraction spots of {002}. In contrast, when the electron beam is aligned in the [011] direction, both the (111) and (002) lattice planes of the Pd shell are imaged (see: {002} and {111} diffraction spots in the corresponding FFT pattern). Therefore, the Pd shell grows along the [001] direction and all six surfaces are terminated by {100} facets, which results in rectangularly shaped Pd Shells. It is believed that the competing growth between the {110} and {100} side facets is responsible for the formation of rectangularly shaped Pd shells [59]. Because the surface energy of the {110} surface is higher than that of the {100} surface, a driving force exists to minimize the overall surface energy by changing morphologies to more stable ones. Thus, palladium grows faster along the {110} planes than along the {100} planes. This results in the final disappearance of all unstable {110} facets and, instead, the formation of rectangularly shaped Pd/Au bimetallic nanorods that show only four stable {100} side surface facets.

As a significant extension of this seeded growth strategy, Yang *et al.* developed various bimetallic Pt@Pd core-shell nanopolyhedra by using highly faceted cubic Pt as seeds to direct the epitaxial overgrowth of a secondary shaping metal Pd shell [60]. The conformal shape-controlled overgrowth is found to depend heavily on the structure of the seed and the degree of lattice match produced between seed and shell [60]. The cubic Pt seeds provide a well-defined surface for the overgrowth of the lattice-matched metal Pd, and dictates the final shape of the core-shell heterostructures. As shown in Figure 6.8a, the net epitaxial overgrowth of Pd on Pt nanocubes leads to Pt/Pd bimetallic cubes. Observations made with HAADF-STEM confirmed the presence of a Pt seed at the center of each core-shell

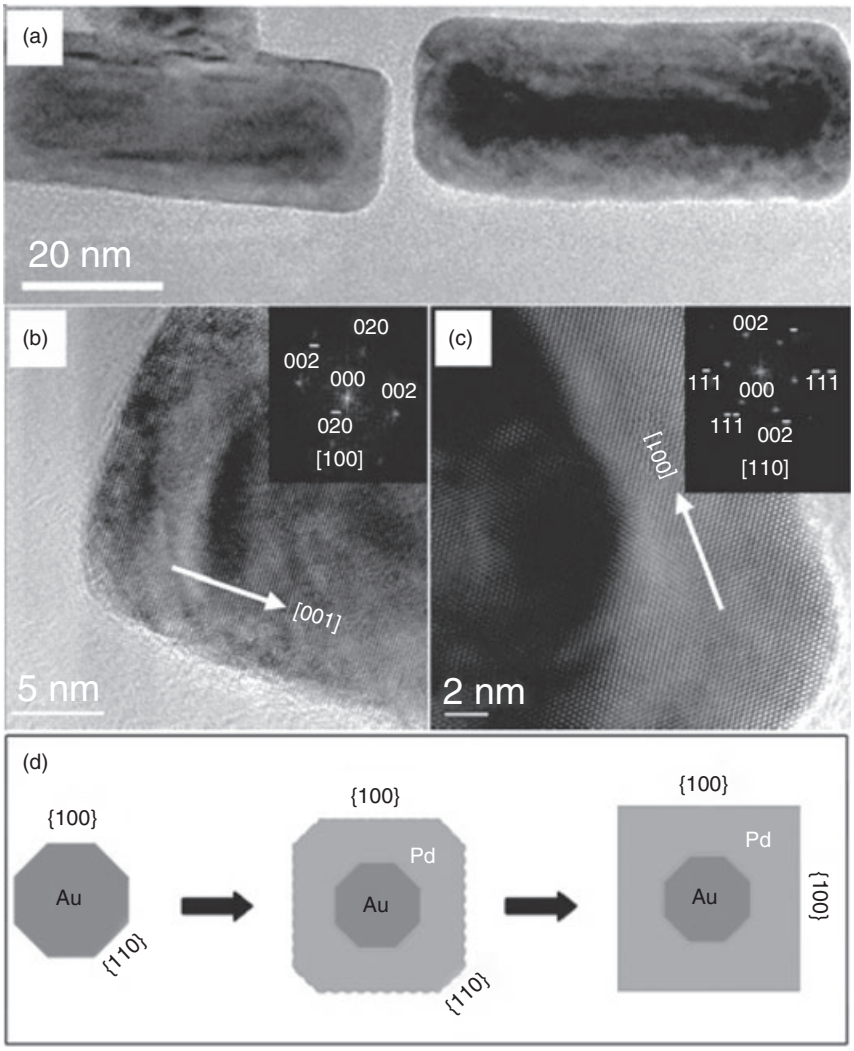

Figure 6.7 (a) Low-resolution TEM image of single bimetallic nanorods; (b, c) HR-TEM images of bimetallic nanorods when the electron beam is aligned in the [001] (b) and [011] (c) directions, showing the distribution of the atoms on the {001} and {111} faces, respectively. The insets show the corresponding fast Fourier transform images; (d) Cross-section showing the morphology transition from pure Au nanorods to Pd/Au bimetallic nanorods. Reprinted with permission from Ref. [59]; © 2006, American Chemical Society.

heterostructured nanocube (Figure 6.8b). Tomographic information, including the mutual orientation of the core and shell, can be extracted from the HAADF-STEM intensity data (Figure 6.8c). The X-ray diffraction (XRD) pattern collected on these core-shell nanocubes is readily indexed to a *fcc* lattice, as Pd and Pt have a small

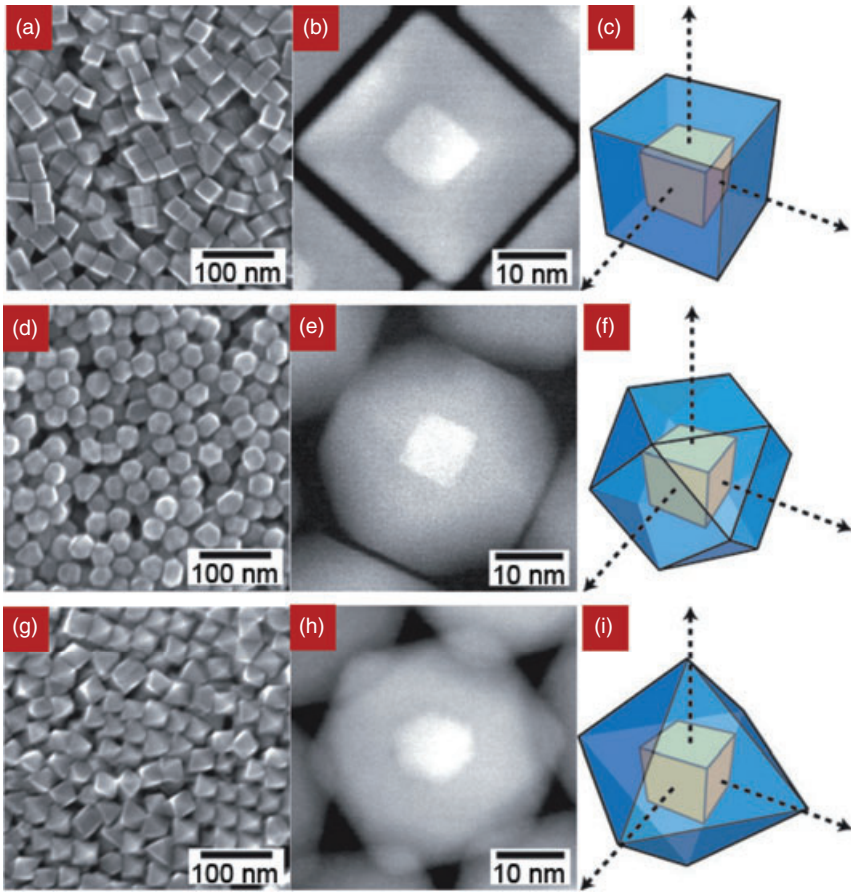

Figure 6.8 Electron microscopy images of cubic (a, b), cubo-octahedral (d, e) and octahedral (g, h) Pt@Pd core-shell nanostructures. (a, d, g) Overall SEM images; (b, e, f) HAADF-STEM images; (c, f, i) Modeling for the orientation of the core and shell for Pt@Pd core-shell cube (c), cubo-octahedra (f) and octahedra (i), respectively, with the axes projecting along the <100> directions through the {100} faces of the central Pt core. Reprinted with permission from Ref. [60]; © 2007, Nature Publishing Group.

lattice mismatch of only 0.77%. In the absence of any seeds, no shape control can be observed. Although heavily influenced by the structure of the seed, the secondary nanocrystal shell growth is subject to external shape-control factors, including the nature of the surface-capping agent and various synthetic conditions of the growth process. The modulation of the surface activity of Pt nanocubes by altering the external shape-controlled factors can allow for the use of the conformal epitaxial overgrowth to produce core-shell particles with other well-defined shapes. For instance, control over the directed growth of Pd on Pt nanocubes is achieved by introducing of increasing amounts of NO_2, since NO_2 can dissociate on Pd

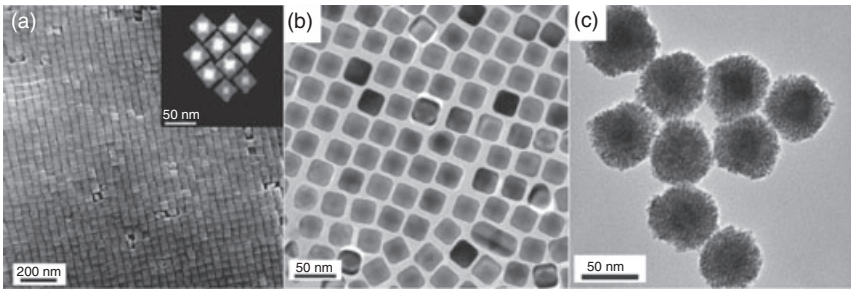

Figure 6.9 (a) SEM images of the overall morphology of Au@Pd nanocubes self-assembled on the Si wafer. The inset in panel (a) shows STEM images of the octahedral Au seed within a cubic Pd shell; (b, c) TEM images of Au@Ag nanocubes (b) and Au@Pt nanoparticles (c). Reprinted with permission from Ref. [61]; © 2008, American Chemical Society.

surfaces to produce adsorbed NO and adsorbed atomic oxygen. An appropriate addition of NO_2 leads to a variation in the Pd growth rates along the <100> and <111> directions to afford Pt/Pd core-shell cubo-octahedra (Figure 6.8d and e) and octahedra (Figure 6.8g and h). An analysis using HAADF-STEM provides the orientations of the cubic Pt seed within the cubo-octahedral and octahedral Pd shells, respectively (Figure 6.8f and i). Seeding with faceted nanocrystals may have a significant potential towards the development of shape-controlled heterostructures with defined interfaces. Similarly, bimetallic core-shell Au@Pd and Au@Ag nanocubes, as well as Au@Pt nanospheres, have also been developed in high yield using a two-step, seed-mediated growth in aqueous solution with Au nanooctahedra of approximately 30 nm diameter as cores (Figure 6.9) [61]. The growth of these heterogeneous metal shells on the Au core involves two different modes: (i) the conformal epitaxial growth for single-crystalline Au@Pd and Au@Ag nanocubes; and (ii) the heterogeneous nucleation and island growth for polycrystalline Au@Pt nanospheres. A complete conversion from octahedral metal cores into heterogeneous single-crystal nanocubes indicates, unambiguously, the fastest growth rate along the <111> directions. A synergetic effect of the lattice match, atomic radius, bond dissociation energy and electronegativity of the core and shell metals is suggested to play a key role in determining which growth mode is at work. Moreover, the shell layer growth rate should be adequately low because the kinetics of the epitaxial growth is influenced considerably by the concentration of surfactant, the reducing agent, the metal ion and the reaction temperature.

6.2.3.2 1-D Bimetallic Heteronanostructures

One-dimensional striped multimetallic heteronanostructures have great potential in biomedical applications, such as biosensors and biovehicles for ultrasensitive detection and gene/drug delivery, and as bionanotools for the separation of biological molecules (e.g., proteins and viruses) [35, 62–64]. The most common strategy

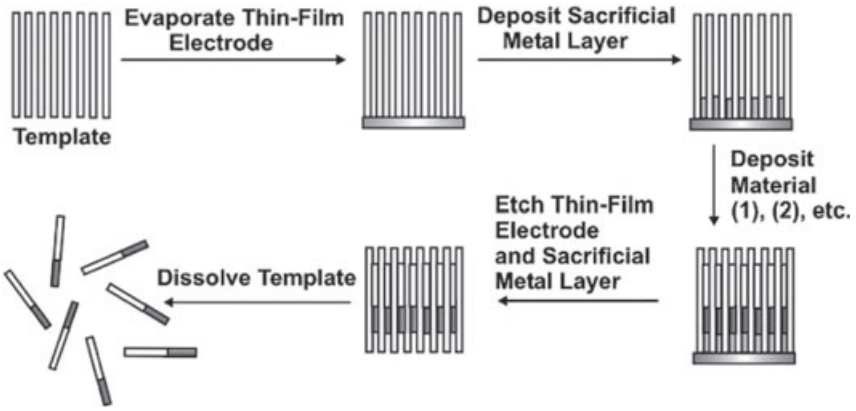

Figure 6.10 General scheme for the synthesis of one-dimensional multimetallic nanostructures by the deposition of metals into nanoporous templates. Reprinted with permission from Ref. [35]; © 2006, Wiley Interscience.

for building 1-D multimetallic heteronanostructures is to deposit either electrochemically or chemically (electroless) – the desired metals into hard templates such as anodic aluminum oxide (AAO) [35, 65]. The general scheme for the creation of multimetallic 1-D nanostructures through electrochemical deposition is shown in Figure 6.10. In the first step of the general process, a thin metal film is evaporated onto one face of the template. This metal film is used as a working electrode that is responsible for electrodepositing materials in the pores. Typically, before the desired metallic components are deposited, a layer of sacrificial metal is deposited into the pores to prevent a 'puddling' effect, which causes one end of the rod to have a deformed mushroom shape. Deposition of the desired components is then performed sequentially. After deposition of the desired components, the multimetallic 1-D nanostructures (nanorods/nanowires) can be released by chemically dissolving the thin film electrode, sacrificial metal layer and template. The diameters of the multisegmented nanostructures are dictated by the pore size of the template, while their lengths are directly related to the amount of negative charge passed through the system, according to Faraday's law. Specifically, a pulsed electrochemical deposition technique [66] has been developed for the preparation of multisegmented 1-D multimetallic nanostructures with precise interfaces. In this technique, a single electrolyte bath, containing multiple metal ions, is used. In the two-component bath system, for example, the more noble metal is kept at a low concentration, and the relatively less noble metal at a much higher concentration. If the two metals have well-separated redox potentials, then as the potential of the system is held at the less-negative potential, the more noble metal will be deposited exclusively. However, as the potential is pulsed to a more negative value, the less-noble metal will be deposited, along with only a small amount of the more noble metal. This method allows multilayers to be grown with monolayer precision. Compared to other methods for the synthesis of 1-D multimetallic nanostructures,

electrochemical deposition does not require any expensive instrumentation, high temperatures or low-vacuum pressures. The method is also not time-consuming, as nanomaterials grown in this fashion have a high growth rate. Hence, multisegmented metal rods can be synthesized simply by changing the plating solution and accordingly varying the potential of the deposition. In addition, by varying the shape of the electrical pulse bringing about the deposition, the interface between multiple electrodeposited components can be controlled.

Although the building of metallic heteronanostructures without hard templates is very attractive, it is also relatively difficult owing to the distinct reduction rates and lattice mismatch of the different components, and the precise control of the reaction conditions. Yang *et al.* developed an anisotropic overgrowth strategy for building bimetallic Pd-Au nanorod heterostructures based on lattice-mismatch by using highly faceted cubic Pt as seeds (Figure 6.11) [60]. As shown in Figure 6.11a, the TEM image displayed a rod-like morphology of the resultant particles, with a Pt seed present on each of the rods, which were ~185 nm long and ~25 nm in diameter. The HR-TEM image clearly revealed a single Pt cube partially embedded in an Au rod (Figure 6.11b). It was believed that the relatively large lattice mismatch between the two metals (4.08% lattice mismatch for Pt/Au) effectively prevented conformal overgrowth on the Pt nanocubes to shaping core-shell polyhedra, and instead produced heterostructures in which both the seed and the secondary metal were exposed [60]. In this growth mode, following the nucleation of Au on the Pt cube, crystal growth would occur on the high-energy Au nucleus, rather than on the Pt seed, as a result of its smaller size and twinning defects. Further growth would occur bidirectionally, resulting in a Pt-Au rod-like heteronanostructure with a Pt seed present on each rod. Using a similar growth strategy, Song *et al.* synthesized multisegmented Ag—Au—Ag heterometallic nanorods through

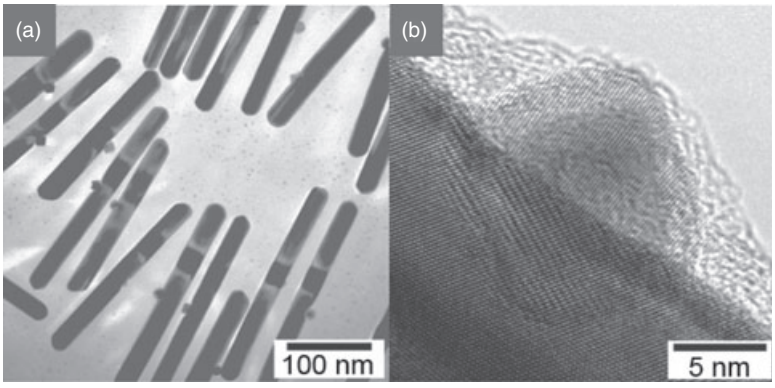

Figure 6.11 Epitaxial overgrowth of lattice-mismatched Au on cubic Pt seeds to give anisotropic growth of Au rods. (a) TEM image and (b) HR-TEM image of multiple metallic rods. Reprinted with permission from Ref. [60]; © 2007, Nature Publishing Group.

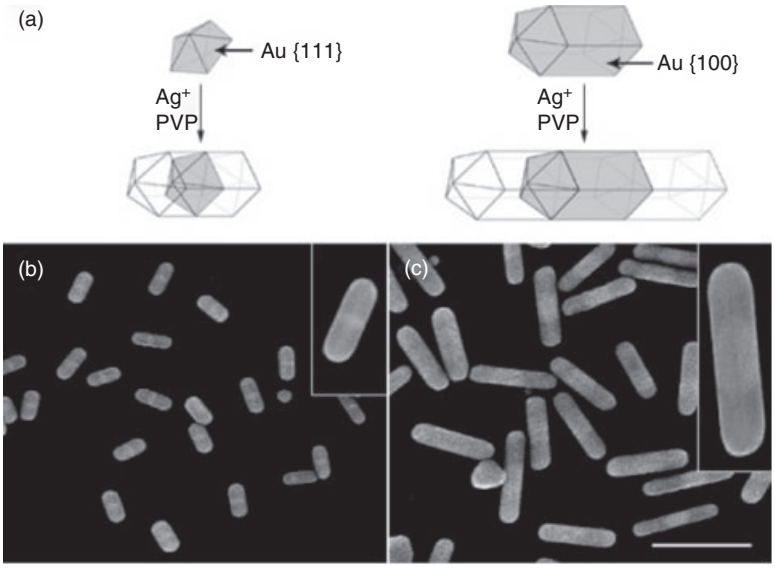

Figure 6.12 (a) Synthesis of Ag–Au–Ag heterometallic nanorods from gold decahedrons and rods; (b, c) SEM images of Ag–Au–Ag heterometallic nanorods grown from (b) gold decahedrons and (c) rods. Scale bar = 500 nm. Reprinted with permission from Ref. [67]; © 2008, American Chemical Society.

directed overgrowth from multiply twinned gold decahedron/rod seeds by adding silver ions and PVP [67]. As shown in the scanning electron microscopy (SEM) image (Figure 6.12), each nanorod had a bright strip at the center, indicating that a heterometallic component with high reflectivity (Au) was symmetrically sandwiched by the two silver segments in the structure. The nanorods were estimated to be 194 ± 17 nm long and 76 ± 9 nm in diameter, with an average aspect ratio of 2.6 ± 0.5. The diameter of the gold segments was almost unchanged from that of the original seeds, and consistent with that of Ag segments after the overgrowth. The gold decahedron/nanorods could be successfully regenerated by the selective dissolution of silver components with HNO_3, and there was no indication of Ag–Au alloy formation in the interface. The clear selected area electron diffraction (SAED) spot pattern and continuous HR-TEM lattice fringe images at the gold–silver junction lend strong support to the idea that the silver segments are grown epitaxially on the end surface planes of Au decahedron and rod [67]. In this synthetic case, the silver deposition on the decahedral seeds and gold nanorods with a fivefold symmetry would lead to the formation of high-energy surfaces, such as {100} and {110}, where PVP could bind more efficiently than on the {111} surface. Consequently, the silver segments would grow rapidly along the longitudinal direction of the nanorods, but slowly along the lateral direction, due to PVP blocking of the high-energy surfaces, producing final multisegmented

Ag—Au—Ag heterometallic nanorods. Xia and coworkers reported the synthesis of some new types of dumbbell- and tadpole-shaped Pd—Au heteronanostructures, with the Au nanoparticle 'head' at both ends and at one end of a Pd nanorod seed, respectively (Figure 6.13) [68]. The initial Pd nanorods had an octagonal cross-section, with the side surface enclosed by a mix of {100} and {110} facet, and had an average diameter of 4.0 ± 0.3 nm and a length of 17.4 ± 2.4 nm. This synthesis was based on the galvanic replacement reaction between sacrificial single-crystal Pd nanorod seeds and $AuCl_4^-$ ions. Although Pd oxidation occurs from any place on the entire surface of a nanorod, including the {100} and {110} side faces and the {100} ends, the nucleation and deposition of Au is localized only to the two ends of a Pd nanorod, leading to the formation of a Pd—Au heterodumbbell at the earlier stages of the reaction (Figure 6.13a). This can be attributed to the fact that the electrons resulting from the oxidation of Pd tend to be pushed to the two ends of a nanorod, due to a strong repulsion between them. The localized deposition of Au is unique for Pd nanorods, and no such phase segregation can be observed when Pd nanoparticles are used in place of the rods. With further addition of $AuCl_4^-$ ions, more Pd will dissolve from the nanorod, accompanying further deposition of Au onto both ends. Then, when the Au tips have grown and reached a critical size, a transition from two-end to one-end growth would occur as a result of Ostwald ripening, to produce a Pd—Au tadpole consisting of an Au head and a Pd tail (Figure 6.13b). The driving force for this ripening process derives from the different stabilization of one Au head relative to another on each nanorod, since the size difference between these two Au heads becomes sufficiently large as the tips grow and reach a critical size. In this scenario, the difference in surface energy favors the growth of larger particles at the expense of smaller ones. In addition, the presence of a Pd segment between the two Au heads greatly facilitates the ripening process, as the Pd nanorod can provide a conductive path for electron

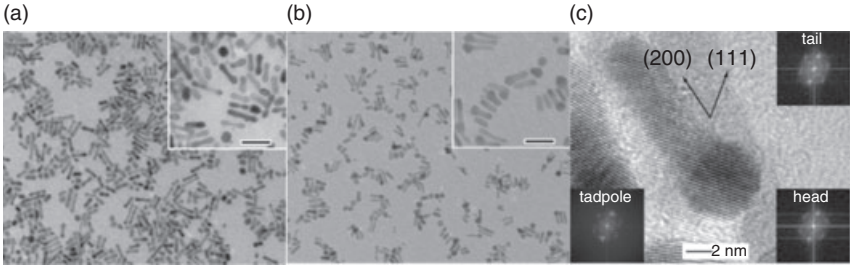

Figure 6.13 TEM images of (a) dumbbell-shaped Pd—Au nanorods and (b) Pd—Au tadpoles by using Pd nanorods as seeds. Scale bars in the insets = 20 nm; (c) High-resolution TEM image recorded along [110] for the Pd—Au tadpoles shown in (b). The insets show FFT operations for the Pd tail, Au head, and for the overall tadpole. In all cases, a hexagonal pattern of six points is observed, as expected for both *fcc* Au and Pd in the [011] beam direction. Reprinted with permission from Ref. [68]; © 2007, American Chemical Society.

migration from one tip to the other. Both, HR-TEM images and FFT patterns of individual tadpole nanostructures confirm that the Pd—Au nanostructure is a piece of single crystal, which in turn suggests that the Au atoms can nucleate and grow epitaxially from the end faces of a Pd nanorod along the [100] direction.

6.2.3.3 Bimetallic Alloy Nanostructures

Nanostructured alloys and intermetallic compounds have been the subject of increasing interest due to a greatly extended range of physical and chemical properties that depend on their size, geometric shape, compositions and atom ordering [33]. A wide variety of alloy nanostructures, ranging from solid nanospheres to hollow nanoshells, have been well developed by different building approaches [33, 69–73]. Stucky *et al*. reported a facile one-step–one-phase synthetic route to achieve monodisperse Au—Ag alloyed nanoparticles by a simultaneous amine–borane complex reduction of mixed corresponding metal sources in organic solvent [69]. The use of amine–borane complexes is essential for the syntheses of monodisperse alloyed nanoparticles. Compared to commonly used reducing agents (e.g., $NaBH_4$, $LiBH_4$), amine–borane complexes have a weaker reducing ability, which can slow the reducing rate of noble metallic cations and allow control over the balanced nucleation and growth rates of alloyed nanoparticles. The resultant alloyed nanoparticles have a narrow size distribution, and can further function as building blocks for the construction of higher-ordered superlattices directly from the reaction mixtures.

Hollow alloyed shells (e.g., hollow spheres, boxes and cages) with nanometer to submicrometer diameters are of particular interest because of their potential applications in encapsulation and the site-specific delivery of drug/gene, catalysis, chemical sensors and cancer therapy. However, a major problem when building hollow alloyed nanostructures is how to control the rapid diffusion of the different atoms to form homogeneous alloys, while simultaneously forming hollow shells. Recently, Li *et al*. reported the general synthesis of hollow alloyed polycrystalline spheres by the direct reduction of templated hollow vesicles that form from Bu_4NBr and the mixture of corresponding noble metal compounds [70]. Figure 6.14 shows a series of resultant bimetallic and multimetallic hollow spheres, including AuPd, AgPd, AuPdAg, CoPtPd and AuPdPt. As shown in Figure 6.14a, the brighter center than edge in each sphere indicates that the spheres possess a hollow interior. In this case, the sizes of the hollow spheres can be tuned by changing the types of metal in the alloys: the constituent Ag decreases the size of the spheres, whereas Pt increases the sphere sizes. For example, under the same synthetic conditions, the sizes of AuPdAg and AuPdPt hollow spheres are 90–150 nm and 200–550 nm, respectively (Figure 6.14a, b and d). The SAED pattern, XRD pattern and EDS analysis confirm a single-phase *fcc* alloy structure and polycrystalline nature of the hollow spheres.

Xia and coworkers have demonstrated the synthesis of Au—Ag alloyed nanocages by using Ag nanocubes and truncated Ag nanocubes as starting templates [71]. The synthesis is based on the galvanic replacement reaction between Ag nanocubes and aqueous $HAuCl_4^-$. Figure 6.15 shows the major steps involved in

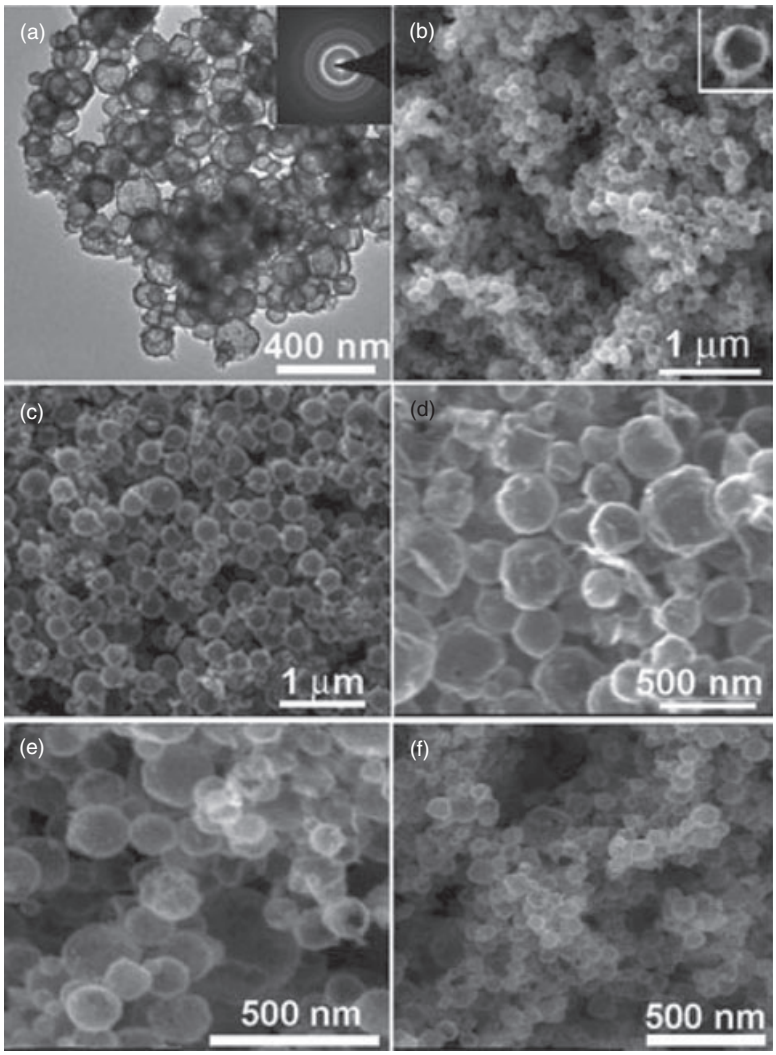

Figure 6.14 (a) TEM image of AuPdAg, Inset: SAED pattern. (b–f) SEM images of (b) AuPdAg (inset, enlarged view of a broken hollow sphere); (c) CoPtPd; (d) AuPdPt; (e) PdAu; (f) PdAg. Reprinted with permission from Ref. [70]; © 2006, Wiley Interscience.

the formation of Au—Ag alloyed nanocages, with well-controlled pores at the corners from truncated Ag nanocubes. A key feature of this synthetic procedure is the use of templated Ag nanocubes, the sharp corners of which have been truncated in advance via a thermal annealing process in the presence of PVP (a capping polymer commonly used in the polyol synthesis of Ag nanostructures) [72]. The mechanism of truncation is that PVP tends preferentially to cover the

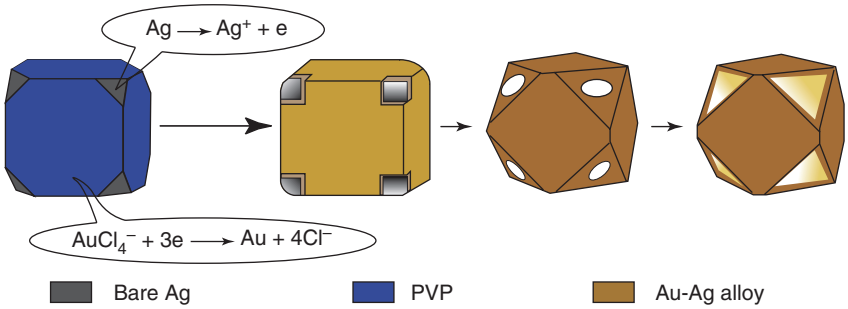

Figure 6.15 Schematic illustration detailing the major steps involved in the formation of Au–Ag nanocages with well-controlled pores at the corners. The success of this synthesis relies on the use of Ag nanocubes bearing truncated corners at {111} facets to react with aqueous $HAuCl_4$. The pore size is mainly determined by the molar ratio of $HAuCl_4$ to Ag. Reprinted with permission from Ref. [71]; © 2006, American Chemical Society.

{100} rather than the {111} facets. Then, if the Ag nanocubes with sharp corners are thermally aged in ethylene glycol in the presence of a small amount of PVP, those {111} facets poorly capped by PVP will develop at the corners, leading to the truncation of all corners. When added into an aqueous solution of $HAuCl_4$, those corner regions unprotected by PVP will serve as primary sites for the dissolution of Ag, and eventually become well-defined pores at all corners of a nanobox. So, by controlling the facets exposed on the surface of Ag nanocubes, the facet-selective protection of PVP and the amount of $HAuCl_4$ added, Au–Ag alloyed nanocages containing hollow interiors and controllable pores at all corners can be obtained routinely (Figure 6.16). As a control experiment, when Ag nanocubes bearing sharp corners (mean edge length 94 ± 14 nm; see Figure 6.16a) were mixed with aqueous $HAuCl_4$, the galvanic replacement reaction occurred immediately. Specifically, at the early stage, the reaction is initiated randomly from any one of the six {100} facets of an Ag nanocube through a pitting process (Figure 6.16b). With further progress of the reaction, nanoboxes (Figure 6.16c) form through a combination of replacement and alloying between Ag and Au. As seen in Figure 6.16c, although the obtained alloyed hollow structures contain small pores in the surface, the size and shape of these pores are poorly defined and their positions are randomly distributed across the surface. At the late stage of the reaction (or when a large amount of $HAuCl_4$ has been added), the Ag atoms in the alloy walls are selectively extracted through a dealloying process to generate nanocages with compositions approaching pure gold. In this dealloying process, Au atoms are concurrently produced and deposited onto the walls, causing additional changes to both the wall thickness and the porosity. Such an unwanted coupling between Ag dealloying and Au deposition makes it difficult to fine-tune or precisely control the wall thickness, porosity – and thus the optical properties – of the resultant nanocage. On the other hand, when Ag nanocubes with truncated corners are employed as the sacrificial template in the experimental procedure, it is found that the pores become more regular and better controlled. Figure 6.16d–f shows

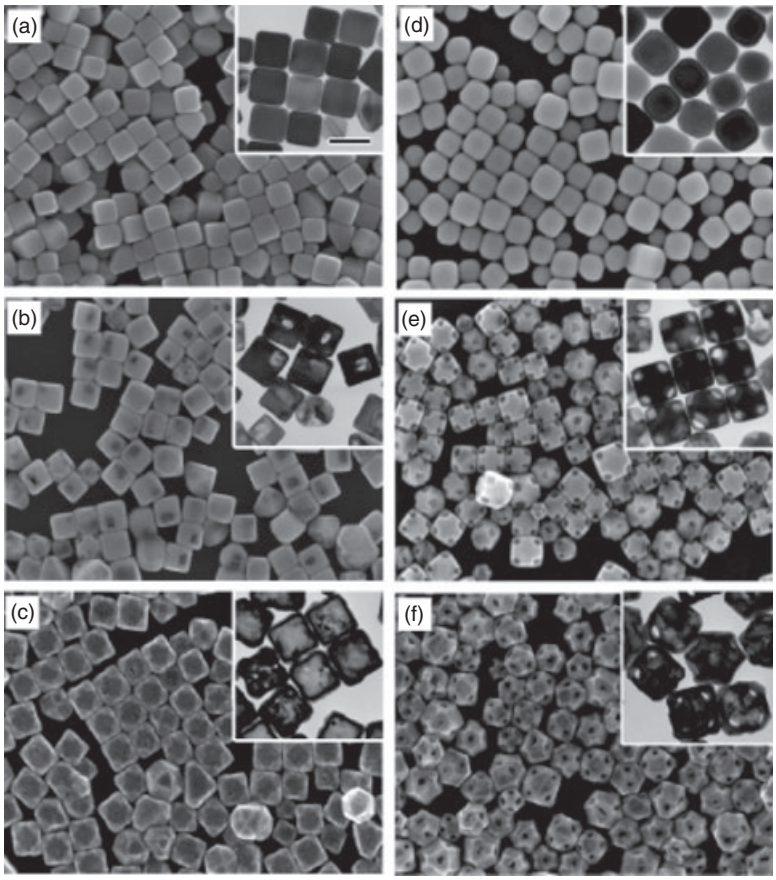

Figure 6.16 SEM and TEM (inset) images of different stages of galvanic replacement reaction with Ag nanocubes serving as the sacrificial template for Au–Ag alloyed nanocages. (a–c) Ag nanocubes with sharp corners titrated with increasing the amount of $HAuCl_4$ (0.1 m*M* $HAuCl_4$, 0, 0.6, and 1.6 ml, respectively); (d–f) Ag nanocubes with truncated corners reacted with the same volumes of 0.1 m*M* $HAuCl_4$ as for the sharp cubes. Scale bar = 100 nm for all TEM images. Reprinted with permission from Ref. [71]; © 2006, American Chemical Society.

SEM and TEM images of the nanostructures obtained at different stages of the reaction, after the Ag nanocubes with truncated corners have been mixed with aqueous $HAuCl_4$. Unlike the cubes with sharp corners, the reaction starts preferentially from all corners of a truncated nanocube at the early stage, while Au atoms are deposited mainly on the six side faces (Figure 6.16e). As a result, cubic nanocages with well-defined pores at all corners (Figure 6.16f) are obtained. During the course of this reaction the area ratio of {111} to {100} facets increases as a result of the surface reconstruction. As the pores are located on the {111} facets, their sizes are gradually enlarged without dealloying until the area of {111} facets can no longer be increased. In both cases, spotted EDS patterns recorded from the

individual cage walls confirm the fact that the Ag atoms can also diffuse into the lattice of deposited Au to form a single crystalline alloy shell. The same group has also shown that the use of an aqueous etchant based on $Fe(NO_3)_3$ or NH_4OH other than $HAuCl_4$ for the dealloying process, will allow a better control of the wall thickness and porosity of resultant nanocages, because there is no concurrent deposition of Au on the side walls during the entire course of the dealloying process [73]. In all these cases, by varying the amount of aqueous etchants ($HAuCl_4$, $Fe(NO_3)_3$ or NH_4OH) used for the galvanic replacement reaction – and thus the optimization of the percentage of Au in the alloy nanoboxes/nanocages – the SPR peaks of the alloyed cage nanostructures can be continuously tuned from the visible to the NIR region, to match the transparent window of biological samples.

One-dimensional encoded alloy nanowires/nanorods have received close attention as tagging systems for a variety of bioanalytical or product-tracking/identification/protection applications. Recently, Wang *et al.* reported the synthesis of single-segment In—Pb—Bi nanowires using a one-step, template-guided electrodeposition from single plating solutions containing different concentrations of corresponding metal ions [74]. The synthesis protocol for compositionally encoded alloy nanowire tags is similar to that for striped nanowires/nanorods based on sequential plating steps from different metal solutions (see Figure 6.10), but is substantially faster and simpler than the latter. Because the barcode patterns are 'built-in' the same alloy materials, rather than using spatially resolved wire segments or mixing different dyes or quantum dots, 1-D encoded alloy nanostructures possess a high coding capacity with a large number of distinguishable voltammetric/X-ray fluorescence signatures which reflect the predetermined composition of the metal mixture plating solution (and hence the nanowire composition). However, such a greatly simplified preparation route is compromised by the corresponding destructive [74] or expensive [75] readout tools. In order to resolve this key bottleneck, Wang and coworkers demonstrated that multisegment Au—Ag alloy nanowire barcodes with distinct optical-reflectance striping patterns and large coding capacities could be prepared by using a template-assisted electrodeposition from a single gold–silver plating solution mixture in connection to different potentials [76]. The different reduction rates of silver and gold at different plating potentials over the –0.50 to –1.20 V range (versus Ag/AgCl) [77] led to alloy segments of different Au—Ag compositions and to three or four optically distinct, readily decoded alloy segments [76]. Hence, extremely wide varieties of optical-reflectance striping patterns can be produced by plating these alloy segments in different orders and charges. This new preparation route to multisegment alloy nanowires greatly simplifies code production compared to the solution-changing, sequential deposition of common bimetal nanowire barcodes (see Figure 6.10). The template-assisted electrodeposition of the multisegment alloy nanowires is illustrated in Figure 6.17. The different deposition potentials are applied sequentially in a predetermined order and for different durations (routes A, B, C) to produce alloy segments of controlled length. This is followed by the template dissolution (route D) and optical readout of the reflectance patterns (E). Compared

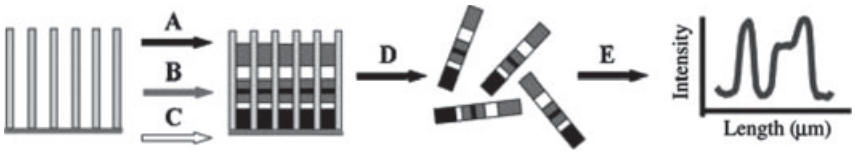

Figure 6.17 Synthesis of multisegment alloy nanowire barcodes using one gold–silver mixture plating solution with electrodeposition of segments occurring at different potentials (routes A, B, C) in various preset orders and durations. Routes D and E represent the template dissolution and optical reflectance (intensity profile) readout, respectively. Reprinted with permission from Ref. [76]; © 2008, @ Wiley Interscience.

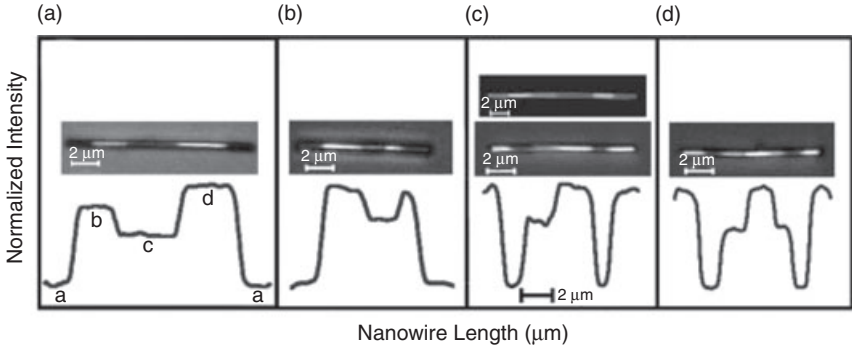

Figure 6.18 Reflectance images (top) and intensity lines (bottom) for different multisegment alloy nanowire barcodes prepared from an 85/15 (v/v) Au/Ag plating solution. The sequences of the deposition potentials for each nanowire image are (from left to right): (a) –1.20, –0.73, –0.96, –0.50 and –1.20 V; (b) –1.20, –0.50, –0.85, –0.50 and –1.20; (c) –0.50, –1.20, –0.85, –0.50, –1.20 and –0.50 V; (d) –0.50, –1.20, –0.85, –0.50, –0.85, –1.20 and –0.50 V. The upper image in panel (c) shows the corresponding SEM image. Reprinted with permission from Ref. [76]; © 2008, Wiley Interscience.

to above-discussed single-segment alloy nanowire electrochemical [74] and X-ray fluorescence [75] barcodes, the new striped alloy nanowires can be readily decoded on the basis of differences in optical reflectivity (a faster and cheaper diagnostic method). Such an ability to tune the optical properties by adjusting the deposition potential and to generate multisegment alloy nanowires with distinct optical reflectance barcode patterns from a single plating solution, is illustrated in Figure 6.18. An optical microscopy image and the corresponding intensity profile for a five-segment nanowire involving four different alloy compositions is shown in Figure 6.18a. This nanowire is prepared from an 85/15 (v/v) Au/Ag plating solution by applying four different potentials in the following sequence: (a) –1.20; (b) –0.73; (c) –0.96; (d) –0.50; and (e) –1.20 V (versus Ag/AgCl). Such sequential deposition from the same solution results in four alloy segments that can be distinguished on the basis of the intensity of their reflectivity. As will be illustrated below, the four intensity levels reflect the stepwise increase of the gold content in the alloy

upon increasing the deposition potential from –0.50 to –1.20 V. The corresponding intensity (line) profile (lower part of Figure 6.18a) clearly illustrates the ability to distinguish between the four segments of different alloy compositions. Each segment yields a characteristic intensity level, allowing the convenient distinction of adjacent alloy stripes and of the four compositions. A large number of unique codes can thus be prepared by simply varying the deposition conditions while using the same plating solution. For example, Figure 6.18b–d shows reflectance images (top) and intensity lines (bottom) for three nanowires prepared by applying different potentials (–0.50, –0.85 and –1.20 V versus Ag/AgCl) using different preset orders and charges. Such changes in the deposition conditions result in distinct striping patterns involving three visibly distinguishable reflectance intensity levels (bright, dark and intermediate), corresponding to the individual alloy segments. Also shown in Figure 6.18c is an SEM image of the corresponding nanowire; here, the individual segments are clearly visible, while their intensities are the opposite of the corresponding optical-reflectance intensities.

In addition, Yeh *et al*. have developed a new class of complex Au_xAg_{1-x} nanostructures with dendrite morphology and a hollow interior based on a galvanic replacement reaction between Ag dendrites and an aqueous solution of $HAuCl_4$ [78]. The hollow Au_xAg_{1-x} dendrite particles are 500–600 nm in size and are built up of many tubular stems with an asymmetric arrangement. Each stem is approximately 400 nm in length, 65 nm in diameter, and 10.5 nm in wall thickness, and is composed of small, asymmetric branches 28 nm in diameter (Figure 6.19). The composition of Au_xAg_{1-x} can be tuned by adjusting the amounts of $HAuCl_4$ to the Ag dendritic solution, leading to a SPR shift to the NIR region. Specifically, the $Au_{0.3}Ag_{0.7}$ dendrites display a strong absorption in the NIR region and good biocompatibility, which allows them to serve as photothermal absorbers for the photothermal therapy of cancer cells.

6.2.4
3-D Mesoscale Bimetallic Patterning

The building of mesoscale metallic patterning has formed the exciting content of many research projects in recent years, because of the promising collective tunable properties and complex functions of the patterned nanostructures [49, 50, 79, 80]. However, there remains a major challenge in building desired three-dimensional (3-D) ordered systems from different types of metallic building blocks, for example to realize novel magnetic, plasmonic and photonic metamaterials. A conceptually simple idea to overcome this problem is the use of ‘encodable’ interactions between building blocks to achieve the cocrystallization of particles; this can, in principle, be implemented in straightforward manner by functionalizing particles with biomolecules (e.g., complementary DNA strands) [81, 82]. Here, although biomolecule hybridization or pairing ‘locks’ the particles together when they come into contact, the strong irreversible ‘snapping’ of the particles into place does not allow ordered cocrystallization. Consequently, colloidal cocrystallization requires a precise adjustment of the attraction between oppositely charged nanoparticles,

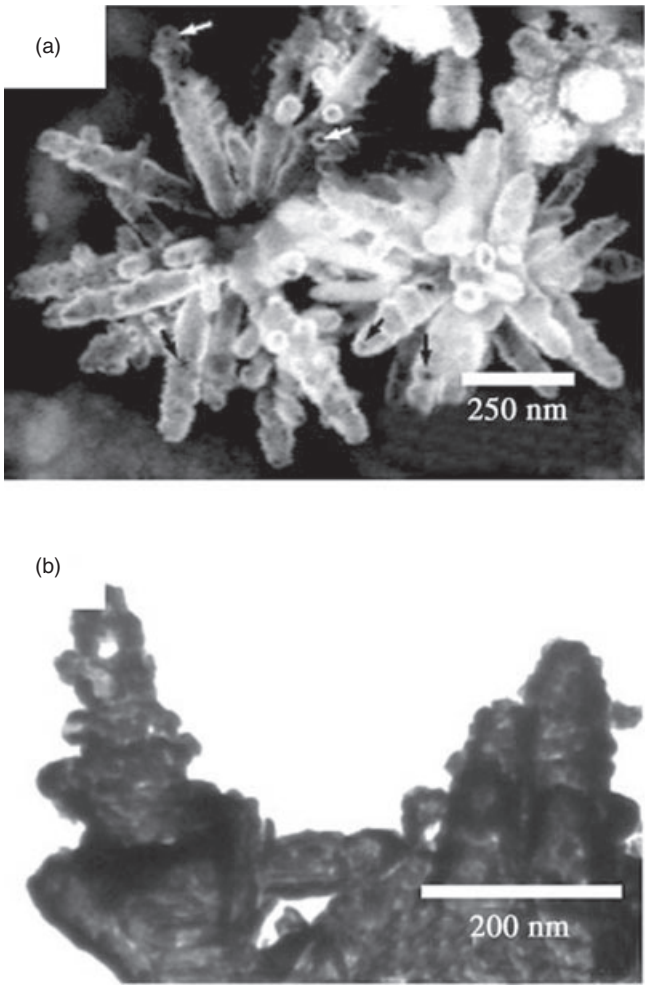

Figure 6.19 (a) SEM and (b) TEM images of core-free $Au_{0.3}Ag_{0.7}$ dendrite nanostructures. The arrows in (a) show the voids on the tips of the stems of the dendrites. Reprinted with permission from Ref. [78]; © 2008, Wiley Interscience.

within a certain small range. Recently, Grzybowski *et al*. reported the evaporation-induced cocrystallization of oppositely charged, almost equally sized metallic Au and Ag nanoparticles into large 3-D microscale sphalerite supracrystals (each composed of several millions of nanoparticles) with diamond-like packing and various morphologies by controlled electrostatic self-assembly, in which each nanoparticle has four oppositely charged neighbors [49]. The constituent Ag and Au nanoparticles are coated with a single layer of ω-functionalized alkane thiols: $HS(CH_2)_{10}COOH$ (MUA) and $HS(CH_2)_{11}NMe_3^+Cl^-$ (TMA), respectively. The dimensions and quality of the self-assembled supracrystals can be controlled

by changing the relative nanoparticles' polydispersity, the nanoparticle concentrations, and the pH of the aqueous solutions. In this method, excess nanoparticles of either polarity will terminate the self-assembly process at desired stages by forming charged, stabilizing shells around the growing aggregates. As a result, average supracrystal sizes can be tuned from several micrometers down to tens of nanometers. The fabricated larger supracrystals precipitate from the growing solution, while those smaller than approximately 400 nm will be stabilized in the solution. At this point, DLVO (Deryaguin–Landau–Verwey–Overbeek) theory seems applicable to the observed threshold size for solubility [83]. The formation of these non-close-packed structures is a consequence of electrostatic effects specific to the nanoscale, where the thickness of the screening layer is commensurate with the dimensions of the assembling objects. As a result of the electrostatic stabilization of larger crystallizing particles by their smaller counterparts (that do not scale up to interactions between microspheres), better-quality crystals can be obtained from more polydisperse nanoparticle solutions. Further, Grzybowski *et al.* demonstrated a straightforward synthesis of macroscopic supracrystal materials using a two-step method in which the different types of individual metal nanoparticles first self-assembled into deformable hybrid spherical aggregates ('supraspheres') and then 'glued' together (much like pieces of clay) into millimeter-sized structures (Figure 6.20) [50]. The individual metal nanoparticles, stabilized in solution with a dodecylamine (DDA) capping agent and didodecyldimethylammonium bromide (DDAB) surfactant, were then connected by using photoswitchable, long-chain *trans*-azobenzene dithiol (ADT) ligands [50]. This long spacer, which connected the two terminal thiol groups, endowed the resultant aggregates with flexibility, while the incorporated azobenzene unit in dithiol crosslinkers allowed for precise control of the assembly process and of the dimensions of the formed spheres by ultraviolet (UV) light. Because an excess of the surfactant and capping agents prevents the spontaneous crosslinking of nearby nanoparticles through their divalent ADT ligands, the nonirradiated solutions proved to be stable for many weeks. Unfortunately, UV irradiation causes a rapid *trans-cis* isomerization of the ADTs and induces molecular dipoles on the azobenzene units (electric dipole moment, m, = 4.4 debye for the *cis* form compared to 0 debye for *trans*), which in turn will cause the molecules to aggregate and crosslink into supraspheres. The diameters and elemental compositions of supraspheres can be controlled by changing the concentration and ratio of the different metal nanoparticles and/or the concentration of the ADT crosslinkers. The supraspheres are highly deformable and sticky upon contact with other spheres (or surfaces), and this enables their further assembly into macroscopic materials. The formed macroscopic materials may also be plastic and capable of being molded into arbitrary shapes. Alternatively, they may be thermally hardened into structurally uniform porous, polycrystalline metal monoliths, in which the composition at every probed location is equal to that of the supraspheres used. In contrast, when nanoparticles are simply crosslinked without forming the intermediate supraspheres, they form precipitates that cannot be assembled, molded or hardened.

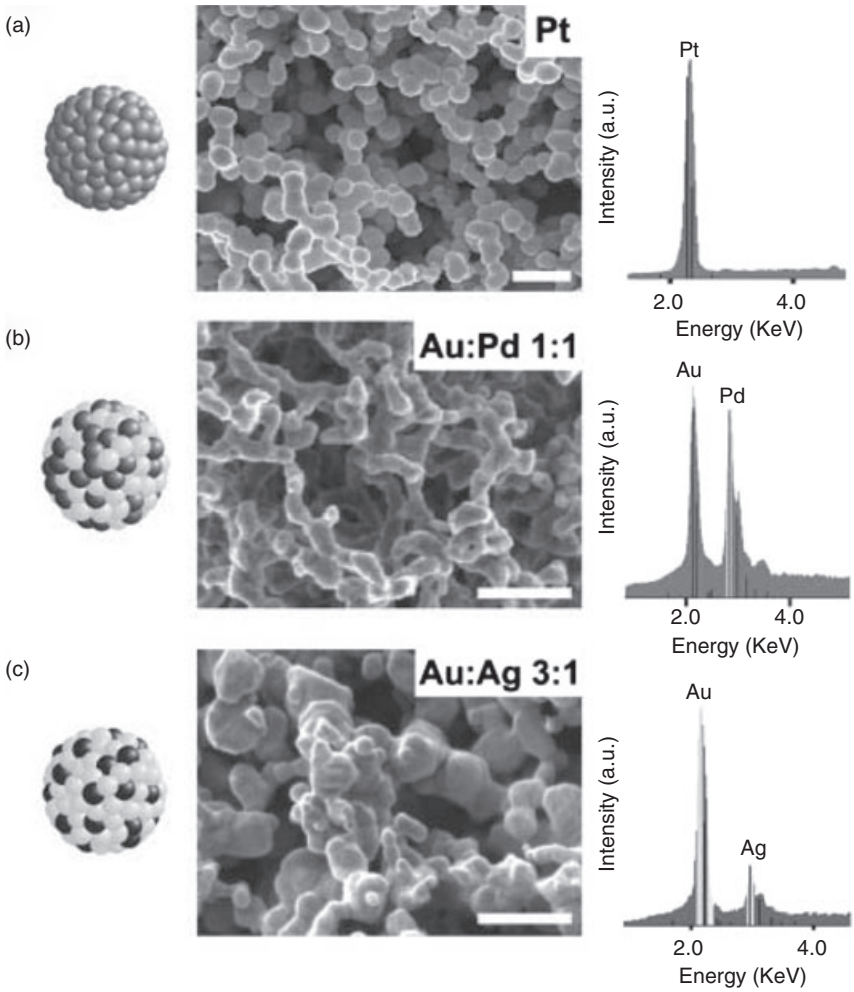

Figure 6.20 Assembly schemes, SEM images and energy-dispersive X-rays (EDX) spectra of nanoporous materials made from: (a) pure platinum; (b) 1:1 gold-palladium; (c) 3:1 gold-silver. To verify the spatially uniform composition of the bimetallic materials, EDX spectra were taken by focusing the beam at different regions of the same sample. a.u. = arbitrary units. Scale bars = 500 nm. Reprinted with permission from Ref. [50]; © 2007, American Association for the Advancement of Science.

6.3
Current and Future Applications in the Life Sciences

Because of their good biocompatibility and dimensional similarities to biomacromolecules, biomolecule functionalized metal-based nanostructures have immense potential applications in the life sciences, such as biodetection and imaging, gene regulation, protein and DNA sensing, biomedical diagnostics, drug delivery and targeted therapeutics, as well as roles in molecular and cell biology.

Previously, noble metal nanoparticles have been used for intracellular gene regulation, biomedical imaging *in vitro* and *in vivo*, and also in cancer diagnosis and therapy on the basis of their strong, tunable SPR-enhanced light scattering and absorption [5, 14, 30, 31, 84]. One particular extension of this type of application is the use of NIR SPR multimetallic nanostructures for deep-tissue *in vivo* molecular imaging, since altering the shapes and compositions of metallic nanostructures can provide dramatic variations in their SPR absorption and scattering properties. For example, the conjugation of Au nanoparticles to biomolecular ligands, such as antibodies, peptides and small molecule antagonists, specifically targeted to biomarkers on cancer cells, will permit the molecular-specific imaging and detection of cancer cells [14]. Au nanoparticles and bimetallic Au_xAg_{1-x} dendrite nanostructures with different sizes and compositions can efficiently convert the strongly absorbed NIR radiation light into localized heat and provide a sufficient increase in temperature for the rapid killing of cancer cells (Figure 6.21), without injuring adjacent healthy cells and tissue, and this effect has been exploited for the selective laser photothermal therapy of cancer [5, 78] and bacterial infection [85], with reduced human toxicity and cytotoxicity. The laser wavelength used in this technique is located in the NIR region, at which tissue transmission is optimal due to low-energy absorption, thus providing maximum penetration of the radiation through the tissues. This site-specific photothermal cancer therapy technique with NIR laser radiation provides a minimally invasive alternative to the conventional surgical treatment of solid tumors. Furthermore, hollow metallic nanospheres, nanoboxes and nanocages/nanoframes can be utilized as both contrast agents and nanovehicles for the remote manipulation of both chemical (e.g., hydrophobic cancer drugs) and biological microenvironments for applications in cell engineering, tissue engineering, and also for delivery to difficult-to-reach regions [86]. It should be noted here that one important aspect of bimetallic nanostructures as biolabels is their extreme stability against photobleaching, their lack of cytotoxicity, and their narrow, strong SPR spectra that allow the real-time monitoring or tracking of intracellular processes over long periods (from hours to days). In this way, they may possess important advantages over organic dyes such as malachite green and rhodamine-6G [87], fluorescent proteins and cytotoxic semiconductor probes. Another key advantage is that the simultaneous multicolor imaging of multiple targets, either inside living cells or on the cell surface, can be achieved with a single white light source by plasmonic nanoparticles of different sizes, shape and compositions when conjugated to different probe molecules [14]. This obviates the need for the complex photoprocessing and image overlaying which is common to multicolor fluorescent probe techniques, and is especially useful for the early detection and identification of cancer tumors based on multiple markers at the cellular or molecular level.

Metallic nanostructures – especially 1-D striped multimetallic nanorods/nanowires – can be used as optical reflectance nanobarcodes (NBCs) for the simultaneous ultrasensitive detection and multiplexed, high-throughout analysis of genes and proteins [26, 35, 88]. Here, the metal segments in each nanostructure show distinguishable contrast in both optical and electron microscopy, with varying

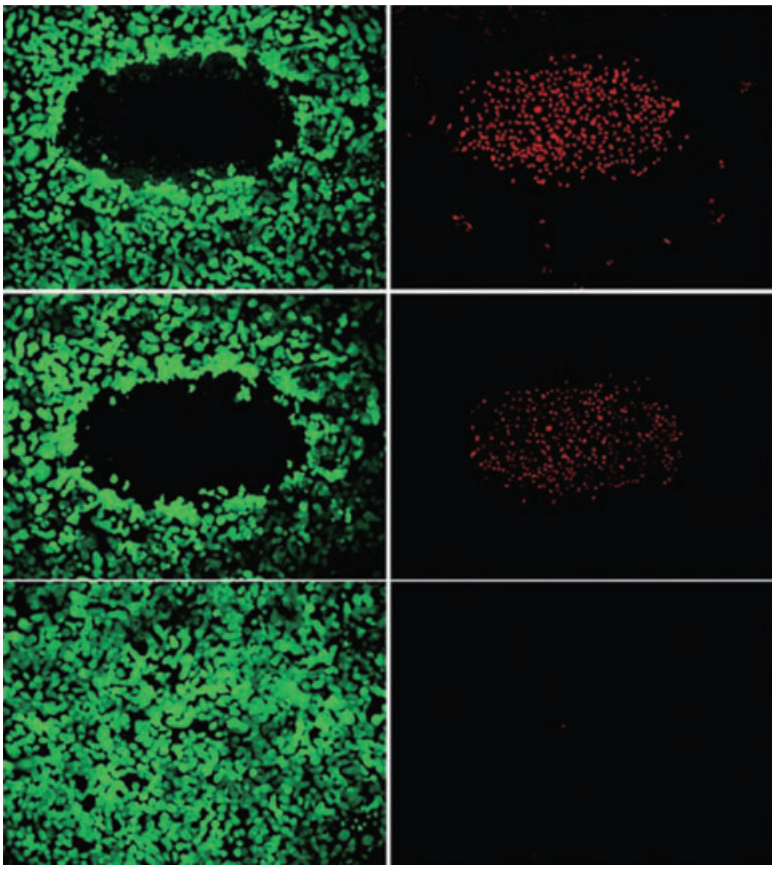

Figure 6.21 A549 cancer cells that were treated with anti-EGFR (epidermal growth factor receptor)–$Au_{0.3}Ag_{0.7}$ dendrite (150 mg ml^{-1}) conjugates and then irradiated with laser dosages of 20 W cm^{-2} (top row), 15 W cm^{-2} (middle row) and 10 W cm^{-2} (bottom row) for 4 min, respectively. A clear circular zone of dead cells was revealed by calcein AM assay (left column), where the green fluorescence dye indicates living cells, and ethidium homodimer-1 (EthD-1) assay, where the red fluorescence color indicates cell death (right column). Reprinted with permission from Ref. [78]; © 2008, Wiley Interscience.

thickness and composition. In this way, NBCs with different metallic patterns (e.g., 10010 and 01000, where 0 = Au and 1 = Ag) can be distinguished by using optical microscopy in reflectance mode. Yet, when detecting different analytes (e.g., proteins, peptides or oligonucleotides), these patterns can be used as an identification system that can be conveniently read-out using optical microscopy. Multiple striping patterns can be used to identify multiple species simultaneously in solution. In theory, by varying the number of distinguishable reflectance intensities, segment length and ordering, it is possible to generate an unlimited number of NBCs. Moreover, the coding capacity can be formulated as n^m, where n is the

number of intensity levels (i.e., alloy compositions) and m is the number of segments in the nanowire (assuming that the direction of the nanowire can be determined) [89]. Recently, Keating and coworkers reported details of the multiplexed detection and assays of DNA, antigens, nucleic acids, viruses and proteins using the striped multimetallic Ag—Au nanowires as biobarcodes [62–64].

Macroscopic patterned multimetallic nanostructures also possess great potential for applications in bioseparation and tissue engineering. It has been proposed that porous macroscopic supracrystal aggregates may be used in separation sciences, such as protein filtration [50]. It has also been shown that the surface patterning of nanostructures can be used to selectively control cell growth, and thus actively to promote the functional regeneration of a host tissue [90]. Living cells have the ability to respond sensitively to surface features of micrometer and nanometer scale, such as grooves, ridges and wells [91]; hence, the interaction of cells with the walls of nanopits on a biomaterial substrate may cause sufficient local biomechanical deformation so as to activate specific signaling cascades that regulate cellular growth and, eventually, differentiation. Both, microstructured and nanostructured surfaces may serve a variety of purposes, such as controlling and guiding cellular recolonization in host tissues by inducing osteogenesis and suppressing the formation of fibrous tissue. For example, by using a simple controlled chemical oxidation of Ti_6Al_4V, a network of nanopits/nanopores with or without a superimposed microtopography has been fabricated and applied to manipulate the growth of cells from different tissues [90]. Such a nanoporous network is able to signal the cells directly by offering physical cues that are within the range of the cellular sensing apparatus.

6.4 Summary and Outlook

To summarize, in recent years a host of impressive advances have been made while developing strategies for the construction of multicomponent metal nanostructures, notably with regards to size-/composition-tunable bimetallic nanostructures of various shapes. The optimization of size, shape and chemical composition enhances the optical properties and biocompatibility of metallic nanostructures, and so enables them to be applied extensively within the life sciences. Notwithstanding the successful initial demonstrations of the synthesis and use of multimetallic nanostructures in biomedical applications, many further investigations must be conducted in order to achieve strictly reproducible processes and high-quality products, including:

- A sound understanding of the fundamental mechanisms that control the synthesis, surface defect nature and real origin of the synergetic enhanced properties of multicomponent nanostructures.
- Investigations of the exact relationships between processing, properties and biomedical applications, which to date have received little attention.

- Improving synthetic control over single-component metal nanoparticles at low cost, optimizing their hybrid self-assemblies to create a broad range of materials to explore, and investigating the new phenomena that emerge in self-assembled hybrid supracrystals.
- Investigations of long-term mechanical and environmental (e.g., heated, cooled, different solvents) stability, biocompatibility and *in vivo* biotoxicity of the metallic nanostructures produced.

The pursuit of these goals, and the subsequent practical applications, will surely constitute an exciting and challenging task. Indeed, it is likely that during the coming decades the emerging ability to control not only the build-up of metallic nanostructures but also their desired properties and mature biomedical applications, may be key to the solution of many biomedical problems ranging from the early diagnosis of cancer to its effective therapy.

Acknowledgments

These studies were supported financially by a start-up grant (U2141) from the University of Sydney.

References

1 Elghanian, R., Storhoff, J.J., Mucic, R.C., Letsinger, R.L. and Mirkin, C.A. (1997) Selective colorimetric detection of polynucleotides based on the distance-dependent optical properties of gold nanoparticles. *Science*, **277**, 1078–81.

2 Verma, A. and Rotello, V.M. (2005) Surface recognition of biomacromolecules using nanoparticle receptors. *Chemical Communications*, 303–12.

3 Bruchez, M., Jr, Moronne, M., Gin, P., Weiss, S. and Alivisatos A.P. (1998) Semiconductor nanocrystals as fluorescent biological labels. *Science*, **281**, 2013–15.

4 Chan, W.C.W. and Nie, S. (1998) Quantum dot bioconjugates for ultrasensitive nonisotopic detection. *Science*, **281**, 2016–18.

5 Huang, X., El-Sayed, I.H., Qian, W. and El-Sayed, M.A. (2006) Cancer cell imaging and photothermal therapy in the near-infrared region by using gold nanorods. *Journal of the American Chemical Society*, **128**, 2115–20.

6 Whitesides, G.M. (2003) The 'right' size in nanobiotechnology. *Nature Biotechnology*, **21**, 1161–5.

7 Salata, O.V. (2004) Applications of nanoparticles in biology and medicine. *Journal of Nanobiotechnology*, **2** (3), 1–6.

8 Sokolova, V. and Epple, M. (2008) Inorganic nanoparticles as carriers of nucleic acids into cells. *Angewandte Chemie – International Edition*, **47**, 1382–95.

9 Niemeyer, C.M. (2001) Nanoparticles, proteins, and nucleic acids: biotechnology meets material science. *Angewandte Chemie – International Edition*, **40**, 4128–58.

10 Bailey, R.E. and Nie, S. (2004) *Core-Shell Semiconductor Nanocrystals for Biological Labeling in the Chemistry of Nanomaterials: Synthesis, Properties and Applications*, Vol. 2 (eds C.N.R. Rao, A. Müller and A.K. Cheetham), Wiley-VCH Verlag GmbH, Weinheim, pp. 405–17.

11 Rosi, N.L. and Mirkin, C.A. (2005) Nanostructures in biodiagnostics. *Chemical Reviews*, **105**, 1547–62.

12 Michalet, X., Pinaud, F.F., Bentolila, L.A., Tsay, J.M., Doose, S., Li, J.J., Sundaresan, G., Wu, A.M., Gambhir, S. S. and Weiss, S. (2005) Quantum dots for live cells, in vivo imaging, and diagnostics. *Science*, **307**, 538–44.

13 Medintz, I.L., Uyeda, H.T., Goldman, E.R. and Mattoussi, H. (2005) Quantum dot bioconjugates for imaging, labelling and sensing. *Nature Materials*, **4**, 435–46.

14 Jain, P.K., El-Sayed, I.H. and El-Sayed, M.A. (2007) Au nanoparticles target cancer. *Nanotoday*, **2** (1), 18–29.

15 Arruebo, M., Fernández-Pacheco, R., Ibarra, M.R. and Santamaría, J. (2007) Magnetic nanoparticles for drug delivery. *Nanotoday*, **2** (3), 22–32.

16 Voura, E.B., Jaiswal, J.K., Mattoussi, H. and Simon, S.M. (2004) Tracking metastatic tumor cell extravasation with quantum dot nanocrystals and fluorescence emission-scanning microscopy. *Nature Medicine*, **10**, 993–8.

17 Gao, X., Cui, Y., Levenson, R.M., Chung, L.W.K. and Nie, S. (2004) In vivo cancer targeting and imaging with semiconductor quantum dots. *Nature Biotechnology*, **22**, 969–76.

18 Loo, C., Lowery, A., Halas, N., West, J. and Drezek, R. (2005) Immunotargeted nanoshells for integrated cancer imaging and therapy. *Nano Letters*, **5**, 709–11.

19 Salem, A.K., Searson, P.C. and Leong, K.W. (2003) Multifunctional nanorods for gene delivery. *Nature Materials*, **2**, 668–71.

20 Wang, D., He, J., Rosenzweig, N. and Rosenzweig, Z. (2004) Superparamagnetic Fe_2O_3 beads-CdSe/ZnS quantum dots core-shell nanocomposite particles for cell separation. *Nano Letters*, **4**, 409–13.

21 Pellegrino, T., Kudera, S., Liedl, T., Javier, A.M., Manna, L. and Parak, W.J. (2005) On the development of colloidal nanoparticles towards multifunctional structures and their possible use for biological applications, *Small*, **1**, 48–63.

22 Link, S. and El-Sayed, M.A. (2003) Optical properties and ultrafast dynamics of metallic nanocrystals. *Annual Review of Physical Chemistry*, **54**, 331–66.

23 Taton, T.A., Mirkin, C.A. and Letsinger, R.L. (2000) Scanometric DNA array detection with nanoparticle probes. *Science*, **289**, 1757–60.

24 Park, S.J., Taton, T.A. and Mirkin, C.A. (2002) Array-based electrical detection of DNA with nanoparticle probes. *Science*, **295**, 1503–6.

25 Cao, Y.W.C., Jin, R. and Mirkin, C.A. (2002) Nanoparticles with Raman spectroscopic fingerprints for DNA and RNA detection. *Science*, **297**, 1536–40.

26 Nam, J.M., Thaxton, C.S. and Mirkin, C.A. (2003) Nanoparticle-based bio-bar codes for the ultrasensitive detection of proteins. *Science*, **301**, 1884–6.

27 Reichert, J., Csáki, A., Kohler, J.M. and Fritzsche, W. (2000) Chip-based optical detection of DNA hybridization by means of nanobead labeling. *Analytical Chemistry*, **72**, 6025–9.

28 Li, C.Z., Male, K.B., Hrapovic, S. and Luong, J.H.T. (2005) Fluorescence properties of gold nanorods and their application for DNA biosensing. *Chemical Communications*, 3924–6.

29 Li, C.Z., Liu, Y. and Luong, J.H.T. (2005) Impedance sensing of DNA binding drugs using gold substrates modified with gold nanoparticles. *Analytical Chemistry*, **77**, 478–85.

30 Rosi, N.L., Giljohann, D.A., Thaxton, C.S., Lytton-Jean, A.K.R., Han, M.S. and Mirkin, C.A. (2006) Oligonucleotide-modified gold nanoparticles for intracellular gene regulation. *Science*, **312**, 1027–30.

31 Yguerabide, J. and Yguerabide, E.E. (1998) Light-scattering submicroscopic particles as highly fluorescent analogs and their use as tracer labels in clinical and biological applications. *Analytical Biochemistry*, **262**, 157–76.

32 Norman, T.J., Grant, C.D., Magana, D., Zhang, J.Z., Liu, J., Cao, D., Bridges, F. and Buuren, A.V. (2002) Near infrared optical absorption of gold nanoparticle aggregates. *The Journal of Physical Chemistry B*, **106**, 7005–12.

33 Ferrando, R., Jellinek, J. and Johnston, R.L. (2008) Nanoalloys: from theory to applications of alloy clusters and nanoparticles. *Chemical Reviews*, **108**, 845–910.

34 Skrabalak, S.E., Chen, J., Au, L., Lu, X., Li, X. and Xia, Y. (2007) Gold nanocages for biomedical applications. *Advanced Materials*, **19**, 3177–84.

35 Hurst, S.J., Payne, E.K., Qin, L. and Mirkin, C.A. (2006) Multisegmented one-dimensional nanorods prepared by hard-template synthetic methods. *Angewandte Chemie–International Edition*, **45**, 2672–92.

36 Lu, L. and Eychmüller, A. (2008) Ordered macroporous bimetallic nanostructures: design, characterization and applications. *Accounts of Chemical Research*, **41**, 244–53.

37 Wang, H., Brandl, D.W., Nordlander, P. and Halas, N.J. (2007) Plasmonic nanostructures: artificial molecules. *Accounts of Chemical Research*, **40**, 53–62.

38 Skumryev, V., Stoyanov, S., Zhang, Y., Hadjipanayis, G., Givord, D. and Nogués, J. (2003) Beating the superparamagnetic limit with exchange bias. *Nature*, **423**, 850–3.

39 Lauhon, L.J., Gudiksen, M.S., Wang, D. and Lieber, C.M. (2002) Epitaxial core-shell and core-multishell nanowire heterostructures. *Nature*, **420**, 57–61.

40 Erwin, S.C., Zu, L., Haftel, M.I., Efros, A.L., Kennedy, T.A. and Norris, D.J. (2005) Doping semiconductor nanocrystals. *Nature*, **436**, 91–4.

41 Klimov, V.I., Ivanov, S.A., Nanda, J., Achermann, M., Bezel, I., McGuire, J.A. and Piryatinski, A. (2006) Single-exciton optical gain in semiconductor nanocrystals. *Nature*, **447**, 441–6.

42 Peng, X., Schlamp, M.C., Kadavanich, A.V. and Alivisatos, A.P. (1997) Epitaxial growth of highly luminescent CdSe/CdS core/shell nanocrystals with photostability and electronic accessibility. *Journal of the American Chemical Society*, **119**, 7019–29.

43 Casavola, M., Buonsanti, R., Caputo, G. and Cozzoli, P.D. (2008) Colloidal strategies for preparing oxide-based hybrid nanocrystals. *European Journal of Inorganic Chemistry*, 837–54.

44 Tovmachenko, O.G., Graf, C., van den Heuvel, D.J., van Blaaderen, A. and Gerritsen, H.C. (2006) Fluorescence enhancement by metal-core/silica-shell nanoparticles. *Advanced Materials*, **18**, 91–5.

45 Liu, N., Prall, B.S. and Klimov, V.I. (2006) Hybrid gold/silica/nanocrystal-quantum-dot superstructures: synthesis and analysis of semiconductor-metal interactions. *Journal of the American Chemical Society*, **128**, 15362–1536.

46 Han, Y., Jiang, J., Lee, S.S. and Ying, J.Y. (2008) Reverse microemulsion-mediated synthesis of silica-coated gold and silver nanoparticles. *Langmuir*, **24**, 5842–8.

47 Lee, J., Park, J.C. and Song, H. (2008) A nanoreactor framework of an $Au@SiO_2$ yolk/shell structure for catalytic reduction of p-nitrophenol. *Advanced Materials*, **20**, 1523–8.

48 Sakai, H., Kanda, T., Shibata, H., Ohkubo, T. and Abe, M. (2006) Preparation of highly dispersed core/shell-type titania nanocapsules containing a single Ag nanoparticle. *Journal of the American Chemical Society*, **128**, 4944–5.

49 Kalsin, A.M., Fialkowski, M., Paszewski, M., Smoukov, S.K., Bishop, K.J.M. and Grzybowski, B.A. (2006) Electrostatic self-assembly of binary nanoparticle crystals with a diamond-like lattice. *Science*, **312**, 420–4.

50 Klajn, R., Bishop, K.J.M., Fialkowski, M., Paszewski, M., Campbell, C.J., Gray, T.P. and Grzybowski1, B.A. (2007) Plastic and moldable metals by self-assembly of sticky nanoparticle aggregates. *Science*, **316**, 261–264.

51 Alayoglu, S., Nilekar, A.U., Mavrikakis, M. and Eichhorn, B. (2008) Ru–Pt core-shell nanoparticles for preferential oxidation of carbon monoxide in hydrogen. *Nature Materials*, **7**, 333–8.

52 Gaikwad, A.V., Verschuren, P., Eiser, E. and Rothenberg, G. (2006) A simple method for measuring the size of metal nanoclusters in solution. *The Journal of Physical Chemistry B*, **110**, 17437–43.

53 Cheng, D., Wang, W. and Huang, S. (2006) The onion-ring structure for Pd-Pt bimetallic clusters. *The Journal of Physical Chemistry B*, **110**, 16193–6.

54 Pedersen, D.B., Wang, S., Duncan, E.J.S. and Liang, S.H. (2007) Adsorbate-induced diffusion of Ag and Au atoms out of the cores of Ag@Au, Au@Ag, and Ag@AgI core-shell nanoparticles. *The Journal of Physical Chemistry C*, **111**, 13665–72.

55 Hunyadi, S.E. and Murphy, C.J. (2006) Bimetallic silver–gold nanowires: fabrication and use in surface-enhanced Raman scattering. *Journal of Materials Chemistry*, **16**, 3929–35.

56 Ferrer, D., Torres-Castro, A., Gao, X., Sepúlveda-Guzmán, S., Ortiz-Méndez, U. and José-Yacamán, M. (2007) Three-layer core/shell structure in Au-Pd bimetallic nanoparticles. *Nano Letters*, **7**, 1701–5.

57 Williams, D.B. and Carter, C.B. (1996) *Transmission Electron Microscopy. A Text for Materials Science*, Plenum Press, New York.

58 Xue, C., Millstone, J.E., Li, S. and Mirkin, C.A. (2007) Plasmon-driven synthesis of triangular core-shell nanoprisms from gold seeds. *Angewandte Chemie – International Edition*, **46**, 8436–9.

59 Xiang, Y., Wu, X., Liu, D., Jiang, X., Chu, W., Li, Z., Ma, Y., Zhou, W. and Xie, S. (2006) Formation of rectangularly shaped Pd/Au bimetallic nanorods: evidence for competing growth of the Pd shell between the {110} and {100} side facets of Au nanorods. *Nano Letters*, **6**, 2290–4.

60 Habas, S.E., Lee, H., Radmilovic, V., Somorjai, G.A. and Yang, P. (2007) Shaping binary metal nanocrystals through epitaxial seeded growth. *Nature Materials*, **6**, 692–7.

61 Fan, F.R., Liu, D.Y., Wu, Y.F., Duan, S., Xie, Z.X., Jiang, Z.Y. and Tian, Z.Q. (2008) Epitaxial growth of heterogeneous metal nanocrystals: from gold nano-octahedra to palladium and silver nanocubes. *Journal of the American Chemical Society*, **130**, 6949–51.

62 Stoermer, R.L. and Keating, C.D. (2006) Distance-dependent emission from dye-labeled oligonucleotides on striped Au/Ag nanowires: effect of secondary structure and hybridization efficiency. *Journal of the American Chemical Society*, **128**, 13243–54.

63 Stoermer, R.L., Cederquist, K.B., McFarland, S.K., Sha, M.Y., Penn, S.G. and Keating, C.D. (2006) Coupling molecular beacons to barcoded metal nanowires for multiplexed, sealed chamber DNA bioassays. *Journal of the American Chemical Society*, **128**, 16892–903.

64 Brunker, S.E., Cederquist, K.B. and Keating, C.D. (2007) Metallic barcodes for multiplexed bioassays. *Nanomedicine*, **2**, 695–710.

65 Martin, C.R. (1994) Nanomaterials: a membrane-based synthetic approach. *Science*, **266**, 1961–6.

66 Yahalom, J. and Zadok, O. (1987) Formation of composition-modulated alloys by electrodeposition. *Journal of Materials Science*, **22**, 499–503.

67 Seo, D.II, , Yoo, C., Jung, J. and Song, H. (2008) Ag-Au-Ag heterometallic nanorods formed through directed anisotropic growth. *Journal of the American Chemical Society*, **130**, 2940–1.

68 Camargo, P.H.C., Xiong, Y., Ji, L., Zuo, J.M. and Xia, Y. (2007) Facile synthesis of tadpole-like nanostructures consisting of Au heads and Pd tails. *Journal of the American Chemical Society*, **129**, 15452–3.

69 Zheng, N., Fan, J. and Stucky, G.D. (2006) One-step one-phase synthesis of monodisperse noble-metallic nanoparticles and their colloidal crystals. *Journal of the American Chemical Society*, **128**, 6550–1.

70 Zhang, X. and Li, D. (2006) Metal-compound-induced vesicles as efficient directors for rapid synthesis of hollow alloy spheres. *Angewandte Chemie – International Edition*, **45**, 5971–4.

71 Chen, J., McLellan, J.M., Siekkinen, A., Xiong, Y., Li, Z.Y. and Xia, Y. (2006) Facile synthesis of gold-silver nanocages with controllable pores on the surface. *Journal of the American Chemical Society*, **128**, 14776–7.

72 McLellan, J.M., Siekkinen, A., Chen, J. and Xia, Y. (2006) Comparison of the surface-enhanced Raman scattering on sharp and truncated silver nanocubes. *Chemical Physics Letters*, **427**, 122–6.

73 Lu, X., Au, L., McLellan, J., Li, Z.Y., Marquez, M. and Xia, Y. (2007) Fabrication of cubic nanocages and nanoframes by dealloying Au/Ag alloy nanoboxes with an aqueous etchant based on $Fe(NO_3)_3$ or NH_4OH. *Nano Letters*, **7**, 1764–9.

74 Wang, J. and Liu, G. (2006) Templated one-step synthesis of compositionally encoded nanowire tags. *Analytical Chemistry*, **78**, 2461–4.

75 Sattayasamitsathit, S., Burdick, J., Bash, R., Kanatharana, P., Thavarungkul, P. and Wang, J. (2007) Alloy nanowires bar codes based on nondestructive X-ray fluorescence readout. *Analytical Chemistry*, **79**, 7571–5.

76 Bulbarello, A., Sattayasamitsathit, S., Crevillen, A.G., Burdick, J., Mannino, S., Kanatharana, P., Thavarungkul, P., Escarpa, A. and Wang, J. (2008) Striped alloy nanowire optical reflectance barcodes prepared from a single plating solution. *Small*, **4**, 597–600.

77 Ji, C., Oskam, G., Oskam, Y., Ding, Y., Erlebacher, J.D., Wagner, A.J. and Searson, P.C. (2003) Deposition of $Au_xAg_{1-x}/Au_yAg_{1-y}$ multilayers and multisegment nanowires. *Journal of the Electrochemical Society*, **150**, C523–8.

78 Hu, K.W., Huang, C.C., Hwu, J.R., Su, W.C., Shieh, D.B. and Yeh, C.S. (2008) A new photothermal therapeutic agent: core-free nanostructured Au_xAg_{1-x} dendrites. *Chemistry – A European Journal*, **14**, 2956–64.

79 Nykypanchuk, D., Maye, M.M., van der Lelie, D. and Gang, O. (2008) DNA-guided crystallization of colloidal nanoparticles. *Nature*, **451**, 549–52.

80 Park, S.Y., Lytton-Jean, A.K.R., Lee, B., Weigand, S., Schatz, G.C. and Mirkin, C.A. (2008) DNA-programmable nanoparticle crystallization. *Nature*, **451**, 553–6.

81 Alivisatos, A.P., Johnsson, K.P., Peng, X.G., Wilson, T.E., Loweth, C.J., Bruchez, M.P. and Schultz, P.G. (1996) Organization of 'nanocrystal molecules' using DNA. *Nature*, **382**, 609–11.

82 Mirkin, C.A., Letsinger, R.L., Mucic, R.C. and Storhoff, J.J. (1996) A DNA-based method for rationally assembling nanoparticles into macroscopic materials. *Nature*, **382**, 607–9.

83 Kalsin, A.M. and Grzybowski, B.A. (2007) Controlling the growth of 'Ionic' nanoparticle supracrystals. *Nano Letters*, **7**, 1018–21.

84 Mitchell, P. (2001) Turning the spotlight on cellular imaging – Advances in imaging are enabling researchers to track more accurately the localization of macromolecules in cells. *Nature Biotechnology*, **19**, 1013–7.

85 Zharov, V.P., Mercer, K.E., Galitovskaya, E.N. and Smeltzer, M.S. (2006) Photothermal nanotherapeutics and nanodiagnostics for selective killing of bacteria targeted with gold nanoparticles. *Biophysical Journal*, **90**, 619–27.

86 Ye, H., Randall, C.L., Leong, T.G., Slanac, D.A., Call, E.K. and Gracias, D.H. (2007) Remote radio-frequency controlled nanoliter chemistry and chemical delivery on substrates. *Angewandte Chemie – International Edition*, **46**, 4991–4.

87 Bugaj, J.E., Achilefu, S., Dorshow, R.B. and Rajagopalan, R. (2001) Novel fluorescent contrast agents for optical imaging of in vivo tumors based on a receptor-targeted dye-peptide conjugate platform. *Journal of Biomedical Optics*, **6**, 122–33.

88 Nicewarner-Pena, S.R., Freeman, R.G., Reiss, B.D., He, L., Pena, D.J., Walton, I.D., Cromer, R., Keating, C.D. and Natan, M.J. (2001) Submicrometer metallic barcodes. *Science*, **294**, 137–41.

89 Walton, I.D., Norton, S.M., Balasingham, A., He, L., Oviso, D.F., Gupta, D., Raju, P.A., Natan, M.J. and Freeman, R.G. (2002) Particles for multiplexed analysis in solution: detection and identification of striped metallic particles using optical microscopy. *Analytical Chemistry*, **74**, 2240–7.

90 Richert, L., Vetrone, F., Yi, J.H., Zalzal, S.F., Wuest, J.D., Rosei, F. and Nanci, A. (2008) Surface nanopatterning to control cell growth. *Advanced Materials*, **20**, 1488–92.

91 Craighead, H.G., James, C.D. and Turner, A.M.P. (2001) Chemical and topographical patterning for directed cell attachment. *Current Opinion in Solid State and Materials Science*, **5**, 177–84.

Abstract

Metallic nanostructures hold great potential for biomedical research such as biodetection and bioimaging, disease-causing gene expression profiling, biodiagnostics, drug delivery and targeted therapeutics, and tissue engineering. A plethora of high-quality metallic nanomotifs have been well developed to date. In this chapter we review the latest advances in the chemical build-up of nonmagnetic metal@oxide and bimetallic nanostructures, as well as their current and future applications in the life sciences. Because of their unique size-, shape- and composition-dependent properties, the simultaneous detection of multiple signals with high stability, and dimensional similarities to biomacromolecules, nanostructured metals may be used to address key problems in the life sciences, from early cancer diagnostics to therapeutics.

Keywords

bimetal; core@shell; nanostructure; colloidal synthesis; shaping crystal; self-assembly; surface plasmon resonance; biomedical applications.

7
Biofunctionalization of Spherical and Anisotropic Bimetallic Nanomaterials

Davide Prosperi, Laura Polito, Carlo Morasso and Diego Monti

7.1
Introduction

The biomedical applications of nanostructured materials have received an impressive boost at the start of the twenty-first century. Indeed, the development of a new generation of metal nanoparticles integrated into biological systems is expected to revolutionize the conventional approaches to biosensing, drug/gene delivery, diagnostic investigations and therapeutic efforts up to the human clinical level [1–9]. Besides the accurate modulation of the physical properties of nanoparticle metal core types, their controllable surface functionalization with biomolecules represents a major challenge in order to fabricate reliably active bioorganic–inorganic hybrid nanostructures [10–13]. It has been well documented, indeed, that the immobilization of biomolecules onto solid surfaces may lead to partial – or even complete – deactivation of their biological functionalities [14, 15]. In this context, the development of biofunctionalized noble metal nanoparticles has imparted a major impact on the current 'season' of nanobioscience. Individual gold and silver nanoparticles, in particular, have proven to be extremely effective and versatile nanomaterials for a range of biomedical applications including biosensing [16], imaging [17, 18], medical diagnostics [19], biophysical investigations [20, 21] and cancer thermotherapy [22–26]. Such a wide applicability mainly resides in their unique electronic and optical properties, including large field enhancement, which promotes strong absorption and scattering of light. This field enhancement is due to a physical process known as 'localized surface plasmon resonance', which is a resonant oscillation of free electrons on the surface of the noble metal in response to a light radiation. This effect may lead to the scattering of light by the metal surface, which is useful for imaging and other optical purposes or, alternatively, to the radiative energy conversion into heat. The latter process is referred to as 'absorption', and is exploited in the hyperthermic treatment of malignant tumors [27]. In the case of monometal particles, these optical properties are largely dependent on multiatom cluster shape and size. However, the incorporation of more than one metal species into the nanoparticle assembly to form a bi/multimetal

Nanomaterials for the Life Sciences Vol. 3: Mixed Metal Nanomaterials. Edited by Challa S. S. R. Kumar

ISBN: 978-3-527-32153-7

alloy is able to confer privileged optical enhancement and fine-tuning to the crystal structure, by introducing a further component that can be modulated, such as the metal composition ratio. Although the great majority of the earliest applications of bimetal nanoparticles have focused on the quest for new catalysts [28], a strong interest for their potential in biology and medicine is rapidly emerging. Once again, together with the development of tunable bimetal probes, much effort is being spent on integrating the metal core into suitable biomolecular systems capable of specific recognition and targeting to living cells and tissues. In this chapter, we review the recent reports of methods used to accomplish the active biofunctionalization of noble bimetal spherical and anisotropic nanoparticles, and place particular emphasis on those approaches which show a real potential applicability to biological systems.

To achieve this, we have divided the chapter into three main sections, each related to the interatomic organization of the two metal elements constituting the nanoparticle core, thus giving rise to: (i) core-shell architectures; (ii) rod-shaped segmented structures; and (iii) randomly assembled nanoalloys. The chapter focuses on polyatomic clusters deriving essentially from noble metals, although we have exceptionally included some examples in which noble metals are associated with intrinsically magnetic elements (e.g., cobalt and nickel) in order to highlight some relevant conceptual advances in nanometal bioconjugation strategies.

Although the number of reports in this field is increasing exponentially, a substantial overview of the current development of methods for bimetal nanoparticle biofunctionalization directed to biological applications is still missing and largely desirable. For this reason, we believe that this chapter will provide a useful introduction to approach the state of the art of this subject area, and provide some suggestions for the next generation of noble metal-based optical bioprobes.

7.2
Spherical Core-Shell Bimetallic Nanoparticles

7.2.1
Ag_{Core}/Au_{shell} Nanoparticles

Ag nanoparticles represent interesting building blocks in nanobiotechnology because they exhibit a number of optical and electrochemical properties that differ widely from those of the more extensively investigated Au nanoparticles. For example, Ag colloids have a surface plasmon band between 390 and 420 nm, depending on the particle size (for Au, this is in the range 520–580 nm), while the extinction coefficient of the surface plasmon band is approximately fourfold larger than that of an Au particle of similar size. However, Ag nanoparticles appear to be less stable than Au nanoparticles in aqueous media, and are not generally considered to be biocompatible. Consequently, several research groups are currently

investigating the idea of preparing a class of Ag-core Au-shell nanoparticles which show the physical properties of silver but the surface chemistry and stability of gold, and which can be readily functionalized with proteins or DNA for bioanalytical tasks.

Mirkin and coworkers reported a synthesis of Ag nanoparticles of ~12 nm covered by a monolayer of Au atoms, that show an ultraviolet (UV) spectrum which is very similar to that of citrate-stabilized pure Ag particles. These particles were thus functionalized with thiol-capped DNA as pure Au particles by adding the deprotected thiolated oligonucleotides to the colloidal solution [29]. Functionalization was carried out in a 10 m*M* phosphate buffer (NaH_2PO_4/Na_2HPO_4) after which, in a subsequent salt-aging process, the colloids were brought in four steps to a 0.3 *M* salt concentration by the dropwise addition of a 2 *M* NaCl solution. This process resulted in an effective loading of oligonucleotides onto the nanoparticles surface, and has been studied in some detail for the pure gold system [30]. Significantly, no conjugation of Ag pure particles has been observed with this method; rather, they aggregate irreversibly when heated in a solution with a salt concentration suitable to effect DNA hybridization (0.05 *M* NaCl).

Such a bimetallic system can be used for the accurate investigation of recognition events between complementary biological species and for the detection of specific biomolecules, including proteins and DNA. The key factor here is the possibility to discriminate between the chromatic responses of individual Au and Ag_{core}/Au_{shell} nanoparticles, based on their respective inherent optical properties. This concept was exploited for the analytical determination of DNA sequences through the development of a 'spot test' performed on a C18-reverse-phase alumina thin-layer chromatography (TLC) plate. The use of a mixed system of Au and Ag/Au nanoparticles makes it possible to identify, unequivocally, DNA sequences at a sensitivity of a single base mutation simply by observing the color changes within the nanoparticle dispersion which, in turn, is related to the complementarities of the different sequences anchored on the nanoparticle surface [31]. When the DNA sequences are complementary to those adsorbed onto the monometal Au nanoparticles, the spot test shows a chromatic shift from red to blue; alternatively, if the complementarities are for the sequences on Ag/Au nanoparticles, this results in a yellow-to-brown wavelength shift (Figure 7.1).

Ag/Au core shell nanoparticles may also be functionalized with proteins, such as immunoglobulins, and the resultant hybrid nanosystem was used in an immunoassay based on surface-enhanced Raman scattering (SERS) for the large enhancement of the Raman signal [32].

The preparation of these nanoparticles involves a two-step sequence. In the first step, the nanoparticles and a Raman probe molecule, such as thiophenol (TP) or *p*-aminothiophenol (PATP), are mixed in ethanol and allowed to react for the activation of the nanoparticle system by surface adsorption. A second step is required for the immobilization of different immunoglobulin G (IgG) proteins on the reporter-labeled colloids, allowing them to react in a borate buffer (pH 9). In order to ensure that no bare sites are left on the particle, some bovine serum albumin (BSA) is eventually added [33].

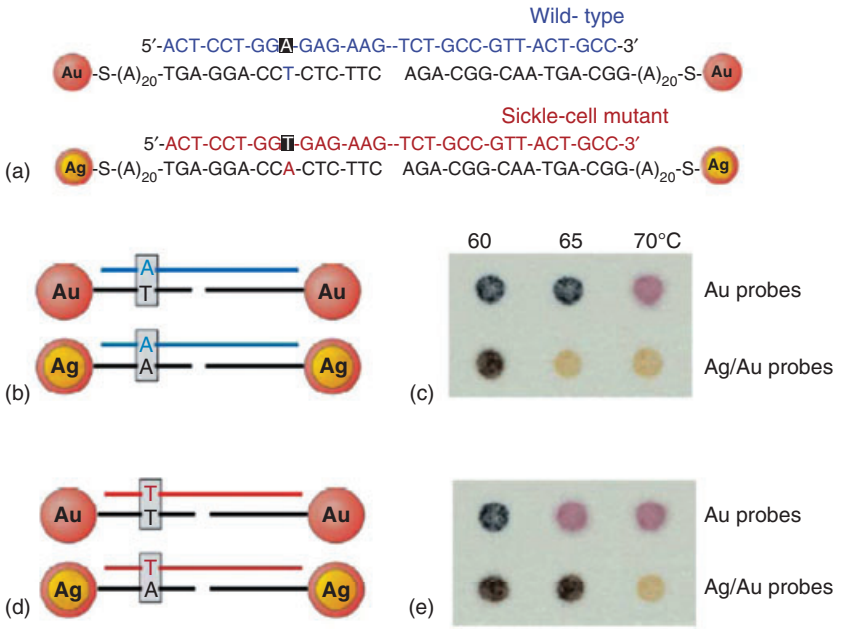

Figure 7.1 (a) Mercaptoalkyl oligonucleotide modified Ag/Au core-shell and pure-gold particles, and their oligonucleotide targets; (b) Scheme for the parallel detection experiments in the presence of wild-type targets; (c) Spot-test results in the presence of wild-type targets; (d) Scheme for the parallel detection experiments in the presence of mutant targets; (e) Spot-test result in the presence of mutant targets. Reproduced with permission from Ref. [31].

The importance of the Ag core is evidenced by the fact that when these types of particle are labeled with PATP, they give rise to a remarkably different spectral feature with respect to that observed with gold nanoparticles, despite the relative intensity of the two signals being very similar (Figure 7.2). In this way, by labeling the different particles with different IgG molecules, it is possible to perform a simultaneous multianalyte immunoassay based on SERS [33].

In a similar system, immunoconjugate core-shell nanoparticles were also used as label-free amperometric biosensors [34]. Unlike the previously described situation, instead of a molecular probe the nanoparticles were labeled with cysteine molecules that bound the gold surface by means of their thiol group; the positive charge on the amino group allowed for adsorption of the conjugated particles onto the surface of microelectrodes modified with Nafion, a negatively charged PTFE-like polymer (Figure 7.3).

A careful comparison of the response of core-shell nanoparticles with respect to those of pure Ag or Au showed better results. However, this was most likely related also to a well-retained bioactivity of the IgG immobilized on a surface with high biocompatibility, and a more liable construct sequence besides an adsorbed concentration effect.

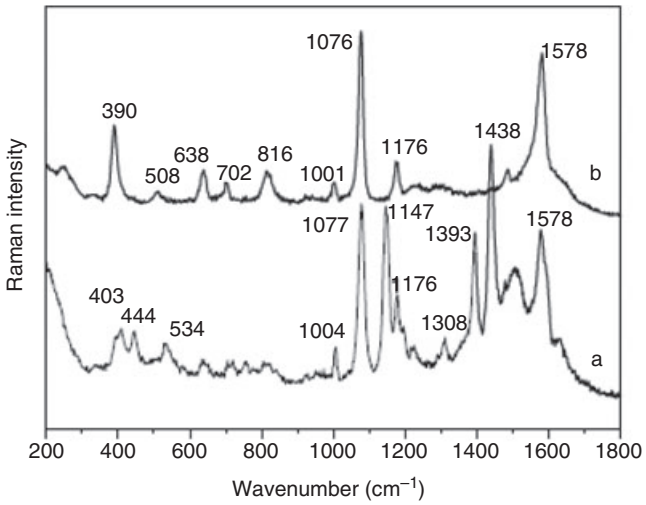

Figure 7.2 SERS spectra of *p*-aminothiophenol adsorbed onto Ag/Au bimetallic nanoparticles (a) and onto pure-Au nanoparticles (b). The spectra profiles are clearly distinguishable. Reproduced with permission from Ref. [33].

7.2.2
Au_{Core}/Ag_{shell} Nanoparticles

The use of Au/Ag core-shell nanoparticles is mainly based on the tremendous enhancement of Raman scattering intensity that is observed when many molecules are adsorbed onto their surfaces; indeed, such response allows for the detection of a dye molecule down to the single-molecule level [35].

This type of colloid may be directly functionalized with a biopolymer alginate layer within the particle fabrication by exploiting an UV photoactivation technique [36]. In this system, alginate acts both as a reducing agent under UV irradiation and as a colloid stabilizer. The saccharide constituents present in sodium alginate, β-D-mannuronic acid and α-L-guluronic acid, contain a secondary hydroxyl function, and hence it is possible for the alginate to act as a photochemically activated reducing agent, while no reducing activity is detected in the absence of light. Alginate is able simultaneously to reduce both Au and Ag ions. In order to obtain core-shell nanoparticles, it is first necessary to generate the Au seeds by adding a solution of $HAuCl_4$ to an alginate solution. The Ag^+ is then added to the stabilized gold seeds, which function as nucleation centers such that, instead of individual silver nanoparticles, an Ag shell is created on gold that presents alginate in a more external layer.

Both, monosaccharide- and disaccharide-functionalized bimetallic nanoparticles may be obtained by a straightforward reduction of gold and silver ions in the presence of the corresponding carbohydrates. In particular, fructose proved to be highly effective in producing variably sized Au/Ag nanoparticles by both inducing

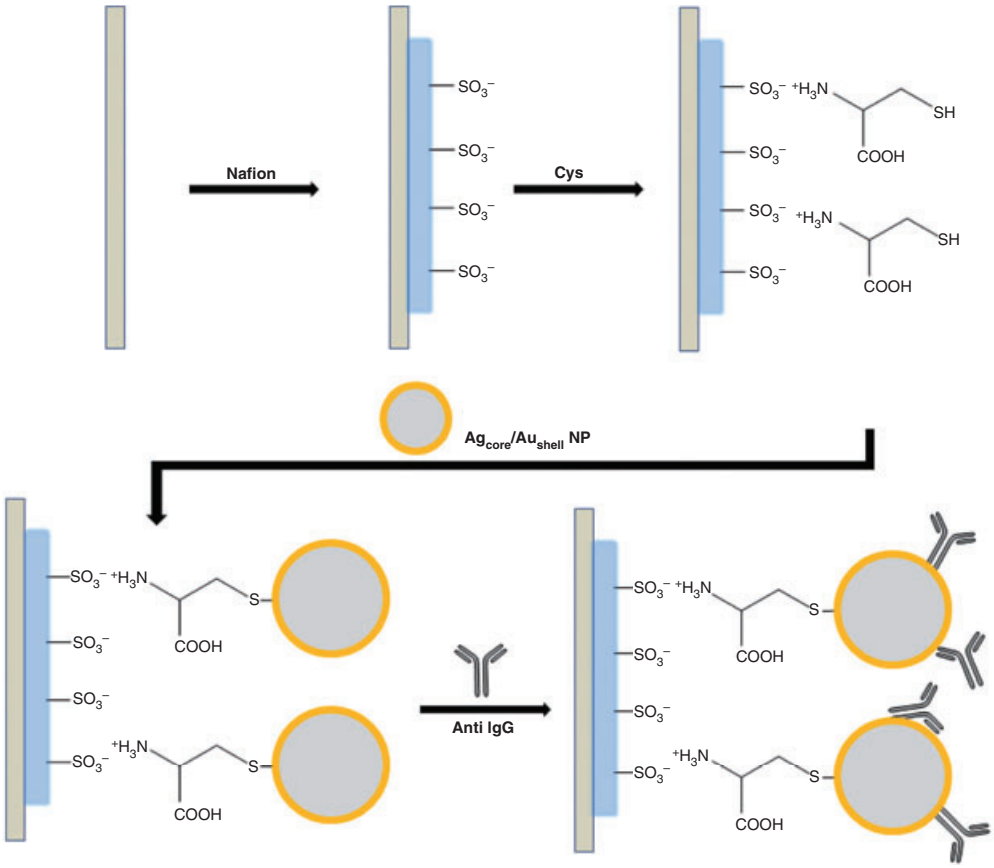

Figure 7.3 Schematic illustration of the preparation of the Ag@Au core-shell nanoparticle-based amperometric immunosensor.

metal reduction and stabilizing the final nanoparticles [37]. Once again, the Au nanoparticle seeds were first prepared by growing from Au^{3+} ions, using the sugar as the only reducing agent. In a second step, a $AgNO_3$ solution was added, followed by a further sugar-assisted reduction, resulting in the final carbohydrate-stabilized bimetallic nanoparticles. The resultant core-shell model nanoparticles have potential for the development of bimetallic nanohybrids that are useful for biomedical applications, on the basis of a favorable combination of effects due to the carbohydrate's chemical properties, such as elevated water solubility, good biocompatibility, tumor targeting efficiency and their involvement in several affinity biorecognitions and metabolic processes.

β-Cyclodextrin (β-CD) has weak reducing capability, and can be used for the synthesis of core-shell bimetallic nanoparticles by acting both as a reducing agent for metal ions and as a capping agent. Analogous to the other above-mentioned

carbohydrate-based examples, of particular interest is the fact that β-CDs in alkaline media are able to reduce Au^{3+} and Ag^{+} ions without the need for any supplementary reducing agent. In this way it is possible to obtain Au_{core}/Ag_{shell} and Ag_{core}/Au_{shell} composites by preparing monometallic seeds of one metal and then, by changing the alternate ions present in solution, to create a surface layer of a different material that is already stabilized by the presence of β-CD [38].

The SERS of this type of particle has been utilized in a number of biological detection tests, including immunoassays. Au_{core}/Ag_{shell} nanoparticles used in such applications are prepared from an Au seed functionalized with a Raman probe, such as 4-mercaptobenzoic acid (MBA), that is adsorbed through its thiol group. The silver shell is then formed by a hydroquinone reduction of Ag^{+} ions in the presence of such gold seeds. This procedure requires a delicate set-up of the preparative conditions, as the final thickness of the silver layer is extremely important for biosensor effectiveness. Typically, a correctly thin layer will provide the desired enhancement of signal, but if the silver layer is too thick then the probe will become localized at a position too far from the external surface, and a remarkable reduction in the signal is observed [39]. As a further development of these bimetallic SERS-based biosensors, it is also possible to functionalize the silver shell. Ji *et al*. reported on the conjugation of a mouse monoclonal antibody against hepatitis B surface antigen to the surface of Au@Ag colloids, and prepared a silicon chip with a polyclonal antibody for the same target immobilized on the surface. The antigen was captured by the chip, which in turn was exposed to the solution of nanoparticles. When the antigen was present, the nanoparticles remained attached to the chip and could be detected using a Raman spectrometric analysis [40].

Recently, the possibility of using this type of core-shell nanoparticle for highly sensitive SERS imaging through biomarker detection in cancer cells was explored [41]. To this aim, the Raman probe rhodamine 6G (R6G) was first adsorbed onto 13 nm gold seeds by electrostatic interaction, after which small amounts of BSA were added to prevent aggregation. Subsequently, the R6G-adsorbed nanoparticles were coated with silver to maximize the Raman signal, yielding silver-coated gold nanoprobes with an average diameter of 30 nm.

In order to target cancer cells, a secondary anti-mouse IgG was conjugated to the metal nanoparticle surface. In particular, *ortho*-pyridyldisulfide polyethylene glycol *N*-succinimidyl propionate (OPSS-PEG-NHS) was used as linker for the antibody conjugation (Figure 7.4). The linker was first conjugated with the antibody using the succinimidyl propionate terminal group that reacts with protein amines. The S–S terminal group of OPSS was then cleaved and chemically bound onto the metal surface. The use of a polyethylene glycol (PEG) linker helps to space out the antibody from the probe surface, and allows for a more favorable protein mobility, thus greatly improving the efficiency of the subsequent antibody–antigen interaction. The secondary IgG-conjugate is able to recognize a primary mouse antibody that specifically targets the cancerous cell, and the cancerous primary antibody-marked cell can then be detected using Raman microscopy. It was suggested by the authors that such nanoprobes, when used for SERS

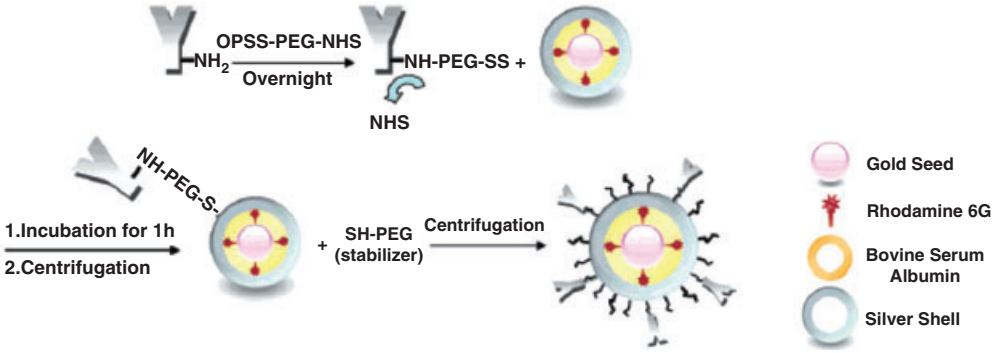

Figure 7.4 Antibody conjugation onto the Au_{core}–Ag_{shell} nanoprobes. OPSS-PEG-NHS was used for antibody conjugation. The S–S terminal group of orthopyridyldisulfide (OPSS) was cleaved and chemically linked to the metal surfaces. The other terminal group, succinimidyl propionate, was bound to the amine group of the antibody. When polyethylene glycol (PEG) was used, the space between the probe and the antibody was enlarged, and the more favorable movement of antibody greatly improved the efficiency of the antibody–antigen interaction. Finally, the PEG-thiol was used to occupy the remaining adsorption sites on the particle surface. Reproduced with permission from Ref. [41].

measurements, are very stable, as no aggregation was identified during the experiments and the declared limit of detection for R6G-adsorbed nanoprobes was within the picomolar range.

7.2.3 Silver Enhancement of Gold Nanoparticles

The examples reported above highlight the fact that the enhancement of an electro-optical signal provided by a silver layer deposited on gold nanoparticles is a phenomenon so massive that it allows for a major improvement in the detection limits of many bioanalytical tools based on metal nanoparticles. In many cases, gold nanoparticles functionalized with thiolated DNA or immunoglobulins are used as markers that can recognize a complementary sequence or an antigen with a particular biological relevance. In general, the silver nanolayer is obtained via a solution of $AgNO_3$ in the presence of hydroquinone. Under these conditions, silver ions are reduced to the zerovalent metal directly onto the nanogold seeds, thus creating a biofunctionalized core shell system. However, careful attention should be paid to the silver enhancer solution, which must be frequently replaced (usually every 2–3 min) in order to avoid the formation of a pure silver particulate [42].

This type of bimetallic system can be detected using a number of different methods. For example, if gold seeds are placed on a silica wafer in a continuous manner between two microelectrodes using a DNA sequence that is in part complementary to a sequence attached to the wafer and, in another part, complemen-

tary to a second sequence linked to the nanoparticles, then after the silver staining a connection will be created that is responsible for closing the circuit [42]. Other optical detection methods such as Raman spectroscopy of suitably dye-labeled nanoparticles [43, 44], light scattering [45] or scanometric detection [46] could also be employed, which are amplified by at least two order of magnitude by the silver staining procedure.

The silver staining of gold nanoparticles is used also in different histological experiments, and today a number of different gold nanoparticles labeled with streptavidin or with immunoglobulin are commercially available. As a result of their small sizes, these materials exhibit good tissue and nucleus permeation. When the gold nanoparticles-labeled tissue are silver-stained, this gives rise to bimetallic nanoparticles that can be easily observed using bright-field microscopy, even in the presence of standard histological stains. Moreover, it also allows for the electron microscope detection of ultrastructural localizations [47].

7.2.4
DNA-Assisted Synthesis of Core-Shell Nanoparticles

Metal nanoparticles, as described above, can be specifically functionalized with thiol-modified DNA sequences. However, in the presence of small particles, a nonspecific passivation of DNA is also possible in order to obtain a stabilization that allows an improvement in both stability and biocompatibility. This approach has been used, for instance, in the biofunctionalization of CdS quantum dots (QDs) by different research groups, and also provides different results in the presence of sequences with different length and composition [48]. With metal and bimetallic nanoparticles, such an effect is less important, although the adsorption of DNA strands independent of the specific base sequence has been reported, which caused the inhibition of DNA hybridization [49]. This effect has been observed not only for single-stranded DNA; rather, the interaction between the oligonucleotide backbone and small nanoparticle surface is sufficiently strong as to disrupt the hydrogen bonds formed between complementary oligonucleotides, such that the thus-hybridized DNA was separated into single strands.

DNA may also be used as a polymer template for the synthesis of metal nanoparticles [50]. This is especially significant because DNA is a linear polymer the composition of which can be precisely controlled, and it has also shown a great affinity for certain metal ions, including Ag^+. When these ions are complexed by DNA bases, they act as light harvesters and sensitizers, triggering photoreduction of the complexed silver ions on exposure to UV light at 254 nm [51]. Such complexation in turn promotes the formation of small (<3 nm) silver clusters. Indeed, as prolonged UV exposure causes DNA strand breakage, only short irradiation times can be used. The silver clusters act as nucleation centers for the electroless deposition of nickel, which originates an outer shell on the cluster surface. In similar fashion, DNA has been used for the preparation of Pd_{core}/Ni_{shell} nanoparticles using dimethylamine borane (DMAB) as reducing agent for Pd^+ ions [52].

7.2.5
Biofunctionalization for the Construction of Core-Shell Bimetallic Nanostructures

Whilst under different circumstances, polymers and biomolecules have been used for the preparation of core-shell bimetallic nanostructures, the degree of complexity of the resultant nanosystems may differ widely.

In a preliminary and simple model, Wang and Sim reported a methodology that utilizes the reactivity between carboxyl groups and $Ru_3(CO)_{12}$ for the attachment of Ru dicarbonyl groups to well-defined Au nanoparticles, through a mercaptopropanoate linker [53]. The first step of the procedure involves attachment of the linker to gold nanoparticles by exploiting the spontaneous chemisorption of thiol to the gold surface. The carboxylic moiety of the linker is then available for ruthenium complexation, thus promoting the generation of an outer metallic shell. These organometallic complexes may serve as potential precursors for the preparation of completely bimetallic systems, such as Au_{core}/Ru_{shell} nanoparticles, that may be useful for catalytic applications.

This evidence leads to a more general consideration that nanoscale building blocks can assemble into bimetallic composite superstructures by exploiting their differentiated chemistry and the chemistry of their surface ligands. During the past three decades, combinatorial peptide chemistry has provided sets of synthetic peptides capable of recognizing and binding to inorganic substrates, including metals and metal ions. By exploiting the very different reactivities of various metals towards the respective ligand functionalities, it is possible to generate peptide sequences suitable for the assembly of bimetallic particles. In particular, the relatively easy development of multifunctional peptide architectures has the potential to lead to the design of peptide templates containing three different domains. Here, two orthogonal metal-targeted domains may be programmed for binding with the respective metal ions, while the third sequence could be used for bioconjugation. In principle, the resulting bimetallic nanoparticles are not true core-shell structures, as distinct monometal clusters are assembled in an ultimate hybrid structure. Indeed, particle self-organization is randomly directed, providing an unpredictable, irregular metal distribution. For example, a peptide ligand consisting of an Au-binding domain, a Pd ion-binding domain and a short sequence suitable for antibody recognition, have been used for the preparation of hybrid bimetallic composite nanostructures in which a gold nanoparticle core was surrounded by Pd nanoclusters connected through a functional organic material [54]. The bimetallic nanohybrid preparation involves three steps (Figure 7.5):

- Peptide capture and reduction of Au^{3+} ions to form peptide-linked gold nanoparticles.
- Pd^{4+} ion coordination by surface peptide templates which guides the nucleation.
- A final reduction with $NaBH_4$ to form Pd nanoparticles that decorate the gold nanoparticle core. In some cases, a complete Pd nanoshell was obtained.

In this way, polymers could be used for the decoration of silver nanowires with gold nanoparticles, and with a greatly enhanced SERS ability [55]. The assembly

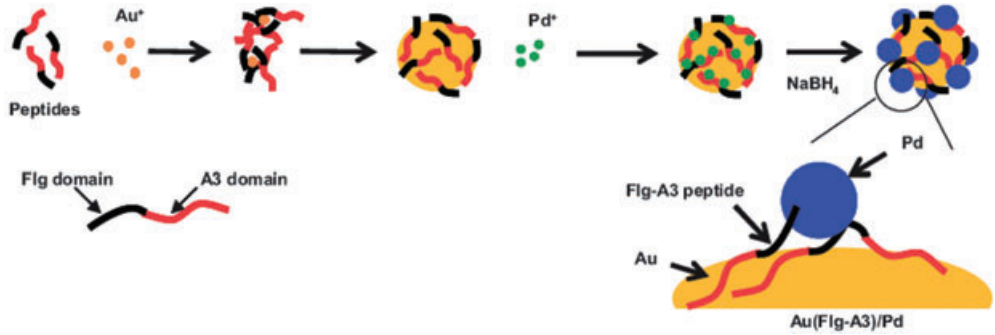

Figure 7.5 Schematic representation of the formation of Pd-on-Au bimetallic nanoparticles promoted by a multifunctional peptide. Reproduced with permission from Ref. [54].

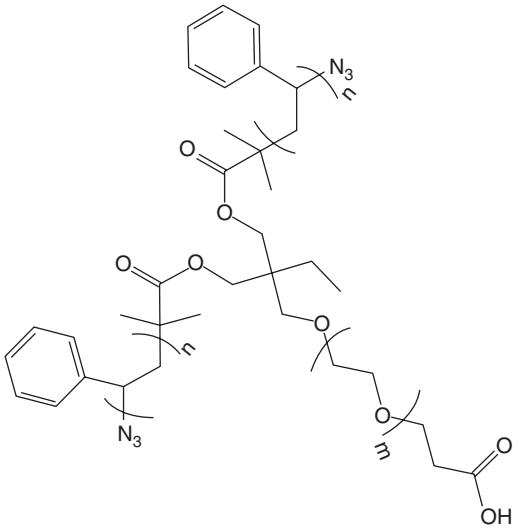

Figure 7.6 Chemical structure of the copolymer $(COOH\text{-}PEO)_1$-*S*-$(PS\text{-}N_3)_2$, obtained by (*tert*-butyldiphenylsilane-polyethyleneoxide)-*S*-(polystyrene-*N*-bromine).

of preformed gold spherical nanoparticles of 4.1 nm diameter, on the surface of one-dimensional (1-D) silver nanowires (65 nm diameter, 6 µm length) was achieved with the aid of a three-arm star polymer with functional terminal groups, that acted both as a linker and a shell. The polymer, *tert*-butyldiphenylsilane-polyethyleneoxide-*S*-polystyrene-*N*-bromine $[TBDPS\text{-}PEO)_1\text{-}S\text{-}(PS\text{-}Br)_2]$ was modified to obtain $(COOH\text{-}PEO)_1\text{-}S\text{-}(PS\text{-}N_3)_2$ (Figure 7.6). The functionalization of the polystyrene (PS) arms with azide terminal groups provides a means for the chemical grafting of propynyl-terminated gold nanoparticles around silver nanowires by an azide–alkyne 'click' reaction.

Silver nanowires were stabilized with 11-mercaptoundecanol. The esterification reaction between the three-arm star polymer linkers and the hydroxyl groups on 11-mercaptoundecanol-functionalized silver nanowires was carried out in *N,N*-dimethylformamide. For the spherical gold nanoparticles, propynyl-11-mercaptoundecanoate was used as the ligand. Click chemistry afforded the grafting of functionalized gold nanoparticles to the azide-bearing nanowires.

Nanocomposite films with Pd–PdO nanoparticles uniformly anchored onto the inner surface of TiO_2 nanotubes can be achieved through a stepwise bioredox/artificial oxygenation approach by using the natural eggshell membrane (ESM) as a template (Figure 7.7) [56]. Not only the macroscopic architecture but also the microscopic structure of the ESM template is faithfully reproduced by Pd–PdO/TiO_2.

The formation of Pd nanoparticles consists of two steps: (i) the nanoporous structure; and (ii) the absent oxygen linkage of the ESM biofibers constitute effective nanoreactors for the *in situ* reduction of Pd^{2+} when the ESM is immersed in the $PdCl_2$ solution. In addition, the coordination is insufficient to maintain isolated metal atoms in the glycoprotein matrix, because of their high mobility and reactivity. Therefore, when the ESM is immersed in the $PdCl_2$ solution, $[PdCl_4]^{2-}$ ions can be reduced by various ESM radicals to form Pd nanoparticles. During soaking in Ti-sol solution in succession, as a result of the strong affinity of the ESM glycoprotein mantle, the Ti-colloids are quickly arrested by various functional groups (notably hydroxyls) of the ESM macromolecules on the ESM fiber surface, attended

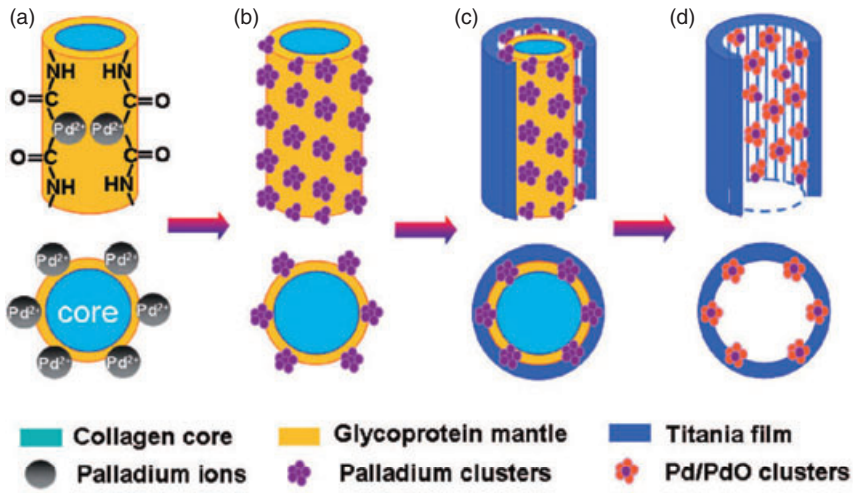

Figure 7.7 Schematic of the synthesis of hierarchical Pd–PdO/TiO_2 nanocomposites through the eggshell membrane-directed interfacial sol–gel process. (a) Interaction between Pd ions and glycoproteins; (b) *In situ* reducing formation of Pd nanoclusters; (c) Formation of TiO_2 films; (d) Pd–PdO-reinforced tubular TiO_2 after calcination treatment.

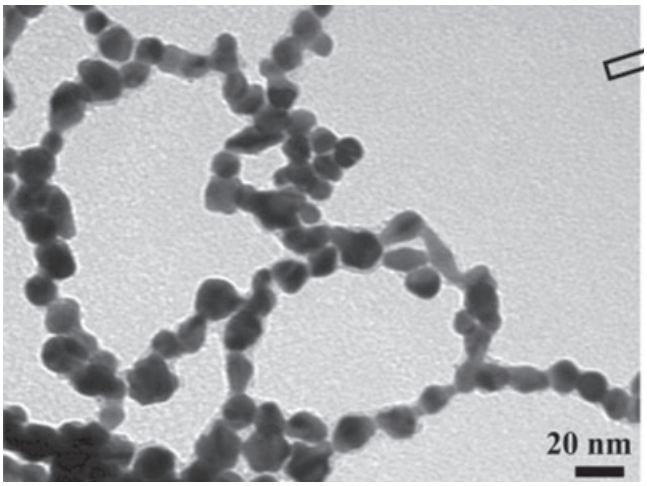

Figure 7.8 Pearl necklace-type gold–silver bimetallic nanoparticle capped by DMPG (1,2-dimyristoyl-*sn*-glycero-3-[phospho-*rac*-(1-glycerol)]). Reproduced with permission from Ref. [57].

by a condensation reaction. Thus, the Ti-impregnated ions are tightly anchored on the host ESM fiber surface, further forming a uniform guest coating. The amorphous coating can be fixed by the former Pd/glycoprotein hybrids, which might weaken the shrinkage of the sinters to realize perfect replication in size by the calcination. Upon calcination, the ESM template is removed, giving rise to the self-supporting TiO_2 hierarchical textile.

Phospholipids can be used in the preparation of a 'pearl-necklace' arrangement of gold and silver nanoparticles [57]. The phospholipids may serve as excellent capping agents for the synthesis of noble metal nanoparticles, as they provide both steric and charge stabilization to the colloidal metal nanoparticles by forming a lipid bilayer on the surface of the nanoparticles. The presence of a bilayer thus prevents anisotropic growth and leads to the formation of 1-D monodisperse nanoparticles. The origin of the pearl-necklace arrangement is thought to arise from the fusion of lipid bilayers around the different nanoparticles (Figure 7.8).

7.3 Anisotropically Shaped Nanoparticles: Nanorods and Nanowires

Multisegment nanowires (NWs) and nanorods (NRs) represent a unique platform for engineering multifunctional nanoparticles for a wide range of applications.

Both, NWs and NRs show peculiar characteristics which are dependent on their size, with the greatest effects observed in the 1–10 nm size range; this is due mainly to the large surface area-to-volume ratio of nanoparticles, which increases

the surface free energy to a point that is comparable with the lattice energy. NW/NR building blocks are of particular interest as their inherent shape anisotropy offers additional degrees of freedom for manipulation compared to spherical particles. In addition, as with core-shell and alloy nanoparticles, multisegmented nanoparticles exhibit characteristic electronic, optical and catalytic properties, which are significantly different from those of their individual constituent metals. Indeed, it is for this reason that NWs/NRs are of considerable interest in the basic and applied biotechnology sciences [58, 59]. The introduction of multiple segments along the length of NWs/NRs can lead to additional versatility associated with an ability to introduce multiple, well-differentiated chemical functionalities. Recently, in fact, the properties of NWs/NRs have been exploited and designed for specific biological applications by taking advantage of the supplemental degrees of freedom associated with their shapes.

The chemical modification of NWs/NRs can be used to tailor the surface properties, including hydrophilicity, charge and charge distribution, to impart a specifically determined chemical reactivity, and to introduce molecular recognition for small molecules (e.g., drugs), biopolymers, protein assemblies and other nanoparticles. The ability to control these parameters is largely dependent on the synthesis or fabrication technique. During the past few years, a huge number of reports describing new synthetic methods for the preparation of NWs/NRs have been reported [59]. The main strategies include high-temperature catalytic processes [60], pulsed-laser ablation/chemical vapor deposition (PLA-CVD) [61], vapor–solid–liquid (VLS) growth processes [62, 63], the evaporation of mixed powders [64], epitaxial growth processes [65, 66], and deposition into hard templates [67–71]. The latter approach will undoubtedly become the most frequently used method for the synthesis of multisegmented rods, based on its lower cost and ease of production.

In line with the scope of this chapter, we will in the following sections restrict our survey to recent methods for the functionalization of bimetallic nanowires and nanorods with biomolecules, with special attention being paid to their potential biomedical applications. The synthesis and potential catalytic activity of bimetallic stripes rods, despite representing a huge and important application, will not be considered here [72].

7.3.1 Surface Modifications

One major challenge in synthetic nanotechnology is not only to customize the size, shape and composition of nanoparticles, but also to optimize their functionality. The introduction of different metals in a single architecture allows for the selective functionalization of portions of the nanoparticles and avoids the molecular interferences that often occur with randomly distributed groups. In order to achieve successful functionalization, NWs/NRs should be cleaned and isolated, and each reaction should correspond to the appropriate surface chemistry of the metal. For example, gold wires are most often functionalized with thiols, nickel is

usually functionalized with carboxylic acids and siloxanes, which bind to the native oxide layer on the metal, while isocyanides bind strongly to platinum and palladium. Other examples of preferred adsorption of ligands to metal surfaces are listed in Table 7.1 [73].

In 1999, the orthogonal functionalization of Au–Pt–Au striped bimetallic nanorods (Figure 7.9a), based on the differential reactivity of platinum and gold [74], was successfully accomplished, giving an entry point into the construction of two- and possibly three-dimensional structures by self-assembly. The nanorods were synthesized using electrochemical methods, producing metal rods with lengths ranging from 200 to 300 nm. The bare bimetallic nanorods were first solvated with 1-butaneisocyanide and then treated with 2-mercaptoethylamine. The affinity of thiols for gold was able to displace isonitriles from Au, such that the nanorods were recovered selectively. Finally, fluorescent Rhodamine B isothiocyanate was reacted with the previously amino-functionalized gold segment of nanowires. An examination using fluorescence microscopy revealed that the orthogonal method

Table 7.1 Ligands and surface linkages.

Ligand	Metallic surface	Linkage
R—S—H	Au, Ag, Cu, Hg, Fe	R—S—
R—S—S—R'	Pt, Pd	R'/R—S—
R—C≡N	Metal oxides	R—C≡N—
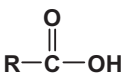	Metal oxides	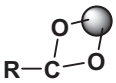
		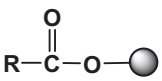
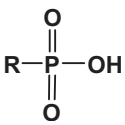	Metal oxides	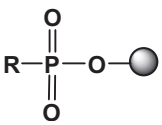
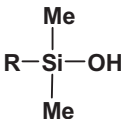	Metal oxides	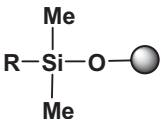
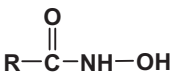	Metal oxides	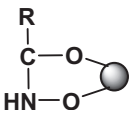

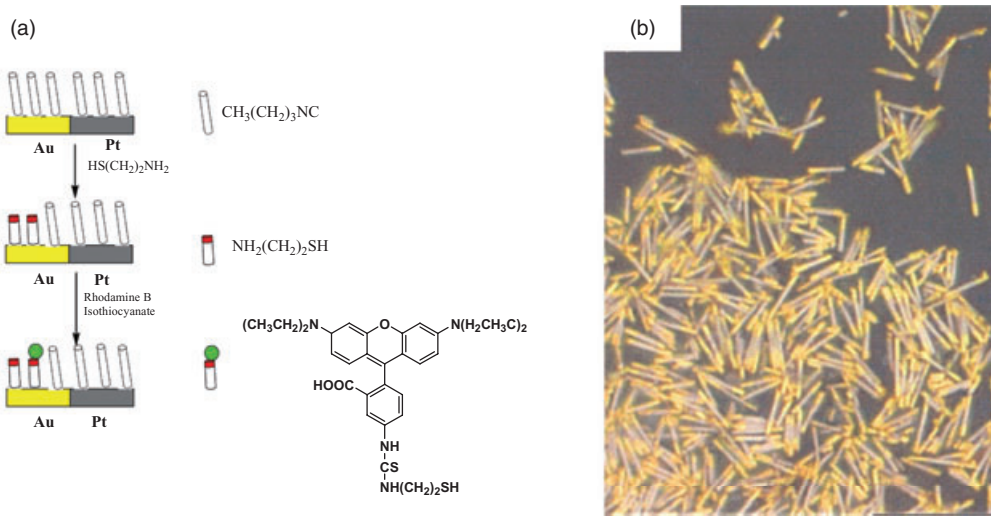

Figure 7.9 (a) Schematic representation of the strategy used for the orthogonal self-assembly on gold and platinum; (b) Bright-field optical micrograph of Au/Pt/Au nanorods. Adapted from Ref. [74].

set-up reported by Mallouk and coworkers was working successfully, leading to selectively functionalized multisegmented nanorods (Figure 7.9b).

Meyers and coworkers used a related approach to show that orthogonal self-assembly is also effective with a two-segment nickel–gold nanowire (Scheme 7.1) [75, 76]. These nanowires, which were synthesized by electrodeposition within alumina templates, were about 350 nm in diameter and typically 12–22 μm in length. The NWs were first reacted with 11-aminoundecanoic acid and 1,9-nonanedithiol, after which the functionalized wires were coupled to two different activated organic dye molecules that selectively reacted with the thiols and with amine groups. The result was a type of nanowire that emitted light of different colors on each segment, as observed with fluorescence microscopy.

7.3.2
NW/NR Functionalization with Protein Molecules

The relative binding affinities and the order of functionalization are crucial for achieving elective functionalization of multisegment NWs/NRs. Functionalizing with proteins and other biomolecules is further complicated by the fact that biomolecules – and particularly proteins – bind nonspecifically to ionic and hydrophobic surfaces. Therefore, the difficulty resides in selectively removing the proteins or in making the surface selectively protein-resistant. In a fundamental contribution to this field [77], four methods for the selective functionalization of Ni/Au and Pt/Au NWs/NRs with proteins through the formation of strong cova-

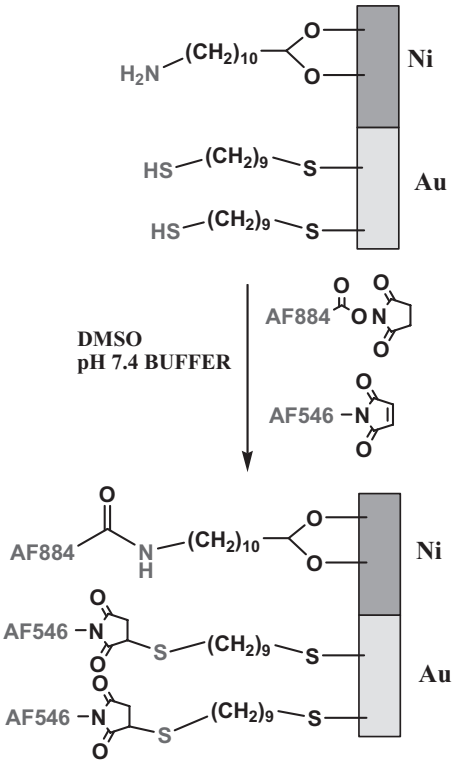

Scheme 7.1 Orthogonal self-assembly on gold and nickel.

lent linkages were presented. As shown in Scheme 7.2a, a protein is selectively bound to the gold end of a gold/nickel nanowire by a thiol linkage. To minimize protein adsorption onto the Ni segment, the surfaces of the NRs were first exposed to an amine-terminated siloxane, which has a very high affinity for nickel, and further functionalized with a PEG layer, which provided a hydrophilic surface with a low affinity for proteins. On the other hand, thiol groups conjugated to the protein were able to displace any nonspecifically bound siloxane from the Au segment, leading to the selectively functionalized NRs.

A similar approach to functionalize a bimetallic nanowire made from Au and Pt segments is shown in Scheme 7.2b. Here, the NWs were first treated with 1-butane-isocyanide, which has a strong affinity for Pt but is bound nonspecifically to the Au segment. When the NWs were treated in the presence of a thiolated protein, isocyanides were displaced from the Au segment, leading to protein-functionalized NWs. Such Au/Pt NWs exhibited a significant advantage as compared to Au/Ni NWs, as they did not show important aggregation phenomena. Scheme 7.3 shows two additional methods for the selective introduction of a protein onto a multisegmented nanowire. In both cases, the protein was bound to NWs through a biotin–avidin–biotin system. The Pt segments were first functionalized with

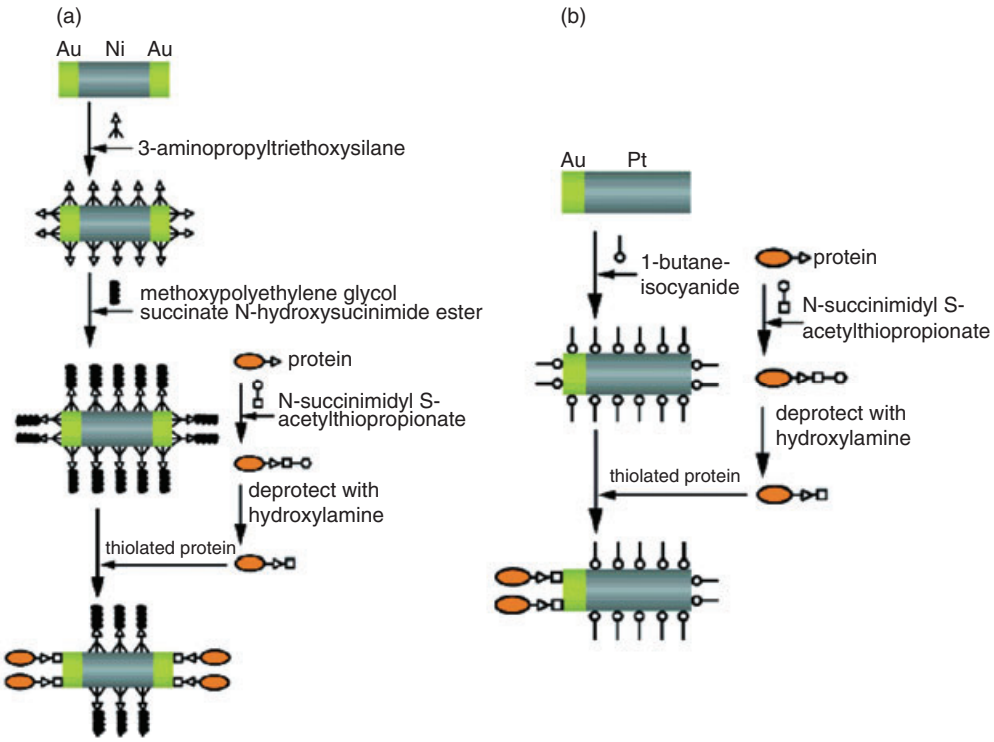

Scheme 7.2 (a) Thiolated KE2 antibody bound to Au segments on Au/Ni/Au nanowires; (b) Thiolated ActaA-NH_2 protein bound to Au segments on Au/Pt nanowires. Adapted from Ref. [77].

1-butane-isocyanide to minimize protein adsorption, after which the Au was decorated with an amine-terminated thiol. The NWs were then exposed to a biotin-terminated succinimide with a PEG spacer, which bound to the Au surface, and avidin was then attached to the biotin on the nanowires. In Scheme 7.3a, the protein was biotinylated through a terminal cysteine residue and then linked to the surface of NWs by avidin. In Scheme 7.3b, the protein was biotinylated by reacting with sulfosuccinimidyl-6-(biotinamido)-hexanoate (sulfo-NHS-LC-biotin) and successively linked to NWs via a biotin–avidin linkage. The selective protein functionalization was demonstrated for each method using light and fluorescence microscopy.

Biotin–avidin coupling, which is recognized as one of the strongest biological interactions [78], is commonly exploited for the bioconjugation of various types of organic and hybrid materials. This method was used by Searson in 2004 to direct the end-to-end assembly of Au/Pt/Au multisegment nanowires [79] that were 300 nm in diameter and 4.5 μm in length. Selective functionalization was achieved through a thiol linkage on the gold segments and an isocyanide linkage on the

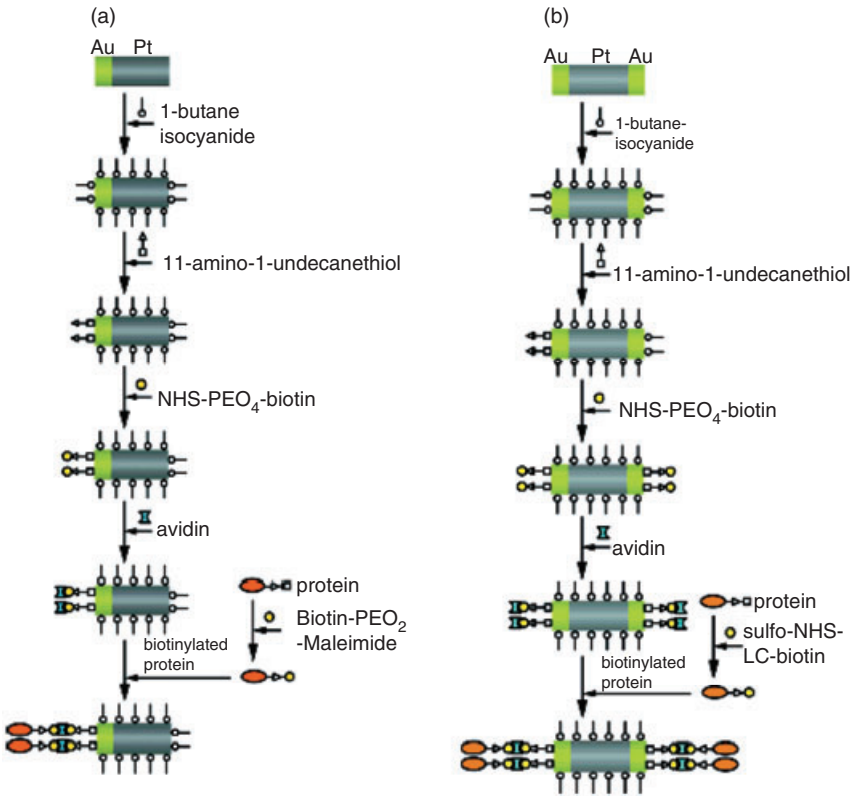

Scheme 7.3 (a) Biotinylated ActA-Cys bound to Au segments on Au/Pt nanowires; (b) Biotinylated ActA-NH_2 protein bound to Au segments on Au/Pt/Au nanowires. Adapted from Ref. [77].

central platinum segment, as shown schematically in Scheme 7.4. In this case, the goal of the functionalization was to improve and control the connection of a single nanowire to assemble higher-order structures through particle–particle interaction. To achieve this goal, a biotin-terminated thiol (BPT) was bound to the gold segment and avidin was bound to the biotin groups of a small portion of bifunctionalized nanowires. The final coupling between nanowires and avidin-terminated gold end segments resulted in directed end-to-end assembly. Butane isocyanide functionalization of platinum segment was essential to avoid nonspecific binding and hence minimize lateral assembly.

As already mentioned, the surface functionalization of metallic nanoparticles generally occurs via the formation of self-assembled monolayers (SAMs). These monolayers can be further modified either by the formation of new covalent bonds (see above) or through a noncovalent linkage of the protein to one of the metallic segments (Scheme 7.5) [75, 80]. Noncovalent interactions are extremely relevant in many biological systems, including the complex tertiary structure of proteins

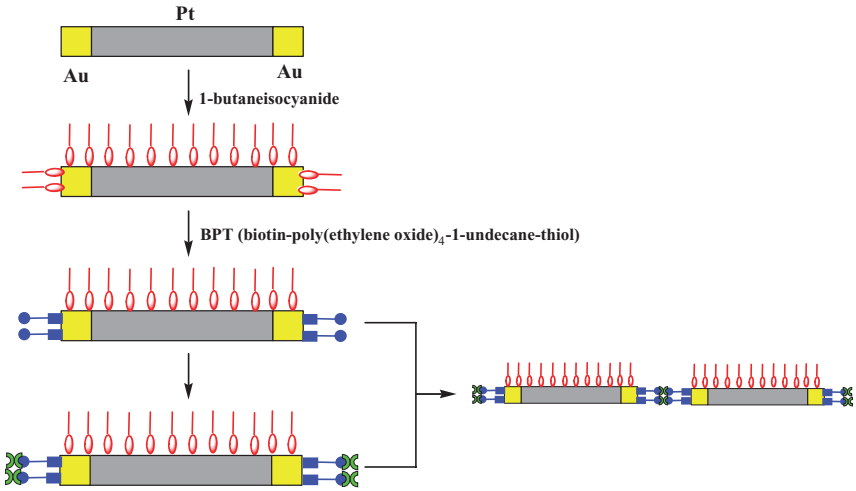

Scheme 7.4 Schematic illustration of a general approach for directed end-to-end assembly of Au/Pt/Au nanowires.

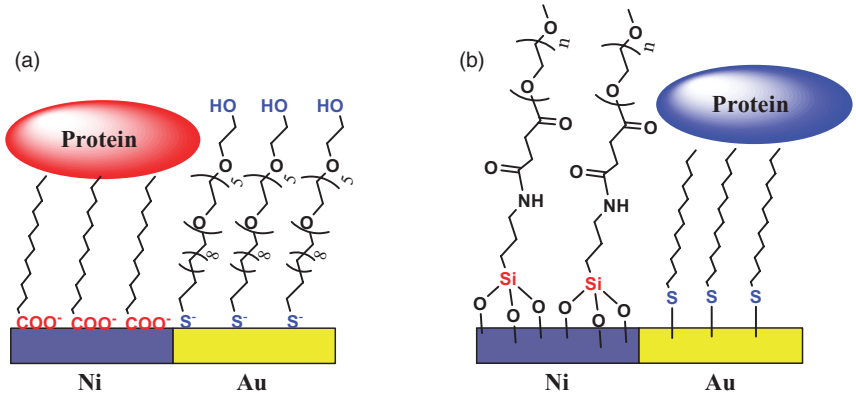

Scheme 7.5 (a) Selective protein adsorption on nickel surface of Au/Ni nanowires; (b) Selective protein adsorption on gold surface of Au/Ni nanowires.

and the hydrogen bonding network that holds together complementary strands of DNA. Starting from a pioneering study of Whitesides [81], a mixture of hydrophobic and hydrophilic compounds have been attached on nanowire surfaces to selectively introduce proteins via noncovalent linkages.

In a first example (Scheme 7.5a), gold was chosen as the protein-resistant segment: to create the resistant surface, Au was functionalized with (1-mercaptoundec-11-yl)-hexaethylene glycol (EG_6-SH). Nickel, on the other hand, was treated with a solution of palmitic acid to create a hydrophobic, alkyl-terminated surface. In order to investigate the interaction of proteins with these NWs (diam-

eter 200 nm, 10–25 μm long), an antibody which was covalently bound to a fluorescent molecule was used. In general, it was observed that the Ni segment showed a bright fluorescence, in contrast to Au segment, demonstrating that proteins are adsorbed preferentially onto the hydrophobic nickel surfaces. More recently, Fond *et al.* presented further results and the details of an inverse functionalization on a gold–nickel nanowire (Scheme 7.5b) [82]. In this latter case, the gold segment was functionalized with a solution of nonylmercaptan to obtain a hydrophobic surface, which was then used for protein adsorption. In contrast, the nickel segment was first treated with 3-aminopropyltriethoxysilane, to decorate the surface with free amine-terminated groups. The NH_2 groups were then used to introduce a hydrophilic surface by treatment with methoxypolyethylene glycol succinate *N*-hydroxysuccinimide ester. Both protein nanowires were used to evaluate protein selective adsorption by fluorescence-labeled anti-rabbit IgG. As expected, the gold and nickel surfaces covered by oligoethylene chains were not available for protein adsorption due to their hydrophilicity. The surfaces functionalized with hydrophobic monolayers, yielded a better protein adsorption in the case of gold functionalization, while methyl-functionalized nickel surfaces proved to be moderately wettable. An explanation for this difference can be found in the strong structural stability of alkanethiolate monolayer on gold (Scheme 7.5b) while the nickel segment can present monolayer defects for the presence of a native oxide layer on nickel segment (Scheme 7.5a). Despite this minimal difference, the fluorescence assay confirmed a selective functionalization of the two bimetallic nanowires, showing that multicomponent nanostructures can be modified at the molecular level to yield new materials which may find useful applications, for example in the study of cell–cell interactions.

What we have described so far provides the impression that there is a broad, growing interest in the use of nanoparticles and/or nanorods in aqueous solution as substrates for the attachment of various chemical and biochemical species. The NRs and NWs along their length provide interesting enhanced capabilities for applications such as control and detection. The use of metallic particles in aqueous solution requires the control of aggregation, adhesion and transport of the particles. Recently, Rose and coworkers reported the results of their experiments aimed at the measurement of the zeta potential of metallic and bimetallic nanorod particles in aqueous media [83]. The zeta potential is defined as the effective surface potential at the hydrodynamic 'shear plane' close to the solid–liquid interface, and represents a key parameter governing the electrophoretic mobility of particles in solution. Thus, larger zeta potentials of like-sign maximize the electrostatic repulsive force and therefore minimize the aggregation. The authors synthesized mono and bimetallic (Au and Ag) nanorods characterized by a SAM using thiol linkages formed in the presence of mercaptoundecanoic acid. Some particles were subsequently derivatized with proteins by attaching them to the carboxyl groups at the free ends of the mercaptoundecanoic acid (Scheme 7.6).

In the case of bimetallic nanorods, the zeta potential is a function of pH, and the profile is a reasonable mean between the zeta potential values measured on each individual metal nanorod. Moreover, all the results are useful to predict and

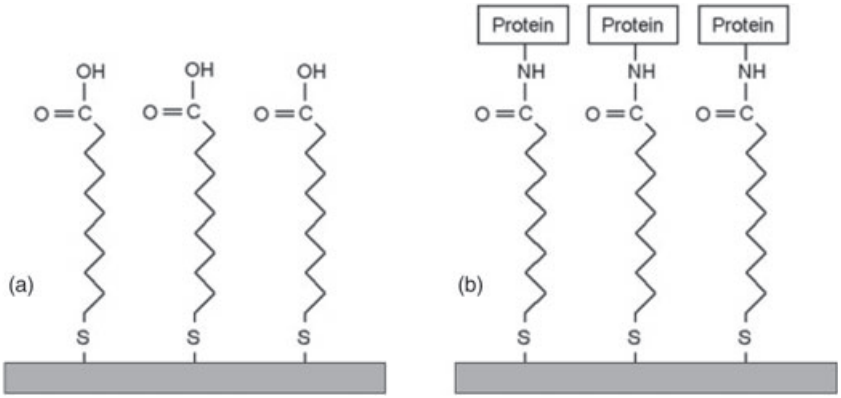

Scheme 7.6 Schematic representation of Au/Ag nanowire functionalization. Reproduced with permission from Ref. [83].

control the aggregation, adhesion and transport of such particles. They also suggest that, in order to minimize aggregation and adhesion, acidic solutions should be avoided: in fact, the value of the zeta potential is higher at moderate pH and lowest at a very acidic pH.

7.3.3 NW/NR Functionalization by DNA

The ability of multisegmented nanowires to lead favorably to selective functionalization opens the doors to multiple sophisticated applications such as gene therapy, vaccine field or cancer cell recognition. The challenge in these applications is represented by the efficiency in DNA surface immobilization and in cell recognition. Currently, synthetic gene-delivery systems have been limited by the control of nanosized delivery systems, and by limits in their ability to incorporate foreign DNA inside a target cell. Fabrication of the segmented wires can face these problems to provide an outlet of control in nanosized dimensions, being engineered with different functionalities. In fact, Au/Ni nanorods and their selective functionalization have been used to offer a precise control of antigen placement, and also to have the possibility of stimulating multiple immune responses [84]. The goal of gene therapy for therapeutics is to introduce foreign genes into somatic cells, either to supplement defective genes or to provide additional biological functions. In their studies, Salem *et al.* presented a no-viral gene-delivery system based on intelligent bimetallic nanowires capable of binding simultaneously and selectively to DNA plasmid and targeting ligands (Scheme 7.7).

In these studies, the authors were able to bind DNA to Ni segments by suspending NRs in a solution of 3-[(2-aminoethyl)dithio]propionic acid (AEDP). The carboxylic functionality of AEDP bound to the native oxide on the nickel segment, while the primary amine was used in a second step to conjugate plasmids to the nanowires. To further compact the DNA bound to the nanorods for more efficient

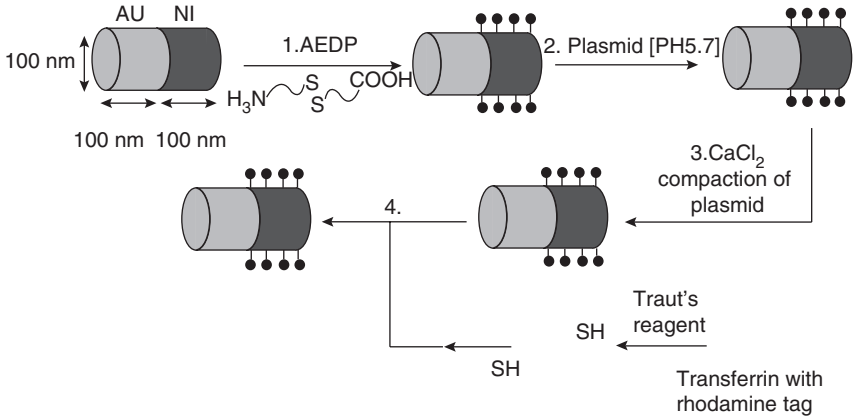

Scheme 7.7 Selective binding of DNA plasmids and transferrin to multisegmented nanowires. Adapted from Ref. [84].

cell entry, and to protect the DNA against enzymatic degradation, the NRs were incubated in a solution of Ca^{2+}, which has a high affinity for DNA. A gold segment was used instead to attach a cell-targeting protein, transferrin, which is one of the first proteins exploited for receptor-mediated gene delivery. The transferrin was bound to the gold segments via a thiol linkage, converting the primary amine groups to sulfhydryl groups. A rhodamine tag on the transferrin provided a mechanism to confirm the presence of NRs inside the cells. Moving on, the same group carried out investigations on the potential of this system in genetic vaccination [85], where the goal was to prepare antigen nanowires that would subsequently be taken up by macrophages or dendritic cells. For this, they anchored plasmids or the antigen ovalbumin (which is involved in a number of pathologic conditions related to infant diseases) to the different segments (Au or Ni), as described above. The ovalbumin was bound to the gold segment of the NRs through a thiolate linkage, following the conversion of a small portion of the primary amine groups of ovalbumin to sulfhydryl groups. DNA was instead bound to nickel segments by electrostatic interactions, using AEDP as a suitable linker. In order to evaluate the genetic vaccination potential of these nanorods, antibody and CD8+ T-cell responses were measured. The authors noted that the coaddition of plasmids, which act as a strong immunostimulatory adjuvant to antigen, and the ovalbumin antigen on the nanorods generated a significant increase in CD8 response compared to the nanorods bound to ovalbumin alone. Therefore, multicomponent nanowires potentially might provide an advantage in gene therapy applications. These results paved the way for an exciting application of the selective functionalized nanorods in vaccine field, extending this approach to other gene targets.

Another very attractive area where nanowires have been used is in the development of advanced molecular binders, with greatly improved properties for cellular studies. Tan and coworkers used Au/Ag nanorods as nanodevices to monitor

multivalent binding by multiple aptamers (RNA or DNA) on the rods to increase both the signal and binding strengths of these aptamers in cancer cell recognition [86]. In fact, the molecular assembly of aptamers on the NR surfaces also significantly improved the binding affinity with cancer cells, through simultaneous multivalent interactions with cell membrane receptors. These investigators incorporated the aptamers onto NR surfaces through simple thiol linkages. The aptamers were decorated with a linker that comprised three segments: (i) a thioalkane hydrocarbon, that promoted the self-assembly of a monolayer; (ii) a hydrophilic segment of ethylene glycol that separated the alkanethiol from the aptamer and avoided steric hindrance with proteins interacting with aptamers; and (iii) the recognition unit of aptamer, which is the 'real' molecular probe. The aptamer loading on the NR surface was determined by fluorescence measurements of fluorescein-labeled oligonucleotides. The group obtained very interesting results, being able to demonstrate the use of NRs as an efficient multivalent platform for the molecular assembly of aptamers for target cell recognition. The target cells were clearly visualized via their strong fluorescence due to the multiple aptamers for the molecular imaging of cells, while the binding affinity of the NR–aptamer conjugates was greatly increased compared to that of single aptamer molecules. Such strong affinity of NR–aptamer conjugates for carcinoma cells meant that these nanomaterials showed great promise for use in cancer cell studies and for targeted therapy, such as hyperthermia in photothermal therapy.

7.3.4 Detection and Sensing

Although, when considering nanomaterials, biosensing has been regarded as a very popular topic during the past few years, multiplexing and miniaturization have also been seen to correlate directly with the major results in this field of research. In fact, the push to measure ever-increasing numbers of species from smaller sample volumes has led to innovative devices for sample manipulation and ingenious approaches to multiplexing analysis (i.e., from microarray to micropolymeric beads).

One very interesting application of multisegmented nanorods is as 'barcoded' particles in multiplexed bioanalysis. Among the metals used as segments in these particles, Au and Ag are particularly attractive due to the large difference in reflectivity between them, which provides a high contrast for the readout of the striping pattern [87, 88]. Keating and collaborators synthesized two barcoded particles made from Au/Ag/Au (4 μm long) and Au/Ni/Au (8 μm long) stripes, which they used to encode information [89]. The particles were derivatized with 16-mercaptohexadecanoic acid, to which the capture antibody was covalently attached using carbodiimide chemistry. The Au/Ag/Au NRs were derivatized with the capture antibody to human IgG, while Au/Ni/Au NRs with the capture antibody to rabbit IgG (Figure 7.10). The functionalized nanorods were first exposed to both analytes (human IgG and rabbit IgG), and then incubated with a mixture of the secondary detection antibodies (rabbit IgG and human IgG), these being differently labeled

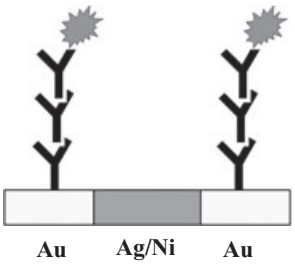

Figure 7.10 Schematic representation of rabbit and human IgG detection.

to test the selectivity of the respective chemistries. The production of barcodes that could be read using conventional brightfield reflectance optical microscopy confirmed that the specific capture chemistries of the two classes of particles were each able to selectively bind their target analytes. Moreover, the results showed that simultaneous immunoassays could be performed on nanowires, and that the reflectivity image was sufficient to identify the capture chemistry on a particle. Considering that it is possible to incorporate several different metals (Au, Ag, Pt, Pd, Ni, Co, Cu) in various lengths and in many stripe combinations, it is easy to understand the potential behind the development of such a biosensor.

Recently, the same group studied in depth the different aspects of this type of applications, and found that it was possible, by an appropriate choice of fluorophore and metals for the barcode stripes, either to accentuate or to obscure the underlying striping pattern in fluorescence images [87].

The application of nanowires to biomolecule detection has provided a major boost for research in this field. One of the current methods used for the real-time sensing of DNA in solution is to apply molecular beacons [90–92]; these are nucleic acid probe molecules designed with complementarity at their 3′ and 5′ ends such that they fold into a stem-and-loop (hairpin) structure. Normally, fluorophores and quenchers are attached to opposing ends of the sequence, and the presence of DNA complementary to the loop sequence leads to a fluorescence emission upon hybridization. However, when the loop is in the hairpin conformation the quencher is held close to the fluorophore, and this results in the fluorescence being quenched. During the past few years, several reports have been made on molecular beacon assays, in which the quencher is a single metal nanoparticle or a metal surface [93–95].

In 2005, Penn and coworkers applied molecular beacon methodology to bimetallic striped nanowires technology to overcome the limitations of using molecular beacons in solutions, notably the need for an organic quencher and a limited multiplexability [96]. Metal surfaces can, indeed, efficiently quench the emission from dyes located within a few nanometers from the surface, without the requirement of an organic dye. This well-documented phenomenon is referred to as Förster resonance energy transfer (FRET). Nanowire technology also has the ability to generate a library of encoded wires, simply by changing the order of the strip (gold and silver), and thereby achieving the goal of multiplexing. The

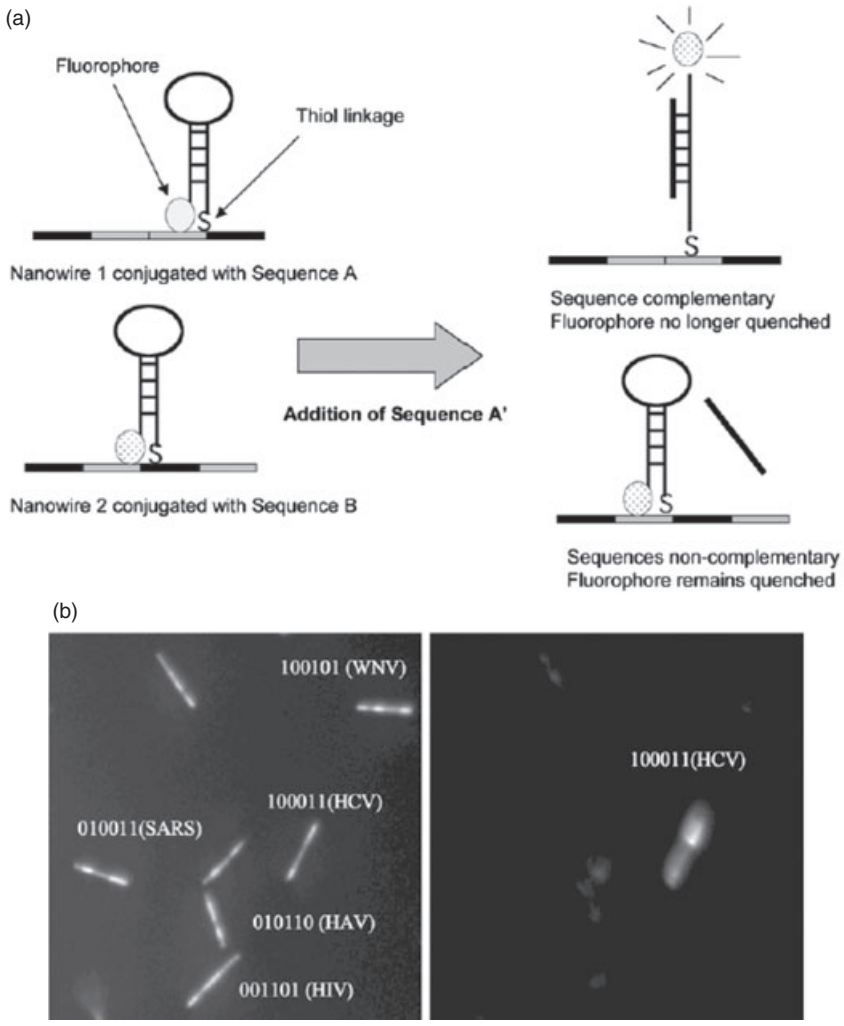

Figure 7.11 (a) Schematic description of the molecular beacons/nanowires experiment; (b) Representative experimental image. In the presence of the complementary viral DNA, fluorescence of the corresponding DNA-functionalized nanowire segment is restored. Reproduced with permission from Ref. [96].

nanowires used in these experiments were approximately 250 nm wide and 6 μm long; a schematic representation of the experiment is shown in Figure 7.11.

The oligonucleotides were decorated with a fluorophore on one side and a thiol group on the other, this being used for conjugation on the metallic segment of nanowires. The oligonucleotide contained a 10-base hairpin structure which forced the fluorophore into contact with the metallic surface, thus producing FRET. Upon

the addition of a target complementary DNA, the resultant DNA hybrid caused the fluorophore to move far from the surface, thus restoring the original fluorescence emission. As a proof of concept, the system was simultaneously applied to the detection of five viral pathogens, including hepatitis A virus (HAV), hepatitis C virus (HCV), West Nile virus (WNV), human immunodeficiency virus (HIV) and severe acute respiratory syndrome (SARS) (Figure 7.11b). The reflectance image (left) and the fluorescence image (right) provided examples of the success of these experiments.

A further study on the efficiency of the system, based both on the different dye positions in a single multiplexed experiment and on the differences in emission for probes attached to the two metals, was also conducted (for details on these conclusions, the reader is referred to Refs [97, 98]).

In addition to the potential for changing emission intensities by using metal-striped nanowire–dye conjugates for the detection of analytes, a number of studies have been conducted to determine if the use of sensors might minimize the complexity of the system. The separation of fluorescence-based sensing chemistry from the metal surface has the advantage to reduce – or in some cases even to eliminate – the interference occurring between the metal and dye, thereby increasing sensor performance. This evidence led to the development of a new type of multiplexing sensor which was based on Au/Ag striping nanowires and covered by a silica layer of variable thickness (from 6 to 150 nm), and capable of detecting three different target sequences simultaneously [99]. A further difference between the coated and bare systems was the type of chemistry used to anchor the probes onto the surface of nanowires. When a glass coating was introduced onto the metallic surface, oligonucleotides could be attached by using a siloxane-based modification rather than conventional thiol chemistry. However, this difference introduced an interesting advantage, as the DNA probe attachment seemed to be more stable, even at the high temperatures required for thermocycling reactions.

Within biosensor applications, nanowire-based field-effect transistors (FETs) have been widely used for the detection of a variety of biological and chemical species, pH value, metal ions, viruses and proteins. In most cases, the sensor is based on the functionalization of homogeneous monometallic nanowires. During recent years there has been a growing interest in fabricating multicomponent nanowires, which show major potential for applications in different fields, ranging from nanoelectronics to self-assembly. For these reasons, CdTe has become one of the most attractive semiconductors because of its optimum energy band gap and high absorption coefficient. The synthesis of striped nanowires comprising CdTe–Au–CdTe sequences has been achieved via a template method to yield NWs that were 230 nm in diameter and 5 μm in length, to study the sensing capability of multisegment nanowires for single-strand DNA (ssDNA) fragments [100]. Modulation of the nanowire's conductance before and after binding, and hybridization of the specific DNA target molecule, were detected using a back-gated current–voltage measurement. One major advantage in the use of a multisegmented nanowire resides in the fact that it is much more sensitive than a single metallic

nanowire. In experiments conducted elsewhere, ssDNA fragments with a thiol functional group at one end were bound selectively and efficiently to the gold surface of the heterostructure nanowires and served as the receptor groups. In order to control the outcome of the experiment, DNA-modified nanowires were incubated in a buffer solution, with a complementary single strand DNA (cDNA) and with a mismatching ssDNA. Hybridization with the cDNA strand was seen to be successful and was detected at very low concentrations; the authors also demonstrated that cDNA was not involved in any nonspecific binding with the metal surface.

Another interesting biofunctionalization of nanowires was introduced in 2006 by Ren and coworkers [101], who were interested in constructing hybrid devices by integrating nanowires with F_1-ATPase motors. This would offer exciting potential applications in the development of advanced biosensors for use in medical and therapeutic areas. In the past, motor proteins have attracted much attention for their ability to convert the chemical energy derived from ATP hydrolysis into mechanical work. Further, an ATPase motor can rotate in different directions, it is ubiquitous among organisms from bacteria to man, and it is the best characterized protein in terms of its atomic structure and biochemistry. In order to synthesize the hybrid devices, the authors created a multicomponent nanowire made from three segments of nickel/gold/nickel, which could be selectively functionalized to direct the binding of the F_1-ATPase motor to specific regions of the wire. The gold segments of NWs were functionalized by thiol groups of a modified and fluorescent ssDNA, while the nickel segment was decorated with a fluorescein isothiocyanate (FITC)-labeled biotinylated peptide. As a result of this selective functionalization, the F_1-ATPase motor could be bound to the nickel segment of NWs using biotin–streptavidin technology. Thus, it was shown – by a sequence of fluorescent images – that the multimetal NWs, when used as efficient propellers of motors, showed a rotation driven by the F_1-ATPase motor. In this way it would also be possible to control the arrangement of the different biomolecules on the designed nanoscale structures.

7.4 Profunctional Bimetallic Alloys

Bimetallic alloy nanoparticles exhibit unique electronic, catalytic and optical properties that are often remarkably different from those of the corresponding individual metal nanoparticles [102, 103]. The great majority of current synthetic efforts with bimetal alloys is directed to improve the catalytic activities of the metal substrates. However, some of the preparative methods employed to this purpose, might be conceptually transferred to the organic surface derivatization, thus paving the way towards the next generation of metal nanohybrids for biomedical applications. In particular, noble bimetal particles, such as gold–silver or gold–palladium alloys, exhibit exciting optical and electronic properties which make them suitable for consideration as nanostructured agents for biosensing and therapeutic targets.

Indeed, in contrast to core/shell type structures and segregated bimetals, for which two distinct plasmon bands are generally observed [104], bimetal alloys show a relatively sharp intermediate plasmon band, shifting between the two individual nanometal intrinsic bands. This results in the potential to develop sets of noble metal hybrid particles with finely tunable optical properties in a continuous wavelength absorption within the visible-NIR range, by varying composition, atomic ordering and cluster size. In light of this, we provide here a few illustrative examples of recent advances in the fabrication of alloy conjugates, and introduce a perspective which, in some cases, goes beyond the declared original intent of the respective investigators.

7.4.1
Dendrimer-Encapsulated Bimetal Nanoparticles

Dendrimer-encapsulated bimetal nanoparticles (DENPs) are self-organized hybrid nanostructures comprised of a metal core and an organic multibranched shell [105]. Dendrimers are monodispersed macromolecules with a repetitive, well-defined 3-D architecture. The interest in dendrimers for biological applications mainly resides in the multiple presentation of ligands in a controlled fashion [106], which usually results in a cooperative enhancement in the affinity for the respective receptors in recognition phenomena [107].

It is possible to control the physico-chemical properties of DENPs by tuning the number and nature of the side branches and the terminal functional groups, which are easily accessible for post-synthetic bioconjugation. Currently, DENPs are almost exclusively employed for applications in efficiency-enhanced catalysis. Interest in DENPs as catalysts resides in a number of concurrent factors, notably:

- The control of composition, immobilization and solubilization of nanoparticles is readily achievable.
- The organic wrapping stabilizes the nanoparticles in solution and prevents their aggregation, without passivating the metal surface, which would largely compromise its catalytic activity.
- Depending on the number of generations and substituents, it is possible to discriminate selectively between different substrates by controlling access to the encapsulated nanoparticles.
- Particles are easily recovered and redispersed for further utilization. Actually, the most widely explored among the various dendrimer sources are the low-generation hydroxyl-terminated poly(amidoamine) (PAMAM) dendrimers, because of the availability of amino groups for metal complexation (Figure 7.12) [108].

While the common synthesis of monometal DENPs usually makes use of a two-step strategy involving the intradendrimer amine complexation of metal ions,

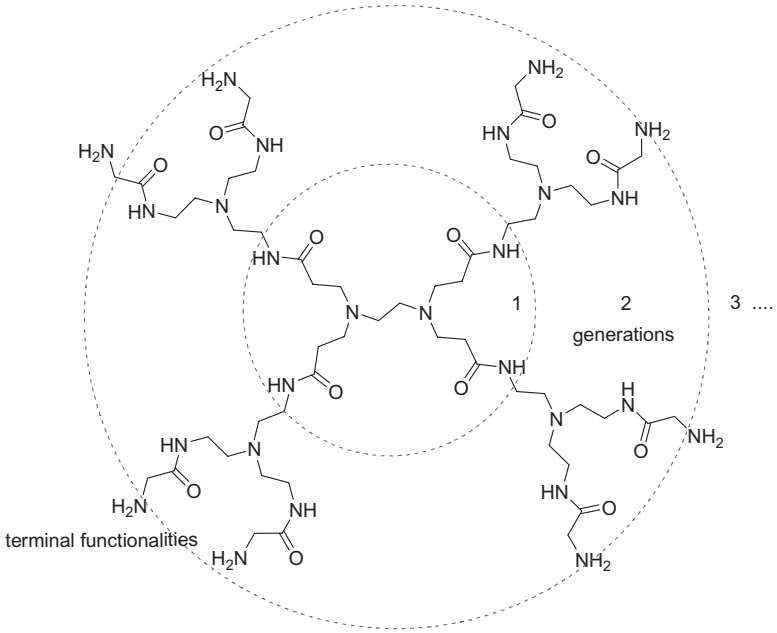

Figure 7.12 Representation of generation 2 PAMAM dendrimer.

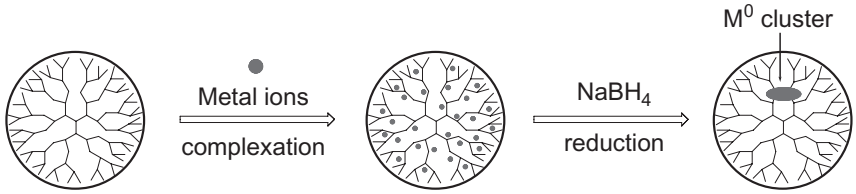

Scheme 7.8 Stabilization of metal nanoparticles by PAMAM dendrimers. Metal ions are first stabilized by complexation with the inner nitrogen atoms of tertiary amines within branches; reduction with $NaBH_4$ then leads to M^0, followed by metal clustering to form the nanoparticle.

followed by reduction to zerovalent metal atoms and aggregation to form the final nanocluster (Scheme 7.8), three different routes have been proposed for the generation of bimetallic DENPs (Scheme 7.9) [109]. The simultaneous co-complexation of two different metal ions, followed by a single reduction step, essentially leads to bimetallic alloys, while the partial displacement and sequential loading methods provide either alloy or core/shell nanoparticles, depending on the nature of the two metals.

In the preparation of mixed-metal intradendrimer nanoparticles by the co-complexation method, the absorption spectrum of a solution containing PAMAM,

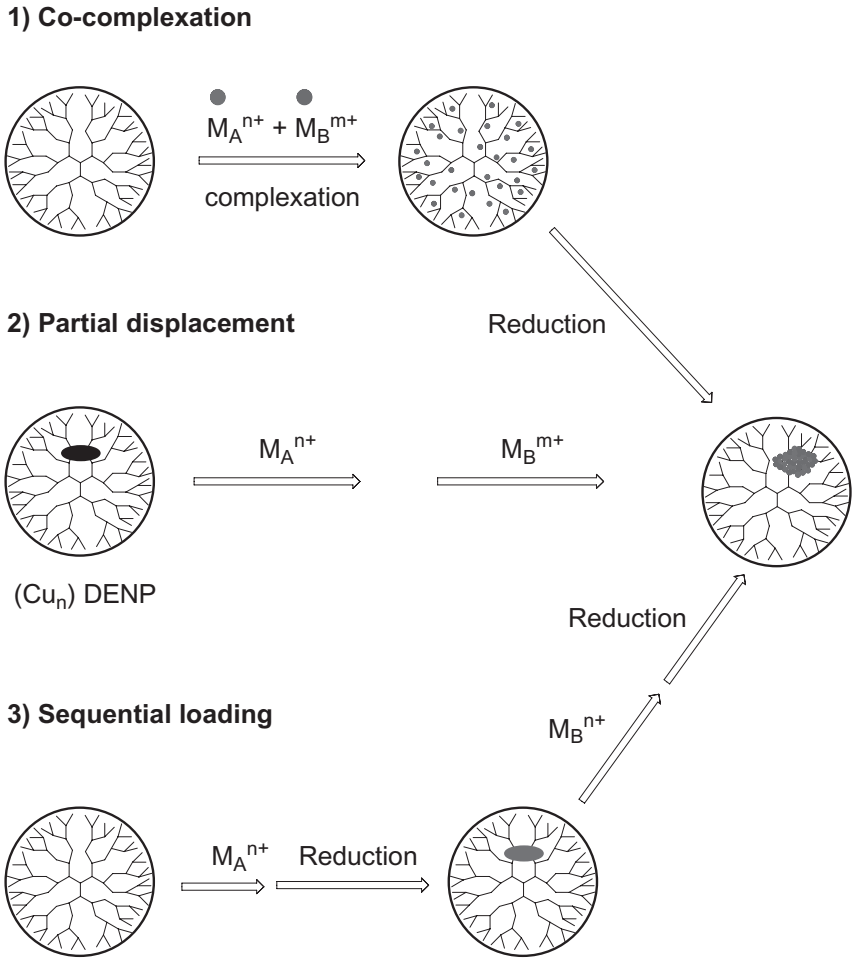

Scheme 7.9 Proposed mechanisms for the formation of bimetallic dendrimer-encapsulated bimetal nanoparticles.

$PtCl_4^{2-}$ and $PdCl_4^{2-}$ is the sum of the spectra of a solution containing generation 4 PAMAM + $PtCl_4^{2-}$ and a separate solution containing generation 4 PAMAM + $PdCl_4^{2-}$ [110]. This observation accounts for a co-complexation of Pt^{2+} and Pd^{2+} within dendrimers. After reduction of the complexed ion, a new interband transition with an intensity which is different from those of pure Pt–PAMAM and Pd–PAMAM nanoparticles, is recovered. Besides Pt–Pd nanoparticles, the co-complexation of two metal precursors has been exploited for the preparation of Pd–Rh [111], Pd–Ag [112] and Pt–Au nanoparticles [113]. The partial displacement method represents an extension of the displacement approach which is generally used for the synthesis of single metal nanoparticles. For instance, if a less than stoichiometric amount of Pd^{2+}, Pt^{2+}, Ag^{+} or Au^{3+} is added to PAMAM(Cu_n), it is possible to form

dendrimer-encapsulated Pd/Cu, Pt/Cu, Ag/Cu, Au/Cu bimetallic alloy nanoparticles, respectively [114].

When using the sequential loading method, bimetallic nanoparticles are prepared by two successive steps: (i) a solution containing PAMAM(Pt_{55}) is prepared by direct reduction; and (ii) $PdCl_4^{2-}$ is added to this solution to form a mixed metal-ion composite PAMAM [(Pt_{55}) + $(Pd_{55})^{2+}$] within dendrimer branches by exploiting the residual free amines. Once again, the interband transition due to the formation of the bimetallic nanoparticles appears, while that corresponding to the tertiary amine–Pd(II) complex disappears. Transmission electron microscopy (TEM) also confirmed a significant increase in particle size following the second reduction step.

7.4.2
Surface Stabilization by Ligand Exchange

As for the core/shell and multisegmented rod-shaped structural cluster organizations mentioned above, a general approach for the targeted surface modification of alloy nanoparticles consists of a thiol–ligand exchange. By adding a suitable excess of the target material, the thiol's high affinity for noble metal substrates allows for complete replacement of the ligand sphere, under several circumstances [115]. It should be noted that each individual metal element shows a characteristic affinity for thiols and other organic functional groups (see Table 7.1). For example, gold exhibits an extremely high affinity for thiols, while Pd prefers to coordinate with isocyanides [74, 116]. In this way, by exploiting the different reactivity of various metals towards thiols, carboxylates, amines, isocyanides and other metal-sensitive functional groups, it is possible – in principle – to introduce and differentiate any type of (bio)organic molecular structure through a post-synthetic surface ligand exchange by modulating the metal composition at the nanoparticle surface.

7.4.3
DNA Metallization

In the field of electronic circuitry, continuous miniaturization has reached a level where new methodologies and ideas are needed to overcome drawbacks, such as minimal sizes and costs, associated with conventional top-down fabrication processes, such as lithography. In this scenario, DNA plays a fundamental role on the basis of its potential to be highly programmable, stable, and readily available to be used as a template for the fabrication of nanoscale electronic building blocks. During recent years, the results of many pioneering studies on DNA metallization have been reported [117–119], comprising a seminal investigation of the first assembly of a FET based on a metallized DNA template [120]. In 2007, Simon and coworkers reported a peculiar method for the selective metallization of artificial DNA duplexes that were functionalized by incorporating a modified cytosine which carried an alkyne group [121]. This alkyne group was used to 'click' sugar

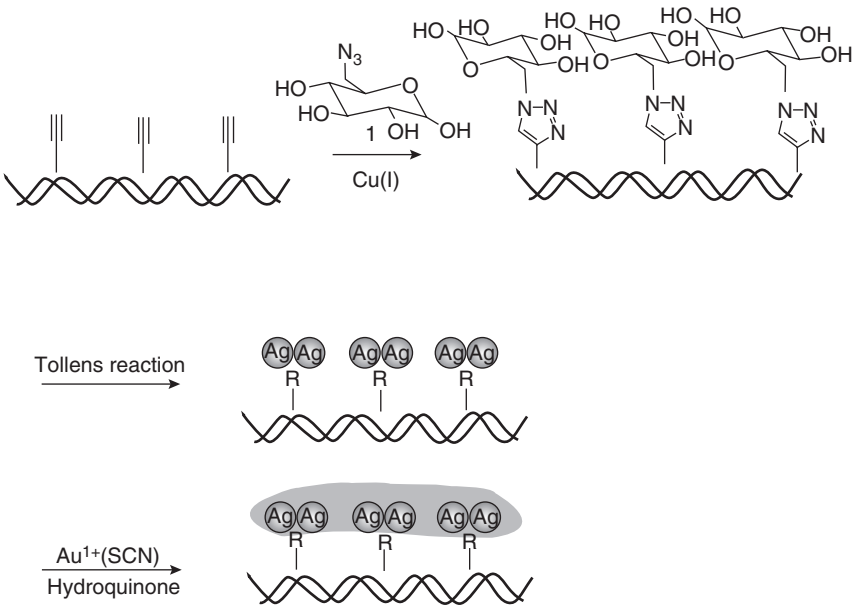

Scheme 7.10 Metallization of synthetic alkyne-derivative DNA. Reproduced with permission from Ref. [121].

azide derivatives along DNA strands via the copper(I)-catalyzed Huisgen 1,3-dipolar cycloaddition – this became known as 'click-chemistry' (Scheme 7.10). Both, the alkyne-tagged and sugar-modified DNA strands showed a length of approximately 300 nm, which coincided with the length of a 394 base pair DNA fragment.

The final metallization was accomplished in two steps. Initially, Tollens reagent was used to generate Ag^0 metallization around the sugar modification sites of DNA. Subsequently, the DNA strands were incubated in the presence of a solution of $KAuCl_4$ and KSCN to have a gold enhancement. The result was a DNA template coated with a homogeneous and dense metal layer with a diameter less than 10 nm, which could be useful in the fabrication of nanoscale electrical building blocks.

7.4.4
Miscellaneous

Anisotropic hollow nanodendrites with a bimetallic Au_xAg_{1-x} organization have been proposed as biocompatible systems for nanoparticle-assisted photothermal therapy against lung cancer cells (Figure 7.13) [122]. Here, the particles were fabricated by using a replacement reaction between Ag dendrite seeds and different concentrations of an aqueous solution of tetrachloroauric acid. $Au_{0.3}Ag_{0.7}$ nanodendrites exhibited the strongest absorption in the NIR region, which could be

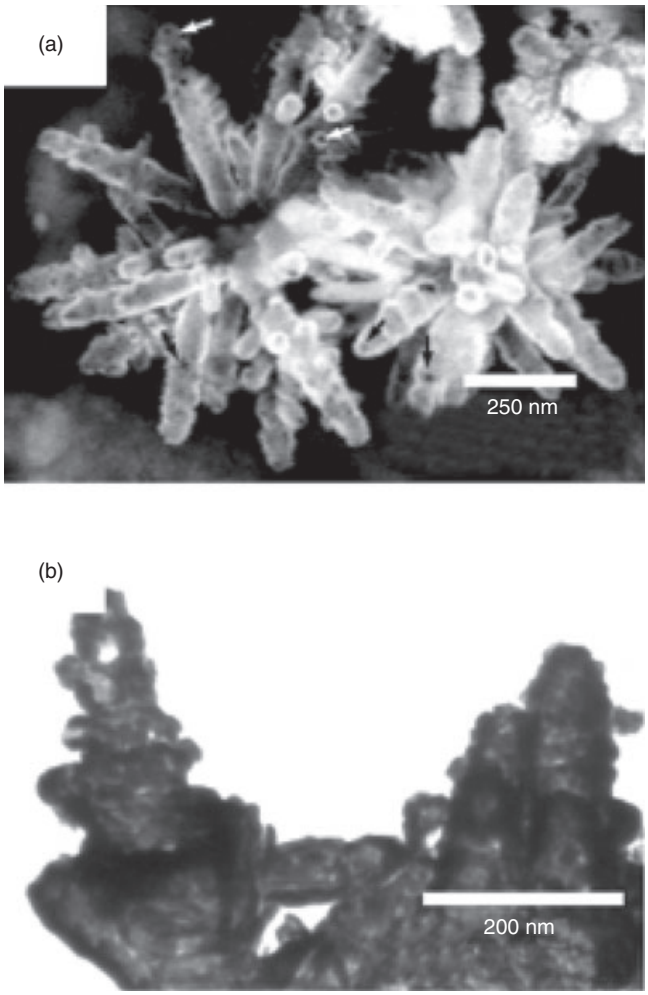

Figure 7.13 (a) SEM and (b) TEM images of core-free $Au_{0.3}Ag_{0.7}$ dendrites. The arrows in (a) show the voids on the tips of the stems of the dendrites. Reproduced with permission from Ref. [122].

exploited to transform an imparted NIR radiation into heat, thus providing a temperature increment which resulted in malignant tumor cell death (Figure 7.14). Since the A549 lung cancer cells used in that study overexpress the epidermal growth factor receptor (EGFR), such particles were conjugated with anti-EGFR monoclonal antibodies (mAbs) to evaluate their cancer cell-killing activity. The anti-EGFR mAb contains a positively charged domain, which allowed a tight electrostatic adsorption onto the strongly negatively charged surface of Au/Ag nanodendrites. Notably, anti-EGFR-conjugated nanodendrites maintained an elevated affinity for the EGFR receptors on the cell surface.

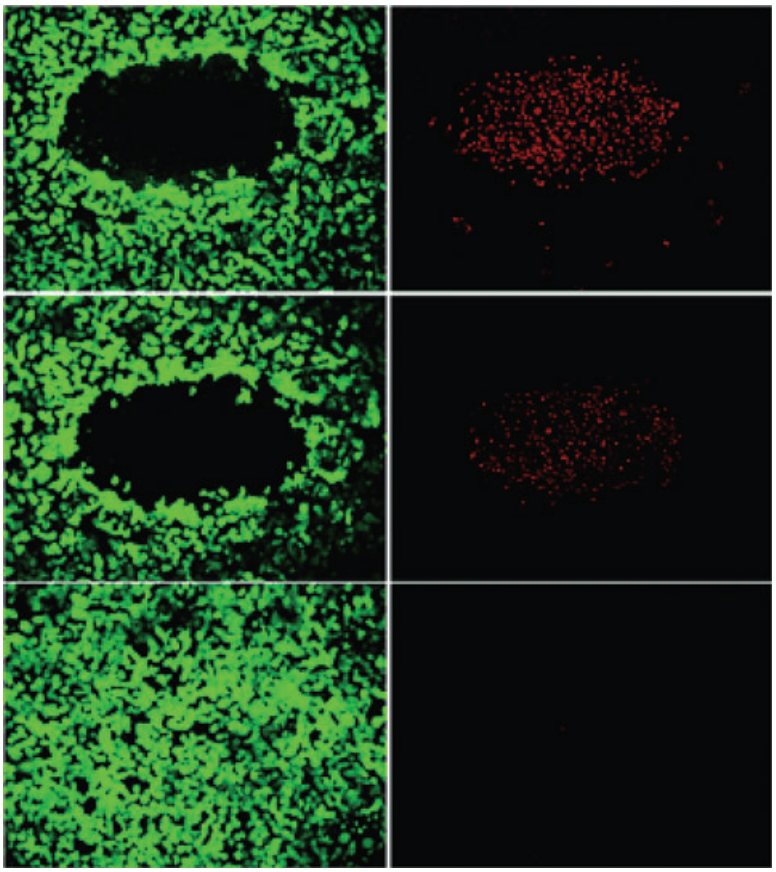

Figure 7.14 A549 cancer cells treated with anti-EGFR conjugated with $Au_{0.3}Ag_{0.7}$ dendrites were irradiated by laser dosages of 20 W cm^{-2} (top row), 15 W cm^{-2} (middle row) and 10 W cm^{-2} (bottom row). The left column shows staining with the green fluorescent dye, calcein AM, for living cells. The right column displays staining with EthD-1, in which the red fluorescence indicates cell death. Reproduced with permission from Ref. [122].

Stabilized biocomposite Au–Ag alloys nanoparticles were directly generated in a foam matrix using BSA as template [123]. The BSA zwitterionic character at the protein isoelectric point was exploited to simultaneously coordinate both (Ag^+) and ($AuCl_4^-$) ions in the foam. This hybrid metal complex promoted the subsequent formation of the protein-coated zerovalent bimetallic nanoparticles obtained by reduction of the coordinated ions, which was carried out by passing hydrazine hydrate vapors through the dry foam; this led to a dramatic coloring of the protein matrix. The thus-synthesized alloy nanoparticles were crystalline and substantially spherical in shape, and their size varied from 5 to 15 nm (as determined with TEM). Both, size and absorbance wavelength were dependent on the Au/Ag ratio. The authors noted that the optimal ratio for having a stable particle

dispersion was 3 Au:1 Ag. In principle, such an approach might represent a model system for producing variably substituted peptide-capped Ag–Au nanoparticles with tunable size, absorbance and a maximal wavelength within the 400–600 nm range.

McMillan *et al.* used a genetically engineered crystalline protein for patterning binary alloy nanoparticles. The octadecameric double-ring chaperonin TF55β exhibits a spontaneous tendency to arrange itself into 2-D hexagonal packing crystals (Figure 7.15). For this reason, it is particularly suitable for use as a tem-

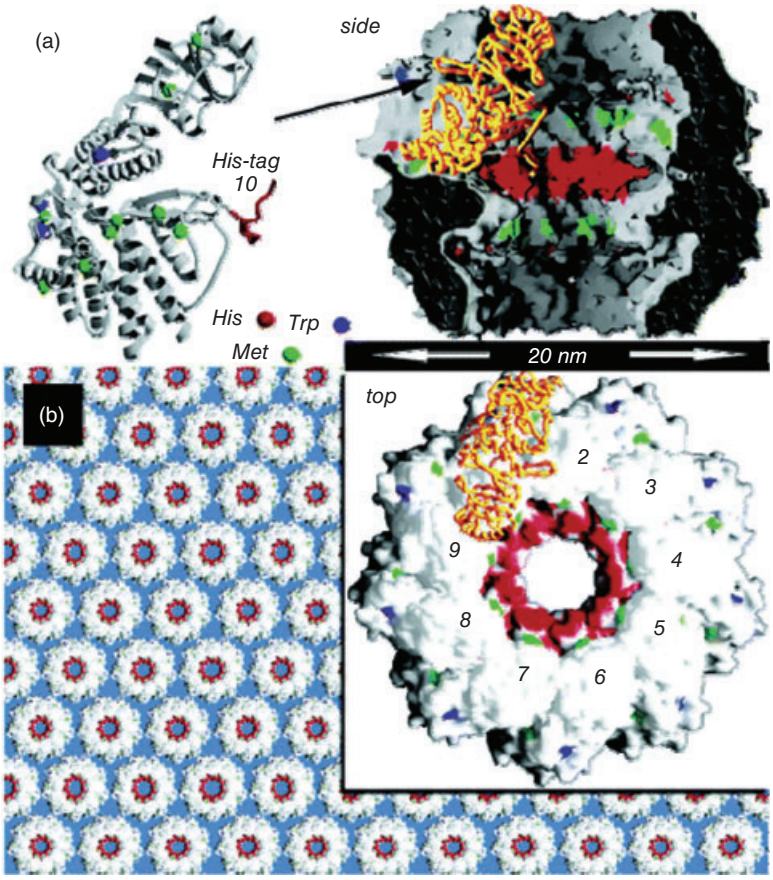

Figure 7.15 Assembly of engineered chaperonin templates. (a) Structures of the subunit (left) and the assembled chaperonin (right: cross-section side- and top-views) highlight (in red) the accessible 10 nm-diameter core functionalized with His; (b) Hexagonal packing of chaperonins into 2-D crystals serves as the basis for patterning nanoparticle arrays. Reproduced with permission from Ref. [124].

plate for highly ordered nanoparticle fabrication. Thus, both Ni–Pd and Co–Pd bimetallic nanoparticles were created by genetically replacing the peptide loop, which originally occluded the natural cavities, with an added polyhistidine sequence capable of coordinating metal ions. Such a procedure provided arrays of bimetal alloys with an extremely narrow size distribution, encapsulated within the self-assembled chaperonin biotemplate (Figure 7.16) [124].

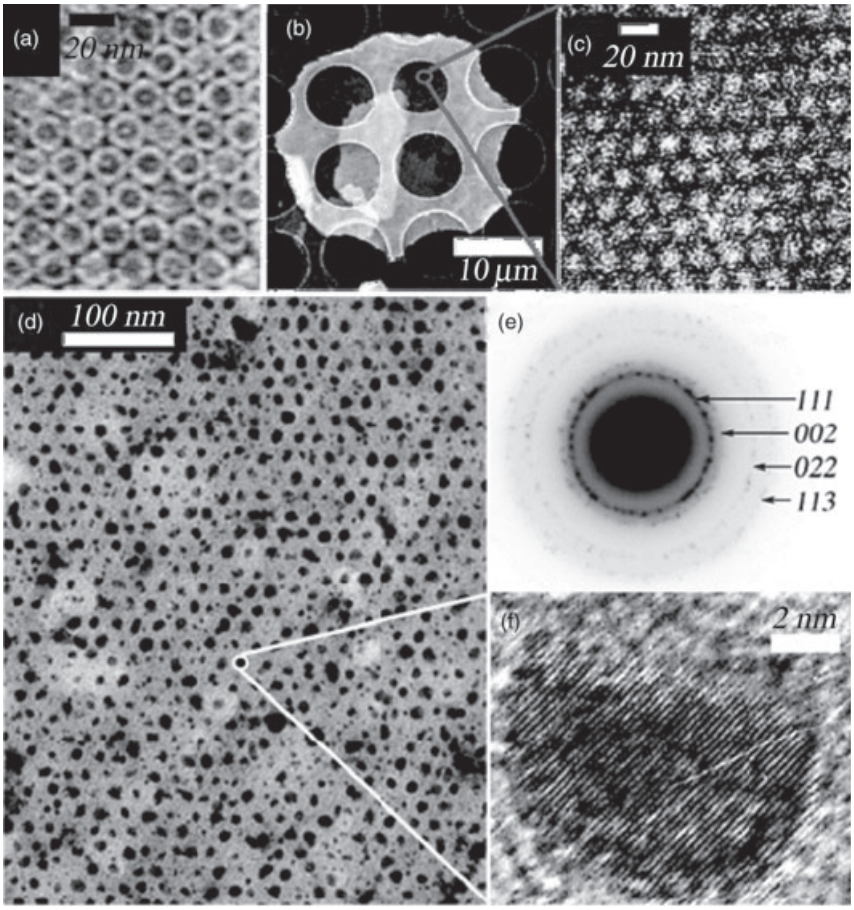

Figure 7.16 TEM imaging of a patterned array. (a) Uranyl acetate staining enables visualization of chaperonins in the 2-D crystal templates; (b) Synthesis of Ni–Pd nanoparticles enhances the contrast of the template in HAADF-STEM mode (unstained Ni–Pd array on Quantifoil, 200 kV); (c) Enlargement of a suspended region reveals a hexagonal array of clusters of small nanoparticles; (d) Imaging at 60 kV (bright-field TEM) coalesces the clusters to form larger nanoparticles that are 8–10 nm in diameter and retain the hexagonal arrangement; (e) SAED pattern of the array indexes to *fcc*; (f) HR-TEM lattice imaging indicates that the coalesced Ni–Pd nanoparticles are crystalline. Reproduced with permission from Ref. [124].

7.5 Outlook

As nanoparticle probes are of the same size scale as biological systems, it is possible for them to be incorporated into cells and living organisms [3]. Nowadays, the development of general and effective strategies for the conjugation of metal nanoparticles with active biomolecules for the targeting, recognition and triggering of signaling phenomena allows us to set up nanosystems with high specificity and low toxicity for biomedical tasks. Since the optical cross-sections of metal nanoparticles in the range 10 to 100 nm are up to five orders larger than those of the classical dye molecules, due to surface plasmon enhancement [125], each metal nanocluster must be considered as an optical probe equivalent to thousands to millions of dye molecules, while remaining photostable and resistant to photobleaching [21]. A number of fundamental applications may derive from these optical and electronic characteristics, both in terms of tunable radiative properties, ranging from bioimaging in the visible-NIR spectral region to optical sensing (e.g., SERS-based biosensors), and nonradiative properties, including their use as light-activated nanosized heaters for photothermal cancer therapy. All of these enhanced optical properties are associated with 'localized surface plasmon resonance' which, in turn, is dependent on the nanoparticle's size, shape and composition. In light of this, the advent of bimetallic nanoparticles has considerably expanded the potential for metal nanoparticles, based on their outstanding aptitude to give rise to optical and electronic properties that differ from those of each individual metal source, and which can be finely modulated in response to specific experimental requirements. Further, the fabrication of multisegmented anisotropic nanoparticles, including nanorods and nanowires, allows for the discrete patterning of biomolecular architectures onto the surfaces of nanoparticles – an ability which is extremely useful for the optimization of multifunctional targeting and task-diversified therapeutic agents.

Although the pioneering applications of bimetallic nanoparticles have been focused largely on organic/inorganic catalysis, the exciting inherent properties of these materials, as offered by the incorporation of different metal elements into one molecular device, combined with the increasing demand for advanced biohybrid nanoscale materials, hold tremendous promise for the development of a new generation of optical/radiative nanotools for biotechnology and medicine.

References

1 Labhasetwar, V. and Leslie-Pelecky, D.L. (2007) *Biomedical Applications of Nanotechnology*, Wiley-VCH Verlag GmbH.

2 Kumar, C.S.S.R. (2007) *Nanomaterials for Medical Applications, Kirk Othmer Encyclopedia of Chemical Engineering*, Wiley-VCH Verlag GmbH, Weinheim.

3 Whitesides, G.M. (2003) The 'right' size in nanobiotechnology. *Nature Biotechnology*, **21**, 1161–5.

4 Minchin, R. (2008) Nanomedicine: sizing up targets with nanoparticles. *Nature Nanotechnology*, **3**, 12–13.

5 Katz, E. and Willner, I. (2004) Integrated nanoparticle-biomolecule hybrid systems: synthesis, properties, and applications. *Angewandte Chemie – International Edition* **43**, 6042–108.

6 Michalet, X., Pinaud, F.F., Bentolila, L. A., Tsay, J.M., Doose, S., Li, J.J., Sundaresan, G., Wu, A.M., Gambhir, S.S. and Weiss, S. (2005) Quantum dots for live cells, in vivo imaging, and diagnostics. *Science*, **307**, 538–44.

7 Reiner, P. (2006) Nanoscopic medicine: the next frontier. *Small*, **2**, 452–6.

8 Azzazy, H.M.E., Mansour, M.M.H. and Kazmierczak, S.C. (2006) Nanodiagnostics: a new frontier for clinical laboratory medicine. *Clinical Chemistry*, **52**, 1238–46.

9 Yezhelyev, M.V., Gao, X., Xing, Y., Al-Hajj, A., Nie, S. and O'Regan, R.M. (2006) Emerging use of nanoparticles in diagnosis and treatment of breast cancer. *The Lancet Oncology*, **7**, 657–67.

10 Kumar, C.S.S.R. (2006) *Biofunctionalization of Nanomaterials*, Wiley-VCH Verlag GmbH, Weinheim.

11 Polito, L., Monti, D., Caneva, E., Delnevo, E., Russo, G. and Prosperi, D. (2008) One-step bioengineering of magnetic nanoparticles via a surface diazo transfer/azide-alkyne click reaction sequence. *Chemical Communications*, 621–3.

12 White, M.A., Johnson, J.A., Koberstein, J.T. and Turro, N.J. (2006) Toward the syntheses of universal ligands for metal oxide surfaces: controlling surface functionality through click chemistry. *Journal of the American Chemical Society*, **128**, 11356–7.

13 Geneviève, M., Vieu, R.C., Carles, R., Zwick, A., Brière, G., Salomé, L. and Trévisiol, E. (2007) Biofunctionalization of gold nanoparticles and their spectral properties. *Microelectronic Engineering*, **84**, 1710–13.

14 Prosperi, D., Morasso, C., Tortora, P., Monti, D. and Bellini, T. (2007) Avidin decorated core-shell nanoparticles for biorecognition studies by elastic light scattering. *ChemBioChem*, **8**, 1021–8.

15 Zhu, H. and Snyder, M. (2003) Protein chip technology. *Current Opinion in Chemical Biology*, **7**, 55–63.

16 Elghanian, R., Storhoff, J.J., Mucic, R.C., Letsinger, R.L. and Mirkin, C.A. (1997) Selective colorimetric detection of polynucleotides based on the distance-dependent optical properties of gold nanoparticles. *Science*, **277**, 1078–80.

17 Alivisatos, A.P. (2004) The use of nanocrystals in biological detection. *Nature Biotechnology*, **22**, 47–52.

18 Sokolov, K., Follen, M., Aaron, J., Pavlova, I., Malpica, A., Lotan, R. and Richards-Kortum, R. (2003) Real-time vital optical imaging of precancer using anti-epidermal growth factor receptor antibodies conjugated to gold nanoparticles. *Cancer Research*, **63**, 1999–2004.

19 Rosi, N.L. and Mirkin, C.A. (2005) Nanostructures in biodiagnostics. *Chemical Reviews*, **105**, 1547–62.

20 Reinhard, B., Sheikholeslami, S., Mastroianni, A., Alivisatos, A.P. and Liphardt, J. (2007) Use of plasmon coupling to reveal the dynamics of DNA bending and cleavage by single EcoRV restriction enzymes. *Proceedings of the National Academy of Sciences of the United States of America*, **104**, 2667–72.

21 Sönnichsen, C., Reinhard, B.M., Liphardt, J. and Alivisatos, A.P. (2005) A molecular ruler based on plasmon coupling of single gold and silver nanoparticles. *Nature Biotechnology*, **23**, 741–5.

22 Huang, X., Jain, P.K., El-Sayed, I.H. and El-Sayed, M.A. (2007) Gold nanoparticles: interesting optical properties and recent applications in cancer diagnostics and therapy. *Nanomedicine*, **2**, 681–93.

23 Hirsch, L.R., Stafford, R.J., Bankson, J.A., Sershen, S.R., Rivera, B., Price, R.E., Hazle, J.D., Halas, N.J. and West, J.L. (2003) Nanoshell-assisted tumor ablation using near infrared light under magnetic resonance guidance. *Proceedings of the National Academy of Sciences of the United States of America*, **100**, 13549–54.

24 Loo, C.A., Lowery, A., Halas, N., West, J. and Drezek, R. (2005) Immunotargeted nanoshells for integrated cancer imaging and therapy. *Nano Letters*, **5**, 709–11.

25 Jain, P.K., El-Sayed, I.H. and El-Sayed, M.A. (2007) Au nanoparticles target cancer. *Nano Today*, **2**, 18–29.

26 Huang, X., El-Sayed, I.H., Qian, W. and El-Sayed, M.A. (2006) Cancer cell imaging and photothermal therapy in the near-infrared region by using gold nanorods. *Journal of the American Chemical Society*, **128**, 2115–20.

27 Jain, P.K., Huang, X., El-Sayed, I.H. and El-Sayed, M.A. (2008) Noble metals on the nanoscale: optical and photothermal properties and some applications in imaging, sensing, biology, and medicine. *Accounts of Chemical Research*, **41**, 1578–86.

28 Lu, L. and Eychmuller, A. (2008) Ordered macroporous bimetallic nanostructures: design, characterization, and applications. *Accounts of Chemical Research*, **41**, 244–53.

29 Cao, Y.W., Jin, R. and Mirkin, C.A. (2001) DNA-Modified core-shell Ag/Au nanoparticles. *Journal of the American Chemical Society*, **123**, 7961–2.

30 Jin, R., Wu, G., Li, Z., Mirkin, C.A. and Schatz, G.C. (2003) What controls the melting properties of DNA-linked gold nanoparticle assemblies? *Journal of the American Chemical Society*, **125**, 1643–54.

31 Cao, Y.W., Jin, R., Thaxton, S. and Mirkin, C.A. (2005) A two-color-change, nanoparticle-based method for DNA detection. *Talanta*, **67**, 449–55.

32 Cui, Y., Ren, B., Yao, J.-L., Gu, R.-A. and Tian, Z.-Q. (2006) Synthesis of Ag_{core}/Au_{shell} bimetallic nanoparticles for immunoassay based on surface-enhanced Raman spectroscopy. *The Journal of Physical Chemistry B*, **110**, 4002–6.

33 Cui, Y., Ren, B., Yao, J.-L., Gu, R.-A. and Tian, Z.-Q. (2007) Multianalyte immunoassay based on surface-enhanced Raman spectroscopy. *Journal of Raman Spectroscopy*, **38**, 896–902.

34 Tang, D., Yuan, R. and Chai, Y. (2006) Ligand-functionalized core/shell Ag@Au nanoparticles label-free amperometric immune-biosensor. *Biotechnology and Bioengineering*, **94**, 996–1004.

35 Mandal, M., Jana, N.R., Kundu, S., Ghosh, S.K., Panigrahi, M. and Pal, T. (2004) Synthesis of Au_{core}-Ag_{shell} type bimetallic nanoparticles for single molecule detection in solution by SERS method. *Journal of Nanoparticle Research*, **6**, 53–61.

36 Pal, A. and Esumi, K. (2007) Photochemical synthesis of biopolymer coated Au_{core}-Ag_{shell} type bimetallic nanoparticles. *Journal of Nanoscience and Nanotechnology*, **7**, 2110–15.

37 Panigrahi, S., Kundu, S., Ghosh, S.K., Nath, S. and Pal, T. (2005) Sugar assisted evolution of mono- and bimetallic nanoparticles. *Colloids and Surfaces A*, **264**, 133–8.

38 Pande, S., Ghosh, S.K., Praharaj, S., Panigrahi, S., Basu, S., Jana, S., Pal, A., Tsukuda, T. and Pal, T. (2007) Synthesis of normal and inverted gold-silver core-shell architectures in β-cyclodextrin and their applications in SERS. *The Journal of Physical Chemistry C*, **111**, 10806–13.

39 Xu, S., Zhao, B., Xu, W. and Fan, Y. (2005) Preparation of Au-Ag coreshell nanoparticles and application of bimetallic sandwich in surface-enhanced Raman scattering (SERS). *Colloids and Surfaces A*, **257–258**, 313–17.

40 Ji, X., Xu, S., Wang, L., Liu, M., Pan, K., Yuan, H., Ma, L., Xu, W., Li, J., Bai, Y. and Li, T. (2005) Immunoassay using the probe-labeled Au/Ag core-shell nanoparticles based on surface-enhanced Raman scattering. *Colloids and Surfaces A*, **257–258**, 171–5.

41 Lee, S., Kim, S., Choo, J., Shin, S.Y., Lee, Y.H., Choi, H.Y., Ha, S., Kang, K. and Oh, C.H. (2007) Biological imaging of HEK293 cells expressing PLCγ1 using surface-enhanced Raman microscopy. *Analytical Chemistry*, **79**, 916–22.

42 Park, S.J., Taton, A. and Mirkin, C.A. (2002) Array-based electrical detection of DNA with nanoparticle probes. *Science*, **295**, 1503–6.

43 Cao, Y.W.C., Jin, R. and Mirkin, C.A. (2002) Nanoparticles with Raman spectroscopic fingerprints for DNA and RNA detection. *Science*, **297**, 1536–40.

44 Xu, W., Xu, S., Ji, X., Bo, S.B., Yuan, H., Ma, L. and Bai, Y. (2005) Preparation of gold colloid monolayer by immunological identification. *Colloids and Surfaces B*, **40**, 169–72.

45 Xu, X., Georganopoulou, D.G., Hill, H.D. and Mirkin, C.A. (2007) Homogeneous detection of nucleic acids based upon the light scattering properties of silver-coated nanoparticle probes. *Analytical Chemistry*, **79**, 6650–4.

46 Taton, T.A., Mirkin, C.A. and Letsinger, R.L. (2000) Scanometric DNA array detection with nanoparticle probes. *Science*, **289**, 1757–60.

47 Zehbe, I., Hacker, G.W., Su, H., Hauser-Kronberger, C., Hainfeld, J.F. and Tubbs, R. (1997) Sensitive in situ hybridization with catalyzed reporter deposition, streptavidin-nanogold, and silver acetate autometallography. *American Journal of Pathology*, **150**, 1553–61.

48 Ma, N., Yang, J., Stewart, K.M. and Kelley, O.S. (2007) DNA-passivated CdS nanocrystals: luminescence, bioimaging, and toxicity profiles. *Langmuir*, **23**, 12783–7.

49 Yang, J., Lee, J.Y., Too, H.P. and Chow, G.M. (2006) Inhibition of DNA hybridization by small metal nanoparticles. *Biophysical Chemistry*, **120**, 87–95.

50 Berti, L. and Burley, G.A. (2008) Nucleic acid and nucleotide-mediated synthesis of inorganic nanoparticles. *Nature Nanotechnology*, **3**, 81–7.

51 Berti, L., Alessandrini, A., Menozzi, C. and Facci, P. (2006) Controlled DNA-templated metal deposition: towards ultra-thin nanowires. *Journal of Nanoscience and Nanotechnology*, **6**, 2382–5.

52 Gu, Q., Cheng, C., Suryanarayanan, S., Dai, K. and Haynie, D.T. (2006) DNA-templated fabrication of nickel nanocluster chains. *Physica E*, **33**, 92–8.

53 Wang, S. and Sim, W.S. (2006) Au nanoparticles encapsulated in Ru carbonyl carboxylate shells. *Langmuir*, **22**, 7861–6.

54 Slocik, J.M. and Naik, R.R. (2006) Biologically programmed synthesis of bimetallic nanostructures. *Advanced Materials*, **18**, 1988–92.

55 Gunawidjaja, R., Peleshanko, S., Ko, H. and Tsukruk, V.V. (2008) Bimetallic nanocobs: decorating silver nanowires with gold nanoparticles. *Advanced Materials*, **20**, 1544–9.

56 Su, H., Dong, Q., Han, J., Zhang, D. and Guo, Q. (2008) Biogenic synthesis and photocatalysis of Pd-PdO nanoclusters reinforced hierarchical TiO_2 films with interwoven and tubular conformations. *Biomacromolecules*, **9**, 499–504.

57 Bakshi, M.S., Possmayer, F. and Petersen, N.O. (2007) Role of different phospholipids in the synthesis of pearl-necklace-type gold-silver bimetallic nanoparticles as bioconjugate materials. *The Journal of Physical Chemistry C*, **111**, 14113–24.

58 Pearce, M.E., Melanko, J.B. and Salem, A.K. (2007) Multifunctional nanorods for biomedical applications. *Pharmaceutical Research*, **24**, 2335–52.

59 Hurst, S.J., Payne, E.K., Qin, L. and Mirkin, C.A. (2006) Multisegmented one-dimensional nanorods prepared by hard-template synthetic methods. *Angewandte Chemie – International Edition*, **45**, 2672–92.

60 Hu, J., Ouyang, M., Yang, P. and Lieber, C.M. (1999) Controlled growth and electrical properties of heterojunctions of carbon nanotubes and silicon nanowires. *Nature*, **399**, 48–50.

61 Wu, Y., Fan, R. and Yang, P. (2002) Block-by-block growth of single-crystalline Si/SiGe superlattice nanowires. *Nano Letters*, **2**, 83–6.

62 Gudiksen, M.S., Lauhon, L.J., Wang, J., Smith, D.C. and Lieber, C.M. (2002) Growth of nanowire superlattice structures for nanoscale photonics and electronics. *Nature*, **415**, 617–20.

63 Björk, M.T., Ohlsson, B.J., Sass, T., Persson, A.I., Thelander, C., Magnusson, M.H., Deppert, K., Wallenberg, L.R. and Samuelson, L. (2002) One-dimensional steeplechase for electrons realized. *Nano Letters*, **2**, 87–9.

64 Jie, J., Wang, G., Han, X. and Hou, J.G. (2004) Synthesis and characterization of ZnO: In nanowires with superlattice structure. *The Journal of Physical Chemistry B*, **108**, 17027–31.

65 Herman, M.A. and Sitter, H. (1989) *Molecular Beam Epitaxy*, Springer, New York.

66 Hu, J., Odom, T.W. and Lieber, C.M. (1999) Chemistry and physics in one

dimension: synthesis and properties of nanowires and nanotubes. *Accounts of Chemical Research*, **32**, 435–45.
67 Sioss, J.A. and Keating, C.D. (2005) Batch preparation of linear Au and Ag nanoparticles chains via wet chemistry. *Nano Letters*, **5**, 1779–83.
68 Martin, C.R. (1994) Nanomaterials: a membrane-based synthetic approach. *Science*, **266**, 1961–6.
69 Martin, C.R. (1996) Membrane-based synthesis of nanomaterials. *Chemistry of Materials*, **8**, 1739–46.
70 Hulteen, J.C. and Martin, C.R. (1997) A general template-based method for the preparation of nanomaterials. *Journal of Materials Chemistry*, **7**, 1075–88.
71 Wade, T.L. and Wegrowe, J.-E. (2005) Template synthesis of nanomaterials. *The European Physical Journal Applied Physics*, **8**, 3–22.
72 Liu, F., Lee, J.Y. and Zhou, W.J. (2005) Multisegment PtRu nanorods: electrocatalysts with adjustable bimetallic pair sites. *Advanced Functional Materials*, **15**, 1459–64.
73 Laibinis, P.E., Hickman, J.J., Wrighton, M.S. and Whitesides, G.M. (1989) Orthogonal self-assembled monolayers: alkanethiols on gold and alkane carboxylic acids on alumina. *Science*, **245**, 845–7.
74 Martin, B.R., Dermody, D.J., Reiss, B. D., Fang, M., Lyon, F.L., Natan, M.J. and Mallouk, T.E. (1999) Orthogonal self-assembly on colloidal gold-platinum nanorods. *Advanced Materials*, **11**, 1021–5.
75 Birenbaum, N.S., Lai, B.T., Chen, C.S., Reich, D.H. and Meyer, G.J. (2003) Selective noncovalent adsorption of protein to bifunctional metallic nanowire surfaces. *Langmuir*, **19**, 9580–2.
76 Bauer, L.A., Reich, D.H. and Meyer, G. J. (2003) Selective functionalization of two-component magnetic nanowires. *Langmuir*, **19**, 7043–8.
77 Wildt, B., Mali, P. and Searson, P.C. (2006) Electrochemical template synthesis of multisegment nanowires: fabrication and protein functionalization. *Langmuir*, **22**, 10528–34.
78 Salem, A.K., Cannizzaro, S.M., Davies, M.C., Tendler, S.J.B., Roberts, C.J., Williams, P.M. and Shakesheff, K.M. (2001) Synthesis and characterization of a degradable poly(lactic acid)-poly(ethylene glycol) copolymer with biotinylated end groups. *Biomacromolecules*, **2**, 575–80.
79 Salem, A.K., Chen, M., Hayden, J., Leong, K.W. and Searson, P.C. (2004) Directed assembly of multisegment Au/Pt/Au nanowires. *Nano Letters*, **4**, 1163–5.
80 Bauer, L.A., Birenbaum, N.S. and Meyer, G.J. (2004) Biological applications of high aspect ratio nanoparticles. *Journal of Materials Chemistry*, **14**, 517–26.
81 Prime, K.L. and Whitesides, G.M. (1991) Self-assembled organic monolayers: model systems for studying adsorption of proteins at surfaces. *Science*, **252**, 1164–7.
82 Fond, A.M., Birenbaum, N.S., Felton, E. J., Reich, D.H. and Meyer, G.J. (2007) Preferential noncovalent immunoglobulin G adsorption onto hydrophobic segments of multi-functional metallic nanowires. *Journal of Photochemistry and Photobiology A. Chemistry*, **186**, 57–64.
83 Dougherty, G.M., Rose, K.A., Tok, J.B.-H., Pannu, S.S., Chuang, F.Y.S., Sha, M.Y., Chakarova, G. and Penn, S.G. (2008) The zeta potential of surface-functionalized metallic nanorod particles in aqueous solution. *Electrophoresis*, **29**, 1131–9.
84 Salem, A.K., Searson, P.C. and Leong, K.W. (2003) Multifunctional nanorods for gene delivery. *Nature Materials*, **2**, 668–71.
85 Salem, A.K., Hung, C.F., Kim, T.W., Wu, T.C., Searson, P.C. and Leong, K.W. (2005) Multi-component nanorods for vaccination applications. *Nanotechnology*, **16**, 484–7.
86 Huang, Y.-F., Chang, H.-T and Tan, W. (2008) Cancer cell targeting using multiple aptamers conjugated on nanorods. *Analytical Chemistry*, **80**, 567–72.
87 Nicewarner-Peña, S.R., Carado, A.J., Shale, K.E. and Keating, C.D. (2003) Barcoded metal nanowires: optical reflectivity and patterned fluorescence. *The Journal of Physical Chemistry B*, **107**, 7360–7.

88 Stoermer, R.L., Sioss, J.A. and Keating, C.D. (2005) Stabilization of silver metal in citrate buffer: barcoded nanowires and their bioconjugates. *Chemistry of Materials*, **17**, 4356–61.

89 Nicewarner-Peña, S.R., Freeman, R.G., Reiss, B.R., He, L., Peña, D.J., Walton, I.D., Cromer, R., Keating, C.D. and Natan, M.J. (2001) Submicrometer metallic barcodes. *Science*, **294**, 137–41.

90 Tyagi, S. and Kramer, F.R. (1996) Molecular beacons: probes that fluoresce upon hybridization. *Nature Biotechnology*, **14**, 303–8.

91 Fang, X., Li, J.J., Perlette, J., Tan, W. and Wang, T. (2000) Molecular beacons: novel fluorescent probes. *Analytical Chemistry*, 747A–753A.

92 Broude, N.E. (2002) Stem-loop oligonucleotides: a robust tool for molecular biology and biotechnology. *Trends in Biotechnology*, **20**, 249–56.

93 Du, H., Disney, M.D., Miller, B.L. and Krauss, T.D. (2003) Hybridization-based unquenching of DNA hairpins on Au surfaces: prototypical 'molecular beacon' biosensors. *Journal of the American Chemical Society*, **125**, 4012–13.

94 Du, H., Strohsahl, C.M., Camera, J., Miller, B.L. and Krauss, T.D. (2005) Sensitivity and specificity of metal surface-immobilized 'molecular beacon' biosensors. *Journal of the American Chemical Society*, **127**, 7932–40.

95 Dubertret, B., Calame, M. and Libehaber, A.J. (2001) Single-mismatch detection using gold-quenched fluorescent oligonucleotides. *Nature Biotechnology*, **19**, 365–70.

96 Sha, M.Y., Yamanaka, M., Walton, I.D., Norton, S.M., Stoermer, R.L., Keating, C.D., Natan, M.J. and Penn, S.G. (2005) Encoded metal nanoparticles-based molecular beacons for multiplexed detection of DNA. *NanoBiotechnology*, **1**, 327–35.

97 Stoermer, R.L. and Keating, C.D. (2006) Distance-dependent emission from dye-labeled oligonucleotides on striped Au/Ag nanowires: effect of secondary structure and hybridization efficiency. *Journal of the American Chemical Society*, **128**, 13243–54.

98 Stoermer, R.L., Cedequist, K.B., McFarland, S.K., Sha, M.Y., Penn, S.G. and Keating, C.D. (2006) Coupling molecular beacons to barcoded metal nanowires for multiplexed, sealed chamber DNA bioassays. *Journal of the American Chemical Society*, **128**, 16892–903.

99 Sioss, J.A., Stoermer, R.L., Sha, M.Y. and Keating, C.D. (2007) Silica-coated, Au/Ag striped nanowires for bioanalysis. *Langmuir*, **23**, 11334–41.

100 Wang, X. and Ozkan, C.S. (2008) Multisegment nanowire sensors for the detection of DNA molecules. *Nano Letters*, **8**, 398–404.

101 Ren, Q., Zhao, Y.-P., Yue, J.C. and Cui, Y.B. (2006) Biological application of multi-component nanowires in hybrid devices powered by F_1-ATPase motors. *Biomedical Microdevices*, **8**, 201–8.

102 Ferrando, R., Jellinek, J. and Johnston, R.L. (2008) Nanoalloys: from theory to applications of alloy clusters and nanoparticles. *Chemical Reviews*, **108**, 845–910.

103 Schmid, G. (1994) *Clusters and Colloids*, Wiley-VCH Verlag GmbH, Weinheim.

104 Mandal, S., Selvakannan, P.R., Pasricha, R. and Sastry, M. (2003) Keggin ions as UV-switchable reducing agents in the synthesis of Au core-Ag shell nanoparticles. *Journal of the American Chemical Society*, **125**, 8440–1.

105 Scott, R.W.J., Wilson, O.M. and Crooks, R.M. (2005) Synthesis, characterization, and applications of dendrimer-encapsulated nanoparticles. *The Journal of Physical Chemistry B*, **109**, 692–704.

106 Ambade, A.V., Chen, Y. and Thayumanavan, S. (2007) Controlled functional group presentations in dendrimers as a tool to probe the hyperbranched architecture. *New Journal of Chemistry*, **31**, 1052–63.

107 Lundquist, J.J. and Toone, E.J. (2002) The cluster glycoside effect. *Chemical Reviews*, **102**, 555–78.

108 Chandler, B.D. and Gilbertson, J.D. (2008) PAMAM dendrimer templated nanoparticle, in *Nanoparticles and Catalysis*, Wiley-VCH Verlag GmbH, Weinheim, pp. 129–60.

109 Durán Pachón, L. and Rothenberg, G. (2008) Transition-metal nanoparticles: synthesis, stability and the leaching issue. *Applied Organometallic Chemistry*, **22**, 288–99.

110 Scott, R.W.J., Datye, A.K. and Crooks, R.M. (2003) Bimetallic palladium-platinum dendrimer-encapsulated catalysts. *Journal of the American Chemical Society*, **125**, 3708–9.

111 Chung, Y.-M. and Rhee, H.-K. (2003) Partial hydrogenation of 1,3-cyclooctadiene using dendrimer-encapsulated Pd–Rh bimetallic nanoparticles. *Journal of Molecular Catalysis A–Chemical*, **206**, 291–8.

112 Chung, Y.-M. and Rhee, H.-K. (2004) Dendrimer-templated Ag-Pd bimetallic nanoparticles. *Journal of Colloid and Interface Science*, **271**, 131–5.

113 Lang, H., Maldonado, S., Stevenson, K.J. and Chandler, B.D. (2004) Synthesis and characterization of dendrimer templated supported bimetallic Pt-Au nanoparticles. *Journal of the American Chemical Society*, **126**, 12949–56.

114 Crooks, R.M., Zhao, M., Sun, L., Chechik, V. and Yeung, L.K. (2001) Dendrimer-encapsulated metal nanoparticles: synthesis, characterization, and applications to catalysis. *Accounts of Chemical Research*, **34**, 181–90.

115 Gehl, B., Aleksandrovic, V., Erbacher, M., Jürgens, B., Schürenberg, M., Kornowski, A., Weller, H. and Bäumer, M. (2008) Ligand exchange with thiols: effects on composition and morphology of colloidal CoPt nanoparticles. *ChemPhysChem*, **9**, 821–5.

116 Hickman, J.J., Laibinis, P.E., Auerbach, D.I., Zou, C., Gardner, T.J., Whitesides, G.M. and Wrighton, M.S. (1992) Toward orthogonal self-assembly of redox active molecules on Pt and Au: selective reaction of disulfide with Au and isocyanide with Pt. *Langmuir*, **8**, 357–9.

117 Braun, E., Eichen, Y., Sivan, U. and Ben-Yoseph, G. (1998) DNA-templated assembly and electrode attachment of a conducting silver wire. *Nature*, **391**, 775–8.

118 Keren, K., Krueger, M., Gilad, R., Ben-Yoseph, G., Sivan, U. and Braun, E. (2002) Sequence-specific molecular lithography on single DNA molecules. *Science*, **297**, 72–5.

119 Eichen, Y., Braun, E., Sivan, U. and Ben-Yoseph, G. (1998) Self-assembly of nanoelectronic components and circuits using biological templates. *Acta Polymerica*, **49**, 663–70.

120 Keren, K., Berman, R.S., Buchstab, E., Sivan, U. and Braun, E. (2003) DNA-templated carbon nanotube field-effect transistor. *Science*, **302**, 1380–2.

121 Fischler, M., Simon, U., Nir, H., Eichen, Y., Burley, G.A., Gierlich, J., Gramlich, M.E. and Carell, T. (2007) Formation of bimetallic Ag-Au nanowires by metallization of artificial DANN duplexes. *Small*, **3**, 1049–55.

122 Hu, K.-W., Huang, C.-C., Hwu, J.-R., Su, W.-C., Shieh, D.-B. and Yeh, C.-S. (2008) A new photothermal therapeutic agent: core-free nanostructured Au_0Ag_{1-x} dendrites. *Chemistry–A European Journal*, **14**, 2956–64.

123 Singh, A.V., Bandgar, B.M., Kasture, M., Prasad, B.L.V. and Sastry, M. (2005) Synthesis of gold, silver and their alloy nanoparticles using bovine serum albumin as foaming and stabilizing agent. *Journal of Materials Chemistry*, **15**, 5115–21.

124 McMillan, R.A., Howard, J., Zaluzec, N.J., Kagawa, H.K., Mogul, R., Li, Y.-F., Paavola, C.D. and Trent, J.D. (2005) A self-assembling protein template for constrained synthesis and patterning of nanoparticle arrays. *Journal of the American Chemical Society*, **127**, 2800–1.

125 Jain, P.K., Lee, K.S., El-Sayed, I.H. and El-Sayed, M.A. (2006) Calculated absorption and scattering properties of gold nanoparticles of different size, shape, and composition: applications in biological imaging and biomedicine. *The Journal of Physical Chemistry B*, **110**, 7238–48.

Keywords

bimetallic nanoparticles; bioconjugation; biosensors; antitumor agents; biomimetics; core-shell materials; nanocomposites; nanorods.

8
Multielemental Nanorods (Nanowires): Synthesis, Characterization and Analytical Applications

Yang-Wei Lin, Zong-Hong Lin, Chih-Ching Huang and Huan-Tsung Chang

8.1
Introduction

Nanoscience focuses on the synthesis, characterization and application of materials of which the sizes typically range from 1 to 100 nm [1, 2]. Such small sizes of nanomaterials (colloids), which are referred to as nanoparticles (NPs), have attracted enormous interest in a wide variety of fields including catalysis, electronics, optics, separation processes and imaging. The unique physical and chemical properties of NPs differ greatly from those of their corresponding bulk materials, and depend heavily on the size, shape and surface morphology of the NP, as well as the environment. A number of organic and inorganic NPs have been prepared, including carbon nanotubes, nanodiamond, NPs made from TiO_2, SiO_2 and Te, polymeric NPs, peptide-based nanotubes, quantum dots (QDs) and metallic NPs. Among these NPs, the metallic variant are particularly interesting because they may serve not only as effective catalysts but are also useful materials for the fabrication of photovoltaic, electronic and magnetic devices. Moreover, after undergoing bioconjugation, they may also serve as selective and sensitive biosensors [3–7]. The recent years have witnessed the growth and progression of nanoscience at an unprecedented rate, with huge numbers of successful examples suggesting that the field is highly interdisciplinary, encompassing aspects of chemistry, physics, biology, materials science, engineering and medicine.

Initially, nanoscience research focused on the study of isotropic, novel metallic colloids or sols in solution phase [8, 9]. During this time, a number of synthetic methods – including wet-chemical, template-based growth, membrane-based synthesis, pulsed-laser ablation/chemical vapor deposition (CVD), vapor–solid–liquid growth and lithographic methods – have been developed for the preparation of differently sized and shaped nanomaterials in liquid, gas and solid phases [10–18]. Today, these methods are used to prepare isotropic NPs and anisotropic nanostructures such as rods, wires and branched structures [13–18]. Of these methods, the wet-chemical approaches are the most popular, mainly due to their advantages

Nanomaterials for the Life Sciences Vol. 3: Mixed Metal Nanomaterials. Edited by Challa S. S. R. Kumar

ISBN: 978-3-527-32153-7

of simplicity, low energy consumption and safety. In addition, NPs prepared in the liquid (especially aqueous) phase are usually more biocompatible.

Nanomaterials prepared from various metal ions have also been demonstrated. Most often, metal elements that are used for the preparation of nanomaterials include Ag, Au, Ti, Fe, Cd, Zn, Cu, Pd, Pt and Ni. Nanomaterials consisting of different compositions have various physical and chemical properties. With regards to optical properties, NPs consisting of Au and Ag atoms and QDs from elements in Groups III to V of the Periodic Table are the most popular. Following (bio)conjugation, Au NPs and CdTe QDs have been used for the detection of analytes of interest at low concentrations, including thiol compounds, metal ions, proteins and DNA [19–23]. Fe and Co ions are especially interesting materials for the preparation of magnetic NPs [24–27], with bioconjugated magnetic NPs being especially useful in the purification of proteins and the separation of cells. Both, Pt and Pd are frequently used for the preparation of catalytic nanomaterials. Indeed, when compared to their disordered alloys, Pt–Pb, Pt–Bi and Pt–In NPs have shown superior electrocatalytic properties towards the oxidation of small organic molecules in fuel cells [28].

In addition to shape- and size-dependence, the physical and chemical properties of NPs can be tuned by controlling the species and contents of the metal elements. For example, the optical properties of Au–Ag nanomaterials differ significantly from those of individual Au and Ag NPs. The molar absorptivity of Au–Ag nanorods (NRs) at a maximum wavelength (845 nm) of the longitudinal plasmon band is $5.5 \times 10^9 M^{-1} cm^{-1}$, which is higher than that ($1.0 \times 10^9 M^{-1} cm^{-1}$) of spherical Au NPs at 520 nm and of spherical Ag NPs at 400 nm ($3.9 \times 10^9 M^{-1} cm^{-1}$). Multielemental NPs prepared from mixtures consisting of several different metal ions (e.g., Co, Fe, Pt, Ni) possess unique magnetic and/or catalytic properties. For example, FePt and CoPt NPs have been demonstrated as being useful materials for data storage, magnets and catalysis [24–27]. Au–Ni–Au NRs functionalized with polyhistidine have been used for the efficient separation of mixtures of anti-histidine proteins from control antibodies by applying a magnetic field [21]. Pt–Ru NRs have shown greater catalytic efficiency for electro-oxidation of methanol at low temperature [29].

Clearly, numerous successful examples have demonstrated the great practicality of metallic NPs in many fields, including biosensing, drug delivery, catalysis, optics and electronics [19, 23, 24]. Because of their excellent physical and chemical properties – and great practicality – many reports and excellent reviews have been provided during the past three years [6, 7]. In this chapter, we discuss the different synthetic methods, characterization, physical and chemical properties and applications of multisegment, one-dimensional (1-D) NRs. Initially, details of the organic- and aqueous-phase syntheses of multisegmented 1-D NRs, including bimetallic, semiconductive and multisegmented NRs are discussed, with particular emphasis placed on polyol, thermal decomposition, wet-chemical, seed growth, nanoporous template growth, micelle-based and hydrothermal methods. The characterization and unique physical and chemical properties, including absorption, emission, surface-enhanced Raman scattering (SERS), catalysis and magnetism of the as-

prepared multielemental NRs are then discussed in great detail. Emphasis is placed on analytical applications, notably in the detection of biomarkers, cells and bacteria of the multisegmented NRs, based mainly on their applications. Details are also provided of the application of as-prepared multielemental NRs, including the electrochemical detection of gaseous molecules, the optical detection of metal ions, and the detection and separation of biological molecules such as proteins, DNA and bacteria. The chapter concludes with a brief summary of the present and future research directions of multisegmented 1-D NRs.

8.2 Synthetic Strategies

8.2.1 Organic-Phase Synthesis

Solvothermal synthesis is usually conducted at elevated temperature and/or pressure to increase the solubility of solids and to speed up the reactions. In a typical method, precursor(s) and possibly reagent(s) capable of regulating and/or templating the crystal growth are added into a solvent, at certain concentrations. This mixture is then placed in an autoclave at elevated temperature and pressure to allow the growth of NRs. Ideally, this approach allows the preparation of NRs from any solid materials if suitable solvents, including alkanes, amines and aromatic compounds, are available. The disadvantages of this approach include a requirement for extra energy (elevated temperatures) and the use of organic solvents that may be toxic and require particular waste treatment. It is also difficult to understand the reaction and growth mechanisms because the solvothermal process itself is inherently complex.

8.2.1.1 Bimetallic NRs

Polyol methods are commonly applied to the preparation of metallic NRs from reducing their ionic salts in organic solution. In general, mixtures of precursors, polymer surfactants and other necessary reagents in organic solvents such as ethylene glycol were heated in oil baths for several hours. To speed up the reaction, microwave heating has been coupled with polyol methods for the preparation of metallic NRs. Microwave heating is fundamentally different from conventional heating processes that generally require a higher reaction temperature and a longer reaction time. As a result of internal and volumetric heating in microwave, much smaller thermal gradients are created in the solution than that by conventional heating. A microwave–polyol method was applied to the preparation of Au seeds from $HAuCl_4 \cdot 4H_2O$ in ethylene glycol aqueous solution containing polyvinylpyrrolidone (PVP) [30]. When Ag^+ was reduced by ascorbic acid and deposited on these Au seeds, Au–Ag NRs/nanowires having Ag shells were prepared. Changes in the adsorption selectivity of PVP from {111} facets of Au to {100} facets of Ag play an important role in controlling the morphology of the as-prepared nanomaterials.

PtPb NRs were synthesized by simultaneously reducing platinum acetylacetonate ($Pt(acac)_2$) and lead acetylacetonate ($Pb(acac)_2$) with a *tert*-butylamine–borane complex in a mixture of diphenyl ether, adamantanecarboxylic acid, hexadecanethiol and hexadecylamine at 180 °C [31]. While *tert*-butylamine–borane was a key factor in controlling the shape of the PtPb NRs, the molar ratios of other reagents, including hexadecylamine, adamantanecarboxylic acid and hexadecanethiol, and also the reaction time, were critical for obtaining the PtPb intermetallic NRs. These NRs had an average length of 45 ± 12 nm and a width of 5.9 ± 3.4 nm, with an average aspect ratio (length-to-width ratio) of 8.2 ± 2.8. The formation of a rod-like morphology is attributed to the difference in the numbers of coordination sites along various low-index surfaces of the hexagonal crystal structure of PtPb. Figure 8.1a displays the hexagonal cell of PtPb viewed from ⟨00-1⟩ direction. Careful crystallographic examination reveals that crystal growth perpendicular to the c-axis

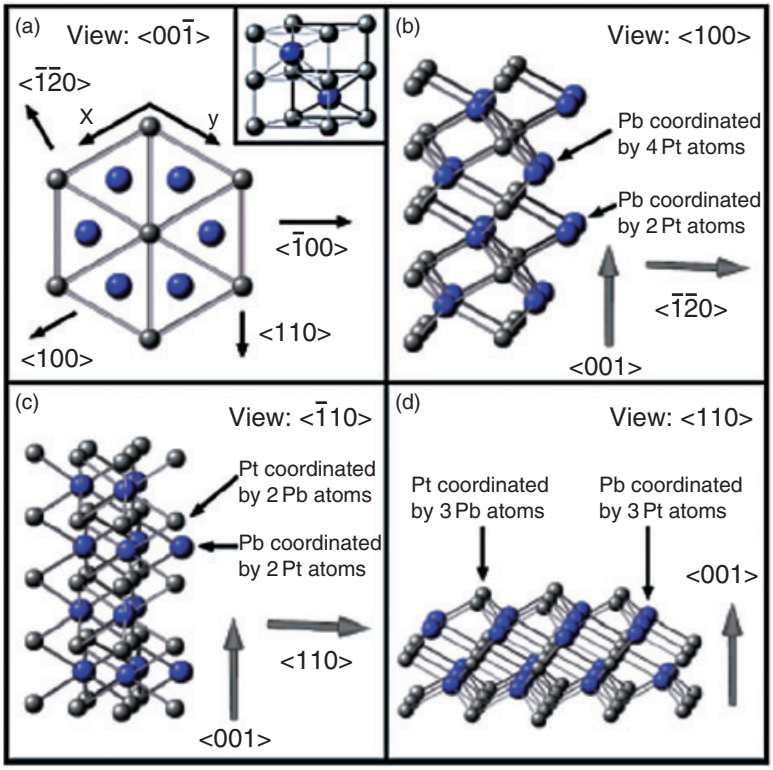

Figure 8.1 (a) The PtPb crystal structure and (b–d) the growing surfaces viewed along (a) ⟨00-1⟩, (b) ⟨100⟩, (c) ⟨-110⟩, and (d) ⟨110⟩ directions, respectively. The inset in panel (a) is the unit cell of intermetallic PtPb. Only the growth along [001] directions involved threefold sites, while those along [110] or [100] directions involved at least one type of twofold binding site. The viewing directions of panels (b–d) were slightly offset for clarity. The gray and blue balls represent Pt and Pb atoms, respectively. Reprinted with permission from Ref. [31].

is unfavorable owing to relatively low numbers of binding sites for adatom incorporation. Growth in the ⟨-1-20⟩ direction of intermetallic PtPb involved two types of lead adatom site – one in which the adsorbed lead atom is coordinated by four platinum atoms, and the other by two platinum atoms (Figure 8.1b). The lead atom coordinated by two platinum atoms is unstable, leading to limited growth in the equivalent [-1-20] directions. Growth in the ⟨110⟩ direction involved sites where the platinum atoms are coordinated by two lead atoms and vice versa, suggesting that growth in the equivalent [110] directions is also unfavorable (Figure 8.1c). Growth in the [001] directions (the unique c-axis), however, involves threefold coordinated sites for both platinum and lead adatoms.

The thermal decomposition of low-valent transition metal complexes (usually organometallic compounds and clusters or labile noble metal salts) has been used to synthesize bimetallic NRs, particularly those containing noble metals. Monodispersed FePt NRs were prepared through the confined decomposition of $Fe(CO)_5$ and reduction of $Pt(acac)_2$ in a surfactant liquid-crystal mesophase [32]. Formation of the surfactant mesophase was critical on the controlled formation of FePt NRs having an average diameter of 2.1 nm and a length of 11.3 nm (Figure 8.2a, b and c). The X-ray diffraction pattern (Figure 8.2d) of the FePt NRs shows the strongest (111) peak at ~40.2° and a (200) peak at ~47°, corresponding to the standard face-center cubic (fcc) structure with a random crystalline orientation. Composition analysis using energy-dispersed X-ray spectroscopy (EDS) (Figure 8.2e) shows an Fe/Pt atomic ratio of ~40/60. In addition, by controlling nucleation and growth kinetics in the confined environment, it is possible to achieve control over the Fe/Pt composition, NR uniformity and NR aspect ratio. Under an external magnetic field, FePt NRs tend to assemble, leading to the formation of two-dimensional (2-D) hexagonal ordered arrays, parallel to the substrate. The arrays provided a uniform anisotropic magnetic platform for varied applications, including enhanced data storage and magnetoelectron transport.

8.2.1.2 **Semiconductor NRs**

Diluted magnetic semiconductors have attracted considerable research interest in recent years due to their great potential applications in the fabrication of spintronic devices, such as spin field-effect transistors, nonvolatile memory devices and quantum computers [33, 34]. With its broad band gap, a large excitation binding energy of 60 meV and ultraviolet (UV) lasing properties at room temperature, ZnO has been a good candidate for creating diluted magnetic semiconductors after being doped with transition metals. Another feature of the transition metal-doped ZnO NPs is that their Curie temperature (T_c) is above room temperature [35]. The excellent optical properties, combined with the room-temperature ferromagnetism of transition metal-doped ZnO NPs, allow the fabrication of magnetic-optic devices.

Co-doped ZnO (ZnO : Co) NRs were prepared by slowly mixing the precursor solutions ($Zn(ac)_2 \cdot 2H_2O$ and $Co(ac)_2 \cdot 4H_2O$) in 1-butanol at the elevated temperature of boiling 1-butanol in the presence of ethylenediamine molecules that acted as ligands [36]. The cations form complexes with ethylenediamine in the precursor

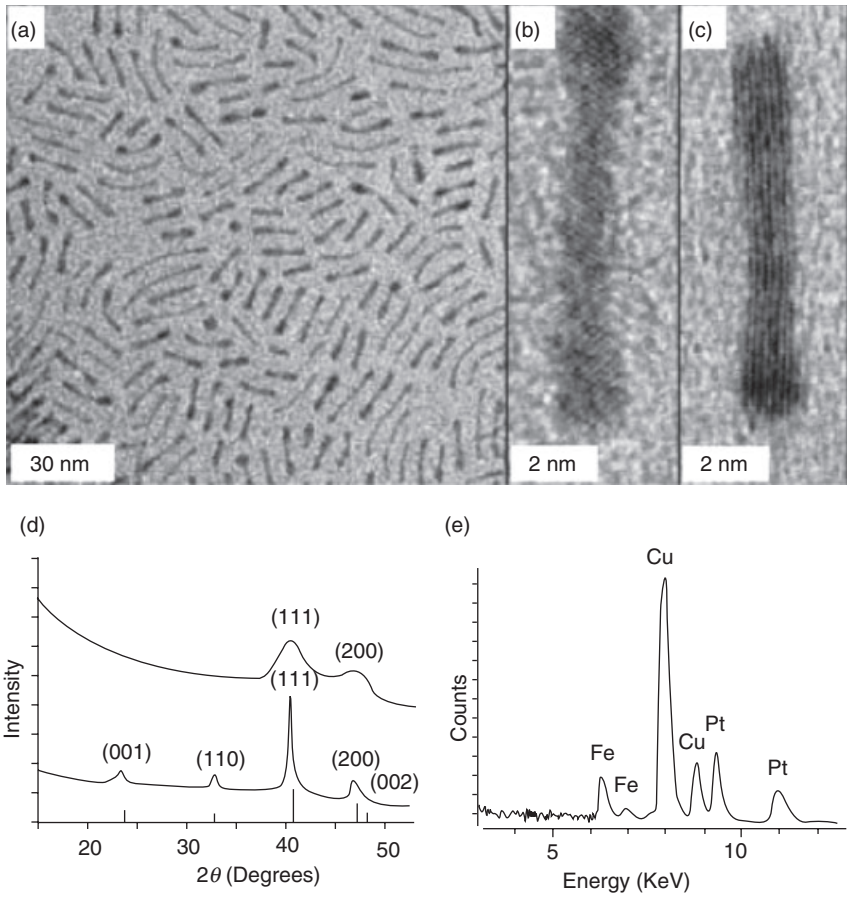

Figure 8.2 Transmission electron microscopy (TEM) images of FePt nanoparticles. (a) TEM images of FePt nanorods; (b) High-resolution TEM of FePt nanorods with {110} faces; (c) FePt nanorods with {100} faces; (d) X-ray diffraction patterns of $Fe_{40}Pt_{60}$ nanorods. Upper curve, as-prepared; lower curve, annealed under 5% H_2/95% N_2 at 700 °C for 1 h; (e) Energy-dispersed X-ray spectroscopy of $Fe_{40}Pt_{60}$ nanorods. Reprinted with permission from Ref. [32].

solution, leading to a better solubility in BuOH. Hence, only a few seeds were formed during the early stages of the reaction, which allowed the growth of longer ZnO:Co NRs (diameters of 20 nm and lengths up to 150 nm). Diluted magnetic semiconductor $Zn_{1-x}Ni_xO$ NRs with nominal Ni doping concentrations of $x = 0\%$, 1%, 5% and 10%, have been synthesized through a simple solvothermal route at low temperature (140 °C) [37]. The required amounts of zinc acetate $[Zn(ac)_2 \cdot 2H_2O]$ and nickel acetate $[Ni(ac)_2 \cdot 4H_2O]$ were dissolved in absolute ethanol, after which NaOH (0.8 *M*) dissolved in absolute ethanol was added under magnetic stirring, followed by 8.0 ml of PEG-400 solution. The mixed solution was transferred to a Teflon-lined stainless autoclave of 50 ml capacity, and the tank placed in an electric

oven at 140 °C for 24 h. The as-prepared $ZnO_{0.95}Ni_{0.05}O$ NRs (1 μm in length, 10 nm in diameter) are single crystalline wurtzite structures, which do not contain any other secondary phases.

Panda and coworkers demonstrated the preparation of CdS/ZnS core-shell NRs having diameters of about 35 nm and lengths of 180–200 nm, and with a smooth surface, by conducting a three-step wet-chemical synthesis approach [38]. Compared to the chemical vapor deposition (CVD) process, the solvothermal synthesis is simple and inexpensive. Jang and coworkers demonstrated the preparation of CdS/ZnS core-shell NRs of diameter 22 nm by using a solvent-coordinating molecular template of ethylenediamine [39]. First, the CdS NRs were prepared from CdO and elemental sulfur at 180 °C for 30 h. In order to improve the stability of the as-prepared CdS core NRs in aqueous solution, they were subjected to liquid exchange in the presence of mercaptopropionic acid. For the synthesis of CdS/ZnS core-shell NRs, an appropriate amount of $Zn(NO_3)_2 \cdot 6H_2O$ was added to the previously prepared CdS colloidal solution, and stirred for 1 h. Equal amounts of $Na_2S \cdot 9H_2O$ and $Zn(NO_3)_2$ were added to the colloidal solution, after which the mixture was refluxed at 70 °C for 1 h. Through Zn–S bonding, the as-prepared NRs were capped with mercaptopropionic acid molecules with the carboxylic groups towards the bulk solution; this led to an increase in coulombic repulsion among the NRs, and thus to an increase in their stability in aqueous solution.

Linear CdTe–CdSe–CdTe heterostructured NRs were synthesized using a colloidal sequential reactant injection technique [40]. A mixture of CdO, *n*-tetradecylphosphonic acid and trioctylphosphine oxide was degassed for 2 h and then heated under nitrogen to 340 °C to form the Cd–tetradecylphosphonic acid complex. Separately, the selenium and tellurium precursors were prepared by dissolving Se and Te powders in trioctylphosphine and then heating the solutions under nitrogen at 120 °C. The CdSe NRs were then synthesized by injecting 0.5 ml of Se–trioctylphosphine solution into the Cd-tetradecylphosphonic acid solution at 3 min intervals. Following the final injection of Se–trioctylphosphine, three further injections (each of 0.5 ml) of Te–trioctylphosphine solution were added every 2 min to elicit an epitaxial growth of the CdTe extensions onto the CdSe core NRs. Following the final injection of Te–trioctylphosphine, the reaction flask was cooled to room temperature and the NR product then precipitated from the crude mixture, using ethanol. After centrifugation, the NRs were subsequently redispersed into organic solvents for further study. Photoluminescence (PL) was observed to occur from electron-hole recombination in both the CdSe core and across the heterojunction.

$AgInSe_2$, a semiconductor with a band gap of 1.19 eV, is a ternary analogue of CdSe which has been used for the fabrication of electronic devices [41]. 1-D $AgInSe_2$ NRs were prepared from a single-source precursor ($(PPh_3)_2AgIn(SeCOPh)_4$) through thermal decomposition in a mixed solution of oleylamine and dodecanethiol [42]. The precursor solution was first degassed for 15 min in a vacuum and then heated to 185 °C in an oil bath for 17 h under flowing Ar gas. The as-prepared $AgInSe_2$ NRs were close to being monodispersed, with dimensions of $50.3 \pm 5.0\,\text{nm} \times 14.5 \pm 1.8\,\text{nm}$. The study results suggested that dodecanethiol and

oleylamine were equally important in the synthesis of $AgInSe_2$ NRs; the oleylamin acted as both activating and capping agent, while dodecanethiol appeared to guide the particles to grow in a 1-D structure.

8.2.2 Aqueous-Phase Synthesis

From the viewpoint of 'green' techniques, the preparation of multielemental nanomaterials in aqueous solution is advantageous over those in organic solution. In addition, multielemental nanomaterials prepared in aqueous solution are usually ready for bioconjugation and then for bioapplication.

8.2.2.1 Bimetallic NRs

Turkevich proposed a mechanism for the stepwise formation of colloidal nanoclusters based on nucleation, growth and subsequent agglomeration [43]. Modern analytical experiments have shown that this mechanism is essentially correct, generally proceeding via a 'seed' particle (<1 nm in diameter) which is relatively stable to dissolution and acts as a nucleus for further growth ('ripening'). Using a seed-growth method, Chang and coworkers demonstrated an easy procedure for the preparation of differently shaped and size Au/Ag NRs (Figure 8.3) in various amino acid solutions – arginine, cysteine, glycine, glutamate, glutamine, histidine, lysine and methionine, respectively – at pH values ranging from 8.0 to 11.5 [44]. The pH, the nature of the amino acid and its concentration all have significant impact on the preparation Au/Ag NRs; these factors exhibit their effects mainly through control over the reducing ability of ascorbate and its recognition capability, as well as through control over the surface charges of the amino acids on the Au NRs. The controlled synthesis of bifunctional Au/Pt hybrid NRs has been realized through a simple wet-chemical approach [45]. The Au NRs were first prepared according to a seed-mediated growth method, which then acted as the seed (core) in a solution to react with metal ions ($PtCl_6^{2-}$). Pt ions were chemically reduced on the core surface to form a shell layer of Pt. These Au–Pt hybrid NRs have dual functions, allowing them to be used as substrates in SERS and/or as catalysts for O_2 reduction.

Ag NRs were prepared directly on a silicon surface by using seed-mediated growth [46]. The procedure involved attaching gold seeds to a functionalized silicon surface and growing them into NRs by placing the substrates in a growth solution. The surface-grown Ag NRs were then used to react with salts of palladium, platinum and gold via galvanic exchange reactions to form high-surface-area 1-D structures of the Ag/Pd, Ag/Pt and Ag/Au core-shell NRs. The growths of gold and silver nanomaterials from their corresponding colloidal seeds on glass substrates were separately demonstrated (Figure 8.4) [47]. The glass substrates were treated with 3-mercaptopropyltrimethoxysilane (MPTMS) and then with gold or silver nanoparticle seeds (AuNPSs or AgNPSs) at different concentrations. Following separate immersion of the thus-prepared MPTMS-AuNPS and MPTMS-AgNPS glass substrates in aqueous solutions containing cetyltrimethylammonium

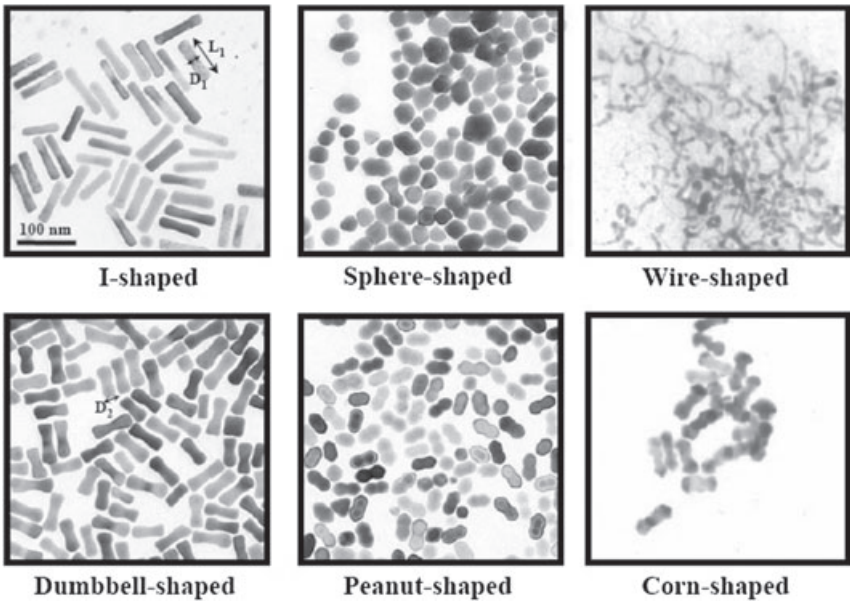

Figure 8.3 TEM images of the differently shaped Au–Ag nanocomposites prepared from AuNR seeds in different amino acid solutions (0.1 *M*) under alkaline conditions (pH > 8.0). The amino acid solutions (arginine, cysteine, glycine, glutamate, glutamine, histidine, lysine, methionine) all contained 0.19 m*M* Au ions, 0.049 m*M* Ag ions, 0.27 m*M* ascorbic acid and 0.05 *M* CTAB. The reactions were conducted overnight at ambient temperature and pressure. Reprinted with permission from Ref. [44].

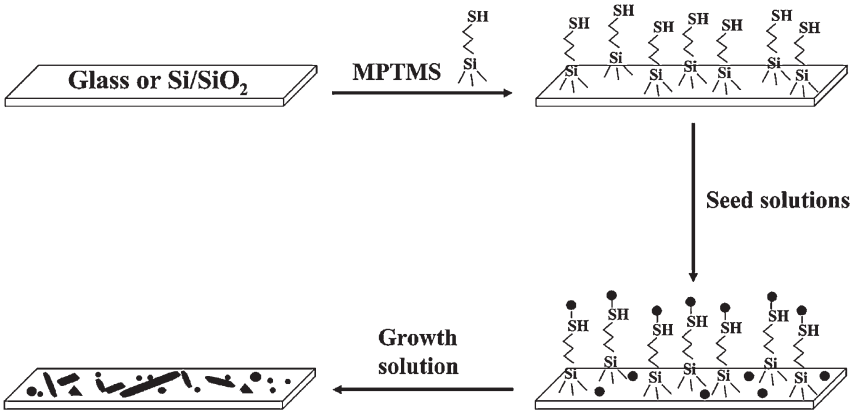

Figure 8.4 Cartoon depicting the seed-mediated growth of NRs on MTPMS-treated glass substrates. Reprinted with permission from Ref. [47].

bromide (CTAB), ascorbic acid and gold or silver ions, Au and Ag nanomaterials of different sizes and shapes were obtained and characterized using scanning electron microscopy (SEM) and dark-field microscopy. At 0.001× concentrations of the AuNPSs and AgNPSs (i.e., 1000-fold-diluted solutions of the as-prepared samples), Au and Ag nanomaterials with lengths of 1.36 and 5.21 μm and aspect ratios of 11 and 24 were prepared, with yields of 27% and 54%, respectively.

8.2.2.2 **Multisegmented NRs**

Nanoporous, template-based growth is routinely applied to prepare 1-D multisegmented NRs such as Au–Ni–Au and Au–Co–Ni, with great yields, mainly because of the uniform and dense pores in the substrates (membranes) [6, 48]. In addition to the desired pore or channel size, morphology, size distribution and density of the pores, the template materials must meet certain requirements. First, they must be compatible with the processing conditions; for example, an electrical insulator is required for a template to be used in electrochemical deposition. The template materials should also be chemically and thermally inert during the synthesis and any following processing steps. Second, deposition of the materials or solution must cause wetting of the internal pore walls. Third, the deposition should start from the bottom or one end of the template channels and proceed from one side to the other. Materials such as aluminum oxide (AAO), zeolites, glass, mica, polycarbonate (PC) and copolymer films are all useful templates for the fabrication of NRs. When used as a template, PC provides the advantages of easy handling and easy removal by means of pyrolysis at elevated temperature. However, the distortion of PC membranes during the heating process and removal of the template will generally occur before complete densification of the NRs, which would result in their being broken and deformed. Although AAO is more rigid and resistant to high temperature (allowing the preparation of a larger surface area of fairly free-standing and unidirectionally aligned NR arrays), it is very difficult to remove completely after the NR growth.

Electrochemical deposition has been used frequently to deposit materials into AAO templates and PC membranes [6]. Typically, a thin metal film such as silver is evaporated onto one face of the template in the first step of the general process. This metal film is used as a working electrode that is responsible for electrodepositing materials in the pores. Before the desired components are deposited, a layer of sacrificial metal (e.g., silver) is deposited into the pores to prevent the formation of a deformed mushroom shape at one end of the NRs. Deposition of the desired components is then carried out, after which concentrated nitric acid and 3 *M* sodium hydroxide solutions are often used to chemically dissolve the thin film electrode, sacrificial metal layer and template to produce free NRs. Electrochemical deposition is fast and usually conducted at ambient conditions, thus avoiding the use of heating and vacuum systems. Electrochemical deposition is convenient in the preparation of multisegmented NRs, simply by changing the plating solution, potential magnitude and the shape of the electrical pulse. Multisegmented rods such as Au–Ni–Au, Au–CdS–Au and Au–Ag have been prepared by electrochemical deposition using AAO membranes [48–50].

Wang and Ozkan fabricated CdTe–Au–CdTe NRs by conducting electrochemical deposition using AAO as a template with 200 nm-diameter pores [51]. Briefly, a silver film was coated on one side of an AAO template by thermal evaporation (this silver film served as the working electrode in a standard three-electrode electrochemical cell). Before depositing the CdTe, Ag was deposited galvanostatically using a commercially available electrolyte (Techni Silver Cyless II) at 1 mA cm^{-2} for 5 min as sacrificial layer. CdTe segments of the nanowires were deposited at room temperature from the electrolyte at 10 mA cm^{-2} for 15 min, while Au segments were deposited from a commercial solution (Techni Gold 25 ES) at 2 mA cm^{-2} for 15 min. Finally, another segment of CdTe was deposited for 15 min. On completion of the deposition, the silver electrode and silver segment inside the pores were removed by dipping the template into a 70 vol% nitric acid solution, while the template was dissolved in a 6 *M* NaOH solution. Both, SEM and TEM images confirmed the formation of CdTe–Au–CdTe nanowires of 230 nm diameter and 5 μm length. Electrical characterization indicated that the as-prepared CdTe–Au–CdTe nanowires possessed a p-type behavior in a back-to-back Schottky diode configuration.

Electrochemical deposition at –0.95 V was applied to the preparation of Au–Ni NRs from Gold Orotemp 24 and nickel sulfamate RTU solution, using AAO as the templates. By controlling the charge passed through the cell, the length of each block was also controlled. In order to grow 100 nm blocks of Au and Ni, 0.03 and 0.1 coulombs were required, respectively [48]. The field emission scanning electron microscopy (FESEM) image confirmed the formation of Au–Ni NRs that were 83 nm in diameter and 260–510 nm long. The optically inactive component Ni was seen to play a relaying role in the surface plasmon coupling both for the dipole mode and for the higher-order modes of gold blocks. The study results suggested that the free electrons in Ni could participate in an optical coupling phenomenon, and that plasmon excitations in the Au blocks induced the free electrons in Ni to oscillate.

Five-segment (Pt–Ru–Pt–Ru–Pt, Pt–Ni–Pt–Ni–Pt and Pt–RuNi–Pt–RuNi–Pt) NRs with the same overall rod length and same total Pt segment length were prepared by sequential electrodeposition of the metals into the pores of AAO membranes [29]. Platinum was electrodeposited from an aqueous solution of H_2PtCl_6 (0.01 *M*) and H_2SO_4 (0.2 *M*) at a constant current density of –0.44 mA cm^{-2} and at 50 °C. Nickel electrodeposition was carried out at –0.87 V for 60 s from a mixture (pH 3–5) of $NiSO_4 \cdot 6H_2O$ (300 g l^{-1}) and H_3BO_3 (40 g l^{-1}) in water at 50 °C. Ru segments were deposited from a solution of $Ru(NO)Cl_3$ (3.5 g l^{-1}) and NH_2SO_3H (10 g l^{-1}) at –0.6 V and 50 °C for 240 s. The deposition of RuNi segments from an aqueous solution (pH 3–5) containing $NiSO_4 \cdot 6H_2O$ (30 g l^{-1}), H_3BO_3 (4.0 g l^{-1}), $Ru(NO)Cl_3$ (3.15 g l^{-1}) and NH_2SO_3H (9.0 g l^{-1}) was carried out at 50 °C and –0.87 V for 300 s. For the preparation of segmented NRs consisting of alternating sequences of Pt and the oxophilic metal(s) (Ni, Ru or RuNi), one metal was plated at a time, followed by rinsing of the membrane with ultrapure water and the application of a constant current density of –0.44 mA cm^{-2} until the potential was more negative than –4.0 V. This process was repeated four times to form the five-segment

Pt–(oxophilic metal) NRs. An examination using FESEM showed the NRs to be about 210 nm in diameter and about 1.5 mm long. The use of segmented NRs with identifiable Pt–oxophilic metal(s) interfaces removes many of the ambiguities in the interpretation of experimental data from conventional alloy catalysts, thereby enabling a direct comparison of the activities of various types of pair sites in methanol oxidation.

8.2.2.3 **Bimetallic/Trimetallic Oxide NRs**

$CoFe_2O_4$ ferrite has large magnetocrystalline anisotropy with a reasonable magnetization, which holds great potential for the fabrication of high-density magnetic recording media and high-performance electromagnetic devices. A solution-based micelle method was used to prepare high-yield $CoFe_2O_4$ NRs from cobalt nitrite ($Co(NO)_3$), iron chloride ($FeCl_2$), oxalic acid, cyclohexane, *n*-pentanol and CTAB [52]. The NRs were initially amorphous, but nucleated internally and crystallized through a calcination process upon heating. The overall dimensions of the NRs were 50–100 nm diameter and 10–20 μm length. The study results suggested that the cetyltrimethylammonium ions served not only as an emulsifier for the generation of 1-D amorphous precursor composites but also as a low-temperature organic molten-salt medium for directional alignment during the early stage of calcination.

Cadmium tungstate ($CdWO_4$) NRs, with lengths of 250–400 nm and widths of 30–60 nm, were successfully synthesized at 70 °C via a hydrothermal process [53]. Appropriate amounts of starting materials (Na_2WO_4 and $Cd(NO_3)_2$) were dissolved in distilled water to form aqueous solutions, separately, and then mixed together with strong magnetic stirring at room temperature. The suspension solution was poured into a 1000 ml stainless steel autoclave which was sealed and maintained at 70 °C for 10 h, and then cooled to room temperature. The $CdWO_4$ NRs showed a PL emission peak at 435 nm. Single-crystalline $CoWO_4$ NRs with an average diameter of 20 nm and lengths of 100 to 300 nm were successfully synthesized from $CoCl_2$ and Na_2WO_4 in aqueous solution, using a hydrothermal method [54]. This straightforward method does not require any seed, catalyst, surfactant or template, and thus shows great promise for the large-scale and low-cost production of $CoWO_4$ NRs. Because no surfactants or templates were introduced into the reaction system, the formation of $CoWO_4$ NRs was thought to be due to the crystal structures. In fact, it has been suggested that the crystal growth is controlled by both extrinsic and intrinsic factors, including the degree of supersaturation, the diffusion of the reaction, surface energy and crystal structure in the solution reaction system [55, 56]. Yu *et al*. reported the synthesis of single-crystal tungstate NRs such as MWO_4 (M = Zn, Mn, Fe), Bi_2WO_6, Ag_2WO_4 and $Ag_2W_2O_7$ by the hydrothermal process, without using templates or surfactants [57]. These authors found that the formation mechanism of the NRs could be easily explained by the spherical diffusion model, in which a layer of solute is located around each crystal during the diffusion-controlled lateral growth.

A hydrothermal method was also used to prepare $ZnAl_2O_4$ NRs in large quantities [58]. The temperature and pH values for the hydrothermal synthesis are

essential to affect the characteristics of the resultant nanomaterials, in terms of their morphology and catalytic properties. The effect of hydrothermal synthesis temperature on the particle size and shape of the resultant nanomaterial became clear when the freshly synthesized nanomaterials were calcined at 750 °C for 5 h. When synthesized at 180 °C, all NPs are found to be tangentially connected with each other, without any clear boundaries for each NP. However, the 1-D nanomaterials generated were well dispersed and randomly grouped with clear NR shapes when the synthesis was conducted at 200 °C. This difference in overall morphology was attributed to the degree of crystallinity at different synthesis temperatures. The study results also suggested that the pH of solution is an important parameter for controlling the surface morphology of the resultant calcined nanomaterials. Although the near-neutral conditions produced the largest NPs, with a surface area of 68.9 $m^2 g^{-1}$, the sizes of the $ZnAl_2O_4$ nanostructures synthesized at pH 5.5 and pH 10 were much smaller, with larger surface areas of 141.8 and 113.4 $m^2 g^{-1}$, respectively. The as-prepared $ZnAl_2O_4$ nanomaterials showed a superior catalytic activity and selectivity for the reduction of NO_x in the presence of excess oxygen.

Ternary oxide zinc stannate, Zn_2SnO_4, is an interesting semiconductor material, with the same band gap energy as that of SnO_2 (E_g = 3.6 eV). Zn_2SnO_4 is a promising material for the fabrication of photovoltaic devices to detect combustible gases and humidity, photoelectrochemistry, functional coatings and transparent conducting electrodes, mainly due to its high electron mobility, high electrical conductivity and low visible absorption. Yao and coworkers reported the preparation of single-crystalline Zn_2SnO_4 NRs with diameters of 2–4 nm and a length of 20 nm by using a simple hydrothermal process with hydrazine hydrate as an alkaline mineralizer [59]. Prior to the hydrothermal process, hydrazine hydrate reacted immediately with $ZnCl_2$ and $SnCl_4$ to form a slurry-like white precipitate (complex clusters); this is regarded as a very important step for the formation of Zn_2SnO_4 NRs. Hydrazine hydrate, the hydrothermal temperature and the molar ratio of $ZnCl_2$: $SnCl_4$ are three key factors for the hydrothermal formation of ultrafine NRs that display a noticeable blue-shift from the band gap of the bulk Zn_2SnO_4 crystal.

YVO_4 nanowires with diameters of 140 to 250 nm and lengths up to 50 μm were synthesized from Y^{3+} at pH 5–6 via a hydrothermal reaction using $(NH_4)_{0.5}V_2O_5$ nanowires as the templates [60]. The YVO_4 nanowires were formed through the self-assembly of YVO_4 NPs, which have almost the same morphology as that of the templates. The PL spectrum of the Eu-doped YVO_4 (YVO_4 : Eu) nanowires exhibited four strong luminescence peaks at 594, 619, 645 and 698 nm under the excitation of 316 nm. YVO_4 : Eu nanorods (5 atom% Eu) having a rectangular cross-section of about 35 × 60 nm^2 and a length of about 220 nm were synthesized using a hydrothermal reaction [61]. In a typical synthesis, 124.6 mg of Y_2O_3 and 10.2 mg of Eu_2O_3 were heated to dissolve in a 5 ml solution of nitric acid and NH_3 (1 : 1; pH 6–7). NH_4VO_3 (136 mg) was slowly added to the suspension, and then diluted with deionized water to 35 ml. After stirring for 10 min, the mixture was transferred to a 50 ml Teflon-lined stainless steel autoclave. A few porous silicon substrates that had been prepared by hydrothermally treating silicon substrates with

30% HF solution for 5 h at 140 °C were added to the autoclave, which was then sealed and maintained at 170 °C for 58 h. After cooling, the precipitates in the solution were filtered to remove the porous silicon substrates and washed three times with deionized water.

$LaVO_4$: Eu nanowires were prepared by applying an ethylenediaminetetraacetic acid (EDTA)-mediated hydrothermal method [62]. In a typical synthesis procedure, a stoichiometric ratio of $La(NO_3)_3 \cdot 6H_2O$ and $Eu(NO_3)_3 \cdot 6H_2O$ aqueous solution and appropriate EDTA dissolved in ammonia were added to distilled water in a 100 ml flask under vigorous stirring to prepare the chelate complexes. When $Na_3VO_4 \cdot 12H_2O$ was added dropwise to the flask the solution turned yellow immediately. Finally, the mixture was transferred into a Teflon-lined stainless steel autoclave of 100 ml capacity, the temperature of which was maintained at 180 °C for several days. The $LaVO_4$: Eu NRs were rod-like in shape with diameters of approximately 100 nm and lengths ranging from 0.5 to 1.0 μm. It was found that Eu^{3+} had replaced La^{3+} to enter the $LaVO_4$ crystalline host lattice, and consequently the unit cell parameters of $LaVO_4$: Eu nanowires became smaller. Owing to the effect of the 4f-electron of the Eu^{3+} ions, the $LaVO_4$ nanowires doped with Eu^{3+} ions led to noticeable improvements in both luminescent and magnetic properties.

Uniform core-shell heterostructured $ZnWO_4/MWO_4$ (M = Mn, Fe) NRs have been synthesized using a simple refluxing method under mild conditions, in which the crystallization event of MWO_4 occurred on the backbone of $ZnWO_4$ single crystalline NRs (average diameter 40 nm, length up to 500 nm) in a ligand-free system [63]. Typically, 0.2 mmol $ZnWO_4$ NRs dispersed in 40 ml of water in a flask was refluxed at 120 °C; 0.02 mmol $MnCl_2$ (or $(NH_4)_2Fe(SO_4)_2 \cdot 6H_2O$) and 0.02 mmol Na_2WO_4 solutions were then added sequentially to the precursor solution. The $ZnWO_4$ NR-directed oriented aggregation mechanism has been clearly observed for the formation of heterostructured $ZnWO_4/MWO_4$ NRs. The as-prepared NRs possess both optical and antiferromagnetic properties; however, by changing the molar ratio of these precursors the shell thickness of MWO_4 could be tuned over the range 10–13 nm.

8.2.2.4 **Semiconductor NRs**

Fe-doped ZnO (ZnO : Fe) NRs were prepared through an *in situ* low-temperature hydrothermal synthetic route [64]. A p-type Si wafer was used to grow ZnO NRs. For this, a ZnO seed layer was deposited on the wafer using a ZnO target by applying a radiofrequency sputtering at 13.56 MHz in an Ar environment. The wafer in the Teflon holder was suspended with surface facing down in the growth solution (30 m*M* zinc nitrate hexahydrate, 30 m*M* iron acetate, 2 ml ammonium hydroxide, 80 ml of deionized water) at 60 °C for 6 h. Fe doping has shown to be effective for improving the optical properties of ZnO NRs.

A direct wet-chemical method was used to synthesize single crystalline Co-doped ZnO NRs [65]. By introducing pure ZnO seeds as the nucleation centers, $Zn_{1-x}Co_xO$ grew to form a rod-shaped nanocrystal through two-step processes. The first step leads to the formation of ZnO seeds, which act as the nucleation center of the $Zn_{1-x}Co_xO$ NRs having lengths between 300 and 600 nm and diameters

between 30 and 60 nm. In the second step, the ZnO seeds were added into a solution of the hexamethylenetetramine in the flask, after which the mixture was heated to 85 °C. Finally, a mixture of zinc nitrate and cobalt nitrate solution was injected slowly into the flask with vigorous stirring at 85 °C for 2 h. The study results suggested that a seed-mediated synthetic route would be required to avoid the phase segregation of $Zn_{1-x}Co_xO$ to ZnO and CoO in the solution.

AlO_x/ZnO core-shell NRs arrays have been successfully synthesized by soaking the ZnO NRs in the sol–gel solution of $Al(NO_3)_3$ and NH_4OH at room temperature [66]. The SEM image shows that the AlO_x/ZnO core-shell NRs can be only grown perpendicularly on the ZnO_f/Si substrate under solution at pH 6–7. After being annealed at 400 °C in N_2 atmosphere, a strong photoluminescence peak corresponding to blue emission (450 nm) was detected from the AlO_x/ZnO core-shell NRs that may result from the induced defects due to interaction between the AlO_x shell and the ZnO NRs.

Water-soluble CdHgTe NRs were prepared in an aqueous medium containing $Hg(CH_3COOH)_2$ using CdTe NRs as templates [67]. First, $Cd(ClO_4)_2$ and NaHTe were refluxed in water in the presence of a mixed-ligand system (thioglycolic acid and cysteine) to form CdTe NRs. Different amounts of $Hg(CH_3COOH)_2$ solutions were then added to the CdTe NRs solution under vigorous stirring. After reaction at room temperature, CdHgTe NRs with diameters of 10–20 nm and 60–300 nm in the short and long axes of the NRs, respectively, were formed. The CdHgTe NRs were of similar size to the CdTe NRs. The emission of the CdHgTe NRs was tunable in the near-infrared region (694–830 nm), depending on the composition of the CdHgTe NR. However, CdHgTe NRs cannot be used directly for cell applications because of their heavy-metal toxicity. Surface coatings of CdHgTe NRs with low-toxicity chemicals such as ZnS, or biopolymers such as bovine serum albumin (BSA), have been demonstrated to significantly reduce cytotoxicity.

Chalcopyrite ternary semiconductor $CuAlS_2$ nanowires were prepared using a wet-chemical method [68]. Here, equimolar amounts of analytical grade aluminum nitrate [$Al(NO_3)_3 \cdot 9H_2O$] and cuprous chloride (CuCl) were dissolved in a solution of water and 2-propanol (1 : 3, v/v) in a three-necked flask. The solution was homogenized by stirring in a nitrogen atmosphere at 45 °C, and an excess of thiourea solution was then added dropwise to the homogenized solution. Following addition of the thiourea, the solution was heated to 60 °C for a few minutes to form $CuAlS_2$ nanowires that were uniformly tetragonal in shape, with diameters of 100 to 300 nm in lengths of 1000 to 5000 nm. The $CuAlS_2$ nanowires displayed a sharp absorption edge at 377.5 nm, and a strong near band edge emission at 3.45 eV (360 nm).

8.3 Properties

The advantages of multielemental NRs over single-component NRs include multifunctional properties, and also the possible enhancement of both their chemical

and physical properties. In addition to their shapes and sizes, the components, relative contents and structures (e.g., alloys, core/shell and multisegments) also determine the physical and chemical properties of multielemental NRs. For example, Au/Pt NRs possess unique catalytic and optical properties, while FePt NRs have high magnetic and catalytic properties. Recently, multielemental NRs have attracted interest in many fields, including catalysis, sensing, separation, electronics, optics and therapeutics. Yet, in order to understand their practical applications, attention must be paid to the absorbance, emission, SERS effects, catalytic efficiency and magnetism of multielemental NRs.

8.3.1 Absorption

Owing to their unique optical properties that originate from surface plasmon resonance (SPR), metallic nanomaterials have attracted much interest in areas of chemical and biochemical sensing, diagnostic and therapeutics and cell imaging. The scattering efficiency and their relative contribution to the total extinction have been shown to depend on the nanomaterial's size, shape, metal composition and surrounding medium. With regards to their thermally therapeutic applicability, small sizes of NRs are favorable, mainly because their optical absorption has a dominant effect. As a result of thermal decay following the absorption of light, local heating takes place which can be used to kill abnormal tissues. Metallic NRs have at least two SPR bands, namely transversal (shorter wavelengths) and longitudinal (longer wavelengths). When compared to the same components of spherical nanomaterials, NRs have greater molar absorptivity values at the longitudinal absorption wavelengths. From the viewpoint of sensitivity, metallic NRs are at the center of attention. Typically, the molar absorptivity and wavelengths of the SPR bands for NRs depend heavily on their compositions and geometrical parameters, such as the aspect ratio and shell thickness (only for core-shell NRs). The effect of geometrical parameters on the shift in wavelength is more easily expected; a red shift occurs on increasing the aspect ratio of NRs. For example, the SPR bands for high-quality Au NRs can be easily expected based on a classical electrostatic theory [69]. The effect that the composition has on changes in the absorption of NRs is relatively complicated and difficult to predict, mainly because their absorption and refractive index are strongly related to the components of the NRs. In order to understand the composition dependence of absorption for NRs, discrete dipole approximation (DDA) calculations were carried out for Ag–Au alloy metallic NRs with different Ag compositions (x_{Ag} = 0, 0.2, 0.5 and 1.0) [70]. In the past, the DDA method has been regarded as one of the most powerful and flexible electrodynamic methods for computing the optical scattering of particles with an arbitrary geometry. Figures 8.5a–c summarize the results of DDA calculations of binary AgAu alloy NRs with an aspect ratio of 3.4 as a function of Ag concentration. From Figure 8.5a, it is observed that the resonance wavelength is sensitive to the refractive index of the surrounding medium, although the sensitivity is independent of the Ag concentration in the alloy (as seen from Figure 8.5b). Figure 8.5a and c show that

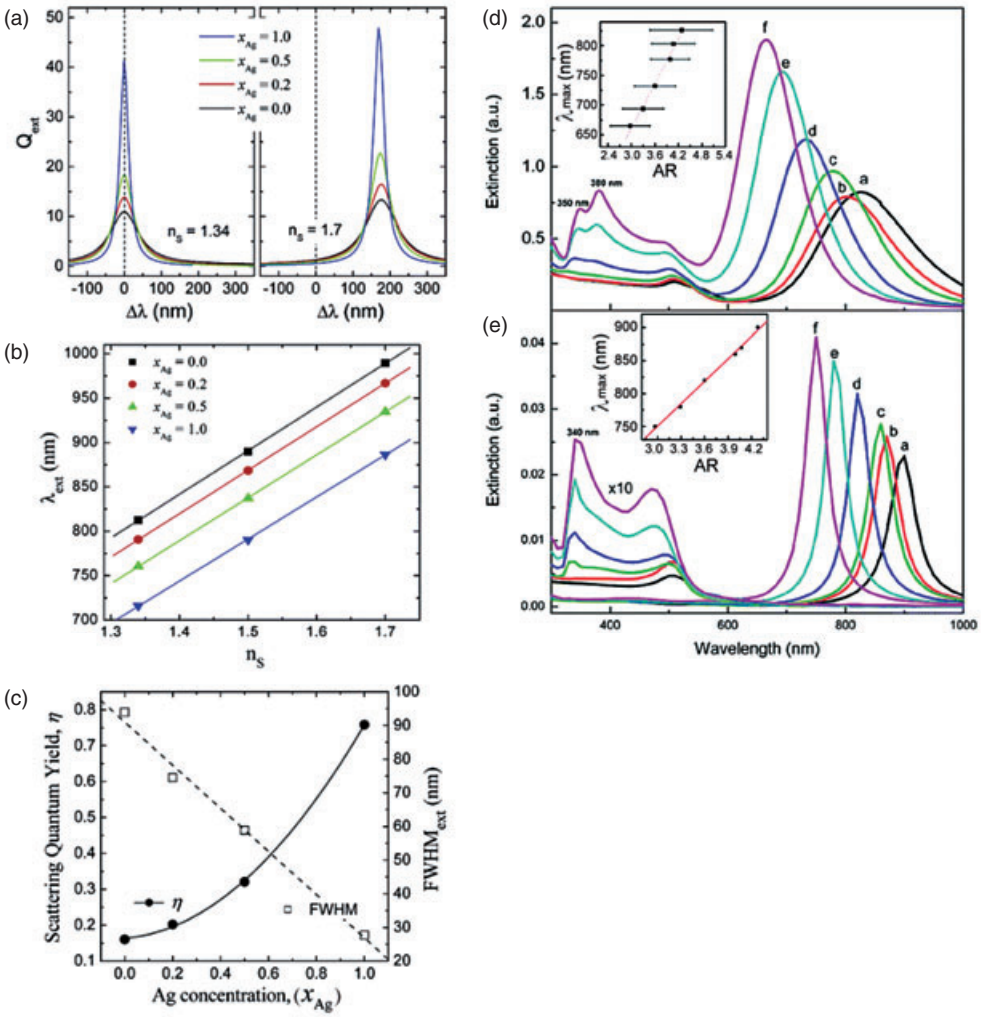

Figure 8.5 (a) Calculated spectra of optical extinction efficiencies of the longitudinal plasmon mode for an AgAu alloy metallic NR with a fixed aspect ratio of 3.4 and different Ag concentrations as a function of relative wavelength shift with change in the medium refractive index from 1.34 to 1.7; (b) The quantitative dependence of SPR wavelength responses on the Ag concentration as a function of the refractive index of the surrounding medium; (c) Scattering quantum yield and full width at half-maximum of the SPR peak as a function of Ag concentration in AgAu alloy metallic NRs when $n_S = 1.34$; (d) UV-visible extinction spectra of (a) the as-prepared Au NRs (61.2 ± 6.7 and 14.3 ± 1.7 nm) and (b–f) the homogeneously coated Ag shell/Au core dispersions with sizes (length and width) of (62.9 ± 4.5 nm and 15.4 ± 1.7 nm), (63.1 ± 4.1 and 15.8 ± 1.4 nm), (63.3 ± 6.6 and 17.6 ± 1.4 nm), (63.9 ± 5.9 and 19.4 ± 2 nm) and (64.3 ± 6.2 and 21.6 ± 2.3 nm), respectively. The inset shows the relationship between the average aspect ratio and the SPR position; (e) Calculated extinction spectra for single Ag shell/Au core NR by DDA simulation. The inset shows the relationship between the average aspect ratio and the calculated longitudinal SPR position. Panels (a–c) reprinted with permission from Ref. [70]. Panels (d, e) reprinted with permission from Ref. [73].

the plasmon bandwidth is also sensitive to the fraction of Ag in the alloy; indeed, as the Ag fraction increases the plasmon band becomes sharper and increases in intensity. A narrower bandwidth allows a much easier detection of the change in the SPR in response to refractive index changes in the surrounding medium.

Core/shell Au/Ag NRs were synthesized and their absorption behavior has been investigated in detail [44, 71–73]. The extinction spectra and theoretical extinction spectra of core/shell Au/Ag NRs obtained using DDA method were compared [73]. Figure 8.5d shows that, on increasing the Ag shell thickness, the longitudinal SPR band gradually blue-shifts and becomes greater. The maximum wavelengths of the longitudinal SPR band show a good linear relationship with the aspect ratio (Figure 8.5d, inset). At shorter wavelength regions, however, apart from the transverse SPR band of pure Au NRs at 510 nm, two new peaks at 340 and 380 nm appear. In the calculated DDA spectra (Figure 8.5e), the longitudinal dipole resonance blue-shifts and enhances upon increasing Ag shell thickness. A good linear relationship between the aspect ratio and the calculated longitudinal SPR bands is also observed (Figure 8.5e, inset). At the shorter wavelength regions, in addition to the transverse SPR of the gold NR, a new peak at 340 nm appears and becomes dominant in the NRs having a thick shell (>16 nm); this reveals that such a peak is due to a transverse dipole resonance of the Ag shell.

8.3.2 Emission

One particularly interesting characteristics of some semiconductor NRs is that they have emission over the range from the ultraviolet to the infrared region [74–76]. Semiconductor NRs provide advantages over organic fluorophores, including chemical stability, a high photobleaching threshold and narrow emission spectra profiles. With such advantages, these materials have attracted much interest for sensing and for the fabrication of optical devices. 'Heterostructures' of NRs consisting of a NR core of one material sandwiched between two ends of a different material, are also of interest [40, 77]. The photoluminescent intensity of CdTe–CdSe–CdTe NRs was quenched upon the addition of CdTe end caps (part c of Figure 8.6a); the quantum yield drops more than an order of magnitude after the first injection of Te–trioctylphosphine (from 0.24 to 0.01%) and remains essentially unchanged after further Te–trioctylphosphine injections. Due to the staggered type II band offset, however, there is an energy barrier that prevents electron transfer from the CdSe core into the CdTe ends, whereas the hole transfer from the CdSe core into the CdTe ends is energetically downhill. As the end caps lengthen, the relative likelihood of electron-hole recombination at the CdSe–CdTe interface increases, and this leads to a decreased photoluminescent quantum yield [78]. Core/shell deposition of the smaller band gap semiconductor, CdTe, is expected to shift the absorption edge to a longer wavelength [79, 80], but this is not observed (part a of Figure 8.6a). For rods longer than the Bohr exciton diameter, but thinner than the Bohr exciton diameter, the NR diameter is solely responsible for energy level quantization and the size-dependent shift in the optical

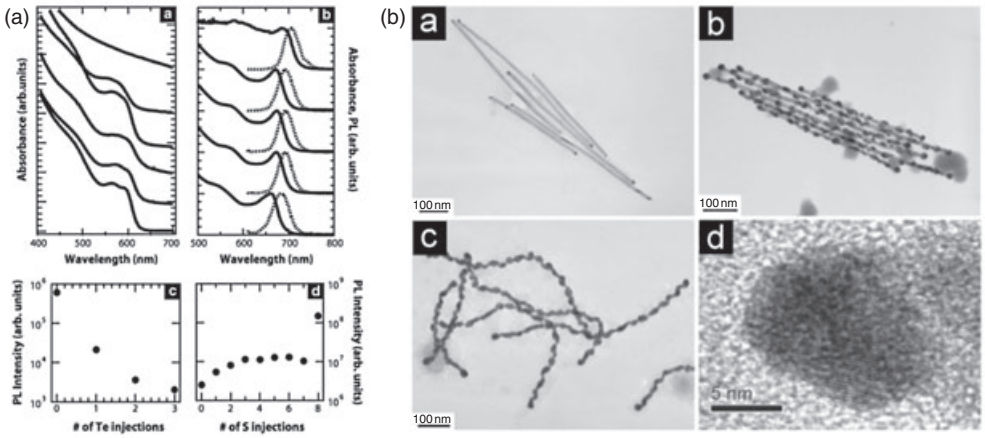

Figure 8.6 (a) Optical properties of CdTe–CdSe–CdTe and CdS–CdTe–CdS heterojunction nanorods. Panel (a) shows absorbance spectra for CdTe–CdSe–CdTe heterojunction rods with multiple chalcogen precursor injections; at long reaction times, ripening increases the particle size past the Bohr diameter, giving the appearance of bulk material at long times. Photoluminescence is not reported as it is quenched due to the type II band offset. Panel (b) shows absorbance and photoluminescence of CdS–CdTe–CdS heterostructure NRs. Panels (c, d) show photoluminescent peak intensity as a function of precursor injections. The type II band offset of CdTe–CdSe–CdTe results in quenching, whereas the type I band offset CdS–CdTe–CdS increases the photoluminescent quantum yield. (λ_{ex} = 550 nm for CdTe/CdSe/CdTe at 550 nm; λ_{ex} = 610 nm for CdS–CdTe–CdS); (b) TEM images of SERS substrates. Panel (a) Au–Te NDBs, panel (b) Au–Te NPPs, panel (c) Au PNNs, and panel (d) HRTEM of (a). (a) Reprinted with permission from Ref. [77]. (b) Reprinted with permission from Ref. [94].

spectra [15, 81]. The fact that the absorbance spectra do not noticeably shift to longer wavelengths with increasing amounts of CdTe deposition indicates that CdTe deposits selectively at the {002} end cap faces of the CdSe NRs. The optical properties of the CdS–CdTe–CdS NRs are also consistent with heterostructure NR formation with sequential precursor injection; the addition of CdS enhances the photoluminescent intensity of the CdTe NRs (part d of Figure 8.6a). The quantum yield increases an order of magnitude, from 0.37% for bare initial CdTe rods to 1.70%, as additional CdS is added epitaxially. If the mixture is slowly cooled to room temperature, CdS grows gradually so as to minimize the surface defects, and this leads to an enhanced photoluminescence of up to 20% (part d of Figure 8.6a). The absorbance spectra are again consistent with NR formation, with the absorption edge staying fixed at one wavelength with addition of the CdS (part b of Figure 8.6a). The core/shell particles would also be expected to exhibit these types of change in the optical properties [82]. In contrast to CdTe–CdSe–CdTe NRs, the CdS–CdTe–CdS NRs do not undergo ripening over long reaction times, this differing qualitatively from the situation that occurs with the CdTe NRs.

Alternatively, ZnO NRs which have a direct band gap of 3.37 eV and are less toxic compared to CdS and CdTe, are also often used in the preparation of

multielemental semiconductor NRs. A previous report described the results of ZnO NR arrays doped with different amounts of Fe [64]. Each sample has two emission peaks, one in the UV region (~374 nm) and another in the visible region (~520 nm). The UV emission peak results from an excitonic recombination corresponding to the near-band-edge emission of ZnO [83]. On the other hand, the visible emission is green or yellow, depending on the availability of oxygen states. The green emission, which is referred to as a deep-level emission (DLE), is attributed to the recombination of electrons trapped in singly ionized oxygen vacancies with holes [84, 85], whereas the yellow emission results from the interstitial oxygen ions [86]. As the Fe concentration in the synthesis solution is increased, the peak intensity of the UV emission is also increased, while the visible emission intensity is decreased. A reduced peak intensity of green emission indicates that the lattice of Fe^{3+}-doped ZnO NRs has fewer oxygen vacancies when compared to undoped ZnO NRs. The peak ratio (I_{UV}/I_{DLE}) increased upon increasing Fe concentration in the synthesis solution. These results reveal that Fe^{3+}-doped ZnO NRs exhibit improved optical properties, presumably resulting from fewer oxygen vacancies.

Rod-, olive-, pineapple- and particle-like nanocrystals of the YVO_4:Eu (ca. 5% Eu) all have unique photoluminescent properties [61]. When measuring the photoluminescence excitation spectra of four different YVO_4:Eu samples under an emission of 618 nm, all of these samples have two excitation peaks at 307 and 328 nm, with varying intensities. The intense transitions observed in the luminescence spectrum originate from the $^5D_0$ level that is not split by the crystal field ($J = 0$) under the excitation of 328 nm. The peaks at 593, 618, 652 and 698 nm are attributed to electric dipole transitions from the $^5D_0$ level to sublevel of $^7F_1$, $^7F_2$, $^7F_3$ and $^7F_4$, respectively, whereas the weak peak at 537 nm is attributed to transition from $^5D_1$ to $^7F_1$ [87]. The emission intensities of the four samples are different, most likely due to the change in symmetry of the crystal fields around Eu^{3+} ions. These different sizes and shapes result in different combinative abilities between the surface and the adsorbed species, leading in turn to different quenching abilities to the emission from Eu^{3+} ions. The luminescence intensity of the olive-like NRs is clearly stronger than that of other samples, most likely because the nanostructures can prevent the adsorbed species on the surface from quenching the emission from Eu^{3+} ions.

8.3.3
Surface-Enhanced Raman Scattering

Since its first inception by Fleishmann in 1974, SERS has attracted considerable interest in several fields, including surface science, electrochemistry, biology and materials science. Three metals (Au, Ag and Cu) have shown major effects on enhancing the SERS signals of many solutes of interest. SERS occurs when molecules are adsorbed onto rough metal surfaces or onto aggregated metallic NPs [88]. Relative to spherical Ag NPs, spherical Au NPs have the beneficial properties of long-term stability and a narrow size distribution [89–91]. Nevertheless, the

Raman enhancement factors of molecules adsorbed onto Au NPs are usually 100- to 1000-fold lower than those on Ag NPs. The SERS signals of 4-mercaptopyridine produced from pure Au NRs are weak, but can be enhanced by using Au/Ag core/shell NRs [92]. Coating the Au NR surface with a thin Ag layer (1–25 nm) caused an increase in SERS sensitivity of between 10- and 100-fold. The effect of local environment on SERS of *p*-nitroso-*N,N*-dimethylaniline utilizing Au, Ag and Ag–Au striped NR array substrates was investigated [93]. The intensity ratio between the ring-breathing mode at 1600 cm^{-1} and the dimethyl-amino stretch at 1400 cm^{-1}, referred to as the polarization ratio (I_{ratio}), for Au and Ag substrates was consistently different. The spectra of Au samples exhibited similar peak intensities for these two modes, while the peak intensity of the methyl-amino stretch was always higher than the ring stretch for Ag samples. The peak shapes and relative intensities of the peak heights at 1400 and 1600 cm^{-1} did not change significantly in the spectra taken from different regions of the striped samples. The peak position and I_{ratio} data suggested that the SERS experiments were probing the entire length of the rod and not only the upper region at this array length scale. For these striping patterns, the I_{ratio} indicated that the binding of the analyte was similar to that binding on Ag-only NRs, revealing that the analyte molecules adsorbed onto the silver component of the rods dominated the spectrum.

Three SERS-active substrates – namely, gold–tellurium nanodumbbells (Au–Te NDBs), gold–tellurium nanopeapods (Au–Te NPPs) and gold pearl-necklace nanomaterials (Au PNNs) – have been prepared using Te nanowires with length/diameter ratios of 550/15 nm (Figure 8.6b) [94]. A near-infrared (NIR) laser (785 nm) was used to obtain Raman spectra of rhodamine 6G (R6G) on the as-prepared nanomaterials. When using the Au–Te NDBs as substrate, the SERS spectrum of R6G showed an enhancement factor of only 48 compared to conventional Raman spectroscopy. This small enhancement effect was due to: (i) the small content of Au NPs (present only at the ends of the nanowires (NW)s) in the as-prepared Au–Te NDBs; and (ii) the distance between the pair of Au NPs within each NW being too large to generate a sufficiently high electromagnetic field. Au–Te NPPs provide more intense SERS signals (2.2×10^6-fold) than the Au–Te NDBs, mainly due to the generation of intense local electromagnetic fields as the distance between pairs of adjacent Au NPs in each Au–Te NPP were shorter (average ca. 23.0 nm) [95, 96]. This value was similar to that reported from SERS analyses employing Au nanodisk arrays that had been prepared using relatively complex on-wire lithography techniques [97]. The largest SERS enhancement factor (5.1×10^9) was achieved by using Au PNNs, in which the Au NPs were closely connected within the nanowires. Under optimum conditions, the limit of detection for R6G was 2.5 p*M*. Unlike the situation when using aggregated nanomaterials, the SERS signals of R6G from four different batches of Au PNNs were reproducible (relative standard deviation 9.6% from five runs).

SERS effects are advantageous when directly monitoring the catalytic effects of nanomaterials; for example, the SERS effects and catalytic activities of Au/Pt hybrid NRs containing different amounts of Pt clusters for 4-aminothiophenol have been reported [45]. The Au NRs beneath the Au/Pt hybrid NRs were shown

to possess a significant local field enhancement under 1064 nm excitation; however, because the Pt clusters were not fully coated on the Au NRs the uncoated Au NRs provided some important positions for the SERS enhancement of 4-aminothiophenol. In comparison, when Pt NPs (6 nm) were investigated, only minimal noise was observed, without any enhancement effect. The electrocatalytic activity of hybrid NRs for dioxygen reduction has also been investigated.

8.3.4 Catalytic Properties

Direct methanol fuel cells have attracted interest as possible power sources for portable electronic devices, because of their characteristics of high-energy density and quick start, the convenience of generating energy, and low levels of environmental pollution. Although platinum has shown an excellent initial catalytic activity in the electrochemical oxidation of methanol at low temperatures, the chemisorbed CO intermediates generated during the methanol activation process cause poisoning of the fuel cells. Hence, in order to minimize these limitations, oxophilic metals such as Ru and Ni may be incorporated into Pt to form bimetallic or ternary alloy electrocatalysts. Pt–Ru is currently the most extensively investigated Pt alloy catalyst for the low-temperature electro-oxidation of methanol, mainly because of its resistance to electrolyte dissolution and low cost. The electrocatalytic oxidation of methanol in multisegment Pt–Ru–Pt–Ru–Pt, Pt–Ni–Pt–Ni–Pt and Pt–RuNi–Pt–RuNi–Pt (codeposited) NRs had almost the same overall rod length, and the same total Pt segment length was investigated [98]. Figure 8.7a shows the steady-state cyclic voltammograms of room-temperature (25 °C) methanol oxidation on 1.453 μm Pt–Ru–Pt–Ru–Pt, Pt–Ni–Pt–Ni–Pt and Pt–RuNi–Pt–RuNi–Pt with a total Pt segment length of 1.097 μm, using pure Pt NRs with a length of 1.097 μm as the control. Generally, methanol oxidation to CO_2 on Pt cannot occur below 0.3 V, and this was confirmed experimentally. However, the measured onset potentials for the Pt–Ru–Pt–Ru–Pt, Pt–Ni–Pt–Ni–Pt and Pt–RuNi–Pt–RuNi–Pt NRs were all less than 0.3 V, which suggested that the anodic overpotentials for water dissociation on RuNi, Ru and Ni sites might be correspondingly lower than that on Pt sites. Among the three multisegmented NR catalysts, the anodic overpotentials for dissociation of water were seen to be in the increasing order: Pt–RuNi < Pt–Ru < Pt–Ni NRs. The long-term catalyst performance of four NRs Pt–Ru–Pt–Ru–Pt, Pt–Ni–Pt–Ni–Pt and Pt–RuNi–Pt–RuNi–Pt and Pt-only NRs was investigated by measuring current–time curves (Figure 8.7b). The Pt–RuNi–Pt–RuNi–Pt NRs provided the highest oxidation current density at 0.89 mA cm^{-2}, followed by the Pt–Ru–Pt–Ru–Pt NR (0.50 mA cm^{-2}) and the Pt–Ni–Pt–Ni–Pt NR (0.18 mA cm^{-2}), while the Pt-only NR exhibited the lowest oxidation current density of 0.004 mA cm^{-2}. The Pt sites remote from the Pt-oxophilic metal(s) interface were rapidly deactivated and contributed negligibly to the overall activity. The current decayed precipitously within the first few seconds of potential application due to deactivation of the Pt sites by CO-like intermediates formed during the dissociation of methanol. Platinum-containing intermetallic polycrys-

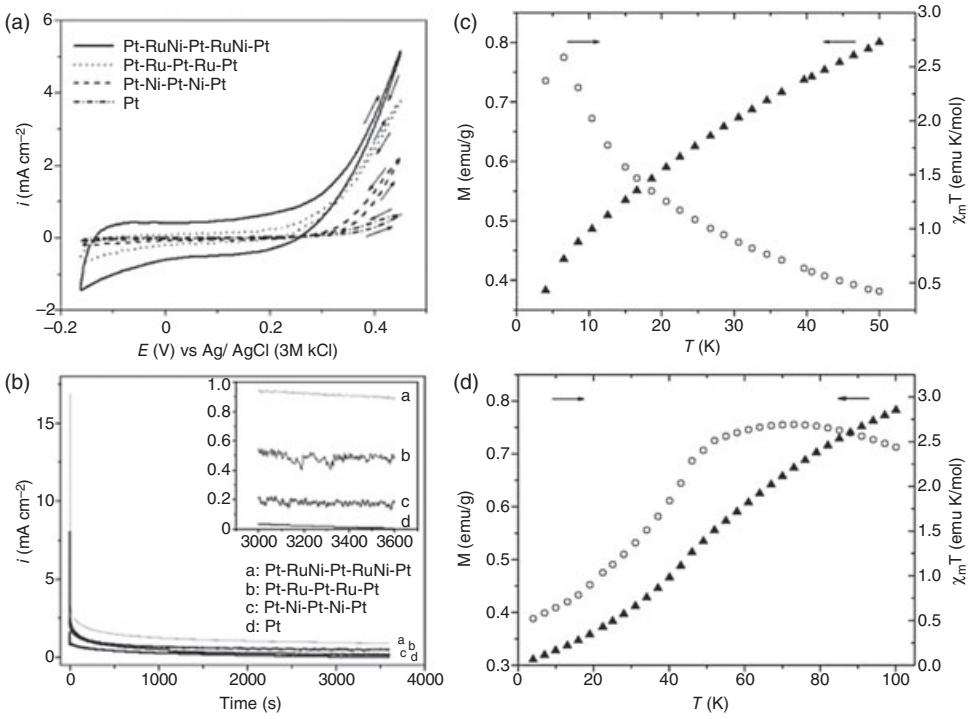

Figure 8.7 (a) Cyclic voltammograms of the as-prepared NRs and Pt-only NRs in N_2-purged $HClO_4$ (0.1 *M*) and CH_3OH (0.5 *M*) between −0.16 V and +0.45 V versus Ag/AgCl at 20 mV s^{-1} at room temperature; (b) Current–time plots of the as-prepared NRs and Pt-only NRs in N_2-purged $HClO_4$ (0.1 *M*) and CH_3OH (0.5 *M*) polarized at a constant potential of 0.4 V versus Ag/AgCl at room temperature. Temperature dependence of the magnetization and the $\chi_m T$ of (c) $ZnWO_4$@$MnWO_4$ heterostructures and (d) $ZnWO_4$@$FeWO_4$ heterostructures. ○ denotes the long moment, ▲ denotes the $\chi_m T$. Panels (a, b) reprinted with permission from Ref. [98]. Panels (c, d) Reprinted with permission from Ref. [63].

tallines such as PtPb, PtBi and PtIn show superior electrocatalytic properties towards the oxidation of small organic molecules such as ethylene glycol [31]. The peak mass current density was above 700 mA mg^{-1} Pt, which was significantly higher than that of a commercial PtRu/C catalyst (30 wt% Pt and 15 wt% Ru; Johnson-Matthey) when normalized to the unit mass of Pt.

8.3.5 Magnetism

FePt nanomaterials have been shown useful in the development of nanocrystal arrays for applications in information storage, permanent-magnet nanocomposites and catalysis. FePt alloys are chemically stable owing to the spin-orbit coupling and hybridization between Fe 3d and Pt 5d states. Moreover, by simply controlling

the atomic ratio of Fe and Pt in the alloy structure, it is possible to tune their magnetic properties. Aligning these nanocrystals magnetically has been a constant problem, as the magnetic axes of the nanocrystals in the assemblies are oriented randomly in three dimensions. The synthesis and self-assembly of FePt nanocubes suggests that elongated nanocrystals may be used to achieve texture and magnetic alignment, which is essential for the fabrication of single-particle recording media with ultrahigh density, magnetic nanocomposites with maximum energy product, and for magnetotransport devices with optimum magnetoresistivity [99]. Alternative gradient magnetometry measurements on FePt NRs have shown ferromagnetism with a coercivity of ~5 kOe at room temperature [32]. The magnetic properties of the Ni-doped ZnO NRs have also been investigated [37], with hysteresis loops with a coercive field H_C ~72 Oe having been observed at 300 K, and showing obvious ferromagnetic characteristic. The saturated magnetization was up to 0.4 emu g^{-1}, this being larger than in previous reports on Ni-doped ZnO NPs [100]. One possible reason for the ferromagnetic behavior of Ni-doped ZnO NRs is the formation of a nanoscale Ni-related secondary phase. However, the NiO phase can be easily ruled out, as bulk NiO is antiferromagnetic with a Neel temperature of 520 K. Metallic Ni is also an unlikely source of this ferromagnetism, because the synthesis of Ni-doped ZnO NRs is performed in an ethanolic solvent containing trace amounts of water, as well as OH^- which can prevent the formation of metallic Ni nanoclusters to some extent. Thus, ferromagnetism in the Ni-doped ZnO NRs could be considered to be the result of an exchange interaction between free delocalized carriers (hole or electron from the valence band) and the localized d spins on the Ni ions. The presence of free carriers is a compulsory condition for the appearance of ferromagnetism in Ni-doped NRs [101]. Pure $MnWO_4$ and $FeWO_4$ display distinct antiferromagnetic behaviors that have potential applications in the field of giant magnetoresistant materials [63]. The magnetic properties of the $ZnWO_4/MWO_4$ core/shell NRs were investigated by using a superconducting quantum interference device. The temperature dependence of the magnetization and $\chi_m T$ of ZnWO4/MnWO4 occurs between 4 and 50 K (see Figure 8.7c); antiferromagnetic ordering is also observed at about 6.5 K, with the reported value being about 8 K for pure $MnWO_4$. Such as difference is due mainly to the shape and morphology dependence of antiferromagnetic behavior and the existence of a $ZnWO_4$ core. When the temperature dependence of the magnetization and $\chi_m T$ of the $ZnWO_4/FeWO_4$ core/shell NRs was investigated over a temperature range of 4 to 100 K (Figure 8.7d), it was revealed that antiferromagnetic ordering was observed at about 76 K, which was in good agreement with reported values [102].

8.4 Analytical Applications

High-aspect ratio NRs with a large surface-to-volume ratio possess high degrees of functional and dimensional control for functionalization. Prior to their analytical application, multielemental NRs are usually subjected to conjugation with

specific chemicals, polymers and biopolymers that recognize analytes of interest, including small molecules, small ionic solutes, proteins and DNA. Functionalized multielemental NRs exhibit recognition and unique physical properties, which have in turn become materials of great interest in many applications, including catalysis, sensing and separation. In the following section, attention is focused on applications in the sensing analytes of interest, including gases, metal ions, proteins, DNA, pathogens and bacteria.

8.4.1
Detection of Gaseous Molecules

Sensors for detecting toxic and flammable gases, such as H_2S, CO, C_2H_6O and H_2, have attracted much attention due to growing concerns about environmental protection, industrial and traffic safety. Semiconductive metal oxide sensors are of special interest because of their low costs, high sensitivity, rapid response and compatibility with silicon microelectronics. Examples of semiconductive metal oxide sensors include SnO_2, ZnO, TiO_2, MoO_3 and Fe_2O_3 [103–105]. ZnO, a chemically and thermally stable n-type semiconductor, is widely used to detect toxic and combustible gases [106–111]. Likewise, 1-D ZnO nanowires have attracted considerable attention as they provide much larger length-to-diameter and surface-to-volume ratios than do bulk ZnO materials and ZnO films. Many metal-based catalysts, such as Au, Pt, Pd and Ag, have been added to the sensing layer to modulate the change of depletion width, and this has resulted in an improved sensitivity for the detection of gases [112, 113]. Recently, the use of Au and Pd NP-coated ZnO nanowires that had been grown on $Ga/SiO_2/Si$ templates, was demonstrated for the sensing of carbon monoxide and ethanol, respectively [113, 114]. Here, the limit of detection (LOD) for carbon monoxide at 250 °C was 5 ppm; moreover, the response of the fabricated sensor for carbon monoxide was rapid, stable and reversible [114]. Highly sensitive and rapidly responding ethanol sensors were produced by coating 4 nm Au NPs onto ZnO nanowires (15 ± 5 nm diameter, 1 μm length) [115]. When compared to bare ZnO nanowire-fabricated devices, both the small diameter and the Au coating on the sensor caused the surface-depletion effect to become more pronounced, and this in turn led to an increased sensitivity, a lower operation temperature, and a decreased response time. Thus, a sensitivity of 100 ppm ethanol was obtained with response time less than 2 s at 300 °C, while the operation temperature could be as low as 150 °C. When Pd NP-coated ZnO nanowires on patterned $ZnO : Ga/SiO_2/Si$ templates were fabricated for sensing ethanol [113], the detection limit (500 ppm ethanol) was increased up to 2.4-fold at 170 °C and 1.7-fold at 230 °C, compared to those sensors using bare ZnO nanowires.

8.4.2
Detection of Metal Ions

Heavy-metal pollutants exert adverse effects not only on the environment but also on human health [116]. Thus, sensitive and selective approaches towards the

detection of metal ions in biological and environmental samples are important with regards to concerns over toxic exposure to metal ions. Although inductively coupled plasma mass spectrometry represents a powerful technique for the determination of metal ions, it is expensive and not suitable for on-site analysis [117]. Thus, new techniques such as nanoprobes are being studied extensively for monitoring aqueous metal ion concentrations. Indeed, metal NPs are emerging today as important colorimetric reporters because of their extremely high visible-region extinction coefficients (10^8–$10^{10}\,M^{-1}\,cm^{-1}$), which are often several orders of magnitude higher than those of organic dyes. Recently, a simple approach for the selective sensing of Fe^{2+} ions using CTAB-stabilized Au–Ag NRs (CTAB–Au–Ag NRs) in the presence of poly(sodium 4-styrenesulfonate) (PSS) has been demonstrated [118]. The prepared CTAB–Au–Ag NRs exhibit an intense longitudinal SPR absorption ($>10^9\,M^{-1}\,cm^{-1}$ at 827 nm) in the NIR region. As a result of attractive electrostatic interactions between PSS and CTAB, an agglomeration of the CTAB–Au–Ag NRs induces a change in the absorption at 827 nm (Figure 8.8). Because Fe^{2+} ions interact selectively with PSS, the degree of agglomeration and change in absorption at 827 nm is dependent on the concentration of Fe^{2+} ions. The concentrations of CTAB–Au–Ag NRs and PSS are both important parameters in determining the sensitivity and selectivity of the present approach towards sensing Fe^{2+} ions. Under optimum conditions (34 p*M* CTAB–Au–Ag NRs, 5×10^{-6}% PSS, pH 7.2), the LOD for Fe^{2+} ions at a signal-to-noise ratio of 3 was 1.0 μ*M*. When this nanosensor system was applied to the determination of Fe^{2+} in ferritin and aqueous environmental samples, the approach was seen to have advantages of simplicity, accuracy and precision (the relative standard deviation from five runs with each sample was <3%). Similarly, CTAB–Au–Ag NRs in the presence of poly(acrylic acid) (PAA) were used for the detection of Pb^{2+} [119]. The PAA-capped Au–Ag NRs (PAA–Au–Ag NRs) were prepared as a result of the electrostatic interactions between PAA and the positively charged bilayers of CTAB on the surfaces of the Au–Ag NRs. In the presence of 0.0001% PAA, the PAA–Au–Ag NRs were stable and possessed an intense longitudinal SPR absorption ($>10^9\,M^{-1}\,cm^{-1}$ at 807 nm) in the NIR region. In the presence of Pb^{2+}, the as-prepared PAA–Au–Ag NRs were aggregated as the result of a complexation between the Pb^{2+} ions and PAA. Subsequent zeta-potential measurements confirmed that the extent of agglomeration was highly dependent on the surface charge density of the PAA–Au–Ag NRs. Under optimum conditions (51 p*M* PAA–Au–Ag NRs, 0.0001% PAA, pH 7.0) the nanosensor provided a LOD of 0.05 μ*M* for Pb^{2+}.

Mercury, at parts-per-trillion levels, in tap water samples were determined by reducing Hg^{2+} to Hg(0) that was deposited on Au NRs [120]. Following the deposition of Hg(0) on Au NRs (average aspect ratio 1.6), a blue shift of the maximum absorption wavelength of the longitudinal mode band ($\Delta\lambda_{max}$) of Au NRs was seen to take place. A calibration curve was constructed by plotting the wavelength shift of the first absorption derivative as a function of the Hg(II) molar concentration.

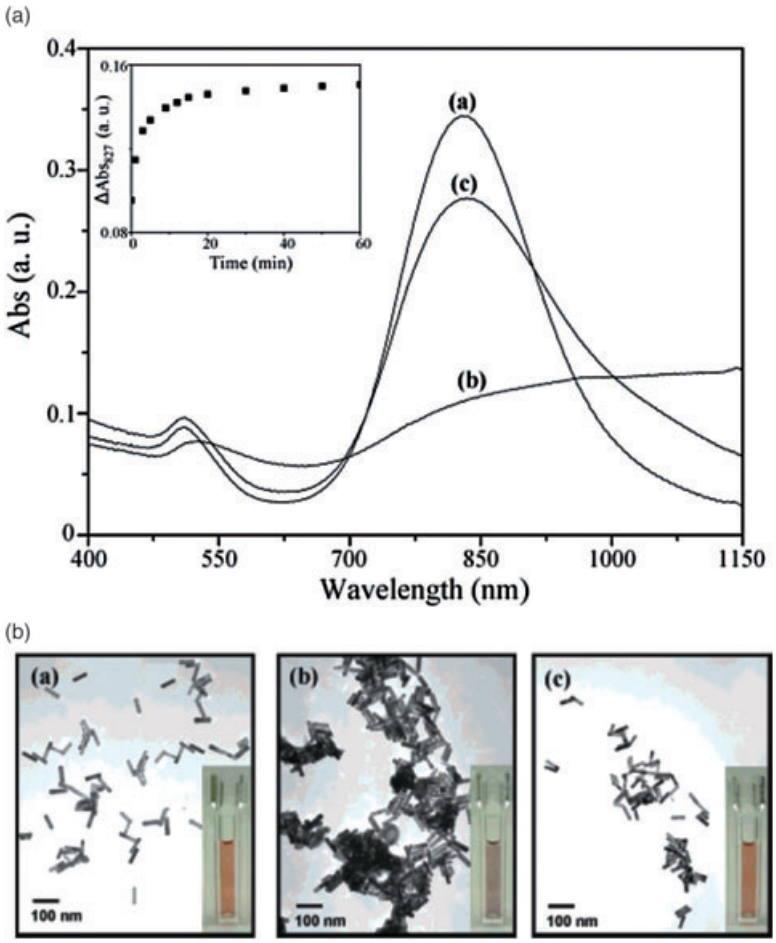

Figure 8.8 (a) UV-visible absorption spectra and (b) TEM and photographic images of CTAB–Au–Ag NR solutions in the (curve and image a) absence and (curves and images b, c) presence of 5×10^{-6}% PSS. Curves/images a, b = no Fe^{2+} ions; curve/image c = 10.0 μM Fe^{2+} ions. Inset to (a): Time-course measurements of ΔAbs_{827} for CTAB–Au–Ag NRs upon addition of a mixture of PSS (5×10^{-6}%) and Fe^{2+} (10.0 μM). The concentration of the CTAB–Au–Ag NRs in 1.0 m*M* Tris–HCl solution (pH 7.2) was 34 p*M*. Reprinted with permission from Ref. [118].

8.4.3
Separation and Sensing of Proteins

The specific attachment of different recognition molecules to individual segments of nanowires to prepare multifunctional metallic nanowires represents a particular challenge. Hence, two-component Au–Ni nanowires were selectively functionalized to yield both a hydrophilic segment (hexa(ethylene glycol)-terminated

monolayers) and a hydrophobic segment (alkylterminated monolayers) [121]. The hydrophilic and hydrophobic groups were then directed to either the Au or Ni portion by the specific interactions of Au–thiol and Ni–carboxylic acid, such that the two-component Ni–Au nanowires were functionalized to yield both a hydrophilic segment and a hydrophobic segment. The adsorption of Alexa Fluor 594-labeled goat antimouse immunoglobulin G (IgG) fluorescently tagged antibody proteins to these bifunctional nanowires was studied and quantified by using optical and fluorescence microscopy. A weak nonspecific adsorption of IgG to the hydrophilic nanowire segments was observed, whereas the IgG bound much more strongly to the hydrophobic nanowire segments. Isotherms were well described by the Langmuir model, from which a limiting surface coverage close to that expected for a monolayer ($6.0 \pm 0.5 \times 10^{-11}$ mol cm^{-2}) and an equilibrium constant of $K = 3 \pm 2 \times 10^{6} M^{-1}$ were obtained.

Triblock magnetic NRs with Au end blocks and Ni interior blocks (Au–Ni–Au) were used as novel materials for the efficient separation of mixtures of biomolecules [122]. The Ni portion of the nanostructure provides a docking site for His-tagged proteins and is ferromagnetic, allowing their selective and efficient removal from solution with an appropriately applied magnetic field. In contrast, the Au portions of the rods were passivated with thiolated poly(ethylene glycol) to minimize the nonspecific binding of proteins to Au surfaces, and also to minimize any aggregation caused by bare Au surface–surface interactions. The use of Au–Ni–Au as affinity templates for the simultaneous and efficient separation of biotin- and histidine-tagged proteins from a mixed solution was also demonstrated [21]. Here, the gold blocks were first selectively functionalized with 11-amino-1-undecanethiol, after which glutaraldehyde was used to effect the covalent attachment of nitrostreptavidin. As the histidine-tagged proteins bound to the nickel block, and the biotin-tagged proteins to the functionalized gold ends, this allowed the separation of a mixture of three proteins with a single material (Figure 8.9). Subsequently, each surface-bound protein can be released selectively, using imidazole for the histidine-tagged protein and biotin for the biotinylated protein.

Silica-coated gold NR ($Au_{rod}@SiO_2$) structures with an aspect ratio of 2.0 ± 0.8 (length 70.1 ± 5.7 nm, width 35.1 ± 2.9 nm) for the Au NR cores, and a uniform thickness of the silica shell of approximately 9 nm, have been successfully prepared using the Stöber method [123]. The self-assembly of $Au_{rod}@SiO_2$ films on poly(4-vinylpyridine)-modified quartz substrates has also been used successfully for the colorimetric detection of human immunoglobulin G (h-IgG). These core/shell NRs have a pure-silica surface, which permits the straightforward and rapid self-assembly of $Au_{rod}@SiO_2$ films onto poly(4-vinylpyridine)-modified quartz substrates. Subsequently, the $Au_{rod}@SiO_2$ was subjected to reaction with (3-amin opropyl)trimethoxysilane, which provided the amino functional groups for further covalent conjugation with goat anti human immunoglobulin G (anti-h-IgG) molecules; the latter process serves as a model reaction for the colorimetric detection of h-IgG. Remarkably, the protein recognition event on the $Au_{rod}@SiO_2$ films can be monitored not only via changes in light absorption but also by the naked eye.

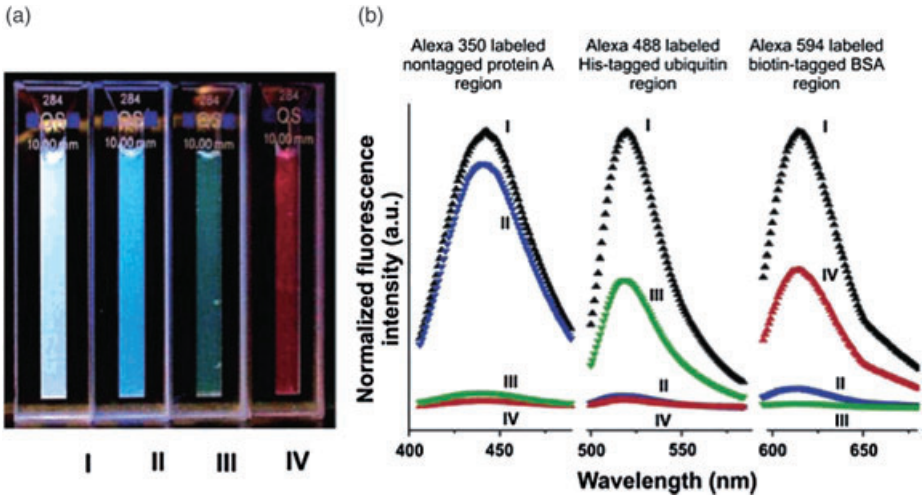

Figure 8.9 (a) Photograph of four protein solutions in cuvettes. (I) Solution mixture containing Alexa 488-labeled His-tagged ubiquitin, Alexa 594-labeled biotin-tagged BSA and Alexa 350-labeled nontagged protein A before separation. (II) After separation of Alexa 350-labeled nontagged protein A from two other proteins with NRs. (III) Green solution formed after release of Alexa 488-labeled His-tagged ubiquitin in the elution buffer from NRs. (IV) Red solution formed after release of Alexa 594-labeled biotin-tagged BSA in the elution buffer from NRs; (b) Fluorescence spectra corresponding to Figure 8.9a. The fluorescence spectrum of solution (I) is in black; that of solution (II) is in blue; that of solution (III) is in green; and that of solution (IV) is in red. Reprinted with permission from Ref. [21].

Hence, the blue-pink $Au_{rod}@SiO_2$ films on which anti-h-IgG had been immobilized were immersed in solutions containing different concentrations of h-IgG. The increase in dielectric constant that occurred close to the $Au_{rod}@SiO_2$ surface following the adsorption of h-IgG led to both a red-shift in wavelength and an increase in absorption intensity. In addition, as the h-IgG concentration was increased, red-shifts and increases in the intensity of the longitudinal plasmon absorption band were observed following the protein-recognition event.

8.4.4 DNA Detection

Multisegmented NRs provide platforms for the simultaneous detection and separation of multiple species in complex solution, as well as multiple modes for the identification of various species. Nanobarcodes composed of Ag and Au segments were prepared and used for the detection of both DNA and proteins [50]. The DNA detection strategy employed a sandwich assay, in which NeutrAvidin-modified Au–Ag NRs were first functionalized with a biotin-12-nucleotide capture sequence capable of binding a 24-nucleotide target sequence. Following capture, the target sequence was then detected by the addition of a fluorophore-tagged 12-nucleotide

probe sequence which was complementary to the remaining bases of the target strand. Similarly, a universal, short oligonucleotide-based ligation strategy using Ag–Au multisegment NRs (nanobarcodes) was demonstrated for single-nucleotide polymorphism genotyping [124]. Because the nanobarcodes are intrinsically encoded by virtue of the different reflectivity of adjacent metal stripes, the generation of many thousands of unique encoded substrates is possible. For example, in this it was shown that the number of combinations for a 9 μm-long particle with 11 stripes composed of only two metals – gold and silver – was 1056. The nanobarcodes were used for the simultaneous genotyping of 15 single-nucleotide polymorphisms within the cytochrome P450 gene family (this is important in drug metabolism and cancer risk susceptibility). In order to further demonstrate the applicability of the nanobarcodes, 160 genotypes were determined from multiplex polymerase chain reaction products of 20 genomic DNA samples.

For detecting specific single-strand DNA (ssDNA) sequences, CdTe–Au–CdTe multisegment nanowires displaying a p-type behavior in a back-to-back Schottky diode configuration were used [51]. The CdTe–Au–CdTe multisegment nanowires, after being functionalized with thiol-ended ssDNA receptors to the Au segment, were able to fabricate sensors with a field-effect transistor configuration that could be used for the ultrasensitive detection of 1 n*M* complementary DNA (cDNA) fragments based on the modulation of nanowire conductance (Figure 8.10). The

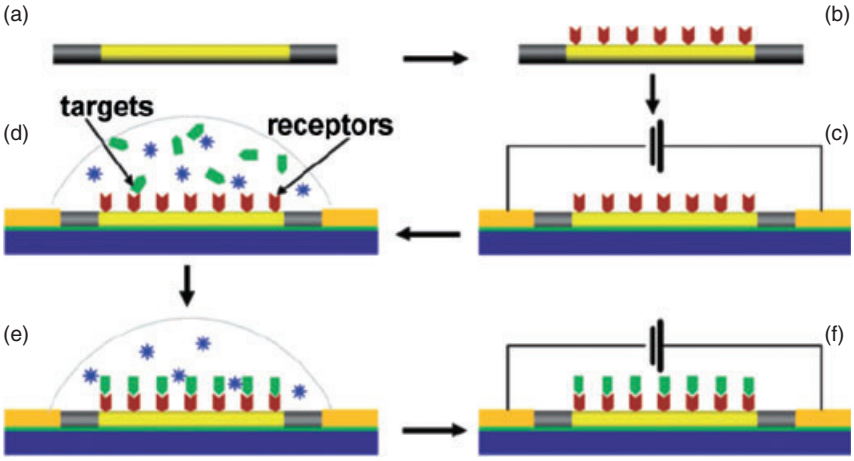

Figure 8.10 Schematic illustration of the application of CdTe–Au–CdTe striped nanowires for sensing specific biomolecules. (a) An individual CdTe–Au–CdTe multisegment nanowire, which is fabricated by electrochemistry; (b) Surface functionalization on the Au segment with thiol-terminated molecules; (c) Fabricated modified nanowire FET device using lithography; (d) Immersing the nanowire into the solution containing different biospecies; (e) Specific biomolecules (targets) are self-assembled to the receptors at the nanowire surface; (f) Sensitive conductance responses from the device are reflected by *I*–*V* curves after being bound with targets. Reprinted with permission from Ref. [51].

CdTe segments at both ends served to modulate the equilibrium Fermi level of the heterojunction device upon hybridization of the cDNA to the ssDNA over the Au segment.

8.4.5
Detection of Pathogens and Bacteria

An approach using multistriped Au–Ag metallic nanowires (diameter ~250 nm, length ~6 μm) in a suspended format was developed for the rapid and sensitive detection of biowarfare agent simulants in single and multiplex immunoassays [125]. Ni segments (50 nm) were deposited at both ends of the multistriped Au–Ag metallic nanowires to form magnetic NRs in order to facilitate magnetic field manipulation of the nanowires. The degree of binding of the antibody-conjugated multistriped metallic nanowires with a fluorophore-tagged antigen target was investigated. The hybridization and capture kinetics of the objective analyte in solution favored the NRs over standard fixed array-based formats. In order to detect *Salmonella*, a heterostructured Si–Au NR array was functionalized with anti-*Salmonella* antibodies and organic dye Alexa Fluor 488 molecules [126]. *Salmonella* is one of the major causes of bacterial gastroenteritis in humans, and a source of many food-related outbreaks. The vertically aligned Si NRs are fabricated on the Si substrate, such that the subsequent oxidation process provides the hydroxyl groups on the NR surfaces. A thin layer of Au is then sputter-coated onto the NRs. The silica surface is silanized with amine groups by 3-aminopropyltriethoxysilane, and then reacted with the amine-reactive carboxylic groups in the Alexa 488-succinimide dye. In order to immobilize antibodies onto the NRs, a dithiobis-succinimidyl propionate crosslinker was modified to the Au surface by Au–S bonding, after which conjugation of the anti-*Salmonella* antibody to Au was achieved by release of the *N*-hydroxysuccinimide leaving groups via the primary amines. *Salmonella* which were fixed through reactions with the functionalized heterostructured NRs were detected through signaling mediated by multiple Alexa 488 dye molecules bound on the Si NRs. Owing to the high-aspect ratio nature of the Si NRs, Alexa Fluo 488 molecules attached to the Si NRs produced an enhanced fluorescence upon capture of *Salmonella*. As a result, a single bacterium was captured by the antibodies conjugated on the Au and detected by thousands of dye molecules immobilized on the Si NRs.

8.5
Conclusions

In this chapter, we have discussed recent advances in the preparation of multielemental NRs (nanowires), as well as their unique physical and chemical properties and analytical applications. Notably, wet-chemical approaches for their preparation in organic and aqueous solution, including solvothermal reaction, hydrothermal

method, polyol reaction, microwave synthesis, thermal decomposition, hard template synthetic method and seed-mediated growth, have been outlined. By carefully controlling the species and molar ratios of the precursors, capping agents, temperature, pH, reaction time and/or applied potential, different morphologies of multielemental NRs can be prepared. The physical and chemical properties of these nanomaterials depend heavily on their compositions, sizes and shapes. Examples of functionalized multielemental NRs have been provided to highlight their great potential for analytical applications. Undoubtedly, with their multifunctional properties, these nanomaterials will continue to show promise for roles in catalysis, optics, electronics, sensing and separation. Although the 'real' applications of the multielemental NRs are rare, it is our strong belief that they will become even more popular when large-scale and high-quality production strategies are developed.

Abbreviations

NRs	nanorods
NPs	nanoparticles
QDs	quantum dots
EDS	energy dispersed X-ray spectroscopy
Tc	Curie temperature
Au NPSs	gold nanoparticle seeds
Ag NPSs	silver nanoparticle seeds
CTAB	cetyltrimethylammonium bromide
SEM	scanning electron microscopy
AAO	aluminum oxide
PC	polycarbonate
TEM	transmission electron microscopy
FESEM	field emission scanning electron microscopy
SERS	surface-enhanced Raman scattering
SPR	surface plasmon resonance
DDA	discrete dipole approximation
DLE	deep-level emission
Au-Te NDBs	gold–tellurium nanodumbbells
Au-Te NPPs	gold–tellurium nanopeapods
Au PNNs	gold pearl-necklace nanomaterials
PSS	poly(sodium 4-styrenesulfonate
PAA	poly(acrylic acid
$Au_{rod}@SiO_2$	silica-coated gold NRs
h-IgG	human immunoglobulin G
anti-h-IgG	anti-human immunoglobulin G
ssDNA	single-stranded DNA
cDNA	complementary DNA

References

1 Mirkin, C.A. (1999) Nanotechnology: tweezers for the nanotool kit. *Science*, **286**, 2095–2096.
2 Mirkin, C.A. (2005) The beginning of a small revolution. *Small*, **1**, 14–16.
3 Ferrando, R., Jellinek, J. and Johnston, R.L. (2008) Nanoalloys: from theory to applications of alloy clusters and nanoparticles. *Chemical Reviews*, **108**, 845–910.
4 Murphy, C.J., Gole, A.M., Hunyadi, S.E., Stone, J.W., Sisco, P.N., Alkilany, A., Kinard, B.E. and Hankins, P. (2008) Chemical sensing and imaging with metallic nanorods. *Chemical Communications*, 544–77.
5 Hu, K.-W., Huang, C.-C., Hwu, J.-R., Su, W.-C., Shieh, D.-B. and Yeh, C.-S. (2008) A new photothermal therapeutic agent: core-free nanostructured Au_xAg_{1-x} dendrites. *Chemistry – A European Journal*, **14**, 2956–64.
6 Hurst, S.J., Payne, E.K., Qin, L. and Mirkin, C.A. (2006) Multisegmented one-dimensional nanorods prepared by hard-template synthetic methods. *Angewandte Chemie – International Edition*, **45**, 2672–92.
7 Xia, Y., Yang, P., Sun, Y., Wu, Y., Mayers, B., Gates, B., Yin, Y., Kim, F. and Yan, H. (2003) One-dimension nanostructures: synthesis, characterization, and applications. *Advanced Materials*, **15**, 353–89.
8 Feldhein, D.L. and Foss, C.A., Jr, (2002) *Metal Nanoparticles: Synthesis Characterization, and Application*, Marcel Dekker, New York.
9 Nalwa, H.S. (2000) *Handbook of Nanostructured Materials and Nanotechnology*, Academic Press, New York.
10 Burda, C., Chen, X., Narayanan, R. and El-Sayed, M.A. (2005) Chemistry and properties of nanocrystals of different shapes. *Chemical Reviews*, **105**, 1025–102.
11 Martin, C.R. (1996) Membrane-based synthesis of nanomaterials. *Chemistry of Materials*, **8**, 1739–46.
12 Gates, B.D., Xu, Q., Stewart, M., Ryan, D., Wilson, C.G. and Whitesides, G.M. (2005) New approaches to nanofabrication: molding, printing, and other techniques. *Chemical Reviews*, **105**, 1171–96.
13 Martin, C.R. (1994) Nanomaterials: a membrane-based synthetic approach. *Science*, **266**, 1961–6.
14 Peng, Z.A. and Peng, X. (2002) Nearly monodisperse and shape-controlled CdSe nanocrystals via alternative routes: nucleation and growth. *Journal of the American Chemical Society*, **124**, 3343–53.
15 Peng, X., Manna, L., Yang, W., Wickham, J., Scher, E., Kakavanic, A. and Aliveisatos, A.P. (2000) Shape control of CdSe nanocrystals. *Nature*, **404**, 59–61.
16 Hu, J., Odom, T.W. and Lieber, C.M. (1999) Chemistry and physics in one dimension: synthesis and properties of nanowires and nanotubes. *Accounts of Chemical Research*, **32**, 435–45.
17 Manna, L., Milliron, D.J., Meisel, A., Scher, E.C. and Alivisatos, A.P. (2003) Controlled growth of tetrapod-branched inorganic nanocrystals. *Nature Materials*, **2**, 382–5.
18 Hao, E., Bailey, R.C., Schatz, G.C., Hupp, J.T. and Li, S. (2004) Synthesis and optical properties of "branched" gold nanocrystals. *Nano Letters*, **4**, 327–30.
19 Nusz, G.J., Marinakos, S.M., Curry, A.C., Dahlin, A., Holo, F., Wax, A. and Chilkoti, A. (2008) Label-free plasmonic detection of bimolecular binding by a single gold nanorod. *Analytical Chemistry*, **80**, 984–9.
20 Marinakos, S.M., Chen, S. and Chilkoti, A. (2007) Plasmonic detection of a model analyte in serum by a gold nanorod sensor. *Analytical Chemistry*, **79**, 5278–83.
21 Oh, B.-K., Park, S., Millstone, J.E., Lee, S.W., Lee, K.-B. and Mirkin, C.A. (2006) Separation of tricomponent protein mixture with triblock nanorods. *Journal of the American Chemical Society*, **128**, 11825–9.
22 Li, X., Wang, L., Zhou, C., Guan, T., Li, J. and Zhang, Y. (2007) Preliminary studies

of application of CdTe nanocrystals and dextran-Fe_3O_4 magnetic nanoparticles in sandwich immunoassay. *Clinica Chimica Acta*, **378**, 168–74.

23 Weng, J., Song, X., Li, L., Qian, H., Chen, K., Xu, X., Cao, C. and Ren, J. (2006) Highly luminescent CdTe quantum dots prepared in aqueous phase as an alternative fluorescent probe for cell imaging. *Talanta*, **70**, 397–402.

24 Sun, S. (2006) Recent advances in chemical synthesis, self-assembly, and applications of FePt nanoparticles. *Advanced Materials*, **18**, 393–403.

25 Chen, W., Kim, J., Sun, S. and Chen, S. (2006) Electro-oxidation of formic acid catalyzed by FePt nanoparticles. *Physical Chemistry Chemical Physics*, **8**, 2779–86.

26 Hou, Y., Kondoh, H., Che, R., Takeguchi, M. and Ohta, T. (2006) Ferromagnetic FePt nanowires: solvothermal reduction synthesis and characterization. *Small*, **2**, 235–8.

27 Wang, Y. and Yang, H. (2005) Synthesis of CoPt nanorods in ionic liquids. *Journal of the American Chemical Society*, **127**, 5316–17.

28 Casado-Rivera, E., Volpe, D.J., Alden, L., Lind, C., Downie, C., Vázquez-Alvarez, T., Angelo, A.C.D., DiSalvo, F.J. and Abruna, H.D. (2004) Electrocatalytic activity of ordered intermetallic phases for fuel cell applications. *Journal of the American Chemical Society*, **126**, 4043–9.

29 Liu, F., Lee, J.Y. and Zhou, W.J. (2006) Segmented Pt/Ru, Pt/Ni and Pt/RuNi nanorods as model bifunctional catalysts for methanol oxidation. *Small*, **2**, 121–8.

30 Tsuji, M., Miyamae, N., Lim, S., Kimura, K., Zhang, X., Hikino, S. and Nishio, M. (2006) Crystal structures and growth mechanisms of Au@Ag core-shell nanoparticles prepared by the microwave-polyol method. *Crystal Growth and Design*, **6**, 1801–7.

31 Maksimuk, S., Yang, S., Peng, Z. and Yang, H. (2007) Synthesis and characterization of ordered intermetallic PtPb nanorods. *Journal of the American Chemical Society*, **129**, 8684–5.

32 Chen, M., Pica, T., Jiang, Y.-B., Li, P., Yano, K., Liu, J.P., Datye, A.K. and Fan, H. (2007) Synthesis and self-assembly of fcc phase FePt nanorods. *Journal of the American Chemical Society*, **129**, 6348–9.

33 Sarma, S.D. (2003) A giant appears in spintronics. *Nature Matters*, **2**, 292–4.

34 Pearton, S.J., Abernathy, C.R., Overberg, M.E., Thaler, G.T., Norton, D.P., Theodoropoulou, N., Hebard, A.F., Park, Y.D., Ren, F., Kim, J. and Boatner, L.A. (2003) Wide band gap ferromagnetic semiconductors and oxides. *Journal of Applied Physics*, **93**, 1–13.

35 Dietl, T., Ohno, H., Matsukura, F., Cibert, J. and Ferrand, D. (2000) Zener model description of ferromagnetism in zinc-blende magnetic semiconductors. *Science*, **287**, 1019–22.

36 Büsgen, T., Hilgendorff, M., Irsen, S., Wilhelm, F., Rogalev, A., Goll, D. and Giersig, M. (2008) Colloidal cobalt-doped ZnO nanorods: synthesis, structural, and magnetic properties. *The Journal of Physical Chemistry C*, **112**, 2412–17.

37 Chen, C., Xu, G., Zhang, H. and Luo, Y. (2008) Hydrothermal synthesis Ni-doped ZnO nanorods with room-temperature ferromagnetism. *Material Letters*, **62**, 1617–20.

38 Datta, A., Panda, S.K. and Chaudhuri, S. (2007) Synthesis and optical and electrical properties of CdS/ZnS core/Shell nanorods. *The Journal of Physical Chemistry C*, **111**, 17260–4.

39 Kim, M.R., Kang, Y.-M. and Jang, D.-J. (2007) Synthesis and characterization of highly luminescent CdS@ZnS core-shell nanorods. *The Journal of Physical Chemistry C*, **111**, 18507–11.

40 Saunders, A.E., Koo, B., Wang, X., Shih, C.-K. and Korgel, B.A. (2008) Structural characterization and temperature-dependent photoluminescence of linear CdTe/CdSe/CdTe heterostructure nanorods. *ChemPhysChem*, **9**, 1158–63.

41 Joseph, C.M. and Menon, C.S. (1996) Electrical conductivity, optical absorption and structural studies in $AgInSe_2$ thin films. *Semiconductor Science and Technology*, **11**, 1668–71.

42 Ng, M.T., Boothroyd, C.B. and Vittal, J.J. (2006) One-pot synthesis of new-phase AgInSe2 nanorods. *Journal of the American Chemical Society*, **128**, 7118–19.

43 Turkevich, J., Sterenson, P.C. and Hillier, J. (1951) A study of the nucleation and growth processes in the synthesis of colloidal gold. *Discussions of the Faraday Society*, **11**, 55–75.

44 Huang, Y.-F., Lin, Y.-W. and Chang, H.-T. (2006) Growth of various Au-Ag nanocomposites from gold seeds in amino acid solutions. *Nanotechnology*, **17**, 4885–94.

45 Guo, S., Wang, L., Wang, Y., Fang, Y. and Wang, E. (2007) Bifunctional Au@Pt hybrid nanorods. *Journal of Colloid and Interface Science*, **315**, 363–8.

46 Slawinski, G.W. and Zamborini, F.P. (2007) Synthesis and alignment of silver nanorods and nanowires and the formation of Pt, Pd, and core/shell structures by galvanic exchange directly on surfaces. *Langmuir*, **23**, 10357–65.

47 Lee, K.-H., Huang, K.-M., Tseng, W.-L., Chiu, T.-C., Lin, Y.-W. and Chang, H.-T. (2007) Manipulation of the growth of gold and silver nanomaterials on glass by seeding approach. *Langmuir*, **23**, 1435–42.

48 Kim, S., Shuford, K.L., Bok, H.-M., Kim, S.K. and Park, S. (2008) Intraparticle surface Plasmon coupling in quasi-one-dimensional nanostructures. *Nano Letters*, **8**, 800–4.

49 Kovtyukhova, N.I., Kelley, B.K. and Mallouk, T.E. (2004) Coaxially gated in-wire thin-film transistors made by template assembly. *Journal of the American Chemical Society*, **126**, 12738–9.

50 Nicewarner-Pena, S.R., Freeman, R.G., Reiss, B.D., He, L., Pena, D.J., Walton, I.D., Cromer, R., Keating, C.D. and Natan, M.J. (2001) Submicrometer metallic barcodes. *Science*, **294**, 137–41.

51 Wang, X. and Ozkan, C.S. (2008) Multisegment nanowire sensors for the detection of DNA molecules. *Nano Letters*, **8**, 398–404.

52 Zhang, Z., Rondinone, A.J., Ma, J.-X., Shen, J. and Dai, S. (2005) Morphologically templated growth of aligned spinel $CoFe_2O_4$ nanorods. *Advanced Materials*, **17**, 1415–19.

53 Wang, Y., Ma, J., Tao, J., Zhu, X., Zhou, J., Zhao, Z., Xie, L. and Tian, H. (2007) Low-temperature synthesis of $CdWO_4$ nanorods via a hydrothermal method. *Ceramics International*, **33**, 1125–8.

54 Zhen, L., Wang, W.-S., Xu, C.-Y., Shao, W.-Z. and Qin, L.-C. (2008) A facile hydrothermal route to the large-scale synthesis of $CoWO_4$ nanorods. *Material Letters*, **62**, 1740–2.

55 Siegfried, M.J. and Choi, K.S. (2005) Directing the architecture of cuprous oxide crystals during electrochemical growth. *Angewandte Chemie – International Edition*, **44**, 3218–23.

56 Siegfried, M.J. and Choi, K.S. (2004) Electrochemical crystallization of cuprous oxide with systematic shape evolution. *Advanced Materials*, **16**, 1743–6.

57 Yu, S.-H., Liu, B., Mo, M.-S., Huang, J.-H., Liu, X.-M. and Qian, Y.-T. (2003) General synthesis of single-crystal tungstate nanorods/nanowires: a facile, low-temperature solution approach. *Advanced Functional Materials*, **13**, 639–47.

58 Shen, S., Hidajat, K., Yu, L.E. and Kawi, S. (2004) Simple hydrothermal synthesis of nanostructured and nanorod Zn-Al complex oxides as novel nanocatalysts. *Advanced Materials*, **16**, 541–5.

59 Zhu, H., Yang, D., Yu, G., Zhang, H., Jin, D. and Yao, K. (2006) Hydrothermal synthesis of Zn2SnO_4 nanorods in the diameter regime of sub-5 nm and their properties. *The Journal of Physical Chemistry B*, **110**, 7631–4.

60 Wu, X., Tao, Y., Mao, C., Liu, D. and Mao, Y. (2006) In situ hydrothermal synthesis of YVO_4 nanorods and microtube using $(NH_4)_{0.5}V_2O_5$ nanowires templates. *Journal of Crystal Growth*, **290**, 207–12.

61 Wu, X., Tao, Y., Song, C., Mao, C., Dong, L. and Zhu, J. (2006) Morphological control and luminescent properties of YVO_4:Eu nanocrystals. *The Journal of Physical Chemistry B*, **110**, 15791–6.

62 Wang, N., Chen, W., Zhang, Q. and Dai, Y. (2008) Synthesis, luminescent, and magnetic properties of $LaVO_4$:Eu nanorods. *Material Letters*, **62**, 109–12.

63 Zhang, Q., Chen, X., Zhou, Y., Zhang, G. and Yu, S.-H. (2007) Synthesis of $ZnWO_4$@MWO_4 (M = Mn, Fe) core-shell nanorods with optical and

antiferromagnetic property by oriented attachment mechanism. *The Journal of Physical Chemistry C*, **111**, 3927–33.

64 Baek, S., Song, J. and Lim, S. (2007) Improvement of the optical properties of ZnO nanorods by Fe doping. *Physica B*, **399**, 101–4.

65 Wang, H., Wang, H.B., Yang, F.J., Chen, Y., Zhang, C., Yang, C.P., Li, Q. and Wong, S.P. (2006) Structure and magnetic properties of $Zn_{1-x}Co_xO$ single-crystalline nanorods synthesized by a wet chemical method. *Nanotechnology*, **17**, 4312–16.

66 Hsiaoa, C.-S., Chena, S.-Y. and Cheng, S.-Y. (2008) Synthesis and physical characteristics of AlO_x-coated ZnO nanorod arrays grown in aqueous solution at low temperatures. *Journal of Physics and Chemistry of Solids*, **69**, 625–8.

67 Tang, B., Yang, F., Lin, Y., Zhuo, L., Ge, J. and Cao, L. (2007) Synthesis and characterization of wavelength-tunable, water-soluble, and near-infrared-emitting CdHgTe nanorods. *Chemistry of Materials*, **19**, 1212–14.

68 Harichandran, G. and Lalla, N.P. (2008) Facile synthesis of $CuAlS_2$ nanorods. *Material Letters*, **62**, 1267–9.

69 Chang, Y.-Y., Yu, S.-S., Lee, C.-L. and Chris Wang, C.R. (1997) Gold nanorods: electrochemical synthesis and optical properties. *The Journal of Physical Chemistry B*, **101**, 6661–4.

70 Lee, K.-S. and El-Sayed, M.A. (2006) Gold and silver nanoparticles in sensing and imaging: sensitivity of plasmon response to size, shape, and metal composition. *The Journal of Physical Chemistry B*, **110**, 19220–5.

71 Yang, Z. and Chang, H.-T. (2006) Anisotropic syntheses of boat-shaped core-shell Au–Ag nanocrystals and nanowires. *Nanotechnology*, **17**, 2304–10.

72 Huang, Y.-F., Huang, K.-M. and Chang, H.-T. (2007) Synthesis and characterization of Au core–Au–Ag shell nanoparticles from gold seeds: impacts of glycine concentration and pH. *Journal of Colloid and Interface Science*, **301**, 145–54.

73 Xiang, Y., Wu, X., Liu, D., Li, Z., Chu, W., Feng, L., Zhang, K., Zhou, W. and Xie, S. (2008) Gold nanorod-seeded growth of silver nanostructures: from homogeneous coating to anisotropic coating. *Langmuir*, **24**, 3465–70.

74 Yin, M., Gu, Y., Kuskovsky, I.L., Andelman, T., Zhu, Y., Neumark, G.F. and O'Brien, S. (2004) Zinc oxide quantum rods. *Journal of the American Chemical Society*, **126**, 6206–7.

75 Panda, A.B., Glaspell, G. and El-Shall, M.S. (2006) Microwave synthesis of highly aligned ultra narrow semiconductor rods and wires. *Journal of the American Chemical Society*, **128**, 2790–1.

76 Rogach, A.L., Eychmüller, A., Hickey, S.G. and Kershaw, S.V. (2007) Infrared-emitting colloidal nanocrystals: synthesis, assembly, spectroscopy, and applications. *Small*, **3**, 536–57.

77 Shieh, F., Saunders, A.E. and Korgel, B.A. (2005) General shape control of colloidal CdS, CdSe, CdTe quantum rods and quantum rod heterostructures. *The Journal of Physical Chemistry B*, **109**, 8538–42.

78 Milliron, D.J., Hughes, S.M., Cui, Y., Manna, L., Li, J., Wang, L.-W. and Alivisatos, A.P. (2004) Colloidal nanocrystal heterostructures with linear and branched topology. *Nature*, **430**, 190–5.

79 Kim, S., Fisher, B., Eisler, H.J. and Bawendi, M. (2003) Type-II quantum dots: CdTe/CdSe (core/shell) and CdSe/ZnTe (core/shell) heterostructures. *Journal of the American Chemical Society*, **125**, 11466–7.

80 Chen, C.-Y., Cheng, C.-T., Cheng, J.-K., Yu, S.-C., Pu, Y.-M., Chou, P.-T., Chou, Y.-H. and Chiu, H.-T. (2004) Spectroscopy and femtosecond dynamics of Type-II CdSe/ZnTe core-shell semiconductor synthesized via the CdO precursor. *The Journal of Physical Chemistry B*, **108**, 10687–91.

81 Steiner, D., Katz, D., Millo, O., Aharoni, A., Kan, S., Mokari, T. and Banin, U. (2004) Zero-dimensional and quasi one-dimensional effects in semiconductor nanorods. *Nano Letters*, **4**, 1073–7.

82 Qian, C., Kim, F., Ma, L., Tsui, F., Yang, P. and Liu, J. (2004) Solution-phase

synthesis of single-crystalline iron phosphide nanorods/nanowires. *Journal of the American Chemical Society*, **126**, 1195–8.

83 Wen, J.G., Lao, J.Y., Wang, D.Z., Kyaw, T.M., Foo, Y.L. and Ren, Z.F. (2003) Self-assembly of semiconducting oxide nanowires, nanorods, and nanoribbons. *Chemical Physics Letters*, **372**, 717–22.

84 Vanheusden, K., Seager, C.H., Warren, W.L., Tallant, D.R. and Voigt, J.A. (1996) Correlation between photoluminescence and oxygen vacancies in ZnO phosphors. *Applied Physics Letters*, **68**, 403–5.

85 Wu, X.L., Siu, G.G., Fu, C.L. and Ong, H.C. (2001) Photoluminescence and cathodoluminescence studies of stoichiometric and oxygen-deficient ZnO films. *Applied Physics Letters*, **78**, 2285–7.

86 Liu, M., Kitai, A.H. and Mascher, P. (1992) Point defects and luminescence centres in zinc oxide and zinc oxide doped with manganese. *Journal of Luminescence*, **54**, 35–42.

87 Levine, A.K. and Palilla, F.C. (1964) A new, highly efficient red-emitting cathodoluminescent phosphor (YVO_4:Eu) for color television. *Applied Physics Letters*, **5**, 118–24.

88 Moskovits, M. (1985) Surface-enhanced spectroscopy. *Reviews of Modern Physics*, **57**, 783–825.

89 Sutherland, W.S. and Winefordner, J.D. (1992) Colloid filtration: a novel substrate preparation method for surface-enhanced Raman spectroscopy. *Journal of Colloid and Interface Science*, **148**, 129–41.

90 Mirkin, C.A., Letsinger, R.L., Mucic, R.C. and Storhoff, J.J. (1996) A DNA-based method for rationally assembling nanoparticles into macroscopic materials. *Nature*, **382**, 607–9.

91 Mann, S., Shenton, W., Li, M., Connolly, S. and Fitzmaurice, D. (2000) Biologically programmed nanoparticle assembly. *Advanced Materials*, **12**, 147–50.

92 Jana, N.R. and Pal, T. (2007) Anisotropic metal nanoparticles for use as surface-enhanced Raman substrates. *Advanced Materials*, **19**, 1761–5.

93 Broglin, B.L., Andreu, A., Dhussa, N., Gerst, J.A., Jr, Heath, J., Dudley, B., Holland, D. and El-Kouedi, M. (2007) Investigation of the effects of the local environment on the surface-enhanced Raman spectra of striped gold/silver nanorod arrays. *Langmuir*, **23**, 4563–8.

94 Lin, Z.-H. and Chang, H.-T. (2008) Preparation of gold-tellurium hybrid nanomaterials for surface-enhanced Raman spectroscopy. *Langmuir*, **24**, 365–7.

95 Gunnarsson, L., Rindzevicius, T., Prikulis, J., Kasemo, B., Käll, M., Zou, S. and Schatz, G.C. (2005) Confined plasmons in nanofabricated single silver particle pairs: experimental observations of strong interparticle interactions. *The Journal of Physical Chemistry B*, **109**, 1079–87.

96 Schuck, P.J., Fromm, D.P., Sundaramurthy, A., Kino, G.S. and Moerner, W.E. (2005) Improving the mismatch between light and nanoscale objects with gold bowtie nanoantennas. *Physical Review Letters*, **94**, 017402.

97 Qin, L., Zou, S., Xue, C., Atkinson, A., Schatz, G.C. and Mirkin, C.A. (2006) Designing, fabricating, and imaging Raman hot spots. *Proceedings of the National Academy of Sciences of the United States of America*, **103**, 13300–3.

98 Yu, Q., Guan, P., Qin, D., Golden, G. and Wallace, P.M. (2008) Inverted size-dependence of surface-enhanced Raman scattering on gold nanohole and nanodisk array. *Nano Letters*, **8**, 1923–8.

99 Chen, M., Kim, J., Liu, J.P., Fan, H. and Sun, S. (2006) Synthesis of FePt nanocubes and their oriented self-assembly. *Journal of the American Chemical Society*, **128**, 7132–3.

100 Li, B.B., Xiu, X.Q., Zhang, R., Tao, Z.K., Chen, L., Xie, Z.L., Zheng, Y.D. and Xie, Z. (2006) Study of structure and magnetic properties of Ni-doped ZnO-based DMSs. *Materials Science in Semiconductor Processing*, **9**, 141–5.

101 Kittilstved, K.R., Liu, W.K. and Gamelin, D.R. (2006) Electronic structure origins of polarity-dependent high-T_C ferromagnetism in oxide-diluted magnetic semiconductors. *Nature Materials*, **5**, 291–7.

102 Wegner, F. (1973) On the magnetic phase diagram of (Mn, Fe)WO_4 wolframite. *Solid State Communications*, **12**, 785–7.

103 Yamazoe, N. and Miura, N. (1995) Development of gas sensors for environmental protection. *IEEE Transactions on Components and Packaging Technologies A*, **18**, 252–6.

104 Seal, S. and Shukla, S. (2002) Nanocrystalline SnO gas sensors in view of surface reactions and modifications. *Journal of the Minerals, Metals and Materials Society*, **54**, 35–8.

105 Ménil, F., Coillard, V. and Lucat, C. (2000) Critical review of nitrogen monoxide sensors for exhaust gases of lean burn engines. *Sensors and Actuators B–Chemical*, **67**, 1–23.

106 Hazra, S.K. and Basu, S. (2006) Hydrogen sensitivity of ZnO p–n homojunctions. *Sensors and Actuators B–Chemical*, **117**, 177–82.

107 Wagh, M.S., Jain, G.H., Patil, D.R., Patil, S.A. and Patil, L.A. (2006) Modified zinc oxide thick film resistors as NH_3 gas sensor. *Sensors and Actuators B–Chemical*, **115**, 128–33.

108 Wöllenstein, J., Plaza, J.A., Cané, C., Min, Y., Böttner, H. and Tuller, H.L. (2003) A novel single chip thin film metal oxide array. *Sensors and Actuators B–Chemical*, **93**, 350–5.

109 Ferro, R., Rodríguez, J.A., Jiménez, I., Cirera, A., Cerdà, J. and Morante, J.R. (2005) Gas-sensing properties of sprayed films of $(CdO)x(ZnO)_{1-x}$ mixed oxide. *IEEE Sensors Journal*, **5**, 48–52.

110 Huang, G.-G., Wang, C.-T., Tang, H.-T., Huang, Y.-S. and Yang, J. (2006) ZnO Nanoparticle-modified infrared internal reflection elements for selective detection of volatile organic compounds. *Analytical Chemistry*, **78**, 2397–404.

111 Hsueh, T.-J., Chen, Y.-W., Chang, S.-J., Wang, S.-F., Hsu, C.-L., Lin, Y.-R., Lin, T.-S. and Chen, I.-C. (2007) ZnO nanowire-based CO sensors prepared at various temperatures. *Journal of the Electrochemical Society*, **152**, J393–6.

112 Kohl, D. (1990) The role of noble metals in the chemistry of solid-state gas sensors. *Sensors and Actuators B–Chemical*, **1**, 158–65.

113 Hsueh, T.-J., Chang, S.-J., Hsu, C.-L., Lin, Y.-R. and Chen, I.-C. (2007) Highly sensitive ZnO nanowire ethanol sensor with Pd adsorption. *Applied Physics Letters*, **91**, 053111–13.

114 Chang, S.-J., Hsueh, T.-J., Chen, I.-C. and Huang, B.-R. (2008) Highly sensitive ZnO nanowire CO sensors with the adsorption of Au nanoparticles. *Nanotechnology*, **19**, 175502.

115 Li, C., Li, L., Du, Z., Yu, H., Xiang, Y., Li, Y., Cai, Y. and Wang, T. (2008) Rapid and ultrahigh ethanol sensing based on Au-coated ZnO nanorods. *Nanotechnology*, **19**, 035501.

116 Stern, A.H. (2005) A review of the studies of the cardiovascular health effects of methylmercury with consideration of their suitability for risk assessment. *Environmental Research*, **98**, 133–42.

117 Leermakers, M., Baeyens, W., Quevauviller, P. and Horvat, M. (2005) Mercury in environmental samples: speciation, artifacts and validation. *Trends in Analytical Chemistry*, **24**, 383–93.

118 Huang, Y.-F., Lin, Y.-W. and Chang, H.-T. (2007) Control of the surface charges of Au-Ag nanorods: selective detection of iron in the presence of poly(sodium 4-styrenesulfonate). *Langmuir*, **23**, 12777–81.

119 Huang, Y.-F., Lin, Y.-W. and Chang, H.-T. (••) Poly(acrylic acid) capped Au-Ag nanorods for colorimetric detection of lead ions. *Journal of Nanoscience and Nanotechnology*, accepted.

120 Rex, M., Hernandez, F.E. and Campiglia, A.D. (2006) Pushing the limits of mercury sensors with gold Nanorods. *Analytical Chemistry*, **78**, 445–51.

121 Fond, A.M., Birenbaum, N.S., Felton, E.J., Reich, D.H. and Meyer, G.J. (2007) Preferential noncovalent immunoglobulin G adsorption onto hydrophobic segments of multi-functional metallic nanowires. *Journal of Photochemistry and Photobiology A–Chemistry*, **186**, 57–64.

122 Lee, K.-B., Park, S. and Mirkin, C.A. (2004) Multicomponent magnetic nanorods for biomolecular separations. *Angewandte Chemie–International Edition*, **43**, 3048–50.

123 Wang, C., Ma, Z., Wang, T. and Su, Z. (2006) Synthesis, assembly, and biofunctionalization of silica-coated gold nanorods for colorimetric biosensing. *Advanced Functional Materials*, **16**, 1673–8.

124 Sha, M.Y., Walton, I.D., Norton, S.M., Taylor, M., Yamanaka, M., Natan, M.J., Xu, C., Drmanac, S., Huang, S., Borcherding, A., Drmanac, R. and Penn, S.G. (2006) Multiplexed SNP genotyping using nanobarcode particle technology. *Analytical and Bioanalytical Chemistry*, **384**, 658–66.

125 Tok, J.B.-H., Chuang, F.Y.S., Kao, M.C., Rose, K.A., Pannu, S.S., Sha, M.Y., Chakarova, G., Penn, S.G. and Dougherty, G.M. (2006) Metallic striped nanowires as multiplexed immunoassay platforms for pathogen detection. *Angewandte Chemie – International Edition*, **45**, 6900–4.

126 Fu, J., Park, B., Siragusa, G., Jones, L., Tripp, R., Zhao, Y. and Cho, Y.-J. (2008) An Au/Si hetero-nanorod-based biosensor for *Salmonella* detection. *Nanotechnology*, **19**, 155502.

Abstract

Metallic nanomaterials have become one of the most fascinating materials in modern sciences, mainly because of their unique optical, electronic, magnetic and catalytic properties. They have been widely used in many fields, including sensing, separation, catalysis, drug delivery, electronics and optics. Unlike spherical nanomaterials, nanorods have interesting anisotropic properties that are highly dependent on their aspect ratios and compositions. In order to provide multifunctional properties, multielemental nanorods have been prepared. In this chapter, we focus on the preparation, physical and chemical properties, as well as the analytical applications of multielemental nanorods. Several advanced synthetic approaches in aqueous and organic phases are briefly discussed. The absorption, emission, surface-enhanced Raman scattering effect, magnetic properties and catalytic effect of the multielemental nanorods are provided to demonstrate their great practicality in sensing and catalysis. Bioconjugated strategies for improving the selectivity of multielemental nanorods toward analytes of interest are briefly reviewed. We highlight the potential of multielemental nanorods in analytical applications. The advantages and disadvantages of various multielemental nanorods in separation and detection of analytes, cells and bacteria of interest are also emphasized.

Keywords

nanoparticles; nanorods; surface plasmon resonance; surface-enhanced Raman scattering; sensing; catalyst.

9
Spherical and Anisotropic Nonmagnetic Core-Shell Nanomaterials: Synthesis and Characterization

Tewodros Asefa, Abhishek Anan, Cole Duncan and Youwei Xie

9.1
Introduction: Core-Shell Nanomaterials and Their Biological/Medical Applications

The fields of nanoscience and nanotechnology have come a long way over the past few decades, and have now reached a point where many of their promises have become reality. At the same time, the development of new nanostructured building blocks with a variety of structures and shapes, as well as range of unique properties, has continued to be actively researched in chemistry, physics, materials science and engineering and medical disciplines. The assembly of these building blocks into 'active' nanoscale materials and devices for various applications in nanoelectronics, catalysis, drug delivery, bioimaging and sensors is also being explored by many research teams. Nanostructured materials have also allowed the study of fundamental optical, magnetic, electronic, chemical and physical properties of matter at the nanoscale by the virtue of their sizes, which lie between those of molecules/atoms and bulk matter. The latter point further helps in our understanding of the size- and shape-dependent nanoscale properties, in our prediction of structure–property relationships at the nanoscale, and in the development of systematic and rational synthetic methods for other new classes of nanomaterials.

Of particular interest in nanomaterials research has been the investigation of the interaction of nanomaterials with biological species, and the application of nanomaterials in the life sciences – all of which is based on nanomaterials and many biomolecules having the same length scale and size domain. This area of research – which often is also referred to as 'nanobiotechnology' – has many far-reaching implications and potential applications in biology and medicine, including drug delivery, biodiagnostics, biosensors and bioimaging. In fact, by using a range of nanomaterials and nanostructures, including nanoparticles, nanowires and nanoporous materials, many different biological and medical applications have already been successfully demonstrated during the past few years. In fact, the research outcomes of nanobiotechnology are far closer to broad commercialization so as to make a difference to society than any of the other subdisciplines in nanoscience and nanotechnology.

Nanomaterials for the Life Sciences Vol. 3: Mixed Metal Nanomaterials. Edited by Challa S. S. R. Kumar

ISBN: 978-3-527-32153-7

Although nanomaterials exhibit unique size- and shape-dependent physical, optical, electronic and chemical properties, many sometimes cannot be used directly, especially for biological and medical applications, often because of their possible cytotoxicity and hydrophobicity. For biological and medical applications, nanoparticles generally must have controlled composition and sizes across the endocytic/phagocytic size ranges, show neither aggregation nor fusion, have appropriate surface properties and surface functional groups, be biocompatible, and show low toxicity. Consequently, the choice of material synthesis that can satisfy these requirements is among the first steps to realize the applications of these materials. Coating the nanomaterials' surfaces with a shell of secondary substance to create core-shell nanostructures is among the easiest ways to make nanomaterials biocompatible, noncytotoxic and stable, or to have a suitable composition and surface properties for specific biological or medical applications. The coating of shells over nanomaterials may also allow the modified colloids to be stable over a wider range of experimental parameters, including pH, ionic strength, solvent and temperature. The design and synthesis of core-shell nanostructures, therefore, has continued to attract a broad range of interest worldwide.

Core-shell nanomaterials are stable nanostructured materials that contain two or more nanoscale structures – some as cores and others as shells (Figure 9.1) [1]. Many nanomaterials, especially metal nanoparticles, can in fact be considered as core-shell nanoparticles themselves because of the presence of their surface passivating organic monolayer shells around the metal cores. However, in this chapter and in many traditionally labeled core-shell nanomaterials, a distinct layer of a second nanoscale structure other than such passivating organic groups must be present in order that the nanomaterial be designated a core-shell.

Core-shell nanomaterials can be prepared with nanoparticle, nanorod and nanowire shapes, with their synthesis involving a variety of approaches, including

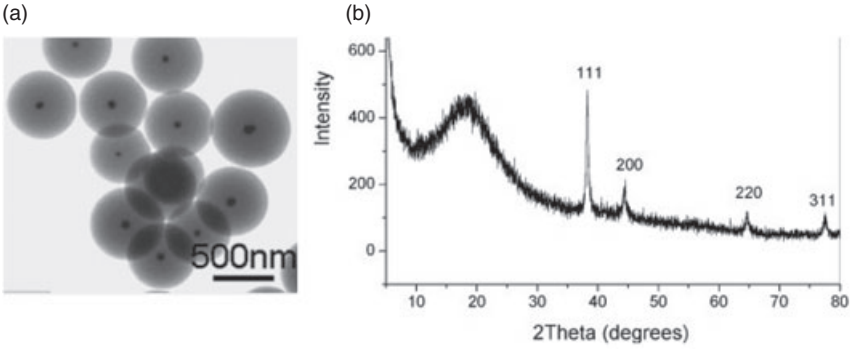

Figure 9.1 (a) Example of core-shell nanoparticles containing metal (Ag) nanoparticle cores and metal oxide (silica) shell; (b) Characterization of the core-shell nanoparticles by powder X-ray diffraction, showing the Bragg reflections of the metal cores in the core-shell nanostructure. Reproduced with permission from Ref. [1].

wet-synthesis, electrodeposition and chemical vapor deposition (CVD). Details of the various synthetic methods used to prepare core-shell nanostructures are outlined in the subsections of this chapter. Because of the different composition, sizes, shapes and thickness of the cores and shells, it is possible to produce a broad range of core-shell nanomaterials that have tunable properties. The design and synthesis of core-shell nanomaterials with different structures, composition and properties has attracted an increasing amount of interest, not only for improving the stability and surface chemistry of the core nanomaterials but also for obtaining unique structures, properties and multifunctional properties that combine those characteristics of the components or properties that are not attainable by one nanomaterial alone. By synthesizing nanomaterials with core-shell structures of different composition, it is also possible to improve their biocompatibility, surface hydrophilicity or hydrophobicity, as well as their binding with biological molecules. For instance, while many semiconductor quantum dots (QDs) or nanorods have important luminescent properties that are useful for bioimaging and other biological applications, their potential cytotoxicity has limited their utilization in biological and medical applications. Consequently, the coating of their surfaces with biocompatible polymers or silica makes possible their use for delivery and uptake by cells, and also as noncytotoxic *in vivo* imaging systems.

The creation of nanomaterials with a core-shell structure also allows the introduction of secondary functional groups or multifunctional sites into the materials (Figure 9.2) [2]. For example, multifunctional poly(lactic-*co*-glycolic acid) (PLGA)-Mn/Au core-shell nanostructures containing near-infrared (NIR)-resonant rhodamine molecules and metallic nanoparticles have been developed for photothermally

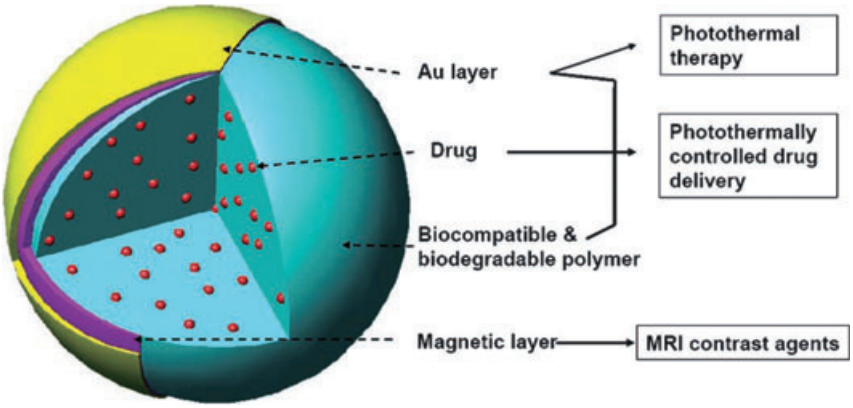

Figure 9.2 Schematic diagram of a drug-loaded polymer–metal multifunctional core-shell nanoparticle. Various drug molecules can be loaded into the biocompatible and biodegradable polymer layer, in which a magnetic Fe_3O_4 and metallic Au nanoshell can be deposited. The latter provide additional functionality such as photothermal therapy, photothermally controlled drug delivery and MRI contrast enhancement. Reproduced with permission from Ref. [2].

controlled drug delivery and for use in magnetic resonance imaging (MRI) applications (Figure 9.2). By irradiating the metal nanoparticles with NIR light, the release rate of rhodamine from the core-shell nanostructure is increased compared to the corresponding material containing no metal nanoparticles. Other similar NIR-responsive multifunctional core-shell nanomaterials consisting of poly(*N*-isopropylacrylamide-*co*-acrylamide) (poly-(NIPAAm-*co*-AAm))—Au/Au_2S core-shell nanocomposite structure with embedded methylene blue, ovalbumin or bovine serum albumin (BSA) have also been reported [3].

The materials of choice in the synthesis of core-shell nanostructures often depends on the types of compositions and properties being sought in the final nanomaterials. Previously reported core-shell nanomaterials have included core materials with compositions ranging from metal, metal oxide, inorganic, polymeric and hybrid organic–inorganic, whilst at the same time the composition of the shells also constitutes one of these. The core-shell nanostructures may also demonstrate unique and interesting optical, magnetic, luminescent and catalytic properties associated with the cores or shells [4]. The structures of the cores and shells can be designed and synthesized to have a spherical shape, to have the form of a nanorod or nanowire, and/or to be nanoporous. Such an aspect offers the additional possibility to tune the structures, as well as possessing the basic properties of core-shell nanomaterials. For example, core-shell nanomaterials containing both multiple metallic cores and multiple shells – the so-called core-shell–shell nanomaterials (Figure 9.3) [1] – may be synthesized, either systematically or accidentally.

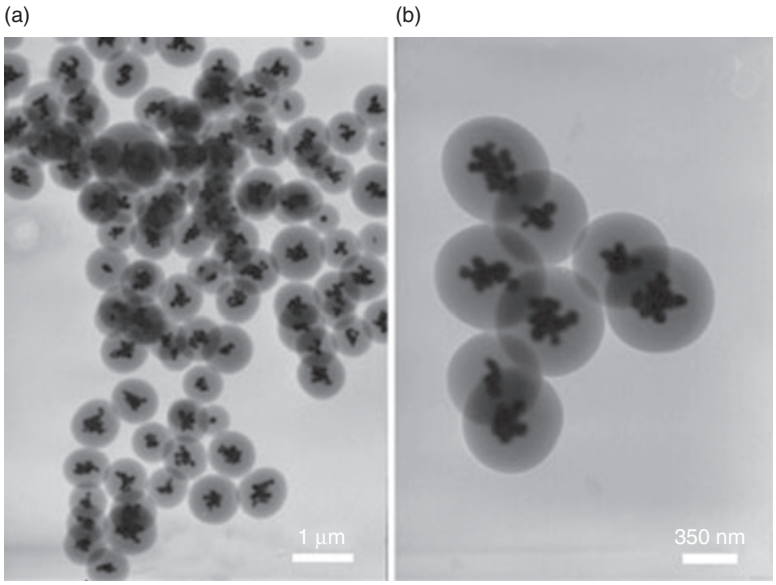

Figure 9.3 Core-shell nanoparticles containing multiple cores.
Reproduced with permission from Ref. [1].

The main part of this chapter will focus on those core-shell nanomaterials that have no magnetic properties. In recent years, many reports and reviews have been prepared describing magnetic based core-shell nanomaterials and their applications [5]. Although much has been written about nonmagnetic core-shell nanomaterials [6], such reports either discuss a specific class of materials, a single type of synthetic strategy, or are focused on a particular application. In this chapter, we provide a comprehensive review, together with selected examples, of nonmagnetic core-shell nanomaterials, with special emphasis on their classification, on the synthetic and characterization methods used for their preparation, and their potential applications in various areas, notably in the life sciences.

Among the reviews on magnetic core-shell nanomaterials are included [5, 6]:

- Salgueiriño-Maceira *et al.* [5a,d] have described the synthesis of different types of magnetic core-shell nanomaterial and magnetic core-shell nanoparticles that contain biocompatible groups or a directly connected, coupled, or isolated second functionality.
- Jun *et al.* [5b] have reported advances in the development of magnetic nanoparticles with a focus on multicomponent heterostructured nanoparticles including alloys, core-shells and binary superlattices synthesized via nonhydrolytic methods.
- Camargo *et al.* [5c] have presented advances prior to 2007 on the synthesis of core-shell monodispersed colloidal nanospheres containing superparamagnetic components such as Fe_3O_4-SiO_2 and chalcogenides and the potential applications of the core-shell nanostructures for fabricating photonic crystals, the band structures of which can be configured using an external magnetic field.

Reviews and other texts concerning nonmagnetic core-shell nanostructured materials include:

- Shan *et al.* [6a] reviewed reports published between 2004 and early 2007 on metal–organic (metal–polymer) core-shell nanoparticles and polymer-protected gold nanoparticles and their properties and applications.
- Liu *et al.* [6b] have reviewed the synthetic approaches involving femtosecond fiber laser ablation for preparing crystalline and polycrystalline nanocubes and core-shell nanostructured materials.
- Weiler *et al.* [6c] have reviewed the synthesis of inorganic $LaPO_4$:Ce,Tb and $CePO_4$:Tb–$LaPO_4$ core-shell nanophosphors with polymer and bioligand shells for *in vitro* diagnostic applications.
- Gravano *et al.* [6d] have reviewed synthetic methods for core-shell nanomaterials containing inorganic cores other than Au and SiO_2.
- Ballauff *et al.* [6e] have reviewed recent studies on the preparation, characterization and application of 'smart' thermosensitive core-shell microgel particles that contain a polystyrene core and a crosslinked poly(*N*-isopropylacrylamide) (PNIPA) shell.

- Torimoto *et al.* [6f] reported progress prior to ~2006 on the preparation of monodispersed semiconductor nanoparticles by the size-selective photoetching technique and their application.
- Nayak *et al.* [6g] reviewed responsive hydrogel nanoparticles and their potential applications as bioresponsive sensors, drug-delivery systems, implantable biomaterials, biotesting and targetable chemotherapy agents.
- Zhong *et al.* [6h] have discussed the synthesis and inter-particle structural and spatial properties of a hydrogen-bonding-mediated assembly of core-shell nanoparticles consisting of a metal nanocrystal core and organic monolayer shells.
- Sastry *et al.* [6i] described synthetic methods to prepare phase-pure core-shell nanoparticles by immobilizing UV- and pH-dependent reducing agents on the surface of the core nanoparticles.
- Chavez *et al.* [6j] have reviewed the synthesis and properties of various core-shell nanostructures containing dyes, porphyrins, drugs, cells and other active agents as cores, and of polymers, dendrimers and microemulsions as shells.
- Scott *et al.* [6k] recently reviewed various reports on the synthesis, characterization and applications of dendrimer-encapsulated nanoparticles (DENs).
- Avgoustakis *et al.* [6l] detailed the preparation, properties and potential drug delivery applications of various biocompatible and biodegradable polymeric core-shell.
- He *et al.* [6v] have reviewed the synthesis and characterization of various biocompatible core-shell nanoparticles and their applications in biomedicine.
- Kickelbick *et al.* [6v] have reviewed the synthetic procedures and some selected properties of core-shell nanoparticles.
- Choi *et al.* [6o] have reviewed synthetic methods for the preparation of polymer-functionalized core-shell nanoparticles, and the advantages of these materials for site-specific and oral delivery applications.
- Zhong *et al.* [6p] have reviewed the synthesis and catalytic properties of various core-shell assemblies containing metals and alloy nanomaterials.
- Shipway and Willner [6q] have reviewed the synthesis of various core-shell assemblies containing metal and semiconductor nanoparticle arrays crosslinked by molecular receptors, photosensitizer/electron-acceptor bridges and nucleic acids.
- Fujimoto *et al.* [6r] have presented preparative techniques in polymeric nanoparticles and core-shell nanostructures that can be potentially used as drug delivery systems, as well as details of their biological properties.
- Schartl [6s] has reviewed reports prior to 2000 in the field of crosslinked core-shell nanoparticles that have potential use as optical tracer systems.

- Wooley [6t] has reviewed a general approach involving the organization of polymers into micellar assemblies, followed by stabilization through covalent intramicellar crosslinking to form shells around different types of core domains having glassy, fluid-like and crystalline morphologies.
- Sung *et al*. [6u] focused their attention on drug delivery and molecular imaging applications of core-shell nanomaterials.
- Liz-Marzan [6v] has also reviewed the different techniques used for the construction of nanoscale patterns using core-shell nanoparticles as building blocks, and their optical properties.
- Liz-Marzan *et al*. [6w] have also reviewed fabrication methods for various core-shell nanomaterials with compositions consisting of dielectric/dielectric, metal/metal, metal/dielectric, dielectric/metal and semiconductor/semiconductor. They have also described the properties of these materials, and the forces involved in their stabilization.

In this chapter, we provide a general introduction to nanomaterials, core-shell nanomaterials and their biological applications, and compare the magnetic and nonmagnetic variations of these nanomaterials. Details of the different types of cores and shells used for their creation, the synthetic methods utilized for such purpose, and the properties and characterization of the final product are then described. The potential applications of different core-shell nanomaterials, with special emphasis on biological and medical applications, are discussed, followed by a brief outline of the future outlook for these materials.

9.2
Nonmagnetic Core-Shell Nanomaterials

Like many magnetic core-shell nanomaterials [5a–d], nonmagnetic core-shell nanostructures also have several unique properties and potential applications in the life sciences [5e–z]. For instance, metal-insulator-semiconductor core-shell-shell nanowires such as Ag—SiO_2—CdSe nanowires, as reported by Fedutik *et al*. [7], exhibit unique optical properties. In these nanostructures, the excitation of surface plasmons (SPs) of the metal (Ag) core nanostructure by the CdSe QDs in the shells results in important light-matter interaction and nanoplasmonics or the coupling of nanocrystal excitons with SPs in the composite core-shell nanomaterial system (Figure 9.4). This allows for transformation of any light that is absorbed (and re-emitted) by the semiconductor nanocrystals (NCs) into the SPs of the metal nanoparticle, and back to photons. In this case, the light-emitting nanoparticles in the shells may serve not only as tiny localized dipole emitters, but also as receivers in an energy back-conversion from plasmons to excitons. These unique and tunable optical properties of the core-shell nanomaterials can be used for potential bioimaging applications.

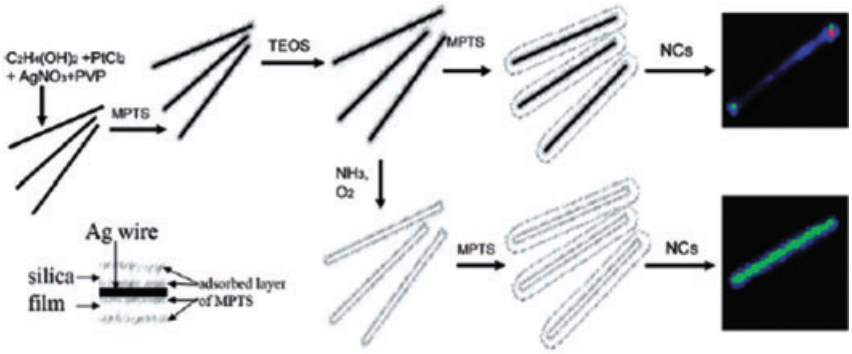

Figure 9.4 Synthesis of composite core-shell Ag–SiO_2 and core-shell-shell Ag–SiO_2–CdSe nanowires and hollow SiO_2 nanowires capped with CdSe nanocrystals and their optical properties. Reproduced with permission from Ref. [7].

9.3
Synthesis of Cores in Core-Shell Nanostructures

The preparation of core-shell nanomaterials often begins with the synthesis of the core nanomaterial, which may be composed of stable metal nanospheres, or nanorods and nanowires that are passivated with organic layers. Alternatively, metal oxide and polymeric nanospheres that are either electrostatically or sterically stabilized as colloidal dispersions can be used as the core nanomaterials. The cores can be coated with the shell nanostructure in subsequent steps. The thickness of both the core and the shell can be varied by changing the synthesis conditions and the concentrations of the reagents used.

9.3.1
Metal Cores

The most widely used synthetic approach to produce metallic cores involves solution-phase chemical reactions to stabilize metal nanoparticles that are passivated with organic groups [8]. By using this approach, a broad range of metallic nanoparticles may be used as cores. While noble metal nanoparticles composed for example of Au, Pd and Ag with different sizes and shapes are synthesized by reducing their corresponding salt solutions in the presence of passivating ionic species, organic groups such as alkanethiols and alkylamines, metal nanoparticles composed of elements such as Fe, Co and Ni can be synthesized by the decomposition of an organometallic precursor [9]. For instance, Au nanoparticles can be synthesized using the Turkevitch method [10], which involves the reduction of $HAuCl_4$ in a boiling sodium citrate solution, or with reductants such as sodium borohydride and ascorbic acid in the presence of sodium citrate at room temperature. This results in citrate-capped gold nanoparticles with sizes ranging from 10 to 100 nm,

depending on the concentration of $HAuCl_4$ and sodium citrate used. Another popular method involves a two-phase reduction synthesis reported by Brust *et al.* [11], which utilizes polar and a nonpolar solvents and a phase-transferring reagent. The latter carries $[AuCl_4]^-$ ions that are present in the aqueous (polar) phase into the organic phase where they undergo reduction in the presence of alkanethiols. This method results in very stable, so-called 'alkanethiol-protected' or 'monolayer-protected' Au nanoparticles. By extending the Brust synthetic method, many other nanoparticles composed of materials such as Ag and Pd, with a variety of alkanethiols, have also been successfully synthesized [12]. The sizes of the nanoparticles can be controlled by changing the relative ratio of the concentrations of the alkanethiol to the gold ions in the solution. Alternatively, the metal nanoparticles can also be produced in a one-phase synthesis [13]. In this case, an appropriate solvent in which the metal ions, reducing agent and alkanethiols are all soluble must be used. Although these three methods are more suitable to the synthesis of noble metal nanoparticles cores, by optimizing the synthetic conditions other metal nanoparticles – including those from transition elements – can also be synthesized. For instance, Li *et al.* [14] have synthesized zerovalent Fe nanoparticles by reducing metal salt solutions in different solvents. In this case, the strong passivation of the metal surfaces is important to keep the metals from being oxidized to the metal oxide and hydroxide. This step is particularly necessary if the nanomaterials are to be used for catalytic and environmental remediation applications, when the metal's surface will need to be exposed. In particular, the decomposition of organometallic complexes and metal–organic chemical vapor deposition (MOCVD) precursors in colloidal solutions can result in a variety of stable transition metal nanoparticles.

In addition to spherical nanoparticles it is possible that, by modifying the synthetic conditions as well as by introducing additives into the synthetic mixtures, a number of shaped metal nanoparticles, nanorods and even nanowires, can be created [15]. These materials may also have similar functional groups to the nanospheres, and may be used coated with the shells to create the core-shell nanostructures.

9.3.2 Metal Oxide Cores

The metal oxide nanomaterials, which can also be used as cores, are commonly synthesized using two different methods: (i) the Stöber synthetic method [16]; and (ii) the microemulsion synthesis [17]. The Stöber method, which over the years has been most widely used, involves the sol–gel process of hydrolysis and condensation of tetraethoxysilane (TEOS) in an ethanol solution containing water and ammonia catalyst to create monodisperse, spherical, electrostatically stabilized nanospheres. By using a slight modification of the Stöber synthesis, it is possible also to synthesize a number of other metal oxide nanosphere cores. The second, commonly used, method is that of reverse microemulsion, which relies on a controlled aqueous environment within surfactant-confined micelles in a nonpolar solvent to create monodisperse spherical colloids. The reverse micelle

microreactors allow the growth of silica and metal oxide nanospheres with controlled sizes. In addition to making pure silica and metal oxide microspheres, this method can also be used for preparing fluorescent nanospheres by physically or chemically entrapping chromophores such as metallo-organic, tris(2,2′-bipyridyl) dichlororuthenium and chromophore dyes [18]. Chromophore or fluorophore immobilization in silica can involve either physisorption or covalent attachment. A covalent attachment of the dyes into the metal overcomes any possible leaching problems of the dye molecules and also maintains their brightness.

9.3.3
Polymeric Cores

Polymers can also used to prepare core materials in the synthesis of core-shell nanostructures. Their synthesis often involves a well-known emulsion polymerization technique [19] where, first, a colloidal microemulsion containing monomers is produced in solution. Polymerization of the monomers inside the microemulsions is then initiated either photochemically or chemically. Upon completion of the polymerization, the microemulsion is broken with solvents and the polymeric nanospheres produced inside the microemulsions are collected. By changing the types of the monomer or by using multiple monomers, a variety of polymeric microsphere cores can be synthesized using this method.

9.3.4
Semiconductor Cores

A variety of semiconductor nanoparticles and nanowires have been successfully used as cores for the synthesis of different types of core-shell nanomaterials [20]. Several types of synthetic methods have now been reported for the synthesis of different types of semiconductors nanomaterial.

9.4
Deposition of Shells over the Core Nanomaterials

The deposition of shells over the core nanomaterial can be achieved in various ways, but depends on the presence of appropriate functional groups on the core nanomaterials such that a favorable deposition can take place. Placement of the correct functional groups over the nanoparticle surface can be achieved using one of five approaches:

- The direct attachment of functional sites as a terminal group on organic passivating groups such as alkanethiols on gold and silver nanoparticles.
- Further modification of the terminal functional groups, such as hydroxyl, carboxylic acid and glycidyl, that exist on the pre-made core nanoparticles, into other more reactive groups that are favorable for shell formation.

- A ligand exchange of organic or other groups on the core nanoparticles with new ligands, which enables the formation of shells.
- Simple physisorption of the shells, or of the molecules that form the shells, onto the surface of the core nanomaterials.
- The covalent attachment of shells onto the core surface.

Whilst the first three methods are more commonly used for the deposition of shells over metallic core surfaces, the latter two are typically applied for polymeric core nanomaterials.

9.5 Types of Core-Shell Nanomaterial

Because of the different types of composition, size, shape and structure that can be chosen and synthesized, core-shell nanomaterials can be subdivided in many ways. The classification of core-shell nanomaterials can be achieved on the bases of the types of material used (both the cores and shells), as well as the types of synthetic method used. By using the former approach core-shell nanomaterial are broadly classified as metal–insulator, metal–semiconductor, polymer–metal, insulator–semiconductor, metal–metal oxide, metal–polymer, metal oxide–polymer, semiconductor–metal, and so on.

9.5.1 Metal–Insulator Core-Shell Nanomaterials

Metal–insulator core-shell nanomaterials have a core which is composed of a metal, and a shell composed of an insulating material. The metal core can be made from noble or transition metals such as Au, Ag, Pd and Fe, and with shapes that include nanospheres, nanorods and nanowires. The insulator shell can be composed of a metal oxide or a metal hydroxide such as silica, MgO and $Mg(OH)_2$, or a polymeric material such as PMMA, polystyrene or polyaniline. This combination can result in a wide range of core-shell nanomaterials such as Au—SiO_2, Ag—SiO_2, Pb—SiO_2, Au—TiO_2, Au—poly(styrene), Au—poly(methyl methacrylate), and with shapes such as nanospheres, nanorods and nanowires. Metal–insulator-type core-shell nanoparticles exhibit a variety of interesting properties. For example, the metal cores can influence the optical and fluorescence emission properties of optically active insulating shells; for example, the metal nanoparticles can quench the fluorescence of chromophores, if they exist in the shell. Schneider and Decher [21] reported a distance-dependent fluorescence quenching of organic chromophores placed in metal–polyelectrolyte core–polymer nanoparticles containing different polyelectrolyte shells. The materials were synthesized using the layer-by-layer (LBL) deposition of oppositely charged polyelectrolytes onto 13 nm-diameter gold nanoparticle (AuNP) cores, where nonfluorescent polyelectrolytes are spacer

layers and fluorescent organic dyes are deposited. Such fluorescently labeled metal–polymer core-shell nanoparticles with tunable fluorescent properties may have potential applications in diagnostic or sensing devices.

Because of the wide range of possible metal–insulator type core-shell nanomaterials, and their wide range of properties, metal–insulator core-shell nanomaterials may be further subdivided based on the type of shell used.

9.5.1.1 Metal-Dense Metal Oxide Core-Shell Nanomaterials

The terminal groups of the organic layers of metal cores (nanoparticles, nanorods and nanowires) can be functionalized to allow the growth of metal oxide shells. In the case of silica shells, silanes with terminal thiol, amines or carboxylic acid groups are used as coupling agents to achieve this. The thiol, amine and carboxylic acid groups of the silanes anchor onto the surface of the metal nanoparticle cores, while the silyl groups hydrolyze and initiate the growth of silica around the cores. By using this method, a number of metal–metal oxide nonmagnetic nanospheres have been synthesized [5]. Similarly, by coating metal nanorods and nanowires, the synthesis of metal–metal oxide nanorods and nanowires has been successfully demonstrated for gold nanorods (Figure 9.5) [22]. This synthesis has proved to be equally applicable to other metal nanoparticles, nanorods and nanowires, including Ag—SiO_2 and Pd—SiO_2. Similarly, metal oxides other than silica (e.g., TiO_2, CeO_2, Cu_2O) may also be deposited and thus produce the shells.

The coating of metal cores, particularly with a silica shell, is attractive by the virtue of the latter being chemically inert. Moreover, a robust material is produced and the method requires only a simple sol–gel synthesis for its preparation and to control silica thickness. Furthermore, as silica is optically transparent in the visible region, it enables probing of the core materials by spectroscopy and allows possible light emission from the cores for biological diagnostics applications. The

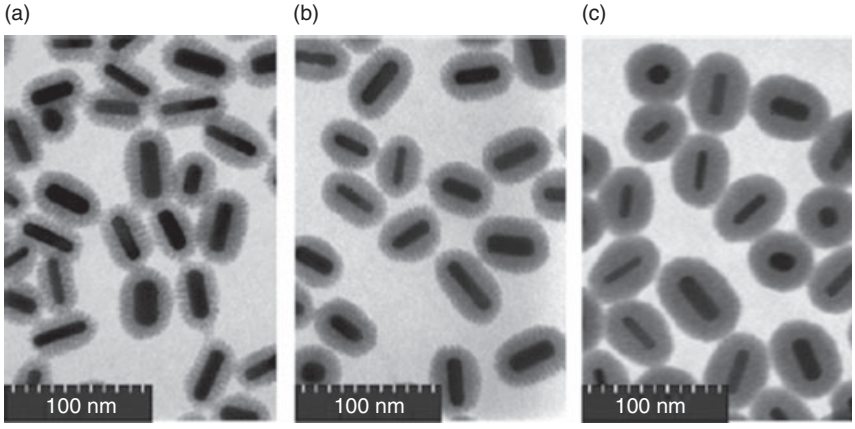

Figure 9.5 Transmission electron microscopy images of mesoporous silica coated gold nanorods after (a) 1 h, (b) 10 h and (c) 500 h of deposition of silica from tetralkoxysilane solution. Reproduced with permission from Ref. [22].

ease with which the thickness of the silica can be controlled also allows a straightforward separation between the different particles, or a tailoring of the collective optical or magnetic coupling behavior of the core metal nanoparticles.

The robust structure of silica allows the synthesis of metal–silica core-shell structures to be achieved also in a reverse process. For example, in a report made by Dae *et al.* [23], hollow spherical silica shells were first prepared by solvent-etching of a-Se with CS_2 or N_2H_4 from a-Se—Pt-silica core-shell-shell nanospheres. By using the resultant hollow structure, nanoparticle cores were then deposited inside. After etching, the Pt shell was transformed into Pt nanoparticle cores, the size and number of which were dependent on the thickness of the Pt layer and the temperature used.

Metal oxides other than silica can also be used to create shells around metal-containing cores. This process, in fact, allows the introduction of other interesting properties associated with the shell. For example, luminescent nanoparticles containing Eu^{3+}-doped Y_2O_3 core nanoparticles of different sizes covered with Y_2O_3 shells were synthesized by urea hydrolysis of the corresponding metal salts in ethylene glycol at a 140 °C, followed by heating at 500 and 900 °C [24]. Luminescence studies showed that, for a fixed concentration of Eu^{3+} doping, there was a reduction in Eu^{3+} emission intensity for core-shell nanoparticles compared to that of core nanoparticles, this being attributed to a concentration dilution effect.

The preparation of metal–metal oxide nanomaterials can also be accomplished by surface oxidization of the metal (Figure 9.6). For instance, Ag—Ag_2O core-shell nanoparticles were synthesized by thermal treatment of Ag nanoparticles at 200–360 °C in the gas phase, or in an organic solvent [25]. The formation of such a core-shell structure was proved by cyclic voltammetry, using Nafion-containing C particles as the matrix to encapsulate the core-shell nanoparticles. These experiments also proved the validity of electrochemical methods in the characterization of core-shell nanostructures, in addition to the use of techniques such as

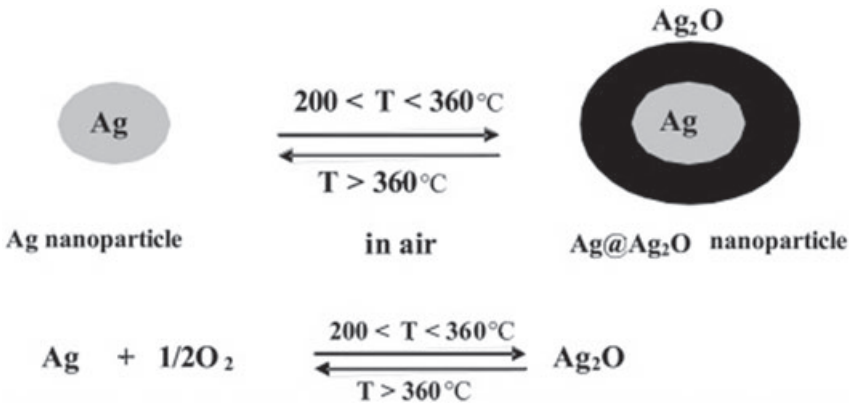

Figure 9.6 Synthetic scheme to Ag–Ag_2O core-shell nanomaterials. Reproduced with permission from Ref. [25].

transmission electron microscopy (TEM), scanning electron microscopy (SEM), X-ray photoelectron spectroscopy (XPS) or X-ray diffraction (XRD), and optical techniques such as UV-visible absorption spectroscopy.

9.5.1.2 Metal-Functionalized Metal Oxide Core-Shell Nanoparticles

One interesting property of silica shells is that they can be decorated rather easily using various organic groups, which in turn enables the surface properties of the core-shell nanomaterial to be tuned [26]. The immobilization of organic groups in silica can be achieved either by post-functionalization or copolymerization with organoalkoxysilanes [27]. The addition of organosilanes such as 3-aminopropyltriethoxysilane, phenyltriethoxysilane and vinyltriethoxysilane, either as monomers during copolymerization with tetra-alkoxysilane or as terminators during deposition of the metal oxide shells around the metal cores, produces hybrid organosilica shells that contain the organic functional groups in the shell material. The thickness, size and morphology of the core-shell nanostructures can be controlled by altering the relative molar ratio of the tetra-alkoxysilane and organosilane, the solvent, and the reaction temperature and time [28]. The formation and composition of the organosilica shells can be verified by combinations of solid-state nuclear magnetic resonance (NMR), Raman and Fourier transform infrared (FTIR) spectroscopy, wide angle X-ray scattering (WAXS) and thermogravimetry.

The possible inclusion of organic groups (including fluorophores) within the silica structures, either by physisorption or covalent attachment, allows optically active silica shells to form. Furthermore, the optical properties of these fluorescent molecules can be tuned or changed by the metal nanoparticle cores, which can produce a near-field electrodynamic environment around the fluorophores. Such property changes may include an enhancement or quenching of the fluorescence of the organic groups in the shells, depending on the distance between the molecule and the metal surface. While nonradiative energy transfer to the surface plasmons of the metal nanoparticles such as gold and silver occurs at short distances, the electromagnetic field enhancement due to surface plasmons occurs possibly at longer distances [29]. Tovmachenko *et al.* [30] have recently demonstrated this point by synthesizing Au or Ag nanoparticle cores, a SiO_2-spacer shell and a dye-doped secondary SiO_2 shell by solution-phase synthesis (Figure 9.7). The materials containing the Ag-core and Au-core and carboxyfluorescein-labeled silica shells with a dye–metal spacer distance of 24–25 nm showed fluorescence enhancement factors of ~12.5 and 6.8, respectively, while the Au-core particles with a dye–metal distance of ~15 nm exhibited significant fluorescence quenching.

9.5.1.3 Metal–Porous Metal Oxide Core-Shell

In addition to dense silica and dense organosilica shells around metal core nanoparticles, much interest has been expressed in preparing porous metal oxide shells in order to create high-surface-area core-shell nanomaterials, to immobilize important functional groups into the materials, or to provide easy access to the metal cores. The synthesis of nanoporous metal oxide shells can be achieved by a

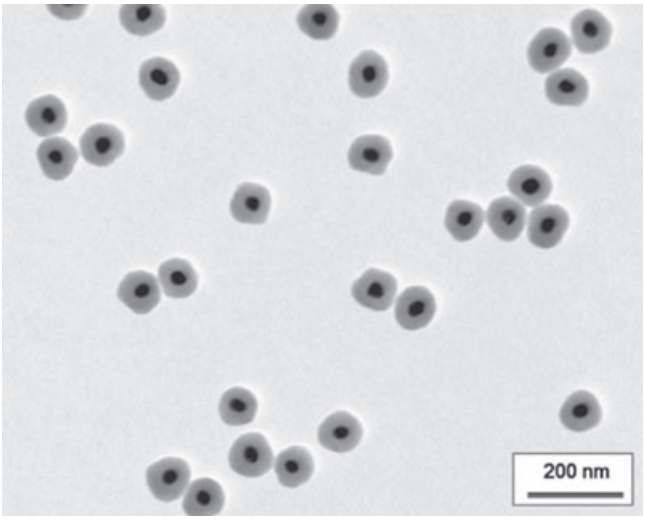

Figure 9.7 TEM image of gold–silica–carboxyfluorescein silica core-shell-shell nanospheres with core sizes of 30 nm. The thickness of the silica spacer is varied, which results in a tunable fluorescence. Reproduced with permission from Ref. [30].

combination of sol–gel processing and surfactant (template) self-assembly – as shown with mesoporous materials [31] – or by a hydrothermal synthesis [32]. Either approach produces a metal oxide–surfactant self-assembled structure around the metal cores. In the former, removal of the surfactant templates by calcination or solvent-washing results in porous metal oxide shells around the metal cores [33]. In another elegant study, a dense silica shell around the metal was transformed into nanoporous silica shell under hydrothermal treatment [32]. These two methods may also be utilized to synthesize other nanoporous metal oxide shells.

9.5.1.4 **Metal–Polymer Core-Shell Nanoparticles**

Insulating shells can also be synthesized by depositing polymeric materials around the metal core nanostructures. Polymer shells that are both biocompatible and biodegradable are particularly appealing not only for biological applications but also to enable the uptake of nanomaterials by cells. In order to synthesize polymer shells around metal nanomaterials (nanoparticles, nanorods and nanowires), the terminal groups in the organic passivating groups of the metal core nanomaterials must be chosen systematically, synthesized to produce polymerizable groups, or be capable of anchoring a pre-made polymer. An excellent review on metal–polymer core-shell nanoparticles containing gold nanoparticle cores was recently provided by Shan and Tenhu [34]. Currently, four major routes are employed that will result in polymer shells being deposited around metallic-core nanomaterials.

9.5.1.4.1 **Post-Polymerization Technique** Polymeric brushes or shells can be anchored onto the surface of metal nanoparticle cores by placing polymerization initiators on the terminal functional groups of the organic passivating agents of the metal cores. For example, by using a living/controlled radical polymerization over functionalized metal nanoparticles in the presence of a polymerization initiator, metal–polymer core-shells that have polymer brush shells with controlled molecular weights and well-defined chain architectures have been synthesized [35]. By changing the monomer concentration and synthetic conditions in the polymerization reaction, it is also possible to control the thickness of the polymer shells and the grafting density. Placement of the polymerization initiators can be achieved by either of three methods:

- By the direct attachment of passivating groups containing initiators onto the surface of the metal nanomaterial.
- By the surface modification of functional groups (e.g., hydroxyl, carboxylic acid, glycidyl) that exist on the alkyl passivating groups of the metal nanoparticles into initiators.
- By ligand exchange of the functional groups of the metal-passivating groups with those containing polymeric initiators. For example, gold-poly(methyl methacrylate) (PMMA) core-shell nanoparticles were synthesized using an atom transfer radical polymerization method over protective ligands [36].

Typically, alkanethiol ligands are first replaced with 3-mercaptopropyltrimethoxysilane by a place exchange reaction, after which the silanes are subjected to hydrolysis and condensation into a crosslinked silica-primer layer. In the same way, ring-opening polymerization or a Michael addition reaction can be used to create polymeric shells from crosslinkable polyfunctional alkanethiols around the 3 nm-diameter gold nanoparticles [37]. The resultant core-shell nanoparticles showed an increased stability towards thermal treatment and oxidative etching, as a result of the polymer shell's presence. In other studies, both temperature- and pH-sensitive polymers such as poly(*N*-isopropylacrylamide) (PNIPAM) and poly(4-vinylpyridine) (P4VPy) were also used to produce shells around metal cores. For example, Li *et al.* [38] prepared a thermosensitive polymer containing Au–PNIPAM core-shell nanoparticles that were capable of encapsulating other nanoparticles, biomolecules, dyes or drugs and releasing drug molecules at different temperatures.

9.5.1.4.2 **One-Pot Synthesis** A second commonly used method to produce polymer shells around metal cores is the direct anchoring of polymeric species onto the metal surface in a one-pot synthesis. This method is rather simple compared to the multistep, post-polymerization synthetic method. In this synthesis, polymers with functional groups such as dithioester, trithioester, thiol, thioether, amine, phosphonic acid and disulfide that are capable of binding to the metal surface, are chosen or synthesized and then allowed to bind onto the nanoparticles surface, either by Brust synthesis [11] or by a ligand exchange reaction [13] (see

Section 9.3.1). In addition to being easier and less complicated, this method also enables a direct covalent attachment of the polymer to the cores, thus achieving a high surface graft density of the polymer shell. As an example, Corbierre *et al.* [39], synthesized AuNPs protected with thiolated polymers (polystyrene, PS–SH). This method also allowed the placement of amphiphilic polymers such as polystyrene-*block*-PNIPAM on metal nanoparticles in a one-pot reaction. The amphiphilicity of the resultant core-shell nanoparticles can be tuned by varying either the relative ratio or the chain lengths of the block polymers. Because of the amphiphilicity of the polymer shell, such core-shell nanoparticles are capable of assembling into different array structures.

Biopolymers such as polypeptides, biocompatible block copolymers and conducting polymers can also be used to create the polymer shell around metal cores with a one-pot synthesis. For example, Higashi *et al.* [40] have reported the synthesis of gold–polypeptide core-shell nanoparticles containing poly(c-benzyl-L-glutamate) groups by using terminal disulfide S—S groups of the polymer to passivate the gold nanoparticles in the Brust synthesis [11]. Biocompatible and biodegradable poly(ethylene oxide) (PEO)-*block*-poly(caprolactone) (PCL) polymers have also been used to produce polymeric shells around noble metal nanoparticles in a one-pot synthesis [41]. Thermosensitive thiol-terminated polymers such as poly(glycidyl methacrylate) (PGMA) and PNIPAM can be placed with similar strategy to produce Au–polymer core-shell nanomaterials for potential stimuli-responsive drug-release applications [34].

9.5.1.4.3 **Ligand Exchange and Micellization** The placement of polymeric species by exchanging organic passivating groups around metal cores is also possible. Block copolymer shells around metal nanoparticles can simply be placed by exchanging passivating groups such as citrates in citrate-capped gold nanoparticles with 1-dodecanethiol, followed by stirring the resultant nanomaterials in a polymer solution containing the block copolymer PS-*b*-PAA (Figure 9.8) [42]. The resultant nanoparticles undergo an interesting micellization in water, where the PS block and the alkanethiol groups are not miscible. The crosslinking of the poly(acrylic acid) (PAA) groups leads to the core-shell nanostructures being permanently fixed.

9.5.1.4.4 **Physisorption** Surfactants and block copolymer reverse micelles have long been used as nanoreactors to produce various nanoparticles. By self-assembling block copolymers that contain hydrophilic and hydrophobic blocks into reverse micelle microreactors, and by immobilizing and reducing metal ions inside the block copolymer micelles, metal–polymer core-shell nanoparticles can be produced. The binding of the polymers over the metal nanoparticles in the resultant core-shell structures is strictly by physisorption or due to electrostatic/covalent interactions. For example, block copolymers containing hydrophobic polymers such as PS, PMMA and poly(*tert*-butylmethacrylate) (PtBMA), as well as hydrophilic block polymers such as poly(styrene)-*block*-poly(4-vinylpyrollidone) (PS-*b*-P4VP) block copolymer can form such reverse micelles. While the

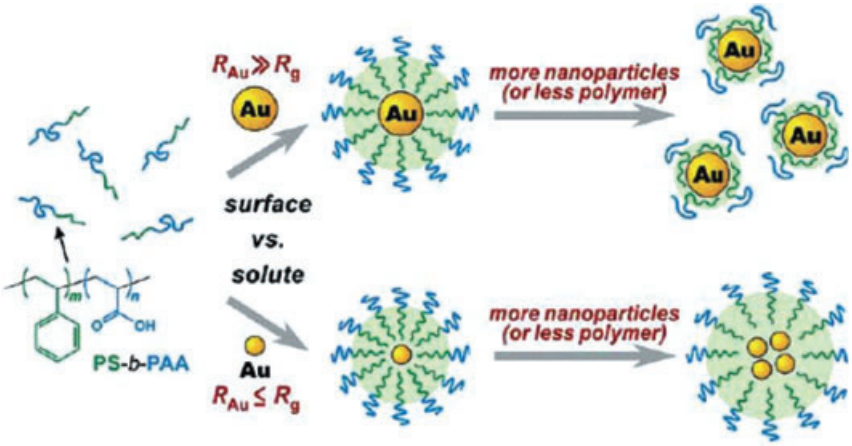

Figure 9.8 Examples of synthesis of metal–polymer core-shell nanoparticles by place exchange and micellization. Reproduced with permission from Ref. [42].

hydrophobic polymers are unable to coordinate with metal ions, the hydrophilic block polymers such as PS-*b*-P4VP that form the cores can coordinate to metal ions which, upon reduction, form metal nanoparticles such as Au, Ag and Pd *in situ*. Hou *et al*. [43] have used this method to synthesize gold nanoparticles in PS-*b*-P4VP reverse micelles prepared in chloroform. Here, an aqueous solution of $HAuCl_4$ is first encapsulated in the hydrophilic P4VP, and then reduced with hydrazine hydrate to produce Au-PS-*b*-P4VP core-shell nanoparticles.

9.5.1.5 Hollow Metal–Metal Oxide Shells by Controlled Core-Dissolution

Metal–metal oxide core-shell nanoparticles containing hollow structures can also be synthesized by a controlled partial etching of the core materials (Figures 9.9 and 9.10). For example, Choi *et al*. [44] have synthesized silica- or goethite-coated melamine-formaldehyde (MF) core-shell microspheres, which then were subjected to a controlled dissolution of the cores with NH_4OH solution to produce hollow silica- or goethite-coated MF core-shell nanospheres. The deposition of metals inside the hollow structure, which is effected by the reduction of metal ions such as $AuCl_4^-$, results in the synthesis of gold–silica core-shell nanoparticles (Figure 9.9b).

By using a similar procedure, other metal core-shell nanoparticles containing hollow cores have been synthesized from Pt–silica core-shell nanomaterials (Figure 9.11) [23, 45]. First, *a*-Se–Pt-silica core-shell nanoparticles are synthesized by reacting H_2SeO_3 solution in ethylene glycol with another solution containing hydrazine hydrate and ethylene glycol. Poly(4-vinylpyrollidone) (PVP) dissolved in ethylene glycol was then added to the *a*-Se colloidal solution, followed by deposition of the Pt layer from the reduction of H_2PtCl_6 in ethylene glycol, which serves as both a solvent and a reducing agent. Finally, silica was deposited by the sol–gel process.

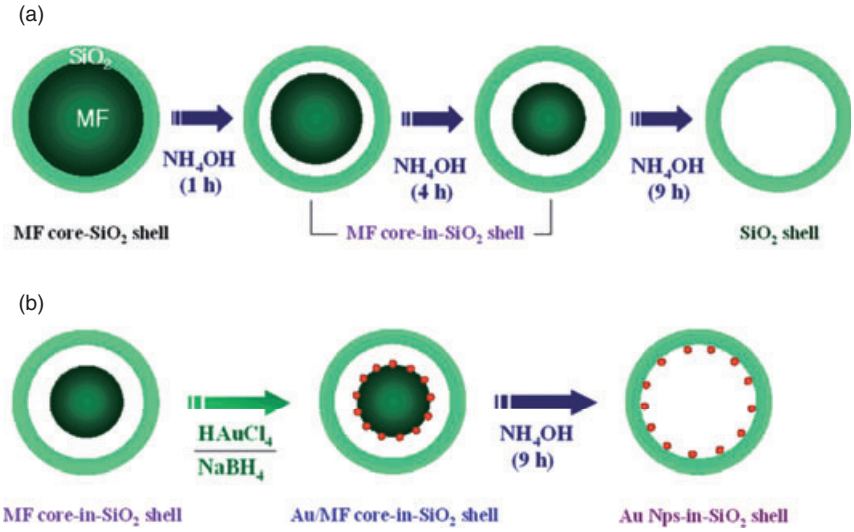

Figure 9.9 Schematics for (a) the synthesis of melamine–formaldehyde (MF)–SiO_2 core-shell microparticles with controllable core size and (b) the encapsulation of gold nanoparticles into the interior of the SiO_2 shell. Reproduced with permission from Ref. [44].

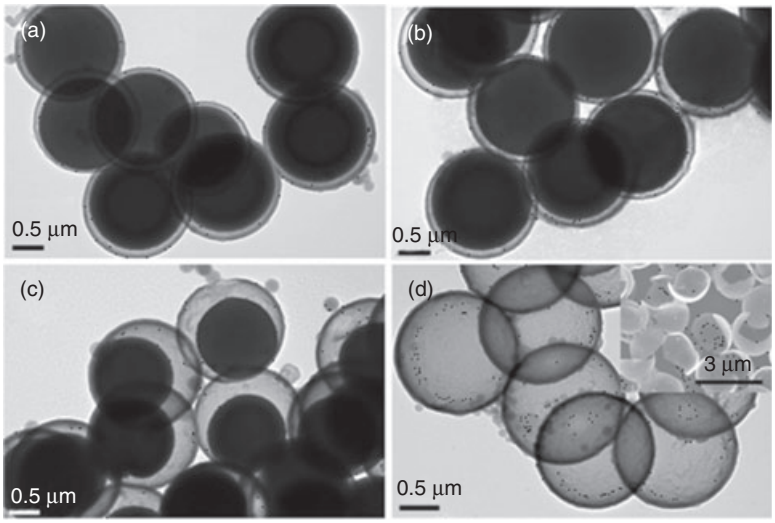

Figure 9.10 TEM images of melamine–formaldehyde (MF)–silica core-shell nanoparticles with various core sizes as a function of increasing exposure time of (a) 1, (b) 2, (c) 4 and (d) 9 h in NH_4OH solution. The inset SEM image in (d) shows broken SiO_2 capsules formed during the dissolution of the MF core under HCl treatment. MF cores were completely dissolved within 5 s under HCl treatment, which may induce rapidly increased osmotic pressure inside the SiO_2 capsules. Reproduced with permission from Ref. [44].

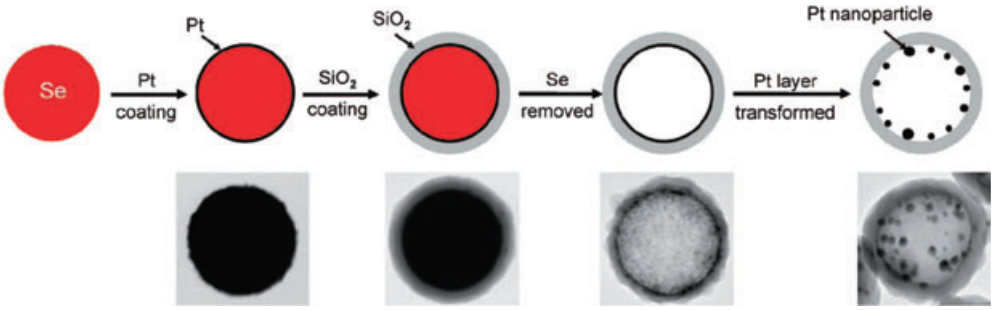

Figure 9.11 Upper: Schematics of the formation of Pt nanoparticles core-in-SiO_2 shell nanoparticles with controllable core size. Lower: TEM images of the particles at the different stages of the synthesis. Reproduced with permission from Ref. [23].

By a solvent etching process in CS_2 and hydrazine (N_2H_4), the *a*-Se core was etched to produce hollow Pt–silica core-shell nanoparticles. The Pt layer could be further transformed into Pt nanoparticle cores at different temperatures; for example, at an elevated temperature (65 °C) in alcohol, the nanoparticles were aggregated and rearranged into large nanoparticles.

9.5.1.6 Metal Core–Dendrimer Core-Shell Nanoparticles

Metal–dendrimer core-shell nanomaterials can be synthesized by the simple deposition of metal ions in dendrimer structures, followed by their reduction *in situ*. Recently, several groups have demonstrated the synthesis of a variety of metal–dendrimer core-shell structures for a range of metals including Cu, Ag, Pd, and Au on nanoparticles inside dendrimer shells [46]. Dendrimer structures, such as the poly(amidoamine) (PAMAM) groups of various generations of dendrimer, may serve as the nanoreactor template to sequester metal ions. Subsequent reduction of the metal ions by various reducing agents produces zerovalent metal nanoparticles within the dendrimer shells or metal–dendrimer nanostructures.

Dendritic hyperbranched polymers that have a double-layered shell, composed of hydrophobic alkyl groups (C18) linked to a hydrophilic monomethyl poly(ethylene oxide) chain outer shell, can also be used to stabilize or coat metal core nanoparticles [47]. The metal cores are synthesized by reducing metal ions in the presence of the polymer.

9.5.1.7 Metal Core–Semiconducting Metal Oxide Shell Nanoparticles

Metal–metal oxide core-shell nanomaterials containing semiconducting metal oxide shells can be produced by a variety of synthetic methods [48]. For instance, Cu—ZnO core-shell nanoparticles were synthesized by combinations of digestive ripening and solvated metal atom dispersion (SMAD) of Cu and Zn nanoparticles [49]. Both, copper nanoparticles (2.1–3.0 nm) and zinc nanoparticles (~3.9 nm)

were first synthesized using SMAD, after which the solutions containing the two different nanoparticles were digestively ripened together, in the presence of a passivating agent to produce Cu—ZnO core-shell nanoparticles.

9.5.2 Insulator–Metal Core-Shell Nanomaterials

Insulator–metal core-shell nanomaterials have an inverse structure compared to those discussed in Section 9.3.1, and consequently their preparation also involves a reverse synthetic approach. The core nanomaterial with metal oxide or polymer composition is synthesized first, and then coated with metallic shells using a variety of methods. Such core-shell nanomaterials can be further divided into several subclasses.

9.5.2.1 Metal Oxide–Metal Core-Shell Nanostructures

For the synthesis of metal oxide cores, the various solution-phase synthetic methods to metal oxide shells discussed in Section 9.3.1 are used. The resultant metal oxide nanomaterial cores are then allowed to react with various coupling agents (often organosilanes such as 3-mercaptopropyltriethoxysilane, 3-aminopropyltriethoxysilane and 3-cyanopropyltriethoxysilane) to leave functional groups such as thiol, amino- and cyano groups on the surface of the cores. These functional groups are then used to anchor metal nanoparticles. Alternatively, the terminal functional groups of the silanes may be converted into other more suitable functional groups, such as carboxylic acids and imines, by further reaction in order to scavenge metals or to anchor metallic shells. By applying this method, Halas and others [50] have synthesized silica–gold core-shell nanospheres with tunable optical properties (Figure 9.12). By altering the relative sizes of the core and the thickness of the metal shell, the sizes and – most importantly – the surface plasmon resonance (SPR) properties of the particles, can be broadly tuned. This method also allows for the deposition of isolated metal nanoparticles as a shell over the metal oxide cores. These colloidal metal oxide–metal core-shell nanomaterials have important metal/dielectric architectures. In addition to their tunable optical absorption properties, the materials' absorption properties in the NIR spectrum – to which the body's tissues are transparent – can be used to kill cancer cells by heating them with these materials. A similar synthetic strategy can also be employed to deposit metal nanoshells onto metal oxide nanotubes and nanowires to produce metal oxide–metal core-shell nanotubes.

9.5.2.2 Polymer–Metal Core-Shell Nanostructures

Polymers can be used as the cores of the insulator–metal core-shell nanomaterials. For example, Shi *et al.* [51] synthesized PS–gold nanoparticle core-shell nanostructures by using thiol-modified PS beads to deposit Au nanoparticles ranging from 1 to 20 nm in size. Moreover, by using the Au nanoparticles as seeds, a continuous growth of gold nanoshells by the reduction of additional gold ions around the PS nanospheres was achieved. The size, shell thickness and roughness could be

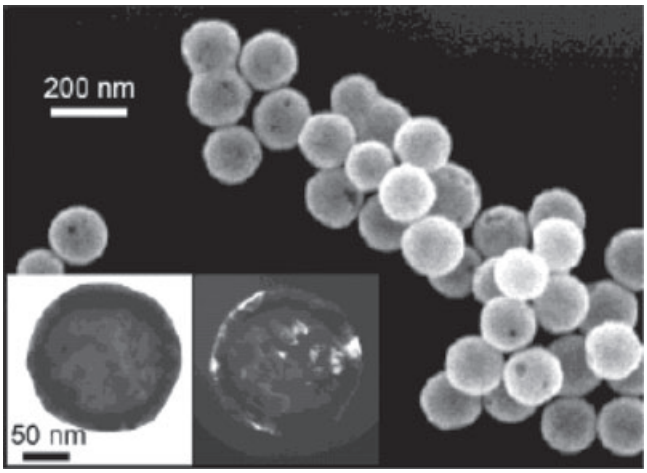

Figure 9.12 Scanning electron microscopy images of silica-gold core-shell nanoparticles having a ~122 nm-diameter silica core and a ~12 nm-thick silica shell. Reproduced with permission from Ref. [50b].

controlled by changing the size of the nanoparticle seeds, as well as the synthetic conditions.

9.5.3 Insulator–Insulator Core-Shell Nanoparticles

9.5.3.1 Polymer–Metal Oxide Core-Shell Nanomaterials

Colloidal polymer nanomaterials can be encapsulated with metal oxides using the Stöber process. For example, Agrawal *et al.* [52] have demonstrated the encapsulation of PS beads with titania of controlled shell thickness between 100 and 130 nm, by varying the concentration of the titania precursor, $Ti(OEt)_4$. Removal of the polymer cores, either by calcination or chemical dissolution, led to the formation of hollow titania nanospheres. The characterization of the core-shell and hollow microspheres was achieved using SEM, TEM, FTIR spectroscopy, XRD and thermogravimetric analysis.

In another example, crosslinked micellar polymer–silica core-shell nanoparticles have been synthesized using a combination of self-assembly and sol–gel process (Figure 9.13) [53]. Polymeric surfactants such as pluronics and F127 ($EO_{106}PO_{70}EO_{106}$) self-assembled into micellar structures in solvents and controlled the polymerization of silicates from tetraethoxysilane (TEOS) in the hydrophilic shell (PEO) region of the self-assembled block-copolymer spherical micelles, resulting in the formation of block copolymer–silica core-shell nanospheres. The addition of a small amount (5 wt% with respect to F127 and TEOS) of diethoxydimethylsilane ($Me_2Si(OEt)_2$) terminated the silicate condensation and prevented intermicellar aggregation and particle growth.

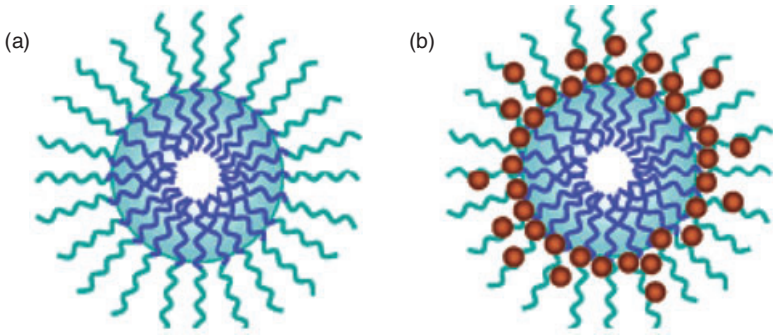

Figure 9.13 (a) Polymeric micelles and (b) silica crosslinked, micellar core-shell nanoparticles. Reproduced with permission from Ref. [53].

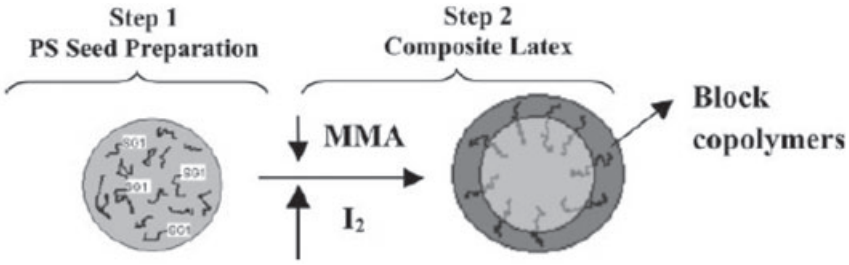

Figure 9.14 Schematic representation of the polymerization steps used to synthesize polymer–polymer core-shell nanoparticles by nitroxide-mediated free-radical miniemulsion polymerization method. Reproduced with permission from Ref. [54].

9.5.3.2 **Polymer–Polymer Core-Shell Nanomaterials**

When both the core and shell nanostructures are polymers, the result is a polymer–polymer-type core-shell nanomaterial (Figure 9.14) [54]. Some polymer–polymer core-shell nanomaterials are also often referred to as core-shell hydrogels or nanogels. Hydrogel nanoparticles, in general, consist of randomly oriented, crosslinked, water-soluble polymers. Some hydrogel core-shell nanomaterials may contain temperature-sensitive polymers such as PNIPAM, or pH-sensitive polymers such as PAA. The structures of these nanomaterials may swell or shrink under external stimuli such as pH or temperature changes and they are, therefore, useful for stimuli-responsive applications, such as drug release. Consequently, polymer–polymer hydrogels – and particularly those containing stimuli-responsive polymers – have recently been the center of attention in the development of stimuli-responsive drug delivery, biomaterials, biosensing, tissue regeneration and chemical separations. They are often synthesized by a two step-synthesis (Figures 9.14 and 9.15). For example, PS nanoparticle cores are synthesized by a first emulsion

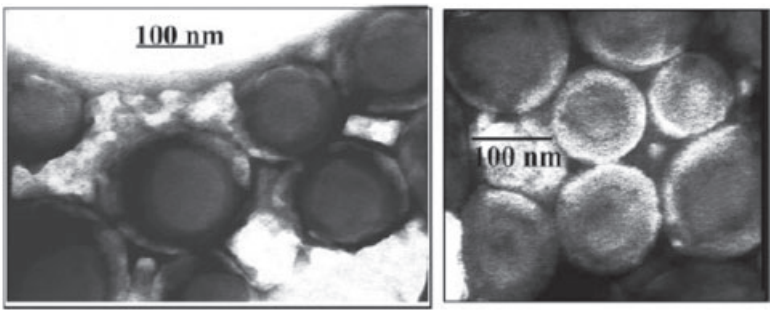

Figure 9.15 (a) Representative TEM images of PS/PMMA core-shell nanoparticles. Reproduced with permission from Ref. [54].

polymerization, followed by a second seeded emulsion polymerization of 5 wt. % *N*-isopropylacrylamide (NIPA) to produce PNIPAM shells on the PS core nanoparticles. Similarly, by using a multistep emulsion polymerization, various types of other thermosensitive core-shell polymer–polymer nanoparticles such as PMMA-thermosensitive PNIPAM and poly(acrylamide-*co*-styrene)-poly(acrylamide-acrylic acid) core-shell polymer–polymer nanoparticles have been synthesized [55].

Other polymerization methods may also be employed for the synthesis of polymer–polymer core-shell nanoparticles. For instance, Blackburn and Lyon [56] have reported the synthesis of monodisperse 100 nm-diameter polymer–polymer core-shell nanoparticles by the free-radical precipitation polymerization of NIPA or *N*-isopropylmethacrylamide as the main monomer, with acrylic acid or 4-acrylamidofluorescein as a comonomer and *N,N'*-methylenebis(acrylamide) as cross-linker. By varying the surfactant and initiator concentrations, the particle sizes of the core-shell nanoparticles could be controlled. Likewise, by decorating the surface of the resultant polymer–polymer core-shell nanoparticle with amine groups, and by the subsequent bioconjugation of folic acid onto the amine groups, the potential of these materials as a targeted drug delivery system has been demonstrated.

Recently, Levins *et al.* [57] succeeded in synthesizing core-shell nanoparticles containing a metal-complex/polymer composite core and a polymer shell via a metal–ligand complexation strategy. These authors synthesized and self-assembled ruthenium–terpyridine molecules into amphiphilic, block copolymer spherical micelles (Figure 9.16). Cleavage of the metal–ligand bond in the complex resulted in hollow, polymeric core-shell nanoparticles.

9.5.3.3 Biomolecule (Protein) Core–Polymer Shell Core-Shell Nanoparticles

The shells or cores of core-shell nanomaterials can be prepared from bioactive materials by a variety of synthetic routes. For instance, lysozymes have been used to produce the cores of lysozyme–dextran core-shell nanogels using Maillard dry-heat and heat-gelation processes [58]. Here, a lysozyme–dextran conjugate was first synthesized by the Maillard reaction, and then heated in solution above the denaturation temperature of lysozyme to produce spherical shaped, ~200 nm-diameter

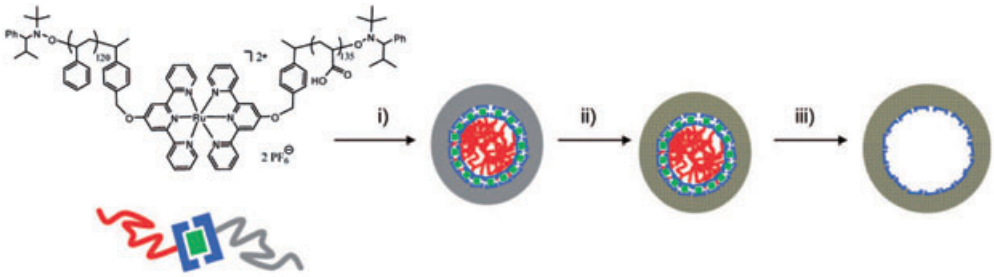

Figure 9.16 Core-shell nanoparticles containing metal–complex/polymer composite core and polymer shell via a metal–ligand complexation strategy. Reproduced with permission from Ref. [57].

nanogels that had a swelling ratio of ~30. The materials' stability under various conditions, and its ability to adsorb the drug ibuprofen at different pH values via electrostatic and hydrophobic interactions, were also investigated.

9.5.3.4 Metal Oxide–Metal Oxide Core-Shell Nanomaterials

Core-shell nanostructures containing only metal oxides as cores and shells can be synthesized by multistep sol–gel processing. Silica nanospheres prepared via a Stöber synthesis (or via a modified Stöber synthesis) [16] have been used as substrate to place a variety of metal oxide shells such as titania and iron oxides by a second sol–gel process involving the corresponding precursor of the second metal oxide under a variety of conditions.

9.5.3.5 Metal Oxide–Dye-Doped Silica and Dye-Doped Silica–Metal Oxide Core-Shell Nanostructures

By modifying the Stöber synthesis [16], organic fluorophores can be incorporated into the silica core or silica shell matrix by using organosilanes containing organic chromophores. This concept was demonstrated for tetramethylrhodamine isothiocyanate (TRITC) dye-doped silica (Figure 9.17) [59]. The silica or the secondary metal oxide shell helps to protect the encapsulated dyes in the cores from being lost by leaching. Using a similar method, several types of luminescent core-shell metal oxide/metal oxide core-shell nanomaterials have been synthesized [59] and, indeed, some of these fluorescent organic dye-silica-based core-shell nanoparticles have per-particle brightness levels close to those of QDs. The brightness of the particles may be controlled by encapsulating the fluorophores in the core of the core-shell nanoparticles, and by altering the sizes of either the cores and shells or of the core-shell nanoparticles (Figure 9.17).

9.5.3.6 Metal Oxide–Polymer Core-Shell Nanoparticles

Various polymerization reactions can be performed on colloidal metal oxide nanoparticles to produce polymer–metal oxide core-shell nanostructures. To achieve this, functional groups that are suitable as polymerization initiators for

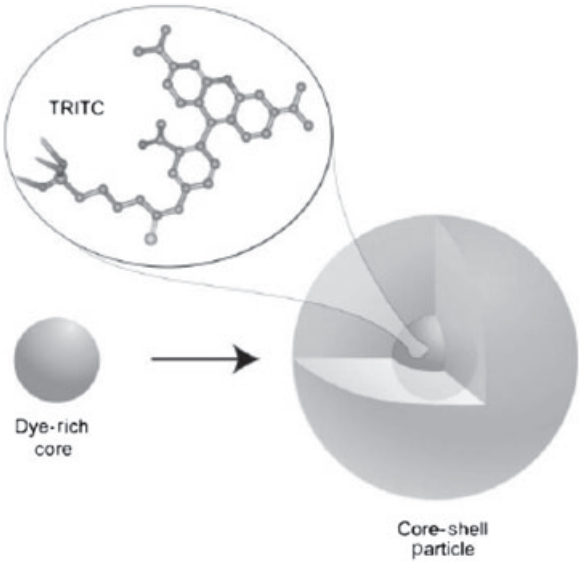

Figure 9.17 A schematic representation of the dye-rich core–shell architecture of dye-doped silica-silica core-shell nanoparticles containing covalently incorporated organic dye tetramethylrhodamine isothiocyanate (TRITC). Reproduced with permission from Ref. [59].

the atom transfer radical polymerization (ATRP) or radical polymerization are first placed on the silica surface. As an example, a polymer shell has been synthesized around silica nanospheres by using the ATRP method (Figure 9.18) [60].

Motornov *et al.* [61] recently synthesized core-shell nanoparticles which consisted of a silica core with a responsive block copolymer brush, poly[styrene-*block*-(4-vinylpyridine)]. The responsive polymer shell was used to tune and stabilize the secondary aggregates of the core-shell nanoparticles into an appropriate size and morphology in an aqueous environment. By using this method, superhydrophobic coatings on silica core were produced by casting the polymer solution on the cores and then heating the core-shell nanoparticles above the polymer's glass transition temperature.

9.5.3.7 **Other Inorganic Materials Cores: Metal Oxide Shells**

Many other examples exist of core-shell nanomaterials that contain 'nontraditional' inorganic materials as cores and shells. For example, Darbani *et al.* [62] have reported the synthesis of luminescent YF_3-SiO_2 core-shell nanoparticles with morphologies ranging from spherical to elongated structures (pearl necklace), using a one-pot microemulsion synthetic method. Core-shell nanoparticles exhibiting NIR luminescence and with superparamagnetic properties have also been synthesized using a combination of layer-by-layer (LbL) and modified Stöber synthetic methods [63]. Magnetic Fe_3O_4 nanoparticles were synthesized onto which

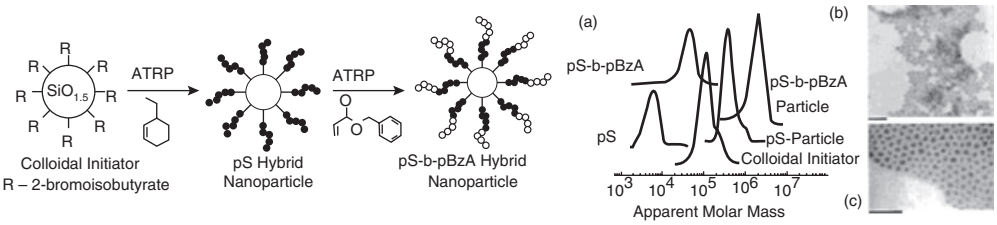

Figure 9.18 Left: Synthesis scheme of silica–polymer core-shell nanoparticles by a combination of microemulsion and atom-transfer radical polymerization (ATRP) methods. Right: (a) Size-exclusion chromatography of polysilosesquioxane colloidal initiator; polysilosesquioxane (pS)-grafted core nanoparticles prepared by ATRP; polysilosesquioxane-*block*-poly(benzyl acrylate) (pS-*b*-pBzA)-grafted particles; cleaved pS homopolymer, $M_{nSEC} = 5230$; $M_w/M_n = 1.22$; cleaved pS-*b*-BzA copolymer, $M_{nSEC} = 27280$; $M_w/M_n = 1.48$; (b) TEM image of polysilsesquioxane colloidal initiators; (c) TEM image of pS hybrid nanoparticles (M_n pS = 5230, $M_w/M_n = 1.22$). Scale bar = 100 nm. Reproduced with permission from Ref. [60].

$NaYF_4:Ln^{3+}$ (Ln = Nd, Er, Pr, Ho) and silica shells were deposited, the shells ultimately helping to improve the chemical stability and photostability of the core-shell nanoparticles. Characterization by XRD patterns enabled the crystal structures of the Fe_3O_4 to be probed, while energy dispersive X-ray (EDX) spectroscopy confirmed the material's composition. An examination using TEM confirmed the spherical morphology of the particles.

9.5.4
Semiconductor–Insulator Core-Shell Nanomaterials

Semiconductor QDs, because of their unique size-dependent fluorescence and symmetric emission profile, have attracted considerable interest in the recent past. For example, semiconductor QDs have been used successfully as biolabeling materials for versatile biological and biomedical diagnostic applications [64]. However, several drawbacks such as ultrasensitivity [65], cytotoxicity [66], heavy metal ion-release [67] and poor chemical and colloidal stabilities have greatly limited their wide application. In order to overcome these deficiencies, the coating of semiconductors with various materials such as silica has been considered. This strategy reduces the cytotoxicity of the semiconductors, impedes their heavy metal release, and also enhances their stability [68]. The general methods used to synthesize metal oxide and silica coatings around semiconductor cores include reverse microemulsion [69], LbL deposition [70] and one-pot syntheses [71]. Several parameters employed in these syntheses can be altered to tune the properties of the semiconductor–semiconductor core-shell nanomaterials. For example, the composition of the semiconductor core [72] and the thickness of the silica shell can be altered, while a void space can be introduced between the core and shell for fine-tuning of the materials' properties. Recently, by using size-selective photoetching, Torimoto and coworkers [70] have created an adjustable void space between the core and shell of semiconductor-metal oxide core-shell nanoparticles.

9.5.5
Semiconductor–Semiconductor Core-Shell Nanomaterials

Semiconductor–semiconductor QDs, nanorods and nanowires represent a very important class of materials because of their many potential applications in biological fields, opto-electronics and light-emitting devices [73]. The coating of one semiconductor nanoparticle with another allows the properties of the materials, such as luminescence efficiency, to be tuned. As an example, the coating of a CdS shell over the CdSe core causes a significant increase in the quantum yield (QY) of the original CdSe QDs.

Chalcogenide core-shell semiconductor–semiconductor nanomaterials, such as CdSe—ZnS and CdSe—CdS QDs and Si/CdS and CdSe/CdS nanowires, are commonly synthesized by a high-temperature decomposition of the corresponding organometallic or inorganic compounds such as diethyl zinc (Et_2Zn), zinc and manganese stearate, dimethyl manganese (Me_2Mn) or CdO, in solutions containing Se, S and thiourea in the presence of trioctylphosphine or trioctylphosphine oxide (TOPO), in high-boiling solvents such as oleylamine and oleic acid [74]. Typically, the metal-containing compounds or reagents are injected into the reaction mixture, either in one step or in several steps. For example, Ehlert *et al.* [75] have synthesized highly luminescent ZnS—Mn/ZnS core-shell nanoparticles for bioanalytical applications via a high-temperature decomposition of $MnCl_2$, zinc acetate in dimethylformamide (DMF) in the presence of oleic acid, trioctylamine and hexadecanethiol at 300 °C under nitrogen, followed by the decomposition of zinc acetate and S. By using a slightly modified procedure which involved the decomposition of the reagents in a microemulsion, Li *et al.* [76] also synthesized ZnS—Mn/ZnS core-shell nanoparticles.

In addition to chalcogenides, semiconductor–semiconductor core-shell nanoparticles from metal oxide semiconducting nanomaterials have also been synthesized using similar multistep reactions. As an example, indium oxide (In_2O_3) nanoparticles (which are direct, wide band-gap metal oxide semiconducting nanomaterials) have been coated with indium sulfide (In_2S_3), which is a visible-light-sensitive semiconductor having a narrow band-gap [77]. This was achieved by the synthesis of In_2O_3 nanoparticles, followed by the sulfidization of their surfaces into In_2S_3 with CS_2 to produce In_2O_3—In_2S_3 core-shell nanoparticles.

9.5.6
Semiconductor–Semiconductor–Dendrimer Core-Shell-Shell Nanoparticles

Multiple nanoscale shells can be coated on a core nanomaterial to produce core-shell-shell nanostructures, and this has been demonstrated with a variety of nanomaterials. Recently, Asefa's group reported the synthesis of silica–gold–silica core-shell-shell nanoparticles via a multistep synthesis [78]. In another report, dendritic galactoside was deposited on the core-shell on ZnS/CdSe QDs to produce core-shell-shell nanoparticles that were more biocompatible with cells and also useful as a hydrophilic, fluorescent, multivalent probe for metastatic lung cancer

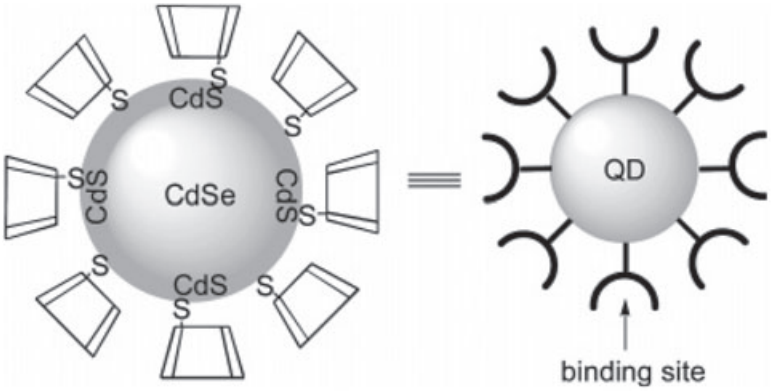

Figure 9.19 β-Cyclodextrin (β-CD)-modified CdSe—CdS core-shell-shell nanoparticles. Reproduced with permission from Ref. [80].

cells [79]. The synthesis was performed by synthesizing appropriate hydrophilic dendrons and covalently linking them onto pre-made CdSe—ZnS core-shell nanoparticles that were subsequently characterized using ^{1}H NMR. Their uptake by lung cancer cells was then probed using confocal microscopy.

Other core-shell-shell nanomaterials such as water-soluble β-cyclodextrin (β-CD)-modified CdSe—β-CD—CdSe and β-CD—CdSe—CdS QDs were synthesized in a single phase in aqueous solution (Figure 9.19) [80]. These receptor-modified QDs were found to be dispersible in water and stable over a wide range of pH values and ionic strengths. Furthermore, they produced a 46% quantum yield in water.

In addition to spherical morphologies, shaped semiconductor–semiconductor core-shell nanomaterials, including nanorods and nanowires, have been reported. For example, Zhang *et al.* [81] have synthesized nail-shaped CdSe—CdS-polyethylene glycol (PEG) core-shell-shell nanoparticles. Subsequent studies using confocal microscopy of the cellular uptake, cytotoxicity and inflammatory properties of these nanoparticles in human epidermal keratinocytes revealed that these core-shell nanoparticles could penetrate through the uppermost stratum corneum layers of the epidermis. Additional TEM studies indicated that the particles were located within in the intercellular lipid bilayers of the stratum corneum.

9.5.7
Insulator–Semiconductor Core-Shell Nanomaterials

Insulator–semiconductor core-shell nanomaterials are simply an inversion of the materials described in Section 9.5.4 where, instead of a semiconductor core sheathed by an insulator metal oxide or silica shell, the silica or polymeric spheres are covered by semiconductor nanoparticles or nanoshells. The general method for producing these materials is to functionalize both the core particles (e.g., silica spheres) and the smaller semiconductor nanoparticles with different functional

groups, so that they can interact with each other and allow semiconductor nanoparticle deposition on the silica nanospheres. Both, Ma *et al.* [82] and Hebalkar *et al.* [83] utilized this strategy to prepare SiO_2–ZnO and SiO_2–CdS, respectively. It was found that, at a low loading of nanoparticles, a discrete and uniform attachment onto silica particles was obtained, whereas a higher loading led to the formation of a thick compact shell of the semiconductor.

An alternative procedure reported by Hao *et al.* and Blomberg *et al.* [84] involved the coating of silica nanospheres with polymer shells. In the study of Hao *et al.*, the polymer was further coated by CdSe nanocrystals (Figure 9.20). Similar to results reported by Ma *et al.* [82] and Hebalkar *et al.* [83], the CdS nanoparticles were changed from nanoparticles to nanoshells as their loading increased. These core-shell nanostructures could be further modified to form new nanostructures; for example, the silica core in the silica–semiconductor core-shell nanoparticles could be etched away with HF solution to form hollow nanostructures (Figure 9.20) [84], which might lead to a broadening of the applications of the materials.

9.5.8
Metal–Metal Core-Shell

Metal–metal bimetallic and trimetallic core-shell nanomaterials such as Ag–Au, Ag–Pt, Ag–Ru, Au–Pt, Au–Ru and Pt–Ru nanoparticles are among the most common types of core-shell nanostructure [85]. Their synthesis typically involves the successive deposition of one metal over the surface of another metal nanostructure, or the galvanic replacement of part of the core surface by a second metal.

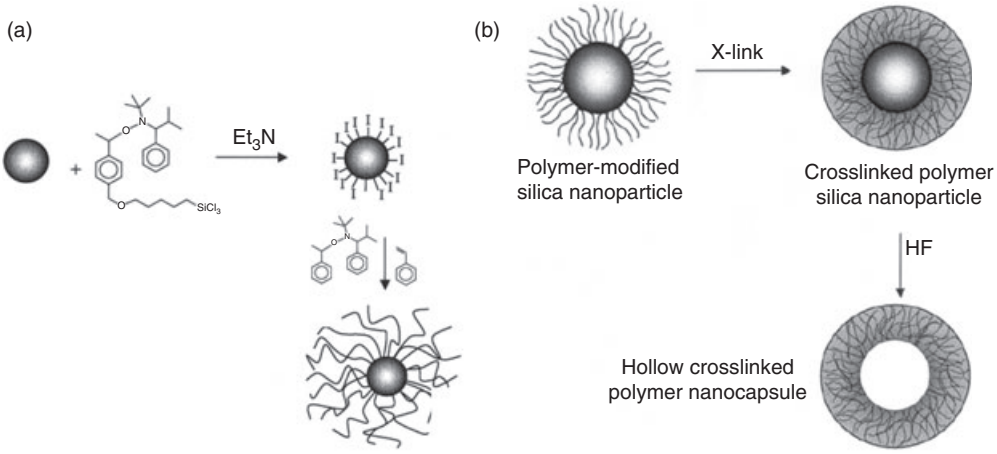

Figure 9.20 (a) Synthesis of polymer-modified silica nanoparticles; (b) Schematic representation of the formation of hollow, crosslinked polymer nanocapsules from silica–polymer core-shell nanospheres. Reproduced with permission from Ref. [84b].

For instance, Harada *et al*. [86] have synthesized Pt—Rh core-shell bimetallic colloidal nanoparticles in polymer solutions by reducing Pt(IV)/Rh(III) ionic solutions with borohydride in the presence of poly(*N*-vinyl-2-pyrrolidone). The size and structure of the nanoparticles were examined using TEM and extended X-ray absorption fine structure (EXAFS) analyses. More recently, the synthesis of Au—Ag, Au—Pd and Au—Pt core-shell nanoparticles using a similar method, or by successive decomposition of the corresponding metal–organic compounds, was reported [87].

Various bimetallic core-shell Au—Ag, Ag—Au nanoparticles, which show surface-enhanced Raman scattering (SERS), have been synthesized by sequential wet-reduction syntheses from the corresponding metals [88]. Likewise, CVD can be used to produce bimetallic core-shell nanoparticles. For example, the deposition of Pd by CVD over 12 nm Au nanoparticle seeds can lead to Au—Pd nanoparticles with controllable sizes ranging from 35 to 100 nm [89]. The core-shell nature of the materials was confirmed using TEM and UV-visible absorption spectroscopy. These core-shell nanoparticles also exhibited high SERS properties.

Galvanic replacement is among the most common methods used to prepare metal–metal core-shell nanostructures. For instance, bimetallic Pd—Au core-shells with compositions ranging from $Pd_{68}Au_{32}$ and $Pd_{45}Au_{55}$ alloy nanostructures from Pd nanowires were synthesized using a galvanic replacement reaction between Pd nanowires of 2.4 nm diameter and >30 nm length and $AuCl_3$ in toluene [90]. The structures and composition of the resultant nanomaterials were characterized using TEM, XRD, energy-dispersive X-ray spectrometry (EDS), UV-visible absorption and EXAFS spectroscopy.

Ferrer *et al*. have reported a three-layer bimetallic Pd—Au—Pd core-shell-shell nanostructure by successive reduction of the constituent metal ions (Figure 9.21) [91]. Various electron microscopic, spectroscopic and diffraction methods were used to determine the structures and compositions of the materials, in particular, to probe whether an alloy or a core-shell structure was formed (Figures 9.21 and 9.22).

Other unique approaches, such as a direct synthesis from aerosols of metal salts, have been used successfully to create metal–metal core-shell nanostructures. For example, Ru—Ni core-shell nanoparticles were synthesized by the controlled decomposition of an aqueous aerosol containing ruthenium chloride and nickel chloride that was formed by nebulizing the solution with an ultrasonic atomizer [92]. First, the aqueous precursor containing the metal solution was nebulized to generate an aerosol, and this was subsequently decomposed to produce uniformly distributed Ru—Ni bimetallic nanoparticles.

A microwave-polyol synthesis involving the two-step reduction of $AuCl_4^-$ and Ag^+ ions with ethylene glycol in the presence of PVP as a capping reagent was also used for the rapid synthesis of Au—Ag core-shell nanostructures [93]. In addition to bimetallic core-shell nanomaterials, a variety of trimetallic core-shell-shell nanostructures such as Au—Pt—Rh nanoparticles were synthesized using a multi-step synthetic procedure which involved a combination of reduction and self-assembly using PVP as both dispersant and stabilizer [94]. Similarly, trimetallic

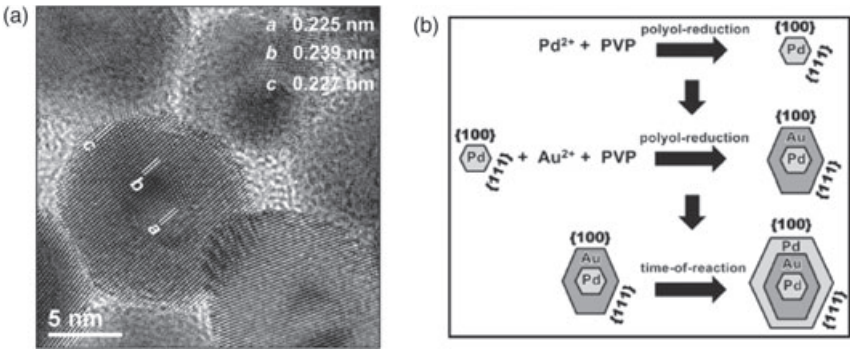

Figure 9.21 (a) High-resolution TEM image displaying the lattice fringes of the Au–Pd nanoparticle; (b) Model proposed for the formation of three-layer core/shell structure. Reproduced with permission from Ref. [91].

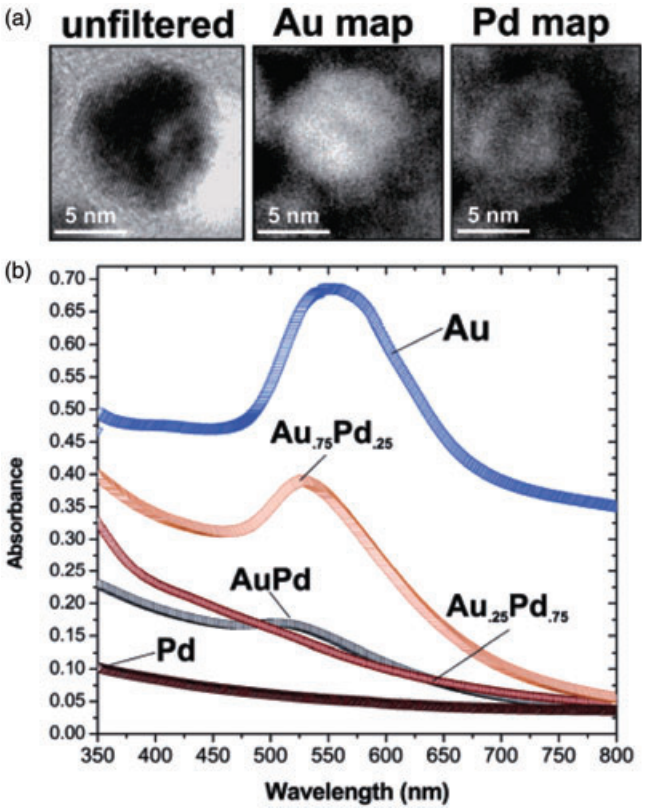

Figure 9.22 (a) Energy filtering images of Au–Pd nanoparticles. The map of gold clearly shows that the intermediate regions of the nanoparticle are rich in gold. On the other hand, the external shell and inner-core contain signals of palladium; (b) UV-visible absorption spectra of the studied bimetallic nanoparticles show the influence of composition on the position of the surface plasmon resonance peak. Reproduced with permission from Ref. [91].

polymer-protected Pd—Ag—Rh trimetallic colloidal dispersions were synthesized by mixing and self-organizing colloidal dispersions of polymer-protected Rh nanoparticles with polymer-protected Pd—Ag bimetallic core-shell nanoparticles that had been pre-prepared using a sacrificial hydrogen-reduction method [95].

9.5.9
Insulator–Metal Core-Shell Nanoparticles

Metal-coated polymer nanoparticles can be synthesized by the deposition and reduction of metal ions over polymer nanosphere surfaces. For example, the synthesis of palladium coated cross-poly(4-vinylbenzyl chloride) (PVBC) nanospheres has been reported (Figure 9.23) [96]. Here, polymer nanospheres of 100 nm diameter were first synthesized by the emulsion copolymerization of vinylbenzyl chloride (VBC) and a *p*-divinylbenzene crosslinking agent. Subsequent modification of the nanosphere surfaces via a surface-initiated ATRP of 4-vinylpyridine by using the VBC units of PVBC on the nanosphere surface as the macroinitiators, led to the production of covalently tethered 24 to 27 nm-thick poly(4-vinylpyridine) (P4VP) shells. The deposition of $PdCl_2$ on P4VPy, and subsequent reduction of the Pd^{2+} ions with CO or H_2S gas, produced densely dispersed palladium or palladium sulfide nanoparticle shells.

9.5.10
Carbon-Containing Core-Shell Nanomaterials

9.5.10.1 Metal Oxide–Carbon Core-Shell Nanoparticles

Silica cores coated with glucose, followed by a hydrothermal carbonization synthesis, results in the production of silica–carbon core-shell nanospheres (Figure 9.24) [97]. These materials can be further coated with silica to produce silica–C–silica core-shell-shell nanospheres; subsequent etching of the carbon then allows the synthesis of hollow silica–silica core-shell nanospheres. Upon deposition of the metal in the hollow space, noble metal nanoparticle-loaded silica–metal nanoparticles–silica core-shell-shell nanospheres resulted which had unique structures and would most likely find applications as catalyst supports, adsorbents and nanoreactors.

9.5.11
Other Carbon-Containing Core-Shell Nanomaterials

The use of insulated carbon-based core-shell nanomaterials with an insulating layer has been shown as a promising avenue in the production of nanoscale electronic and photoelectronic devices such as field-effect transistors (FETs), chemical sensors and catalysts. Carbon sources (e.g., single or multiwalled carbon nanotubes, activated carbon, graphite, fullerene), all of which are either metallic or semiconducting in nature, are viewed as favorable replacements for silicon-based electronics [98]. Carbon materials generally participate in nonbinding interactions such as van der Waals forces, and have caused difficulties in the uniform

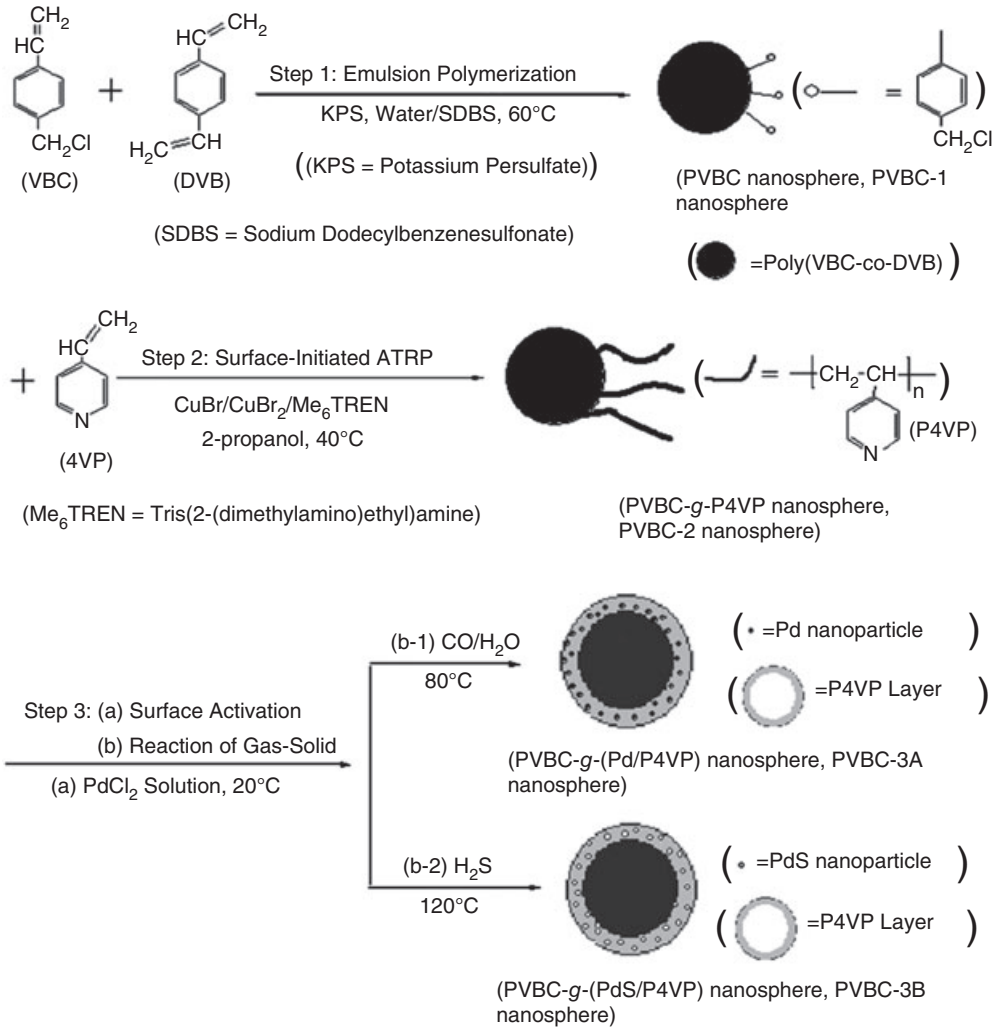

Figure 9.23 Synthetic scheme of polymer–metal core-shell nanoparticles. Reproduced with permission Ref. [96].

formation of external shells by covalent modification. Hence, these nanomaterials are usually coated by materials that forming external layers via noncovalent interactions; these coatings, such as metal oxides [99] or organic polymers [100], generally exhibit a wide band gap which allows for the creation of electronics that are less susceptible to malfunction. Some examples of relevant and current methodologies are introduced in the following section.

One popular route taken in the insulation of carbon core-shell materials is the use of polymeric materials. The addition of high-molecular-weight fluorinated poly(methyl vinyl ether-*alt*-maleic anhydride) onto multi-walled carbon nanotubes

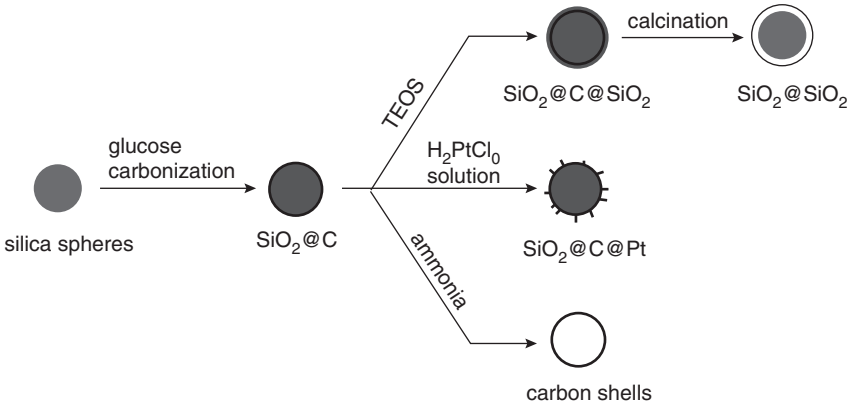

Figure 9.24 Schematic illustration of synthesis of silica–carbon core-shell nanoparticles. Reproduced with permission from Ref. [97].

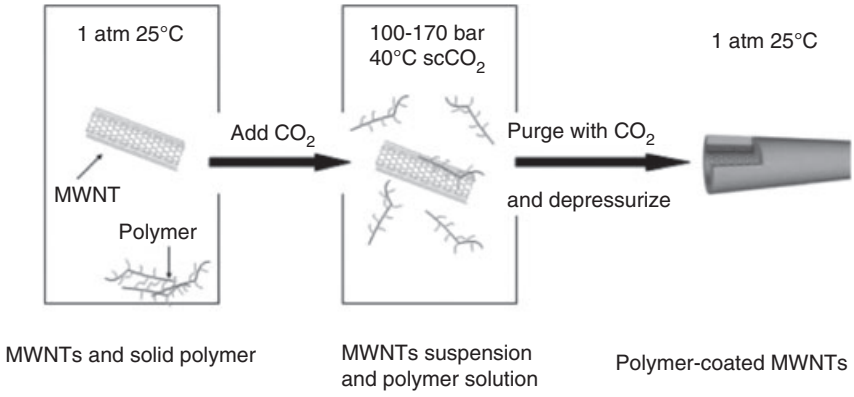

Figure 9.25 Multiwalled nanotube (MWNT) coated with fluorinated graft poly(methyl vinyl ether-*alt*-maleic anhydride) copolymer in supercritical CO_2. Reproduced with permission from Ref. [101].

(MWCNTs) in supercritical carbon dioxide ($scCO_2$) led to the formation of a MWCNT with an average coating layer of ~2 nm thickness (Figure 9.25) [101].

The results of recent studies have shown that some metal oxides serve as good insulators for carbon core materials [102, 103]. Fu *et al.* [102] have recently developed a procedure for the coating of aluminum oxide, Al_2O_3, on MWCNTs. The thickness of the alumina sheath could be regulated by modifying the reagent concentrations to form (8 nm-diameter coatings by the reaction of aluminum nitrate nonahydrate and MWCNTs (formed by CVD) in ethanol and $scCO_2$ (Figure 9.26) [103]. Similar methodologies may be tailored for the fabrication of other metal

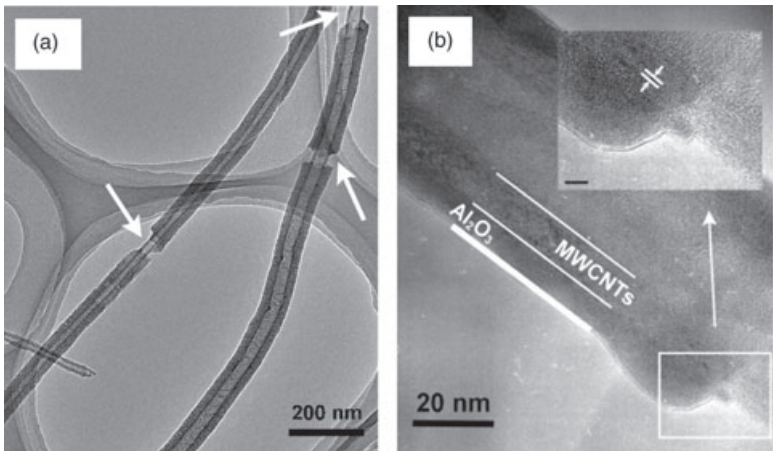

Figure 9.26 (a) TEM image of Al_2O_3-coated multiwalled carbon nanotubes (MWCNTs). The arrows indicate the uncoated regions; (b) Enhancement (×10) of the tube wall image. Reproduced with permission from Ref. [102].

oxide-coated CNTs, such as SiO_2, HfO_2, ZrO_2 and TiO_2 or other wide band gap metal oxides, and this procedure will undoubtedly be expanded in the future.

9.5.12 Synthetic Methods to Create Core-Shell Nanomaterials, and their Characterizations

As demonstrated many times above, the synthesis of core-shell nanomaterials often involves a combination of several wet-synthetic methods including polymerization, solid-state inorganic synthesis, sol–gel processing, hydrothermal synthesis, sulfidization, carbonization and the high-temperature decomposition of various inorganic materials. The synthetic methods are involved mainly in multistep reactions in order to allow growth of the core materials, followed by an appropriate strategy to coat the shell over the core materials. During these multistep synthetic methods, similar requirements are necessary for passivating the intermediate and final nanomaterials to prevent aggregation either by electrostatic, covalent or steric interactions, as are required for classic colloidal nanoparticles. By using one or many of these methods, the creation of monodisperse nanocrystals of many transition metals, metal oxides and metal sulfides, without size selection, can be accomplished [104]. The thermal decomposition of metal–surfactant complexes yields monodisperse spherical nanocrystals of metals (Fe, Cr, Cu, Ni, Pd), metal oxides (Fe_3O_4, $CoFe_2O_4$, $MnFe_2O_4$, NiO, MnO) and metal sulfides (CdS, ZnS, PbS, MnS). By using thermolysis, ultra-large-scale or multi-gram-scale syntheses of monodisperse nanocrystals metal–oleate complexes can be achieved. As an example, the multi-gram-scale syntheses of CdS, ZnS, PbS and MnS have been achieved via the thermolysis of metal–surfactant complexes in the presence of sulfur [104].

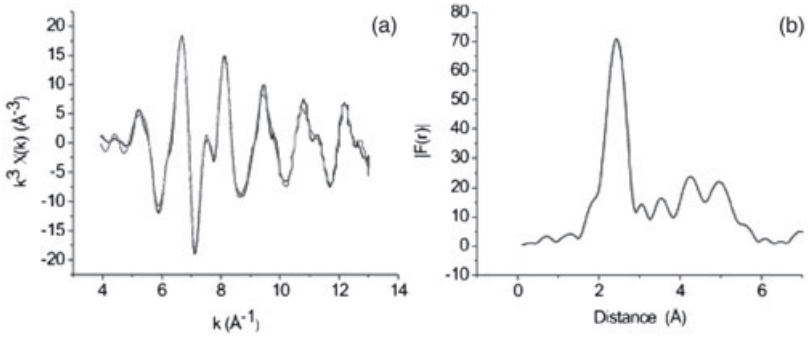

Figure 9.27 (a) A typical EXAFS experimental $k^3\chi(k)$ (black) and the corresponding theoretical fit (gray) for the Co edge of an as-synthesized Ge–Co core-shell heterostructure obtained by adding successive backscattering shells around the central Co atom; (b) Absolute values of the Fourier transform of $k^3\chi(k)$ into r space for the Ce–Co core-shell heterostructure at the Co K-edge. Reproduced with permission from Ref. [106].

The methods used to characterize core-shell nanomaterials have also advanced over the past few years. As mentioned above, a variety of tools can be used for this purpose, including TEM, SEM, FTIR, NMR, UV-visible spectroscopy and electrochemical methods. These approaches are often used in complementary fashion to probe and obtain crucial information about the materials, including their structures, shapes and composition. In recent years, EXAFS in particular has been used to characterize core-shell and alloy Ag—Au bimetallic clusters. For example, Chen *et al.* [105] used EXAFS to characterize Ag—Au core-shell and alloy nanoparticles that had been synthesized by successive synthesis, while Daly *et al.* [106] employed the same technique with great success to characterize Ge—Co core-shell nanoparticles (Figure 9.27). Notably, in addition to absorption spectra and TEM images, EXAFS aids in probing the environment surrounding the core atoms of the core-shell and alloy nanoparticles [105]. The absorption maxima at 520 and 410 nm, which correspond to the absorption plasmon of Au and Ag nanoparticles, respectively, are changed upon the formation of core-shell or alloy structures.

9.6 Applications

9.6.1 Applications in Biology and Medicine

The combination of diverse structures, shapes, sizes and morphologies of core-shell nanomaterials, their tunable optical, biological, chemical, photophysical, electronic and magnetic properties, and their compatibility (in terms of size) with biomacromolecules such as proteins, cells, antibodies, bacteria and cells, has induced considerable interest in core-shell nanomaterials with regards to their

potential applications in the life sciences. Potential examples include bioimaging, targeted drug delivery, cancer treatment and biosensing.

9.6.1.1 Bioimaging and Immunoassay

Wiesner and coworkers [107, 108] have used a number of core-shell fluorescent probes for the bioimaging of a variety of cells, including as rat basophilic leukemia mast cells (RBL-2H3), by confocal fluorescence imaging. The same group has also synthesized antibody-functionalized core-shell nanoparticles and utilized the antibody nanoconjugates for targeted imaging.

The use of core-shell nanoparticles with complex structures and properties for simultaneous imaging and biosensing has been extensively demonstrated [107, 108]. Such core-shell nanoparticle sensors are capable of dual-emission-based ratiometric pH sensing for quantitative *in vitro* chemical imaging and spectrofluorometric analysis (Figure 9.28). Here, the core-shell nanostructures contained a pH-sensitive fluorescein isothiocyanate (FITC) dye, which significantly changes its quantum yield upon protonation/deprotonation of the hydroxyl groups of the xanthene backbone. Covalent attachment of the dye in the core-shell structure minimized possible leaching, and led to the creation of a stable nanosensor with a low background signal. The core-shell nanoparticles may also allow intracellular ratiometric pH imaging and quantitative chemical measurements to be performed inside individual cells for the spatial and temporal mapping of intracellular

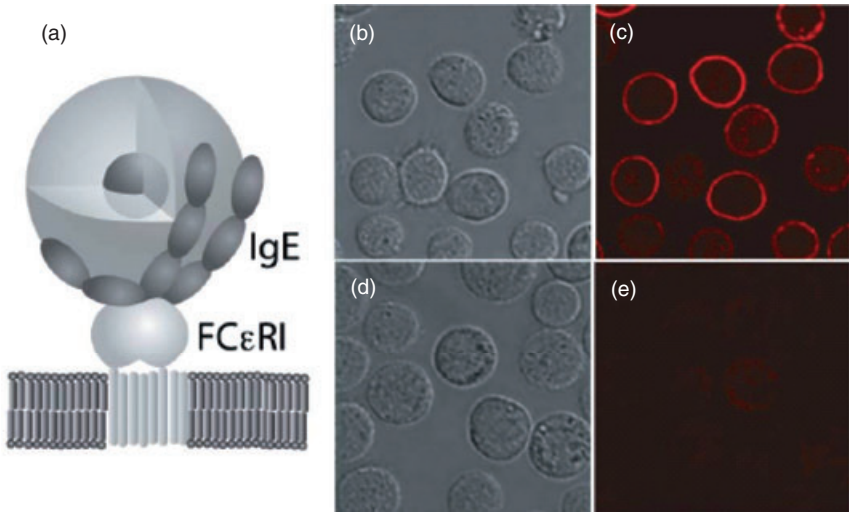

Figure 9.28 (a) Schematic illustration of a fluorescent core-shell silica nanoparticle attached noncovalently to an immunoglobulin E (IgE) antibody specifically attached to the FcεR1 cell surface receptor of an RBL cell; (b) bright field and (c) confocal fluorescence images of RBL cells with IgE-mediated cell surface labeling. As a control, (d) bright field and (e) fluorescence images of RBL cells quenched with free IgE after exposure to C dot complexes showing minimal nonspecific cell surface binding. Reproduced with permission from Ref. [107].

metabolic parameters. This has important implications for determining the concentrations of biologically active ions (e.g., H^+), and may also help to provide an understanding of the metabolic processes and growth of tumor cells.

In another example, a novel Au—dye-doped silica core-shell nanoparticle with dye-embedded silica has been synthesized and its potential demonstrated as a SERS tag for the ultrasensitive immunoassay of human IgG antigen (detection limit of 4.9 ng ml^{-1}) [109]. The reaction between surface silanols and citrate anion groups on citrate-capped gold nanoparticles was used in silica layer deposition to synthesize this material.

Bioimaging with core-shell QDs with intrinsic luminescent properties has also been demonstrated, both *in vitro* and *in vivo*. Here, CdSe—ZnS core-shell QDs, loaded with solid lipid nanoparticles and exhibiting high fluorescence and narrow/symmetrical emission spectra, were used successfully for both *in vitro* and *in vivo* bioimaging applications [110].

9.6.1.2 Drug or Biomolecular Delivery Vehicles

Core-shell nanomaterials have been widely considered as suitable vehicles for transporting bioactive molecules through cell membranes, and several different examples have been reported. For example, Yin *et al.* [111] have synthesized core-shell-shell fluorescent nanocontainers consisting of a fluorescent perylene-3,4,9,10-tetracarboxdiimide chromophore in the center and hydrophobic poly(phenylene) and flexible hydrophilic polymer multishells, and used these materials as molecular transport vehicles in cell membranes. Very recently, Guo *et al.* [1] synthesized a biocompatible, green luminescent silver–phenol–formaldehyde resin core-shell nanospheres with sizes ranging from 180 to 1000 nm and with centric, eccentric and coenocytic shapes, by employing a hydrothermal synthesis. Subsequently, the *in vivo* bioimaging of human lung cancer H1299 cells, demonstrating the endocytosis of these materials, was achieved successfully and without any cytotoxic effects.

Multifunctional core-multishell nanoparticles with external stimuli-induced tunable properties have also been reported. Core-half-shell nanoparticles containing NIR-resonant rhodamine in PLGA—Mn—Au half-shell nanoparticles were synthesized by depositing metal multilayers on PLGA for the photothermal control of drug release, and also for magnetic resonance imaging [112]. Upon NIR irradiation, the rate at which rhodamine was released from the PLGA nanoparticles was reported to be almost twice that without NIR irradiation.

9.6.2 Core-Shell Nanomaterials for Catalysis

Core-shell nanomaterials have also found application in heterogeneous catalysis where, in some situations, the core materials have been used as support materials to place an active catalyst. In other cases, the core-shell structure itself has been shown to offer a suitable active surface for the catalytic reactions. Core-shell nanomaterials can also be synthesized within the structure of another solid substrate to

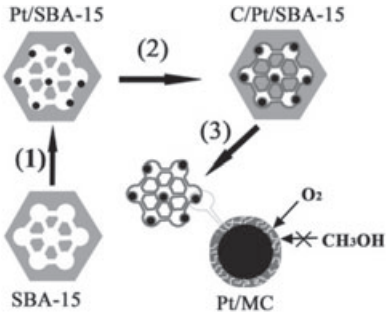

Figure 9.29 Schematic illustration of the synthetic procedure of Pt–C–Mesoporous carbon (MC) core-shell nanostructures. This includes: (1) deposition of Pt in the nanochannels of mesoporous silica, SBA-15; (2) polymerization of glucose; and (3) carbonization and removal of SBA-15. Reproduced with permission from Ref. [1].

produce supported core-shell nanocatalysts. The synthesis of core-shell Pt—C nanostructures has been achieved by the *in situ* deposition of Pt, followed by polymerization and carbonization of glucose within the mesoporous channels of mesoporous silica, SBA-15 (Figure 9.29) [113]. This material was used as an efficient methanol-tolerant cathode electroreduction catalyst in direct methanol fuel cells.

Park *et al.* [114] have synthesized Cu—Cu_2O core-shell nanoparticles from the thermal decomposition of copper acetylacetonate, followed by air oxidation for catalysts for Ullmann-type amination coupling reactions of aryl chlorides. The same authors have also reported the synthesis of Ni—Pd core-shell-like bimetallic nanoparticles from the consecutive thermal decomposition of corresponding metal–surfactant complexes, and their ability to catalyze various Sonogashira coupling reactions.

Trimetallic nanomaterials such as Au—Pt—Rh core-shell-shell nanoparticles, which are synthesized by a combination of reduction and self-assembly in the presence of PVP as dispersant and stabilizer, showed superior catalytic activity in hydrogenation reactions compared to monometallic and bimetallic nanoparticles, due to their unique electronic properties. Trimetallic nanomaterials such as Pd—Ag—Rh nanoparticles were also shown to exhibit high catalytic activity for the hydrogenation of methyl acrylate. A wide variety of metal–dendrimer core-shell nanomaterials have also been used successfully as catalysts for both hydrogenation [115, 116] and Suzuki coupling [117] reactions.

9.7 Conclusions and Future Prospects

During the past two decades, we have witnessed the development of a wide variety of synthetic techniques for the creation of multifunctional nanomaterials. The

same might also be said of core-shell nanomaterials. By using these various methods – or a combination of multiple synthetic methods – core-shell nanostructures with a wide range of compositions, sizes and structures have been synthesized. Equally important has been the investigation of the unique properties of the resultant materials, and their potential applications. The aim of this chapter has been to review the different methods available for the creation of core-shell nonmagnetic nanomaterials, and to assess their properties and applications – specifically in biological and medical applications. Due to the vast amount of literature available, this chapter is intended not to be exhaustive but rather to highlight pertinent examples of those studies that have been conducted over the past few years on these exciting classes of nanomaterials. Research in this area is expected to continue and, with the use of more rational and systematic synthetic approaches, to lead to the development of more complex, 'smart' and predictable nanostructures suitable for both biological and medical applications.

Acknowledgments

The authors gratefully acknowledge the financial assistance from the US National Science Foundation (NSF), CAREER Grant No. CHE-064534 for studies in nanostructured catalysis, and also National Science Foundation (NSF) NSF DMR-0804846. They also wish to thank Krishna K. Sharma for his continued contribution on research projects in catalysis in their research group.

References

1 Guo, S.-R., Gong, J.-Y., Jiang, P., Wu, M., Lu, Y. and Yu, S.-H. (2008) Biocompatible, luminescent silver@phenol formaldehyde resin core/shell nanospheres: large-scale synthesis and application for in vivo bioimaging. *Advanced Functional Materials*, **18**, 872–9.

2 Park, H., Yang, J., Seo, S., Kim, K., Suh, J., Kim, D., Haam, S. and Yoo, K.-H. (2008) Multifunctional nanoparticles for photothermally controlled drug delivery and magnetic resonance imaging enhancement. *Small*, **4**, 192–6.

3 Sershen, S.R., Westcott, S.L., Halas, N.J. and West, J.L. (2000) Temperature-sensitive polymer-nanoshell composites for photothermally modulated drug delivery. *Journal of Biomedical Materials Research*, **51**, 293–8.

4 Ghosh, P., Oliva, J., De la Rosa, E., Haldar, K.K., Solis, D. and Patra, A. (2008) Enhancement of upconversion emission of $LaPO_4$:Er@Yb core-shell nanoparticles/nanorods. *The Journal of Physical Chemistry C*, **112**, 9650–8.

5 (a) Salgueiriño-Maceira, V. and Correa-Duarte, M.A. (2007) Increasing the complexity of magnetic core / shell structured nanocomposites for biological applications. *Advanced Materials*, **19**, 4131–44;
(b) Jun, Y.W., Choi, J.S. and Cheon, J. (2007) Heterostructured magnetic nanoparticles: their versatility and high performance capabilities. *Chemical Communications*, 1203–14;
(c) Camargo, P.H.C., Li, Z.Y. and Xia, Y. (2007) Colloidal building blocks with potential for magnetically configurable

photonic crystals. *Soft Matter*, **3**, 1215–22;
(d) Salgueiriño-Maceira, V., Correa-Duarte, M.A., Spasova, M., Liz-Marzan, L.M. and Farle, M. (2006) Composite silica spheres with magnetic and luminescent functionalities. *Advanced Functional Materials*, **16**, 509–14.

6 (a) Shan, J. and Tenhu, H. (2007) Recent advances in polymer protected gold nanoparticles: synthesis, properties and applications. *Chemical Communications*, 4580–98;
(b) Liu, B., Hu, Z. and Che, C. (2007) Ultrafast lasers produce nanoparticles. *Laser Focus World*, **43**, 74–8;
(c) Weiler, V., Haase, M., Walter, C., Hoheisel, W. and Hummel, H. (2007) Luminescent nanoparticles for molecular medicine. *Proceeding of the SPIE – The International Society for Optical Engineering*, **6633**, 66332J/1–66332J/7;
(d) Gravano, S.M., Patten, T.E. (2007) Hybrid organic inorganic objects, in *Macromolecular Engineering*, Vol. **2** (eds K. Matyjaszewski, Y. Gnanou and L. Leibler), Wiley-VCH, Weinheim, pp. 1179–20;
(e) Ballauff, M. and Lu, Y. (2007) "Smart" nanoparticles: preparation, characterization and applications. *Polymer*, **48**, 1815–23;
(f) Pal, B., Torimoto, T., Iwasaki, K., Shibayama, T., Takahashi, H. and Ohtani, B. (2005) Synthesis of metal-cadmium sulfide nanocomposites using jingle-bell-shaped core-shell photocatalyst particles. *Journal of Applied Electrochemistry*, **35**, 751–6;
(g) Nayak, S. and Lyon, L.A. (2005) Soft nanotechnology with soft nanoparticles. *Angewandte Chemie – International Edition*, **44**, 7686–708;
(h) Liz-Marzan, L.M., Correa-Duarte, M. A., Pastoriza-Santos, I., Mulvaney, P., Ung, T., Giersig, M. and Kotov, N.A. (2001) Core-shell nanoparticles and assemblies thereof, in *Hand Book of Surfaces and Interfaces of Materials* (ed. H.S. Nalwa), Vol. **3**: *Nanostructured Materials, Micelles and Colloids*, Ch. 5, pp. 189–237;
(i) Sastry, M., Swami, A., Mandal, S. and Selvakannan, P.R. (2005) New approaches to the synthesis of anisotropic, core-shell and hollow metal nanostructures. *Journal of Materials Chemistry*, **15**, 3161–74;
(j) Chavez, J.L., Wong, J.L., Jovanovic, A.V., Sinner, E.K. and Duran, R.S. (2005) Encapsulation in sub-micron species: a short review and alternate strategy for dye encapsulation. *IEE Proceedings: Nanobiotechnology*, **152**, 73–84;
(k) Scott, R.W.J., Wilson, O.M. and Crooks, R.M. (2005) Synthesis, characterization, and applications of dendrimer-encapsulated nanoparticles. *The Journal of Physical Chemistry B*, **109**, 692–704;
(l) Avgoustakis, K. (2004) Pegylated poly(Lactide) and poly(Lactide-Co-Glycolide) nanoparticles: preparation, properties and possible applications in drug delivery. *Current Drug Delivery*, **1**, 321–33;
(m) He, X., Lin, X., Wang, K., Chen, L., Wu, P., Yuan, Y. and Tan, W. (2004) Biocompatible core-shell nanoparticles for biomedicine. *Encyclopedia of Nanoscience and Nanotechnology*, **1**, 235–53;
(n) Kickelbick, G. and Liz-Marzán, L.M. (2004) Core-shell nanoparticles. *Encyclopedia of Nanoscience and Nanotechnology*, **2**, 199–220;
(o) Choi, S.W., Kim, W.S. and Kim, J.H. (2003) Surface modification of functional nanoparticles for controlled drug delivery. *Journal of Dispersion Science and Technology*, **24**, 475–87;
(p) Zhong, C.-J. and Maye, M.M. (2001) Core-shell assembled nanoparticles as catalysts. *Advanced Materials*, **13**, 1507–11;
(q) Shipway, A.N. and Willner, I. (2001) Nanoparticles as structural and functional units in surface-confined architectures. *Chemical Communications*, 2035–45;
(r) Fujimoto, K. (2001) Preparative techniques of nanoparticles for drug delivery. *Drug Delivery System*, **16**, 155–64;
(s) Schartl, W. (2000) Crosslinked spherical nanoparticles with core-shell topology. *Advanced Materials*, **12**, 1899–908;
(t) Wooley, K.L. (2000) Shell crosslinked polymer assemblies: nanoscale constructs inspired from biological systems. *Journal of Polymer Science Part A – Polymer*

Chemistry, **38**, 1397–407;
(u) Han, S.K., Kim, R.S., Lee, J.H., Tae, G., Cho, S.H. and Yuk, S.H. (2007) Core-shell nanoparticles for drug delivery and molecular imaging, in *Nanotechnologies for the Life Sciences* (ed. C. Kumar), Wiley-VCH Verlag GmbH;
(v) Liz-Marzán, L.M. (2003) Design of nanoscale materials using silica-coated metal nanocolloids. *Nanoscale Materials*, 227–46;
(w) Liz-Marzán, L.M., Correa-Duarte, M.A., Pastoriza-Santos, I., Mulvaney, P., Ung, T., Giersig, K. and Kotov, N.A. (2001) Core-shell nanoparticles and assemblies thereof, in *Handbook of Surfaces and Interfaces of Materials*, Vol. **3** (ed. H.S. Nalwa), Academic Press, New York, pp. 189–237.

7 Fedutik, Y., Temnov, V., Woggon, U., Ustinovitch, E. and Artemyev, M. (2007) Exciton-plasmon interaction in a composite metal-insulator-semiconductor nanowire system. *Journal of the American Chemical Society*, **129**, 14939–45.

8 Daniel, M.-C. and Astruc, D. (2004) Gold nanoparticles: assembly, supramolecular chemistry, quantum-size-related properties, and applications toward biology, catalysis, and nanotechnology. *Chemical Reviews*, **104**, 293–346.

9 Cozzoli, P.D., Pellegrino, T. and Manna, L. (2006) Synthesis, properties and perspectives of hybrid nanocrystal structures. *Chemical Society Reviews*, **35**, 1195–208.

10 Turkevich, J., Stevenson, P.C. and Hillier, J. (1951) A study of the nucleation and growth processes in the synthesis of colloidal gold. *Discussions of the Faraday Society*, **11**, 55–75.

11 Brust, M., Walker, M., Bethell, D., Schiffrin, D.J. and Whyman, R. (1994) Synthesis of thiol-derivatized gold nanoparticles in a 2-phase liquid-liquid system. *Journal of the Chemical Society, Chemical Communications*, 801–2.

12 (a) Zang, J. and Lakowicz, J.R. (2005) Enhanced luminescence of phenyl-phenanthridine dye on aggregated small silver nanoparticles. *The Journal of Physical Chemistry B*, **109**, 8701–6;
(b) Aslam, M., Gopakumar, G; Shoba, T. L., Mulla, I.S., Vijayamohanan, K., Kulkarni, S.K., Urban, J. and Vogel, W. (2002) Formation of Cu and Cu_2O nanoparticles by variation of the surface ligand: preparation, structure, and insulating-to-metallic transition. *Journal of Colloid and Interface Science*, **255**, 79–90.

13 Yee, C.K., Jordan, R., Ulman, A., White, H., King, A., Rafailovich, M. and Sokolov, J. (1999) Novel one-phase synthesis of thiol-functionalized gold, palladium, and iridium nanoparticles using superhydride. *Langmuir*, **15**, 3486–91.

14 Li, X., Elliott, D.W. and Zhang, W. (2006) Zero-valent iron nanoparticles for abatement of environmental pollutants: materials and engineering aspects. *Critical Reviews in Solid State and Materials Sciences*, **31**, 111–22.

15 (a) Shi, W., Zeng, H., Sahoo, Y., Ohulchanskyy, T.Y., Ding, Y., Wang, Z.L., Swihart, M. and Prasad, P.N. (2006) A general approach to binary and ternary hybrid nanocrystals. *Nano Letters*, **6**, 875;
(b) Shi, W., Sahoo, Y., Zeng, H., Ding, Y., Swihart, M.T. and Prasad, P.N. (2006) Anisotropic growth of PbSe nanocrystals on Au-Fe_3O_4 hybrid nanoparticles. *Advanced Materials*, **18**, 1889.

16 Stöber, W., Fink, A. and Bohn, E. (1968) Controlled growth of monodisperse silica spheres in the micron size range. *Journal of Colloid and Interface Science*, **26**, 62–9.

17 Chien, A.T., Lee, Y.H. and Lin, K.F. (2008) Crosslinkable poly(vinyl acetate)/clay nanocomposite films cast from soap-free emulsion-polymerized lattices. *Journal of Applied Polymer Science*, **109**, 355–62.

18 Burns, A., Sengupta, P., Zedayko, T., Baird, B. and Wiesner, U. (2006) Core/shell fluorescent silica nanoparticles for chemical sensing: towards single-particle laboratories. *Small*, **2**, 723–6.

19 (a) He, Y., Cao, Y. and Fan, Y. (2008) Using anionic polymerizable surfactants in ultrasonically irradiated emulsion polymerization to prepare polymer nanoparticles. *Journal of Applied Polymer Science*, **107**, 2022–7;
(b) Wen, F., Zhang, W., Wei, G., Wang, Y., Zhang, J., Zhang, M. and Shi, L.

(2008) Synthesis of noble metal nanoparticles embedded in the shell layer of core-shell poly(styrene-*co*-4-vinylpyridine) microspheres and their application in catalysis. *Chemistry of Materials*, **20**, 2144–50.

20 (a) Ai, Z., Wang, Y., Xiao, M., Zhang, L. and Qiu, J. (2008) Microwave-induced catalytic oxidation of RhB by a nanocomposite of $Fe@Fe_2O_3$ core-shell nanowires and carbon nanotubes. *The Journal of Physical Chemistry C*, **112**, 9847–53;
(b) Kim, H.W., Lee, J.W. and Shim, S. H. (2007) Composite nanowires with MgO/ZnO core-sheath structures: study of thin ZnO shell layers. *Journal of Physics and Chemistry of Solids*, **69**, 1491–4.

21 Schneider, G., Decher, G., Nerambourg, N., Praho, R., Werts, M.H.V. and Blanchard-Desce, M. (2006) Distance-dependent fluorescence quenching on gold nanoparticles ensheathed with layer-by-layer assembled polyelectrolytes. *Nano Letters*, **6**, 530–6.

22 Gorelikov, I. and Matsuura, N. (2008) Single-step coating of mesoporous silica on cetyltrimethyl ammonium bromide-capped nanoparticles. *Nano Letters*, **8**, 369–73.

23 Moon, G.D. and Jeong, U. (2008) Decoration of the interior surface of hollow spherical silica colloids with Pt nanoparticles. *Chemistry of Materials*, **20**, 3003–7.

24 Robindro, S.L., Ningthoujam, R.S., Sudarsan, V., Srivastava, I., Singh, S. Dorendrajit; Dey, G.K. and Kulshreshtha, S.K. (2008) Luminescence study on Eu_3^+ doped Y_2O_3 nanoparticles: particle size, concentration and core-shell formation effects. *Nanotechnology*, **19**, 055201/1–055201/8.

25 Ghilane, J., Fan, F.-R.F., Bard, A.J. and Dunwoody, N. (2007) Facile electrochemical characterization of core/shell nanoparticles. Ag core/Ag_2O shell structures. *Nano Letters*, **7**, 1406–12.

26 (a) Sharma, K.K., Anan, A., Buckley, R.P., Ouellette, W. and Asefa, T. (2008) Toward efficient nanoporous catalysts: controlling site-isolation and concentration of grafted catalytic sites on nanoporous materials with solvents and colorimetric elucidation of their site-isolation. *Journal of the American Chemical Society*, **130**, 218–28;
(b) Sharma, K.K. and Asefa, T. (2007) Efficient bifunctional nanocatalysts by simple postgrafting of spatially isolated catalytic groups on mesoporous materials. *Angewandte Chemie – International Edition*, **46**, 2879–82;
(c) Lim, M.H., Blanford, C.F. and Stein, A. (1997) Synthesis and characterization of a reactive vinyl-functionalized MCM-41: probing the internal pore structure by a bromination reaction. *Journal of the American Chemical Society*, **119**, 4090–2;
(d) Sanchez, C., Julian, B., Belleville, P. and Popall, M. (2005) Applications of hybrid organic-inorganic nanocomposites. *Journal of Materials Chemistry*, **15**, 3559–92.

27 (a) Corriu, R.J.P. and Leclercq, D. (1996) Recent developments of molecular chemistry for sol-gel processes. *Angewandte Chemie – International Edition*, **35**, 1421–36;
(b) Sayari, A. and Hamoudi, S. (2001) Periodic mesoporous silica-based organic-inorganic nanocomposite materials. *Chemistry of Materials*, **13**, 3151–68;
(c) Stein, A., Melde, B.J. and Schroden, R.C. (2000) Hybrid inorganic-organic mesoporous silicates – Nanoscopic reactors coming out of age. *Advanced Materials*, **12**, 1403–19;
(d) Sanchez, C., Julian, B., Belleville, P. and Popall, M. (2005) Applications of hybrid organic-inorganic nanocomposites. *Journal of Materials Chemistry*, **15**, 3559–92;
(e) Shea, K.J. and Loy, D.A. (2001) Bridged polysilsesquioxanes. Molecular-engineered hybrid organic-inorganic materials. *Chemistry of Materials*, **13**, 3306–19.

28 Marini, M., Pourabbas, B., Pilati, F. and Fabbri, P. (2008) Functionally modified core-shell silica nanoparticles by one-pot synthesis. *Colloids and Surfaces A*, **317**, 473–81.

29 Xie, F., Baker, M.S. and Goldys, E.M. (2008) Enhanced fluorescence detection

on homogeneous gold colloid self-assembled monolayer substrates. *Chemistry of Materials*, **20**, 1788–97.

30 Tovmachenko, O.G., Graf, C., van den Heuvel, D.J., van Blaaderen, A. and Gerritsen, H.C. (2006) Fluorescence enhancement by metal-core/silica-shell nanoparticles. *Advanced Materials*, **18**, 91–5.

31 (a) Kresge, C.T., Leonowicz, M.E., Roth, W.J., Vartuli, J.C. and Beck, J.S. (1992) Ordered mesoporous molecular sieves synthesized by a liquid-crystal template mechanism. *Nature*, **359**, 710–12; (b) Zhao, D., Feng, J., Huo, Q., Melosh, N., Fredrickson, G.H., Chmelka, B.F. and Stucky, G.D. (1998) Triblock copolymer syntheses of mesoporous silica with periodic 50 to 300 angstrom pores. *Science*, **279**, 548–50; (c) Huo, Q., Margolese, D.I. and Stucky, G.D. (1996) Surfactant control of phases in the synthesis of mesoporous silica-based materials. *Chemistry of Materials*, **8**, 1147–60.

32 Botella, P., Corma, A. and Navarro, M.T. (2007) Single gold nanoparticles encapsulated in monodispersed regular spheres of mesostructured silica produced by pseudomorphic transformation. *Chemistry of Materials*, **19**, 1979–83.

33 Jiang, X. and Brinker, C.J. (2006) Aerosol-assisted self-assembly of single-crystal core/nanoporous shell particles as model controlled release capsules. *Journal of the American Chemical Society*, **128**, 4512–13.

34 Shan, J. and Tenhu, H. (2007) Recent advances in polymer protected gold nanoparticles: synthesis, properties and applications. *Chemical Communications*, 4580–98.

35 Liu, G.Y., Ji, H.F., Yang, X. and Wang, Y. (2008) Synthesis of a Au/silica/polymer trilayer composite and the corresponding hollow polymer microsphere with a movable Au core. *Langmuir*, **24**, 1019–25.

36 Mandal, T.K., Fleming, M.S. and Walt, D.R. (2002) Preparation of polymer coated gold nanoparticles by surface-confined living radical polymerization at ambient temperature. *Nano Letters*, **2**, 3–7.

37 Koenig, S. and Chechik, V. (2006) Shell cross-linked Au nanoparticles. *Langmuir*, **22**, 5168–73.

38 Li, D., He, Q., Cui, Y., Wang, K., Zhang, X. and Li, J. (2007) Thermosensitive copolymer networks modify gold nanoparticles for nanocomposite entrapment. *Chemistry – A European Journal*, **13**, 2224–9.

39 (a) Corbierre, M.K., Cameron, N.S. and Lennox, R.B. (2004) Polymer-stabilized gold nanoparticles with high grafting densities. *Langmuir*, **20**, 2867–73; (b) Corbierre, M.K., Cameron, N.S., Sutton, M., Mochrie, S.G.J., Lurio, L.B., Ruhm, A. and Lennox, R.B. (2001) Polymer-stabilized gold nanoparticles and their incorporation into polymer matrices. *Journal of the American Chemical Society*, **123**, 10411–12.

40 Higashi, N., Kawahara, J. and Niwa, M. (2005) Preparation of helical peptide monolayer-coated gold nanoparticles. *Journal of Colloid and Interface Science*, **288**, 83–7.

41 Azzam, T. and Eisenberg, A. (2007) Monolayer-protected gold nanoparticles by the self-assembly of micellar poly(ethylene oxide)-b-poly(epsilon-caprolactone) block copolymer. *Langmuir*, **23**, 2126–32.

42 Kang, Y. and Taton, T.A. (2005) Controlling shell thickness in core-shell gold nanoparticles via surface-templated adsorption of block copolymer surfactants. *Macromolecules*, **38**, 6115–21.

43 Hou, G., Zhu, L., Chen, D. and Jiang, M. (2007) Core-shell reversion of hybrid polymeric micelles containing gold nanoparticles in the core. *Macromolecules*, **40**, 2134–40.

44 Choi, W.S., Koo, H.Y. and Kim, D.-Y. (2008) Facile fabrication of core-in-shell particles by the slow removal of the core and its use in the encapsulation of metal nanoparticles. *Langmuir*, **24**, 4633–6.

45 Jeong, U., Wang, Y., Ibisate, M. and Xia, Y. (2005) Some new developments in the synthesis, functionalization, and utilization of monodisperse colloidal spheres. *Advanced Functional Materials*, **12**, 1907–21.

46 (a) Crooks, R.M., Zhao, M., Sun, L., Chechik, V. and Yeung, L.K. (2001) Dendrimer-encapsulated metal nanoparticles: synthesis, characterization, and applications to catalysis. *Accounts of Chemical Research*, **34**, 181–90;
(b) Zhao, M., Sun, L. and Crooks, R.M. (1998) Preparation of Cu nanoclusters within dendrimer templates. *Journal of the American Chemical Society*, **120**, 4877–8;
(c) Zheng, J. and Dickson, R.M. (2002) Individual water-soluble dendrimer-encapsulated silver nanodot fluorescence. *Journal of the American Chemical Society*, **124**, 13982–3.

47 Radowski, M.R., Shukla, A., von Berlepsch, H., Bottcher, C., Pickaert, G., Rehage, H. and Haag, R. (2007) Supramolecular aggregates of dendritic multishell architectures as universal nanocarriers. *Angewandte Chemie – International Edition*, **46**, 1265–9.

48 (a) Li, L., Yang, Y.W., Li, G.-H. and Zhang, L.-D. (2006) Conversion of a Bi nanowire array to an array of Bi-Bi_2O_3 core-shell nanowires and Bi_2O_3 nanotubes. *Small*, **2**, 548–53;
(b) Bourlinos, A.B., Chowdhury, S.R., Herrera, R., Jiang, D.D., Zhang, Q., Archer, L.A. and Giannelis, E.P. (2005) Functionalized nanostructures with liquid-like behavior: expanding the gallery of available nanostructures. *Advanced Functional Materials*, **15**, 1285–90.

49 Kalidindi, S.B. and Jagirdar, B.R. (2008) Synthesis of Cu@ZnO core-shell nanocomposite through digestive ripening of Cu and Zn nanoparticles. *The Journal of Physical Chemistry C*, **112**, 4042–8.

50 (a) Hirsch, L.R., Stafford, R.J., Bankson, J.A., Sershen, S.R., Rivera, B., Price, R.E., Hazle, J.D., Halas, N.J. and West, J.L. (2003) Nanoshell-mediated near-infrared thermal therapy of tumors under magnetic resonance guidance. *Proceedings of the National Academy of Sciences of the United States of America*, **100**, 13549–54;
(b) Aguirre, C.M., Kaspar, T.R., Radloff, C. and Halas, N.J. (2003) CTAB mediated reshaping of metallodielectric nanoparticles. *Nano Letters*, **3**, 1707–11.

51 Shi, W.L., Sahoo, Y., Swihart, M.T. and Prasad, P.N. (2005) Gold nanoshells on polystyrene cores for control of surface plasmon resonance. *Langmuir*, **21**, 1610–17.

52 Agrawal, M., Pich, A., Zafeiropoulos, N.E. and Stamm, M. (2008) Fabrication of hollow titania microspheres with tailored shell thickness. *Colloid and Polymer Science*, **286**, 593–601.

53 Hu, Q., Liu, J., Wang, L.-Q., Jiang, Y., Lambert, T.N. and Fang, E. (2006) A new class of silica cross-linked micellar core-shell nanoparticles. *Journal of the American Chemical Society*, **128**, 6447–53.

54 Herrera, V., Pirri, R., Asua, J.M. and Leiza, J.R. (2007) Morphology control in polystyrene/poly(methylmethacrylate) composite latex particles. *Journal of Polymer Science Part A – Polymer Chemistry*, **45**, 2484–93.

55 Jang, J., Kim, S. and Lee, K.J. (2007) Fabrication of CdS/PMMA core/shell nanoparticles by dispersion mediated interfacial polymerization. *Chemical Communications*, 2689–91.

56 Blackburn, W.H. and Lyon, L.A. (2008) Size-controlled synthesis of monodisperse core/shell nanogels. *Colloid and Polymer Science*, **286**, 563–9.

57 Levins, A.D., Moughton, A.O. and O'Reilly, R.K. (2008) Synthesis of core functionalized polymer micelles and shell cross-linked nanoparticles. *Macromolecules*, **41**, 3571–8.

58 Li, J., Yu, S., Yao, P. and Jiang, M. (2008) Lysozyme-dextran core-shell nanogels prepared via a green process. *Langmuir*, **24**, 3486–92.

59 Ow, H., Larson, D.R., Srivastava, M., Baird, B.A., Webb, W.W. and Wiesner, U. (2005) Bright and stable core-shell fluorescent silica nanoparticles. *Nano Letters*, **5**, 113–17.

60 Pyun, J., Matyjaszewski, K., Kowalewski, T., Savin, D., Patterson, G., Kickelbick, G. and Huesing, N. (2001) Synthesis of well-defined block copolymers tethered to polysilsesquioxane nanoparticles and their nanoscale morphology on surfaces. *Journal of the American Chemical Society*, **123**, 9445–6.

61 Motornov, M., Sheparovych, R., Lupitskyy, R., MacWilliams, E. and Minko, S. (2008) Superhydrophobic surfaces generated from water-borne dispersions of hierarchically assembled nanoparticles coated with a reversibly switchable shell. *Advanced Materials*, **20**, 200–5.

62 Darbandi, M. and Nann, T. (2006) One-pot synthesis of YF_3@silica core/shell nanoparticles. *Chemical Communications*, 776–8.

63 Zhang, M., Shi, S., Meng, J.,; Wang, X., Fan, H., Zhu, Y., Wang, X. and Qian, Y. (2008) Preparation and characterization of near-infrared luminescent bifunctional core/shell nanocomposites. *The Journal of Physical Chemistry C*, **112**, 2825–30.

64 Jia, N., Lian, Q., Shen, H., Wang, C., Li, X. and Yang, Z. (2007) Intracellular delivery of quantum dots tagged antisense oligodeoxynucleotides by functionalized multiwalled carbon nanotubes. *Nano Letters*, **7**, 2976–80.

65 (a) Chen, Y. and Rosenzweig, X. (2002) Luminescent CdS quantum dots as selective ion probes. *Analytical Chemistry*, **74**, 5132;
(b) Nazzal, A.Y., Wang, X., Qu, L., Yu, W., Wang, Y., Peng, X. and Xiao, M. (2004) Environmental effects on photoluminescence of highly luminescent CdSe and CdSe/ZnS core/shell nanocrystals in polymer thin films. *The Journal of Physical Chemistry B*, **108**, 5507.

66 (a) Derfus, A.M., Chan, W.C.W. and Bhatia, S.N. (2004) Probing the cytotoxicity of semiconductor quantum dots. *Nano Letters*, **4**, 11;
(b) Kirchner, C., Liedl, T., Kudera, S., Pellegrino, T., Munoz Javier, A., Gaub, H.E., Stolzle, S., Fertig, N. and Parak, W.J. (2005) Cytotoxicity of colloidal CdSe and CdSe/ZnS nanoparticles. *Nano Letters*, **5**, 331.

67 (a) Yang, Y., Jing, L., Yu, X., Yan, D. and Gao, M. (2007) Coating aqueous quantum dots with silica via reverse microemulsion method: toward size-controllable and robust fluorescent nanoparticles. *Chemistry of Materials*, **19**, 4123–8;
(b) Teng, F., Tian, Z., Xiong, G. and Xu, Z. (2004) Preparation of CdS-SiO_2 core-shell particles and hollow SiO_2 spheres ranging from nanometers to microns in the nonionic reverse microemulsions. *Catalyst Today*, **93–95**, 651–7.

68 Yang, Y., Jing, L., Yu, X., Yan, D. and Gao, M. (2007) Coating aqueous quantum dots with silica via reverse microemulsion method: toward size-controllable and robust fluorescent nanoparticles. *Chemistry of Materials*, **19**, 4123–8.

69 Teng, F., Tian, Z., Xiong, G. and Xu, Z. (2004) Preparation of CdS-SiO_2 core-shell particles and hollow SiO_2 spheres ranging from nanometers to microns in the nonionic reverse microemulsions. *Catalysis Today*, **93**–95, 651–7.

70 Torimoto, T., Reyes, J.P., Murakami, S.Y., Pal, B. and Ohtani, B. (2003) Layer-by-layer accumulation of cadmium sulfide core-silica shell nanoparticles and size-selective photoetching to make adjustable void space between core and shell. *Journal of Photochemistry and Photobiology A: Chemistry*, **160**, 69–76.

71 Wang, Y.-L., Lu, J.-P., Huang, X.-F., Long, J.-X. and Tong, Z.-F. (2008) Electrodeposition of Ni–Co/Al_2O_3 composite coating by pulse reverse method under ultrasonic condition. *Material Letters*, **62**, 3413–15.

72 Ge, J.-P., Xu, S., Zhuang, J., Wang, X., Peng, Q. and Li, Y.-D. (2006) Synthesis of CdSe, ZnSe, and ZnxCd1-xSe nanocrystals and their silica sheathed core/shell structures. *Inorganic Chemistry*, **45**, 4922–7.

73 (a) Bruchez, M., Jr, Gin, M., Moronne, P., Weiss, S. and Alivisatos, A.P. (1998) Semiconductor nanocrystals as fluorescent biological labels. *Science*, **281**, 2013;
(b) Chan, W.C. and Nie, S. (1998) Quantum dot bioconjugates for ultrasensitive nonisotopic detections. *Science*, **281**, 2016.

74 (a) Joo, J., Na, H.B., Yu, T., Yu, J.H., Kim, Y.W., Wu, F., Zhang, J.Z. and Hyeon, T. (2003) Generalized and facile synthesis of semiconducting metal sulfide nanocrystals. *Journal of the American Chemical Society*, **125**, 11100–5;

(b) Cozzoli, P.D., Manna, L., Curri, M. L., Kudera, S., Giannini, C., Striccoli, M. and Agostiano, A. (2005) Shape and phase control of colloidal ZnSe nanocrystals. *Chemistry of Materials*, **17**, 1296–306.

75 Ehlert, O., Buecking, W., Riegler, J., Merkulov, A. and Nann, T. (2008) Organometallic synthesis and electrophoretic characterization of high-quality ZnS : Mn/ZnS core/shell nanoparticles for bioanalytical applications. *Microchimica Acta*, **160**, 351–6.

76 Li, D., Wang, Y., Yang, G. and Xu, Z. (2008) *Proceedings of Sixth International Conference on Thin Film Physics and Applications, 6984*.

77 Sun, Z., Kumbhar, A., Sun, K., Liu, Q. and Fang, J. (2008) One-pot synthesis of reverse type-I In_2O_3@In_2S_3 core-shell nanoparticles. *Chemical Communications*, 1920–2.

78 Shi, Y.-L. and Asefa, T. (2007) Tailored core-shell-shell nanostructures: sandwiching gold nanoparticles between silica cores and tunable silica shells. *Langmuir*, **23**, 9455–62.

79 Chen, C.-T., Munot, Y.S., Salunke, S.B., Wang, Y.-C., Lin, R.-K., Lin, C.-C., Chen, C.-C. and Liu, Y.-H. (2008) A triantennary dendritic galactoside-capped nanohybrid with a ZnS/CdSe nanoparticle core as a hydrophilic, fluorescent, multivalent probe for metastatic lung cancer cells. *Advanced Functional Materials*, **18**, 527–40.

80 Palaniappan, K., Xue, C., Arumugam, G., Hackney, S.A. and Liu, J. (2006) Water-soluble, cyclodextrin-modified CdSe-CdS core-shell structured quantum dots. *Chemistry of Materials*, **18**, 1275–80.

81 Zhang, L.W., Yu, W.W., Colvin, V.L., Monteiro, R. and Nancy, A. (2008) Biological interactions of quantum dot nanoparticles in skin and in human epidermal keratinocytes. *Toxicology and Applied Pharmacology*, **228**, 200–11.

82 Ma, X., Shi, W., Yan, Z. and Shen, B. (2007) Fabrication of silica/zinc oxide core–shell colloidal photonic crystals. *Applied Physics. B, Lasers and Optics*, **88**, 245–8.

83 Hebalkar, N., Kharrazi, S., Ethiraj, A., Urban, J., Fink, R. and Kulkarni, S.K. (2004) Structural and optical investigations of SiO_2-CdS core-shell particles. *Journal of Colloid and Interface Science*, **278**, 107–14.

84 (a) Hao, L., Gong, X., Xuan, S., Zhang, H., Gong, X., Jiang, W. and Chen, Z. (2006) Controllable fabrication and characterization of biocompatible core-shell particles and hollow capsules as drug carrier. *Applied Surface Science*, **252**, 8724–33;
(b) Blomberg, S., Ostberg, S., Harth, E., Bosman, A.W., Von Horn, B. and Hawker, C.J. (2002) Production of crosslinked, hollow nanoparticles by surface-initiated living free-radical polymerization. *Journal of Polymer Science Part A – Polymer Chemistry*, **40**, 1309–20.

85 Limmer, S.J., Chou, T.P. and Cao, G. (2003) Formation and optical properties of cylindrical gold nanoshells on silica and titania nanorods. *The Journal of Physical Chemistry B*, **107**, 13313–18.

86 Harada, M. and Einaga, H. (2007) Preparation of Pt/Rh bimetallic colloidal particles in polymer solutions using borohydride-reduction. *Journal of Colloid and Interface Science*, **308**, 568–72.

87 Sao-Joao, S., Giorgio, S., Penisson, J.M., Chapon, C., Bourgeois, S. and Henry, C. (2005) Structure and deformations of Pd-Ni core-shell nanoparticles. *The Journal of Physical Chemistry B*, **109**, 342–7.

88 Yang, Y., Shi, J., Kawamura, G. and Nogami, M. (2008) Preparation of Au-Ag, Ag-Au core-shell bimetallic nanoparticles for surface-enhanced Raman scattering. *Scripta Materialia*, **58**, 862–5.

89 Hu, J.-W., Zhang, Y., Li, J.-F., Liu, Z., Ren, B., Sun, S.-G., Tian, Z.-Q. and Lian, T. (2005) Synthesis of Au@Pd core-shell nanoparticles with controllable size and their application in surface-enhanced Raman spectroscopy. *Chemical Physics Letters*, **408**, 354–9.

90 Teng, X., Wang, Q., Liu, P., Han, W., Frenkel, A.I., Wen, W., Marinkovic, N., Hanson, J.C. and Rodriguez, J.A. (2008) Formation of Pd/Au nanostructures from Pd nanowires via galvanic replacement reaction. *Journal of the American Chemical Society*, **130**, 1093–101.

91 Ferrer, D., Torres-Castro, A., Gao, X., Sepulveda-Guzman, S., Ortiz-Mendez, U. and Jose-Yacaman, M. (2007) Three-layer core/shell structure in Au-Pd bimetallic nanoparticles. *Nano Letters*, **7**, 1701–5.

92 Ingali, K.C., Deng, S. and Rockstraw, D.A. (2007) Direct synthesis of Ru-Ni nanoparticles with core-and-shell structure. *Chemical Engineering Communications*, **194**, 780–6.

93 Tsuji, M., Miyamae, N., Matsumoto, K., Hikino, S. and Tsuji, T. (2005) Rapid formation of novel Au core-Ag shell nanostructures by a microwave-polyol method. *Chemistry Letters*, **34**, 1518–19.

94 Toshima, N., Ito, R., Matsushita, T. and Shiraishi, Y. (2007) Trimetallic nanoparticles having a Au-core structure. *Catalysis Today*, **122**, 239–44.

95 Matsushita, T., Shiraishi, Y., Horiuchi, S. and Toshima, N. (2007) Synthesis and catalysis of polymer-protected Pd/Ag/Rh trimetallic nanoparticles with a core-shell structure. *Bulletin of the Chemical Society of Japan*, **80**, 1217–25.

96 Cheng, Z., Zhang, L., Zhu, X., Kang, E.T. and Neoh, K.G. (2008) Organic/inorganic hybrid nanospheres coated with palladium/P4VP shells from surface-initiated atom transfer radical polymerization. *Journal of Polymer Science A*, **46**, 2119–31.

97 Wan, Y., Min, Y.L. and Yu, S.-H. (2008) Synthesis of silica/carbon-encapsulated core-shell spheres: templates for other unique core-shell structures and applications in *in situ* loading of noble-metal nanoparticles. *Langmuir*, **24**, 5024–8.

98 Baughman, R.H., Zakhidov, A.A. and DeHeer, W.A. (2002) Carbon nanotubes – the route toward applications. *Science*, **297**, 787.

99 (a) Javey, A., Guo, J., Farmer, D.B., Wang, Q., Wang, D., Gordon, R.G., Lundstrom, M. and Dai, H. (2004) Carbon nanotube field-effect transistors with integrated ohmic contacts and high-k gate dielectrics. *Nano Letters*, **4**, 447–50;
(b) Fu, L., Liu, Y., Liu, Z., Han, B., Cao, L., Wei, D., Yu, G. and Zhu, D. (2006) Carbon nanotubes coated with alumina as gate dielectrics of field-effect transistors. *Advanced Materials*, **18**, 181–5;
(c) Li, X., Liu, Y., Fu, L., Cao, L., Wei, D., Wang, Y. and Yu, G. (2007) Synthesis and device integration of carbon nanotube/silica core-shell nanowires. *The Journal of Physical Chemistry C*, **111**, 7661–5.

100 (a) Wang, J., Khlobystov, A.N., Wang, W., Howdle, S.M. and Poliakoff, M. (2006) Coating carbon nanotubes with polymer in supercritical carbon dioxide. *Chemical Communications*, 1670–2;
(b) Han, L., Wu, W., Kirk, F.L., Luo, J., Maye, M.M., Kariuki, N.N., Lin, Y., Wang, C. and Zhong, C.-J. (2004) A direct route toward assembly of nanoparticle-carbon nanotube composite materials. *Langmuir*, **20**, 6019–25;
(c) Lu, Y., Bangsaruntip, S., Wang, X., Zhang, L., Nishi, Y. and Dai, H. (2006) DNA functionalization of carbon nanotubes for ultrathin atomic layer deposition of high kappa dielectrics for nanotube transistors with 60 mV/decade switching. *Journal of the American Chemical Society*, **128**, 3518–19.

101 Wang, J., Khlobystov, A.N., Wang, W., Howdle, S.M. and Poliakoff, M. (2006) Coating carbon nanotubes with polymer in supercritical carbon dioxide. *Chemical Communications*, 1670–2.

102 Fu, L., Liu, Y., Liu, Z., Han, B., Chao, L., Wei, D., Yu, G. and Zhu, D. (2006) Carbon nanotubes coated with alumina as gate dielectrics of field-effect transistors. *Advanced Materials*, **18**, 181–5.

103 Sun, X. and Li, Y. (2004) Colloidal carbon spheres and their core/shell structures with noble-metal nanoparticles. *Angewandte Chemie – International Edition*, **43**, 597–601.

104 Park, J., Joo, J., Kwon, S.G., Jang, Y. and Hyeon, T. (2007) Synthesis of monodisperse spherical nanocrystals. *Angewandte Chemie – International Edition*, **46**, 4630–60.

105 Chen, H.M., Liu, R.S., Jang, L.-Y., Lee, J.-F. and Hu, S.F. (2006) Characterization of core-shell type and alloy Ag/Au bimetallic clusters by using extended X-ray absorption fine structure spectroscopy. *Chemical Physics Letters*, **421**, 118–23.

106 Daly, B., Kulkarni, J.S., Arnold, D.C., Shaw, M.T., Nikitenko, S., Morris, M.A. and Holmes, J.D. (2006) Structural investigation of germanium–cobalt core shell nanocable arrays. *Journal of Materials Chemistry*, **16**, 3861–6.

107 Burns, A., Owb, H. and Wiesner, U. (2006) Fluorescent core-shell silica nanoparticles: towards Lab on a Particle architectures for nanobiotechnology. *Chemical Society Reviews*, **35**, 1028–42.

108 Ow, H., Larson, D.R., Srivastava, M., Baird, B.A., Webb, W.W. and Wiesner, U. (2005) Bright and stable core-shell fluorescent silica nanoparticles. *Nano Letters*, **5**, 113–17.

109 Gong, J.-L., Jiang, J.-H., Yang, H.-F., Shen, G.-L., Yu, R.-Q. and Ozaki, Y. (2006) Novel dye-embedded core-shell nanoparticles as surface-enhanced Raman scattering tags for immunoassay. *Analytica Chimica Acta*, **564**, 151–7.

110 Liu, W., He, Z., Liang, J., Zhu, Y., Xu, H. and Yang, X. (2008) Preparation and characterization of novel fluorescent nanocomposite particles: CdSe/ZnS core-shell quantum dots loaded solid lipid nanoparticles. *Journal of Biomedical Materials Research Part A*, **84A**, 1018–25.

111 Yin, M., Kuhlmann, C.R.W., Sorokina, K., Li, C., Mihov, G., Pietrowski, E., Koynov, K., Klapper, M., Luhmann, H.J., Muellen, K. and Weil, T. (2008) Novel fluorescent core-shell nanocontainers for cell membrane transport. *Biomacromolecules*, **9**, 1381–9.

112 Park, H., Yang, J., Seo, S., Kim, K., Suh, J., Kim, D., Haam, S. and Yoo, K.-H. (2008) Multifunctional nanoparticles for photothermally controlled drug delivery and magnetic resonance imaging enhancement. *Small*, **4**, 192–6.

113 Wen, Z., Liu, J. and Li, J. (2008) Core/shell Pt/C nanoparticles embedded in mesoporous carbon as a methanol-tolerant cathode catalyst in direct methanol fuel cells. *Advanced Materials*, **20**, 743–7.

114 Son, S.U., Park, I.K., Park, J. and Hyeon, T. (2004) Synthesis of Cu2O-coated Cu nanoparticles and their successful application to the Ullmann-type amination coupling reactions of aryl chloride. *Chemical Communications*, 778–9.

115 Zhao, M. and Crooks, R.M. (1999) Homogeneous hydrogenation catalysis with monodisperse, dendrimer-encapsulated Pd and Pt nanoparticles. *Angewandte Chemie–International Edition*, **38**, 364–6.

116 Niu, Y., Yeung, L.K. and Crooks, R.M. (2001) Size-selective hydrogenation of olefins by dendrimer-encapsulated palladium nanoparticles. *Journal of the American Chemical Society*, **123**, 6840–6.

117 Li, Y. and El-Sayed, M.A. (2001) The effect of stabilizers on the catalytic activity and stability of Pd colloidal nanoparticles in the Suzuki reactions in aqueous solution. *The Journal of Physical Chemistry B*, **105**, 8938–43.

Keywords

core-shell nanoparticles; nonmagnetic nanoparticles; bioimaging; nanomedicine; drug delivery; catalysis; metal oxide nanomaterials.

10
Spherical and Anisotropic Silica Shell Nanomaterials

Chih-Wei Lai, Jong-Kai Hsiao, Yu-Chun Chen and Pi-Tai Chou

10.1
Introduction

In this chapter we focus primarily on silica-encapsulated, commonly encountered nanomaterials such as metals, metal oxide and semiconductors. The silica encapsulation of these core-shell nanoparticles, the aim being to enhance their functionalities such as photophysical properties and biocompatibilities, has been studied extensively over the past decade [1–6]. As a result, several reviews have been published which discuss either the inertness of the silica shell to attenuate cytotoxicities [2, 4], the convenience of the silica in providing a medium for linking materials with different properties [3, 5], or the consequent optical properties [1, 2, 6]. In this chapter, the aim is to examine the subject from a different angle, by providing a complete overview of the silica-coating principle of different core-shell materials. The procedures and characteristics of the currently dominant encapsulation methods will be detailed to affirm the potential applicability of such materials in the fields of nanotechnology or biomedicine.

The chapter is organized systematically on the basis of the unique property being discussed. In Section 10.2, we describe silica-coated nonemissive noble metal cores such as Au and Ag nanoparticles and nanorods, notably with regards to the resultant intensive surface plasmon resonance (SPR) in the presence of an external electrical field. Such a phenomenon can enhance the emissions of doped dyes and/or quantum dots (QDs) in the silica layers or the signals of the Raman tags residing near the metal cores, producing highly sensitive spectroscopic information. Silica-coated emissive materials such as QDs, will then be detailed in Section 10.3. The resultant nanocomposite renders significant reductions in cytotoxicity, as well as a retention of emission properties, thus providing a momentous breakthrough in the area of bioimaging.

A further relevant topic of interest can be ascribed to magnetic nanoparticles with silica coatings (Section 10.4). Previously, these have been conjugated with biomarkers for the specific targeting of tissues or organs of interest, with examples (albeit at the prototype stage) including targeted drug delivery and smart probes

Nanomaterials for the Life Sciences Vol. 3: Mixed Metal Nanomaterials. Edited by Challa S. S. R. Kumar

ISBN: 978-3-527-32153-7

for magnetic resonance imaging (MRI). As an example, a silica-coated MRI contrast agent conjugated with a tumor-specific antibody would be highly effective in tumor diagnosis. However, because details of MRI theory and the corresponding measurements are included in a later volume, the emphasis here is placed on a variety of synthetic methodologies of uniform magnetic metal iron/mesoporous-silica core-shell nanoparticles. This type of core-shell structure combines the advantages of mesoporous silica and magnetic nanoparticles to fabricate a nanocomposite with a high surface area and magnetic susceptibility. Particular attention in this section is paid to FePt, because of its smaller size, easily modified characteristics and superparamagnetic properties. The section also focuses on multifunctionality, with magnetic nanoparticle (MNP) -core and silica shell materials being recognized as much more versatile than their metal-core counterparts. Although the sole use of iron oxide is popular because of its negligible cellular toxicity, many research groups have extended its utility by incorporating MNPs/SiO_2 with other materials such as dyes, photothermal or photodynamic agents.

Last but not least, in Section 10.5, one interesting topic worthy of review is the development of nanospheric cores in hollow SiO_2 balls. This type of advanced material, which incorporates a metallic core with hollow nanomaterials, has double the surface area of typical nanoparticles and is both lightweight and low-density, which in turn entails lower production costs. Taken together, these properties make the nanoparticles suitable for catalysts, biosensors and drug delivery agents.

10.2
Silica-Coated Metal Nanoparticles

The aim here is to introduce different approaches, namely the sol–gel Stöber method and microemulsion system, for coating a silica layer outside metal nanoparticles. By conjugating with biological active ligands, silica-coated metal nanoparticles are suited for a variety of applications. For example, oligo-bioconjugation with nucleotides allows silica-coated metal nanoparticles to act as biosensors to detect biological activities such as DNA hybridization. On the other hand, dye doping confined within the silica layer of coated metal nanoparticles allows surface enhancement in Raman scattering spectroscopy or luminescence preservation in electromagnetic spectroscopy. Another relevant topic of current interest should be credited to silica-capped metal nanorods, which possess extremely high extinction coefficients in the near-infrared (NIR) region and are hence suited to a variety of applications. Finally, the advantages of using silica-coated platinum nanoparticles in catalytic role will be demonstrated.

10.2.1
Noble Metal Nanoparticles: An Overview

In general, gold nanoparticles are prepared through chemical reduction methods. A typical water-phase synthesis of spherical gold nanoparticles, which uses $HAuCl_4$

as a gold precursor and $NaBH_4$ as a reducing agent in sodium citrate aqueous solution, was first reported by Enustun and Turkevich in 1963 [7]. These authors also discovered that gold nanoparticles underwent coalescence or conformational changes as a result of Brownian motion and thermodynamic tendency. Therefore, the addition of a stabilizer (e.g., sodium citrate) was necessary to maintain the size and conformation of the synthesized nanoparticles. As predicted in classical static electric field theory [8], metal core nanoparticles will absorb an electromagnetic wave at a certain degree when the particle sizes are far smaller than the wavelength of the applied electromagnetic wave. Consequently, the surface electrons of metal core nanoparticles will be excited in a resonant manner, named SPR [9]. The characteristic band of SPR is determined based typically on particle size, conformation, metallic characteristics and the dielectric constant of scavengers. As soon as the surface electrons of gold nanoparticles are excited through exposure to light, they will create a transition dipole moment and induce a transition dipole resonance under a certain excitation frequency. As reported by El-Sayed *et al*. [10], the absorptive cross-section of gold nanospheres with a commonly employed size (i.e., 40 nm) is five orders higher than that of conventional dyes, according to theoretical calculations [10]. Likewise, the light-scattering factor is five orders higher with 80 nm-diameter gold nanospheres.

Because the interaction between gold nanoparticles is inversely proportional to the inter-particle distance, a bathochromic shift in the absorption spectrum is observed in an agglomerated suspension of gold nanoparticles [11]. In recent studies, this key characteristic of gold nanoparticles has been ingeniously applied to the point mutation detection of DNA molecules, as reported by Mirkin *et al*. [12]. In their study, gold nanoparticles were separately modified with two complementary single-strand DNA (ssDNA) molecules. Upon mixing, hybridization between two gold nanoparticles can be detected using spectroscopic methods. In addition to the distance control of Au nanoparticles, the application of the photothermal conversion effect has also attracted much attention [13]. Consequently, further studies in biomedical imaging and the selective photothermal destruction of cancer cells by immunotargeted Au nanospheres have been carried out by Halas *et al*. [14] and other research groups [15, 16].

One annoying problem when manipulating metal core nanoparticles is that the stabilizer commonly loses its function upon changing to different solvent systems, consequently inducing coalescence. In order to overcome this hurdle, phase-transfer and surface-modification techniques are both useful. Generally, new soluble ligands with a high affinity to the targeted metallic cores are adopted in the phase-transfer process. Some useful functional groups capable of strong interactions with gold nanoparticles include –SH, $–NH_2$, –CN and $–P(C_6H_5)_2$. In order to provide further protection, as well as to enrich their potential applications, the other terminal of the ligands is also strategically functionalized [17]. One material used typically for chemical modification is tetraethyl orthosilicate (TEOS); this provides great versatility because it is capable of polymerization, and of forming a SiO_2 shell with various functionalities. Owing to rapid increases in numbers of applications, SiO_2 nanoparticles – and hence the metal nanoparticles/SiO_2 core-shell nanocomposites – warrant detailed elaboration.

Silver nanoparticles have also been used for the identification and quantitative measurement of oligonucleotides and proteins. The mechanism by which silver nanoparticles are synthesized is quite similar to that for gold nanoparticles, although in general the silver nanoparticles are produced via the reduction of $AgNO_3$, using $NaHB_4$ as a reducing agent [18]. Another similarity is that silica coating is a common surface modification used to make silver nanoparticles more biocompatible. Hence, many protocols of silver/SiO_2 coated nanomaterials have been designed, based on the same framework as that for silica-coated gold nanoparticles.

10.2.1.1 Sol–Gel method for Silica Coating

10.2.1.1.1 Stöber Method Ever since its first use in 1996, 3-aminopropyltrimethoxysilane (APTES) has been employed as a silane coupling agent to modify the gold surface by displacing citric acid from the surface of gold nanoparticles [19]. The resultant active thin silica monolayer serves as an extension base for further SiO_2 shell growth by sol–gel methods in a water/alcohol cosolvent system. By applying the sol–gel process, Stöber *et al.* first reported the synthesis of homogenous SiO_2 nanoparticles using siloxane as the source and high-concentration ammonium aqueous solutions as catalysts under ethanol [20]. The size of the synthesized particles ranged from 50 to 150 nm (see Figure 10.1a and b). Subsequently, a detailed study of formulaic correlations among particle sizes and the concentrations of silane precursor, ammonia and water, was carried out by Bogush *et al.* [23]. Further investigations of the relationships between particle size and reaction temperature or TEOS concentration within various solvent systems were completed by Sadasivan *et al.* [24]. The study results suggested that the trend of increasing particle size was in the order of 1-butanol > 2-propanol > 1-propanol > ethanol > methanol. A similar investigation was conducted by Park *et al.* [25], who showed that the synthesized particles were not only smaller but also more homogeneous within the high-temperature regime of the reaction. In contrast, the particle became larger, but more inhomogeneous, when the proportion of ammonia or water was increased while the TEOS concentration was held constant.

The pH value was shown to be a critical issue in the formation of homogeneous silica shells. According to studies reported by Iler *et al.* [26], the pH is basic enough for silane to crosslink on the nanoparticle surfaces, but not basic enough to form silica nuclei, under pH 8.0~10.0. This finding is important because the formation of redundant silica nuclei will further grow into SiO_2 balls without metal cores, and these would be difficult to separate from any default products. The concentration of TEOS also plays a key role in the core-shell structure formation, with the optimum molar ratio for TEOS versus gold nanoparticles being approximately 10 [26]. Optically, the thus-synthesized Au/SiO_2 colloids exhibit a significant red shift in absorption compared to the reactant gold nanoparticles. As the dielectric constant around gold nanoparticles is also changed after coating with silica nanoshells, these results can easily be rationalized.

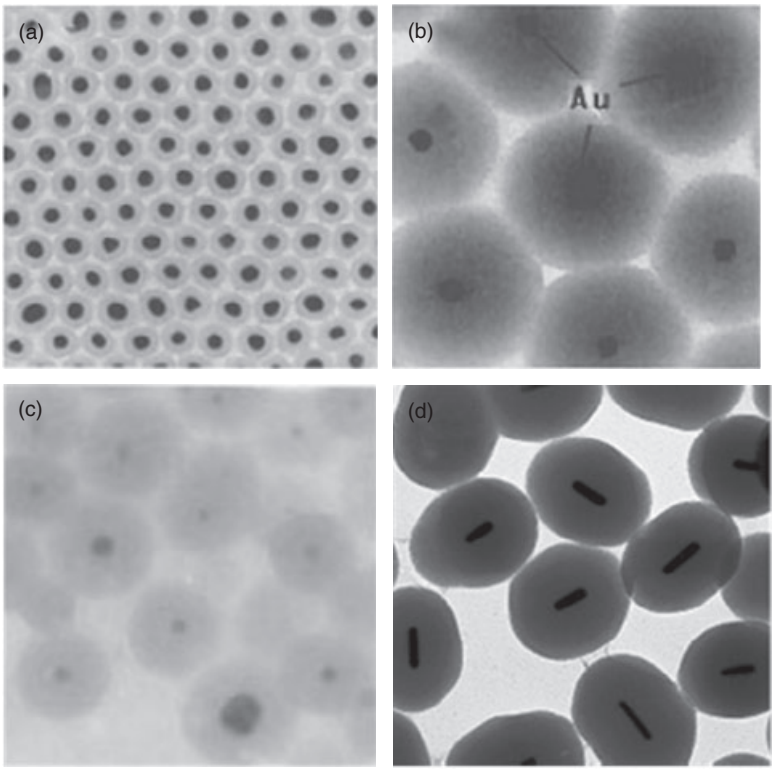

Figure 10.1 Homogeneous silica coating with no free colloidal silica demonstrated in (a,b) gold colloid after APTES activation, (c) in Ag/SiO_2 nanoparticles, (d) in Au rod/SiO_2 nanoparticles. Reproduced with permission from Refs. [19, 21, 22]; © The American Chemical Society.

One challenge which is presented in silica encapsulation is the formation of multicore and core-free silica nanoparticles. Fortunately, these synthetic defects can be avoided with aid from organosilane. Although amine-functional silane coupling agents were the first organosilanes used to react with gold nanoparticles at an earlier stage, because of the strong Au–S bonding, thiols have replaced amines and are now frequently used as a functional group to couple with gold nanoparticles [27]. Thus, thiol-functional silane coupling agents, such as MPTES (3-mercaptopropyltrimethoxysilane), are often used to form an active silica monolayer. Moreover, the alkoxy terminal on the MPTES can be further hydrolyzed and so provide coupling junctions between the organosilanes and the free Si–OH surface groups [28]. The overall synthesis of the SiO_2 shell is completed by adding TEOS in a sol–gel process. Based on a similar framework, polyvinylpyrrolidone (PVP) has been shown to be a good substitute for silane coupling agents [29], as it promotes the silica coating of gold nanoparticles

through a water-to-ethanol phase-transfer process. The synthesis of homogeneous gold core–silica shell structures within a water : 2-propanol cosolvent system free from silane coupling agents (or PVP) was also reported by Xia's group [30], when a linear relationship between the thickness of the silica shells and the TEOS concentration was also observed. Highly homogeneous silica-coated silver nanoparticles may also be synthesized via Stöber methods (see Figure 10.1c) [21].

10.2.1.1.2 **Microemulsion Method** Although, in general, the foundation of silica encapsulation has relied on the Stöber sol–gel process, the inapplicability of this method to hydrophobic materials has stimulated development of the reverse micelle method. Microemulsion is a transparent, isotropic and thermodynamically stable system in which the sizes of the micelles are within the range of a few to tens of nanometers. The size of the micelles in a microemulsion system depends not only on the molar ratio of water and the major surfactant, but also on types and concentrations of solute, cosurfactants and nonpolar solvent presented in the system. During microemulsion formation, the hydrophilic region of a surfactant points to the polar aqueous phase, while the hydrophobic region points to the nonpolar oil phase. Spontaneous micelle formation is thermodynamically driven to minimize unfavorable interactions. Depending on the system conditions and the final conformation, micelles can be classified as either normal or reverse type. In a normal micelle, under an aqueous environment, the hydrophobic region is aggregated at the center while the hydrophilic region is exposed. In contrast, in a reverse micelle the opposite conformation is observed under a water-restricted environment. The size of the micelles in a system can also be modulated, with the volume of water in a water pool under a reverse system determining the micellar dimensions. In a normal system, the volume of the oil phase plays the same role. Commonly used polar surfactants include anionic aerosol OT (sodium di-2-ethylhexyl sulfosuccinate; AOT) and cationic cetyltrimethylammonium bromide (CTAB). Other less-polar surfactants, such as (tetraethyleneglycol) mono-*n*-dodecyl ether ($C_{12}E_4$), TritonX-100 and phosphatidylcholine (PTC) are often encountered.

A reverse micelle system represents a powerful tool for nanoscale synthesis, as a well-controlled water pool can ensure that the product formed will be in the desired magnitude. Osseo-Asare and Arriagada showed that monodisperse SiO_2 spheres could be constructed in the size range of 40–70 nm by the controlled hydrolysis and condensation of tetraethoxysilane within reverse micelles [31]. The synthesis of colloidal silica by the hydrolysis of TEOS in alcohols has also been widely studied [20–26]. Because hydrolysis with water alone is very slow, either an acid or a base catalyst is needed; the former will enhance the growth of gel structures, while the latter will serve as a morphological catalyst, resulting in the production of spherical particles. Stoichiometrically, the reaction proceeds as

$$Si(OC_2H_5)_4 + 2H_2O \rightleftharpoons SiO_2 + 4C_2H_5OH$$

This reaction is actually a hydrolysis

$$Si(OC_2H_5)_4 + 4H_2O \rightleftharpoons Si(OH)_4 + 4C_2H_5OH$$

followed by a condensation step

$$Si(OH)_4 \rightleftharpoons SiO_2 + 2H_2O$$

The polymerization of silic acid may occur in two ways. In an acidic environment, the condensation of silane groups leads to the formation of chainlike or open-branched polymers, which are defined as having a specific molecular weight but are not considered as particles. On the other hand, for polymerization occurring in an alkaline environment, internal condensation and crosslinking leads to the generation of particles consisting of four siloxanes and hydroxyl groups attached only to the surfaces of the particles. The prime advantages of employing a reverse micelle system for a core-shell nanomaterial synthesis are: (i) the capacity to dissolve reactants in the water core; and (ii) the constant exchange of the aqueous phase among micelles. For biomedical applications, the development of efficient large-scale synthetic methods for silica-coated nanoparticles is necessary, and in this respect a direct synthesis towards Au/SiO_2 and Ag/SiO_2 nanoparticles using a reverse microemulsion technique has been developed [32, 33]. Here, the synthesis of gold or silver nanoparticles was carried out under aqueous phase, followed by the Stöber sol–gel synthesis. Ying has also shown that a reverse micelles technique can be applied to the synthesis of gold- or silver-based silica-coated nanoparticles. Ying and colleagues also found the overall yield of the reverse micelles method to be three orders of magnitude higher than that of the Stöber method. In the latter case, the aggregation of silica-coated gold nanoparticles was inevitable only when the reaction was carried out at a lower concentration. In contrast, the reverse microemulsion method enabled a much more successful silica coating at a higher gold particle concentration (up to 1.5×10^{13} particles ml^{-1}). In short, when compared to the Stöber method, only 0.1% of solvent volume was required to silica coat the same amount of nanoparticles via the reverse microemulsion method. In practical terms, this synthetic protocol could also be scaled up towards the gram scale.

Silane-coupled organic dyes, such as fluorescein isothiocyanate (FITC)-APTES [34], have been proven to be stably embedded in silica-coated gold nanoparticles, and not to be eluted by washing. Neither was their emission seen to quenched by gold nanoparticles. Such a result is quite different from that obtained with dye-conjugated gold nanoparticles free from any silica coating, for which the emission is generally quenched due to the SPR. In the reverse micelles case, silver is known to lack long-term stability in ammonium aqueous solution, a situation which might be attributed to the fact that Ag tends to be oxidized in a basic medium to AgOH, and to form soluble $Ag(NH_3)_2OH$. This can be prevented by adding a reducing agent such as 1,2-hexadecanediol to the ammonia solution, thereby improving the yield of Ag/SiO_2.

10.2.2
Silica Shell for Biofunctionalization

In order to enrich the biofunctionality of metal core nanoparticles, bioconjugated ligands are coupled with alkoxysilane agents in the process of silica shell formation. As such, the thickness of the silica shell becomes a pivotal consideration. A new protocol based on silica thin film formation has been developed by Horst *et al.* [35], in which MPTES was used for silica thin film formation prior to the crosslinking of biofunctionalized alkoxysilane agents (see Figure 10.2). The silica shell layer thus formed was much thinner than any previously synthesized. The results also indicated that a lower dosage might be needed in prescriptions. Furthermore, different biofunctionalized alkoxysilane coupling agents could be anchored simultaneously on the surface of silica-coated nanoparticles, with proportional control.

10.2.3
Application of Silica-Coated Metal Nanoparticles

10.2.3.1 Silica Shell Modified with Oligonucleotides

As reported by Han's group, aldehyde-functional silane coupling agents have been successfully conjugated to the surface of silica-coated gold nanoparticles [36]. Aldehyde functional groups easily undergo 'oligo-bioconjugation', forming, for example, amine-terminated oligonucleotides. Similar to gold nanoparticles with thiolated oligonucleotides, these modified nanoparticles have been shown to represent an effective colorimetric detection material for DNA hybridization or protein–protein interaction, because of their unique optical properties. Upon oligonucleotide conjugation, the Au/SiO_2 core-shell nanoparticles have proved to be

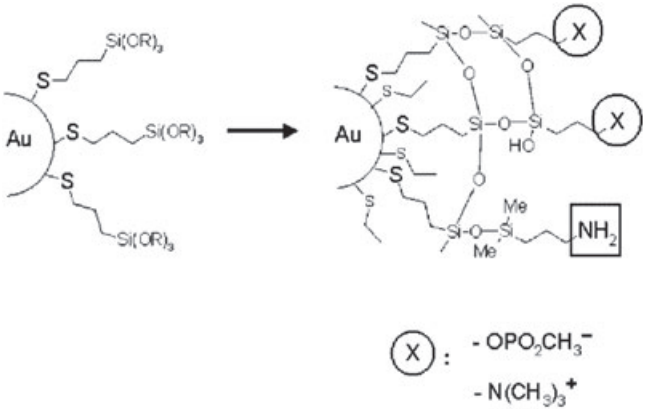

Figure 10.2 Further modification with crosslinking silica linkers to promote biofunctionalities. Reprinted with permission from Ref. [35]; © 2002, Wiley.

capable of oligonucleotide hybridization and, based on this protocol, the synthesis of gram-scale oligonucleotide-conjugated silver/SiO_2 core-shell nanoparticles has been reported [37]. Owing to their rapid, sequence-specific hybridization kinetics, these surface-modified silica-coated silver nanoprobes have also been applied to a rapid colorimetric DNA detection system [37].

10.2.3.2 **Surface-Enhanced Raman Scattering Effect**

The wavelength of scattering light, which was shown by C. V. Raman in 1928 to be related to a molecule's structure or characteristics [38], is referred to as Raman scattering or the Raman effect. Raman scattering provides information on molecular structure, and therefore is an essential technique in molecular structure studies. Since Raman's discovery, Raman spectroscopy has been applied ubiquitously in biochemical examinations, with research projects having been focused on proteins, amino acids, lipids, DNA and RNA. Unfortunately, however, the low intensity of the system makes Raman scattering difficult to analyze. Hence, in 1974, Fleishmann *et al*. showed that the Raman scattering signals of pyridine (C_5H_5N) were increased 10^5-fold when it was adsorbed onto a silver metal [39]. This signal magnification, which resulted from the adhesion to a rough metal surface, is referred to as surface-enhanced Raman scattering (SERS). Despite the fact that the subject has been extensively discussed, the theory of SERS remains somewhat controversial. One plausible mechanism for SERS is known as the electromagnetic effect or the field effect; this specifies that when molecules and metallic surfaces are close enough, an incidence electromagnetic radiation field, combined with an enlarged molecular polarizability, will induce a SPR of the metal surface. Hence, those molecules lying in the locally maximized electromagnetic field will have their Raman scattering signals enhanced [40, 41]. It should be noted that another point of view exists with regards to the SERS effect. In a simplified expression, for example, metal core nanoparticles can be treated as capacitors that store and release energy to nearby molecules within picoseconds, thus enhancing the Raman scattering signals [40, 41].

Many reports have focused on the application of Raman tag-conjugated nanoparticles in SERS detection for bioanalysis [42–44], and in light of this a scanometric detection of complementary DNA-conjugated gold nanoparticles has been developed by Mirkin and coworkers [45]. This method (or device) is composed of an underlying chip in a DNA microarray combined with a Cy3 dye and silver nanoparticles. The inserted Raman tag, Cy3, is localized between the gold nanoparticles and ssDNA molecules. Larger Raman scattering enhancements are observed only when the labeled conjugate nanoparticles are overgrown with Ag, due to the similar wavelength between the characteristic bands of silver nanoparticles and the absorption band of Raman tags. A detection limit of 20 fM has been reported for this technique.

Although the working distance of the SERS effect is within 10 nm, the strongest enhancement occurs when the tag is anchored directly onto the surface of certain metals, such as Au, Ag, Ni, Fe and Co [46–51]. By using SERS techniques, extremely sensitive single-molecule detection techniques can be carried out with the aid of

metal core nanoparticles, with a detection limit reported as 10^{-15} *M*. Recently, silica-coated Raman tags were developed by two different groups. Organic dye-anchored gold core/silica shell colloids were first used for the study of SERS by Doering's group [49]. In this approach, dye molecules with an isocyanate (N=C=S–) group are mixed with MPTES in 1 : 1 ratio in volume, and used for active silica formation. Sodium silicate is then added, whereupon a protective SiO_2 shell is formed outside the nanoparticles that assists the dye molecules to become anchored tightly onto the particle surfaces. The resultant Raman scattering signal is far stronger than for nanoparticles without protective silica shells.

Similar results have been reported by Natan and coworkers [50], who prepared 'glass coated, analyte-tagged' (GAN) nanoparticles for use in multiplexed bioassays. As shown in Figure 10.3, the Raman active tag is first combined with metal

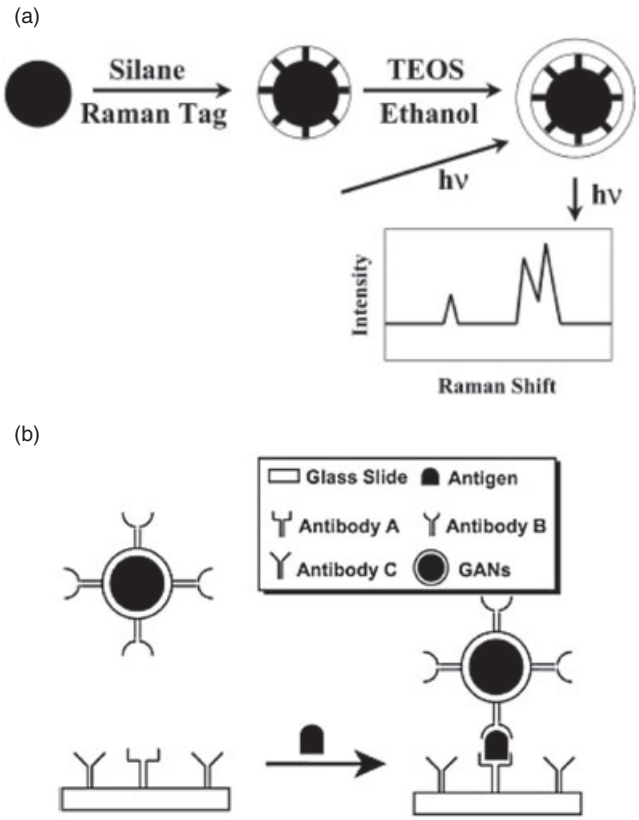

Figure 10.3 (a) Schematic of 'glass coated, analyte-tagged' (GAN) nanoparticle synthesis, and the spectral activity in Raman scattering; (b) Schematic of a modified GAN acting as a reporter antibody in an immunoassay. Reproduced with permission from Ref. [50]; © 2003, The American Chemical Society.

core nanoparticles, followed by a glass shell and silica shell coating. When the SiO_2 shell of the metal core-silica shell nanoparticle and a planar surface are both conjugated with target-specific antibodies, the addition of an antigen will result in a 'sandwich immunoassay'. The characterization of a specific antigen is revealed by the Raman spectrum of the GAN label, with the acquaintance of which antigen an antibody-conjugated GAN is coded. Multiplexed assays have been achieved by conjugating GANs that have different Raman tags with antibodies for recognizing different antigens. The narrow bandwidth of the Raman spectra allows multiple tags to be monitored simultaneously, with high spectral resolution. Furthermore, all tags can be examined with one excitation source, and consequently photobleaching is no longer a problem in Raman spectroscopic studies. Thus, Raman tag-labeled nanoparticles are capable of providing highly sensitive spectroscopic information. In this situation, the silica-coated metallic core colloidal structure reported here has several advantages as a biomarker. First, it is biocompatible and exhibits enhanced Raman scattering signals. Second, it easily undergoes surface modification with a variety of functional groups. Moreover, in certain cases, an increase in the emission quantum yield of the dye molecules has been observed upon incorporating gold or silver metallic nanoparticles as cores.

Adsorption onto rough metal surfaces offers the chance of increasing the Raman intensities of molecules. In contrast to the SPR band of gold nanoparticles (which occurs at 520 nm), silver nanoparticles have an SPR band at 400 nm, which falls within the range of absorption bands for most organic dyes [52]. As a result, the extinction coefficient of silver nanoparticles, which have a narrower SPR band, is almost fivefold higher than that of gold nanoparticles. Moreover, the zeta-potential of silver nanoparticles is less negative than that of gold due to the use of borohydride and citrate during synthesis [51]. In other words, it is much easier for negative analytes, such as oligonucleotides, to be adsorbed onto the surface of silver nanoparticles. This combination of superior characteristics leads to silver nanoparticles having an even wider range of applications than gold nanoparticles, especially in the areas of SERS spectroscopy or nonlinear optical responses for current advanced research.

Nevertheless, the Raman tags reported above suffer from the disadvantage of being unstable when they are dispersed in various solvents or analyte solutions. While studying gold nanoparticle-based Raman tags, a solution to this problem was first provided by Doering and colleagues [49], and also by Natan *et al.* [50]. In both reports, the Raman dyes and gold cores were simultaneously encapsulated inside silica shells. In the case of silver-based Raman tags, a similar solution to the problem was provided by Gong *et al.* [53] via reverse micelle synthesis. This technology employed a surfactant, Igepal CO-520 (polyoxyethylene nonphenyl ether), an aqueous solution of silver nitrate, and isothiocyanate-terminated rhodamine mixtures as the water pool. Compared to the other approaches reported elsewhere, the main advantage proposed here was simplicity, by avoiding the tedious pretreatment steps during the preparation process.

The great potential of silver-based SERS detection in immunoassay has been demonstrated by the same group [54]. Here, a sandwich-type immunoassay

was performed between polyclonal antibody-functionalized Ag/SiO_2 Raman nanoprobes and monoclonal antibody-modified silica-coated magnetic nanoparticles. In this study, rhodamine B isothiocyanate as a Raman tag was embedded in the shell of Ag/SiO_2 core-shell nanoparticles, and synthesized particles were further conjugated with the polyclonal antibody of goat anti-human α-fetoprotein (AFP), which serves as a tumor marker in the diagnosis of hepatocellular carcinoma. By using rat anti-human AFP monoclonal antibody-conjugated magnetic nanoparticles as the immobilization matrix and separation tools, a simple, sensitive and highly specific immunoassay for human AFP detection was developed based on SERS techniques, as shown in Figure 10.4. Using this strategy, concentrations of human AFP as low as 11.5 $pg\,ml^{-1}$ were detected, with the linear relationship holding up to a concentration of 0.12 $\mu g\,ml^{-1}$.

10.2.3.3 **Enhanced Luminescence Intensity**

In a previous study, metal core nanoparticles were shown to have a quenching effect on nearby fluorescent dyes through a nonradiative energy transfer manner, because of SPR [55]. However, contradictory conclusions have also been drawn in different reports [56, 57]. It has been pointed out that the quantum yield of fluorescent dyes or QDs is increased with the distance from nearby metal core nanoparticles. This opposite result is tentatively attributed to the enhanced local electromagnetic field resulting from SPR. A detailed study of the correlation

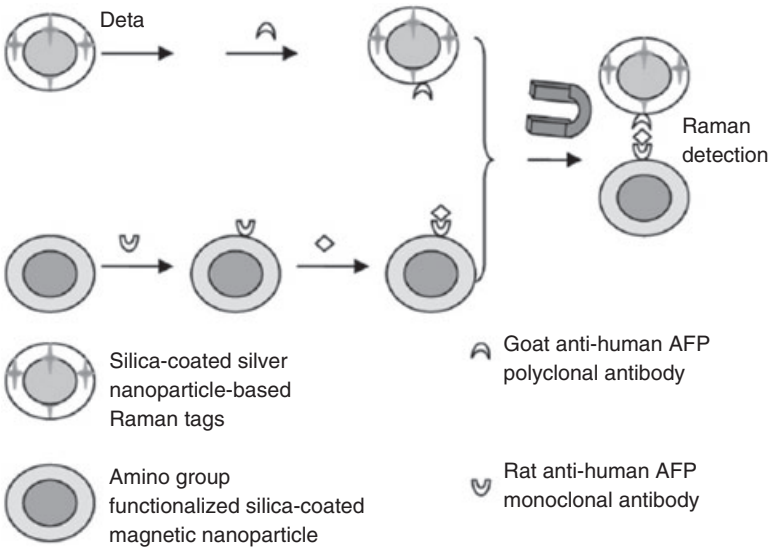

Figure 10.4 A sandwich-type immunoassay of human α-fetoprotein (AFP) using Ag/SiO_2 core-shell nanoparticles embedded with rhodamine B isothiocyanate as SERS tags, and the amino group modified silica-coated magnetic nanoparticle as the immobilization matrix. Reproduced with permission from Ref. [54]; © 2007, Elsevier.

between fluorophore–metal core distances and quenching efficiency was reported by Xu and Tovmachenko *et al.*, and a succinct conclusion was provided, namely that the quenching effects occur only when the fluorophore–metal core distances range from 1 to 16 nm [56, 57]. By using silica-coated gold or silver nanoparticles as a testing model with controllable shell thickness, a testing platform with variable fluorophore–metal core distances was established by Tovmachenko *et al.* [57]. In the case of silver core nanoparticles, a 12.5-fold increase in quantum yield and a shortened radiative lifetime of fluorescent dyes was observed when the fluorophore was 24 nm from the nearby metal cores. However, only a 6.8-fold increase was found in the case of gold core nanoparticles under the same conditions. According to Tovmachenko *et al.*, a shortened radiative lifetime also reflects an increase in transition probability, for example, absorbance. A similar study, using FITC, was carried out by Xu *et al.* [56]. Here, the shortest possible distance between FITC and metal cores was achieved, as FITC can be anchored directly onto the surface of silver nanoparticles via an isothiocyanate (N=C=S–) functional group. In this way, a tunable thickness of silica shells that ranged from 0 to almost 90 nm was extensively studied, as shown in Figure 10.5. For example, a 4.8-fold increase

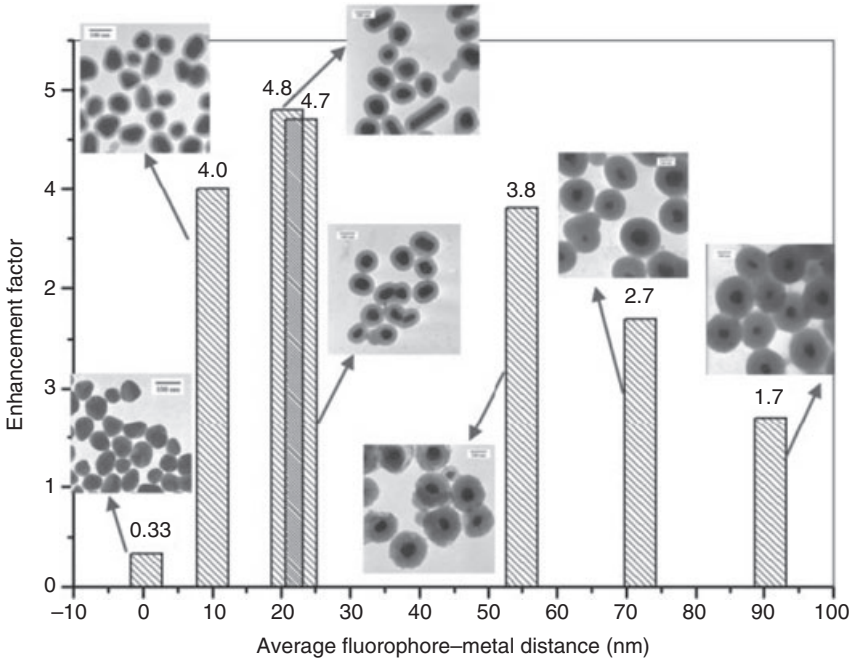

Figure 10.5 Correlations of fluorescence enhancement and distances between organic dyes and Ag nanoparticles. The fluorophore–metal distances were measured from the center of the second SiO_2 layer to the edge of the Ag nanoparticles. Corresponding TEM images are shown in the insets. Reproduced with permission from Ref. [56]; © 2007, The Royal Society of Chemistry.

in quantum yield was seen to occur when the distance between the FITC and the metal core was 21 nm. Although the amplification of emission yields was poorer than previously reported, the calculated correlations in these two related studies matched very well. Hence, Ag/SiO_2-dye core-shell nanocomposites have been proven to have great potential as enhanced fluorescence labels in, for example, single-molecule imaging or bioanalysis.

At this point it is worth noting that a similar theory arose in the case of Au/CdSe and Au/SiO_2/CdSe nanomaterials. For Au/CdSe, some degree of success has been achieved, although the optical emission enhancement via surface plasmon–quantum dot (SP–QD) coupling is rather limited (less than fivefold). It has been shown by Hsieh *et al.* that the SPR-based enhancement and the quenching effect each followed different mechanisms [58]. It was suggested that the quenching effect resulted from an electron-transfer process in which electrons are drawn from CdSe QDs to the Fermi level of gold nanoparticles, thus lowering the quantum yield. Yet, it has also been shown that such enhancement is related to the increase in QD excitation due to locally enhanced electromagnetic fields. Such a finding clarifies any previous ambiguity regarding the control of the emission intensity of semiconductor nanocrystals when coupled with surface plasmon waves. Klimov *et al.* demonstrated similar phenomena by using a Au/SiO_2/CdSe system, in which the photoluminescence intensity of QDs depended on the shell thickness, with quenching for 5 nm thickness but enhancement for 24 nm [59]. Two explanations have been proposed for the distance-dependent light-emitting properties of QDs. The mechanism, as referred to above, is based on an electric field enhancement due to local plasmon excitation and the suppression of photoluminescent blinking, followed by a more effective QD excitation [60]. However, the related mechanisms remain a matter of debate.

10.2.4
Coating Silica Gold Nanorods

According to theoretical predictions, the characteristic band of gold nanoparticles should shift to a longer wavelength as the aspect ratio increases [61]. One-dimensional (1-D) gold nanoparticles exhibit an extremely high extinction coefficient and an absorption capability in the NIR region. In terms of practical application, gold nanorods may be used as a contrast agent in a laser opto-acoustic imaging system for *in vivo* studies [62]. The feasibility of the system lies in the fact that gold nanorods, when compared to gold nanoparticles or nanoshells, have a stronger optical absorption, and this results in detectable acoustic waves upon pulse laser irradiation [10]. Today, several frequently used protocols are available for gold nanorod synthesis. First, Wang and coworkers synthesized gold nanorods with aspect ratios ranging from 3 to 8 by using electrochemical methods with a cationic surfactant such as CTAB as a shape-inducing agent [63]. Second, gold nanorods can also be synthesized via seed-mediated growth methods in the presence of cationic surfactants [64]. In recent studies, CTAB has been shown to exhibit cytotoxicity in *in vitro* viability tests, which also implies that it might cause major problems in

biomedical applications [65]. When excess CTAB is removed, however, the agglomeration of gold nanorods is inevitable, and consequently a range of other substitutes, including polyethyene glycol (PEG), poly(sodium-4-styrenesulfonate) (PSS) and methoxy-polyethylene glycol thiol (mPEG-thiol) have been adopted in order to reduce cytotoxicity whilst maintaining the dispersive properties [66]. In yet another approach, a multistep procedure has been applied for CTAB substitution. This method is accomplished by first forming an intermediate layer upon coating the gold nanorods with polystyrene (PS), PVP or PSS, followed by the addition of MPTES to form the basic silica shell layer. The Stöber method is then used to increase the thickness of the SiO_2 shell under a water/alcohol cosolvent system, yielding the final product as nanorod/SiO_2 core-shell colloids (see Figure 10.1d) [22]. Gold nanorods or nanoparticles are well known to have high photothermal conversion efficiencies under an NIR laser source [10], a property which should facilitate, for instance, drug delivery systems suited for photothermal therapy.

10.2.5
Silica-Encapsulated Platinum

Because of their very high surface-to-volume ratios, high surface energy and excellent adsorption of reactants, platinum nanoparticles have been prepared and developed for investigations into catalysis and sensing techniques [67]. As an example, Han and coworkers prepared larger platinum nanoparticles (~50 nm) by aggregating smaller nanoparticles; the Pt/SiO_2 nanocomposite was then prepared following silica-coating and dye-incorporation, under cocondensation with the dye [(3-dansylaminopropyl) trimethoxysilane] and the silica precursor TEOS [68]. The goal of this research was to use the Pt/SiO_2 nanocomposite to investigate the dye-releasing mechanism, and possibly also to further explore the same mechanism in a drug-releasing process. The Pt/SiO_2 with dye-loaded silica spheres was 'shrunken' under aqueous conditions at pH 11 and 50 °C to reduce the shell thickness from 110 to 20 nm, and to cause a red shift of the dye emission. But, with the temperature held constant, when the pH was lowered to 7.4 the shell's dissolution rate became slower and the dye-releasing efficiency was attenuated to almost 50% of that displayed at pH 11 (Figure 10.6). This unique size-sensitive absorbance resonance in the dye-loaded Pt/SiO_2 suggested the possibility of using amorphous silica as vectors for target loading and controlled release. Both, mesoporous and hollow silica spheres also showed attractive characteristics for target-loading and controlled-release studies. Some further details of hollow silica nanoparticles with Pt infills will be outlined later in this chapter.

10.3
Silica-Coated Quantum Dots

During the past two decades, luminescent nanoparticles made from type II–VI or III–V semiconducting materials – known as QDs – have attracted vast interest.

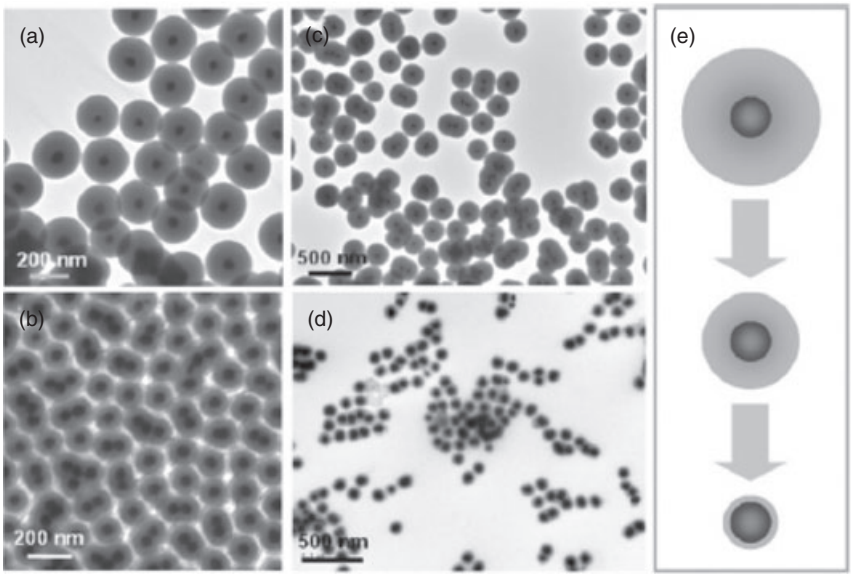

Figure 10.6 Transmission electron microscopy image of Pt/SiO_2 luminescent nanoparticles (LPNs), demonstrating successful reduction of the silica shell from (a) ~110 nm to (b) ~50 nm in radius after treatment at pH 11 and 50 °C for 12 h. An even more noticeable silica shell reduction on dansylamide-loaded Pt/SiO_2 LPNs occurred, from (c) ~110 nm to (d)~20 nm in radius, after treatment at pH 11 and 50 °C for 48 h; (e) Schematic representation of the dissolution process for silica shells reduction. Reproduced with permission from Ref. [68]; © 2007, Wiley.

These QDs, which feature large extinction coefficients, narrow emission widths and high photostability, have been widely exploited in a variety of different fields, including bioimaging and biosensing [69].

The following sections include details of the synthetic strategy and the advantage of coating QDs with silica, a layer of which will reinforce the stability and attenuate the cytotoxicity of QDs under physiological conditions. Although the exact mechanisms involved remain controversial, the principle of silica encapsulation of both hydrophobic and hydrophilic QDs are also discussed.

10.3.1
The Advantages of Coating QDs with Silica

The synthetic routes of QDs have been improved continuously since their discovery. As an example of reagent choice, highly toxic dimethyl cadmium [$Cd(Me)_2$] was replaced by CdO as the precursor of CdSe nanoparticles [70]. Much effort has been expended to render QDs soluble and functional in aqueous buffer solutions for use in biomedical applications. For example, hydrophilic ligands such as mercaptopropionic acid (MAA) can be used to replace hydrophobic trioctylphosphine oxide (TOPO) and hexadecylamine (HDA) ligands on naked QD surfaces, and

subsequently transfer the QDs from an oil phase into an aqueous phase [71]. Since not all hydrophilic ligands work equally well, the type of ligand used must be chosen carefully, as free Cd^{2+} is known to be highly toxic [4]. Shiohara *et al.* have conducted a cytotoxicity evaluation on three mercaptoundecanoic acid (MUA)-coated CdSe/ZnS QDs (520, 570 and 640 nm emission) with three different cell lines (Vero cells, HeLa cells and human primary hepatocytes), and highlighted a dose-dependent cytotoxicity after treating the cells with QD concentrations ranging from 0 to 0.4 mg ml^{-1} over a 24 h period [72]. Hoshino *et al.* also showed that, of the three ligands (MUA, cystamine and thioglycerol) applied to the CdSe/ZnS QDs, the MUA-coated quantum dots exhibited the greatest degree of toxicity [73]. Such evidence of different toxicities with different ligands indicates that toxicity is exerted not only at the core but also at the surface ligand. A possible solution to this problem was proposed by Chan and coworkers after witnessing the liberation of Cd from hydrophilic ligand-coated CdSe QDs during a biological experiment [74]. In order to prevent the release of photo-oxidized Cd, Chan *et al.* coated a layer of ZnS on the outside of the CdSe, and then transferred this nanocomposite into an aqueous phase by surface ligand exchange. On examination, it was found that although the ZnS shell could slow the photoinduced oxidation of the QDs, a complete prevention of Cd ablation was impossible. Although ZnS shells can successfully reduce the cytotoxicity of CdSe, they are less effective than SiO_2 shells. Selvan *et al.* were the first to realize that SiO_2/CdSe QDs were less cytotoxic than either MAA- or PA-coated QDs, and subsequently found that SiO_2/ZnS–CdSe QDs were even less cytotoxic than SiO_2/CdSe QDs [75]. These findings suggested that ZnS capping, combined with a SiO_2 coating, could provide the optimum protection against CdSe dissolution. Likewise, SiO_2 with a low gas permeability could prevent surface oxidization, the result of which causes luminescent quenching.

Silica can also prevent nonspecific adsorption onto the surface and offer more versatile modification routes than can water-soluble ligands, as the silane-coupling agent encloses more functional groups such as thiol, phosphonate and amine. Water-soluble semiconductors (e.g., CdSe/CdS, CdTe) can be improved drastically through silanization via removal of the dynamic stabilizer system (e.g., MAA) and replacement with a permanent silica shell [76].

Finally, by comparison with hydrophilic ligands, silica shell is more inert and stable in aqueous solution, which in turn renders silica-coated nanocrystals soluble in buffer solutions over a wide range of pH values, even at high salt concentrations (up to 200 m*M*), without any loss of their native core-shell structures and optical properties [77]. Under physiological conditions, the silica-coated nanocrystals have demonstrated greater stability than those nanoparticles coated with hydrophilic ligands.

10.3.2
Different Types of Silica-Coated QDs

10.3.2.1 Hydrophobic QDs

In 1998, Alivisatos and colleagues demonstrated the formation of a thin SiO_2 shell layer outside QDs, and used this successfully for *in vivo* bioimaging [78]. Most

QDs/SiO_2 are synthesized using the reverse micelles method; common cores include CdTe, PbSe, CdSe/ZnS and CdSe/CdS/ZnS, and the shell is usually made from SiO_2 [79–84]. In yet another approach, Ying proposed a microemulsion method to convert a hydrophobic ligand (e.g., TOPO or HAD) -coated CdSe and CdSe/ZnS QDs into hydrophilic versions (see Figure 10.8a) [75]. Ying believed that the surfactant Igepal CO-520, when used in the reverse micelles system, could partially or even completely replace the TOPO ligand outside the QDs, allowing transfer of the QDs to the water pool for silanization. Nann performed a detailed investigation on the reaction conditions of a reverse micelles QDs/SiO_2 method, and subsequently proposed two plausible routes by which the QDs could be coated with silica in a reverse micelle system [83]. The corresponding mechanisms are depicted in Figure 10.7. First (and similar to the earlier proposal of Ying *et al.*), the surfactants can interact with QD surfaces via van der Waals forces and form a bilayer to bring QDs into the reverse micelles. However, certain flaws are apparent in this assumption: (i) the magnitude of QDs per silica nanoparticle should increase as the QD concentration is increased, although such a prediction was not observed; (ii) all QDs appeared to be localized at the center of the silica ball, as if

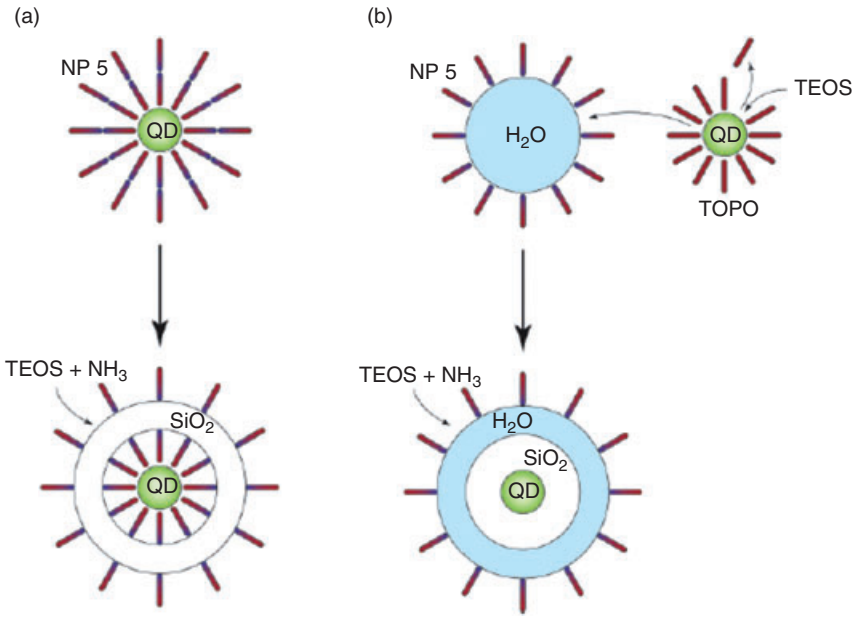

Figure 10.7 Schematic representations of two possible silica deposition mechanisms onto QDs. (a) Silica growth without ligand exchange; (b) Replacement of QD surface surfactant by TEOS, followed by transfer into a reverse micelle water pool before silica coating. Reproduced with permission from Ref. [83]; © 2005, The American Chemical Society.

the silica were grown from QD seeds. Alternatively, the second assumption presumes that the exchange mechanism takes place at the surface of the QDs when the QDs and TEOS are mixed in the presence of an ammonia catalyst. For example, TEOS might exchange with the TOPO ligand of hydrophobic QDs and subsequently transfer them to the hydrophilic phase of the microemulsion for a sol–gel reaction. The absence of a tense 'transition layer' (as verified with transmission electron microscopy; TEM) made the second assumption more convincing.

Both, PbSe and CdTe/CdSe core-shell nanoparticles have excitations and emissions in the NIR region, which is of great benefit for *in vivo* bioimaging. The NIR region is a window where tissues have a low self-absorption and auto-fluorescence, thus allowing excellent deep imaging in organisms with minimum photo-induced damage [85]. However, as is the case for CdSe, PbSe contains a toxic heavy metal (Pb^{2+} ion) that represents a potential threat to living organisms. To date, two groups have successfully encapsulated PbSe inside SiO_2; a TEM image of the $PbSe/SiO_2$ nanoparticles is shown in Figure 10.8b [80, 81]. Although this type of process can be used to reduce the cytotoxicity of PbSe, none of the methods has yet been able to retain the NIR emission after silica coating.

10.3.2.2 **Hydrophilic QDs**

Previously, $CdCl_2$ or $Cd(ClO_4)_2 \cdot 6H_2O$ and NaHTe or H_2Te have been used to produce water-soluble CdTe QDs [86]. Unlike other types of QD, which are easily quenched in aqueous solution, hydrophilic CdTe QDs feature a strong emission. Nevertheless, their high cytotoxicity and difficulties in modification remain the most significant drawbacks [87]. By using a hydrophilic CdTe core and SiO_2 coating, Gao obtained single core per shell luminescent nanoparticles (see Figure 10.8c) [79]. In contrast to the Stöber method, which incorporates the encapsulation of inorganic nanomaterials into an aqueous system, Gao proposed a new method to prepare single core per shell QDs using a reverse micelles system. According

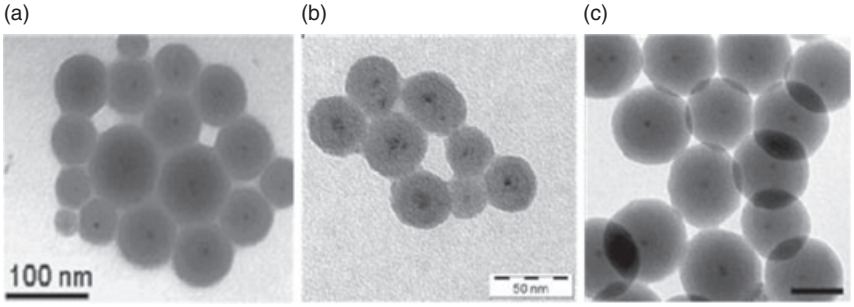

Figure 10.8 Transmission electron microscopy images of nanoparticles after coating with (a) SiO_2; (b) $CdSe/ZnS/SiO_2$; (c) $PbSe/SiO_2$; and (d) $CdTe/SiO_2$. Scale bar = 50 nm. Parts (a), (b) and (c) reproduced with permission from Refs. [75], [80] and [79], respectively; © Wiley and The American Chemical Society.

to Gao, the single core per shell QD phenomenon can be rationalized by the interplay of electrostatic forces. The pH of the system was 11 when NH_4OH was added for catalysis, and such a high pH resulted in a negative charge on the CdTe surface and an electrostatic repulsion between the CdTe particles. Due to this repulsion, only a few CdTe particles would be left in the water-pool, and consequently only one CdTe core would be encapsulated in each SiO_2 ball.

In an effort to improve the low product yield of the microemulsion method, Bakalova and coworkers synthesized CdSe/CdS/ZnS with a high quantum yield (QY) of >30% [84]. Based on the modified layer-by-layer (LBL) method, Bakalova's group sequentially added docusate sodium salt, *n*-octyltriethoxysilane (OTS) and triethoxyvinylsilane (TEVS) for the coating. As a result, the as-prepared QDs retained strong luminescence properties, which were used to demonstrate a bioimaging ability *in vitro* due to a high biocompatibility (see Figure 10.9). The LBL method is believed to form a hydrophobic environment of the micelle to stabilize the QDs and hence increase the QY of the QDs/SiO_2. Recently, Koole *et al*. used a similar reverse micelle system to prepare CdSe/ZnS, PbSe and water-soluble CdTe particles, their aim being to study the SiO_2 coating mechanism [88]. During SiO_2 coating, a time-resolved method was used to measure the change in QD luminescence, while the affinity present at the interface of the surfactant (TEOS) and the QDs was found to weaken their emission. It was also found that purification of the TEOS could abate the level of quenching during the coating process, although the QDs remained heavily quenched after an extended period of time. Based on a (time-resolved) fluorescence spectroscopy analysis, Koole *et al*. discovered that both TEOS and ammonia could alter the QD surfaces and cause quenching. The same group then designed a core-shell-shell structure to increase the thickness of the inorganic shell from 6.4 nm to 7.7 nm, thus enhancing the surface

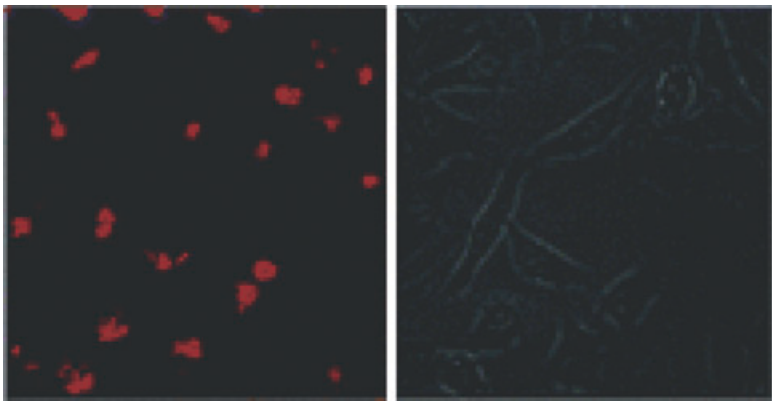

Figure 10.9 Fluorescence confocal microscopy images showing intracellular delivery of silica-shelled single CdSe/CdS/ZnS QD micelles in viable HeLa cells. Left: red fluorescence emissions from the nanoparticles internalized by the cells. Right: corresponding transmission image of intact HeLa cells showing no alternation in cell morphology after treating with the nanoparticles. Reprinted with permission from Ref. [84]; © 2006, The American Chemical Society.

passivation of CdSe during silica coating and preserving a 24% QY in aqueous solution [88]. An enhancement of the QY and a reduction in cytotoxicity continue to be the focal points of recent publications. For example, Alivisatos and coworkers determined that a concentration of up to 80 n*M* PEG-silane-coated QDs was virtually harmless to cells, with minimal apoptosis/necrosis indicated by gene expression measurements [89]. In addition, very few human fibroblast genes showed significant changes under exposure at 8 to 80 n*M*. The ultimate goal of QD research is to eliminate their toxicity, to exploit their unique luminescence properties and, ultimately, to replace the organic dye in the field of bioimaging.

10.4
Silica-Encapsulated Magnetic Nanoparticles

In this section we continue to survey the synthetic improvement of silica encapsulation techniques on different magnetic core compositions, namely pure metal, metal alloy and metal oxide. The main advantage of silica composites is their inertness, which prevents adverse tissue reactions when in contact with the human body; for example, silica implants have been used clinically for breast augmentation in women. Magnetic core nanoparticles play an indispensible role in the area of MRI contrast enhancement. Moreover, by conjugating them with different functional materials, such as sorbents, antibodies, dyes or photosensitizers via the silica shell, the use of these multifunctional hybrid materials can be extended into areas such as optical celullar imaging, photodynamic therapy and drug delivery (see Section 10.4.3).

In comparison to the commonly used metal oxides, nanoscale superparamagnetic metal materials usually have higher magnetizations [90]. For example, the magnetizations of both Co_3O_4 (2.4 emu g^{-1}) and Fe_3O_4 (70–80 emu g^{-1}) are much weaker than that of Co nanoparticles (~162.5 emu g^{-1}) and Fe nanoparticles (~221.9 emu g^{-1}) [3, 91]. Nickel is another extreme case, since NiO – with its antiferromagnetic properties – has a net magnetization close to zero, whereas the Ni nanoparticle has a magnetization up to 57.5 emu g^{-1} [5, 92]. Because a detectable signal under an external magnetic field is extremely valuable in biomedical diagnosis, numerous attempts have been made to synthesize silica-coated magnetic nanoparticles. By using APTES and TEOS as silica precursors, Kobayashi *et al.* first reported the synthesis of monodisperse and amorphous silica-coated cobalt nanoparticles in aqueous solution (Figure 10.10a) [93]. In the same study, the ability of silica shells to prevent cobalt metal from oxidization during high temperature annealing was also demonstrated.

Immediately following the debut of silica-coated cobalt nanomaterial synthesis, a synthetic approach towards silica-encapsulated α-Fe nanocrystals was reported by Tartaj *et al.* [94]. This protocol began with the synthesis of water-soluble iron oxide nanoparticles incorporated with a reverse microemulsion technique. An appropriate amount of the surfactant Igepal CO-520 was added in order to form a water pool. Iron oxide nanoparticles inside the water pool were then embedded

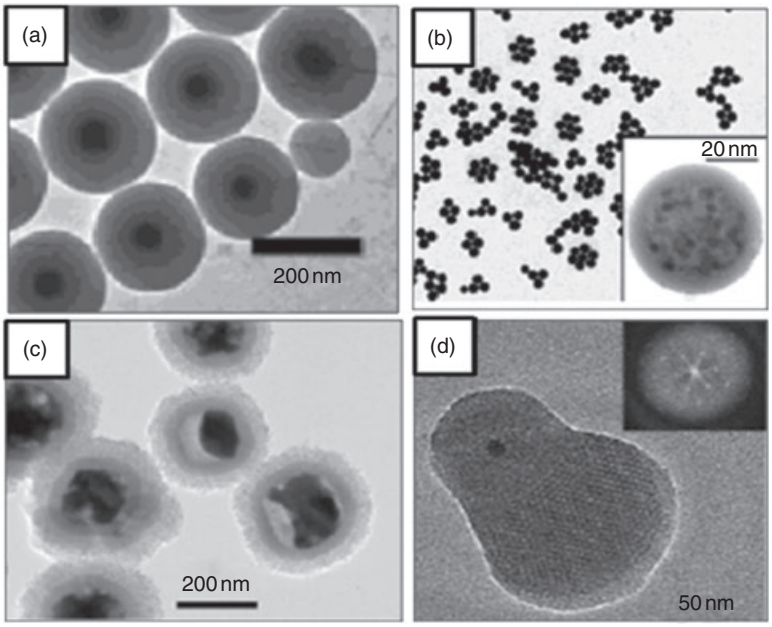

Figure 10.10 Transmission electron microscopy images of amorphous silica coating with: (a) Co core; (b) Fe core; the inset shows single Fe/SiO_2 nanoparticles, where the Fe nanocrystals are embedded in the silica shell; the dark spots correspond to nanoparticles with an R-Fe metallic core; (c) additional mesoporous silica shell on Fe/SiO_2; and (d) a mesoporous nanoparticle with Fe_3O_4/SiO_2. Reproduced with permission from Refs [93–96]; © The American Chemical Society.

in silica nanoparticles under high-temperature hydrogen gas, such that the core was reduced back to iron. As a result, air-stable, monodisperse and superparamagnetic nanomaterials were synthesized (Figure 10.10b).

Another development that has received much attention is the ordered mesoporous materials, first discovered in 1992 [97]. Based on their unique properties of uniform pore size, large pore volume and high surface area, mesoporous materials have been broadly applied in the study of catalysis, separation and drug delivery [97]. The combination of mesoporous materials with magnetic nanoparticles is relatively new, and has become the subject of increasing numbers of reports. It might be possible to combine the advantages of mesoporous silica and magnetic nanoparticles to fabricate a nanocomposite with a high surface area and magnetic susceptibility. Accordingly, it may be feasible to develop a novel adsorbent material and a targeted drug delivery matrix that carries the drug directly to a specific organ or location in the body under an external magnetic field.

The successful synthesis of uniform magnetic metal iron/mesoporous-silica core-shell nanoparticles was first reported by Shi *et al*. [95]. In their study, simultaneous sol–gel polymerization (also called the Stöber process) of TEOS and *n*-octadecyltrimethoxysilane (C_{18}TMS) was carried out after the hematite core

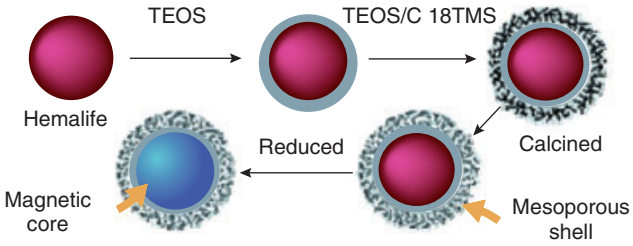

Scheme 10.1 Schematic representation of the synthesis of a mesoporous silica shell on Fe/SiO_2. (Reproduced with permission from Ref. [96]; © 2005, The American Chemical Society.)

(γ-Fe_2O_3) had been synthesized. The organic group of C_{18}TMS served as the porogen during the growth process of the mesoporous layer (Figure 10.10c), and pores were found to be arranged randomly in the mesoporous silica shell following the removal of C_{18}TMS. The hematite core could then be reduced to a metallic state with H_2, forming a uniform mesoporous silica-shell-coated magnetic core nanomaterial of approximately 270 nm diameter. The overall synthetic route is illustrated in Scheme 10.1.

By combining magnetic labeling with optical labeling in mesoporous silica shells, advanced nanocomposites were further developed by Kim *et al.* [98]. In this process, following a thorough mixing of water-insoluble iron oxide and semiconductor nanoparticles (CdSe/ZnS), the sol–gel reaction was carried out and successfully transferred into the water phase, in the presence of CTAB. Any excess CTAB was removed by acetone extraction, yielding a final product of mesoporous silica spheres embedded with monodisperse magnetic and semiconductor nanocrystals. The as-prepared mesoporous nanocomposites were capable of drug delivery. In another report, the prototypical synthesis of a mesoporous silica shell was also applied to coating the surface of nonporous silica with iron oxide nanoparticles [99]. As a result, a well dispersed LBL nanostructure was constructed, designated $Fe_3O_4@n SiO_2@m SiO_2$. (*n:* non-porous; *m:* mesoporous).

In another approach, Lin and coworkers combined mesoporous nanomaterials with nonporous silica-coated iron oxide nanoparticles in a coalescent manner [96]. In their study, multifunctional mesoporous nanoparticles were prepared by adding the organic dye (*N*-1-(3-trimethoxy-silylpropyl)-*N*-fluoresceyl thiourea (FITC-APTES) and nonporous silica-coated iron oxide nanoparticles to an ammonia solution containing dilute TEOS and a low concentration of CTAB. Self-assembled silicate micelles (SSMs) were formed when diluted TEOS was added to an ammonium solution. As the TEOS and FITC-APTES were hydrolyzed in the presence of CTAB, mesoporous silica was further deposited on the surfaces of the SSMs. Simultaneously, the nearby nonporous silica-coated iron oxide nanoparticles coalesced with the SSMs, forming tumbler-like structures. Up to two silica-coated iron oxide nanoparticles on the same mesoporous silicate nanoparticle were observed by TEM (Figure 10.10d). Despite having different synthesis schemata,

this composite mesoporous magnetic nanomaterial is capable of both *in vitro* magnetic resonance and optical imaging studies.

10.4.1 Silica-Coated Alloy Metal Nanoparticles

Whilst magnetic metal core nanoparticles, such as Fe and Co, have been encapsulated with a silica shell and used as biolabeling agents, iron–platinum (FePt) has also attracted much attention because of its smaller size, easily modified characteristics and superparamagnetic properties. In the year 2000, a chemical synthesis toward FePt alloy nanoparticles was explored by Sun *et al.* at IBM, with such research being considered a significant breakthrough in the field of alloy nanomaterials synthesis [100]. It should also be noted that FePt nanoparticles possess a chemically disordered *fcc* structure, and are magnetically soft when deposited. However, they may not necessarily return to a dispersed colloidal state upon removal of the external field, and this results in a consequent particle aggregation.

In oil-phase synthesis, FePt nanoparticles are generally stabilized with alkyl carboxylic acid (RCOOH) and alkylamine (RNH_2). The carboxylic terminal can covalently link to Fe, forming an iron carboxylate (–COO–Fe) framework; in contrast, a primary amine (as an electron donor) prefers to bind on Pt via a coordination bond [101]. The thiol group has also been demonstrated as a good coupling functional group in the phase-transfer process of iron-containing nanoparticles. As a result, a variety of thiol-functionalized, water-soluble ligands, such as 11-mercaptoundecanoic acid and 3-mercaptopropionic acid [102], have been used for phase transfer, making FePt nanoparticles more applicable to biomedical applications. Tsang and coworkers added excess MPTES (a mercaptosilane coupling agent) to FePt colloids to displace the oleic acid and oleylamine stabilizers on the FePt surface [103]. MPTES–FePt underwent further sol–gel reaction to form FePt/SiO_2, a material which displays several advantages, as noted in Tsang's study [103]. First, its magnetization of 70.81 emu g^{-1} is higher than the general published data on FePt nanoparticles, which are usually not high enough to be used as MRI contrast agents. Second, the silica coating helps to lower any interparticle magnetic interactions, which should be avoided during the synthesis of magnetic nanomaterials. Following the transfer of FePt nanoparticles from the oil to water phase, the reverse micelles technique is commonly applied in the process of silica shell formation [104]. As illustrated in Figure 10.11, the thickness of the SiO_2 shell can easily be controlled by adjusting the TEOS concentration. Hence, following this protocol permits the synthesis of a monodisperse FePt/SiO_2 core-shell structure.

Several studies of FePt nanoparticles aimed at biomedical applications have been reported. One interesting approach focused on the capture and rapid detection of vancomycin-resistant enterococci (VRE) and other Gram-positive bacteria, by the addition of FePt nanoparticles at a concentration of ~15 colony-forming units ml^{-1} [105]. In another study, FePt/CoS_2 core-shell nanostructures were reported to have a latent potential as anticancer nanotherapies. Here, when the

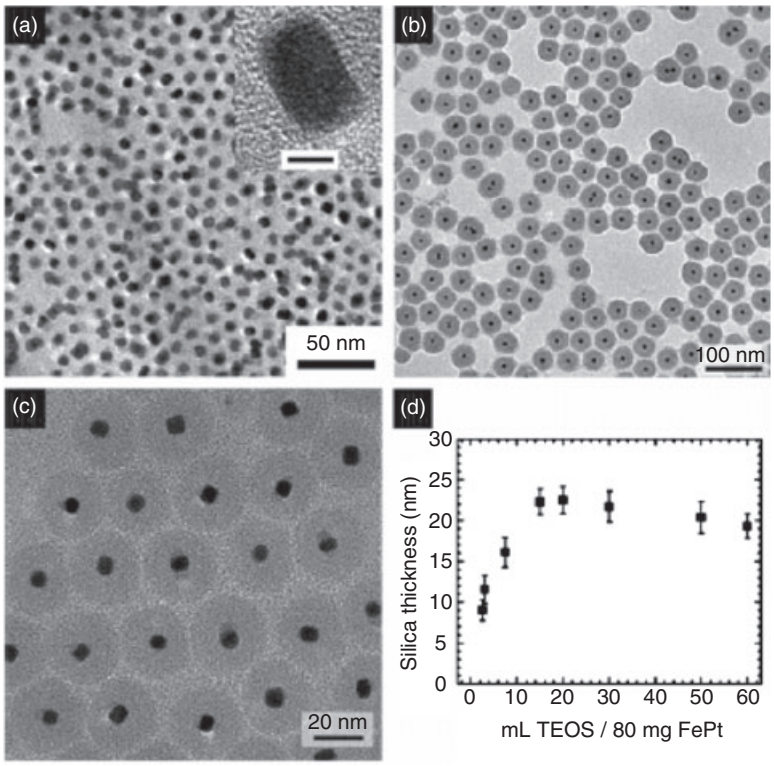

Figure 10.11 (a) Transmission electron microscopy (TEM) images of a bare FePt nanocrystal (for inset, scale bar = 3 nm; (b, c) TEM images of FePt with a SiO_2 coating; (d) concentration-dependence of silica shell thickness on TEOS concentration. Reprinted with permission from Ref. [104]; © 2006, The American Chemical Society.

iron in the FePt core is oxidized within an acidic environment inside the cells, the released Pt^{2+} ions may enter the nucleus and/or mitochondria, inducing apoptosis by binding to double-stranded DNA [106]. The key to this proposal is to have degradable – or at least permeable – shell components for certain molecules or ions. Other hybrid FePt bifunctional nanoparticles, including FePt–CdS [107], FePt–CdSe [108], FePt–Au [109] and FePt–ZnS [110], have recently been shown to possess both optical and magnetic properties that might be applicable to imaging systems.

A great deal of effort has been expended in the development of easily dispersed silica encapsulated FePt nanomaterials with a high coercivity and large saturated magnetization. An easily encapsulating silica shell would prevent FePt nanoparticle aggregation during annealing. Although the magnetization could be enhanced through annealing, the accompanying high coercivity would result in a higher noise level during MR imaging. Moreover, the dehydrated silica surfaces would

make silica-coated FePt nanoparticles difficult to transfer into the water phase. Similar silica coating procedures have also been carried out in alloy materials such as CoPt nanoparticles, the synthesis of which is feasible under either water or oil phase. In a water-phase synthesis, the cobalt and platinum cations were simultaneously reduced by sodium borohydride ($NaBH_4$), with the consequent formation of alloy nanoparticles [111]. In 2003, an oil-phase preparation of $CoPt_3$ nanoparticles was reported by Shevchenko *et al.* [112] where, in the case of water-soluble CoPt alloy nanoparticles, an active silica shell was synthesized through amine-terminated silane coupling agents (e.g., APTES), followed by application of the Stöber method for further encapsulation [113]. In addition to this bottom-up synthesis, a one-step, top-down fabrication of silica-coated CoPt nanoparticles has also been achieved by using a laser ablating technique [114]. By applying such techniques, nanocomposites composed of magnetic CoPt cores covered with amorphous silica shells have been successfully fabricated. However, very few cases have recently been reported that are relevant to the biomedical applications of CoPt core or $CoPt/SiO_2$ core-shell nanoparticles.

10.4.2
Silica-Coated Magnetic Metal Oxide Nanoparticles

Most currently available T_1 contrast agents used in MRI are based on gadolinium chelates. Based on a practical standpoint, Gd^{3+} provides seven unpaired electrons that are capable of interfering with the motion of the H_2O molecule [115, 116], with the most popular gadolinium chelates being Gd-DTPA (diethylenetriamine-penta-acetic acid) and Gd-DOTA (1,4,7,10-tetraazacyclododecane-1,4,7,10-tetraacetic acid) [117, 118]. Recently, Roux and coworkers showed that Gd_2O_3 nanoparticles encapsulated in SiO_2 shells, and with a PEG-modified surface, might be useful as an MRI contrast agent *in vivo* (see Figure 10.12) [119]. Because positive (r_1) contrasting agents rely on the direct interaction of the paramagnetic ion with water, their performance is mainly determined by the amount of water molecules that interact with the surface ions.

Gd_2O_3/SiO_2 was shown to generate a higher r_1 signal compared to a commercial Gd-complex at the same concentration, because the magnitude of r_1 does not only depend solely on the Gd^{3+} ions present at the surface of the crystalline core, but also partially on those inside. Roux and coworkers subsequently conjugated APTES with FITC (an organic dye), to prepare an APTES-FITC silane precursor that they then attached to the Gd_2O_3/SiO_2 shell to produce a bifunctional Gd_2O_3/SiO_2 nanocomposite. When injected intravenously into a nude mouse, these particles could then be imaged using fluorescence reflectance imaging, as shown in Figure 10.13.

The use of a SiO_2 shell has several benefits. First, a silica shell can effectively prevent the leakage of Gd ions; second, the shell can easily be modified compared to complex ligands such as DOTA and DTPA. Multifunctional nanoparticles can be constructed by conjugating dyes, antibodies or other molecules via the functional groups on the silica surface. For example, nanoparticles combined with a

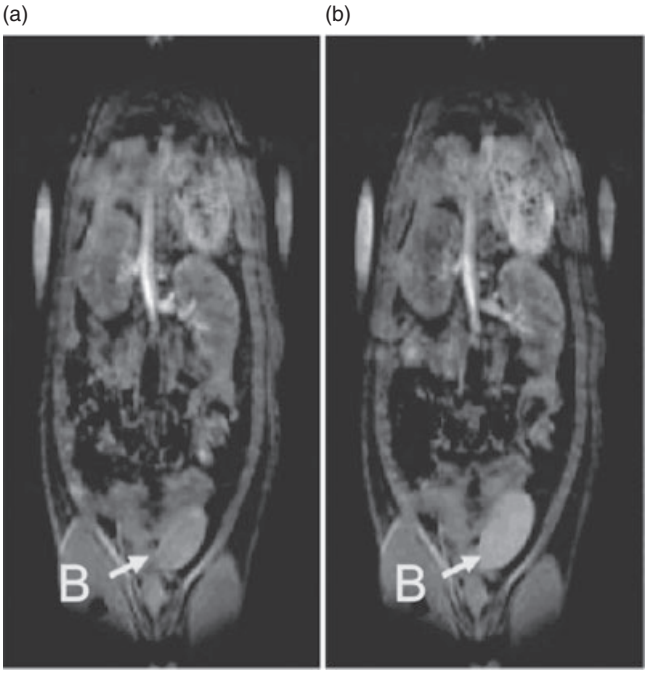

Figure 10.12 T_1-weighted magnetic resonance imaging of a rat (a) before and (b) at 1 h after Gd_2O_3/SiO_2-PEG injection. 'B' indicates the location of the bladder. Reproduced with permission from Ref. [119]; © 2007, The American Chemical Society.

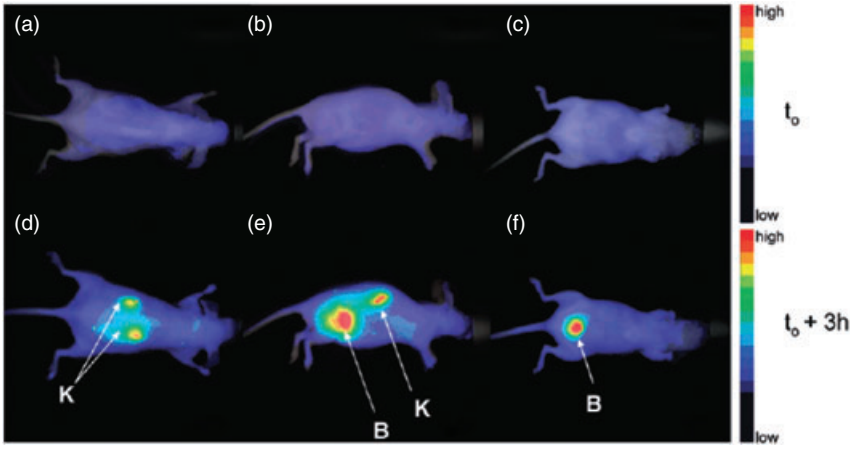

Figure 10.13 Fluorescence reflectance imaging of a nude mouse (a–c) before and (d–f) after 3 h after Gd_2O_3/SiO_2-PEG injection (K = kidneys; B = bladder). Each image was captured with an exposure time of 200 ms. Reproduced with permission from Ref. [119]; © 2007, The American Chemical Society.

magnetic core and a fluorescent dye have received much attention as they can combine high spatial resolution MRI with highly sensitive fluorescence. Here, while florescence detection is highly sensitive and selective, MRI serves as a valuable and complementary method for deep *in vivo* imaging due to poor penetration-depth of light. In fact, the use MRI has achieved prominence in diagnostic clinical medicine, owing to the possibility of obtaining highly resolved three-dimensional images of living organisms [120].

The Mn^{2+}-based MRI contrast agents have been limited to oral forms due to their poor safety rating when monitored in animal models [121]. However, recent studies have shown that Mn^{2+} could be applied safely for brain imaging. Consequently, Hyeon recently extended his expertise with MnO nanoparticles by developing a new method of preparing MnO nanoparticles via the thermal decomposition of a Mn–oleate complex under a nonpolar organic solvent [122]. After transferring the MnO nanoparticles to aqueous phase, either by ligand exchange [123] or silica encapsulation, T_1 enhancement of the MRI signal was successfully obtained; in this respect, silica encapsulation was less popular as the enhancement proved to be smaller [124]. Although the detailed mechanism underlying the use of MnO nanoparticles in MRI contrast enhancement requires further investigation, it is highly possible that paramagnetic Mn^{2+} ions on the surface of the nanoparticles account for a shortening of the T_1 relaxation times.

Compared to T_1 contrast agents, the T_2 agents are composed of metal ions. The clinical application of T_2 contrast agents for MR imaging is that of organ specificity, such that a differentiation can be made between benign and malignant liver tumors. Many reports have focused on the use of silica-embedded iron oxide nanoparticles as a contrast agent in MRI [125]. Both, silica- and alkoxysilane-coated ultrasmall superparamagnetic iron oxide particles have been used to label immortalized progenitor cells [126]. Compared to particles coated with silica, (3-aminopropyl)trimethoxysilane and *N*-(2-aminoethyl)-3-aminopropyl]trimethoxysilane silica-coated iron oxide particles exhibit the highest T_2 relaxivity ($\sim 339.80 \pm 0.22\,s^{-1}\,mM^{-1}$) and are the most effective (in terms of iron load, at 42.1 ± 4.0 pg per cell). These results show that silica-coated iron oxide represents a good candidate for a contrast medium in bioimaging via MRI. In fact, this nanocomposite may provide a tool for both cell therapy and cell biology, due to its easy surface modification from the silica shell. The multifunctional role of this single nanoparticle forms the basis of its widespread use in popular biomedical nanotechnologies [127].

Compared to the SiO_2 coating on semiconductor materials, which prevents the leakage of toxic heavy metals, the SiO_2 coating on magnetite or maghemite nanoparticles (MNPs) cores opens the opportunity for surface modification [22]. From a multifunctional aspect, MNPs/SiO_2 materials are much more versatile than their metal core counterparts [125]. Although the use of iron oxide is popular due to a negligible cellular toxicity, many investigators have extended such use by incorporating MNPs/SiO_2 with other materials such as dyes [128] and photothermal [129] or photodynamic agents [130]. Initially, an adequate – but less direct – method was proposed based on previous experience with surface modification on

pure metals. The coating of amine groups onto the surface of silica-coated magnetite nanoparticles was therefore developed using the condensation of APTES [125]. However, most investigators were dissatisfied with these problematic steps, which included the treatment of a silica coupling agent to silanize the nanoparticle surface. Fortunately, it was soon realized that the presence of hydroxyl functional groups on the metal oxide surface eased the process, such that the use of a coupling agent was no longer necessary [131]. Several methods for the preparation of superparamagnetic iron oxide silica nanocomposites have been reported, including aerosol pyrolysis [132], miniemulsion [133], active silica [18] and reverse micelles [134, 135]. Among these methods, reverse micelles have proved to be the most popular. Whilst appreciating that surfactants can stabilize water molecules in a 'water-in-oil' system to generate a nanoscale water pool, it is also possible to transfer iron oxide nanoparticles from an oil phase into the water pool for sol–gel silica coating. The resultant particles have a size distribution in the range of 30 to 120 nm diameter, which is smaller than for particles prepared using aerosol and/or miniemulsion methods. Although the exact mechanism of core-shell formation in a reverse micelles system has yet to be elucidated, it is generally believed that the reaction starts from the surface interaction of hydrophobic MNPs and TEOS. By the time ammonia is added to the system, the TEOS will have been hydrolyzed and the MNPs transferred from oil phase into the water pool by the newly formed surface hydroxyl group. The MNPs in the water pool will then act as seeds for the subsequent sol–gel silanization. The reverse micelles system will also work well for hydrophobic MNPs, which have been reported to have a layer of silica coated on the spinal ferrite nanoparticles of $CoFe_2O_4$ [136]. Recently, not only hydrophobic but also hydrophilic MNPs were brought into the water pool and acted as seeds for more silica precursors to condense. It should be noted here that hydrophilic MNPs are easier to handle, as the phase-transfer step is omitted [137].

10.4.3
Applications of Silica-Coated Magnetic Nanoparticles

10.4.3.1 Forming Hybrid Materials with Optic Materials Dopant

Iron oxide–silica nanoparticles with a fluorescent signal have also been synthesized by integrating organic dyes into the silica shells, using a modified sol–gel procedure. Although MRI provides a radiation-free and penetration depth-free modality for imaging, the contrast is much poorer than with optical probes, such as fluorescent dyes or proteins. However, optical probes have limited applications for *in vivo* imaging due to their limited body tissue penetration depth and limited resolution. Consequently, dual imaging probes that combine MRI and optical characteristics might provide advantageous applications in biomedical fields such as biolabeling, bioimaging, cell sorting, separation and *in vivo* imaging. The SiO_2 encapsulation of these functional nanoparticles is necessary, since the SiO_2 not only serves as a barrier to prevent solvent-collision and photo-oxidation from oxygen, but also preserves the fluorescence intensity of the organic dyes [138]. Other reports have highlighted the fact that SiO_2 prevents quenching that results

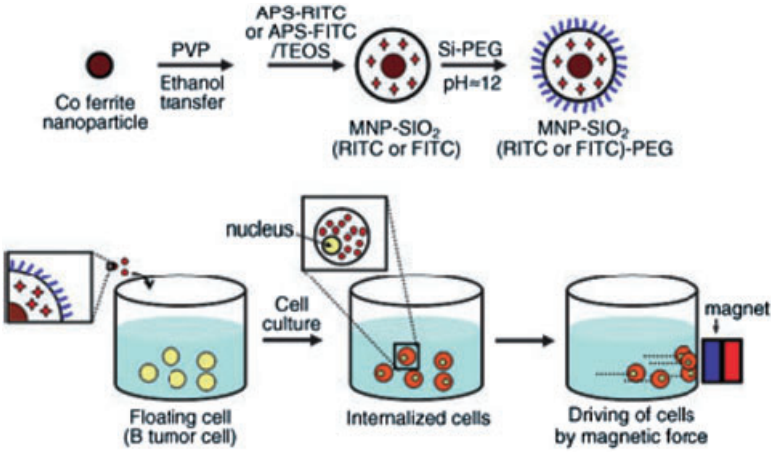

Figure 10.14 Cartoon of MNPs-SiO_2 (RITC)-PEG synthesis and its potential use for cell separation. Reprinted with permission from Ref. [140]; © 2005, Wiley.

from a direct contact between the dye and the MNPs [128]. As a consequence, dyes are usually included in the SiO_2 layer of MNPs/SiO_2 to prevent any quenching effect due to either the MNP cores or the surrounding solvent. In order to achieve such a design in synthesis, dye-modified silyl functional groups are normally prepared by combining APTES and a dye–isothiocyanate (e.g., FITC or RITC (rhodamine isothiocyanate) to form a dye–APTES [139]. Addition of the dye–APTES to the middle of the sol–gel SiO_2 coating leads to a polymerization of the dye–APTES on the SiO_2 shell surface, and the subsequent formation of fluorescent, magnetic bifunctional nanoparticles. A similar approach has been utilized to prepare silica-coated luminescent cobalt ferrite magnetic nanoparticles ($CoFe_2O_4$), for which the mechanism is presented in Figure 10.14 [140].

In addition to integrating dyes such as RITC or FITC into the amorphous silica shell, a surface modification by coating another layer of PEG and antibody immobilization ($Ab_{CD\text{-}10}$ or $Ab_{HER\text{-}2}$), capable of the specific recognition of floating tumor cells, has also been reported [141]. According to these authors, the biocompatible PEG layer – which improved cellular uptake of the nanoparticles and provided an ability to monitor movement of the doped cells under an external magnetic field (see Figure 10.15) – might be valuable for bioseparation and related applications. Other groups, including Farle and coworkers, took advantage of these high-QY and emissions-tunable QDs, and developed a LBL method to assemble CdTe QDs in the MNPs/SiO_2 shell [142]. A microemulsion synthesis to prepare MNPs-QDs/SiO_2 was also reported (see Figure 10.16) [143] in which the QDs and γ-Fe_2O_3 nanoparticles were added to the reaction solution simultaneously. Ammonium hydroxide and TEOS were then added for the sol–gel reaction, after which the silica nanoparticle-embedded QDs and γ-Fe_2O_3 were subsequently obtained. The QY of the QDs was greatly decreased following the silica coating, however. This

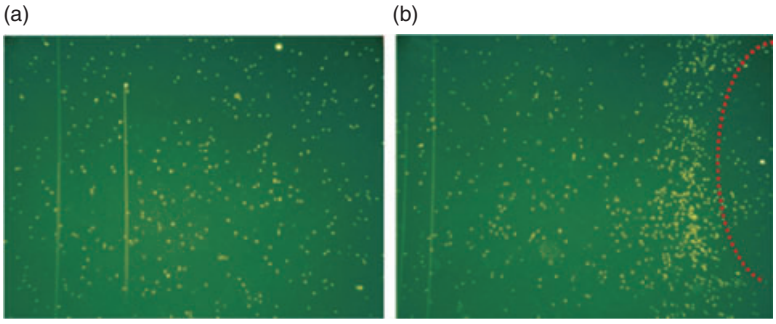

Figure 10.15 Demonstration of a biocompatible magnetic nanocomposite in bioapplication. The mobilization of MNPs/SiO_2 (FITC)-$Ab_{CD\text{-}10}$ treated SP2/0 floating cells (white dots, 10–20 mm) was achieved in the presence of an external magnetic field. The $Ab_{CD\text{-}10}$ antibody permits specific targeting towards SP2/0 cells, while the FITC dye allows the process to be monitored with optical microscopy. (a) Without magnetic field; (b) with magnetic field. The location of the magnet is marked by the red dot circle. Reprinted with permission from Ref. [141]; © 2006, Wiley.

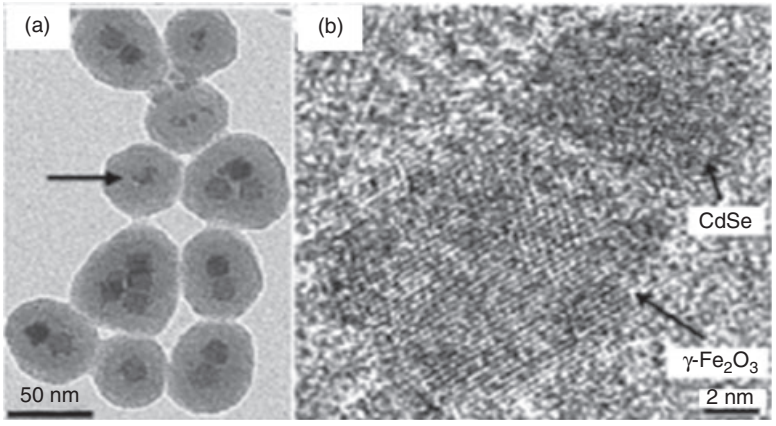

Figure 10.16 (a) SiO_2/MNPs-QDs nanocomposites prepared by the microemulsion method; (b) High-resolution TEM image of the area marked by the arrow in panel (a), showing the presence of both CdSe QDs and γ-Fe_2O_3 MNPs. Reproduced with permission from Ref. [143]; © 2005, The American Chemical Society.

core-shell hybrid, with its unique optical properties and magnetic moieties attributable to the QDs, demonstrated great potential in targeting and bioimaging applications.

Photodynamic therapy (PDT) – which may also be referred to as photoradiation therapy, phototherapy or photochemotherapy – has emerged as an important area in preclinical research and clinical practice [144]. Its therapeutic effect is based on

a chain reaction resulting from excitation of the photosensitizer. When the photosensitizing agent has absorbed sufficient energy, the molecules are promoted from the ground state to a highly unstable excited state. The excited molecules, after intersystem crossing, reside at the triplet state and can transfer their remaining energy to tissue oxygen to generate singlet oxygen ($^1O_2$), which has a very short lifetime (<0.04 μs) and a low mobility (<0.02 μm) [145]. As any excessive reactive oxygen species (ROS), such as singlet oxygen, free radicals and peroxides, are extremely toxic towards cells, the physician can preconcentrate a photosensitizing agent at the tissue of interest, and then apply photoexcitation to create an induced apoptosis [146]. Since, in the absence of light exposure, the photosensitizing agents are harmless to cells, the location of cellular damage can be much more precisely controlled than with conventional surgery. Porphyrine and its derivatives serve as excellent photosensitizers, as their excited states can interact with molecular oxygen to generate cytotoxic singlet oxygen [147]. However, as a photodynamic therapy will lose its purpose if the photosensitizing agent is not delivered to a desired location, it is necessary to conjugate photosensitizers with peptides and antibodies for the active targeting of cell-surface receptors or other biomolecules.

PDT agents have also been encapsulated within silica nanoparticles to solve the problem that most existing photosensitizers are hydrophobic, and aggregation is extensive under physiological conditions [148]. Such silica encapsulation provides additional benefits to the PDT agent, as further chemical medications become possible. For example, Rossi and coworkers have prepared a nanoparticle-based drug carrier composed of a magnetic core and a silica layer containing the PDT drug methylene blue, entrapped in the silica matrix [149]. Chou and coworkers also attached an iridium complex photosensitizer onto a ZnS-capped QD, and demonstrated its PDT effect on cancer cells. The outstanding performance of QDs in optical detection and Ir-complex formation in PDT make Ir–CdSe/ZnS nanocomposites an attractive tool in biomedicine [150]. Chou subsequently duplicated his success, and attached an iridium-complex photosensitizer onto the silica surface of an iron oxide core [130]. The unique point of this study was the artful use of iridium-complex emission. Due to a short radiative lifetime, the efficiency of bimolecular O_2 quenching of the iridium-complex emission was approximately 85%, which left 15% as phosphorescence. As a result, this hybrid material featured trifunctional moieties of MRI, phosphorescence and singlet oxygen generation. Subsequent *in vitro* testing demonstrated the apoptosis of cancer cells treated with Fe_3O_4/SiO_2(Ir) nanoparticles and photodynamic therapy (see Figure 10.17).

Owing to the multifunction capabilities of hybrid silica nanoparticles, several research studies have been conducted into the combination of imaging and drug delivery. In order to enrich the functionality of MNPs/SiO_2, some investigators have taken advantage of the easily modified silica surface by preparing a thin silica layer that was coated onto the magnetic core and served as a platform for APTES–FITC conjugation [151]. They then modified the surface with MPS to generate terminal C=C bonds on the surface of the FITC-labeled magnetic silica microspheres. Here, MPS can act as a polymerization activator while, with aid of potas-

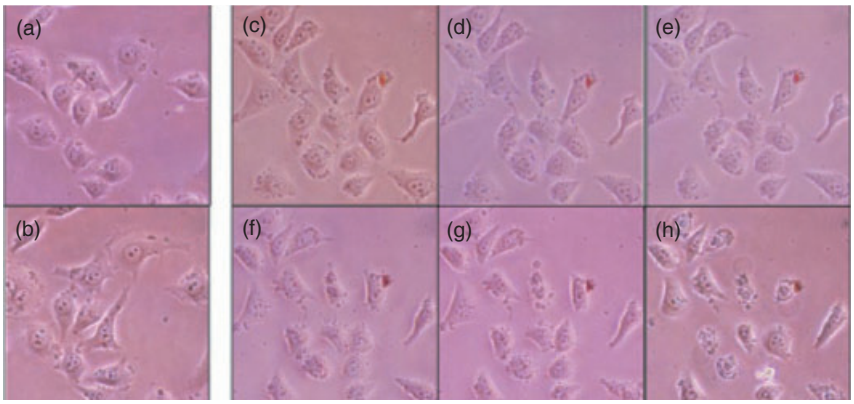

Figure 10.17 Cells treated with 100 mg ml^{-1} Fe_3O_4/SiO_2(Ir) were monitored with light microscopy after photodynamic treatment. Control group without light exposure: (a) 0; (b) 480 min; with light exposure: (c) 0; (d) 90; (e) 180; (f) 210; (g) 390; and (h) 480 min. Reprinted with permission from Ref. [130]; © 2008, Wiley.

sium persulfate (KPS), a polymerization initiator NIPAM (*N*-isopropylacrylamide, monomer) can be coated on top of the MNPs/SiO_2. As the NIPAM shell has a temperature-dependent affinity towards doxorubicin (DOX, a hydrophilic antitumor drug), MNPs/SiO_2–NIPAM can be used for drug delivery. This represents a prototypical example of a multi-stimuli-responsive microsphere with a fluorescence-labeled magnetic core and a thermoresponsive shell.

10.5
Hollow Silica Spherical Structures

While the previous sections have focused on silica shells with filled cores, hollow-sphere structures can also provide distinct advantages in the areas of catalysis and drug delivery. In the following sections, we describe the synthetic development of unique hollow-sphere Au and Pt nanoparticles.

10.5.1
Au and Pt Nanoparticles in Hollow Spheres

Hollow nanomaterials are modern materials that are lightweight; have a low density, entail lower production costs and also have double surface areas – all of which are suitable properties for catalysts, biosensors and drug delivery agents [152, 153]. The generation of a hollow core is usually achieved by coating a thin shell of a desired material onto the surfaces of spherical colloids made from inorganic ceramics, polymers or their hybrids, followed by selective removal of the core via calcination or chemical etching in solution [154]. Although many types of

metallic core can be embedded inside silica nanoparticles for bioapplications, attention has focused recently on one especially interesting study of the development of metallic cores within hollow SiO_2 balls. As an example, the 'yolk-shell' structure of Au is a popular catalyst because of its easy dispersion and separation within reaction mixtures. In catalytic reactions which favor a large metallic support (e.g., the reduction of *p*-nitrophenol to *p*-aminophenol by $NaBH_4$), Au/SiO_2 yolk-shell nonreactors offer reaction rates which may be 10-fold greater than are provided by their Au/SiO_2 core-shell counterparts [155]. This gain in catalytic efficiency is mainly contributed by a partial removal of the silica obstruction in the original Au/SiO_2 core-shell structure. In addition, the turnover frequency (TOF) of the reaction is increased fivefold, from 6.6 to 36 s^{-1}, when the core diameter is reduced from 104 to 43 nm. Multiple edges, high surface roughness and several defect sites on the metal core surface, resulting from stepwise etching, are believed to be the causes of such high levels of activity. The Au/SiO_2 yolk-shell structure is created by a selective etching of the Au cores from the silica-coated particles (Figure 10.18), the mechanism of which is shown in Scheme 10.2. Here, the average dimension of the metal cores can be modulated by employing different amounts of etching agent, such as KCN [154]. The size of the Au core is related to the overall optical properties, as the emission maximum in the UV-visible region is shifted from 594 nm to 587 nm when the core diameter is decreased from 104 to 43 nm; this in agreement with the blue shifts predicted by Mie theory [137]. A higher-activity catalytic metal core (Pt) has been used in the study of nanoreactor framework synthesis, as described below.

In the synthesis of these materials, the Pt metal thin shells are coated onto α-Se cores, followed by coating of the shell with silica. Mixtures of hydrazine, carbon disulfide and alcohol are then used to dissolve the Se from the silica-coated material, leaving the Pt cores untouched. The resultant structure is a hollow SiO_2 ball with Pt nanoparticles scattered inside, as can be seen using TEM [156]. It should be emphasized here that the alcohol-induced transition from α-Se to *t*-Se allows the slow dissolution of isopropyl alcohol in the applied solvents. As Pt is known to be a high-efficiency catalytic material, silica-coated hollow shells containing Pt nanoparticles may serve as useful catalytic nanoreactors for a variety of organic reactions or biocatalysis. By offering an immense catalytic surface area, the Pt nanoparticles inside the silica shell are able to mitigate and catalyze vigorous reactions that otherwise would be undesirable. In addition, the simple retrieval of such materials by centrifugation or filtration leads to a minimal loss of the expensive catalyst.

QD core-shell systems have also been adopted for hollow-ball structures. Although many reports have been made on coating QDs with SiO_2 to maintain the emission properties and prevent heavy metal leakage so as to reduce cytotoxicity, CdSe/ZnS cores in such core-shell structures were recently shown to be unstable after washing and not to remain inside the silica shell [157]. Yet, such instability provides a simple alternative procedure for the formation of hollow SiO_2 nanoparticles. Nann, who used a microemulsion approach to transform CdSe/ZnS from the oil phase to the aqueous phase via silanization, obtained uniform

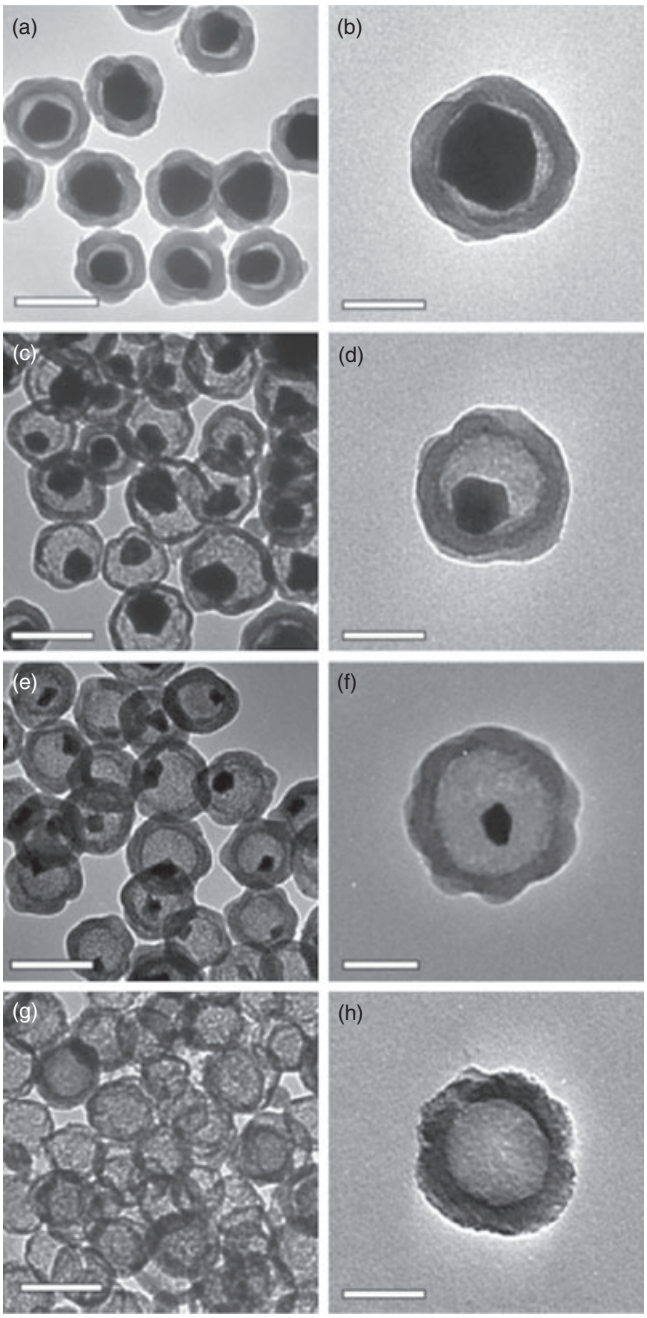

Figure 10.18 Transmission electron microscopy images of Au/SiO_2 'yolk-shell' nanoreactor frameworks of different sizes (a–f) and silica hollow shells (g, h). The gold core diameters are (a,b) 104±9 nm; (c,d) 67±8 nm; (e,f) 43±7 nm. The scale bars represent 200 nm for panels (a,c,e,g), and 100 nm for panels (b,d,f,h). Reproduced with permission from Ref. [155]; © 2008, Wiley.

Scheme 10.2 Scheme of Au/SiO_2 nanoreactor framework synthesis. Reproduced with permission from Ref. [155]; © 2008, Wiley.

semiconductor core/SiO_2 (20~70 nm) with sizes smaller than those produced by the Stöber method, and made several interesting observations on the preparation of hollow silica nanoparticles [157]. Nann showed that the etching of inorganic materials such as CdSe/ZnS inside the SiO_2 shells occurred with an increase in the number of washings. However, experiments conducted by other groups have indicated that several conditions lead to the disappearance of the CdSe/ZnS/SiO_2 semiconductor core. For example, CdSe/ZnS can be dissolved in concentrated ammonia: the pores (average size ~5 Å) on the silica shells are sufficiently large for aqueous ammonia to diffuse through the shell and dissolve the CdSe/ZnS inside. Subsequently, the hollow silica sphere nanoparticles form when the free ions (Cd and Se) have diffused out. Notably, two other conditions can also lead to such a hollow structure:

- The occurrence of hollow silica sphere nanoparticles is often observed immediately after the addition of excessive ammonia as catalyst, although occasionally this may be delayed until after a 3–5 min period of stirring, despite the reaction having reached completion.
- When the stirring is stopped, aqueous ammonia, rather than ethanol, can be used as the washing solvent, to dissolve CdSe/ZnS and to generate the hollow silica sphere nanoparticles; a strong acid (e.g., nitric acid) works equally well in this respect.

This method, which employs QDs as a template, is somewhat more gentle and novel than the use of vesicles, emulsion systems, acoustic cavitations or electrically forced liquid jets, all of which have been reported in detail previously. Such types of hollow silica sphere nanoparticle, which can be prepared in straightforward manner via a homogeneous reaction and functionalized by versatile surface modifications, have great potential in the development of drug-delivery agents.

The template provided by the hollow silica sphere nanoparticles may serve as a growth cavity for gold nanoparticles, thus simultaneously avoiding the need for a stabilizing surfactant and any consequent problems of aggregation. The 'reverse' synthesis of Au cores in hollow silica shells shown in Scheme 10.3 and Figure 10.19 is highly innovative [158], with the added reagents, $HuAuCl_4$ and $NaBH_4$, diffusing through the porous silica and entering into the cavity to form gold

Scheme 10.3 Graphical representation of Au/SiO_2 formation via hollow silica nanoparticles. Reproduced with permission from Ref. [158]; © 2007, The Royal Society of Chemistry.

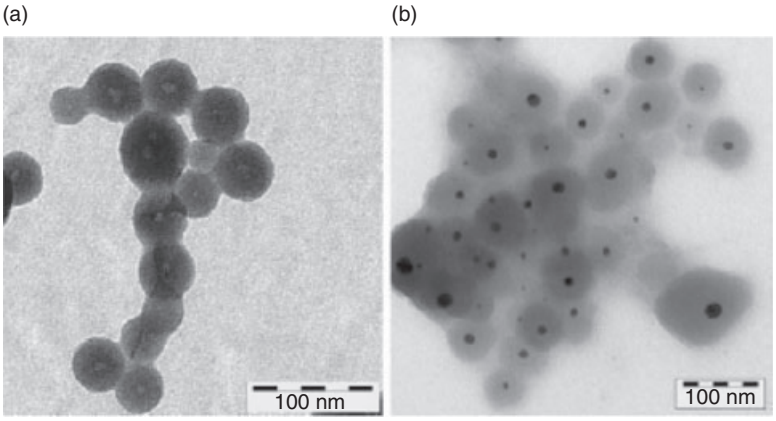

Figure 10.19 (a) Transmission electron microscopy (TEM) image of hollow silica nanoparticles; (b) TEM image of Au/SiO_2 nanocomposites. Reproduced with permission from Ref. [158]; © 2007, The Royal Society of Chemistry.

nanoparticles. The resultant Au/SiO_2 nanoparticles can be extracted by centrifugation.

10.6 Conclusions

By applying a silica coating, a variety of nanomaterials can be used in biocatalysis, bioanalysis or bioimaging. Amid much research progress in this area, it has been shown that not only are these core materials worthy of investigation, but that any surface modification of the silica shell is also critical. Silica shells that can be easily bioconjugated with antibodies or antagonists allow specific targeting, and may also serve as vehicles with different materials either doped inside or anchored on the surface, thus creating a hybrid nanoparticle with multiple functions. Although several reports have shown that silica coatings can induce aggregation at high salt concentrations (this being due to a neutralized surface potential diminishing the electron repulsion between nanoparticles), this problem can be solved simply by

introducing negatively charged ligands at the surface [159]. Yet, this approach is considered controversial, bearing in mind that a negative charge might limit the cellular ingestion of such particles, as the potential at the cell membrane is also negative. Although polymers represent another popular type of surface ligand, they suffer from the apparent impossibility of single nanoparticle modification, which results in undesirable interactions among such nanoparticles when they are in close proximity with one another. Nevertheless, surface modification plays an indispensible role in the application of silica-coated metals, metal oxides and semiconductor nanoparticles.

References

1 LizMarzán, L.M. and Philipse, A.P. (1995) Synthesis and optical properties of gold-labeled silica particles. *Journal of Colloid and Interface Science*, **176**, 459–66.

2 Klostranec, J.M. and Chan, W.C.W. (2006) Quantum dots in biological and biomedical research: recent progress and present challenges. *Advanced Materials*, **18**, 1953–64.

3 Lu, A.-H., Salabas, E.L. and Schuth, F. (2007) Magnetic nanoparticles: synthesis, protection, functionalization, and application. *Angewandte Chemie – International Edition*, **46**, 1222–44.

4 Lewinski, N., Colvin, V. and Drezek, R. (2008) Cytotoxicity of nanoparticles. *Small*, **4**, 26–49.

5 Cai, W.B. and Chen, X.Y. (2007) Nanoplatforms for targeted molecular imaging in living subjects. *Small*, **3**, 1840–54.

6 Pastoriza-Santos, I., Gomez, D., Rez-Juste, J., Liz-Marzán, L.M. and Mulvaney, P. (2004) Optical properties of metal nanoparticle coated silica spheres: a simple effective medium approach. *Physical Chemistry Chemical Physics*, **6**, 5056–60.

7 Enûstûn, B.V. and Turkevich, J. (1963) Coagulation of colloidal gold. *Journal of the American Chemical Society*, **85**, 3317–28.

8 Mulvaney, P. (1996) Surface plasmon spectroscopy of nanosized metal particles. *Langmuir*, **12**, 788–800.

9 Link, S. and El-Sayed, M.A. (2003) Optical properties and ultrafast dynamics of metallic nanocrystals. *Annual Review of Physical Chemistry*, **54**, 331–66.

10 Jain, P.K., Lee, K.S., El-Sayed, I.H. and El-Sayed, M.A. (2006) Calculated absorption and scattering properties of gold nanoparticles of different size, shape, and composition: applications in biological imaging and biomedicine. *The Journal of Physical Chemistry B*, **110**, 7238–48.

11 Elghanian, R., Storhoff, J.J., Mucic, R.C., Letsinger, R.L. and Mirkin, C.A. (1997) Selective colorimetric detection of polynucleotides based on the distance-dependent optical properties of gold nanoparticles. *Science*, **277**, 1078–81.

12 Storhoff, J.J., Elghanian, R., Mucic, R.C., Mirkin, C.A. and Letsinger, R.L. (1998) One-pot colorimetric differentiation of polynucleotides with single base imperfections using gold nanoparticle probes. *Journal of the American Chemical Society*, **120**, 1959–64.

13 Link, S. and El-Sayed, M.A. (1999) Spectral properties and relaxation dynamics of surface plasmon electronic oscillations in gold and silver nanodots and nanorods. *The Journal of Physical Chemistry B*, **103**, 8410–26.

14 Loo, C., Lowery, A., Halas, N., West, J. and Drezek, R. (2005) Immunotargeted nanoshells for integrated cancer imaging and therapy. *Nano Letters*, **5**, 709–11.

15 Kim, J.Y., Lee, J.E., Lee, J.W., Jang, Y.G., Kim, S.W., An, K.G., Jung Ho Yu, J.H. and Hyeon, T.G. (2006) Generalized fabrication of multifunctional

nanoparticle assemblies on silica spheres. *Angewandte Chemie–International Edition*, **45**, 4789–93.
16 Huang, X., Jain, P.K., El-Sayed, I.H. and El-Sayed, M.A. (2006) Determination of the minimum temperature required for selective photothermal destruction of cancer cells with the use of immunotargeted gold nanoparticles. *Photochemistry and Photobiology*, **82**, 412–17.
17 Grabar, K.C., Allison, K.J., Baker, B.E., Bright, R.M., Brown, K.R., Freeman, R.G., Fox, A.P., Keating, C.D., Musick, M.D. and Natan, M.J. (1996) Two-dimensional arrays of colloidal gold particles: a flexible approach to macroscopic metal surfaces. *Langmuir*, **12**, 2353–61.
18 Lee, P.C. and Meisel, D. (1982) Adsorption and surface-enhanced Raman of dyes on silver and gold sols. *The Journal of Physical Chemistry*, **86**, 3391–5.
19 Liz-Marzán, L.M., Giersig, M. and Mulvaney, P. (1996) Synthesis of nanosized gold-silica core-shell particles. *Langmuir*, **12**, 4329–35.
20 Stöber, W., Fink, A. and Bohn, E. (1968) Controlled growth of monodisperse silica spheres in the micro size range. *Journal of Colloid and Interface Science*, **26**, 62–9.
21 Ung, T., Liz-Marzán, L.M. and Mulvaney, P. (1998) Controlled method for silica coating of silver colloids influence of coating on the rate of chemical reactions. *Langmuir*, **14**, 3740–8.
22 Pastoriza-Santos, I., Pérez-Juste, J. and Liz-Marzán, L.M. (2006) Silica-coating and hydrophobation of CTAB-stabilized gold nanorods. *Chemistry of Materials*, **18**, 2465–7.
23 Bogush, G.H., Tracy, M.A. and Zukoski, C.F. (1988) Preparation of monodisperse silica particles: control of size and mass fraction. *Journal of Non-Crystalline Solids*, **104**, 95–106.
24 Sadasivan, S., Dubey, A.K., Li, Y. and Rasmussen, D.H. (1998) Alcoholic solvent effect on silica synthesis-NMR and DLS Investigation. *Journal of Sol-Gel Science and Technology*, **12**, 5–14.
25 Park, S.K., Kim, K.D. and Kim, H.T. (2002) Preparation of silica nanoparticles: determination of the optimal synthesis conditions for small and uniform particles. *Colloids and Surfaces A: Physicochemical and Engineering Aspects*, **197**, 7–17.
26 Iler, R.K. (1959) U.S. Patent No. 2,885366.
27 Weisbecker, C.S., Merritt, M.V. and Whitesides, G.M. (1996) Molecular self-assembly of aliphatic thiols on gold colloids. *Langmuir*, **12**, 3763–72.
28 Obare, S.O., Jana, N.R. and Murphy, C.J. (2001) Preparation of polystyrene- and silica-coated gold nanorods and their use as templates for the synthesis of hollow nanotubes. *Nano Letters*, **1**, 601–3.
29 Graf, C., Vossen, D.L.J., Imhof, A. and van Blaaderen, A.V. (2003) A general method to coat colloidal particles with silica. *Langmuir*, **19**, 6693–700.
30 Lu, Y., Yin, Y., Li, Z.-Y. and Xia, Y. (2002) Synthesis and self-assembly of Au@SiO_2 core-shell colloids. *Nano Letters*, **2**, 785–8.
31 Santra, S., Bagwe, R.P., Dutta, D., Stanley, J.T., Walter, G.A., Tan, W., Moudgil, B.M. and Mericle, R.A. (2005) Synthesis and characterization of fluorescent, radio-opaque, and paramagnetic silica nanoparticles for multimodal bioimaging applications. *Advanced Materials*, **17**, 2165–9.
32 Li, T., Moon, J.H., Morrone, A.A., Mecholsky, J.J., Talham, D.R. and Adair, J.H. (1999) Preparation of Ag/SiO_2 nanosize composites by a reverse micelle and sol-gel technique. *Langmuir*, **15**, 4328–34.
33 Han, Y., Jiang, J., Lee, S.S. and Ying, J.Y. (2008) Reverse microemulsion-mediated synthesis of silica-coated gold and silver nanoparticles. *Langmuir*, **24**, 5842–8.
34 Van Blaaderen, A. and Vrij, A. (1992) Synthesis and characterization of colloidal dispersions of fluorescent, monodisperse silica spheres. *Langmuir*, **8**, 2921–31.
35 Schroedter, A. and Weller, H. (2002) Ligand design and bioconjugation of colloidal gold nanoparticles. *Angewandte Chemie-International Edition*, **41**, 3218–21.
36 Liu, S.H. and Han, M.Y. (2005) Synthesis, functionalization, and

bioconjugation of monodisperse, silica-coated gold nanoparticles: robust bioprobes. *Advanced Functional Materials*, **15**, 961–7.

37 Liu, S., Zhang, Z. and Han, M.Y. (2005) Gram-scale synthesis and biofunctionalization of silica-coated silver nanoparticles for fast colorimetric DNA detection. *Analytical Chemistry*, **77**, 2595–600.

38 Raman, C.V. and Krishnan, K.S. (1928) A New type of secondary radiation. *Nature*, **121** (3048), 501–2.

39 Fleischmann, M., Hendra, P.J. and McQuillan, A.J. (1974) Raman spectra of pyridine adsorbed at a silver electrode. *Chemical Physics Letters*, **26**, 163–6.

40 Campion, A. and Kambhampati, P. (1998) Surface-enhanced Raman scattering. *Chemical Society Reviews*, **27**, 241–50.

41 Vo-Dinh, T. (1998) Surface-enhanced Raman spectroscopy using metallic nanostructures. *Trends in Analytical Chemistry*, **17**, 557–82.

42 (a) Isola, N.R.; Stokes, D.L. and Vo-Dinh, T. (1998) Surface-enhanced Raman gene probe for HIV detection. *Analytical Chemistry*, **70**, 1352; (b) Allain, L.R. and Vo-Dinh, T. (2002). Surface-enhanced Raman scattering detection of the breast cancer susceptibility gene BRCA1 using a silver-coated microarray platform. *Analytica Chimica Acta*, **469**, 149–54.

43 Graham, D., Mallinder, B.J., Whitcombe, D., Watson, N.D. and Smith, W.E. (2002) Simple multiplex genotyping by surface-enhanced resonance Raman scattering. *Analytical Chemistry*, **74**, 1069–74.

44 Ni, J., Lipert, R.J., Dawson, B. and Porter, M.D. (1999) Immunoassay readout method using extrinsic Raman labels adsorbed on Immunogold colloids. *Analytical Chemistry*, **71**, 4903–8.

45 Cao, Y.W.C., Jin, R.C. and Mirkin, C. (2002) Nanoparticles with Raman spectroscopic fingerprints for DNA and RNA detection. *Science*, **297**, 1536–40.

46 Huang, Q.J., Yao, J.L., Mao, B.W., Gu, R.A. and Tian, Z.Q. (1997) Surface Raman spectroscopic studies of pyrazine adsorbed onto nickel electrodes. *Chemical Physics Letters*, **271**, 101–6.

47 Cao, P.G., Yao, J.L., Ren, B., Mao, B.W., Gu, R.A. and Tian, Z.Q. (2000) Surface enhanced Raman scattering from bare Fe electrode surfaces. *Chemical Physics Letters*, **316**, 1–5.

48 Wu, D.Y., Xie, Y., Ren, B., Yan, J.W., Mao, B.W. and Tian, Z.Q. (2001) Surface enhanced Raman scattering from bare cobalt electrode surfaces. *PhysChemComm*, **4**, 89–91.

49 Doering, W.E. and Nie, S.M. (2003) Spectroscopic tags using dye-embedded nanoparticles and surface-enhanced Raman scattering. *Analytical Chemistry*, **75**, 6171–6.

50 Mulvaney, S.P., Musick, M.D., Keating, C.D. and Natan, M.J. (2003) Glass-coated, analyte-tagged nanoparticles: a new tagging system based on detection with surface-enhanced Raman scattering. *Langmuir*, **19**, 4784–479.

51 Aroca, R.F., Alvarez-Puebla, R.A., Pieczonka, N., Sanchez-Cortez, S. and Garcia-Ramos, J.V. (2005) Surface-enhanced Raman scattering on colloidal nanostructures. *Advances in Colloid and Interface Science*, **116**, 45–61.

52 Jin, R.C., Cao, Y.W. and Mirkin, C.A. (2001) Photoinduced conversion of silver nanospheres to nanoprisms. *Science*, **294**, 1901–3.

53 Gong, J.L., Jiang, J.H., Liang, Y., Shen, G.L. and Yu, R.Q. (2006) Synthesis and characterization of surface-enhanced Raman scattering tags with Ag/SiO_2 core-shell nanostructures using reverse micelle technology. *Journal of Colloid and Interface Science*, **298**, 752–6.

54 Gong, J.-L., Liang, Y., Huang, Y., Chen, J.-W., Jiang, J.-H., Shen, G.-L. and Yu, R.-Q. (2007) Ag/SiO_2 core-shell nanoparticle-based surface-enhanced Raman probes for immunoassay of cancer marker using silica-coated magnetic nanoparticles as separation tools. *Biosensors and Bioelectronics*, **22**, 1501–7.

55 Dubertret, B., Calame, M. and Libchaber, A.J. (2001) Single-mismatch detection using gold-quenched fluorescent oligonucleotides. *Nature Biotechnology*, **19** (4), 365–70.

56 Cheng, D.M. and Xu, Q.-H. (2007) Separation distance dependent fluorescence enhancement of fluorescein isothiocyanate by silver nanoparticles. *Chemical Communications*, 248–50.

57 Tovmachenko, O.G., Graf, C., van den Heuvel, D.J., van Blaaderen, A. and Gerritsen, H.C. (2006) Fluorescence enhancement by metal-core/silica-shell nanoparticle. *Advanced Materials*, **18**, 91–5.

58 Hsieh, Y.-P., Liang, C.-T., Chen, Y.-F., Lai, C.-W. and Chou, P.-T. (2007) Mechanism of giant enhancement of light emission from Au/CdSe nanocomposites. *Nanotechnology*, **18**, 415707.

59 Liu, N.G., Prall, B.S. and Klimov, V.I. (2006) Hybrid gold/silica/nanocrystal-quantum-dot superstructures: synthesis and analysis of semiconductor-metal interactions. *Journal of the American Chemical Society*, **128**, 15362–3.

60 Shimizu, K.T., Woo, W.K., Fisher, B.R., Eisler, H.J. and Bawendi, M.G. (2002) Surface-enhanced emission from single semiconductor nanocrystals. *Physical Review Letters*, **89**, 117401–117401.4.

61 van der Zande, B.M.I., Böhmer, M.R., Fokkink, L.G.J. and Schönenberger, C. (2000) Colloidal dispersions of gold rods: synthesis and optical properties. *Langmuir*, **16**, 451.

62 Eghtedari, M., Oraevsky, A., Copl, J.A., Kotov, N.A., Conjusteau, A. and Motamedi, M. (2007) High sensitivity of in vivo detection of gold nanorods using a laser optoacoustic imaging system. *Nano Letters*, **7**, 1914–18.

63 Yu, Y.-Y., Chang, S.-S., Lee, C.-L. and Wang, C.R.C. (1997) Gold nanorods: electrochemical synthesis and optical properties. *The Journal of Physical Chemistry B*, **101**, 6661–666.

64 Gole, A. and Murphy, C.J. (2004) Seed-mediated synthesis of gold nanorods: role of the size and nature of the seed. *Chemistry of Materials*, **16**, 3633–40.

65 Connor, E.E., Mwamuka, J., Gole, A., Murphy, C.J. and Wyatt, M.D. (2005) Gold nanoparticles are taken up by human cells but do not cause acute cytotoxicity. *Small*, **1**, 325–7.

66 Niidome, T., Yamagata, M., Okamoto, Y., Akiyama, Y., Takahashi, H., Kawano, T., Katayama, Y. and Niidome, Y.J. (2006) PEG-modified gold nanorods with a stealth character for in vivo applications. *Journal of Controlled Release*, **114**, 343–7.

67 Ahmadi, T.S., Wang, Z.L., Green, T.C., Henglein, A. and El-Sayed, M.A. (1996) Shape-controlled synthesis of colloidal platinum nanoparticles. *Science*, **272**, 1924–6.

68 Liu, S.H., Wong, Y.V., Wang, Y.B., Wang, D.S. and Han, M.-Y. (2007) Controlled release and absorption resonance of fluorescent silica-coated platinum nanoparticles. *Advanced Functional Materials*, **17**, 3147–52.

69 Murray, C.B., Noms, D.J. and Bawendi, M.G. (1993) Synthesis and characterization of nearly monodisperse CdE (E = S, Se, Te) semiconductor nanocrystallites. *Journal of the American Chemical Society*, **115**, 8706–15.

70 Peng, Z.A. and Peng, X.G. (2001) Formation of high-quality CdTe, CdSe, and CdS nanocrystals using CdO as precursor. *Journal of the American Chemical Society*, **123**, 183–4.

71 Aldana, J., Wang, Y.A. and Peng, X.G. (2001) Photochemical instability of CdSe nanocrystals coated by hydrophilic thiols. *Journal of the American Chemical Society*, **123**, 8844–50.

72 Shiohara, A., Hoshino, A., Hanaki, K., Suzuki, K. and Yamamoto, K. (2004) On the cyto-toxicity caused by quantum dots. *Microbiology and Immunology*, **48**, 669–75.

73 Hoshino, A., Fujioka, K., Oku, T., Suga, M., Sasaki, Y., Ohta, T., Yasuhara, M., Suzuki, K. and Yamamoto, K. (2004) Physicochemical properties and cellular toxicity of nanocrystal quantum dots depend on their surface modification. *Nano Letters*, **4**, 2163–9.

74 Derfus, A.M., Chan, W.C.W. and Bhatia, S.N. (2004) Probing the cytotoxicity of semiconductor quantum dots. *Nano Letters*, **4** (1), 11–18.

75 Selvan, S.T., Tan, T.T. and Ying, J.Y. (2005) Robust, non-cytotoxic, silica-coated CdSe quantum dots with efficient photoluminescence. *Advanced Materials*, **17**, 1620–5.

76 Gaponik, N., Talapin, D.V., Rogach, A.L., Hoppe, K., Shevchenko, E.V., Kornowski, A., Eychmu1ller, A. and Weller, H. (2002) Thiol-capping of CdTe nanocrystals: an alternative to organometallic synthetic routes. *The Journal of Physical Chemistry B*, **106**, 7177–85.

77 Gerion, D., Pinaud, F., Williams, S.C., Parak, W.J., Zanchet, D., Weiss, S. and Alivisatos, A.P. (2001) Synthesis and properties of biocompatible water-soluble silica-coated CdSe/ZnS semiconductor quantum dots. *The Journal of Physical Chemistry B*, **105**, 8861–71.

78 Bruchez, M., Jr, Moronne, M., Gin, P., Weiss, S. and Alivisatos, A.P. (1998) Semiconductor nanocrystals as fluorescent biological labels. *Science*, **281**, 2013–16.

79 Yang, Y.H. and Gao, M.Y. (2005) Preparation of fluorescent SiO_2 particles with single CdTe nanocrystal cores by the reverse microemulsion method. *Advanced Materials*, **17**, 2354–7.

80 Darbandi, M., Lu, W., Fang, J. and Nann, T. (2006) Silica encapsulation of hydrophobically ligated PbSe nanocrystals. *Langmuir*, **22**, 4371–5.

81 Tan, T.T., Selvan, S.T., Zhao, L., Gao, S. and Ying, J.Y. (2007) Size control, shape evolution, and silica coating of near-infrared-emitting PbSe quantum dots. *Chemistry of Materials*, **19**, 3112–17.

82 Nann, T. and Mulvaney, P. (2004) Single quantum dots in spherical silica particles. *Angewandte Chemie–International Edition*, **43**, 5393–6.

83 Darbandi, M., Thomann, R. and Nann, T. (2005) Single quantum dots in silica spheres by microemulsion synthesis. *Chemistry of Materials*, **17**, 5720–5.

84 Zhelev, Z., Ohba, H. and Bakalova, R. (2006) Single quantum dot-micelles coated with silica shell as potentially non-cytotoxic fluorescent cell tracers. *Journal of the American Chemical Society*, **128**, 6324–5.

85 Michalet, X., Pinaud, F.F., Bentolila, L.A., Tsay, J.M., Doose, S., Li, J.J., Sundaresan, G., Wu, A.M., Gambhir, S.S. and Weiss, S. (2005) Quantum dots for live cells, in vivo imaging, and diagnostics. *Science*, **307**, 538–44.

86 Zhang, H., Zhou, Z. and Yang, B. (2003) The influence of carboxyl groups on the photoluminescence of mercaptocarboxylic acid-stabilized CdTe nanoparticles. *The Journal of Physical Chemistry B*, **107**, 8–13.

87 Lovric, J., Cho, S.J., Winnik, F.M. and Maysinger, D. (2005) Unmodified cadmium telluride quantum dots induce reactive oxygen species formation leading to multiple organelle damage and cell death. *Chemistry and Biology*, **12**, 1227–34.

88 Koole, R., van Schooneveld, M.M., Hilhorst, J., Donegá, C.D., 't Hart, C.D., van Blaaderen, A., Vanmaekelbergh, D. and Meijerink, A. (2008) On the incorporation mechanism of hydrophobic quantum dots in silica spheres by a reverse microemulsion method. *Chemistry of Materials*, **20**, 2503–12.

89 Zhang, T., Stilwell, J.L., Gerion, D., Ding, L., Elboudwarej, O., Cooke, P.A., Gray, J.W., Alivisatos, A.P. and Chen, F.F. (2006) Cellular effect of high doses of silica-coated quantum dot profiled with high throughput gene expression analysis and high content cellomics. *Nano Letters*, **6**, 800–8.

90 Gupta, A.K. and Gupta, M. (2005) Synthesis and surface engineering of iron oxide nanoparticles for biomedical applications. *Biomaterials*, **26**, 3995–4021.

91 Jiang, J. and Li, L.C. (2007) Synthesis of sphere-like Co_3O_4 nanocrystals via a simple polyol route. *Material Letters*, **61**, 4894–6.

92 Roth, W.L. (1958) Magnetic structures of MnO, FeO, CoO, and NiO. *Physical Review*, **110**, 1333–41.

93 Kobayashi, Y., Horie, M., Konno, M., Rodríguez-González, B. and Liz-Marzán, L.M. (2003) Preparation and properties of silica-coated cobalt nanoparticles. *The Journal of Physical Chemistry B*, **107**, 7420–5.

94 Tartaj, P. and Serna, C.J. (2003) Synthesis of monodisperse superparamagnetic Fe/Silica nanospherical composites. *Journal of the American Chemical Society*, **125**, 15754–5.

95 Zhao, W.R., Gu, J.L., Zhang, L.X., Chen, H.R. and Shi, J.L. (2005) Fabrication of uniform magnetic nanocomposite

spheres with a magnetic core/mesoporous silica shell structure. *Journal of the American Chemical Society*, **127**, 8916–17.

96 Lin, Y.-S., Wu, S.-H., Hung, Y., Chou, Y.-H., Chang, C., Lin, M.-L., Tsai, C.-P. and Mou, C.-Y. (2006) Multifunctional composite nanoparticles: magnetic, luminescent, and mesoporous. *Chemistry of Materials*, **18**, 5170–2.

97 Kresge, C.T., Leonowicz, M.E., Roth, W.J., Vartuli, J.C. and Beck, J.S. (1992) Ordered mesoporous molecular sieves synthesized by a liquid-crystal template mechanism. *Nature*, **359**, 710–12.

98 Kim, J.Y., Lee, J.E., Lee, J.W., Yu, J.H., Kim, B.C., An, K.J., Hwang, Y.S., Shin, C.-H., Park, J.-G., Kim, J.B. and Hyeon, T. (2006) Magnetic fluorescent delivery vehicle using uniform mesoporous silica spheres embedded with monodisperse magnetic and semiconductor nanocrystals. *Journal of the American Chemical Society*, **128**, 688–9.

99 Deng, Y.H., Qi, D.W., Deng, C.H., Zhang, X.M. and Zhao, D.Y. (2008) Superparamagnetic high-magnetization microspheres with an Fe_3O_4@SiO_2 core and perpendicularly aligned mesoporous SiO_2 shell for removal of microcystins. *Journal of the American Chemical Society*, **130**, 28–9.

100 Sun, S.H., Murray, C.B., Weller, D., Folks, L. and Moser, A. (2000) Monodisperse FePt nanoparticles and ferromagnetic FePt nanocrystal superlattices. *Science*, **287**, 1989–92.

101 Sun, S.H. (2006) Recent advances in chemical synthesis, self-assembly, and applications of FePt nanoparticles. *Advanced Materials*, **18**, 393–403.

102 Bagaria, H.G., Ada, E.T., Shamsuzzoha, M., Nikles, D.E. and Johnson, D.T. (2006) Understanding mercapto ligand exchange on the surface of FePt nanoparticles. *Langmuir*, **22**, 7732–7.

103 Xin, G., Tam, K.Y., Yu, K.M.K. and Tsang, S.C. (2005) Synthesis and characterization of thiol-capped FePt nanomagnetic porous particles. *Small*, **1**, 949–52.

104 Lee, D.C., Mikulec, F.V., Pelaez, J.M., Koo, B. and Korgel, B.A. (2006) Synthesis and magnetic properties of silica-coated FePt nanocrystals. *The Journal of Physical Chemistry B*, **110**, 11160–6.

105 Gu, H.W., Ho, P.-L., Tsang, K.W.T., Wang, L. and Xu, B. (2003) Using biofunctional magnetic nanoparticles to capture vancomycin-resistant enterococci and other gram-positive bacteria at ultralow concentration. *Journal of the American Chemical Society*, **125**, 15702–3.

106 Gao, J., Liang, G., Zhang, B., Kuang, Y., Zhang, X. and Xu, B. (2007) FePt@CoS_2 yolk-shell nanocrystals as a potent agent to kill HeLa cells. *Journal of the American Chemical Society*, **129**, 1428–33.

107 Gu, H., Zheng, R., Zhang, X. and Xu, B. (2004) Facile One-pot synthesis of bifunctional heterodimers of nanoparticles: a conjugate of quantum dot and magnetic nanoparticles. *Journal of the American Chemical Society*, **126**, 5664–5.

108 Gao, J., Zhang, B., Gao, Y., Pan, Y., Zhang, X. and Xu, B. (2007) Fluorescent magnetic nanocrystals by sequential addition of reagents in a one-pot reaction: a simple preparation for multifunctional nanostructures. *Journal of the American Chemical Society*, **129**, 11928–35.

109 Choi, J.S., Jun, Y.W., Yeon, S.I., Kim, H.C., Shin, J.S. and Cheon, J. (2006) Biocompatible heterostructured nanoparticles for multimodal biological detection. *Journal of the American Chemical Society*, **128**, 15982–3.

110 Gu, H., Zheng, R., Liu, H., Zhang, X. and Xu, B. (2005) Direct synthesis of a bimodal nanosponge based on FePt and ZnS. *Small*, **1**, 402–6.

111 Yu, A.C.C., Mizuno, M., Sasaki, Y., Kondo, H. and Hiraga, K. (2002) Structural characteristics and magnetic properties of chemically synthesized CoPt nanoparticles. *Applied Physics Letters*, **81**, 3768–70.

112 Shevchenko, E.V., Talapin, D.V., Schnablegger, H., Kornowski, A., Festin, O., Svedlindh, P., Haase, M. and Weller, H. (2003) Study of nucleation and growth in the organometallic synthesis of magnetic alloy nanocrystals: the role of nucleation rate in size control of CoPt3 nanocrystals. *Journal of the American Chemical Society*, **125**, 9090–101.

113 Kobayashi, Y., Kakinuma, H., Nagao, A., Ando, Y., Miyazaki, T. and Konno, M. (2008) Synthesis and properties of Co–Pt alloy silica core-shell particles. *Journal of Sol-Gel Science and Technology*, **47**, 16–22.

114 Seto, T., Koga, K., Takano, F., Akinaga, H., Orii, T., Hirasawa, M. and Murayamac, M. (2006) Synthesis of magnetic $CoPt/SiO_2$ nano-composite by pulsed laser ablation. *Journal of Photochemistry and Photobiology A: Chemistry*, **182**, 342–5.

115 Caravan, P. (2006) Strategies for increasing the sensitivity of gadolinium based MRI contrast agents. *Chemical Society Reviews*, **35**, 512–23.

116 Sitharaman, B., Kissell, K.R., Hartman, K.B., Tran, L.A., Baikalov, A., Rusakova, I., Sun, Y., Khant, H., Ludtke, S.J., Chiu, W., Laus, S., Toth, E., Helm, L., Merbach, A.E. and Wilson, L.J. (2005) Superparamagnetic gadonanotubes are high-performance MRI contrast agents. *Chemical Communications*, **31**, 3915–391.

117 Gries, H. and Miklautz, H. (1984) Some physicochemical properties of the gadolinium-DTPA complex, a contrast agent for MRI. *Physiological Chemistry and Physics and Medical NMR*, **16**, 105–12.

118 Dubost, J.P., Leger, J.M., Langlois, M. H., Meyer, D. and Schaefer, M. (1991) Structure of a magnetic-resonance-imaging agent the gadolinium-DOTA complex $C_{16}H_{24}N_4O_8NAGD \cdot 5H_2O$. *Comptes rendus de l'Académie des sciences. Série 2, Mécanique, Physique, Chimie, Sciences de l'univers, Sciences de la Terre*, **312**, 349–54.

119 Bridot, J.-L., Faure, A.-C., Laurent, S., Rivière, C., Billotey, C., Hiba, B., Janier, M., Josserand, V., Coll, J.-L., Elst, L.V., Muller, R., Roux, S., Perriat, P. and Tillement, O. (2007) Hybrid gadolinium oxide nanoparticles: multimodal contrast agents for in vivo imaging. *Journal of the American Chemical Society*, **129**, 5076–84.

120 Salgueiriño-Maceira, V. and Correa-Duarte, M.A. (2007) Increasing the complexity of magnetic core/shell structured nanocomposites for biological applications. *Advanced Materials*, **19**, 4131–44.

121 Silva, A.C., Lee, J.H., Aoki, I. and Koretsky, A.P. (2004) Manganese-enhanced magnetic resonance imaging (MEMRI): methodological and practical considerations. *NMR in Biomedicine*, **17**, 532–5.

122 Park, J., Kang, E., Bae, C.J., Park, J.G., Noh, H.J., Kim, J.Y., Park, J.H., Park, H.M. and Hyeon, T. (2004) Synthesis, characterization, and magnetic properties of uniform-sized MnO nanospheres and nanorods. *The Journal of Physical Chemistry B*, **108**, 13594–8.

123 Dubertret, B., Skourides, P., Norris, D.J., Noireaux, V., Brivanlou, A.H. and Libchaber, A. (2002) In vivo imaging of quantum dots encapsulated in phospholipid micelles. *Science*, **298**, 1759–62.

124 Na, H.B., Lee, J.H., An, K., Park, Y.I., Park, M.H., Lee, I.S., Nam, D.H., Kim, S.T., Kim, S.-H., Kim, S.-W., Lim, K.-H., Kim, K.-S., Kim, S.-O. and Hyeon, T.H. (2007) Development of a T_1 contrast agent for magnetic resonance imaging using MnO nanoparticles. *Angewandte Chemie - International Edition*, **46**, 5397–401.

125 Bruce, I.J. and Sen, T. (2005) Surface modification of magnetic nanoparticles with alkoxysilanes and their application in magnetic bioseparations. *Langmuir*, **21**, 7029–35.

126 Zhang, C., Wängler, B., Morgenstern, B., Zentgraf, H., Eisenhut, M., Untenecker, H., Krüger, R., Huss, R., Seliger, C., Semmler, W. and Kiessling, F. (2007) Silica- and alkoxysilane-coated ultrasmall superparamagnetic iron oxide particles: a promising tool to label cells for magnetic resonance imaging. *Langmuir*, **23**, 1427–34.

127 Lu, C.-W., Hung, Y., Hsiao, J.-K., Yao, M., Chung, T.-H., Lin, Y.-S., Wu, S.-H., Hsu, S.-C., Liu, H. -M., Mou, C.-Y., Yang, C.-S., Huang, D.-M. and Chen, Y.-C. (2007) Bifunctional magnetic silica nanoparticles for highly efficient human stem cell labeling. *Nano Letters*, **7**, 149–54.

128 Ma, D.L., Guan, J.W., Normandin, F., Dénommée, S., Enright, G., Veres, T. and

Simard, B. (2006) Multifunctional nano-architecture for biomedical applications. *Chemistry of Materials*, **18**, 1920–192.

129 Salgueiriño-Maceira, V., Correa-Duarte, M.A., Farle, M., López-Quintela, A., Sieradzki, K. and Diaz, R. (2006) Bifunctional gold-coated magnetic silica spheres. *Chemistry of Materials*, **18**, 2701–6.

130 Lai, C.-W., Wang, Y.-H., Lai, C.-H., Yang, M.-J., Chen, C.-Y., Chou, P.-T., Chan, C.-S., Chi, Y., Chen, Y.-C. and Hsiao, J.-K. (2008) Iridium-complex-functionalized Fe_3O_4/SiO_2 core/shell nanoparticles: a facile three-in-one system in magnetic resonance imaging, luminescence imaging, and photodynamic therapy. *Small*, **4**, 218–24.

131 Lu, Y., Yin, Y.D., Mayers, B.T. and Xia, Y.N. (2002) Modifying the surface properties of superparamagnetic iron oxide nanoparticles through a sol-gel approach. *Nano Letters*, **2**, 183–6.

132 Tartaj, P., Gonzalez-Carreno, T., Bomati-Miguel, O., Serna, C.J. and Bonville, P. (2004) Magnetic behavior of superparamagnetic Fe nanocrystals confined inside submicron-sized spherical silica particles. *Physical Review. B, Condensed Matter*, **69**, 094401.

133 Xu, Z.Z., Wang, C.C., Yang, W.L. and Fu, S.K. (2005) Synthesis of superparamagnetic Fe_3O_4/SiO_2 composite particles via sol-gel process based on inverse miniemulsion. *Journal of Materials Science*, **40**, 4667.

134 Santra, S., Tapec, R., Theodoropoulou, N., Dobson, J., Hebard, A. and Tan, W. (2001) Synthesis and characterization of silica-coated iron oxide nanoparticles in microemulsion: the effect of nonionic surfactants. *Langmuir*, **17**, 2900–6.

135 Yi, D.K., Lee, S.S., Papaefthymiou, G.C. and Ying, J.Y. (2006) Nanoparticle architectures templated by SiO_2/Fe_2O_3 nanocomposites. *Chemistry of Materials*, **18**, 614–19.

136 Tago, T., Hatsuta, T., Miyajima, K., Kishida, M., Tashiro, S. and Wakabayashi, K. (2002) Novel synthesis of silica-coated ferrite nanoparticles prepared using water-in-oil microemulsion. *Journal of the American Ceramic Society*, **85**, 2188–94.

137 Henglein, A. (1999) Radiolytic preparation of ultrafine colloidal gold particles in aqueous solution: optical spectrum, controlled growth, and some chemical reactions. *Langmuir*, **15**, 6738–44.

138 Ow, H., Larson, D.R., Srivastava, M., Baird, B.A., Webb, W.W. and Wiesner, U. (2005) Bright and stable core shell fluorescent silica nanoparticles. *Nano Letters*, **5**, 113–17.

139 Verhaegh, N.A.M. and van Blaaderen, A. (1994) Dispersions of rhodamine-labeled silica spheres: synthesis, characterization, and fluorescence confocal scanning laser microscopy. *Langmuir*, **10**, 1427–38.

140 Yoon, T.-J., Kim, J.S., Kim, B.G., Yu, K.N., Cho, M.-H. and Lee, J.-K. (2005) Multifunctional nanoparticles possessing a "magnetic motor effect" for drug or gene delivery. *Angewandte Chemie – International Edition*, **44**, 1068–71.

141 Yoon, T.-J., Yu, K.N., Kim, E.H., Kim, J.S., Kim, B.G., Yun, S.-H., Sohn, B.-H., Cho, M.-H., Lee, J.-K. and Park, S.B. (2006) Specific Targeting, cell sorting, and bioimaging with smart magnetic silica core-shell nanomaterials. *Small*, 209–15.

142 Salgueiriño-Maceira, V., Correa-Duarte, M.A., Spasova, M., Liz-Marzán, L.M. and Farle, M. (2006) Composite silica spheres with magnetic and luminescent functionalities. *Advanced Functional Materials*, **16**, 509–14.

143 Yi, D.K., Selvan, S.T., Lee, S.S., Papaefthymiou, G.C., Kundaliya, D.Y. and Ying, J.Y. (2005) Silica-coated nanocomposites of magnetic nanoparticles and quantum dots. *Journal of the American Chemical Society*, **127**, 4990–1.

144 Dougherty, T.J., Gomer, C.J., Henderson, B.W., Jori, G., Kessel, D., Korbelik, M., Moan, J. and Peng, Q. (1998) Photodynamic therapy. *Journal of the National Cancer Institute*, **90**, 889–905.

145 Dougherty, T.J. (1984) Photodynamic therapy of malignant tumors. *Critical Reviews in Oncology and Hematology*, **2**, 83–116.

146 Snyder, J.W., Lambert, J.D.C. and Ogilby, P.R. (2006) 5,10,15,20-Tetrakis(*N*-methyl-4-pyridyl)-21*H*, 23*H*-porphine (TMPyP) as a sensitizer for singlet oxygen imaging in cells: characterizing the irradiation-dependent behavior of TMPyP in a single cell. *Photochemistry and Photobiology*, **82**, 177–84.

147 Henderson, B.W. and Dougherty, T.J. (1992) How does photodynamic therapy work? *Photochemistry and Photobiology*, **55**, 145–57.

148 Roy, I., Ohulchanskyy, T.Y., Pudavar, H.E., Bergey, E.J., Oseroff, A.R., Morgan, J., Dougherty, T.J. and Prasad, P.N. (2003) Ceramic-based nanoparticles entrapping water-insoluble photosensitizing anticancer drugs: a novel drug-carrier system for photodynamic therapy. *Journal of the American Chemical Society*, **125**, 7860–5.

149 Tada, D.B., Vono, L.L.R., Duarte, E.L., Itri, R., Kiyohara, P.K., Baptista, M.S. and Rossi, L.M. (2007) Methylene blue-containing silica-coated magnetic particles: a potential magnetic carrier for photodynamic therapy. *Langmuir*, **23**, 8194–9.

150 Hsieh, J.M., Ho, M.L., Wu, P.W., Chou, P.T., Tsai, T.T. and Chi, Y. (2006) Iridium-complex modified CdSe/ZnS quantum dots; a conceptual design for bifunctionality toward imaging and photosensitization. *Chemical Communications*, **6**, 15–17.

151 Deng, Y.H., Wang, C.C., Shen, X.Z., Yang, W.L., Jin, L., Gao, H. and Fu, S.K. (2005) Preparation, characterization, and application of multistimuli-responsive microspheres with fluorescence-labeled magnetic cores and thermoresponsive shells. *Chemistry – A European Journal*, **11**, 6006–13.

152 Langer, R. (1998) Drug delivery and targeting. *Nature*, **392**, 5–10.

153 Im, S.H., Jeong, K.U. and Xi, Y.N. (2005) Polymer hollow particles with controllable holes in their surfaces. *Nature Materials*, **4**, 671–5.

154 Giersig, M., Ung, T., Liz-Marzán, L.M. and Mulvaney, P. (1997) Direct observation of chemical reactions in silica-coated gold and silver nanoparticles. *Advanced Materials*, **9**, 570–5.

155 Lee, J.G., Park, J.C. and Song, H.J. (2008) A nanoreactor framework of a Au@SiO_2 Yolk/shell structure for catalytic reduction of *p*-nitrophenol. *Advanced Materials*, **20**, 1523–8.

156 Moon, G.D. and Jeong, U.Y. (2008) Decoration of the interior surface of hollow spherical silica colloids with Pt nanoparticles. *Chemistry of Materials*, **20**, 3003–7.

157 Darbandi, M., Thomann, R. and Nann, T. (2007) Hollow silica nanospheres: in situ, semi-in situ, and two-step synthesis. *Chemistry of Materials*, **19**, 1700–3.

158 Cavaliere-Jaricot, S., Darbandia, M. and Nann, T. (2007) Au–silica nanoparticles by "reverse" synthesis of cores in hollow silica shells. *Chemical Communications*, 2031–3.

159 Hilliard, R.P., Bagwe, L.R. and Tan, W. (2006) Surface modification of silica nanoparticles to reduce aggregation and nonspecific binding. *Langmuir*, **22**, 4357–62.

Keywords

metal; metal oxide; semiconductors; silicates; sol–gel method; bioapplications.

11
Spherical and Anisotropic Core-Shell and Alloy Nanomaterials: Characterization Using X-Ray Absorption Spectroscopy

Loka Subramanyam Sarma, Hung-Lung Chou, Ming-Yao Cheng, Fadlilatul Taufany, Feng-Ju Lai, Meng-Che Tsai, Shih-Hong Chang and Bing-Joe Hwang

11.1
Introduction

The fabrication of fine-metal particles with nanometer-scale dimensions over a range of chemical compositions, sizes and shapes has garnered great attention among nanotechnology disciplines [1]. Remarkable variations in the fundamental electrical, optical and magnetic properties observed in nanoparticles, as one progresses from bulk to nanometer-scale dimensions, makes them attractive for biomedical applications [2–5]. Of particular interest is the ability to shape nanomaterials in the form of core-shell architectures, which can exhibit synergistic properties as a result of second functionality. Consequently, such ability has received significant attention with regards to biomedical applications, including disease diagnosis and treatment [6–10]. In a typical core-shell structured nanomaterial, the core nanoparticle is covered with a uniformly and directly grown shell material. The protective shell imparts superior thermal and chemical stability to the nanoparticle, and makes the nanoparticles suitable for use in harsh environments. When a core nanoparticle is coated with a polymeric layer or an inorganic layer such as silica, synergistic functions can be envisioned as a result of the second functionality making the nanoparticle robust [11]. Further, by proper and convenient surface modification, the shell material may endow biocompatibility and target specificity to the nanoparticle. For example, the modification of gold surfaces with thiol groups leads to biological molecules becoming conveniently tethered to a gold shell–cobalt core nanoparticle. In a recent review, Salgueiriño-Maceira and Correa-Duarte described, and explained meticulously, the biomedical applications of magnetic core-shell-structured nanocomposites [12]. In addition to the structure, shape plays an important role in determining the electrical, magnetic and optical properties of nanoparticles [13, 14]. Subsequently, special-shaped nanoparticles with various anisotropic morphologies such as rods, wires, plates and tetrapods have been extensively studied both for biochemical sensing and imaging [15, 16] and for drug delivery [17, 18]. The properties of anisotropic nanoparticles are largely

Nanomaterials for the Life Sciences Vol. 3: Mixed Metal Nanomaterials. Edited by Challa S. S. R. Kumar

ISBN: 978-3-527-32153-7

governed by the aspect ratio, which is defined as the ratio between the length of the nanoparticle and its cross-sectional dimension [14, 19]. For example, in the case of nanorods and nanowires, an increase in the aspect ratio leads to a splitting of the plasmon band of the metal into longitudinal and transverse plasmon bands. While the longitudinal plasmon band is related to the light absorption and scattering along the long axis of the particle, the transverse plasmon band is contributed by the light absorption and scattering along the short axis of the particle [20, 21]. Metallic nanowires and nanorods with a large aspect ratio are reported to be possess enhanced properties when compared to their spherical counterparts, and find promising applications in areas such as surface-enhanced Raman scattering (SERS), cancer hyperthermia and plasmon resonance tomography [22–24].

Nanomaterials advocated for biomedical applications are required to possess well-controlled structure and composition. The frequent attempts that have been made to impart surface modifications on nanoparticle systems, so as to render them more biocompatible, has led to the development of rigorous characterization techniques capable of providing information about the nanoscale properties that are critically required [25]. For example, parameters such as particle size, deviation from spherical shape (and hence the aspect ratio) and interparticle interactions have a major influence on the plasmon resonance frequency of gold nanostructures [26]. Further, if the nanoparticles are composed of two or more metals, then both the composition and the actual distribution will determine the resultant physico-chemical properties. Thus, surface structure, atomic distribution and composition are other dominant nanostructural properties that require both control and careful characterization. This is because, for nanoparticle applications in biomedical systems, a proper control of the interface is required to produce specific interactions with biology.

In recent years, much attention has been focused on controlling the aspect ratio of inorganic nanomaterials of various anisotropies, such as nanorods and nanowires [27]. Such interest largely stems from the fact that unique and improved optical [26], magnetic [28] and surface-enhanced Raman scattering properties [29] are possible with anisotropic nanomaterials compared to their spherical counterparts. Murphy and coworkers reported the wet-chemical synthesis of relatively monodisperse gold and silver nanorods, and also of silver nanowires [30–32]. Their studies revealed that a control of the ratio of spherical metallic seeds to metal salt (growth solution) in the reduction reaction permits control of the aspect ratio of the resultant nanorods and nanowires. In order to better understand aspect ratio control, it is important to understand the growth mechanism of nanorods and nanowires [33], and in this respect XAS studies are quite helpful [34].

Controlling the core and shell dimensions is also considered to be crucial when tuning the physico-chemical properties of core-shell nanomaterials for biomedical applications. For example, controlling the thickness of the silica coating of Au-core–SiO_2-shell nanoparticles in turn allows their optical properties also to be conveniently tuned. Recently, Oldenburg and coworkers conducted detailed studies of the dependence of optical resonance of gold-coated silica spheres on their core radius and shell thickness [35, 36]. Likewise, Jun *et al*. emphasized the importance

of controlling the core and shell dimensions when they created Co_{core}–Pt_{shell} nanoparticles via a redox transmetallation reaction between $Pt(hfac)_2$ and previously synthesized Co nanoparticles [37]. Following shell formation, the nanoparticles retained their single-domain superparamagnetism. These authors noted that the core and shell dimensions must be precisely controlled in order to minimize the use of Pt as much as possible, for economic reasons. However, if the magnetic core is too small, it will not display a sufficiently strong magnetism for the magnetic recycling process. Likewise, in the case of silver/silica nanoparticles, which are widely used for fluorescence imaging, control of the core-shell ratio is an important aspect as the region of emission is heavily dependent on the thickness of the silica coating. Metal interactions with fluorophores must also be characterized correctly, as they are responsible for the nanoparticles' increased photostability and enhanced fluorescence. Due to the complexity of most biological environments, the number of methods capable of providing useful information on the surface structure of nanomaterials in a complex environment is limited. However, rigorous characterization techniques that can provide detailed information on shape, size and size distribution are equally important.

Several experimental techniques, including microscopy, diffraction and numerous forms of spectroscopy, have been successfully applied to deduce the structural aspects of nanoparticles [38, 39]. For example, size, size distribution, morphology, segregation, alloying extent, atomic distribution, degree of alloying and surface composition represent some of the key properties considered important in the characterization of bimetallic alloy or core-shell nanoparticles [40–42] (also B.J. Hwang *et al.*, unpublished results). Although freely available and capable of providing information regarding the alloy structure of bimetallic nanoparticles, X-ray diffraction (XRD) cannot provide true structural information. This is because XRD lacks the ability to identify short-range ordering (local environment), and can only provide data relating to long-range ordering and periodicities, preferably on single crystals or polycrystals. Hence, conclusions concerning the alloy structure of nanosized particles cannot be simply drawn when using XRD. However, if the lattice spacings of the two metals are distinct, then XRD may provide some information on the degree of mixing [43]. Microscopy techniques such as transmission electron microscopy (TEM) [44, 45] and high-resolution TEM (HR-TEM) [46] can provide only a qualitative understanding of the structure of bimetallic nanoparticles. For example the HR-TEM method enables a distinction to be made between core-shell structures on the basis of observing different lattice spacings and crystal orientations [47, 48]. However, if the core and shell components comprise a similar crystal orientation and lattice spacing, then it would be extremely difficult to identify the core-shell structured nanoparticle using HR-TEM [49]. Rather surprisingly, TEM provides a better understanding of the core-shell structure if the core and shell region comprise metal atoms with a high contrast. Scanning TEM (STEM), which relies on scanning an electron beam across the sample, combined with a HAADF or Z-contrast imaging technique (as the HAADF image contrast is proportional to Z^{α}, where Z is the atomic number and α is in the range 1.5–2), offers the possibility of identifying the internal structure of the nanoparticle [50]. Consequently, by

combining the specific advantages of HR-TEM, STEM, energy filtering TEM (EF-TEM) and convergent-beam electron diffraction (CBED), Ferrer *et al.* studied the complex structure of Au/Pd nanoparticles, which incorporated alternate layers of Au atoms and Pd atoms, for its three-layer morphology [51]. The surface alloying and segregation phenomena of bimetallic nanoparticles can be reasonably obtained by using surface-sensitive techniques such as X-ray photoelectron spectroscopy (XPS) [52], Auger electron spectroscopy (AES) [53] and infrared (IR) spectroscopy [54].

Another parameter which is of major importance when assessing the suitability of core-shell or alloy-structured bimetallic nanoparticles for biomedical applications is that of the surface composition. Surface-sensitive techniques such as electron spectroscopy for chemical analysis (ESCA), secondary ion mass spectrometry (SIMS), ion scattering spectroscopy (ISS), XPS and AES have enabled investigators to obtain reasonably good estimates of the surface compositions of bulk or thin-film alloys [55, 56]. Unfortunately, however, these techniques have severe limitations for analyzing the surface composition of bimetallic nanoparticles (bi-MNPs). For example, due to the escape depth of the Auger electrons and photoelectrons, the application of AES and XPS to particles with diameters of ≤30 Å is restricted [57, 58]. Although SIMS offers depth information in the range of 10 to 20 Å, it does not provide the spatial resolution provided by electron beam techniques such as SEM, TEM and AFS.

One promising method for probing the internal structures of core-shell and alloy-type bimetallic nanoparticles, and of species adsorbed onto them, is that of X-ray absorption spectroscopy (XAS). This in fact consists of both X-ray absorption near-edge structure (XANES) and extended X-ray absorption fine structure (EXAFS) regions. XAS studies conducted in the XANES region (conventionally from below the edge up to ~30–50 eV) can reveal the oxidation state and d-band occupancy of a specific atom in nanoparticles, as well as the size of the nanoparticles [59, 60]. EXAFS (above ~30–50 eV) provides a powerful tool for the analysis of local atomic structure, providing accurate information about the average local atomic environment [61, 62]. EXAFS is particularly sensitive to interatomic distances and local disorder, and has been successfully utilized to resolve subtle nanoparticle structural details [63], whereas XAS has proved to be a powerful technique for the characterization of bimetallic catalysts [64–66].

Recently, some significant contributions were made that highlighted the applicability of the XAS technique to studying various aspects of nanoparticles, including the deduction of structural models and atomic distribution/or alloying extent in bimetallic nanoparticles [42]. The formation mechanism of metallic nanoparticles has been successfully investigated by following *in situ* XAS at various reaction steps during the nanoparticle synthetic process [67–73]. The detailed knowledge obtained from these mechanistic studies with XAS was subsequently utilized to design bimetallic nanoparticles with various atomic distributions, alloying extents and stacking orders. In another study, a general methodology was demonstrated, based on EXAFS techniques, for quantitative determination of the surface and core composition of bi-MNPs by combining modeling and experimental approaches [B.J. Hwang *et al.*, unpublished results].

In this chapter, we will provide an overview of the use of XAS in characterizing the internal structures of spherical and anisotropic core-shell and alloy nanomaterials. Also highlighted are the authors' efforts in developing XAS-based methodologies to probe the mechanism of nanoparticle formation, and subsequently to determine the structure, atomic distribution, alloying extent and surface composition of bimetallic nanoparticles.

11.2
Nanoparticle Systems for Biomedical Applications

The unique electronic, optical and magnetic properties of nanoparticle systems are clearly the main reasons for their proposed application in biomedicine. Nanoparticle systems that have at least one dimension in the range of <100 nm offer possibilities of enhanced robustness, sensitivity and selectivity. As the size and shape of nanoparticles play crucial roles in determining their optical, electronic and magnetic properties [74–77], metallic nanorods and nanowires have been widely developed for promising applications in photonics [78, 79], electronics [80, 81], bioimaging and sensing [16], as well as for drug delivery [17, 18]. Recently, in addition to their anisotropic nanostructures, core-shell-type nanoparticles have received much attention on the basis of their promise in the development of devices and materials with new functions for magnetic recording, and for both biomedical and medical applications [6, 7, 82, 83]. A range of biomedical applications for nanoparticulate systems are briefly discussed in the following sections.

11.2.1
Bioimaging (Magnetic Resonance Imaging)

Magnetic resonance imaging (MRI) is a noninvasive technique that relies especially on an enhancement of the local proton relaxation of water molecules in the presence of a contrast agent [84]. MRI has shown great promise for imaging the biodistribution of magnetically labeled cells, and of providing three-dimensional (3-D) maps of living bodies at the cellular and molecular level, in real time [85–88]. Nanoparticle systems with a core-shell structure in which a magnetic core is coated with a biocompatible organic or inorganic shell have found widespread application as MRI contrast agents. Indeed, a wide variety of superparamagnetic iron oxide (SPIO) -based nanoparticles have been investigated in these areas [89–91]. The details of silica-coated iron oxide [92–94], gold-coated iron oxide [95] and other gold-coated magnetic nanoparticles have each been reported by various research groups [96–99].

Recently, the magnetic properties and biomedical applications of metallic nanoparticles were elaborately described by Krishnan *et al.* [100]. It has been reported that the gold coating on iron oxide provides an optical or luminescent functionality which depends largely on the relative dimensions of the core radii and shell thickness [101]. These gold-coated iron oxide nanoparticles showed

optical resonances with tunable wavelength, from visible to infrared including the near-infrared (NIR) region, where tissue transmissivity is highest, as a result of lowest scattering and absorption [102]. These advantages can provide an imaging and photothermal ablation [35, 36, 103–105]. Silica coating on magnetic nanoparticles has been reported to show promise in preventing the nanoparticles' aggregation, and also to protect the magnetic particles from possible decomposition [106]. The important function of the shell material is to provide stability, biocompatability and additional functionality to the magnetic nanoparticles. Moreover, the chemistry of the silica surface has been well established, and silica-coated nanoparticles can be easily functionalized for specific biocompatibility. For example, Lu *et al*. showed that fluorescent dye molecules such as 7-(dimethylamino)-4-methylcoumarin-3-isothiocyanate (DACITC) and tetramethylrhodamine-5-isothiocyanate (5-TRITC) can be conveniently incorporated into the silica shells coated on SPIO nanoparticles for MRI applications [107]. Fluorescent dyes such as fluorescein isothiocyanate (FITC) [108], Cy5.5 [109], rhodamine [110], ASPI-SH [111] and fluorescent amino polyvinyl alcohol (PVA) [112] have also been reported. Some of these reported fluorescent magnetic nanoparticles have been utilized for stem cell labeling, and subsequently imaged with MRI in clinical conditions with low cell counts.

Another important function of the gold coating on a previously formed SPIO core and silica shell nanoparticles has been suggested to cause separation of biofunctionals, either magnetic or optical. Here, the outer Au optical shell provides an exclusive optical functionality without having any significant influence on the core's magnetic behavior. Similar to the Au-coated $SPIO_{core}$–$silica_{shell}$ nanoparticles, Group II and VI semiconductor materials such as CdTe [113, 114] and CdSe [115, 116] quantum dots (QDs) have also been reported to show promise in providing optical functionality, where these luminescent nanoparticles were deposited onto the surface of silica-coated iron oxide nanomaterials.

In order to fabricate magnetic nanoparticles to meet the requirements of a particular biomedical application, it is necessary to carefully control the size, shape, composition, morphology and surface chemistry, as each of these factors in turn determine the magnetic properties of the nanoparticles [100]. Hence, rigorous characterization techniques to assess the surface chemistry, size, size distribution, shape, crystallinity and composition are of major importance when evaluating and controlling the interaction of nanoparticles with biomolecules, in order to provide promising biocompatibility, targeting, controlled circulation time and specific binding.

11.2.2 Drug Delivery

Surface-modified magnetic nanoparticles with enhanced functionality have been widely used for drug-delivery applications [117–120]. In combination with an external magnetic field, SPIO nanoparticles allow the delivery of particles to a selected target area, and to fix them at a predetermined site while the medication

is released and acts locally [121–124]. Most drug-containing magnetic nanocarriers comprise a magnetic nanoparticulate 'core' with an organic or inorganic 'shell', with the therapeutic drugs being encapsulated within the shell structure. Drug release from these magnetic core-shell nanocarriers can easily be triggered by an external magnet, and this has become known as the 'magnetic motor' for site-specific drug-delivery applications. Hu *et al*. demonstrated the use of polyvinylpyrollidine (PVP)-modified silica/Fe_3O_4 core-shell nanospheres for the controlled release of fluorescent dyes within HeLa (human cervical cancer) cells [92]. Yoon *et al*. reported the use of core-shell-structured Co ferrite–silica MNPs, in which the shell silica contained a luminescent organic dye, such as rhodamine B isothiocyanate (RITC) or FITC on the inside of the silica shell, and a biocompatible polymer (poly(ethylene glycol); PEG) on the outside, in a variety of *in vitro* cell studies [120].

A complete characterization of the nanoparticulate system is necessary to determine whether the use of a nanocarrier system is appropriate for a specific *in vivo* application. In this respect, the particle size, size distribution, shape, surface structure, segregation and morphology – all of which control the properties of the nanoparticle system with regards to drug delivery applications and other biomedical applications – require rigorous characterization.

11.3 Characterization of Spherical and Anisotropic Core-Shell and Alloy Nanomaterials using X-Ray Absorption Spectroscopy (XAS)

X-ray absorption spectroscopy, which comprises both XANES and EXAFS regions, represents an extremely powerful characterization technique when investigating the various structural aspects of nanomaterials. It has been shown previously that investigations at the XANES region (conventionally from below the edge up to ~30–50 eV) can provide information regarding the oxidation state, the fractional d-electron density and the electronic environment of the absorbing atom. Spectra obtained from the region extending from XANES up to 1000 eV above the edge are referred to as EXAFS, and are primarily caused by scattering of the photoelectrons from near-neighbor atoms. The amplitude of the EXAFS function is $\chi(k)$, where k is the wave vector that is proportional to the number of nearest neighbors, and the change of phase with the wavelength of the photoelectron depends on the distance between the emitter and the backscattering atom [125, 126]. The backscattering strength also depends on the type or atomic number of atoms involved in the backscattering process. Thus, an analysis of EXAFS data yields structural details concerning the absorbing atom and its local environment. Due to the short (~10 Å) mean free path of the photoelectron and the rapid core hole lifetime (10^{-16}–10^{-15} s), EXAFS experiments are considered to be both local and instantaneous [63]. By applying these factors, XAS has shown great promise for studying the structural dynamics of finite-sized particles, even in the absence of any long-range order.

11.3.1 XAS Fundamentals

When a beam of X-ray photons travels through a material, it loses its incident intensity by an amount determined by the absorption characteristics of the material being irradiated [127]. When the X-ray energy is scanned through the absorption edge of element of interest, the corresponding change in absorbance or fluorescence of the sample can be conveniently measured. Such absorption (μx) is defined by the well-known Beer–Lambert law:

$$\mu x = \log\left(\frac{I_0}{I_t}\right) \tag{11.1}$$

where μ is the linear absorption coefficient, x is the sample thickness, I_0 is the incident intensity, and I_t is the intensity transmitted through the sample.

When the energy of the incoming photons is large enough to excite an electron from a deeper core level to the continuum, a sharp rise appears in the absorption intensity. This sharp rise is denoted as the threshold energy or absorption edge. At the absorption edge, E_{edge}, the kinetic energy of the electron (E_k) is defined as equal to E_0, which often is referred to as the zero-point energy or 'inner potential'. In the near edge region – which sometimes is referred to as the X-ray near edge structure (XANES) and extends to approximately 30–50 eV near and above the edge – transitions may occur to unfilled bound states and nearly bound states (resonances). In most cases, the XANES region of the XAS spectra exhibit a strong rise in absorption which is known as the 'white line', and which is sensitive to the local symmetry and electronic structure of the absorbing atom. The XANES region provides information on the local characteristics of the absorber, such as its formal oxidation state and the type of bond. For any energy above this XANES region, the photoelectron kinetic energy is given by:

$$E_k = h\nu - E_{binding} \tag{11.2}$$

The outgoing photoelectron can be represented as a spherical wave with a wavelength λ and the corresponding wave number (k) of the photoelectron, which has dimensions of 1/distance can be represented as

$$k = \sqrt{\frac{8\pi^2 m_e}{h^2}(E - E_0)} \tag{11.3}$$

where E_0 is the ionization edge energy, m_e is the electron rest mass and h is Planck's constant.

When the neighboring atoms are involved in the absorption process, the outgoing photoelectron wave is scattered from the neighboring atoms, thus producing an incoming electron wave that interferes either constructively or destructively with the outgoing wave. Hence, the final state wavefunction of the photoelectron

(ψ_f) comprises the wave functions of outgoing electron ($\psi_{outgoing}$) as well as a back-scattered electron ($\psi_{backscattered}$). Interference between these two final-state wave-functions gives rise to an oscillation of the absorption coefficient as a function of the energy of the incident photon. These oscillations, which generally are referred to as EXAFS, which may extend from 40 eV to 1000 eV above the absorption edge, and are described by the fine-structure function $\chi(E)$, as

$$\chi(E) = \frac{\mu(E) - \mu_0(E)}{\Delta\mu_0(E)} \tag{11.4}$$

where $\mu(E)$ is the measured absorption coefficient, $\mu_0(E)$ is a smooth background function representing the absorption of an isolated atom, and $\Delta\mu_0$ is the measured jump in the absorption of $\mu(E)$ at the threshold ionization energy E_0. The oscillation in $\chi(k)$, represents as a summation over all interference patterns (sine waves) scattered from all neighboring atoms:

$$\chi(k) = \sum_{j=1}^{Shells} A_j(k) \cdot \sin[2kR_j + \delta_j(k)] \tag{11.5}$$

where $A_j(k)$ is the amplitude, $\delta_j(k)$ is the phase shift and R_j is the distance to neighboring atoms of type j.

The amplitude $A_j(k)$ is a complex term containing the coordination number (N), and disorder factor (σ), which is the fluctuation in R_j due to thermal motion or structural disorder:

$$A_j(k) = \frac{N_j S_0^2 F_j(k) \cdot e^{-2\sigma_j^2 k^2} \cdot e^{-\frac{2R_j}{\lambda_j(k)}}}{kR_j^2} \tag{11.6}$$

where $F_j(k)$ is the backscattering amplitude of atoms of type j, S_0^2 is the so-called amplitude reduction factor, which takes into account many-body effects such as central atom shake-up and shake-off due to relaxation process after the photo-ionization event. The $e^{-2\sigma_j^2 k^2}$ term describes thermal and static disorder causing an additional damping of the EXAFS amplitude, especially at large k. σ^2 is a Debye–Waller factor, defined as the root mean square displacement of the average nearest-neighbor distance. $\lambda_j(k)$ is the mean-free path of the photoelectron, which is the average distance traveled by a photoelectron before it scatters inelastically or the core-hole is filled.

The complete EXAFS function $\chi^{th}(k)$ can represented as:

$$\chi^{th}(k) = \sum_{j=1}^{Shells} \left(\frac{N_j S_0^2}{kR_j^2} \right) F_j(k) \cdot e^{-2\sigma_j^2 k^2} \cdot e^{-\frac{2R_j}{\lambda_j(k)}} \sin[2kR_j + \delta_j(k)] \tag{11.7}$$

In the usual procedure, the experimentally obtained EXAFS oscillations were Fourier back-transformed by considering the coordination shells of interest, after

which the Fourier back-transformed EXAFS oscillation $\chi(k)$ was submitted to a curve-fitting procedure with the theoretical EXAFS function of $\chi^{th}(k)$. Here, the amplitude is proportional to the number of nearest neighbors, while the change of phase with the wavelength of the photoelectron depends on the distance between the emitter and the backscattering atom. The backscattering strength also depends on the type or atomic numbers of the atoms involved in the back-scattering process. Thus, by analyzing the EXAFS spectra, it is possible to access structural information concerning the absorber and the local structural environment.

11.3.2 XAS Data Collection and Analysis

The extraction of $\chi(k)$ from the experimentally measured intensities involves several steps. First, the raw absorption spectrum in the pre-edge region is fitted to a straight line by a modified Victoreen function in order to subtract the background. After the pre-edge subtraction, the edge energy (E_0) must be identified. Normally, the energy of the maximum derivative of $\mu(E)$ is considered as a systematic choice for E_0. The atomic background above the absorption edge should be determined generally by using a cubic spline. The EXAFS function $\chi(k)$ is then obtained by subtracting the post-edge background from the overall absorption, and then normalized to the edge jump in order to obtain absorption per absorber atom. A common method of determining the edge step is to fit the data within a few hundred eV below the edge, and also above the edge, with low-order polynomials (linear to quadratic), and then extrapolate them to the edge. The difference between the pre-edge and post-edge fits extrapolated to the edge energy is the edge step. At the next stage of XAS analysis, the normalized $\chi(E)$ is transformed from energy space to k-space, where k is the photoelectron wave vector. At this stage, the $\chi(k)$ data consist of damped sine waves corresponding to the different shells of atoms. The $\chi(k)$ data are then usually multiplied by k^n; this can be used to compensate the decay of waves so that a distinction can be made between the high and low Z scattering elements around the absorber element. At the next stage, a Fourier transformation of $\chi(k)$ data within a carefully chosen k-range in a radiation distribution function is carried out to separate the EXAFS contributions from the different coordination shells:

$$FT(R) = \frac{1}{\sqrt{2\pi}} \int_{k_{min}}^{k_{max}} k^n \chi(k) e^{i2kR} dk \tag{11.8}$$

In the most practical cases, the Fourier-transformed EXAFS signal is subjected to Fourier filtration, using the inverse Fourier transformation, which separates the contributions of individual coordination spheres. This analysis is particularly useful when extracting standards for phase shifts and backscattering amplitudes from reference compounds that are required in EXAFS data analysis. When the transferable parameters such as amplitude, phase shifts and amplitude reduction

factor have been estimated for a reference compound, then the EXAFS function for a sample of unknown structure can be conveniently determined.

11.3.3 Structural Characterization: XAS Methodologies

In this section, we will discuss the promising possibilities of XAS in understanding the size, shape, aspect ratio, atomic distribution and/or alloying extent, and surface composition of nanomaterials. Initially, we will discuss the XAS methodologies used to deduce the above structural details, and then provide an overview of those studies which have focused on such structural aspects.

11.3.3.1 Particle Size, Shape and Aspect Ratio of Nanoparticles

The coordination number of elements present in nanomaterials can be conveniently derived using XAS. The coordination number is a strong and nonlinear function of the particle diameter up to 3–5 nm, and has been widely used in EXAFS analysis to determine nanoparticle size. A general relationship between the coordination number and the diameter and/or height of various anisotropic nanomaterials (e.g., nanowires, nanoparticles, nanodiscs/nanoplates) is shown in Figure 11.1. Here, the length of anisotropic nanomaterials is taken to be much larger than that of the diameter and/or height; in fact, the length can be varied to an unlimited degree. The face-centered cubic (*fcc*) structure was considered for various anisotropic nanomaterials in generating the sequence of the average coordination number. In fact, this general relationship can also be extended to various

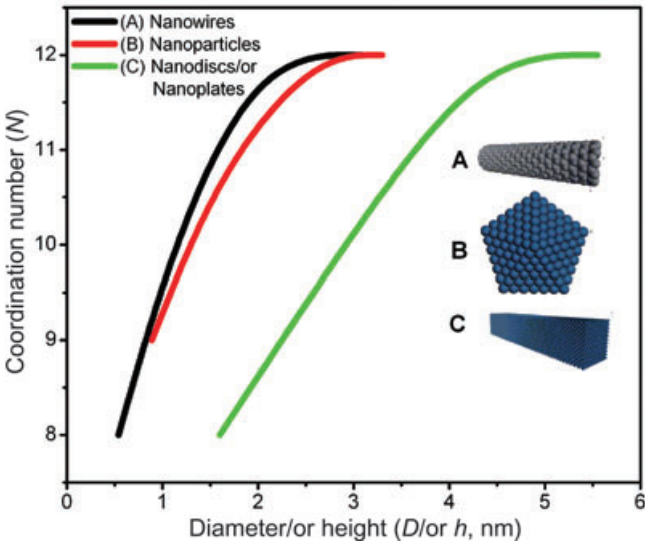

Figure 11.1 Coordination number as a function of the diameter/or height of anisotropic nanomaterials.

anisotropic nanomaterials with body-centered cubic (*bcc*) structure. From the results of XAS studies, the coordination number can be conveniently determined and the corresponding particle diameter/or height estimated, in association with the measured coordination number. When the average coordination number has been obtained via XAS, the shape of the nanomaterials can be reliably determined since, due to differences in the geometry of clusters with different sizes, the shapes each cluster will generate a unique average coordination number [63].

The aspect ratio of an anisotropic nanomaterial is an important feature that requires critical characterization. Generally, the aspect ratio (α) of a shape is defined as the length of the major axis divided by the width of the minor axis ($\alpha = L/D$). XAS has shown promise for determining the average coordination numbers of anisotropic nanomaterials (Figure 11.1). When the diameter/or height of a nanomaterial, in association with the coordination number, has been determined, then the aspect ratio of an anisotropic nanomaterial can be calculated by utilizing information regarding the nanomaterial's length, obtained from TEM measurements.

It is also interesting to note that it is possible to obtain information regarding the surface to total number of atoms (n_{surf}/n_{total}) of *fcc*- and *bcc*-structured nanomaterials associated with the average coordination number (an example for spherical nanoparticles is shown in Figure 11.2). By extracting the coordination number of nanomaterials from experimental XAS measurements, the n_{surf}/n_{total} of the nanomaterial can be determined by utilizing information regarding its orientation, obtained from XRD measurements. If such information is obtained via XAS measurements, then the surface structure and composition of the nanomaterial can also be realized.

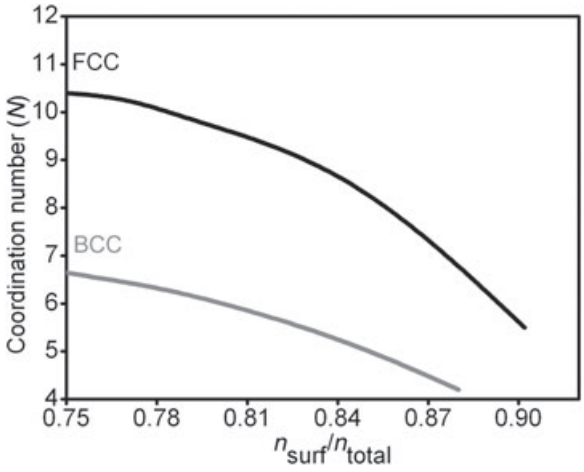

Figure 11.2 Coordination number of *fcc*- and *bcc*-structured nanomaterials as a function of number of surface to total atoms (n_{surf}/n_{total}).

11.3.3.2 Alloy Versus Core-Shell Structure, Atomic Distribution and Degree of Alloying of Nanomaterials: An XAS Methodology

In order to realize the actual structure of nanomaterials of either alloy or core-shell structure, especially when those bimetallic systems are in the subnanometer to 2–3 nm size range, a combination of characterization techniques is required. The ability to tune the X-ray energy to the absorbing edge of each participating metal in a bimetallic system makes EXAFS an attractive technique for elucidating local structures and providing information about the environment for a particular atom. By analyzing the EXAFS spectrum of each metal in a bimetallic nanomaterial concurrently, valuable structural and chemical information (e.g., interatomic distance, coordination number, oxidation state of chemical species) concerning the nanostructures can be obtained conveniently, and such information may also supplement the data obtained with microscopy. Several research groups have been successfully used EXAFS to study the bonding habits, geometry and surface structures of many bimetallic nanoparticles of biomedical importance (e.g., Co/Pt, Pd/Au, Au/Ag), from which the shape, size, morphology and short range order in atomic distributions occurring within the particles were reliably obtained [128–134]. By collecting the XAS data at the absorption edges corresponding to each element in the bimetallic nanoparticle under investigation, the extent of intermixing (alloying extent) and homogeneity (atomic distribution) of the nanoparticle may be assessed [42]. In general, it is possible to assess the core-shell structure of nanomaterials simply from the coordination numbers of participating elements in those core-shell materials. For a homogeneous bimetallic system of A_{core}–B_{shell} cluster, in which the core of the cluster is composed of N atoms of A (N_A) and the surface is made of N atoms of B (N_B), the total coordination number ($N_{AA} + N_{AB}$) for the 'A' atom will be greater than the total coordination for the 'B' atoms ($N_{BA} + N_{BB}$) [135, 136]. If bimetallic nanoparticles possess a random alloyed structure, then the ratios of the coordination number of A and B coordination, $N_{A–A}/N_{A–B}$ and $N_{B–A}/N_{B–B}$, should be consistent with the ratio of the atomic fraction x_A/x_B.

The alloy or core-shell-type structure of metallic nanostructures, as deduced from XAS measurements, may be better understood if information can be obtained about the atomic distribution and alloying extent of the participating elements. This is particularly important because, among the various structural aspects, it is of most important to control the homogeneity, dispersion and alloying extent, as each of these factors has a profound influence on the surface properties that in turn affect the biocompatibility and stability of the bimetallic nanoparticles. It is clear, therefore, that techniques must be developed to obtain further insight into these structural aspects. Although alloying is a well-known phenomenon, detailed studies on the quantitative assessment of alloying extent in bimetallic nanoparticles have been lacking to date. However, in our laboratory we were able to develop a general method to estimate the alloying extent and/or atomic distribution in bimetallic nanoparticles by deriving the structural parameters via an XAS analysis [42].

By estimating the ratio of the coordination number (CN) of A around B and also the CN of B around A to the total CNs, it is possible to estimate very conveniently

the alloying extent of A (J_A) and B (J_B) in A–B bimetallic nanoparticles. The parameters needed to derive the extent of alloying are represented as $P_{observed}$, $R_{observed}$, P_{random} and R_{random}. The parameter $P_{observed}$ can be defined as a ratio of the scattering atoms 'B' CN around absorbing 'A' atoms ($N_{A–B}$) to the total CN of absorbing atoms ($\Sigma N_{A–i}$), ($P_{observed} = N_{A–B}/\Sigma N_{A–i}$). Similarly, $R_{observed}$ can be defined as a ratio of the scattering atoms 'A' CN around absorbing 'B' atoms ($N_{B–A}$) to the total CNs of absorbing atoms ($\Sigma N_{B–i}$), ($R_{observed} = N_{B–A}/\Sigma N_{B–i}$). Whereas, P_{random} and R_{random} can be taken as 0.5 for perfect alloyed bimetallic nanoparticles if the atomic ratio of 'A' and 'B' is 1:1. The J_A and J_B for 1:1 A–B bimetallic nanoparticles can then be estimated by using Equations 11.9 and 11.10, respectively:

$$J_A = (P_{observed}/P_{random}) \times 100\% \tag{11.9}$$

$$J_B = (P_{observed}/P_{random}) \times 100\% \tag{11.10}$$

Based on the $\Sigma N_{A–i}$, $\Sigma N_{B–i}$, J_A and J_B, it is possible to predict the structural models of nanoparticles. For example, if $\Sigma N_{A–i} > \Sigma N_{B–i}$ it appears that the core is rich in 'A' atoms while the shell is rich in 'B' atoms. In this case, if both $J_A < J_B$, then the bimetallic nanoparticle structure is almost close to pure A_{core}–B_{shell} (Case 1 in Figure 11.3). However, if $J_B > J_A$ with a coordination parameter relationship $\Sigma N_{A–i} > \Sigma N_{B–i}$, then the bimetallic nanoparticles possess an 'A'-rich core–'B' rich shell structure (Case 2 in Figure 11.3). If $\Sigma N_{A–i} = \Sigma N_{B–i}$ and J_A and $J_B \approx 100\%$, then bimetallic nanoparticles will adopt an alloy structure (Case 3 in Figure 11.3). If we apply our derived expression for J_A and J_B to calculate the alloying extent of Au and Pd, respectively, for a 1:1 Au–Pd bimetallic nanoparticles reported elsewhere [129], we have achieved the values $J_{Au} = 52\%$ and $J_{Pd} = 125\%$. This indicates that Au atoms are rich in the core and Pd atoms are rich in the shell, similar to the model shown in Case 2 of Figure 11.3. From these J_{Au} and J_{Pd} values, it becomes

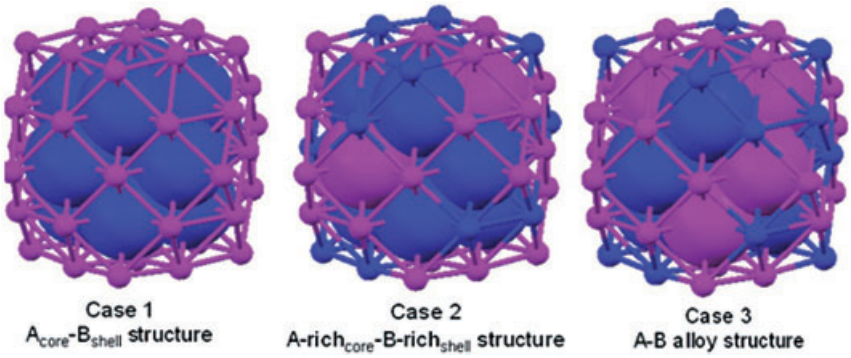

Figure 11.3 Structural models of bimetallic nanoparticles with core-shell and alloy structures deduced from XAS structural parameters. 'A' atoms are shown in blue; 'B' atoms are shown in pink.

clear that the atomic dispersion of Pd is better than the atomic dispersion of Au in the Au–Pd bimetallic nanoparticles. Thus, by deriving the XAS structural parameters ΣN_{A-i}, ΣN_{B-i}, $P_{observed}$, $R_{observed}$, J_A and J_B, the structure and alloying extent and/or atomic distribution in bimetallic nanostructures can easily be determined.

11.3.3.3 Surface and Core Composition in Bimetallic Nanoparticles: An XAS Methodology

Recently, we developed a general methodology based on EXAFS techniques for quantitative determination of the surface and core composition of bi-MNPs by combining modeling and experimental approaches. The advantage of this method is that it can be used to extract the surface and core composition of various bi-MNPs under known reaction conditions (even in the liquid phase), and can be also extended to ternary nanoparticles. The key to this methodology is to use geometric arguments to relate inaccessible surface and core compositions to quantities that can be measured robustly with XAS. By knowing only the basic crystal structure (*fcc*, *bcc*, etc.) and the overall nanoparticle shape (cubo-octahedron, icosahedron, truncated octahedron, etc.), it is possible to write equations for the surface and core compositions of bi-MNPs in terms of measurable quantities. A system of AB bi-MNPs with an *fcc* structure is employed to demonstrate the feasibility of the developed methodology. Based on the cluster model, the dependence of the total number of atoms (n^t), the number of surface atoms (n^s), and the total average surface coordination number ($\underline{N}^s$) on the total average coordination number ($\underline{N}$) for the *fcc* cluster of icosahedron, cubo-octahedron and truncated octahedron shapes can be evaluated. The equations for the surface and core compositions of a system of AB bi-MNPs with an *fcc* structure can be given as follows:

$$X_A^s = \frac{x\left(\sum N_{A-i} - 12\right)}{x\left(\sum N_{A-i} - 12\right) + (1-x)\left(\sum N_{B-i} - 12\right)} \tag{11.11}$$

$$X_B^s = \frac{(1-x)\left(\sum N_{B-i} - 12\right)}{(1-x)\left(\sum N_{B-i} - 12\right) + x\left(\sum N_{A-i} - 12\right)} \tag{11.12}$$

$$X_A^c = \frac{x\left(\underline{N}^s - \sum N_{A-i}\right)}{x\left(\underline{N}^s - \sum N_{A-i}\right) + (1-x)\left(\underline{N}^s - \sum N_{B-i}\right)} \tag{11.13}$$

$$X_B^c = \frac{(1-x)\left(\underline{N}^s - \sum N_{B-i}\right)}{(1-x)\left(\underline{N}^s - \sum N_{B-i}\right) + x\left(\underline{N}^s - \sum N_{A-i}\right)} \tag{11.14}$$

where ΣN_{A-i} and ΣN_{B-i} represent the average coordination numbers of A and B. We can determine the total average coordination numbers of A and B, ΣN_{A-i}, and ΣN_{B-i}, from EXAFS measurements and the bulk composition (x) from the edge jump in XANES measurements. When ΣN_{A-i} and ΣN_{B-i} have been determined, the

surface composition of the nanoparticles can be obtained using Equations 11.11 and 11.12. Meanwhile, the average coordination number of the cluster N can be calculated by

$$\underline{N} = x\sum N_{A-i} + (1-x)\sum N_{B-i} \tag{11.15}$$

The core composition of A and B atoms in the *fcc* nanoparticles with various shapes can be estimated using Equations 11.13 and 11.14, but $\underline{N}^S$ must be obtained from the experimental total average coordination number ($\underline{N}$) associated with the fcc model calculation considering various shapes. In general, the surface composition depends only on the structure of the nanoparticles, whereas the core composition relies not only on the structure but also on the shape of the nanoparticles.

11.3.4
Review of XAS Characterization Methodologies for Nanomaterials

Greegor and Lytle demonstrated the feasibility of EXAFS technique for measuring size and shape of small metal particles [137]. This methodology relies on developing a two-region model for various geometrical shapes such as spheres, cubes and disks, and calculating the EXAFS average coordination number for first, second and third coordination spheres as a function of cluster size. Nuzzo and coworkers have also elaborated the modeling nanoparticle size and shape by using EXAFS [63]. Nuzzo's group considered two-model particles characterized by a common average first-shell coordination number (a value of ~8 for a 92-atom hemispherical and a 55-atom spherical cubo-octahedral cluster). These authors emphasized that the geometry of these two clusters was significantly different with different sizes, shapes or lattice symmetries, so that each cluster can generate a unique sequence of average coordination numbers in the first few nearest-neighbor shells. When such a sequence has been obtained experimentally, then the corresponding cluster size, shape and symmetry may be conveniently determined.

One other important feature of anisotropic nanomaterials that must be assessed is the aspect ratio. Whilst spheres have an aspect ratio of 1, nanorods will generally have aspect ratios less than 1 but higher than 20, with a width ranging from 1 to 100 nm; nanowires will have aspect ratios greater than 20. The aspect ratio of metallic nanorods can be conveniently controlled by using surfactants. As an example, the aspect ratio of Au nanorods may be systematically moderated from ~2 to ~25 by controlling the relative concentrations of the surfactants [19, 138]. The intense interest in controlling the aspect ratio of anisotropic nanomaterials stems largely from an ability to control the optical properties of metallic nanoparticles, depending on their shape. This is especially due to the absorption of visible light, both along the length of the nanorod (the longitudinal plasmon band) and along the width of the nanorod (the transverse plasmon band). In general, the larger the aspect ratio, the more red-shifted the longitudinal plasmon band [139]. Generally, TEM is used to determine the aspect ratios of nanorods and nanowires, although problems with sample preparation and the limited selection of images

for determining nanorod size may make it difficult to obtain statistically correct and reproducible values. Recently, Eustis and El-Sayed have proposed an optical absorption-based method to assess the aspect ratio distribution by using the observed longitudinal surface plasmon resonance (SPR) absorption spectrum of gold nanorods in solution [140]. The use of XAS may provide information regarding the diameter of metallic nanorods, based on the derived coordination parameters, and this information – when coupled with the length obtained using TEM – may provide better information about the aspect ratio than when using TEM alone.

Park *et al*. utilized XAS to characterize the core-shell-type bimetallic interfacial structure of Co_{core}–Pt_{shell}-type super paramagnetic nanoparticles, and monitored their anisotropic phase transition to ferromagnetic solid solution nanoalloys [140-141]. In order to elucidate the interfacial structure, these authors relied on the XAS measurements at both Co K-edge and Pt L_{III}-edge of CoPt nanoparticles. In the $k^3\chi(k)$ Co K-edge Fourier transform (FT) EXAFS spectra, a strong peak was observed at ~2.0 Å and a shoulder at ~2.3 Å, indicative of two different types of neighboring atom around the Co atom in the first shell. The peak at ~2.0 Å was attributed to single scattering by Co_{core}–Co_{core} atoms within the Co_{core} region, while the shoulder at ~2.3 Å corresponded to single scattering by the Co_{core}–Pt_{shell} at the core–shell interfaces. These authors suggested that three different environments were present for Pt atoms, based on the FT of the Pt L_{III}-edge $k^2\chi(k)$ FT-EXAFS spectrum. A strong peak at ~2.3 Å arose from the single scattering of Co_{core}–Pt_{shell} atoms in the interface region, while the shoulder at ~2.7 Å was due to Pt_{shell}–Pt_{shell} interaction within the Pt shell layer. In addition, a peak was observed at ~1.7 Å which corresponded to the scattering with capping molecules on the surface of the Pt shell layer. The authors described a Co_{core}–Pt_{shell} structure to the synthesized nanomaterials based on the position of peaks in FT-EXAFS spectra. If the alloying extent of the Co and Pt and the total coordination number from both edges can be determined, then a better picture can be obtained of the core-shell structure. From the available Co K-edge XAS coordination parameters, the alloying of Co (J_{Co}) can be calculated as 67%, indicating that the segregation of Co is less in nanoparticles. Unfortunately, however, the Pt L_{III}-edge XAS coordination parameters were not provided by these authors to deduce the alloying extent of Pt.

Teng *et al*. presented the structural elucidation of Pd/Au nanostructures with various compositions ($Pd_{68}Au_{32}$ and $Pd_{45}Au_{55}$) generated from Pd nanowires via a galvanic replacement reaction, and assessed the degree of alloying [142]. It was observed that the first-nearest-neighbor (1NN) Pd–Pd coordination number N_{Pd-Pd} decreased monotonically from 9.4 (Pd nanowires) to 0 (Au nanoparticles) as the reaction progressed. Remarkably, the N_{Pd-Au} increased with reaction time faster than did the X_{Au}/X_{Pd} composition ratios (N_{Pd-Au} was increased from 0.3 in $Pd_{68}Au_{32}$ to 4.8 in $Pd_{45}Au_{55}$, compared to the X_{Au}/X_{Pd} increase from 32/68 to 55/45). Based on these trends, the authors demonstrated an increased alloying in Pd/Au nanostructures during the reaction. From the XAS parameters reported in these studies, we calculated the alloying of Pd (J_{Pd}) and Au (J_{Au}) in $Pd_{45}Au_{55}$ nanoparticles based on our XAS methodology [42], and found values of 88 and 89, respectively. The

higher J_{Pd} and J_{Au} values indicated a higher extent of alloying in $Pd_{45}Au_{55}$ nanoparticles, which was consistent with the authors' own observations. The N_{Au-Au} was largest (9.5) for the $Pd_{68}Au_{32}$ sample, decreased for the $Pd_{45}Au_{55}$ sample to 7.2, and then rose to 8.4 for the final product (Au nanoparticles). Based on the fact that the N_{Au-Au}/N_{Au-Pd} ratio (~14) obtained was much greater than the ratio of the compositions X_{Au}/X_{Pd} (~0.47; equality would be expected for a random alloy) for the $Pd_{68}Au_{32}$ nanostructure, the authors emphasized that Au and Pd displayed a significant degree of segregation and proposed the existence of a core-shell-like, nonrandom Pd/Au alloy during the initial stage of the replacement reaction. As the galvanic replacement reaction progressed, the authors observed that the N_{Au-Au}/N_{Au-Pd} ratio (1.58) was comparable to X_{Au}/X_{Pd} (1.22), and proposed the presence of random alloying in the resultant $Pd_{45}Au_{55}$ nanostructures. For $Pd_{68}Au_{32}$ elongated nanoparticles, the 1NN Pd–metal coordination number ($N_{Pd-M} = N_{Pd-Au} + N_{Pd-Pd}$) was shown to be 8.3 ± 1.0, while the 1NN Au–metal coordination number (N_{Au-M}) was 10.2 ± 1.5. Based on the fact that $N_{Pd-M} < N_{Au-M}$, the authors concluded that a large (compared to the statistical average) number of Pd atoms segregated to the surface of the elongated nanoparticles and Au to the core, since atoms on the surface have fewer neighbors than those in the core. Interestingly, the alloying extent of Pd (J_{Pd}) and Au (J_{Au}) in $Pd_{68}Au_{32}$ nanoparticles was found to be 11 and 10, respectively, if the developed XAS methodology was applies. Both, the alloying extent values calculated and the coordination number parameter relationship $N_{Au-M} > N_{Pd-M}$ strongly supported a core-shell structure for $Pd_{68}Au_{32}$ nanoparticles that was consistent with the author's proposed structure. At this point it is worth mentioning that, apart from the coordination number parameter relationship, when considering the alloying extent the reliability in predicting the structure of bimetallic nanoparticles is greatly improved.

We have recently demonstrated the unique application of XAS as a fundamental characterization tool when designing and controlling the architecture of Pd–Au bimetallic nanoparticles within a water-in-oil microemulsion system of water/sodium bis(2-ethylhexyl)sulfosuccinate (AOT)/*n*-heptane [68]. By performing hydrazine reduction and redox transmetallation reactions sequentially within water-in-oil microemulsions, we have generated Pd–Au bimetallic clusters with various Pd–Au atomic stackings. First, by performing a redox transmetallation reaction between Pd_{nuclei} nanoparticles and the Au^{3+} ions, Pd_{nuclei}–$Au_{stack\text{-}1}$ nanoparticles were generated. Following the hydrazine reduction reaction, Pd^{2+} ions were reduced on the preformed Pd_{nuclei}–$Au_{stack\text{-}1}$ nanoparticles in order to fabricate (Pd_{nuclei}–$Au_{stack\text{-}1}$)–Pd_{surf} nanoparticles (Figure 11.4). Both, the redox transmetallation and hydrazine reduction reactions were repeated to manipulate the Pd–Au stacking until (Pd_{nuclei}–$Au_{stack\text{-}3}$)–Pd_{surf} nanoparticles were produced.

Based on the XAS structural parameters, the degree of alloying and extent of atomic distribution could be evaluated. In the case of (Pd_{nuclei}–$Au_{stack\text{-}1}$)–Pd_{surf} stacked Pd–Au bimetallic nanoparticles formed during the second hydrazine reduction reaction, the N_{Au-Au} and N_{Au-Pd} were determined as 8.17 and 1.37, respectively, giving a total coordination number of Au and Pd around Au ($\Sigma N_{Au-i} = N_{Au-Au} + N_{Au-Pd}$) as 9.54. Similarly, the N_{Pd-Pd} and N_{Pd-Au} were determined as 6.37

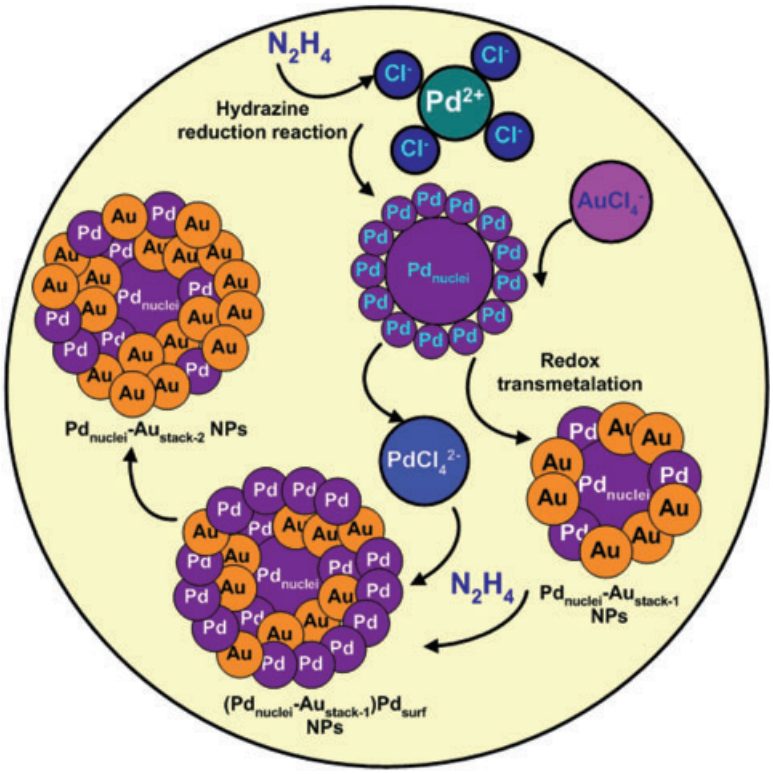

Figure 11.4 Schematic of the architecture of Pd–Au bimetallic nanoparticles as investigated by X-ray absorption spectroscopy. Modified from the original figure of Ref. [68].

and 0.87, respectively, providing a total coordination number of Pd and Au around Pd ($\Sigma N_{\text{Pd–i}} = N_{\text{Pd–Pd}} + N_{\text{Pd–Au}}$) as 7.24. From these values, the structural parameters P_{observed} ($= N_{\text{Au–Pd}}/\Sigma N_{\text{Au–i}}$) and R_{observed} ($= N_{\text{Pd–Au}}/\Sigma N_{\text{Pd–i}}$) were calculated as 0.14 and 0.12, respectively. From the calculated degree of alloying of Au and Pd – that is, J_{Au} (22.9%) and J_{Pd} (30.8%) by our developed methodology – low values of J_{Au} and J_{Pd} indicated that both Pd and Au atoms were segregated in the cluster. Thus, XAS can be conveniently utilized to characterize the segregation in nanomaterials, when the coordination number parameters have been properly extracted.

Several authors have reported that the optical properties of nanoparticles depend heavily on whether the participating elements are alloyed or segregated (core-shell). Although the results for alloys seem to agree fairly well, different interpretations have been proposed for correlating the optical properties of core-shell structures. It has been reported that the position of the plasmon band of Ag–Au nanoparticles is heavily dependent on the alloy composition, and lies between those of pure Ag and pure Au nanoparticles [46, 143–145]. In the case of Au_{core}–Ag_{shell} nanostructures, several groups have reported that the optical properties are

significantly influenced by the core and shell thickness [146]. As discussed earlier, it is fortunate that XAS can reveal information about alloying and segregation phenomena in nanomaterials.

Chen *et al*. have explored the structure of Ag–Au bimetallic nanoparticles by using EXAFS [147]. These authors presented the Au L_{III} edge EXAFS spectra $\chi(k)$ of three Ag–Au alloy samples with various Ag to Au ratios (Ag : Au as 1 : 3, 1 : 1 and 3 : 1). In the case of FT-EXAFS spectra of alloy samples, Au–Ag in the first shell appeared as a doublet in the amplitude, but by increasing the Ag amount the peak intensity at a larger distance was seen to increase relative to that at a smaller distance. Chen and coworkers pointed out that both peaks came from the first neighbor (with a single distance), and appeared at a shorter distance from the actual bond lengths. The same authors surmised that both EXAFS oscillation of $\chi(k)$ and FT of $\chi(k)$ for this series of samples showed a continuous change with increasing amounts of Ag. Unlike the alloy structured samples, in the Au L_{III} edge EXAFS spectra of the Ag–Au core-shell nanoparticles (Ag : Au ratios of 0.4 : 0.2, 0.4 : 0.3 and 0.4 : 0.4), the peak related to the first shell did not separate into two parts. For Ag : Au ratios of 0 : 0.4, 0.4 : 0.2, 0.4 : 0.3 and 0.4 : 0.4, there were no remarkable differences in the FT of $\chi(k)$ and interatomic distance around Au atoms. These results reveal that the surrounding sites around Au atoms are Au atoms, and that the Au atoms formed a uniform layer. Although Chen *et al*. surmised that Ag and Au atoms formed Ag_{core}–Au_{shell} structured nanoparticles, they failed to produce any data from the Ag edge that would permit calculation of the alloying of Ag and Au in order to better understand the alloy versus core-shell structure.

Lee and coworkers have characterized various core-shell-type nanomaterials including Co@Au, Co@Pd, Co@Pt and Co@Cu nanoparticles fabricated using a redox transmetallation reaction [148]. These authors compared the Co K-edge and Au L_{III}-edge XAS of Co–Au nanoparticles with that of pure metallic Co nanoparticles in order to elucidate the local structures around the Co core and the Au shell atoms of the nanoparticles. The core-shell structure of the bimetallic Co–Au nanoparticles was supported by an analysis of the FTs of the EXAFS spectra. Thus, the pure Co nanoparticles showed a symmetric FT peak at ~2.2 Å, while a new FT peak was observed at ~2.6 Å, in addition to that at ~2.2 Å for the Co@Au nanoparticles in the Co K-edge EXAFS spectra. Based on these FT peak features, the authors suggested that the first shell around the central Co atom included two different types of neighboring atoms of core-shell-type nanoparticles. The authors also attributed the shorter FT peak that appeared at ~2.2 Å to a single scattering between the inner Co atoms themselves within the core region, whereas the longer FT peak that appeared at 2.6 Å was ascribed to single scattering between a Co atom in the core surface and an Au atom in the outer shell layer. In the corresponding Au L_{III}-edge EXAFS spectra, FT peaks were observed at ~2.6 and ~2.8 Å, corresponding to the scattering between Co_{core} atoms and Au_{shell} atoms in the interface region of Co@Au and the scattering between Au_{shell} atoms and Au_{shell} atoms within the Au shell layer, respectively. The results of the authors' XAS analysis clearly suggested that the obtained nanoparticles were of Co_{core}–Au_{shell} nanostructure.

Lahiri *et al.* demonstrated EXAFS on bimetallic Ag–Pt and Ag–Pd nanorods that had high aspect ratios and were synthesized using a radiolysis method [149]. The EXAFS data on Ag–Pt nanorods revealed that the first shell did not show any presence of Ag, and that the central Pt was coordinated only by Pt atoms (for $Pt_{0.6}Ag_{0.4}$, the $N_{Pt–Pt}$ is 5 and $N_{Pt–Ag}$ is 2). These authors ruled out the formation of an alloy structure, as there was an absence of any expansion of the lattice parameter of Pt. This implies that, in these Ag core–Pt shell particles, the two metals are not alloyed but rather retain their bulk lattice parameters. In the case of Pd–Ag nanorod samples from the Pd K-edge, the FT-EXAFS spectra showed that the nearest neighbor distance expanded in line with an increase in the molar percentage of Pd. While conducting the analysis for the Ag edge, the authors fixed the Debye–Waller factor from the fit results at the Pd K-edge. Around Ag atoms, a contraction of the first shell was observed, while the FT-EXAFS spectra at the Ag K-edge exhibited a change in the nearest neighbor distance with a change in the molar percentage of Ag within the bimetallic system. Based on these measurements, it was suggested that the alloying of Ag and Pd had occurred in Ag–Pd nanorods.

In another interesting study, XAS was used to elucidate the growth mechanism of gold nanorods [33, 150]. Here, long gold nanorods were fabricated by controlling the volume of the growth solution, and shapes ranging from fusiform nanoparticles to one-dimensional (1-D) rods were observed to evolve. By increasing the growth solution, it was possible to control the length of the nanorods up to 2 μm, with aspect ratios of up to ~70. An analysis with EXAFS confirmed the growth of gold and the environment around the Au atoms during the reaction. The Au L_{III} edge FT-EXAFS spectra of gold nanorods and Au foil exhibited a main peak corresponding to the Au–Au metal bond. For the corresponding foil case, the shape of the main peak was consistent with that of the gold foil, indicating that the local structure of as-prepared Au nanorods was similar to that of gold foil. Based on XAS structural parameters, the authors showed that interatomic distance between the Au_{core} and the nearest neighboring Au atom to be 2.86 Å, and consistent with the value for bulk gold (2.88 Å). The EXAFS data clearly confirmed that gold nanorods prepared using the authors' method were indeed of a *fcc* phase of gold. The coordination number of the gold nanorods appeared to be slightly smaller than that of gold foil, owing to the nature of the nanomaterials. As the size of materials was reduced, the increase in surface-to-volume ratio led to a decrease in the coordination number.

Aruguete *et al.* studied the surface structure of aligned colloidal CdSe nanorods by combining *ab initio* density functional theory (DFT) calculations with EXAFS [151]. By rotating the sample, the authors were able to measure XAS at multiple rod orientations with respect to the polarization of the X-rays. The corresponding XAS data analysis suggested that, in the CdSe nanorods, both the 1NN distance and second nearest-neighbor (2NN) distance were reduced along the c-axis with respect to bulk CdSe. These authors used the coordination number of Se atoms as a probe of the Cd content on the nanorod surfaces, and measured the 1NN and 2NN coordination numbers of Se as 3.6 and 9.98, respectively; these appeared to fall in between the values expected for a completely Cd-terminated wire (1NN, 4;

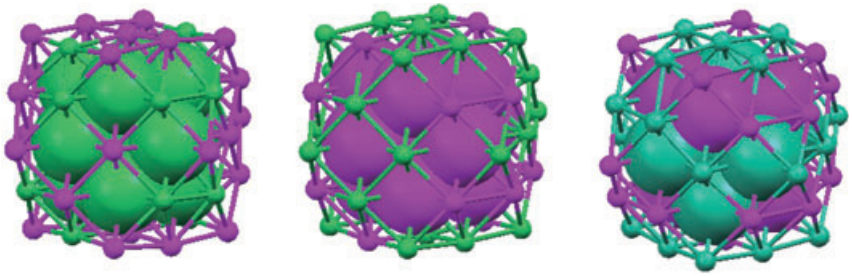

Figure 11.5 Bimetallic nanoparticles with various structures of core-shell and random alloy used for calculating the surface composition. P atoms are shown in pink; R atoms are shown in green.

2NN, 9.94) and those expected for a stoichiometric wire (1NN, 3.4; 2NN, 10.01). Based on these observations, and by comparing the nanowire models with XAS measurements, the authors showed the nanorod surfaces to be Cd-rich, with some unpassivated Se atoms. Unfortunately, not all of the necessary XAS coordination number parameters were available to calculate the alloying of Cd and Se in CdSe nanorods.

Subsequently, we calculated the surface composition of P in P–R bi-MNPs of cubo-octahedral shape with three types of structure, viz., R_{core}-$(P–R)_{shell}$, P_{core}-$(P–R)_{shell}$ and P–R random alloy (as shown in Figure 11.5), with a P : R atomic ratio of 28 : 27, using a developed combined modeling-XAS methodology. For an R_{core}-$(P–R)_{shell}$ structured bimetallic nanoparticle, the coordination numbers of $N_{P–P}$ and $N_{P–R}$ were calculated as 2.43 and 4.07, respectively. These values provide the total coordination of P and R around P; that is, $\Sigma N_{P–i} = N_{P–P} + N_{P–R}$ as 6.50. Similarly, the coordination numbers $N_{R–R}$ and $N_{R–P}$ were calculated as 5.48 and 4.22, respectively, and yielded $\Sigma N_{R–i} = N_{R–R} + N_{R–P}$ as 9.70. By substituting $\Sigma N_{P–i}$ and nanoparticle composition in Equation 11.11, the surface composition of P $\left(x_P^s\right)$ was calculated as 0.70. The $\Sigma N_{P–i}$ and $\Sigma N_{R–i}$ were found to be 9.32 and 6.33, respectively, for the P_{core}-$(P–R)_{shell}$ structured bimetallic nanoparticles, which yielded x_P^s as 0.32. For the P–R random alloy, the extracted $\Sigma N_{P–i}$ and $\Sigma N_{R–i}$ were found to be 7.93 and 7.78, respectively. Based on these values, x_P^s was calculated as 0.50. Although the calculated surface composition discussed here is based on coordination numbers extracted from the model, it is possible to obtain both $\Sigma N_{P–i}$ and $\Sigma N_{R–i}$ from XAS measurements; then, by substituting these values into Equations 11.11 and 11.12, the surface composition of P and R, respectively, can be easily determined.

This methodology was also applied to calculate the surface composition of Au and Pd in bimetallic Pd–Au nanoparticles prepared in microemulsions [68]. Three types of Pd–Au nanoparticle with various Pd–Au stackings, viz., $Pd–Au_{stack-1}$, $Pd–Au_{stack-2}$ and $Pd–Au_{stack-3}$, were generated by performing hydrazine reduction and redox transmetallation reactions sequentially within a water-in-oil microemulsion.

For the Pd–$Au_{stack\text{-}1}$ nanoparticles (atomic ratio, $N_{Au}/N_{Pd} = 0.633$), the total coordination of Au and Pd around Au; that is, $\Sigma N_{Au\text{–}i} = N_{Au\text{–}Au} + N_{Au\text{–}Pd}$ was 9.00. Similarly, the total coordination of Au and Pd around Au; that is, $\Sigma N_{Pd\text{–}i} = N_{Pd\text{–}Pd} + N_{Pd\text{–}Au}$ was 2.38. By substituting $\Sigma N_{Au\text{–}i}$ and $\Sigma N_{Pd\text{–}i}$ in Equations 11.11 and 11.12 along with the Au and Pd compositions, the surface compositions of Au (x^s_{Au}) and Pd (x^s_{Pd}) were calculated as 0.165 and 0.835, respectively. By using the determined coordination parameters from XAS measurements, for the Pd–$Au_{stack\text{-}2}$ nanoparticles, the (x^s_{Au}) and Pd (x^s_{Pd}) were calculated as 0.177 and 0.823, respectively. Similarly, for the Pd–$Au_{stack\text{-}3}$ nanoparticles, the (x^s_{Au}) and Pd (x^s_{Pd}) were calculated as 0.205 and 0.795, respectively. It is interesting to note that the trend in the increase in surface composition of Au for Pd–$Au_{stack\text{-}2}$ and Pd–$Au_{stack\text{-}3}$ nanoparticles, when compared to Pd–$Au_{stack\text{-}1}$ nanoparticles, was consistent with the experimental conditions. Since the outermost layer plays a dominant role in determining the interaction of a nanoparticle with the incoming light, the information regarding surface chemistry is critical when assessing the optical properties of nanoparticles. It is believed that the possibility of XAS providing information that concerns not only the surface composition but also the atomic stacking of nanoparticles, will be valuable for realizing the optical properties of Au-based bimetallic nanoparticles of either core-shell or alloy-type structure.

11.3.5
XAS Characterization of Surface Interactions

The successful application of nanomaterials in biomedical systems, as well as in medical therapy and diagnosis, lies in the engineering of a robust, tailored surface functionality that will ensure biocompatibility and allow specific site targeting. As surface functionalization is believed to alter the electronic structure of nanomaterials, then depending on the intensity of the nanoparticle-capping molecule interaction, the electronic structure can be tuned to modify both magnetic and optical properties. In this respect, Modrow and coworkers have demonstrated the capabilities of XAS to provide an understanding of the surface engineering of Co and FeCo nanoparticles [152]. These authors discussed the Co K-edge XANES spectra of Co nanoparticles that were peptized in water and ethanol by the thiol group of L-cysteine ethyl ester, with the amino acid remaining free. Based on the XANES results, it was found that the surface-modified Co nanoparticles exhibited no drastic changes in white line intensity, which in turn suggested some degree of protection of the cobalt core. When the authors monitored the S K-edge XANES spectrum of the modified Co nanoparticles along with pure cysteine, they identified a significant shift in the position of the shape resonances to a lower energy in the case of surface-modified Co nanoparticles when compared to pure cysteine. Such a shift was attributed to the formation of a sulfur–metal bond, leading to a notable charge transfer towards the sulfur atom.

In another interesting study, Crespo *et al.* utilized XANES to determine how changes in electronic structure affect the magnetic behavior of Au and ZnO nanoparticles, when capped with different organic molecules [153]. From the Au

L_{III} XANES spectra, the intensity of threshold resonance of Au nanoparticles capped with thiol (Au–SR sample) was found to be higher than that of the Au foil, and also of Au nanoparticles capped with a surfactant, tetraoctyl ammonium bromide ($BrN(C_8H_{17})_4$) (Au–NR sample). The study results indicated that the capping of Au nanoparticles with thiols promotes charge transfer from the Au atoms to organic chains, but this is not detected when Au nanoparticles are stabilized with surfactant molecules. Based on the corresponding magnetization curves, the Au–NR sample was shown to exhibit a diamagnetic behavior similar to that of bulk Au, while the Au–SR sample exhibited an unexpected paramagnetic behavior. The increase in the number of holes at the d-band of the Au–SR sample was attributed to paramagnetic behavior.

11.4 Conclusions

During recent years, XAS has been successfully applied to identify the core-shell and alloy structures of nanomaterials. As the technique does not require any long-range ordering of the material of interest, amorphous materials may be also successfully studied. The most striking advantage of XAS is that detailed electronic and structural information about nanomaterials can be obtained, within their active chemical environments, and their structure–performance relationships can be fully understood. Whilst XAS is a 'bulk' technique that provides 'average' information concerning all of the elements present in the material, it is also possible – due to the large number of atoms present on the surface in the case of nanoscale materials – to obtain information about the nanomaterial's surface properties. Such information is critical, since the surface chemistry of nanomaterials predominantly determines their biointerfacial properties. There remains a vast need for characterization techniques to be developed that are capable of providing a complete and comprehensive knowledge of the structure and surface properties of nanomaterials, notably for the design and development of nanodevices for biomedical applications. With the increased availability of sophisticated synchrotron radiation sources worldwide, coupled with major developments in analysis software, XAS may provide solutions to the complex structural problems of nanomaterials, thereby increasing our current knowledge base of nanoscale properties, including that of biocompatibility. It is important to note that, as with any other characterization technique, XAS also has its limitations, and its sole use may fail to provide much needed information regarding the characterization of nanomaterials. However, if XAS is used in conjunction with electron microscopy, then a much better characterization can be achieved. Notably, great care must be taken to ensure the uniformity of nanoparticles, to extract reliable XAS parameters, and to obtain information on particle size and shape, as these are the major requirements for obtaining reliable information on the alloying extent and surface and core compositions of nanomaterials via XAS. It is hoped that this chapter will help the reader to appreciate the promise of XAS for characterizing the structure,

atomic distribution and surface chemistry/composition of core-shell or alloy-type nanomaterials, many of which are today highly attractive in terms of their biomedical applications.

Acknowledgments

The authors gratefully acknowledge financial support from the National Science Council (NSC), and the facilities of the National Synchrotron Radiation Research Center (NSRRC) and the National Taiwan University of Science and Technology (NTUST), Taiwan.

References

1 Ferrari, M. (2005) Cancer nanotechnology: opportunities and challenges. *Nature Reviews. Cancer*, **5**, 161–71.

2 Chan, W.C.W. and Nie, S. (1998) Quantum dot bioconjugates for ultrasensitive nonisotopic detection. *Science*, **281**, 2016–19.

3 Bruchez, M., Moronne, M., Gin, P., Weiss, S. and Alivisatos, P. (1998) Semiconductor nanocrystals as fluorescent biological labels. *Science*, **281**, 2013–16.

4 Nicewarner-Pena, S.R., Freeman, R.G., Reiss, B.D., Pena, D.J., Walton, I.D., Cromer, R., Keating, C.D. and Natan, M.J. (2001) Submicrometer metallic barcodes. *Science*, **294**, 137–41.

5 Taton, T.A., Mirkin, C.A. and Letsinger, R.L. (2000) Scanometric DNA array detection with nanoparticle probes. *Science*, **289**, 1757–60.

6 Mornet, S., Lambert, O., Duguet, E. and Brisson, A. (2005) The formation of supported lipid bilayers on silica nanoparticles revealed by cryoelectron microscopy. *Nano Letters*, **5**, 281–5.

7 Mornet, S., Vasseur, S., Grasset, F. and Duguet, E. (2004) Magnetic nanoparticle design for medical diagnosis and therapy. *Materials Chemistry*, **14**, 2161–75.

8 Kim, D.K., Mikhaylova, M., Zhang, Y. and Muhammed, M. (2003) Protective coating of superparamagnetic iron oxide nanoparticles. *Chemistry of Materials*, **15**, 1617–27.

9 O'Neal, D.P., Hirsch, L.R., Halas, N.J., Payne, J.D. and West, J.L. (2004) Photothermal tumor ablation in mice using near infrared-absorbing nanoparticles. *Cancer Letters*, **209**, 171–6.

10 Gao, X., Cui, Y., Levenson, R.M., Chung, L.W.K. and Nie, S. (2004) In vivo cancer targeting and imaging with semiconductor quantum dots. *Nature Biotechnology*, **22**, 969–76.

11 Kang, S.M., Lee, K.B., Kim, D.J. and Choi, I.S. (2006) Biomimetic approach to the formation of gold nanoparticle/silica core/shell structures and subsequent bioconjugation. *Nanotechnology*, **17**, 4719–25.

12 Salgueiriño-Maceira, V. and Correa-Duarte, M.A. (2007) Increasing the complexity of magnetic core/shell structured nanocomposites for biological applications. *Advanced Materials*, **19**, 4131–44.

13 Pérez-Juste, J., Pastoriza-Santos, I., Liz-Marzán, L.M. and Mulvaney, P. (2005) Gold nanorods: synthesis, characterization and applications. *Coordination Chemistry Reviews*, **249**, 1870–901.

14 Sastry, M., Swami, A., Mandal, S. and Selvakannan, P.R. (2005) New approaches to the synthesis of anisotropic, core-shell and hollow metal nanostructures. *Journal of Materials Chemistry*, **15**, 3161–74.

15 Katz, E. and Willner, I. (2004) Integrated nanoparticle-biomolecule hybrid systems: synthesis, properties, and applications. *Angewandte Chemie – International Edition in English*, **43**, 6042–108.

16 Schultz, D.A. (2003) Plasmon resonant particles for biological detection. *Current Opinion in Biotechnology*, **14**, 13–22.

17 Salem, A.K., Searson, P.C. and Leong, K.W. (2003) Multifunctional nanorods for gene delivery. *Nature Materials*, **2**, 668–71.

18 Tkachenko, A.G., Xie, H., Coleman, D., Glomm, W., Ryan, J., Anderson, M.F., Franzen, S. and Feldheim, D.L. (2003) Multifunctional gold nanoparticle-peptide complexes for nuclear targeting. *Journal of the American Chemical Society*, **125**, 4700–1.

19 Murphy, C.J., Sau, T.K., Gole, A.M., Orendorff, C.J., Gao, J., Gou, L., Hunyadi, S.E. and Li, T.J. (2005) Anisotropic metal nanoparticles: synthesis, assembly, and optical applications. *Physical Chemistry B*, **109**, 13857–70.

20 Kelly, K.L., Coronado, E., Zhao, L.L. and Schatz, G.C. (2003) The optical properties of metal nanoparticles: the influence of size, shape, and dielectric environment. *The Journal of Physical Chemistry B*, **107**, 668–77.

21 Hornyak, G.L., Patrissi, C.J. and Martin, C.R. (1997) Fabrication, characterization, and optical properties of gold Nanoparticle/porous alumina composites: the nonscattering Maxwell-Garnett limit. *The Journal of Physical Chemistry B*, **101**, 1548–55.

22 Tao, A., Kim, F., Hess, C., Goldberger, J., He, R., Sun, Y., Xia, Y. and Yang, P. (2003) Langmuir-Blodgett silver nanowire monolayers for molecular sensing using surface-enhanced Raman spectroscopy. *Nano Letters*, **3**, 1229–33.

23 Imura, K., Nagahara, T. and Okamoto, H. (2004) Plasmon mode imaging of single gold nanorods. *Journal of the American Chemical Society*, **126**, 12730–1.

24 Hanarp, P., Kall, M. and Sutherland, D.S. (2003) Optical properties of short range ordered arrays of nanometer gold disks prepared by colloidal lithography. *The Journal of Physical Chemistry B*, **107**, 5768–72.

25 Grainger, D.W. and Castner, D.G. (2008) Nanobiomaterials and nanoanalysis: opportunities for improving the science to benefit biomedical technologies. *Advanced Materials*, **20**, 867–77.

26 Liz-Marzán, L.M. (2006) Tailoring surface plasmons through the morphology and assembly of metal nanoparticles. *Langmuir*, **22**, 32–41.

27 Murphy, C.J. and Jana, N.R. (2002) Controlling the aspect ratio of inorganic nanorods and nanowires. *Advanced Materials*, **14**, 80–2.

28 Thurn-Albrecht, T., Schotter, J., Kastle, G.A., Emley, N., Shibauchi, T., Krusin-Elbaum, L., Guarini, K., Black, C.T., Tuominen, M.T. and Russell, T.P. (2000) Ultrahigh-density nanowire arrays grown in self-assembled diblock copolymer templates. *Science*, **290**, 2126–9.

29 Kottmann, J.P., Martin, O.J.F., Smith, D.R. and Schultz, S. (2001) Dramatic localized electromagnetic enhancement in plasmon resonant nanowires. *Chemical Physics Letters*, **341**, 1–6.

30 Jana, N.R., Gearheart, L. and Murphy, C.J. (2001) Wet chemical synthesis of silver nanorods and nanowires of controllable aspect ratio. *Chemical Communications*, 617–18.

31 Jana, N.R., Gearheart, L. and Murphy, C.J. (2001) Seed-mediated growth approach for shape-controlled synthesis of spheroidal and rod-like gold nanoparticles using a surfactant template. *Advanced Materials*, **13**, 1389–93.

32 Busbee, B.D., Obare, S. and Murphy, C.J. (2003) An improved synthesis of high-aspect ratio gold nano-rods. *Advanced Materials*, **15**, 414–16.

33 Chen, H.M., Peng, H.C., Liu, R.S., Asakura, K., Lee, C.L., Lee, J.F. and Hu, S.F. (2005) Controlling the length and shape of gold nanorods. *The Journal of Physical Chemistry B*, **109**, 19553–5.

34 Liu, R.S., Chen, H.M. and Hu, S.F. (2007) Synthesis and characterization of long gold nanorods. *IEEJ Transactions on Electrical and Electronic Engineering*, **2**, 468–72.

35 Oldenburg, S.J., Jackson, J.B., Westcott, S.L. and Halas, N.J. (1999) Infrared extinction properties of gold nanoshells. *Applied Physics Letters*, **75**, 2897–9.

36 Oldenburg, S.J., Averitt, R.D., Westcott, S.L. and Halas, N.J. (1998) Nanoengineering of optical resonances. *Chemical Physics Letters*, **288**, 243–7.

37 Jun, C.H., Park, Y.J., Yeon, Y.R., Choi, J.-R., Lee, W.-R., Ko, S.-J. and Cheon, J. (2006) Demonstration of a magnetic field and catalytic Co@Pt nanoparticle as a dual-function platform. *Chemical Communications*, 1619–21.

38 Bradley, J.S. (1994) The Chemistry of Transition Metal Colloids, in *Clusters and Colloids: From Theory to Applications* (ed. G. Schmid), Wiley-VCH Verlag GmbH, Weinheim, pp. 459–544.

39 Toshima, N. and Yonezawa, T. (1998) Bimetallic nanoparticles – novel materials for chemical and physical applications. *New Journal of Chemistry*, **22**, 1179–201.

40 Hwang, B.J., Sarma, L.S., Wang, G.R., Chen, C.H., Liu, D.G., Sheu, H.S. and Lee, J.F. (2007) Heat-induced alterations in the surface population of metal sites in bimetallic nanoparticles. *Chemistry – A European Journal*, **13**, 6255–64.

41 Hwang, B.J., Sarma, L.S., Chen, C.H., Tang, M.T., Liu, D.G. and Lee, J.F. (2007) Depth profile of alloying extent and composition in bimetallic nanoparticles investigated by in situ X-ray absorption spectroscopy. *Applied Physics Letters*, **91**, 023108.

42 Hwang, B.J., Sarma, L.S., Chen, J.M., Chen, C.H., Shih, S.C., Wang, G.R., Liu, D.G., Lee, J.F. and Tang, M.T. (2005) Structural models and atomic distribution of bimetallic nanoparticles as investigated by X-ray absorption spectroscopy. *Journal of the American Chemical Society*, **127**, 11140–5.

43 Ferrando, R., Jellinek, J. and Johnston, R.L. (2008) Nano alloys: from theory to applications of alloy clusters and nanoparticles. *Chemical Reviews*, **108**, 845–909.

44 Srnová-Šloufová, I., Lednický, F., Gemperle, A. and Gemperlová, J. (2000) Core-shell (Ag)Au bimetallic nanoparticles: analysis of transmission electron microscopy images. *Langmuir*, **16**, 9928–35.

45 Chen, Y.H. and Nickel, U. (1993) Superadditive catalysis of homogeneous redox reactions with mixed silver–gold colloids. *Journal of the Chemical Society – Faraday Transactions*, **89**, 2479–85.

46 Link, S., Wang, Z.L. and El-Sayed, M.A. (1999) Alloy formation of gold-silver nanoparticles and the dependence of the plasmon absorption on their composition. *The Journal of Physical Chemistry B*, **103**, 3529–33.

47 Kan, C., Cai, W., Li, C., Zhang, L. and Hofmeister, H. (2003) Ultrasonic synthesis and optical properties of Au/Pd bimetallic nanoparticles in ethylene glycol. *Journal of Physics D: Applied Physics*, **36**, 1609–14.

48 Mizukoshi, Y., Fujimoto, T., Nagata, Y., Oshima, R. and Maeda, Y. (2000) Characterization and catalytic activity of core-shell structured gold/palladium bimetallic nanoparticles synthesized by the sonochemical method. *The Journal of Physical Chemistry B*, **104**, 6028–32.

49 Yang, J., Lee, J.Y., Chen, L.X. and Too, H.P. (2005) A phase-transfer identification of core-shell structures in Ag-Pt nanoparticles. *The Journal of Physical Chemistry B*, **109**, 5468–72.

50 Voyles, P.M., Muller, D.A., Grazul, J.L., Citrin, P.H. and Gossmann, H.-J.L. (2002) Atomic-scale imaging of individual dopant atoms and clusters in highly n-type bulk Si. *Nature*, **416**, 826–9.

51 Ferrer, D., Torres-Castro, A., Gao, X., Sepúlveda-Guzmán, S., Ortiz-Méndez, U. and José-Yacamán, M. (2007) Three-layer core/shell structure in Au-Pd bimetallic nanoparticles. *Nano Letters*, **7**, 1701–5.

52 Polak, M. and Rubinovich, L. (2000) The interplay of surface segregation and atomic order in alloys. *Surface Science Reports*, **38**, 127–94.

53 Batista, J., Pintar, A. and Ceh, M. (1997) Characterization of supported Pd-Cu bimetallic catalysts by SEM, EDXS, AES and catalytic selectivity measurements. *Catalysis Letters*, **43**, 79–84.

54 Lang, H., Maldonado, S., Stevenson, K.J. and Chandler, B.D. (2004) Synthesis and characterization of dendrimer templated supported bimetallic Pt-Au nanoparticles.

Journal of the American Chemical Society, **126**, 12949–56.
55 Somorjai, G.A. (1978) Surface science. *Science*, **201**, 489–97.
56 Ross, P.N. (1991) Characterization of alloy electrocatalysts for direct oxidation of methanol: new methods. *Electrochimica Acta*, **36**, 2053–62.
57 Powell, C.J. (1978) *Quantitative Surface Analysis of Materials* (ed. N.S., McIntyre), ASTM Special Publication 643, American Society for Testing and Materials, Philadelphia, pp. 5–30.
58 Briggs, D. and Seah, M.P. (1990) *Practical Surface Analysis*, Vol. **1**, John Wiley & Sons, Inc., New York.
59 Bazin, D. and Rehr, J.J. (2003) Limits and advantages of X-ray absorption near edge structure for nanometer scale metallic clusters. *The Journal of Physical Chemistry B*, **107**, 12398–402.
60 Bazin, D., Sayers, D., Rehr, J.J. and Mottet, C. (1997) Numerical simulation of the platinum L_{III} edge white line relative to nanometer scale clusters. *The Journal of Physical Chemistry B*, **101**, 5332–6.
61 Konnigsberger, D.C. and Prins, R. (eds) (1988) *X-Ray absorption: Principles, Applications, Techniques of EXAFS, SEXAFS, and XANES*, John Wiley & Sons, Inc., New York, p. 362.
62 Iwasawa, Y. (ed.) (1996) *XAS for Catalysts and Surfaces*, World Scientific, Singapore, p. 113.
63 Frenkel, A.I., Hills, C.W. and Nuzzo, R.G. (2001) A view from inside: complexity in the atomic scale ordering of supported metal nanoparticles. *The Journal of Physical Chemistry B*, **105**, 12689–703.
64 Nitani, H., Nakagawa, T., Daimon, H., Kurobe, Y., Ono, T., Honda, Y., Koizumi, A., Seino, S. and Yamamoto, T. (2007) Methanol oxidation catalysis and substructure of PtRu bimetallic nanoparticles. *Applied Catalysis A: General*, **326**, 194–201.
65 Sinfelt, J.H., Via, G.H. and Lytle, F.W. (1984) Application of EXAFS in catalysis: structure of bimetallic cluster catalysts. *Catalysis Reviews–Science and Engineering*, **26**, 81–140.
66 Bazin, D.C., Sayers, D.A. and Rehr, J.J. (1997) Comparison between X-ray absorption spectroscopy, anomalous wide angle X-ray scattering, anomalous small angle X-ray scattering, and diffraction anomalous fine structure techniques applied to nanometer-scale metallic clusters. *The Journal of Physical Chemistry B*, **101**, 11040–50.
67 Sarma, L.S., Chen, C.H., Kumar, S.M.S., Wang, G.R., Yen, S.C., Liu, D.G., Sheu, H.S., Yu, K.L., Tang, M.T., Lee, J.F., Bock, C., Chen, K.H. and Hwang, B.J. (2007) Formation of Pt–Ru nanoparticles in ethylene glycol solution: an in situ X-ray absorption spectroscopy study. *Langmuir*, **23**, 5802–9.
68 Chen, C.H., Sarma, L.S., Chen, J.M., Shih, S.C., Wang, G.R., Liu, D.G., Tang, M.T., Lee, J.F. and Hwang, B.J. (2007) Architecture of Pd–Au bimetallic nanoparticles in sodium bis(2-ethylhexyl) sulfosuccinate reverse micelles as investigated by X-ray absorption spectroscopy. *ACS Nano*, **1**, 114–25.
69 Chen, C.H., Sarma, L.S., Wang, G.R., Chen, J.M., Shih, S.C., Tang, M.T., Liu, D.G., Lee, J.F., Chen, J.M. and Hwang, B.J. (2006) Formation of bimetallic Ag–Pd nanoclusters via the reaction between Ag nanoclusters and Pd^{2+} ions. *The Journal of Physical Chemistry B*, **110**, 10287–95.
70 Hwang, B.J., Chen, C.H., Sarma, L.S., Chen, J.M., Wang, G.R., Tang, M.T., Liu, D.G. and Lee, J.F. (2006) Probing the formation mechanism and chemical states of carbon-supported Pt–Ru nanoparticles by in situ X-ray absorption spectroscopy. *The Journal of Physical Chemistry B*, **110**, 6475–82.
71 Chen, C.H., Hwang, B.J., Wang, G.R., Sarma, L.S., Tang, M.T., Liu, D.G. and Lee, J.F. (2005) Nucleation and growth mechanism of Pd/Pt bimetallic clusters in sodium bis(2-ethylhexyl)sulfosuccinate (AOT) reverse micelles as studied by in situ X-ray absorption spectroscopy. *The Journal of Physical Chemistry B*, **109**, 21566–75.
72 Hwang, B.J., Tsai, Y.W., Sarma, L.S., Tseng, Y.L., Liu, D.G. and Lee, J.F. (2004) Genesis of bimetallic Pt–Cu clusters in reverse micelles investigated by in situ

X-ray absorption spectroscopy. *The Journal of Physical Chemistry B*, **108**, 20427–34.

73 Tsai, Y.W., Tseng, Y.L., Sarma, L.S., Liu, D.G., Lee, J.F. and Hwang, B.J. (2004) Genesis of Pt clusters in reverse micelles investigated by in situ X-ray absorption spectroscopy. *The Journal of Physical Chemistry B*, **108**, 8148–52.

74 Murphy, C.J. (2002) Nanocubes and nanoboxes. *Science*, **298**, 2139–41.

75 Harris, N., Ford, M.J., Mulvaney, P. and Cortie, M.B. (2008) Tunable infrared absorption by metal nanoparticles: the case for gold rods and shells. *Gold Bulletin*, **41**, 5–14.

76 Skrabalak, S.E., Chen, J., Au, L., Lu, X., Li, X. and Xia, Y. (2007) Gold nanocages for biomedical applications. *Advanced Materials*, **19**, 3177–84.

77 Chen, J., Wiley, B., Li, Z.Y., Campbell, D., Saeki, F., Cang, H., Au, L., Lee, J., Li, X. and Xia, Y. (2005) Gold nanocages: engineering their structure for biomedical applications. *Advanced Materials*, **17**, 2255–61.

78 Maier, S.A., Brongersma, M.L., Kik, P.G., Meltzer, S., Requichia, A.A.G. and Atwater, H. (2001) Plasmonics – a route to nanoscale optical devices. *Advanced Materials*, **13**, 1501–5.

79 Law, M., Sibuly, D.J., Johnson, J.C., Goldberger, J., Saykally, R.J. and Yang, P. (2004) Nanoribbon waveguides for subwavelength photonics integration. *Science*, **305**, 1269–73.

80 Mallouk, T.E. and Kovtyukhova, N.I. (2002) Nanowires as building blocks for self-assembling logic and memory circuits. *Chemistry – A European Journal*, **8**, 4354–63.

81 Huang, Y., Duan, X., Wei, Q. and Lieber, C.M. (2001) Directed assembly of one-dimensional nanostructures into functional networks. *Science*, **291**, 630–3.

82 Skumryev, V., Stoyanov, S., Zhang, Y., Hadjipanayis, G., Givord, D. and Nogués, J. (2003) Beating the superparamagnetic limit with exchange bias. *Nature*, 850–3.

83 Bao, Y., Pakhomov, A.B. and Krishnan, M. (2005) A general approach to synthesis of nanoparticles with controlled morphologies and magnetic properties. *Journal of Applied Physics*, **97**, 10J317.

84 Turner, J.L., Pan, D., Plummer, R., Chen, Z., Whittaker, A.K. and Wooley, K.L. (2005) Synthesis of gadolinium-labeled shell-crosslinked nanoparticles for magnetic resonance imaging applications. *Advanced Functional Materials*, **15**, 1248–54.

85 Bulte, J.W., Douglas, T., Witwer, B., Zhang, S.C., Strable, E., Lewis, B.K., Zywicke, H., Miller, B., van Gelderen, P., Moskowitz, B.M., Duncan, I.D. and Frank, J. (2001) Magnetodendrimers allow endosomal magnetic labeling and in vivo tracking of stem cells. *Nature Biotechnology*, **19**, 1141–7.

86 Lewin, M., Carlesso, N., Tung, C.H., Tang, X.W., Cory, D., Scadden, D.T. and Weissleder, R. (2000) Tat peptide-derivatized magnetic nanoparticles allow in vivo tracking and recovery of progenitor cells. *Nature Biotechnology*, **18**, 410–14.

87 Langereis, S., Kooistra, H.-A.T., Van Genderen, M.H.P. and Meijer, E.W. (2004) Probing the interaction of the biotin–avidin complex with the relaxivity of biotinylated Gd-DTPA. *Organic and Biomolecular Chemistry*, **2**, 1271–3.

88 Caravan, P., Greenwood, J.M., Welch, J.T. and Franklin, S. (2003) Gadolinium-binding helix–turn–helix peptides: DNA-dependent MRI contrast agents. *Chemical Communications*, 2574–5.

89 Mehta, R.V., Upadhyay, R.V., Charles, S.W. and Ramchand, C.N. (1997) Direct binding of protein to magnetic particles. *Biotechnology Techniques*, **11**, 493–6.

90 Babes, L., Denizot, B., Tanguy, G., Jeune, J.J.L. and Jallet, P. (1999) Synthesis of iron oxide nanoparticles used as MRI contrast agents: a parametric study. *Journal of Colloid and Interface Science*, **212**, 474–82.

91 Weissleder, R., Elizondo, G., Wittenberg, J., Rabito, C.A., Bengele, H.H. and Josephson, L. (1990) Ultrasmall superparamagnetic iron oxide: characterization of a new class of contrast agents for MR imaging. *Radiology*, **175**, 489–93.

92 Hu, S.H., Chen, S.Y., Liu, D.M. and Hsiao, C.S. (2008) Core/single-crystal-

shell nanospheres for controlled drug release via a magnetically triggered rupturing mechanism. *Advanced Materials*, **9999**, 1–6.

93 Banerjee, S., Roy, S., Chen, J.W. and Chakravorty, D. (2000) Magnetic properties of oxide-coated iron nanoparticles synthesized by electrodeposition. *Journal of Magnetism and Magnetic Materials*, **219**, 45–52.

94 Barick, K.C. and Bahadur, D. (2006) Assembly of Fe_3O_4 nanoparticles on SiO_2 monodisperse spheres. *Bulletin of Materials Science*, **29**, 595–8.

95 Wu, W., He, Q., Chen, H., Tang, J. and Nie, L. (2007) Sonochemical synthesis, structure and magnetic properties of air-stable Fe_3O_4/Au nanoparticles. *Nanotechnology*, **18**, 145609.

96 Bai, J. and Wang, J.-P. (2007) High-magnetic-moment core-shell-type FeCo-Au/Ag nanoparticles. *Applied Physics Letters*, **87**, 152502.

97 Cho, S.-J., Kauzlarich, S.M., Olamit, J., Liu, K., Gradjean, F., Rebboulh, L. and Long, G.J. (2004) Characterization and magnetic properties of core/shell structured Fe/Au nanoparticles. *Journal of Applied Physics*, **95**, 6804.

98 Zhou, W., Kumbhar, A., Wiemann, J., Fang, J., Carpenter, E.E. and Oconner, C.J. (2001) Gold-coated iron (Fe@Au) nanoparticles: synthesis, characterization, and magnetic field-induced self-assembly. *Journal of Solid State Chemistry*, **159**, 26–31.

99 Lyon, J.L., Fleming, D.A., Stone, M.B., Schiffer, P. and Williams, M.E. (2004) Synthesis of Fe oxide core/Au shell nanoparticles by iterative hydroxylamine seeding. *Nano Letters*, **4**, 719–23.

100 Krishnan, K.M., Pakhomov, A.B., Bao, Y., Blomqvist, P., Chun, Y., Gonzales, M., Griffin, K., Ji, X. and Roberts, B.K. (2006) Nanomagnetism and spin electronics: materials, microstructure and novel properties. *Journal of Materials Science*, **41**, 793–815.

101 Salgueirino-Maceira, V., Correa-Duarte, M.A., Farle, M., Lopez-Quintela, A., Sieradzki, K. and Diaz, R. (2006) Bifunctional gold-coated magnetic silica spheres. *Chemistry of Materials*, **18**, 2701–6.

102 Jain, P.K., El-Sayed, I.H. and El-Sayed, M.A. (2007) Au nanoparticle target cancer. *Nanotoday*, **2**, 18–29.

103 Westcott, S.L., Oldenburg, S.J., Lee, T.R. and Halas, N.J. (1998) Formation and adsorption of clusters of gold nanoparticles onto functionalized silica nanoparticle surfaces. *Langmuir*, **14**, 5396–401.

104 Oldenburg, S.J., Westcott, S.L., Averitt, R.D. and Halas, N.J. (1999) Surface enhanced Raman scattering in the near infrared using metal nanoshell substrates. *The Journal of Chemical Physics*, **111**, 4729–35.

105 (a) Weissleder, R. (2001) A clearer vision for in vivo imaging. *Nature Biotechnology*, **19**, 316–17;
(b) Graf, C. and Van Blaaderen, A. (2002) Metallodielectric colloidal core-shell particles for photonic applications. *Langmuir*, **18**, 524–34.

106 Donselaar, L.N., Philipse, A.P. and Suurmond, J. (1997) Concentration-dependent sedimentation of dilute magnetic fluids and magnetic silica dispersions. *Langmuir*, **13**, 6018–25.

107 Lu, Y., Yin, Y., Mayers, B.T. and Xia, Y. (2002) Modifying the surface properties of superparamagnetic iron oxide nanoparticles through a sol-gel approach. *Nano Letters*, **2**, 183–6.

108 Lu, C.-W., Hung, Y., Hsiao, J.-K., Yao, M., Chung, T.-H., Lin, Y.-S., Wu, S.-H., Hsu, S.-C., Liu, H.-M., Mou, C.-Y., Yang, C.-S., Huang, D.-M. and Chen, Y.-C. (2007) Bifunctional magnetic silica nanoparticles for highly efficient human stem cell labeling. *Nano Letters*, **7**, 149–54.

109 Veiseh, O., Sun, C., Gunn, J., Kohler, N., Gabikian, P., Lee, D., Bhattarai, N., Ellenbogen, R., Sze, R., Hallahan, A., Olson, J. and Zhang, M. (2005) Optical and MRI multifunctional nanoprobe for targeting gliomas. *Nano Letters*, **5**, 1003–8.

110 Bertorelle, F., Wilhelm, C., Roger, J., Gazeau, F., Menager, C. and Cabuil, V. (2006) Fluorescence-modified superparamagnetic nanoparticles: intracellular uptake and use in cellular imaging. *Langmuir*, **22**, 5385–91.

111 Lal, M., Levy, L., Kim, K.S., He, G.S., Wang, X., Min, Y.H., Pakatchi, S. and

Prasad, P.N. (2000) Silica nanobubbles containing an organic dye in a multilayered organic/inorganic heterostructure with enhanced luminescence. *Chemistry of Materials*, **12**, 2632–9.

112 Congelli, F., Maysinger, D., Tschudi-Monnet, F., Montet, X., Corot, C., Petri-Fink, A., Hofmann, H. and Juillerat-Jeanneret, L. (2006) Interaction of functionalized superparamagnetic iron oxide nanoparticles with brain structures. *Journal of Pharmacology and Experimental Therapeutics*, **318**, 108–16.

113 Salgueiriño-Maceira, V., Correa-Duarte, M.A., Spasova, M., Liz-Marzán, L.M. and Farle, M. (2006) Composite silica spheres with magnetic and luminescent functionalities. *Advanced Functional Materials*, **16**, 509–14.

114 Wuister, S.F., Swart, I., van Driel, F., Hickey, S.G. and de Mello Donega, C. (2003) Highly luminescent water-soluble CdTe quantum dots. *Nano Letters*, **3**, 503–7.

115 Yi, D.K., Selvan, S.T., Lee, S.S., Papaefthymiou, G.C., Kundaliya, D. and Ying, J.Y. (2005) Silica-coated nanocomposites of magnetic nanoparticles and quantum dots. *Journal of the American Chemical Society*, **127**, 4990–1.

116 Wang, D., He, J., Rosenzweig, N. and Rosenzweig, Z. (2004) Superparamagnetic Fe_2O_3 beads-CdSe/ZnS quantum dots core-shell nanocomposite particles for cell separation. *Nano Letters*, **4**, 409–13.

117 Giri, S., Trewyn, B.G., Stellmaker, M.P. and Lin, V.S.-Y. (2005) Stimuli-responsive controlled-release delivery system based on mesoporous silica nanorods capped with magnetic nanoparticles. *Angewandte Chemie – International Edition*, **44**, 5038–44.

118 Arruebo, M., Galán, M., Navascués, N., Téllez, C., Marquina, C., Ibarra, M.R. and Santamaría, J. (2006) Development of magnetic nanostructured silica-based materials as potential vectors for drug-delivery applications. *Chemistry of Materials*, **18**, 1911–19.

119 Neuberger, T., Schöpf, B., Hofmann, H., Hofmann, M. and von Rechenber, B. (2005) Superparamagnetic nanoparticles for biomedical applications: possibilities and limitations of a new drug delivery system. *Journal of Magnetism and Magnetic Materials*, **293**, 483–96.

120 Yoon, T.J., Kim, J.S., Kim, B.G., Yu, K.N., Cho, M.H. and Lee, J.K. (2005) Multifunctional nanoparticles possessing a 'magnetic motor effect' for drug and gene delivery. *Angewandte Chemie – International Edition*, **44**, 1068–71.

121 Ström, V., Hultenby, K., Grüttner, C., Teller, J., Xu, B. and Holgersson, J. (2004) A novel and rapid method for quantification of magnetic nanoparticle–cell interactions using a desktop susceptometer. *Nanotechnology*, **15**, 457–66.

122 Lübbe, A.S., Alexiou, C. and Bergmann, C.J. (2001) Clinical applications of magnetic drug targeting. *Surgical Research*, **95**, 200–6.

123 Lübbe, A.S., Bergemann, C., Riess, H., Schriever, F., Reichardt, P., Possinger, K., Matthias, M., Dörken, B., Herrmann, F., Gürtler, R., Hohenberger, P., Haas, N., Sohr, R., Sander, B., Lemke, A., Ohlendorf, D., Huhnt, W. and Huhn, D. (1996) Clinical experiences with magnetic drug targeting: a phase I study with 4′-epidoxorubicin in 14 patients with advanced solid tumors. *Cancer Research*, **56**, 4686–93.

124 Torchilin, V.P. (2000) Drug targeting. *European Journal of Pharmaceutical Sciences*, **11**, S81–91.

125 Teo, B.K. (1986) *EXAFS: Basic Principles and Data Analysis*, Springer, Berlin, Germany.

126 Prins, R. and Koningsberger, D.E. (eds) (1988) *X-Ray Absorption: Principles, Applications, Techniques of EXAFS, SEXAFS, and XANES*. John Wiley & Sons, Inc., New York.

127 Koningsberger, D.C., Mojet, B.L., van Dorssen, G.E. and Ramaker, D.E. (2000) XAFS spectroscopy: fundamental principles and data analysis. *Topics in Catalysis*, **10**, 143–55.

128 Via, G.H., Sinfelt, J.H. and Lytle, F.W. (1979) Extended X-ray absorption fine structure (EXAFS) of dispersed metal catalysts. *The Journal of Chemical Physics*, **71**, 690–9.

129 Toshima, N., Harada, M., Yamazaki, Y. and Asakura, K. (1992) Catalytic activity and structural analysis of polymer-protected Au–Pd bimetallic clusters prepared by simultaneous $HAuCl_4$ and $PdCl_2$. *The Journal of Physical Chemistry*, **96**, 9927–33.

130 Newville, M. (2001) IFEFFIT: interactive XAFS analysis and FEFF fitting. *Journal of Synchrotron Radiation*, **8**, 322–4.

131 Nashner, M.S., Frenkel, A.I., Adler, D.L., Shapley, J.R. and Nuzzo, R.G. (1997) Structural characterization of carbon-supported platinum-ruthenium nanoparticles from the molecular cluster precursor $PtRu_5C(CO)_{16}$. *Journal of the American Chemical Society*, **119**, 7760–71.

132 Davis, R.J. and Boudart, M. (1994) Structure of supported PdAu clusters determined by X-ray absorption spectroscopy. *The Journal of Physical Chemistry*, **98**, 5471–7.

133 Nashner, M.S., Frenkel, A.I., Somerville, D., Hills, C.W., Shapley, J.K. and Nuzzo, R.G. (1998) Core shell inversion during nucleation and growth of bimetallic Pt/Ru nanoparticles. *Journal of the American Chemical Society*, **120**, 8093–101.

134 Sarkar, S.K., Kababya, S., Vega, S., Cohen, H., Woicik, J.C., Frenkel, A.I. and Hodes, G. (2007) Effects of solution pH and surface chemistry on the post deposition growth of chemical bath deposited PbSe nanocrystalline films. *Chemistry of Materials*, **19**, 879–88.

135 Via, G.H. and Sinfelt, J.H. (1996) Applications of EXAFS to Catalyst Characterization – Supported Bimetallic Cluster Catalysts, in *X-Ray Absorption Fine Structure for Catalysts and Surfaces* (ed. Y. Iwasawa), World Scientific, London., pp. 147–72.

136 Bazin, D., Sayers, D. and Rehr, J.J. (1997) Comparison between X-ray absorption spectroscopy, anomalous wide angle X-ray scattering, anomalous small angle X-ray scattering, and diffraction anomalous fine structure techniques applied to nanometer-scale metallic clusters. *The Journal of Physical Chemistry B*, **101**, 11040–50.

137 Greegor, R.B. and Lytle, F.W. (1980) Morphology of supported metal clusters: determination by EXAFS and chemisorption. *Journal of Catalysis*, **63**, 476–86.

138 Gao, J., Bender, C.M. and Murphy, C.J. (2003) Dependence of the gold nanorod aspect ratio on the nature of directing surfactant in aqueous solution. *Langmuir*, **19**, 9065–70.

139 El-Sayed, M.A. (2001) Some interesting properties of metals confined in time and nanometer space of different shapes. *Accounts of Chemical Research*, **34**, 257–64.

140 Eustis, S. and El-Sayed, M.A. (2006) Determination of the aspect ratio statistical distribution of gold nanorods in solution from a theoretical fit of the observed inhomogeneously broadened longitudinal plasmon resonance absorption spectrum. *Journal of Applied Physics*, **100**, 044324.

141 Park, J.-I., Kim, M.G., Jun, J.-W., Lee, J.S., Lee, W.-R. and Cheon, J. (2004) Characterization of superparamagnetic core-shell nanoparticles and monitoring their anisotropic phase transition to ferromagnetic solid solution nanoalloys. *Journal of the American Chemical Society*, **126**, 9072–8.

142 Teng, X., Wang, Q., Liu, P., Han, W., Frenkel, A.I., Wen, W., Marinkovic, N., Hanson, J.C. and Rodriguez, J.A. (2008) Formation of Pd/Au nanostructures from Pd nanowires via galvanic replacement reaction. *Journal of the American Chemical Society*, **130**, 1093–1.

143 Han, S.W., Kim, Y. and Kim, K.J. (1998) Dodecanethiol-derivatized Au/Ag bimetallic nanoparticles. Colloid and Interface. *Science*, **208**, 272–8.

144 Rodríguez-González, B., Sánchez-Iglesias, A., Giersig, M. and Liz-Marzán, L.M. (2004) AuAg bimetallic nanoparticles: formation, silica-coating and selective etching. *Faraday Discussions*, **125**, 133–44.

145 Mallin, M.P. and Murphy, C.J. (2002) Solution phase synthesis of sub-10 nm Au-Ag alloy nanoparticles. *Nano Letters*, **2**, 1235–7.

146 Schatz, G.C. (2001) Electrodynamics of nonspherical noble metal nanoparticles and nanoparticle aggregates. *Journal of*

Molecular Structure: THEOCHEM, **573**, 73–80.

147 Chen, H.M., Liu, R.S., Jang, L.-Y., Lee, J.-F. and Hu, S.-F. (2006) Characterization of core-shell type and alloy Ag/Au bimetallic clusters by using extended X-ray absorption fine structure spectroscopy. *Chemical Physics Letters*, **421**, 118–23.

148 Lee, W.-R., Kim, M.G., Choi, J.-R., Park, J.-I., Ko, S.J., Oh, S.J. and Cheon, J. (2005) Redox-transmetalation process as a generalized synthetic strategy for core-shell magnetic nanoparticles. *Journal of the American Chemical Society*, **127**, 16090–7.

149 Lahiri, D., Chattopadhyay, S., Bunker, B.A., Doudna, C.M., Bertino, M.F., Blum, F., Tokuhiro, A. and Jerry, T. (2005) EXAFS studies of bimetallic Ag-Pt and Ag-Pd nanorods. *Physica Scripta*, T**115**, 776–80.

150 Liu, R.S., Chen, H.M. and Hu, S.F. (2007) Synthesis and characterization of long gold nanorods. *IEEJ Transactions on Electrical and Electronic Engineering*, **2**, 468–72.

151 Aruguete, D.M., Marcus, M.A., Li, L.-S., Williamson, A., Fakra, S., Gygi, F., Galli, G.A. and Alivisatos, P.A. (2007) Surface structure of CdSe nanorods revealed by combined X-ray absorption fine structure measurements and ab initio calculations. *The Journal of Physical Chemistry C*, **111**, 75–9.

152 Behrens, S., Bönnemann, H., Matoussevitch, N., Gorschinski, A., Dinjus, E., Habicht, W., Bolle, J., Zinoveva, S., Palina, N., Hormes, J., Modrow, H., Bahr, S. and Kempter, V. (2006) Surface engineering of Co and FeCo nanoparticles for biomedical application. *Journal of Physics – Condensed Matter*, **18**, S2543–61.

153 Crespo, P., García, M.A. and Fernández-Pinel, E., De la Venta, J., Merino, J.M., Quesada, A. and Hernando, A. (2008) Permanent magnetism in thiol capped nanoparticles: gold and ZnO. *Acta Physica Polonica A*, **113**, 515–20.

Abstract

Nanomaterials, either of the core-shell or alloy type, have attracted significant attention due to their promising use in a host of biomedical applications such as bioimaging, biosensing, drug delivery and cell labeling. Although nanomaterials with well-controlled surface properties and structures can be synthesized and, to a certain extent, also characterized, understanding and validating the structure–property relationships of these materials for biomedical applications requires rigorous characterization techniques. Due to the complexity of most biological environments, the introduction of nanomaterials characterization techniques that can provide useful information on surface structure, atomic distribution, segregation and composition is critical in developing new systems with improved properties. During the past two decades, X-ray absorption spectroscopy (XAS) has been actively employed in investigating the structural aspects of nanomaterials and, in many instances, can provide useful information over many characterization techniques. In this chapter we provide an overview of the current research and developments in applying XAS techniques to the characterization of spherical and anisotropic core-shell and alloy nanomaterials. The importance of understanding the structure and surface properties of nanomaterials, and the capabilities of XAS in developing nanostructured materials, are also discussed.

Keywords

core-shell nanoparticles; alloy nanoparticles; anisotropy; X-ray absorption spectroscopy; nanostructure; atomic distribution; surface composition; biomedical applications.

12
Anisotropic Hexagonal Boron Nitride Nanomaterials: Synthesis and Applications

Wei-Qiang Han

12.1
Introduction

Boron nitride (BN) is a synthetic binary compound located between Group III and Group V elements in the Periodic Table. However, its properties, in terms of polymorphism and mechanical characteristics, are rather close to those of carbon compared with other Group III–V compounds, such as gallium nitride. BN crystallizes into a layered or a tetrahedrally linked structure, similar to those of graphite and diamond, respectively, depending on the conditions of its preparation, and especially on the pressure applied. Such correspondence between BN and carbon readily can be understood from their isoelectronic structures [1, 2]. On the other hand, in contrast to graphite, layered BN is transparent and is an insulator. This material has attracted great interest because, similar to carbon, it exists in various polymorphic forms that exhibit very different properties; however, these forms do not correspond strictly to those of carbon.

Crystallographically, BN is classified into four polymorphic forms: hexagonal BN (h-BN) (Figure 12.1b); rhombohedral BN (r-BN); cubic BN (c-BN); and wurtzite BN (w-BN). BN does not occur in Nature. In 1842, Balmain [3] obtained BN as a reaction product between molten boric oxide and potassium cyanide under atmospheric pressure, and thereafter many methods for its synthesis were reported. Both, h-BN and r-BN are formed under ambient pressure, while c-BN is synthesized from h-BN under high pressure at high temperature, and w-BN is prepared from h-BN under high pressure at room temperature [1].

Each BN layer consists of stacks of hexagonal plate-like units of boron and nitrogen atoms, linked by sp^2 hybridized orbits and held together mainly by van der Waals force (Figure 12.1b). The hexagonal polymorph has two-layered repeating units: AA′AA″ ... that differ from those in graphite: ABAB ... (Figure 12.1a). Within the layers of h-BN there is coincidence between the same phases of the hexagons, although the boron atoms and nitrogen atoms are alternatively located along the c-axis. The rhombohedral system consists of three-layered units: ABCABC ... , the honeycomb layers of which are arranged in a shifted phase, like as those of graphite.

Nanomaterials for the Life Sciences Vol. 3: Mixed Metal Nanomaterials. Edited by Challa S. S. R. Kumar

ISBN: 978-3-527-32153-7

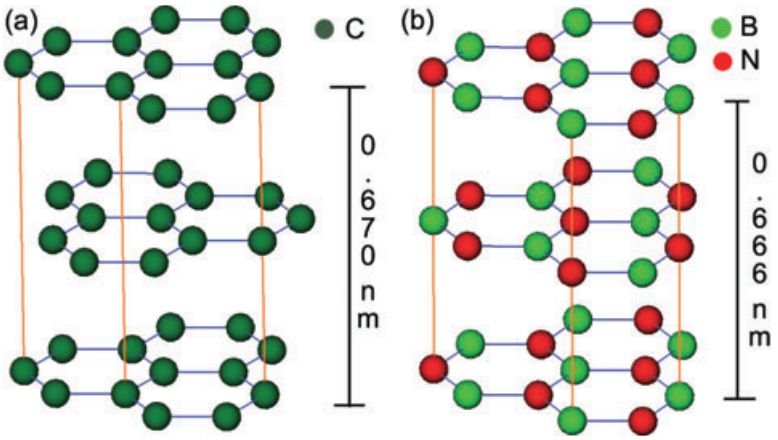

Figure 12.1 Crystal structures of (a) graphite and (b) hexagonal boron nitride.

Reflecting its weak interlayer bond, the h-BN can be cleaved easily along its layers, and hence, is widely used as a lubricant. The material is stable up to a high temperature of 2300 °C before decomposition sets in [2], it does not fuse in a nitrogen atmosphere of 1 atm, and thus, is applicable as a refractory material. Besides having such properties similar to those of graphite, the material is transparent and acts as a good electric insulator, especially at high temperatures ($10^6\,\Omega$m at 1000 °C) [1].

Both, c-BN and w-BN are tetrahedrally linked BN; the former has a cubic sphalerite-type structure, and the latter a hexagonal wurtzite-type structure. c-BN is the second hardest known material (the hardest is diamond), and is referred to as white diamond. It is used mainly for grinding and cutting industrial ferrous materials, because it does not react with molten iron, nickel and related alloys at high temperatures, in contrast to diamond [1]. c-BN also displays the second highest thermal conductivity (6–9 $W\,cm^{-1}\cdot$ °C) after diamond.

In this chapter, attention is focused principally upon information regarding h-BN nanomaterials, mainly BN nanotubes (BNNTs), porous BN and mono- and few-layer-BN sheets. Excellent reviews on c-BN are available in Refs [1, 4–6].

12.2 Synthesis of BN Nanotubes

12.2.1 Introduction

Iijima's discovery of carbon nanotubes (CNTs) in 1991 [7] has occasioned intense experimental and theoretical research investigations during the past decade on other hollow tubular structures – that is, inorganic nanotubes – because of the various intriguing properties associated with their small dimensions, high anisotropy and interesting structures. Among such inorganic nanotubes, BNNTs have

received the most attention. h-BN has a layered structure which is very similar to that of graphite; hence, its tubular forms were predicated on a theoretical basis [8] before being successfully produced [9]. Indeed, in 1981, Ishii *et al.* already had reported the formation of h-BN 'whiskers' (in modern terminology these are known as bamboo-like BNNTs) by heating oxidized BN powder [10]. Electronic-band structure calculations have shown that BNNTs, the diameters of which exceed 0.8 nm, are wide-band-gap semiconductors with a gap value of ~5.5 eV. Interestingly – and in sharp contrast to CNTs – this gap value is independent of their chirality and diameter [11]. The ionic B—N bonding in BNNTs provides richer, but more complex, structural properties than those of CNTs. Accordingly, BNNTs may be more useful than CNTs for certain applications in electronic devices such as nanoscale insulating materials. Besides BNNTs, $B_xC_yN_z$ nanotubes have also been widely studied [12–14]; at this point, however, only noncarbon pure BNNTs will be introduced.

Multiwalled and single-walled BNNTs were first prepared, respectively, in 1995 [9] and 1996 [15]. Figure 12.2a and b are simulated images of a single-walled BNNT (SW-BNNT) (5, 5)* and a double-walled BNNT, respectively. Figure 12.2c shows some high-resolution transmission electron microscopy (TEM) images of BNNTs, ranging from single-layered to four-layered versions. Figure 12.2d shows an electron energy loss spectrum (EELS) of a BNNT. Previously, BNNTs have been synthesized using a variety of methods, including arc discharge [9], laser heating/ablation [16], CNT-substitution reactions [17], chemical vapor deposition (CVD) [18], solid-gas reaction [19], low-temperature autoclave [20], pore-template [21] and arc-jet plasma [22].

12.2.2 Arc Discharge

In 1995, Chopra *et al.* reported the first synthesis of pure crystalline BNNTs by using an arc-discharge method [9]. This synthetic route employs a high-temperature arc plasma similar to that used in the conventional production of CNTs. A tungsten rod loaded with pressed h-BN was arc-discharged against a cooled copper cathode, generating numerous multiwalled BNNTs with B : N ratio of ~1, as confirmed by EELS, and consistent with theoretical predictions. The spacing distance of BNNTs is 0.33 nm, in agreement with the spacing distance of 0.333 nm in bulk h-BN. Later, Loiseau *et al.* also synthesized BNNTs using the arc-discharge method [15]. The establishment of a carbon-free plasma between HfB_2 electrodes in a nitrogen atmosphere led to the formation of BNNTs with very few layers, including single- and double-layer varieties [15].

Cumings and Zettl [23] modified the arc-discharge method by using conductive boron ingots as electrodes. The electrodes are formed by first thoroughly mixing elemental boron (99.5% pure) with 1 at% each of nickel and cobalt. After heating the mixture to its melting point in a copper-hearth arc furnace, it was cooled to

* [(n, m) is a chiral vector, where n and m are integrals of the vector equation $R = n\mathbf{a}_1 + m\mathbf{a}_2$; the values of n and m determine the charility, or 'twist' of the nanotubes].

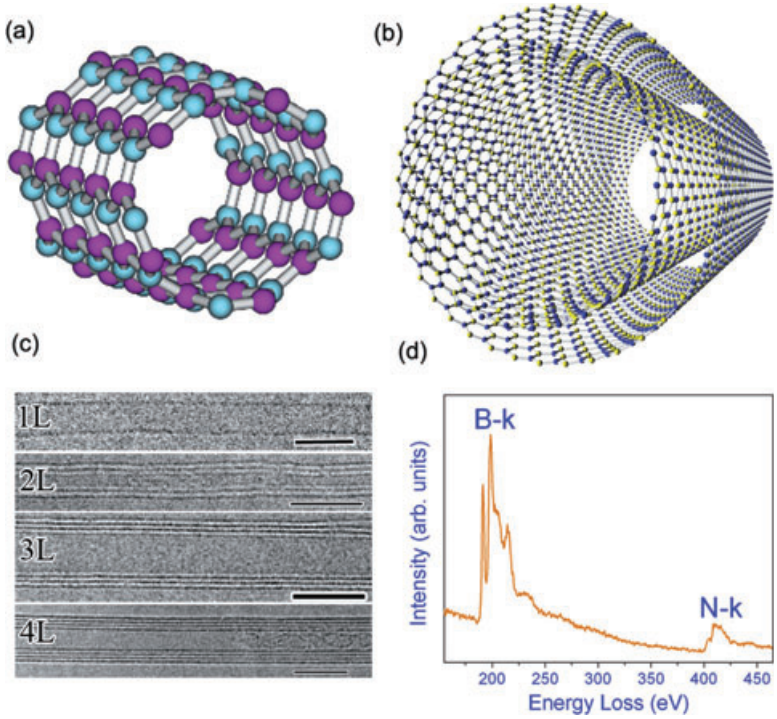

Figure 12.2 (a) Simulated image of a single-walled BNNT (5 5); (b) Simulated image of a double-walled BNNT; (c) High-resolution TEM images of a series of individual nanotubes with numbers of walls from 1 to 4; (d) EELS spectrum of a BNNT.

form a macroscopically homogenous ingot. Using a crude two-probe method, the electrical resistivity of the ingots was measured as $<50\,m\Omega \cdot m$. When the metals are not added, the conductivity of the boron ingots is insufficient to support the arc. The ingots themselves are mounted as both anode and cathode in a conventional-design, water-cooled nanotube direct current arc synthesis chamber (see Figure 12.3). The chamber is evacuated to <30 mTorr and then backfilled with N_2 gas with the pressure dynamically stabilized to 380 Torr. During synthesis, the arc current is sustained nominally at 60 amperes (DC), with the electrode voltage ranging from 30 to 45 V. During the arc, a gray, web-like material grows preferentially near the top of the chamber, while a thin layer of gray soot is deposited on its side walls. Both contain an abundance of BNNTs, although the web-like material is significantly richer. By using this method it is possible to produce about 70% double-walled nanotubes (Figure 12.4), within which is included ~10% single-walled nanotubes and fewer multiwalled nanotubes.

Among the byproducts can be found a large amount of BN fullerene-like nanoparticles (FNPs), which are also known as nanococoons. High-resolution

Figure 12.3 Simulated image of a arc-discharge chamber. The conductive ingots are mounted as both anodes and cathode (the end of yellow lines).

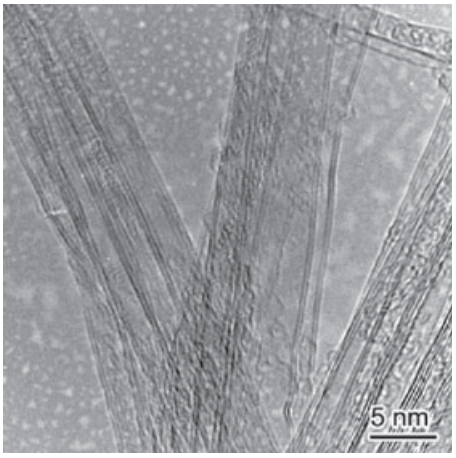

Figure 12.4 High-resolution transmission electron microscopy image of BNNTs prepared using the arc-discharge method.

(HR) TEM images, together with EELS and electron-diffraction data, have shown these nanoparticles to be B-rich nanocrystals coated with a few layers of graphitic BN, although some also contained cobalt and nickel impurities. The BN FNPs ranged widely in size, from 5 to 100 nm. There was no clear correlation between the number of BN layers of the FNPs and their diameter, and in general only a few layers of graphitic BN were observed. Interestingly, however, on many occasions the FNPs consisted of two layers of BN. Two types of contact between the FNPs and nanotubes were apparent. In the first type of contact, the FNPs were found on the side walls of nanotubes, but clearly distinct from them; presumably,

these FNPs were attached by van der Waals forces. The second type of contact took place at the end of the nanotubes, where the BN sheets were continuous between the FNPs and the nanotubes. The nanotube–FNP junctions occurred at the corners, rather than at the facets [24]. In these samples, no transition metals were detected in any particle from which a nanotube grew. Hence, the transition metals may simply serve as dopants, enhancing the conductivity of the boron ingots. The possible growth mechanism is as follows:

- The plasma contains various-sized droplets of molten boron from the ingots, boron vapor and nitrogen vapor.
- The larger droplets fall to the bottom of the chamber, while the smaller ones (which are nanometers in diameter) remain in the plasma.
- During their exposure to the plasma, the boron and nitrogen atoms react on their surfaces to form BN sheets, probably after the droplets have solidified.
- The sheets have one or more layers (with two being the most common configuration), and continue to extend while remaining flat. In order to introduce any curvature there must be defects at the junction of two or more flat sheets (these defects are the loci of nanotube growth).
- As the boron and nitrogen atoms continue to be added to the sheets, they are incorporated into growing nanotubes at the tube's base. The nanotube growth ends when the particle is transported out of the zone of hot gas [24].

BNNTs also were prepared by arc-melting of ZrB_2 [25], NbB_2 [26], YB_6 [26], YB_6/Ni [26] and BN-Ta [27] powders in nitrogen/argon gas mixtures.

12.2.3 Laser Ablation

Golberg *et al.* [16] heated BN with a laser in a diamond anvil cell at high nitrogen pressure (5–15 GPa) to prepare BNNTs with between three and eight layers. These nanotubes were grown either in melted cubic BN, or in hexagonal + amorphous BN that had recrystallized on the specimen's surface from the fluid phase. Yu *et al.* [28] produced BNNTs by using excimer-laser ablation at 1200 °C. The target was a mix of BN powder with Ni and Co nanoparticles (1% each)., and the resultant nanotubes had one or a few layers. The tips of the nanotubes were either flat caps or polygonal terminations, in contrast to the conical ends of CNTs [28]. Continuous CO_2 lasers also were used to generate BNNTs, with or without metal catalysts [29, 30].

Arenal *et al.* [31] demonstrated the production of high-quantity, SW-BNNTs by laser ablation, without using any metal catalyst. The group repeatedly bombarded an h-BN target with a CO_2 (wavelength 10.6 μm) continuous laser under a partial pressure of nitrogen gas [31]. The temperature at the surface of the target was 3200–3500 K (measured using optical pyrometry); the gas temperature was also monitored using coherent anti-Stokes Raman scattering (CARS), as a function of

the distance to the target's surface [32]. Reportedly, the nitrogen gas near the target's surface is heated up to temperature and acts as a local furnace. However, above the target the temperature decreases first rapidly, and then more slowly until, at a distance of 7 mm above the target's surface, it is approximately 1200 K. The optimized power was found to lie between 1000 and 1200 W, equivalent to a temperature at the target's surface of >2400 °C. The yield of the raw products was approximately 0.5 g h^{-1}, and the reaction products were collected both on the filter and also in a trap located in the outlet of the reactor chamber. An examination of the product revealed 80% of the nanotubes to be single walled, and the remainder to be multiwalled with very few layers. The typical length and diameter of the nanotubes were several hundred nanometers and 2 nm, respectively.

By combining the techniques of TEM and EELS [33], Arenal and colleagues later reported that near-spherical nanoparticles (or so-called cages) generally consist of a core of a pure boron particle covered by a thin layer of boron oxide, wrapped with h-BN shells. The same nanoparticles often are found at the ends of nanotubes. Although these nanoparticles are only a few nanometers (≤10 nm) in size, they very often are larger than the tubes; occasionally, a few tubes assembled into a bundle appear to emerge from the same particle.

Based on these results, Arenal *et al.* proposed a root-growth mechanism originating in pure boron particles for the formation of BNNTs. Their modified vapor–liquid–solid (VLS) growth model for the formation of SW-BNNTs is illustrated in Figure 12.5. According to the thermodynamic phase diagram of the B—N system, upon heating with the laser beam the h-BN compound of the target does not sublimate (as does graphite), but rather decomposes above 2600 K into gaseous nitrogen and liquid boron. The boron then is vaporized, despite the equilibrium vaporization temperature being far from that realized at the target's surface. Above 1800 °C, the boron oxide also decomposes and vaporizes, such that two sources of boron are available to form the nanotubes (though the efficiency of formation is less with boron oxide). On cooling within the temperature gradient created by the flow of nitrogen gas, the boron vapor condenses into small droplets which, as the temperature falls below 2700 K, react with the nitrogen gas to form a sp^2 BN structure. Despite the extreme stability of the nitrogen molecule, the high reactivity of the liquid boron's surface at 2700 K can cause this molecule to degrade. The source of the nitrogen gas is either the carrier gas, or that issued from decomposition of the BN target; the latter was confirmed as the source by using argon as the carrier gas [31]. As a consequence of the chemical reaction, B—N_2 (a sp^2 BN cap) is formed at the surface of the particle (step I in Figure 12.5), which is then progressively transformed into a tube by the continuous supply and decomposition of nitrogen at the particle surface (step II in Figure 12.5). This finding implies that, initially, the size of the BN cap is less than that of the particle, and therefore its surface would be ensured free access to the nitrogen gas. The nucleation process implies a root growth mechanism wherein nitrogen and boron atoms are incorporated into the BN network at the foot of the nanotube via its interface with the particle's surface, where the bonds are the most active. In this mechanism, the boron particle has a dual role, serving both as a support for growth and as a reactant.

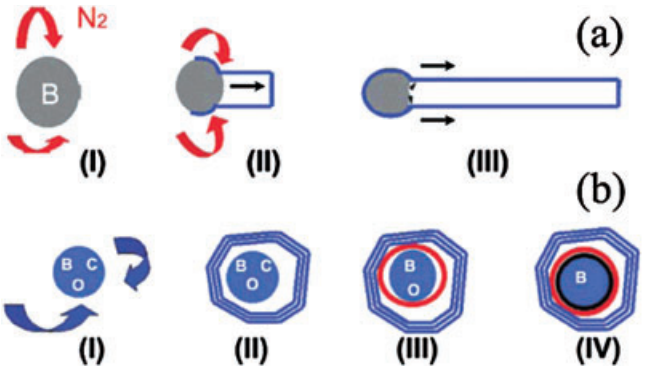

Figure 12.5 Sketches showing the phenomenological model for the formation of the tubes (a), and of the cages of BN (b). (a) The model is as follows: (a,I) Formation of boron drops from the decomposition of h-BN and from the boron oxide of the target; (a,II) Reaction of these drops of boron with the nitrogen injected into the reaction chamber and with that coming from the h-BN target. Recombination of the boron and nitrogen to form boron nitride; (a,III) Incorporation of the nitrogen atoms at the root of the boron particle from which the tube grows. With regards to the cages and the carbon and boron oxide filling them (carbon may also be found inside some BNNTs), the growth mechanism is (b,I) and (b,II); these steps correspond to (a,I) to (a,III), taking into account the dissolution of oxygen and carbon in the boron drops; (b, III) and (b,IV) correspond to the segregation of the carbon and oxygen. For carbon, the segregation occurs at temperatures close to 2000 °C, whereas oxygen segregation occurs at lower temperatures, around 700 °C. Reproduced with permission from Ref. [31]; © 2007, The American Chemical Society.

This pattern of growth persists as long as the boron particle remains liquid (i.e., as long as the temperature is >2300 K; step II in Figure 12.5). The boron particle begins to solidify in a zone of the reactor chamber where the cooling rate is between 100 and 200 $K\,ms^{-1}$. Accordingly, the growth of the tubes stops abruptly, which explains the relatively short length of SW-BNNTs compared to their carbon analogues synthesized via a continuous CO_2 laser vaporization of a NiCo-graphite target [34]. Finally, when the boron solidifies, the nitrogen atoms remaining at the surface of the particle react with surface boron atoms to build a BN sheet encapsulating the B particle.

In summary, the growth process involves three steps:

- The laser-induced decomposition of boron oxide contained in the target's binder and in its h-BN crystallites into nitrogen gas and liquid boron, both of which finally are vaporized.
- Upon cooling, boron vapor condenses into small boron liquid droplets that react with nitrogen gas that is either derived from the carrier gas or is issued from decomposition of the target, to form BN caps at the droplets surface.
- Growth of the nanotubes from the progressive incorporation of nitrogen and boron at the interface between the cap and the particle. The growth stops on the solidification of this core particle of boron.

Plasma-enhanced pulsed-laser deposition (PE-PLD) was used to generate multiwalled BNNTs directly on substrates at 600 °C. Oxidized Si substrates with Fe films (12.5 nm) were installed on the heater and sealed inside the vacuum chamber at base pressures up to ~5×10^{-7} mbar. By using a radiofrequency (RF) generator (13.56 MHz) capacitively coupled to a steel substrate holder, plasma was generated on the substrate's surface over a 10 min period. The RF plasma-induced negative DC voltages on the substrates (the so-called substrate bias) then accelerate the positive ions in the RF plasma and the BN vapor so as to bombard the substrate surface at between –360 and –450 V. When the kinetic energies of these ions are sufficient, the deposition rate of the BN film is balanced by the rate of resputtering [35].

Studies using scanning electron microscopy (SEM) have revealed that multiple BNNTs grown from adjacent Fe catalyst particles tend to form vertical bundles; BNNTs grown at –380 V appear conical in shape (see Figure 12.6a), whereas samples grown at a higher substrate bias (–450 V) form individual BNNTs inside the bundles. Such formation seems to occur because of the increase in diameter (~20 nm) of the individual BNNTs grown from the larger Fe nanoparticles formed by enhanced plasma heating (Figure 12.6b). The bundling configurations of BNNTs with small (left) and large (right) diameters are depicted in Figure 12.6c. Such BNNT bundles can be grown into arrays of regular patterns (Figure 12.6d), with a patterned Fe film created by a shadow mask. Taken together, these results

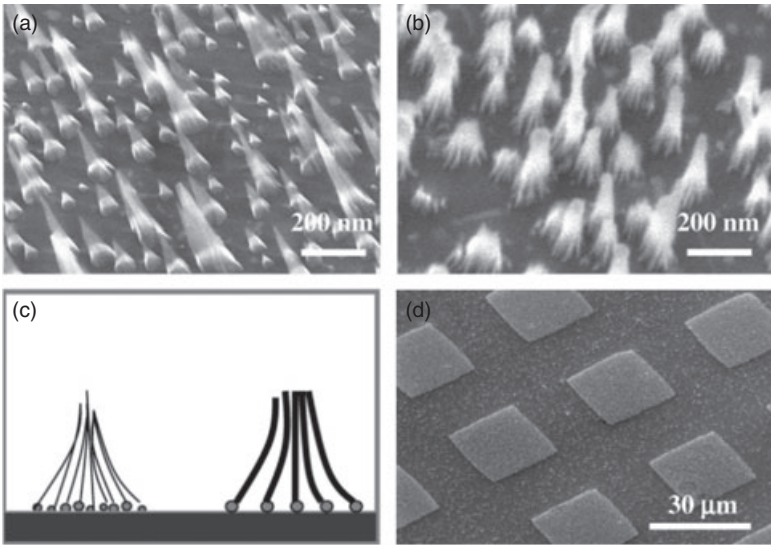

Figure 12.6 Scanning electron microscopy images of BNNT bundles grown at a substrate bias of (a) –380 V, (b) –450 V, and (c) their corresponding bundling configurations (left and right, respectively); (d) Patterned growth of BNNTs. Reproduced with permission from Ref. [35]; © 2005, The American Chemical Society.

showed that the location of BNNTs can be controlled during their growth by manipulating the patterns of the Fe nanoparticles [35].

Growth of the BNNTs is achieved through an optimum combination of the Fe film's thickness, the laser's energy density (deposition rate) and the substrate bias. For example, for a substrate with a 12.5 nm-thick Fe film, at a substrate bias of −300 V, the resultant excessive deposition rate generates a coating of BN films on the Fe nanoparticles (Figure 12.7a). These insulating BN coatings can be recognized by their charging effect during SEM measurements, although in such cases the growth of the BNNTs may be difficult to identify. Under these conditions, the deposition rate of the BN films is faster than the diffusion rate of the BN growth species into the Fe catalyst particles. Hence, the BN films coated on the catalyst will terminate contact between the Fe and the reactive growth species (Figure 12.7a) – a phenomenon known as the poisoning effect. The thickness of the BN films gradually decreases as the substrate bias increases (Figure 12.7b), with BNNTs starting to grow at a higher substrate bias as a balance is reached between the rate of film deposition and the resputtering rate (Figure 12.7c). Within this total resputtering region there is a suppression of the deposition of BN thin films. BNNTs grow on the Fe nanoparticles according to the VLS mechanism. Here, the RF plasma creates a directional flux of the BN growth species with sufficient kinetic energies so as to diffuse into the Fe nanoparticles. In this way, the Fe captures the energetic BN growth species and confines them within a nanoscopic space; otherwise, they may be resputtered from the surface. Supersaturation of the Fe nanoparticles with BN vapor causes the BN species to condense into ordered nanotubular structures [35].

12.2.4
Carbon Nanotubes-Substitution Reaction

One important application for CNTs is their use as templates to prepare other one-dimensional (1-D) nanomaterials, such as filling, coating and other nanorods

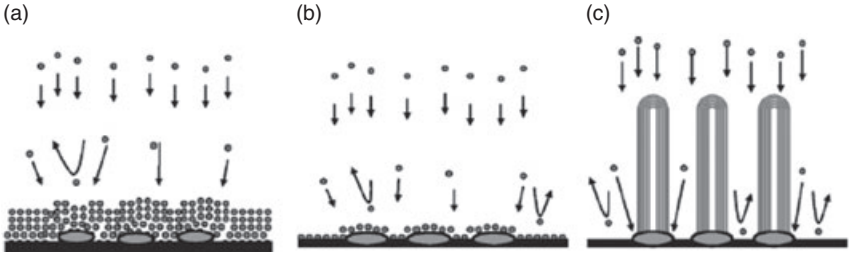

Figure 12.7 Schematic drawing representing the growth region of BNNTs. (a) Deposition of BN films on Fe nanoparticles due to low resputtering rate of the growth species; (b) Reduced growth rate of BN films with an energetic growth species; (c) Total resputtering region wherein BNNTs grow and BN films are suppressed. Reproduced with permission from Ref. [35]; © 2005, The American Chemical Society.

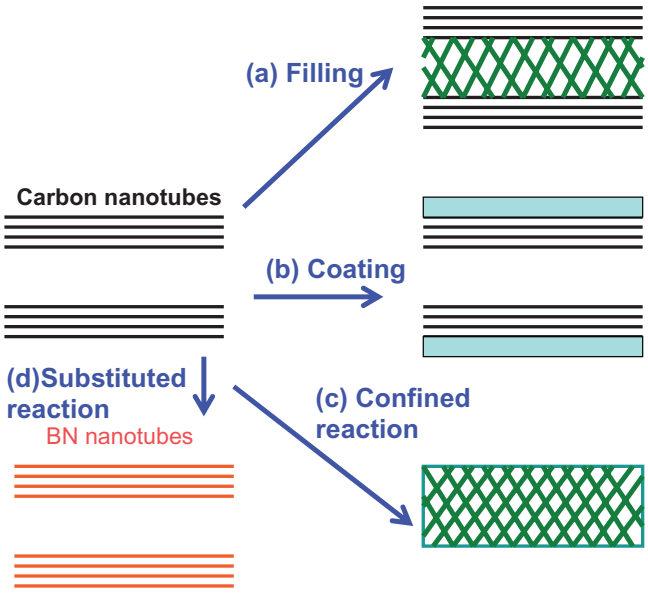

Figure 12.8 Schematic illustrations of using carbon nanotubes (CNTs) as a template to produce new one- dimensional nanoscale materials by (a) filling, (b) coating, (c) CNT-confined reaction to produce carbide and nitride nanorods, and (d) CNT-substituted reaction to produce BNNTs.

(Figure 12.8) [36, 37]. In 1998, Han *et al.* [17] developed a method involving a CNT substitution reaction to synthesize mass quantities of BNNTs. The method involved reacting boron oxide vapor with nitrogen or ammonia at high temperature in the presence of CNTs to form BNNTs, the proposed reaction being:

$$B_2O_3 + 3\,C\,(\text{nanotubes}) + N_2 \rightarrow 2\,BN\,(\text{nanotubes}) + 3\,CO \qquad (12.1)$$

Although the starting multiwalled CNTs are curved and contain many defects, the BNNTs produced are straight, near-perfect, and usually a few nanometers in diameter with only a few shells; their length is similar to that of the starting CNTs (Figure 12.9). Depending upon the temperature and the nature of the starting CNTs, the nanotubes thus formed can either be pure BN or a mixture of pure BN and $B_xC_yN_z$. The CNTS prepared via this latter route may be easily transformed into pure BNNTs by oxidation at 650 °C. In this reaction, metal oxides (e.g., MoO_3) may serve as promoters for the synthesis of BNNTs [38]. Most of the BNNTs prepared in this way have open tips at the both ends [39]. In fact, X-ray diffraction (XRD) spectra showed that both hexagonal (two-layered repeating units) and rhombohedral (three-layered repeating units) nanotubes existed in the final product [17], as confirmed with TEM (Figure 12.10) [40]. Pure BN conical nanotubes were also obtained using this method (Figure 12.11) [41–43], while aligned $B_xC_yN_z$

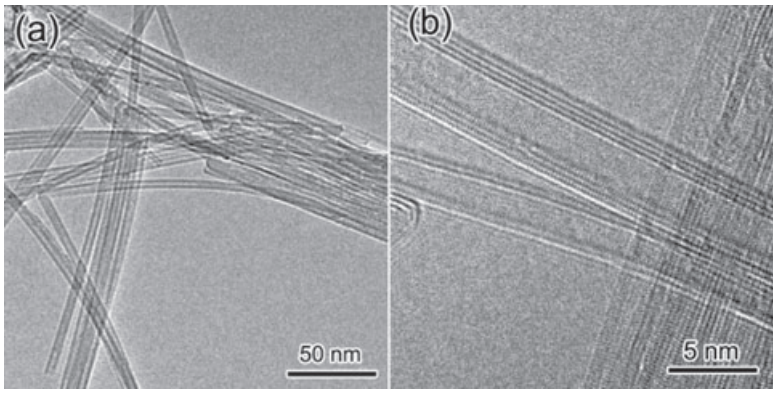

Figure 12.9 (a) Low-magnification TEM image of BNNTs; (b) High-magnification TEM image of BNNTs.

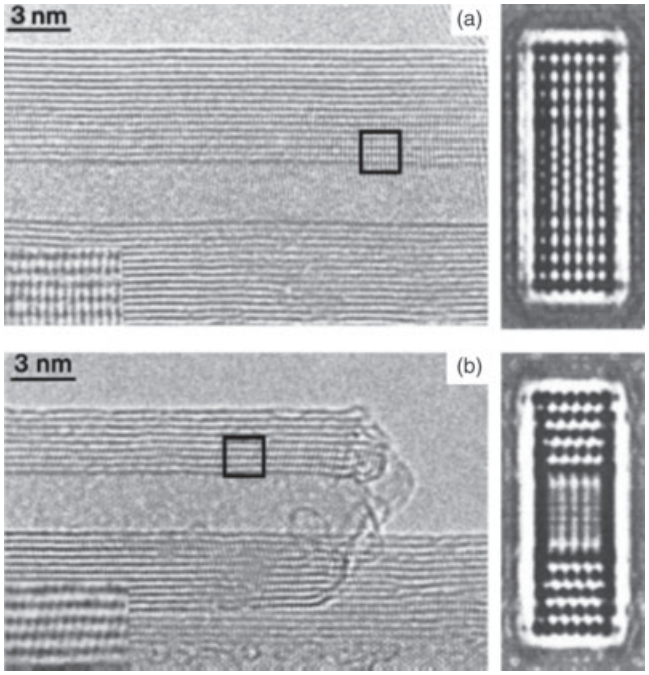

Figure 12.10 HR-TEM images of multiwalled BNNTs. A definite, but different, stacking order is apparent in marked areas in (a) and (b), as highlighted in the insets. Hexagonal-type stacking in (a) and rhombohedral-type stacking in (b) are confirmed by corresponding computer-simulated HR-TEM images (right-hand images) for BNNTs having the axes parallel to the [1 0 –10]orientation (zigzag tubes). Reproduced with permission from Ref. [40]; © 2000, American Institute of Physics.

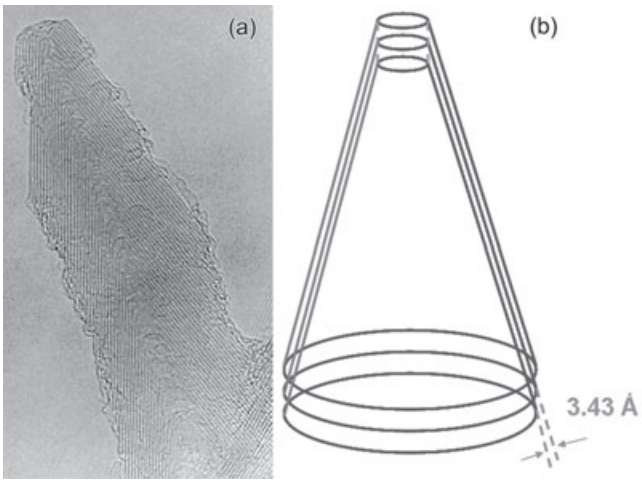

Figure 12.11 TEM image (a) and schematic representation (b) of a conical BNNT.

nanotubes and BNNTs resulted from the use of aligned CNTs and aligned CN_x nanotubes as templates [14, 44].

Han *et al.* showed that CNTs prepared via CVD contain many defects, but that these are the preferred sites for substitution reactions. Advantageously, boron oxide can flow into the hollows of nanotubes with open tips or breaches, so that the reaction can begin from both the outer and/or inner layer [45]. Bando *et al.* confirmed this assumption based on EELS mapping results, and suggested that the conversion of carbon to BN in the tubular layers occurred through an inhomogeneous crystallization of B/N domains onto and within the undulating defective graphite C shells opened by oxidation [46]. These models can provide a simple explanation for the major growth processes, but cannot explain other important phenomena, such as the outer and inner diameters of BNNTs (typically 3–9 nm and 2–4 nm, respectively) being smaller than those of the starting CNTs (typically 8–15 nm and 4–7 nm, respectively), and the decrease in the number of layers.

A detailed growth model was proposed (see Figure 12.12) [47], wherein the oxidation reactions of the carbon layers, defects and tips each played important roles. Although the reaction tube was purged with 99.99% nitrogen before heating (nitrogen also was used as the reaction gas), a small amount of oxygen had remained in the reaction chamber (some remnant oxygen may even derive from the reaction chamber wall). When the temperature rises above about 500 °C, the oxygen will react with the carbon layers, this effect occurring especially in the weakest regions of the CNTs such as the defects and tips. This process leads to the production of small voids in the carbon layers of the CNTs (process a in Figure 12.12). The reaction is expressed as:

$$2\ \mathrm{C\,(nanotube\ layer)} + \mathrm{O_2\ (gas)} \rightarrow 2\ \mathrm{CO\ (gas)} \qquad (12.2)$$

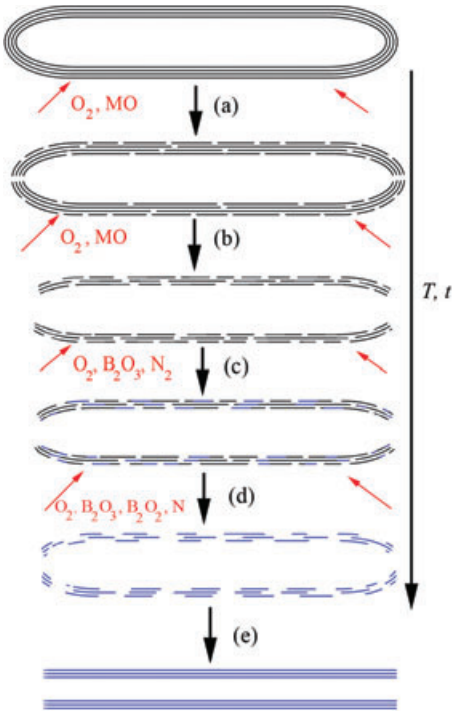

Figure 12.12 A schematic process for the CNT-substitution reaction that develops with temperature (T) and time (t). (a) Areas of voids in carbon layers that are formed by their oxidation reactions with oxygen or metal oxides (MO); (b) More voids form in the carbon layers, and some outer layers peel off; (c) B_2O_3 and nitrogen react with the carbon layers to form BN domains, and more voids are formed in the carbon layers; (d) The substitution reactions are completed with all BN layers having numerous large voids; (e) The inner and outer diameters of BN start to shrink by the rearrangement of B and N atoms, so as to eliminate to the large voids and yield near-perfect layers of BNNTs. Reproduced with permission from Ref. [47]; © 2006, American Institute of Physics.

The vapor pressure of the metal-oxide (MO) additive arising at high temperature also helps to disrupt the carbon layer by the following reaction:

$$\mathrm{MO\,(g) + C\,(nanotube\ layer) \rightarrow M + CO\,(gas)} \tag{12.3}$$

At higher temperatures, larger and more numerous areas of carbon are consumed, and consequently more voids are formed. Some of the outer layers may peel off partially, or even completely (process b in Figure 12.12). This is one reason why the outer diameter is smaller, and the number of layers fewer, in the final BNNTs than in the starting CNTs.

Although, above its melting temperature (ca. 450 °C) boron oxide is molten, its vapor pressure remains quite low until the temperature reaches about 1200 °C, which is sufficiently high to start the reaction. According to experimental results,

the B_2O_3 partial pressure is high enough to create a flow into the CNT area, while temperature is adequate for initiating the carbon-substitution reaction. The BN formation begins from the open edges of the broken areas created by the oxidation reactions (Equations 12.1 and 12.2). Meanwhile, oxygen and the metal oxide continue to react with the carbon layers, a process that leads to the rupture of more areas on the carbon (process c in Figure 12.12). As h-BN is a near-perfect lattice match with graphitic carbon, the substitution-reaction proceeds smoothly.

The carbon layer-substitution reaction occurs at specific areas and is expressed as follows:

$$B_2O_3\,(\text{gas}) + 3\,C\,(\text{layer}) + N_2\,(\text{gas}) \rightarrow 2\,BN\,(\text{layer}) + 3\,CO\,(\text{gas}) \tag{12.4}$$

Should the final reaction temperature be high enough to start the reaction, but not sufficiently high to fully substitute the carbon, then only low-/C ratio $B_xC_yN_z$ nanotubes are formed [46]. At 1500 °C, the main boron oxide is B_2O_2, which is mainly formed by the reaction:

$$B_2O_3\,(\text{liquid}) + CO\,(\text{gas}) \rightarrow B_2O_2\,(\text{gas}) + CO_2\,(\text{gas}) \tag{12.5}$$

The carbon-substitution reaction may then be written as:

$$B_2O_2\,(\text{gas}) + 2\,C\,(\text{layer}) + N_2\,(\text{gas}) \rightarrow 2\,BN\,(\text{layer}) + 2\,CO\,(\text{gas}) \tag{12.6}$$

At a steady temperature of 1580 °C, most (or all) of the carbon layers have been replaced by BN layers via the reactions shown in Equations 12.4 and 12.6, or consumed by oxygen or metal oxide via the reactions shown in Equations 12.2 and 12.3, leaving small or large voids (process d in Figure 12.12).

However, since the temperature is high enough, the BN atoms may be in a near-fusion state and rearrange to eliminate these voids. The diameter of the inner layer of BNNTs will then tend to shrink, such that the B and N atoms in the same layer are numerous enough to settle into a perfect cylinder, which in turn makes the structures more energetically stable. The final inner and outer diameters might be regulated by the size of the open-tips, which can range from very small to a size equal to the original diameters of the nanotubes. Such an rearrangement of BN atoms, which corresponds to a shrinking of the diameter, thus begins from the tip area and extends along the whole length of the tube. This process leads to BNNTs with inner and outer diameters that are much smaller than those of the starting CNTs and, in fact, some B and N atoms can even migrate between the different layers. Hence, the outer layers might be eliminated by the occurrence of such migration to inner layers, to mend the voids therein. In this way, the number of layers in the BNNTs is reduced (process e in Figure 12.12). It appears that processes d and e in Figure 12.12 may even occur simultaneously. The results of EELS studies have shown that the atomic ratio of B/N is usually close to 1, signifying that the B and N atoms rearrange preferentially and migrate as a pair. Frequently, both double and triple-layered BNNTs are identified along with their single-walled

counterparts. The processes of rearrangement and fusion of the B and N atoms are also similar to the graphitization process in the carbon layers of CNTs during heating and irradiation by an electron beam during *in situ* TEM observations [48].

This model is also helpful for explaining the formation of near-perfect $B_xC_yN_z$ nanotubes with very high B/C atomic ratios, that similarly exhibit much narrower outer and inner diameters compared to those of the starting CNTs.

The CO gas formed during the reactions in Equations 12.2, 12.3, 12.4 and 12.6 can also react with B_2O_3 and N_2 to form BN in the following manner:

$$B_2O_3 + 3\ CO + N_2 \rightarrow 2\ BN + 3\ CO_2 \tag{12.7}$$

This reaction may help to mend the voids in BN layers, or to form new BN layers on existing inner or/and outer layers. However, it also represents the main source for the formation of byproducts, such as BN FNPs and BN pieces. If the reaction temperature is too high, then the reaction in Equation 12.7 will predominate, and more BN byproducts will be produced.

Using this route, isotopic ^{10}BN and ^{11}BNNTs respectively were synthesized by replacing natural B_2O_3 with $^{10}B_2O_3$ and $^{11}B_2O_3$ [47, 49].

12.2.5 Chemical Vapor Deposition

Chemical vapor deposition involves the dissociation and/or chemical reactions of gaseous reactants in an activated (heat, light, plasma) environment, followed by the formation of a stable, solid product. The deposition involves homogeneous gas-phase reactions or heterogeneous chemical reactions (which occur either on, or in the vicinity of, a heated surface), or both, leading to the formation of powders, films and 1-D nanomaterials, respectively. While CVD represents a successful route for the synthesis of high-purity and good-quality CNTs, it is also expected to be invaluable for the synthesis of high-purity BNNTs.

Lourie *et al.* used borazine ($B_3N_3H_6$) as a precursor, and nickel boride as a catalyst, to synthesize BNNTs at 1100 °C. The group prepared borazine by an *in situ* reaction of $(NH_4)_2SO_4$ with $NaBH_4$ [18], with the nanotubes produced having large diameters and exhibiting a bamboo-like structure.

Tang *et al.* also prepared BNNTs, by using B and MgO as the starting materials to react with ammonia. At 1300 °C, the boron reacted with MgO to form B_2O_2 and a Mg vapor that was carried by argon into a reaction chamber at 1100 °C, where a flow of ammonia was introduced. The BN was produced by the interaction of B_2O_2 with ammonia [50], the chemical reactions being represented by the following equations:

$$2\ B\ (S) + 2\ MgO\ (S) \rightarrow B_2O_2\ (g) + 2\ Mg\ (g) \tag{12.8}$$

$$B_2O_2\ (g) + NH_3\ (g) \rightarrow 2\ BN\ (s) + 2\ H_2O\ (g) + H_2 \tag{12.9}$$

Extensive follow-up experiments revealed that the quantity, quality and purity of these as-grown BNNTs depended heavily on the growth temperature when a mixture of MgO and boron powder was employed. Below 1100 °C, BNNTs of good quality and purity were obtained, although the yield was only in the region of tens of milligrams. An increase in the growth temperature to 1200 °C improved the yield to hundreds of milligrams, but the nanotube diameters increased dramatically, up to 1 μm. Above 1250 °C, only bulk BN flakes were obtained. A high Mg vapor pressure at high temperature (760 mm Hg at 1100 °C) ensured that the Mg vapor easily reached the tube's growth region and any aggregates present in this low-temperature zone. When growing BNNTs, the catalytic activity of Mg is ideal; although a mixture of MgO and boron powder has proven an effective source of B_2O_2, it is extremely difficult to increase the yield by simply raising the temperature [50].

Transition metals are common catalysts for nanotube growth. Thus, a mixture of MgO, FeO and boron powder was shown to be a good substitute for the precursor as it combines the advantages of MgO and FeO, which are, respectively, an effective B_2O_2-producer and catalyst. The detailed experimental procedures were as fellows: (i) an induction furnace is used to heat the mixture of FeO, MgO and boron powder in a BN crucible to produce B_2O_2, Fe and Mg vapors; (ii) ammonia gas, which is introduced from the top of a BN boat with inner diameter 2 cm, reacts with B_2O_2 in the presence of a Fe catalyst; and (iii) after a 1 h reaction period the BN boat is filled with a large amount of BNNTs.

The use of a mixture of FeO, MgO and boron powder as precursor allows BNNTs to be synthesized over a wide temperature range (1100–1700 °C). Although the temperature does not affect the purity and diameters of the BNNTs, the yield is seen to increase as the growth temperature is raised. Most BNNTs have diameters ranging from 50 nm to 150 nm, while the lengths may extend to a few hundred micrometers (Figure 12.13).

Although the BNNTs lack any notable impurity phases, the metal catalysts occur at the nanotube tips, which suggests that the nanotube growth is occurring via the VLS mechanism [51]. Isotopic ^{10}BN [49] and ^{11}BN [52] nanotubes have both been prepared by replacing naturally occurring B with ^{10}B and ^{11}B, respectively.

BNNTs have also been synthesized via a CVD method using B—N—O precursors, specifically self-forming $B_4N_3O_2H$ intermediate compounds (oxygen content ~27%) or commercial BN powders enriched with oxygen (Denka Co.; oxygen content ~10%) [10, 53, 54]. After heating the precursor in a graphite susceptor with an induction furnace to ~1700 °C under flowing mixed N_2/H_2O or mixed N_2/NH_3 (15 : 1 flow rates), the vapors of boron oxides (B_2O_3 or B_2O_2), which have been decomposed from their precursors, were reduced to BNNTs and deposited on the susceptors at an estimated temperature of ~1200 °C.

A microwave plasma-enhanced CVD method was used to prepare BNNTs with diborane and ammonia as the reactants [55]. The chemical reaction for the formation of BN is:

$$B_2H_6 + 2\ NH_3 \rightarrow 2\ BN + 6\ H_2 \qquad (12.10)$$

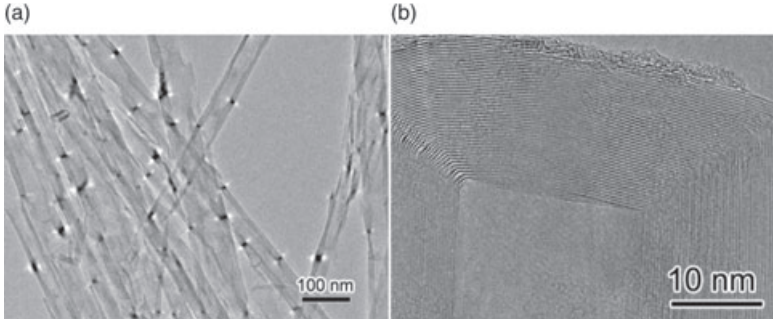

Figure 12.13 (a) Low-magnification TEM image of BNNTs; (b) High-magnification TEM image of the tip of a BNNT.

For the overall reaction in Equation 12.10, the free energy changes are, respectively, $-165\,\text{kcal mol}^{-1}$ and $-177\,\text{kcal mol}^{-1}$, at reaction temperatures of 900 and 1100 K. Thus, BN can be processed at relatively low temperatures by reacting diborane and ammonia due to favorable free-energy exchanges of the reaction. Furthermore, in a plasma environment the dissociation and ionization of gas molecules is enhanced by activated electron and ion collisions. The electron temperature affords a measure of the degree of the dissociation and ionization of the plasma. The average electron temperature is estimated as ~10000 K for the plasma containing B_2H_6-NH_3-H_2 at 800 °C and 800 W. The ratio of diborane to ammonia dominates the formation of different intermediate compounds. In these studies, the $[B_2H_6]/[NH_3]$ ratio was 1.55 : 1 and Ni thin films were used as catalysts. The results of *in situ* quadruple mass spectroscopy (QMS) in B_2H_6-NH_3-H_2 during the deposition of BNNTs (Figure 12.14), allowed the reaction between diborane and ammonia to be described by the following equations, involving four steps: (i) the decomposition of diborane to form B_xH_y; (ii) the dissociation of ammonia to form NH_z; (iii) the reaction of B_xH_y and NH_z to form BNH_γ; and (iv) the dissociation of BNH_γ to form of BN:

$$B_2H_6 \rightarrow B_xH_y + H_2 \ (x = 1\text{–}2, y = 1\text{–}2) \tag{12.11}$$

$$NH_3 \rightarrow NH_z + H_2 \ (z = 0\text{–}2) \tag{12.12}$$

$$B_xH_y + NH_z \rightarrow BNH_\gamma \ (\gamma = 2) \tag{12.13}$$

$$BNH_\gamma \rightarrow BN + H_2 \tag{12.14}$$

Although BN can be deposited on the substrate area with or without Ni catalysts, BNNTs only appear in areas with catalysts. The thickness of the Ni film is one key factor which affects the growth of BNNTs; no 1-D nanostructures are observed on either a bare Si substrate without any catalyst, or on a thick catalyst-film-coated substrate. When the film thickness is <10 nm, the long nanostructures with high

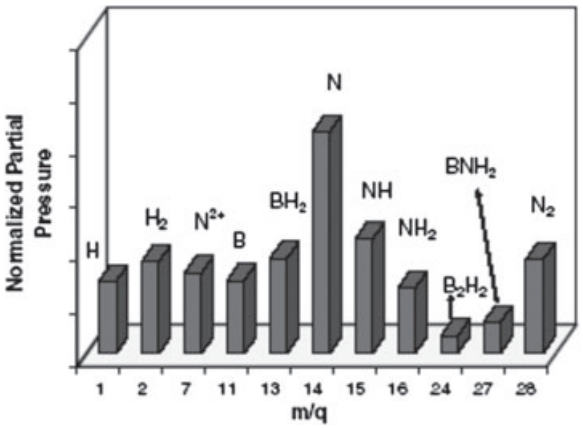

Figure 12.14 Active species detected using quadruple mass spectroscopy (QMS) in B2H6—NH3—H2 plasma during deposition of the BNNTs. The partial pressure of every species is normalized by the total pressure in the reaction chamber. Reproduced with permission from Ref. [55]; © 2008, Institute of Physics.

aspect ratios begin to grow, with such growth becoming significant when the film thickness is <2 nm. No Ni particles were observed attached at the tip of the nanotubes, even though the catalyst is essential for the nanotube growth.

Hexagonal BNNTs and orthorhombic-BN (o-BN) nanotubes were prepared in a thermal CVD furnace using trimethyl borate (TMB) and nitrogen as reactants, with reaction temperatures ranging from 1000 to 1200 °C. A 434 stainless-steel wire, 0.5 mm in diameter, coiled into a disk-like shape, was placed in the center area of the chamber. At temperatures above 1000 °C, Fe, Cr and Mo vaporize and combine with the reactant gases to reach a eutectic composition, forming a partial liquid on the surface and forming BNNTs based on the VLS growth mechanism. The typical diameter of the BNNTs was about 100 nm. At reaction temperatures below 1000 °C or above 1200 °C, BN plates, beads, particles and other morphologies are formed [56].

12.2.6 Solid–Gas Reaction

BNNTs can be generated in a reaction between solids (containing boron sources) and gases (ammonia or nitrogen). One such reaction utilizes pretreated elemental boron powders obtained by ball-milling in an ammonia gas for 150 h at 1000 °C; the powders are then thermally annealed under a nitrogen atmosphere at 1000 °C [19, 57–59]. This method was also shown to yield isotopic ^{10}BN nanotubes [60]. BNNTs were also fabricated by nitriding boron nanowires under a nitrogen atmosphere at 1500 °C for 4 h [61], or a boron thin film under an ammonia atmosphere at 1175 °C for 1 h [62].

For the preparation of BNNTs, Fe_4N/B powders were annealed by exposure to a temperature of 1000 °C for 1 h in a nitrogen atmosphere. The nanotubes, with diameters generally greater than 100 nm, formed a cup-stacked structure [63]. Analysis using XRD showed that the Fe_4N was reduced to Fe by boron at 700 °C, after which the Fe nanoparticles dispersed and adhered to the surface of boron, where they formed a supersaturated solid solution of boron in Fe nanoparticles that reacted with N_2 gas. The BNNTs were then seen to grow from these sites, with the nanotube diameters depending on the Fe particle sizes [64].

12.2.7
Low-Temperature Autoclaving

BNNTs can also be prepared by using a low-temperature autoclaving process. In a typical procedure, $Mg(BO_2)_2 \cdot H_2O$, Mg powder, NH_4Cl and NaN_3 are mixed and placed in an autoclave that is then closed and heated at 600 °C for 60 h. Nanotubes prepared in this way normally have a quite large diameter (several hundreds of nanometers) and contain a large hollow region; they may also be mixed with large amounts of BN nanocages containing large hollows [20]. By using the same strategy, BNNTs were produced with a ~50% yield by copyrolyzing NH_4BF_4, KBH_4 and NaN_3 at temperatures ranging from 450 to 600 °C. The diameters of the resultant BNNTs ranged from 60 to 350 nm, and lengths from 0.5 to 5 μm [65]. BNNTs were also produced when boron trifluoride etherate and sodium azide were used as the reactants in the presence of Fe—Ni powder at 600 °C for 12 h [66].

12.2.8
Pore-Template

Currently, template-aided synthesis is considered to be one of most efficient routes for producing 1-D nanomaterials. However, the correct selection of the templates and precursors is important in order to control the size and shape of the nanomaterials. Various types of template have been utilized to produce many different forms of nanostructured BN [67, 68]. An alumina anodic membrane (AAM) was used to synthesize 1-D nanostructures, based on its tunable pore dimensions, narrow pore-size distribution and good mechanical and thermal stabilities [69]. Borazine ($B_3N_3H_6$) has proved to be an almost ideal precursor because of its high ceramic yield to BN, lack of carbon content, and straightforward conversion to BN upon thermal treatment, without NH_3 [70]. Other effective and well-known precursors include polyvinylpentaborane, polyvinylborazine and dibromoboranedimethyl sulfide, all of which forming BN upon ammonia thermolysis.

One such example involves the use of a borazine oligomer as the precursor. The oligomer was formed from a borazine monomer solution, prepared from a mixture of sodium borohydride ($NaBH_4$) and ammonium sulfate ($(NH_4)_2SO_4$) in tetraglyme at 135 °C in a dynamic vacuum [71]. The borazine solution thus obtained, which contained 97 wt% $B_3N_3H_6$ and 3 wt% BH_3NH_3, was heated and stirred for 40 h at 40 °C in a glass flask sealed with a Teflon cap. On completion of the reaction, a low-viscosity borazine liquid oligomer $(B_3N_3H_4)_x$ had been formed.

In the next stage, a commercially available alumina anodic membrane (60 mm thick, nominal pore diameter 100 nm) functioned as the template (Anodisc 13; Whatman Ltd). These alumina templates were successively cleaned (ultrasonically) in acetone, ethanol and distilled water, and then dried at 50 °C. The template was immersed in the borazine oligomer for periods of 20 and 40 h and 2 weeks, in a glovebox filled with N_2, at room temperature. The template containing the borazine oligomer was then heated at 10 °C min^{-1} from room temperature to 600 °C, held there for 24 h, and subsequently heated to 1200 °C at 10 °C min^{-1}, at which temperature it was maintained for 30 min. The N_2 gas continued to flow into the glovebox during the periods of heating and cooling to room temperature. The template containing BN was then dissolved in 40% NaOH at 60 °C to separate the BN materials from those of the template. The BN nanomaterials were washed carefully several times with water and ethanol. A flow chart showing the production of BN nanomaterials is provided in Figure 12.15.

With a wetting time of 20 h, BNNTs with lengths of several tens of micrometers and diameters of 200–300 nm were formed. Extending the wetting time to 40 h led to the generation of BN 'nanobamboos' that were 40 μm long and 300 nm thick, with walls of 20 nm thickness and a knot that was 30–100 nm thick. Very fine nanoparticles (<100 nm) were also deposited on the nanobamboo's walls. A two-week period of wetting yielded BN nanofibers that were 20 μm long and 300 nm thick, with deposits of small fine nanoparticles less than a few nanometers thick on the external surfaces.

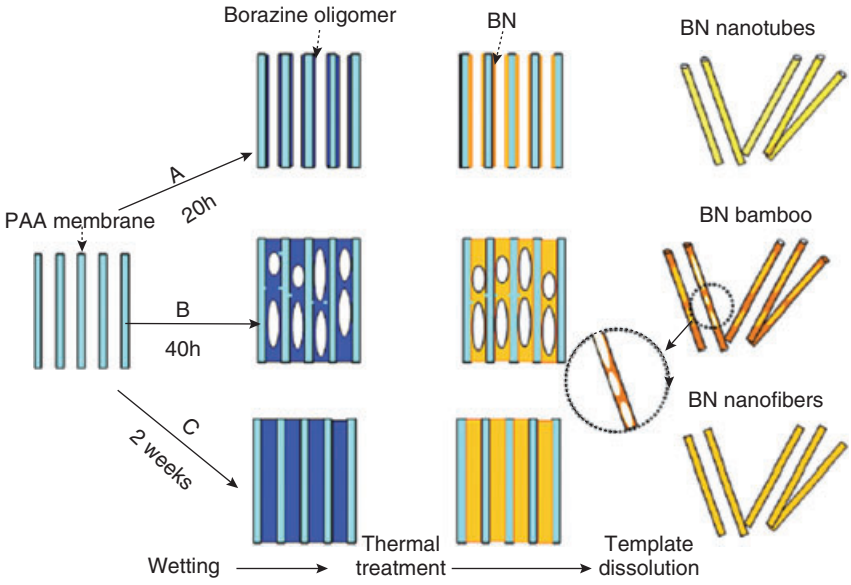

Figure 12.15 A schematic diagram of the formation process of BNNTs, BN nanobamboos and BN nanofibers. Reproduced with permission from Ref. [71]; © 2008, Elsevier.

Shelimove *et al.* grew BNNTs by pyrolyzing 2,4,6-trichloroborazine within the pores of an anodic aluminum oxide (AAO) template at 750 °C [72], while Bechelany *et al.* used liquid polymeric borazine within the pores of AAO also to grow BNNTs [21]. Wang *et al.* derived BNNTs by microwave plasma-enhanced CVD method below 520 °C, under the confinement of an AAO template and using borane/argon and ammonia/nitrogen as the precursors [73].

12.2.9 Arc-Jet Plasma

BNNTs are prepared using an arc-jet plasma process that employs a nontransferred plasma torch (Figure 12.16). The experimental system consists of a DC nontransferred plasma torch, an injector of reactant materials and catalysts, and carbon reaction cylinders. An arc-jet thermal plasma is generated by an arc discharge between a conical tungsten cathode and a copper anode with a cylindrical nozzle in the DC plasma torch; the resultant plasma is ejected from the exit of the anode's nozzle into the inside of the reaction cylinders that join together in front of this exit. A mixture of argon and nitrogen gas constitutes the plasma-forming gas. The flow rates of argon and nitrogen were respectively, 45 slpm (standard liters per minute) and 2 slpm, while the reactant material was a mixture of h-BN as boron source and Ni/Y powder (atomic ratio 9 : 1) as the catalyst. The reactant

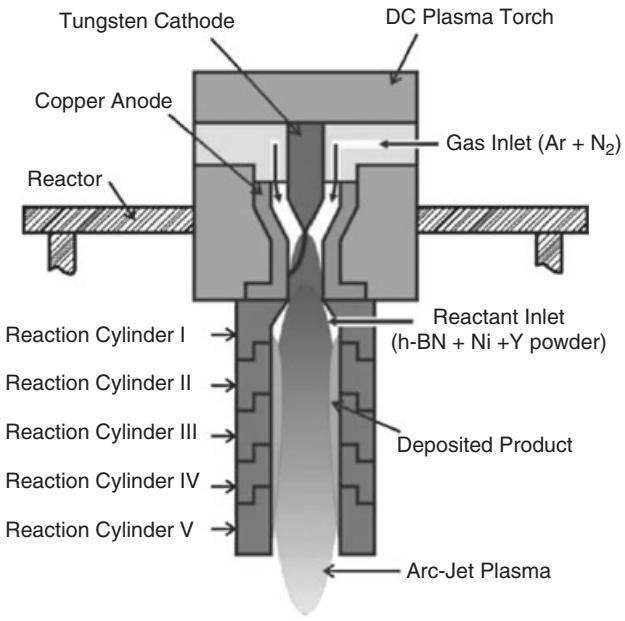

Figure 12.16 Schematic of an arc-jet plasma reactor used for BNNTs synthesis along with a nontransferred plasma torch. Reproduced with permission from Ref. [22]; © 2006, Elsevier.

powder is introduced via an argon carrier gas into the arc-jet plasma flame through injection holes in a reaction cylinder close to the nozzle exit, and then undergoes synthetic reactions in the high-temperature plasma flowing through the reaction cylinders. The carbon reaction cylinders are installed in such a way as to build up a long, high-temperature reaction zone, which enhances the reactants' synthetic reactions. The arc-jet plasma torch is operated with a DC current of 300 A and an applied voltage of 46 V, with ambient pressure being maintained under atmospheric conditions. The samples are collected from the inner wall of the reaction chamber. The nanotubes, which are created only on the wall of reaction cylinder II and are mixed with nanoparticles, have an outer diameter of 3–10 nm and a length of up to several micrometers. Most also have encapsulated catalysts particles at their tips [22].

12.3 BNNT-Based Nano-Objects

In this section, attention is focused on BN nanotube-based nano-objects, including both filled and functionalized BNNTs.

12.3.1 Filled BNNTs

Similar to CNTs, the nanocavity of BNNTs serves as an ideal tool for preparing and studying the properties of confined nanostructures of different materials in different forms. As the nanocavities are very small, the filled materials might be expected to have different physical and/or chemical properties compared to the unfilled materials, Hence, the filled BNNT itself might behave differently from pure BNNT. Filled BNNTs are mainly prepared by either of two methods: (i) *in-situ* filling, where the nanotubes are filled while they grow; and (ii) two-step filling, where the BNNTs are formed first before being filled with a molten or a sublimated material. In principle, filling might occur during all methods of synthesis, although not all materials can be filled by one method, nor even by all known methods.

The first report of filling pure BNNTs was that of SiC-filled BNNTs using CNTs as templates [74]. The CVD-prepared CNTs initially were treated with nitric acid and then heated in air to remove any surface acidic groups. The reaction took place in a conventional horizontal furnace with a sintered alumina tube. A powdered mixture of silica (~68.2 wt%) and silicon (~21.8 wt%) was placed in the central hot zone, while B_2O_3 powder covered with CNTs was placed just outside the central zone (Figure 12.17a). The tube was held in a flowing nitrogen atmosphere at 1753 K for 1 h. After the reaction, the product was collected from the original nanotube bed. A high-resolution (HR) TEM image of a SiC-filled BNNT, revealing a dissimilar number of tubular layers on one side of the nanotube compared to the other, is shown in Figure 12.17c. The interlayer distances in the outer sheath

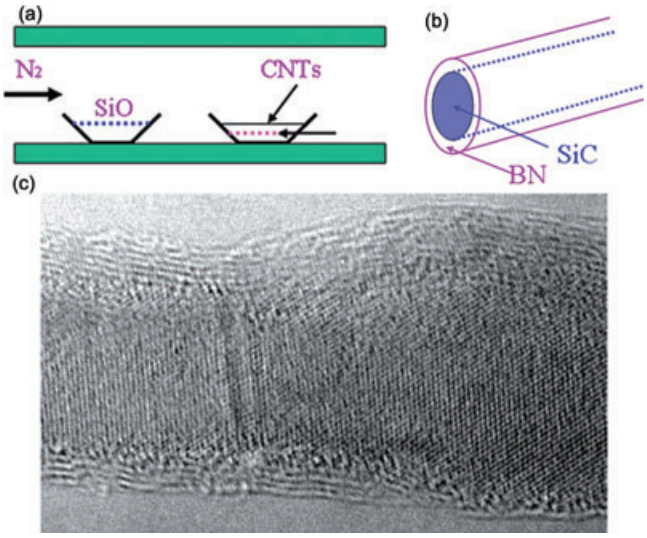

Figure 12.17 (a) Schematic image of experimental set-up; (b) Schematic image of SiC-filled BNNT; (c) High-resolution TEM image of a SiC-filled BNNT.

were approximately 0.33 nm – close to the value of the ~002 spacing of h-BN or graphitic carbon. This method combines both the CNT-substitution reaction and the confined reaction. In the former case, the CNTs react with boron oxide vapor in the presence of nitrogen gas to form BNNTs, the diameters and lengths of which are similar to those of the starting CNTs. Formation of the SiC filling proceeds via the penetration of SiO vapor into the nanotube cavity, and subsequent reaction of the SiO vapor with the inner carbon layers or volatile carbon monoxide in the interior to form SiC nanowires. The filled region may extend for the entire length of the nanotubes. Using the same route, this method has been successfully applied to boron carbide nanowires [75], FeNi nanowires [46], Co nanowires [76], MoO_x clusters and nanowires [77].

In situ filling via CVD processes have been used to prepare Fe nanoparticles [78], AlN nanotubes [79], GaN nanowires [80–82], Si_3N_4 nanowires [83], MgO nanowires [84], SiO_x/Si [85], ZnS [86], $Al_{18}B_4O_{33}$ nanowires [87] and SiC nanowires [83, 88, 89]. BNNTs filled with ZrO_2 nanorods have been obtained via a solid–gas multiphase reaction [90].

A good example of this is the synthesis of GaN-filled BNNTs [80]. In order to create the BN-coated nanowires, Ga_2O_3 and Ga (molar ratio 1 : 4), amorphous boron powder and an iron oxide catalyst supported on an alumina–nanoparticle template were well mixed and placed in a quartz boat that was then inserted into the hot zone of a conventional temperature-programmable furnace. Ammonia was used during the reaction at 1100 °C for 1 h, after which the synthesis product was collected from the quartz boat. The core of GaN nanowire was crystalline, with either a cubic zinc blende or hexagonal wurtzite structure, and was 10–85 nm in

diameter and up to 60 nm in length. The outer coating, which typically was several BN-layers thick, covered the entire GaN nanowire almost uniformly.

The two-step filling method requires the nanotube tips to be opened before they can be filled with BNNTs. This is possible in two ways: either the tips open naturally during nanotube formation, or they can be opened by treating the nanotubes with acid and/or oxidation.

For molten-state materials in a typical filling experiment, the BNNTs are mixed with the desired amount of filler, after which the mixture is vacuum-sealed in a silicon ampoule. The ampoule is then slowly heated to a temperature above the melting point of the filler, and then slowly cooled. The BNNTs were filled with the halides KI, KCl and KBr [91, 92]. The nanotubes were synthesized via a CNT-substitution reaction, followed by oxidation treatment [39]. The BNNTs then were sealed in several evacuated (10^{-6} Torr) quartz ampoules, together with different halides (KI, KCl, KBr) in an approximate 4 : 1 halide : BNNT mass ratio. A high-magnification TEM image of a BNNT filled with KI crystals is shown in Figure 12.18a. Here, the direction of the incident electron beam is along <001>, and the long axis of the crystal is parallel to the crystalline *a* direction. The crystal structure is indexed to rock salt KI.

The sublimation filling method is more restrictive than the molten-state process, because it is applicable only to a very limited number of materials. The reason for such limitation is the need for a filler to sublimate within the thermal stability range of not only the nanotubes but also the silica ampoule and other sealed containers. An example is the filling of BNNTs with C_{60} fullerene molecules [93]. Here, pure BNNTs were synthesized using either a plasma-arc discharge method [23] or a CNT substitution reaction [17, 39]. The as-synthesized arc-nanotube-rich soot was heat-treated in air at 800 °C for 20 min to remove any excess boron nanoparticles and to open the tips of the BNNTs. The gray, heat-treated tubes then were sealed in an evacuated (10^{-6} Torr) quartz ampoule, together with commercially available C_{60} powder at about a 5 : 1 C_{60} : BNNT mass ratio, and then heated uniformly to between 550 ° and 630 °C for 24–48 h. The individual spheres can be seen to fit just inside the cylinder, producing the linear-chain or classic 'peapod' configuration (Figure 12.18b). With increasing inner diameter of the BNNTs, unusual

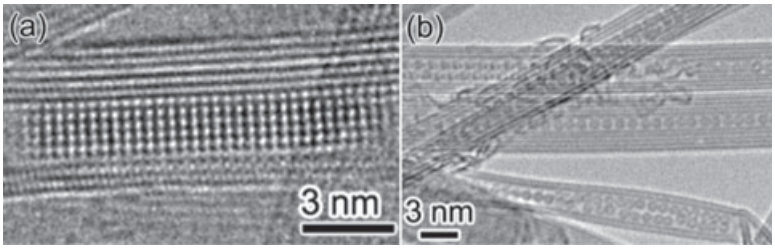

Figure 12.18 (a) High-magnification TEM image of a KI-filled BNNT. The direction of the incident electron beam direction is along the ⟨001⟩, and the long axis of the crystal is parallel to the crystalline *a* direction; (b) BNNTs filled with C_{60}.

C_{60} stacking configurations are obtained (including helical, hollow core and incommensurate) that are unknown among bulk or thin-film forms of C_{60}.

12.3.2 Functionalized BNNTs

As the functionalization of CNTs represents a vital means of tailoring their properties and engineering CNT-based devices, significant efforts have been undertaken in this direction, with especially intense investigations being undertaken into soluble CNTs, CNT composites and CNT compatibility with biological systems [94–97]. Yet, compared to CNTs, much less attention has been centered on the chemical functionalization of BNNTs, one reason being that it is still difficult to obtain large amounts of high-quality, pure BNNTs. Another reason is the inherently low chemical reactivity of the surface of well-crystallized BNNTs, which inhibits many traditional solution-based reactions. Until now, BNNTs have been functionalized by inorganic, polymer and biomaterials.

Han *et al*. reported BNNT functionalization by their full coverage with semiconducting SnO_2 nanoparticles [98]. Bare BNNTs (i.e., unfunctionalized) were synthesized in a CNT-substitution reaction, followed by oxidation treatment, such that the outer diameter of the BNNTs was usually <8 nm. The nanotubes were formed either as isolated units or as tubes arranged in aligned bundles; no attempt was made to separate these different configurations. Tin(II) chloride (1.2 g) dissolved in distilled H_2O (50 ml) was then added, followed by 0.8 ml of HCl (38%, v/v). After incorporating 15 mg of BNNTs, the solution was sonicated for 5 min and then stirred for 1 h at room temperature. The formation of SnO_2 is represented as:

$$2\ SnCl_2 + 2\ H_2O + O_2 \rightarrow 2\ SnO_2 + 4\ HCl.$$

A TEM image of the coated BN nanotube bundles is shown in Figure 12.19. The uniform coating, of average thickness 3 nm, was composed of nanocrystalline particles <5 nm in size. The BN FNPs also were fully coated; thus, the SnO_2 coating layer followed the shape of the supporting nanoparticle template. The composition of the nanoparticles as tetragonal SnO_2 was confirmed using XRD, electron-diffraction patterns and energy-dispersive spectroscopy (EDS) [98].

Soluble multiwalled BNNTs were developed by using amine-terminated oligomeric poly(ethylene glycol) (PEG) surface groups [99]. Stearoyl chloride-functionalized BNNTs were formed via the interactions of COCl groups and amino groups on BNNT walls [100]. In contrast to the starting material (multiwalled BNNTs), which is insoluble in organic solvents, the functionalized BNNTs (f-BNNTs) were soluble in solvents such as chloroform, *N,N*-dimethylacetamide, tetrahydrofuran (THF), *N,N*-dimethylformamide, acetone, toluene and ethanol. The solubility of f-BNNTs in *N,N*-dimethylacetamide was >0.5 $g\,l^{-1}$. Very dilute solutions of BNNT are almost totally transparent, while concentrated solutions have a white appearance and are visually nonscattering. No precipitation was observed when the sample was stored long term under ambient conditions. The results of both,

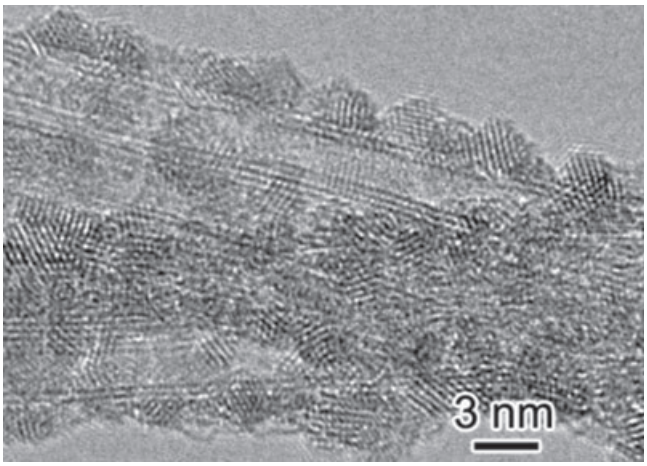

Figure 12.19 High-resolution TEM image of a BNNT bundle fully coated with SnO_2.

cathodoluminescence (CL) and UV/visible absorption experiments, suggested that long alkyl chains might induce drastic changes in the band structure of BNNTs. The effects of functionalization of BNNT with NH_3 and four other amino-functional groups – namely, NH_2CH_3, $NH_2CH_2OCH_3$, NH_2CH_2COOH and NH_2COOH – were investigated on a theoretical basis using density functional theory (DFT) calculations [101]. Although the authors reported few changes in the electronic structure of BNNTs, their chemical reactivity was enhanced owing to the presence of –COOH amino groups. The BNNTs were functionalized and solubilized by interaction with Lewis bases [102], and also functionalized with amine groups via ammonia plasma irradiation [103].

In addition to covalent functionalization, a so-called noncovalent functionalization through wrapping BNNTs with a conjugated polymer, poly [*m*-phenylenevinylene-*co*-(2,5-dioctoxy-*p*-phenylenevinylene)] (PmPV) was also accomplished [104]. As the functionalized BNNTs were totally soluble in many solvents, the experimental process could easily be scaled up. In a typical run, 5 mg of PmPV was dissolved in 20 ml chloroform, and 5 mg of BNNTs then added to the solution. The mixture was sonicated for 2 h at room temperature, and then centrifuged (2000 rpm) to remove any insoluble material. Thus, a homogeneous solution was obtained in which no precipitation was observed during long-term storage at ambient conditions. The dilute BNNT solution was totally transparent. The PmPV-wrapped BNNTs were shown to be totally soluble in chloroform, *N*,*N*-dimethylacetamide and THF, but insoluble in water, ethanol and similar solvents. Both, TEM and CL characterization indicated the existence of strong π–π interactions between BNNTs and PmPV. In addition, functionalization may also be used to purify BNNTs [105] and, most importantly, to tune their band structure [106].

The fact that BNNTs absorb neither visible nor infrared light might prove advantageous for the protection of biological molecules against overheating and damage, as occurs when using CNTs. The natural affinity of a protein for BNNTs has been

demonstrated – that is, proteins can be immobilized directly onto BNNTs without using a coupling reagent. In order to immobilize the proteins, the dispersed BNNTs were simply stirred with dilute protein solutions for several hours. Figure 12.20a shows ferritin molecules (dark contrast particles) immobilized on a BNNT, where the ~6 nm iron core of each ferritin molecule is clearly visible, and the amorphous apoproteins are located around the cores. All of the BNNTs were shown to be coated with immobilized ferritin molecules, the immobilization being verified by EDS analyses, and Fe peaks appearing after immobilization (Figure 12.20b). Some ferritin molecules were also found inside the BNNTs (Figure

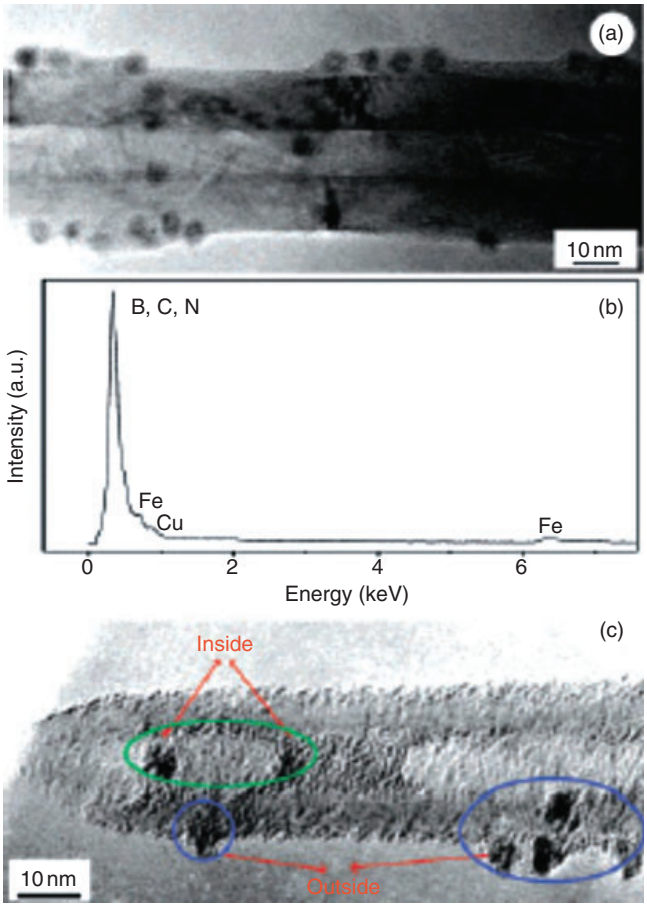

Figure 12.20 (a) TEM image of ferritin molecules on a BNNT; (b) EDS spectrum of a ferritin-covered BNNT. Note the characteristic Fe peak peculiar to ferritin; the Cu signal originates from a TEM grid; (c) Ferritin filled in a BNNT. Reproduced with permission from Ref. [107]; © 2005, The American Chemical Society.

12.20c), most likely due to the presence of numerous open tip-ends. In order to raise the efficiency of the immobilization process, 1-pyrenebutyric acid-*N*-hydroxysuccinimide ester (PAHE) -functionalized BNNTs were utilized to anchor the ferritin protein. For this, the BNNTs and PAHE were mixed and stirred for 2 h in an organic solvent, dimethylformamide (DMF); the solution was then filtered and washed repeatedly with DMF to remove any excess reagent. A highly aromatic pyrenyl group in PAHE, with known strong π–π interactions with the basal plane of graphite and sidewalls of CNTs, was also found to interact strongly with the sidewalls of BNNTs. Typically, BNNTs may have profound interactions with some chemicals via π–π stacking due to the electrical polarization phenomena induced by the BNNT's broken symmetry. Thus, an efficient immobilization may be based upon the formation of an amide bond via the nucleophilic substitution of *N*-hydroxysuccinimide by an amine group on the ferritin [107].

12.4 Porous BN and BN Mesh

Porous solids have applications ranging from adsorbents to purification chromatographic packing to support structures for catalytic processes. A wide variety of porous solids exist, including zeolites, pillared clays, porous polymeric solids and porous carbon [108]. Among these, porous carbon (often called 'activated carbon') displays exceptional porosity, an extended surface area, universal and adsorption capabilities and a high degree of surface reactivity. In the broadest sense, activated carbon can be defined as an amorphous carbon-based material with a high degree of porosity and an extended interparticulate surface area; often, the microscopic structure can be visualized as stacks of flat aromatic sheets cross-linked randomly. Currently, porous carbon is the most popular and economic porous solid in use [109].

h-BN, a material which is structurally closely related to graphite, has an attractive combination of chemical, thermal and electrical properties. The use of activated carbon suggests that an analogous 'activated' BN, exhibiting a high degree of porosity and an extended interparticulate surface area, might be of scientific and economic importance. The nature of the individual B—N bonds introduces a local polar character which is lacking in the carbon structure; thus, as polar sites are considered to improve adsorption, porous BN might represent an effective candidate. Conventionally produced film and particle forms of BN have low surface areas, rendering them relatively useless for adsorption applications [2]. To date, several routes have been suggested for the synthesis of porous BN.

12.4.1 Direct Pyrolyzing Borazinic Precursors

Narula *et al.* prepared porous BN from poly(2,4,6-borazinylamine) with surface areas ranging from 30 to 50 $m^2 g^{-1}$ for powders produced at 900 °C [110]. BN

aerogels formed by the critical point drying of poly(2,4,6-borazinylamine) gels and heated to 1000 °C exhibit low density, are highly porous, and have surface areas of ~400 $m^2 g^{-1}$ [68]. Porous BN materials with surface areas ranging from 437 to 712 $m^2 g^{-1}$ have also been created using similar polymeric precursors [111–113]. An example of this methodology is as follows. A sample of $(Me_2NB)B_2C_2N3H_3$ (3.28 g, 17.0 mmol) was dissolved in 120 ml of chlorobenzene at 23 °C, to which $(Me_3\text{-}Si)_2NH$ (2.74 g, 17.0 mmol) was added via a syringe while stirring the solution. The gel that formed contained some solvent, but this was vacuum evaporated and the remaining solid vacuum-dried for 24 h. The residue (3.12 g) was treated twice with 150 ml of NH_3 (1), held at ~30 °C and then left for 4–5 h with a slow stream of N_2 passing through the flask. The NH_3 (l) slowly evaporated under these conditions, during which time the polymer dissolved in the NH_3 (l). The resultant foamy residue (2.7 g) was vacuum-dried for 30 min. The formed polymer was placed in a quartz or platinum crucible inside a quartz tube, and pyrolyzed *in vacuo* at 800 °C or 1000 °C in a horizontal tube furnace. The porous BN materials thus produced was capable of adsorbing H_2, O_2, CO_2, CO and CH_4. The surface area and pore volume were maximized at pyrolysis temperatures of 800 °C, and essentially eliminated at 1200 °C. These results indicate that the pore structure of polymer-derived boron nitride is a function of both the precursor's polymer structure and the pyrolysis conditions [114, 115]. Such a demonstration of the ability to tailor pore structure and adsorption properties of BN by controlling these parameters represents an important advance in nonoxide, preceramic polymer processing.

12.4.2 Use of Mesoporous Molds

Dibandjo *et al*. prepared porous BN by nanocasting a hexagonally ordered mesoporous carbon (CMK-3) or a cubic mesoporous carbon (CMK-8) with a molecular BN precursor [67, 114, 115]. CMK-3 was prepared using SBA-15 silica as a template, and sucrose as carbon source [114]. CMK-8 is synthesized by nanocasting Ia3d cubic silica (KIT-6) [67]. Tri(methylamino)borazine (MAB) was used as the BN precursor and prepared from 2,4,6-trichloroborazine (TCB) and methylamine. The material was filtered using 2 g of MAB per gram carbon, after which a ceramization step was carried out under nitrogen at 1000 °C, yielding a composite BN-C. The template was then eliminated via a hydrogenation reaction, leaving BN; this step entailed thermal treatment under ammonia at 1000 °C. The resultant XRD spectrum showed two peaks at $2\theta = 26°$ and 43°, and demonstrating the formation of a turbostatic phase of BN. A small-angle diffraction peak of BN appeared at $2\theta = 1.22°$, that was attributed to the (211) reflexion of a cubic I13d phase and the corresponding cell parameter, a = 17.7 nm. Mesoporous BN was shown to have a specific area of 820 $m^2 g^{-1}$, a mesoporous volume of 0.32 $cm^3 g^{-1}$ and a pore size distribution centered on 4.7 nm diameter. Similar experimental conditions were employed in preparing hexagonal ordered mesoporous BN with a specific surface area of 540 $m^2 g^{-1}$, a mesoporous volume of 0.27 $cm^3 g^{-1}$ and a narrow pore-size distribution

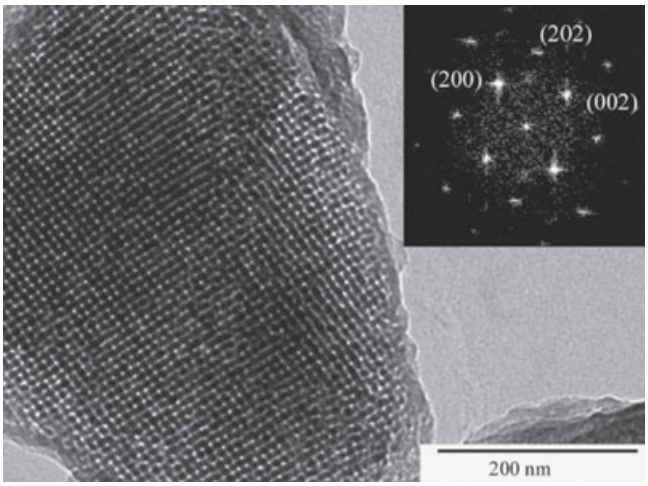

Figure 12.21 Representative transmission electron microscopy image of the boron nitride replication taken with the incident beam parallel to the [010], and corresponding Fourier diffractogram. Reproduced with permission from Ref. [67]; © 2006, Elsevier.

(centered on 4.4 nm diameter) starting with tri(methyl-amino)borazine as the BN source and CMK-3 mesoporous carbon as the template (Figure 12.21). The results of these studies demonstrated that the cubic and hexagonal ordered mesostructure of CMK-8 or CMK-3 were transferred almost fully to the BN replica [67].

12.4.3
Carbon Template-Substitution Reaction

The synthesis routes described above for generating BN with enhanced porosity typically employ expensive and highly toxic borane-based molecular precursors, which limit their use in high-volume production.

An alternative method – the carbon template-substitution reaction – is suitable for obtaining porous BN [116], and has been used to prepare both BN and $B_xC_yN_z$ nanotubes [17, 39]. CNTs and activated carbon each have high specific surface areas that reactant gases (e.g., boron oxide and nitrogen) readily can reach. Hence, based on such similarities, porous BN might well be formed by using porous carbon as a template. The porous carbon used here (obtained commercially from Calgon) had a specific surface area, total pore volume and average pore radius of, respectively, 779.0 $m^2 g^{-1}$, 0.5465 $cm^3 g^{-1}$ and 14.03 Å. The substitution reaction was performed in a horizontal, high-temperature furnace. B_2O_3 powder in an open graphite crucible was covered with activated carbon and held in a flowing nitrogen atmosphere at 1580 °C for 45 min. The $B_xC_yN_z$ intermediate product was collected from the bed of porous carbon and heated in air at 600 °C for 30 min to remove any remaining carbon and/or convert the $B_xC_yN_z$ to pure BN [116].

The TEM images of the starting material and its product are shown in Figure 12.22. In Figure 12.22a–c can be seen the images of activated carbon at successively higher magnification, while Figure 12.22d–f shows the corresponding results for the product, the BN material. At the 80 and 20 nm size scales, the BN-based product is strikingly similar in morphology to the activated carbon template. The matrix of both samples is a uniform, isotropic microtexture. Subtle differences between the carbon starting material and the BN-based product are apparent at high magnification (as seen when comparing Figure 12.22c and f). Here, the BN-based material shows slightly more 'graphitization' – that is, the degree of activation of the BN system appears less than that of the activated carbon template.

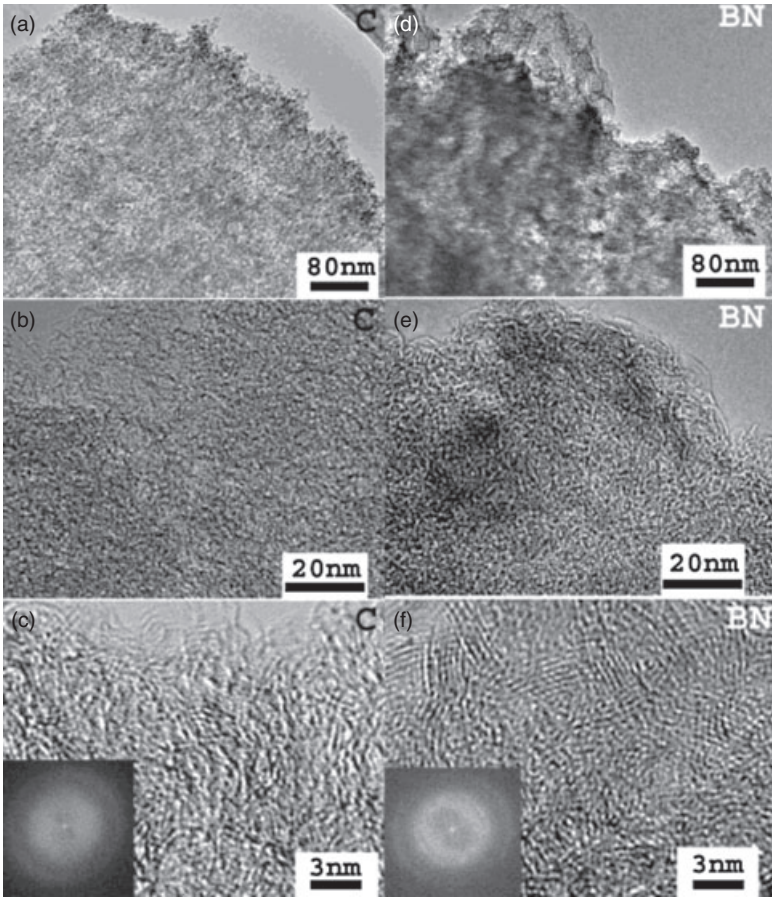

Figure 12.22 TEM images of starting activated carbon (a–c) and product-activated BN (d–f). The insets in (c) and (f) show the FFT diffraction patterns of the corresponding high-resolution images. Reproduced with permission from Ref. [116]; © 2004, The American Chemical Society.

Figure 12.22c shows the pores of the activated carbon to be mostly slit-shaped spaces between twisted aromatic sheets. Small amounts of graphitic ribbons are seen in Figure 12.22c. A fast Fourier transform (FFT) of the image in Figure 12.22c (shown as an inset) revealed the broad 'fuzzy' rings that corresponded to the largely amorphous structure of the activated carbon. From the corresponding TEM image of Figure 12.22f, it was clear that the BN-based product had more and larger crystalline ribbons than the starting activated carbon. The inset of Figure 12.22f shows the FFT of the associated image that, again, evidenced the 'fuzzy' rings corresponding to significant amorphous structures of the activated BN product, although the angular structures in the FFT suggested that the amorphization was not as complete as in activated carbon. XRD measurements supported the conclusion that the BN product had a more crystalline structure than the starting activated carbon. EELS spectra were also recorded during TEM characterization to confirm the stoichiometry of the starting materials and products. Most of the porous structures in the products were pure BN, although a minority of EELS spectra taken from some areas indicated the presence of B, N and a small amount of C. The specific surface area, total pore volume and average pore radius of template-derived activated BN were, respectively, $168\,m^2\,g^{-1}$, $0.27\,cm^3\,g^{-1}$ and 32.2 Å.

Terrones *et al*. used the same route to transfer spherical mesoporous MCM-48 carbon to spherical mesoporous BN (100–400 nm outer diameter) with a specific surface area of $290\,m^2\,g^{-1}$. The porous BN spheres exhibited stable field emission properties at a low-turn-on voltage (e.g., $1–1.3\,V\,\mu m^{-1}$) [117].

12.5
BN Mono- or Few-Layer Sheets

Materials that have same dimensionality, but different numbers of layers, also exhibit significantly diverse physical properties. The properties of single- or double-walled CNTs differ from those of multiwalled CNTs. Today, graphene sheets, comprising one atom-thick two-dimensional (2-D) layers of sp^2-bonded carbon (ML) and a few-graphite-layer sheets, are emerging as materials with unusual properties that show great promise in areas of nanoelectricals (including spintronics), on the basis of the high mobility of their electrons at room temperature. Charge transport in graphene substantially differs from that of conventional 2-D electronic systems because of its linear energy–dispersion relationship near the charge-neutrality point (Dirac point) in the electronic-band structure [119–122].

Hitherto, only a few routes and some experiments have been reported for the synthesis and characterization of BN mono- or few-layer sheets. These experiments have generally focused on depositing ML or few-layer sheets onto atomic flat metal surfaces. Well-ordered h-BN layers can be grown by the thermal decomposition of borazine ($B_3N_3H_6$) on the surface of a transition metal, in most cases one with a hexagonal symmetry [118, 123–126], or on a square lattice (Ni (100)) [127]. Although the layers interact weakly with the metal, they are stable at high temperatures (up to 1000 K) and to air exposure. These important features reflect

the strong lateral interatomic bonds that play a key role in the process of forming h-BN layers on different metal surfaces, while the geometry and lattice constant of the substrate make each system unique. Ultrathin insulating films that are weakly bonded to flat metal surfaces may offer interesting applications in the construction of advanced microelectronic devices, due to the abrupt change in the electronic structure at the interface.

Lattice-matched Ni(111) is often chosen as a substrate for depositing ML h-BN due to its small compressive lattice mismatch of +0.4% between the two systems favoring the formation of commensurate layers; both, ordered and flat terraces – one ML thick – occur over a larger area [128–130]. These syntheses are usually carried out in an ultrahigh vacuum (UHV) chamber. Auwärter *et al.* demonstrated one method in which Ni(111) single crystals were cleaned by exposing them to repeated cycles of Ar^+ bombardment (0.8 kV), to 30 Langmuir O_2, and subsequent annealing to 1000 K [130]. The sample's cleanliness was verified with XPS and/or STM. Subsequently, the Ni(111) surface was held at 1070 K and exposed to borazine, which reacts under hydrogen to form a ML of stoichiometric h-BN. When the first ML is complete, the reaction rate falls by more than two orders of magnitude. Accordingly, a perfect ML of h-BN on Ni(111) can be prepared.

The STM image in Figure 12.23a shows the surface following the formation of a h-BN layer on Ni(111), with a large-area topography scan (1 nA, +100 mV) of atomically flat terraces separated by steps of about 2 Å high; the h-BN layers are seen to grow flat and perfect. The Ni(111) and the h-BN on the Ni(111) surfaces can be distinguished further by their different behaviors towards residual gases or metal vapors. Figure 12.23b shows, at atomic resolution, a h-BN layer on

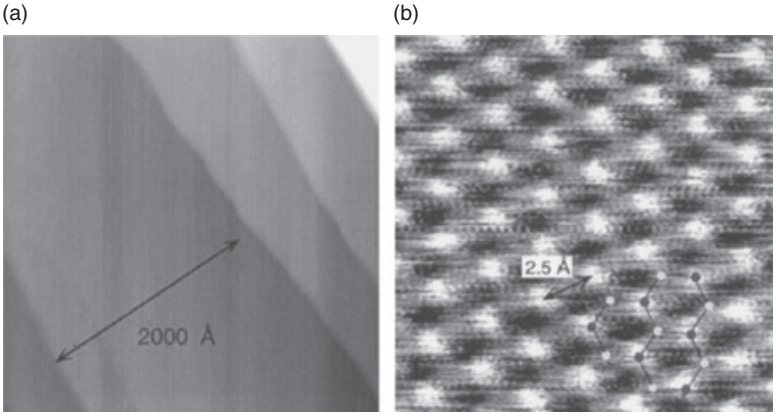

Figure 12.23 STM images of a h-BN layer on Ni(111). (a) Large area topography scan showing atomically flat terraces separated by atomic steps; (b) The atomically resolved picture clearly reveals two hexagonal lattices with a lattice constant of 2.5 ± 0.1 Å, forming a honeycomb pattern. Reproduced with permission from Ref. [130]; © 2008, Elsevier.

Ni(111); this image was recorded at a constant height with a tungsten tip at +4.8 mV bias voltage. Two hexagonal Bravais lattices are apparent that form a honeycomb pattern, while the observed lattice constant of 2.5 ± 0.1 Å corresponds to that of the Ni(111) substrate (2.49 Å). These results represent a well-ordered surface with two distinct atomic species [130].

For h-BN films on Rh(111), the large tensile lattice-mismatch of ~ 6.7% between the over-layer and the substrate leads to the formation of a bilayer nanomesh with a periodicity of 32 ± 2 Å [119].

Recently, 2-D h-BN sheets with few atomic layers (more than five) were obtained using a micromechanical cleavage method [131], in which layers of h-BN can be peeled off with adhesive tape and attached to a 300 nm-thick SiO_2 substrate. h-BN powders of grade AC6004 (Momentive Performance Materials, Inc.), with an average crystal size of about 10 μm, were used as the starting h-BN crystals. An examination using atomic force microscopy (AFM) showed the thinnest region of the BN flakes to be 3.5 nm thick; moreover, as any water adsorbed between the sample and substrate contributed to the measured thickness, the number of layers was, at the most, ten. TEM images showed seven parallel dark lines, giving a clear signature of the number of BN layers in the thinnest region. Because the height of this region was 3.5 nm (as measured with AFM), there was apparently an approximately 1 nm-thick layer of adsorbate between the sheet and substrate. The thickest region measured approximately 80 nm [132].

Two-dimensional BN sheets with mono- and few-layers can be obtained via a chemical-solution-derived method, starting from a single-crystalline h-BN. In this process, a small amount of BN crystals were sonicated in an organic solution to break the crystalline structure and separate the loose single crystals of BN into either mono- or few-layer sheets (W.Q. Han *et al.*, unpublished results).

A two-layered BN sheet is shown in Figure 12.24a, where, the fringe contrast at the edge indicates the number of layers. Another BN sheet with six layers is shown in Figure 12.24b, where the sheet's folding axis is off the [108] direction, causing the folded sheet to rotate with respect to the basal sheet. This HR-TEM image also shows a Moiré (interference) pattern with a spacing of approximately 1.05 nm.

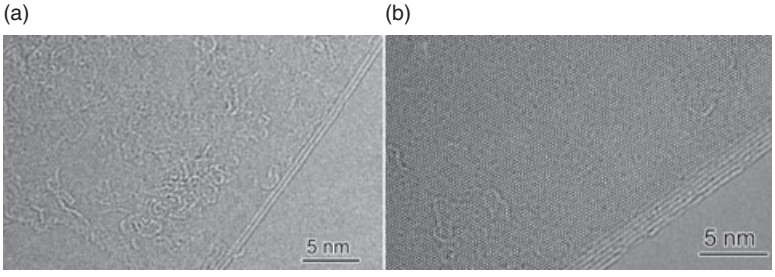

Figure 12.24 (a) High-resolution TEM image of a BN sheet with two layers; (b) High-resolution TEM image of a BN sheet with six layers with a Moiré pattern.

BN sheets can be generated with different numbers of layers, for example single, double and triple. The bandgap of a single-layer BN sheet was calculated, on a theoretical basis, as ~4.5 eV by local density approximation (LDA), and as 6.0 eV by a GW (a combination of the Green function G and the screened Coulomb interaction W) approximation (GWA) [133]. This finding signifies that a single-layer BN sheet retains the insulating feature of BN bulk.

12.6 Physical Properties of h-BN

Although h-BN and h-C have the same crystal structure, with very close cell parameters, their electronic properties are very distinct. The electronic properties of h-C can be metallic, semiconducting or semi-metallic, depending on dimensionality and size, whereas h-BN typically is an insulator for which the bandgap reportedly ranges from 5.3 to 5.9 eV, except for the band-gap narrowing seen in ultrathin nanotubes (diameter <0.8 nm) resulting from sp^3 (π) hybridization induced by high curvature [8, 134, 135]. Multiwalled BN exhibits a strong photoluminescence at room temperature, with a temporal analysis of the PL signals revealing an underlying charge recombination process dominated by fast recombination occurring within individual BN sheets. The slower decay process is attributed to the charge transfer and recombination across different BN sheets, and shows behavior that is consistent with the predicted spatially indirect band gap of multiwalled BNNTs [136]. The direct bandgap of both natural and isotopic BNNTs, which were prepared by a metal-assisted CVD methods [50, 51] and CNT-substitution reaction [14, 37], was determined from CL spectra to be 5.38 eV, independent of the nanotube's size and isotope substitution (Figure 12.25) [49, 137]. At lower energies, several radiative transitions were observed, and an isotope effect was revealed. In particular, it was confirmed that the rich CL spectra between 3.0 and 4.2 eV reflect

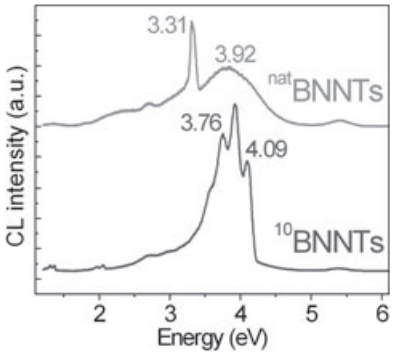

Figure 12.25 Cathodoluminescence spectra taken from thick natural BN and ^{10}BNNTs.

a phonon–electron coupling mechanism, which is characterized by a radiative transition at 4.09 eV. Both, FTIR spectra and DFT calculations suggest that those radiative transitions in BNNTs might be generated by the replacement of some nitrogen atoms with oxygen [49].

As BN materials display far better thermal, chemical and irradiation stabilities than their C counterparts, BN usage is preferable for device applications where a high-temperature environment or a chemically active and/or hazardous environment is expected [37, 138].

CNTs have shown excellent thermal conductivity; with both theoretical calculations and experimental results showing values comparable to those of BNNTs [139–142].

The stress of BNNT was measured as ~1.1–1.3 TPa; thus, BNNTs might be the stiffest insulating fibers known to date [143, 144]. Theory-based calculations have shown that, despite a slightly lower elastic modulus of a single-walled BNNT compared to a single-walled CNT, the resistance of the former to thermal degradation may surpass that of the latter [145].

12.7 Applications

h-BN has many novel advantageous physical properties, including electrical insulation, high thermal and chemical stabilities, high thermal conductivity and excellent mechanical properties, all of which lead to applications in many fields.

12.7.1 Pharmaceutical Table Lubricant

A wide range of lubricants is available for pharmaceutical applications, the most common tablet lubricants being magnesium stearate (MGST), stearic acid (STAC), glycerol esters of fatty acids, D,L leucine and sodium benzoate [146]. A solid oral dosage product must be processed with other excipients, such as 'lubricants', which reduce friction at the interface between a tablet's surface and the die wall during ejection. The aim is to reduce wear on the punches and dies, prevent sticking to the punch faces, and hence to improve the fluidity and filling properties and manufacturing efficiency of solid preparations [147]. An ideal lubricant should reduce both the shear strength at the interface between the tablet and die wall and the coefficient of friction and, in turn, the frictional force at a given load. Such a lubricant should be nontoxic, chemically inert, unaffected by process variables, have no adverse effects on the finished dosage form, and be consistent from batch to batch [148].

h-BN is an interesting compound with the potential of being incorporated as a lubricant into tablet formulations, since it is soft, lubricious, highly heat-stable and an inert material that will not react with other pharmaceutical excipients during

manufacture. h-BN is also considered safe as a 99.9% high-purity material. The first application of h-BN as a table lubricant was carried out by Turkoglu *et al*. in 2005 [149], who calculated the lowest punch ejection force (LPEF) by comparing control and lubricant-containing batches. When evaluated as a new tablet lubricant by comparing its properties with those of MGST, STAC and glyceryl behenate (COMP), h-BN was shown to be as effective as MGST in reducing the LPEF when used at 0.5–1%. As with all conventional lubricants, the higher the concentration of h-BN the lower the mechanical properties of the tablets, due to the hydrophobic character of h-BN [150]. The inclusion of h-BN had no significant effect on the tablet's properties, while a comparison of parameters such as effect on tablet disintegration time and crushing and tensile strengths showed h-BN to be superior to MGST. Taken together, these results showed that h-BN would be highly effective as a lubricant in this technology.

12.7.2 Cosmetic Materials

Cosmetic compositions usually contain components, such as metallic oxides, that confer opacity to the composition. These components may be excellent for evening-out skin tone, but may not be very flattering to certain types of skin. Furthermore, due to their tendency to accumulate in furrows, such components actually may emphasize deeper wrinkles and flaws rather than hide them. Previously, 'soft focus' types of powder were used in cosmetic compositions in an attempt to hide skin flaws; such materials are spherical powders that provide skin with light-scattering properties. Spherical silica, polyethylene or polymethylmethacrylate (PMMA) operate on the principle of diffusing the light which is incident on the face in such a way that the skin's overall appearance is blurred in the viewer's eye, thereby minimizing the ability to detect lines and wrinkles [151].

As BN is transparent, it has been used as a raw powder for cosmetics, primarily as a particulate material in very small quantities ranging from 0.1 to 70 wt%, depending on the type of cosmetic, such as eye-shadows, lipsticks, foundation make-up, powder, blushes, shampoos and conditioners. BN fillers and a host of other fillers have been used in cosmetic compositions, including spherical silica, PMMA, titanium dioxide, walnut shell powder, and mixtures thereof. These fillers may be surface-treated with lecithin, amino acids, mineral oil, silicone oil or various other agents, either alone or in combination, to coat the powder's surface, thus rendering the particles hydrophobic. BN also has been used in diverse cosmetic compositions, from providing sun protection, reducing the shine from oily skin, for cooling (due to its high thermal conductivity), and affording smoothness. The size of BN filler employed in the composition of the prior art ranges from 20 μm to submicrometer. The collapsibility of the spherical BN particles provides a cosmetic composition with an excellent luster. Submicron BN powder, in a formulation such as a foundation, surprisingly creates the illusion of a substantially flawless skin, by blurring the appearance of wrinkles and lines on the wearer's skin while also noticeably covering color blemishes, spots and defects [152].

12.7.3
^{10}BNNTs for Cancer Therapy and Diagnostics

The use of radiation therapy is well established in the treatment cancers, and generally involves the localized delivery of radiation to a tumor site. Radiation therapy relies on the free radical disruption of cellular DNA to destroy cancer cells in a targeted manner, and may derive either from a machine outside the body or from radioactive materials implanted in the body, close to the cancer cells. Systemic radiation therapy uses a radioactive substance (e.g., a radiolabeled monoclonal antibody) that circulates throughout the body, and thus entails the careful selection of a material containing a radioactive isotope capable of delivering the desired type and amount of radiation. Radioisotopes are also used widely in medical diagnostic. Boron neutron capture therapy (BNCT) is an experimental approach to cancer treatment that is based on a dual-step technique: (i) the accumulation of a boron-containing compound within a tumor; and (ii) subsequent exposure to a beam of low-energy neutrons directed at the boron-containing tumor. Subjecting boron atoms to low-energy neutron radiation causes the boron nuclei to disintegrate into alpha particles and lithium isotopes with a kinetic energy of 2.5 MeV; the energy generated in this way in malignant cells is sufficient to destroy them, but without damaging the neighboring cells. Buzatu *et al.* proposed the use of isotopic ^{10}BN nanostructures in BNCT, whereby antibody species are attached to the BN nanostructures to enable them to target tumors. When the BN nanostructure–antibody composite species approaches a tumor it can be activated with transdermal neutrons, so that the ^{10}B atoms emit alpha particles that will destroy cancerous cells [153].

12.7.4
BNNT Composites

Because of their exceptional morphological, electrical, thermal, mechanical and optical (transparent to visible and infrared light) properties, BNNTs may be used especially as reinforcement materials in composites with ceramics or polymer matrices. The key issues to address here include the good dispersion of the nanotubes, the control of the nanotube/matrix bonding, and the densification of bulk composites and thin films.

A barium calcium alumosilicate glass with a 4 wt% BNNT fraction was reinforced by 90% and 35% for ambient-temperature fracture strength and fracture toughness. A subsequent microscopic examination of the fracture surfaces revealed that BNNTs were responsible for these improvements [154]. Common engineering ceramics, such as Al_2O_3 and Si_3N_4, when loaded with 2.5–5.0 wt% BNNT fractions, both became much more deformable at high temperatures. For example, Al_2O_3 with 2.5 wt% BNNT demonstrated an approximately 4.5-fold lower yield stress and a higher true strain-to-fracture than the untreated ceramic; the parameters of high-temperature super-plasticity were also notably improved. By contrast, control experiments on BN micropowders added to these ceramics in the same proportions showed no analogous positive effects [155].

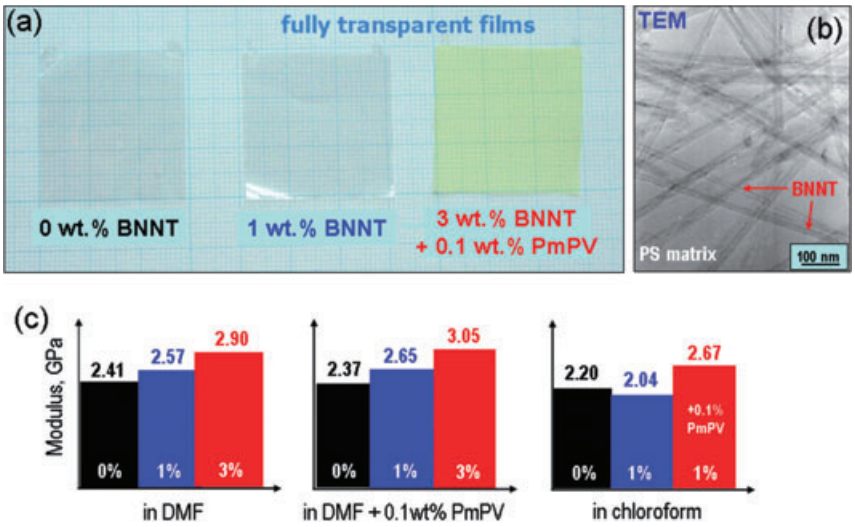

Figure 12.26 (a) Fully transparent polymeric films containing various fractions of BNNTs in polystyrene matrices; (b) TEM image of numerous straight BNNTs randomly and evenly dispersed in a polymer; (c) Histograms demonstrating an increase in the elastic modulus (under tensile tests) of polystyrene films after adding variable BNNT fractions dissolved in different solvents. Reproduced with permission from Ref. [155]; © 2006, Materials Research Society; 2007, Wiley-VCH.

Soluble BNNTs were obtained through noncovalent tube wrapping with a polymer or covalent functionalization. The availability of such solutions allowed investigators to prepare high-quality, self-organized BNNT-reinforced polymer films based on polyaniline [156] and polystyrene [157]. Tensile tests on these materials indicated that the elastic modulus of the films was improved by ca. 21% when only a 1 wt% soluble BNNT fraction was employed (see Figure 12.26). These BNNT composite films showed a better stability to oxidation and a slightly lowered glass transition temperature than the untreated polymers [155].

12.7.5 Gas Adsorption

Increasing concerns about energy and the environment call for a hydrogen economy that entails its safe and efficient production, transportation, conversion and storage [158, 159]. Recently, hydrogen storage has attracted much attention; gas adsorption is inherently safe and potentially more energy-efficient than the use of metal hydrides, compressed gas or liquid storage. However, the main challenge in this field is to identify materials with a reversible high hydrogen sorption capacity (the Department of the Environment's benchmark goal is 6 wt%) at ambient temperature and pressure. Previously, CNTs have been considered as promising materials for hydrogen storage. Although this potential is controversial,

and the adsorption mechanism in these carbon-related materials remains vague, it has been shown that the hydrogen storage capacity of CNTs correlates strongly with the surface accessible to hydrogen [159–161]. In many respects, BNNTs are analogous to CNTs since, because of their dissimilar local electronic structure, the B—N bond has an ionic character that may induce an extra dipole moment. Therefore, the stronger (de)hydriding properties of BN are expected to be better than those of graphite [162].

Wang *et al*. reported that nanostructured h-BN can absorb a concentration of hydrogen up to 2.6 wt% after mechanically milling h-BN powders for 80 h under a hydrogen pressure of 1.0 MPa. Furthermore, in addition to hydrogen desorption starting at about 570 K, nitrogen desorption also was detected at about 700 K; there was also no recrystallization, at least below 1173 K. Thus, nanostructured h-BN possesses the ability to trap (absorb) hydrogen during milling, and to desorb it at elevated temperatures. More importantly, its (de)hydriding properties depend not only on the defective nanostructure itself, but also on the local electronic structure near the specific defects. This information offers a constructive perspective for designing noncarbon materials for hydrogen storage [163].

BNNTs may absorb hydrogen at a level equal to, or even exceeding, that of CNTs. Multiwalled BNNTs [164] and nanofibers (with open-ended edge layers) [165] were found to adsorb 1.8–2.9 wt% hydrogen under approximately 10 MPa pressure at room temperature. Theoretically based studies have shown that BN may serve as an effective hydrogen-storage medium, as the binding energy of hydrogen on BNNTs is increased by up to 40% compared to that on CNTs, this effect being attributed to heteropolar bonding in BN [166]. The results of this study suggest that the binding energy of hydrogen can be systematically increased for sp^2-like bonding nanostructure materials by modifying the sp^2 bonding. It is possible that layered materials of ionic character (more ionic than BN), but with a moderate substitutional doping, might have a substantially large binding energy sufficient for the storage of hydrogen at room temperatures.

An increase in specific surface area (SSA) for BNNTs may represent a solution for increasing the operating temperature and capacity for hydrogen storage. The calculated binding energy of hydrogen on activated BNNTs (those with well-developed pore structures) was found to be as high as 22 kJ mol^{-1}, well within the correct range for room-temperature hydrogen storage. The most active pores for hydrogen binding were those terminated by oxygen atoms. Additional theory-based calculations by Wu *et al*. [167] showed that the adsorption energy and site can be modified by the radial deformation. When the deformation is small, H prefers to adsorb onto the boron atom, which creates an acceptor state in the gap; however, when the deformation is large enough the H is adsorbed preferentially onto the nitrogen atom in the high curvature region of the radially deformed BNNT, thus creating a donor state.

BNNTs prepared via the CVD method, using $LaNi_5$/B mixture and nickel powders, may be capable of storing hydrogen by an electrochemical method, although the storage capacity is low [168]. The hydrogen desorption of nonelectrochemical recombination in cyclic voltammograms, which is considered as the slow

reaction at BNNTs, suggests the possible existence of a strong chemisorption of hydrogen, and this may lead to the lower discharge capacity of BNNTs.

12.7.6
Electrical Nanoinsulators

The electric insulating feature of BNNTs offers a promising means of preparing electrically insulated nanocables with embedded metallic or semiconducting nanowires. Such cables might be utilized in downsized electrical devices and complex multicable circuits [74–93]. BNNTs also can enhance the field emission characteristics of filled semiconductors.

12.7.7
Ultraviolet Lasers and LEDs

GaN and related semiconductors have been used commercially to fabricate high-power and blue-light laser devices [169–171]. Demand is increasing for compact ultraviolet lasers with even shorter wavelengths, as they are essential in applications such as storage, photocatalysts, sterilization, ophthalmic surgery and nano-surgery. h-BN is a promising material for such devices because it has a direct bandgap in the ultraviolet region. Pure h-BN single-crystals, prepared using a high-pressure flux method, show a stable dominant luminescence peak and a series of s-like excitation absorption bands around 215 nm, proving this to be a direct-bandgap material [172]. The laser-emission spectrum for the BN single-crystal sample with well-cleaved surfaces reveals room-temperature ultraviolet lasing at 215 nm. The longitudinal mode is enhanced, even at a flux density of $0.2\,mA\,cm^{-2}$ and an electron-beam accelerating voltage of 20 kV. This signifies that the threshold power is lower than $4\,W\,cm^{-2}$, which is of the same order as for optical lasing for ZnO [173]. Kubota *et al.* developed a new synthetic route to prepare high-purity h-BN crystals at atmospheric pressure, using a nickel–molybdenum solvent. The h-BN crystals obtained in this way also emitted an intense 215 nm luminescence at room temperature [174].

12.7.8
BN as Support for Catalysts

The most popular materials used as supports for catalytically active phases include oxides, such as alumina, silica and mixture of silica–alumina. In order to improve stability and catalytically activity, other materials with high thermal conductivity and thermal stability might (tentatively) be employed as supports for catalytically active phases. Besides these features, BN has other attributes, such as a high surface area, and hydrophobic (thus preventing moisture condensation on its surface) and weak chemical support–active species interaction that might lead to it being a good catalyst. Wu *et al.* showed that porous BN-supported Pt Sn catalysts were highly efficient for the selective hydrogenation of α,β-unsaturated aldehyde

into unsaturated alcohol [175]. Although butyraldehyde and butanol in crotonaldehyde hydrogenation are favorable (based on the thermodynamic equilibrium), the product selectivity can be shifted towards crotyl alcohol by controlling the reaction kinetics on the Pt–Sn/BN catalyst. The yield of crotyl alcohol rose to 38% on Pt–Sn(0.75)/BN at 80 °C, while crotyl alcohol selectivity reached 80% at a conversion of 10% at ca. 40 °C. Pd-loaded porous BN was shown to be an effective catalyst that could be used under difficult conditions (e.g., methane oxidation or hydrocarbon cracking), without exhibiting any decrease in activity [176].

12.8 Concluding Remarks

h-BN has been the focus of much research for many decades, with BNNTs, porous BN and mono- and few-layer BNs having received a great deal of attention during recent years. Although, h-BN is less popular than its h-C counterpart, it exhibits certain advanced properties and promising applications, and consequently further efforts are warranted to realize its potential. Yet, this field faces many challenges, including the synthesis of pure single-walled BNNTs, well-aligned BNNTs, porous BNs with very high specific surface areas and separated monolayer BN sheets. Further explorations of the novel physical properties and new applications of these h-BN nanostructures should be encouraged.

Acknowledgments

The author is very grateful for support grants from the U.S. DOE under contract DE-AC02-98CH10886 and Laboratory Directed Research and Development Fund of Brookhaven National Laboratory, and thanks L.J. Wu, N. Bodzin and H.G. Yu for their help in providing the illustrations.

References

1 Sato, T. (1987) Studies on hexagonal and rhomobohedral layered boron nitrides: synthesis, crystal growth, and transformation under high pressure, Report of National Institute for Research in Inorganic Materials, Tsukuba, Japan.
2 Pouch, J.J. and Alterovitz, S.A. (1990) *Synthesis and properties of boron nitride*. Trans Tech Publications, Aedermannsdorf, Switzerland.
3 Balmain, W.H. (1842) *Journal für Praktische Chemie*, **27**, 422.
4 Meng, Y., Mao, H.-K., Eng, P.J., Trainor, T.P., Newville, M., Hu, M.Y., Kao, C., Shu, J., Hausermann, D. and Hemley, R.J. (2004) The formation of sp^3 bonding in compressed BN. *Nature Materials*, **3**, 111–14.
5 Zhang, W.J., Bello, I., Lifshitz, Y. and Lee, S.T. (2003) Recent advances in cubic boron nitride deposition. *MRS Bulletin/Materials Research Society*, 184–8.
6 Mirkarimi, P.B., McCarty, K.F. and Medlin, D.L. (1997) Review of advances in cubic boron nitride film synthesis.

Materials Science and Engineering, R, **21**, 47–100.
7 Iijima, S. (1991) Helical microtubules of graphitic carbon. *Nature*, **354**, 56–8.
8 Rubio, A., Corkill, J.L. and Cohen, M.L. (1994) Theory of graphitic boron-nitride nanotubes. *Physical Review B*, **49**, 5081–4.
9 Chopra, N.G., Luyken, R.J., Cherrey, K., Crespi, V.H., Cohen, M.L., Louie, S.G. and Zettl, A. (1995) Boron nitride nanotubes. *Science*, **269**, 966–7.
10 Ishii, T., Sato, T., Sekikawa, Y. and Iwata, M. (1981) Growth of whiskers of hexagonal boron nitride. *Journal of Crystal Growth*, **52**, 285–9.
11 Blasé, X., Rubio, A., Louie, S.G. and Cohen, M.L. (1994) Stability and band-gap constant of BN nitride nanotubes. *Europhysics Letters*, **28**, 335–40.
12 Stephan, O., Ajayan, P.M., Colliex, C., Redlich, P., Lanbert, J.M., Bernier, P. and Lefin, P. (1994) Doping graphite and carbon nanotubes structures with boron and nitrogen. *Science*, **266**, 1683–5.
13 Suenaga, K., Colliex, C., Demoncy, N., Loiseau, A., Pascard, H. and Willaime, F. (1997) Synthesis of nanoparticles and nanotubes with well-separated layers of boron nitride and carbon. *Science*, **278**, 653–5.
14 Han, W.Q., Cumings, J., Hunag, X., Bradley, K. and Zettl, A. (2001) Synthesis of aligned $B_xC_yN_z$ nanotubes by a substitution-reaction route. *Chemical Physics Letters*, **346**, 368–72.
15 Loiseau, A., Willaime, F., Demoncy, N., Hug, G. and Pascard, H. (1996) Boron nitride nanotubes with reduced numbers of layers synthesized by arc discharge. *Physical Review Letters*, **76**, 4737–40.
16 Golberg, D., Bando, Y., Eremets, M., Takemura, K., Kurashima, K. and Yusa, H. (1996) Nanotubes in boron nitride laser heated at high pressure. *Applied Physics Letters*, **69**, 2045–7.
17 Han, W.Q., Bando, Y., Kurashima, K. and Sato, T. (1998) Synthesis of boron nitride nanotubes from carbon nanotubes by a substitution reaction. *Applied Physics Letters*, **73**, 3085–7.
18 Louie, O., Jones, C.R., Bartlett, M., Gibbons, P.C., Ruoff, R.S. and Buhro, W.E. (2000) CVD growth of boron nitride nanotubes. *Chemistry of Materials*, **12**, 1808–10.
19 Chen, Y., Gerald, J., Williams, J. and Bulcock, S. (1999) Synthesis of boron nitride nanotubes at low temperature using reactive ball milling. *Chemical Physics Letters*, **299**, 260–4.
20 Xu, L., Peng, Y., Meng, Z., Yu, W., Zhang, S., Liu, X. and Qian, Y. (2003) A co-pyrolysis method to boron nitride nanotubes at relative low temperature. *Chemistry of Materials*, **15**, 2675–80.
21 Bechelany, M., Bernard, S., Brioude, A., Cornu, D., Stadelmann, P., Charcosset, C., Fiaty, K. and Miele, P. (2007) Synthesis of boron nitride nanotubes by a template-assisted polymer thermolysis process. *The Journal of Physical Chemistry C*, **111**, 13378–84.
22 Lee, C.M., Choi, S.I., Choi, S.S. and Hong, S.H. (2006) Synthesis of boron nitride nanotubes by arc-jet plasma. *Current Applied Physics*, **6**, 166–70.
23 Cumings, J. and Zettl, A. (2002) Mass-production of boron nitride double-wall nanotubes and Nanococoons. *Chemical Physics Letters*, **316**, 211–16.
24 Altoe, M.V.P., Sprunck, J.P., Gabriel, J.C.P. and Bradley, K. (2003) Nanococoon seeds for BN nanotube growth. *Journal of Materials Science*, **38**, 4805–10.
25 Terauchi, M., Tanaka, M., Matsumoto, T. and Saito, Y. (1998) Electron energy-loss spectroscopy study of the electronic structure of boron nitride nanotubes. *Journal of Electron Microscopy*, **47**, 319.
26 Narita, I. and Oku, T. (2003) Synthesis of boron nitride nanotubes by using NbB_2, YB_6 and YB_6/Ni powders. *Diamond and Related Materials*, **12**, 1912–17.
27 Terrones, M., Hsu, W.K., Terrones, H., Zhang, J.P., Ramosa, S., Hare, J.P., Castlllo, R., Prassldes, K., Cheetham, A.K., Kroto, H.W. and Walton, D.R.M. (1996) Metal particle catalysed production of nanoscale BN structures. *Chemical Physics Letters*, **259**, 568–73.
28 Yu, D.P., Sun, X., Lee, C., Bello, I., Lee, S., Gu, H., Leung, K., Zhou, G., Dong, Z. and Zhang, Z. (1998) Synthesis of boron nitride nanotubes by means of excimer

laser ablation at high temperature. *Applied Physics Letters*, **72**, 1966–8.
29 Lee, R.S., Gavillet, J., Lamy de la Chapelle, M., Loiseau, A., Loisau, A., Cochon, J.L., Pigache, D., Thibault, J. and Willaime, F. (2001) Catalyst-free synthesis of boron nitride single-wall nanotubes with a preferred zig-zag configuration. *Physical Review B*, **64**, 121405.
30 Laude, T., Matsui, Y., Marraud, A. and Jouffrey, B. (2000) Long ropes of boron nitride nanotubes grown by a continuous laser heating. *Applied Physics Letters*, **76**, 3239–41.
31 Arenal, R., Stephan, O., Cochon, J.L. and Loiseau, A. (2007) The root-growth mechanism for single-walled boron nitride nanotubes in laser vaporization technique. *Journal of the American Chemical Society*, **129**, 16183–9.
32 Cau, M., Dorval, N., Cao, B., Attal-Trétout, B., Cochon, J.L., Loiseau, A., Farhat, S. and Scott, C.D. (2006) Spatial evolutions of Co and Ni atoms during single-walled nanotubes formation: measurements and molding. *Journal of Nanoscience and Nanotechnology*, **6**, 1298–308.
33 Arenal, R., Stephan, O., Loiseau, A. and Colliex, C. (2007) Nanoscale bond mapping in complex nanostructures using EELS. *Microscopy and Microanalysis*, **179**, 1240.
34 Gavillet, J., Loiseau, A., Journet, C., Willaime, F., Ducastelle, F. and Charlier, J.C. (2001) Root-growth mechanism for single-walled carbon nanotubes. *Physical Review Letters*, **87**, 275504.
35 Wang, B.J., Kayastha, V.K., Yap, Y.K., Fan, Z., Lu, J.G., Pan, Z., Ivanov, I.N., Puretzky, A.A. and Geohegan, D. (2005) Low temperature growth of boron nitride nanotubes on substrates. *Nano Letters*, **5**, 2528–32.
36 Dai, H., Wong, E., Lu, Y., Fan, S. and Lieber, C.M. (1995) Synthesis and characterization of carbide nanorods. *Nature*, **375**, 769–1.
37 Han, W.Q., Fan, S., Li, Q. and Hu, Y. (1997) Synthesis of gallium nitride nanorods through a carbon nanotube-confined reaction. *Science*, **277**, 1287–9.
38 Golberg, D., Bando, Y., Kurashima, K. and Sato, T. (2000) Promoted synthesis of multi-walled BN nanotubes from C nanotube templates. *Chemical Physics Letters*, **323**, 185–91.
39 Han, W.Q., Mickelson, W., Cumings, J. and Zettl, A. (2002) Transformation of $B_xC_yN_z$ nanotubes to pure BN nanotubes. *Applied Physics Letters*, **81**, 1110–12.
40 Golberg, D., Bando, Y., Bourgeois, L., Kurashima, K. and Sato, T. (2000) Insights into the structure of BN nanotubes. *Applied Physics Letters*, **77**, 1979–81.
41 Han, W.Q., Bourgeois, L., Bando, Y., Kurashima, K. and Sato, T. (2000) Formation and structure of boron nitride conical nanotubes. *Applied Physics A*, **71**, 83–5.
42 Bourgeois, L., Bando, Y., Han, W.Q. and Sato, T. (2000) Structure of boron nitride nanoscale cones: order stacking of 240° and 300° disclinations. *Physical Review B*, **61**, 7686–9.
43 Xu, F.F., Banod, Y., Ma, R., Golberg, D., Li, Y. and Mitome, M. (2003) Formation, structure, and structural properties of a new filamentary tubular form: hollow conical-helix of graphitic boron nitride. *Journal of the American Chemical Society*, **125**, 8032–8.
44 Deepak, F.L., Vinod, C.P., Mukhopadhyay, K., Govindaraj, A. and Rao, C.N. (2002) Boron nitride nanotubes and nanowires. *Chemical Physics Letters*, **353**, 345–52.
45 Han, W.Q., Banado, Y., Kurashima, K. and Sato, T. (1999) Formation of BN fullerene- like nanoparticles and $(BN)_xC_y$ nanotubes by using carbon nanotubes as templates. *Japanese Journal of Applied Physics Part 2*, **38**, L755–7.
46 Bando, Y., Ogawak, K. and Golberg, D. (2001) Insulating 'nanocables' invar Fe-Ni alloy nanorods inside BN nanotubes. *Chemical Physics Letters*, **347**, 349–54.
47 Han, W.Q., Todd, P.J. and Strongin, M. (2006) Formation and growth mechanism of ^{10}BN nanotubes via a carbon nanotube-substitution reaction. *Applied Physics Letters*, **89**, 173103.
48 Yusuda, A., Kawase, N., Banhart, F., Mizutani, W., Shimizu, T. and Tokumoto, H. (2002) Graphitization

mechanism during the carbon-nanotube formation based on the in-situ HRTEM observation. *The Journal of Physical Chemistry B*, **106**, 1849.

49 Han, W.Q., Yu, H.G., Zhi, C., Wang, J., Liu, Z., Sekiguchi, T. and Bando, Y. (2008) Isotope effect on bandgap and radiative transitions properties of boron nitride nanotubes. *Nano Letters*, **8**, 491.

50 Tang, C., Bando, Y., Sato, T. and Kurashima, K. (2000) A novel precursors for synthesis of pure boron nitride nanotubes. *Chemical Communications*, 1290–1.

51 Zhi, C., Bando, Y., Tang, C. and Golberg, D. (2005) Effective precursor for high yield synthesis of pure BN nanotubes. *Solid State Communications*, **135**, 67–70.

52 Chang, C.W., Fennimore, A.M., Afanasiev, A., Okawa, D., Ikuno, T., Garcia, H., Li, D.Y., Majumdar, A. and Zettl, A. (2006) Isotope effect on the thermal conductivity of boron nitride nanotubes. *Physical Review Letters*, **97**, 085901.

53 Ma, R., Bando, Y., Sato, T. and Kurashima, K. (2001) Growth, morphology, and structure of BN nanotubes. *Chemistry of Materials*, **13**, 2965–71.

54 Ma, R., Bando, Y., Sato, T. and Kurashima, K. (2001) Thin boron nitride nanotubes with unusual large inner diameters. *Chemical Physics Letters*, **350**, 434–40.

55 Guo, L. and Singh, R.N. (2008) Selective growth of boron nitride nanotubes by plasma-enhanced chemical vapor deposition at low substrate temperature. *Nanotechnology*, **19**, 1–6.

56 Lin, F., Jus, C., Tang, T., Kang, P. and Yang, F. (2008) Thermal-heating CVD synthesis of BN nanotubes from trimethyl borate and nitrogen gas. *Materials Chemistry and Physics*, **107**, 115–21.

57 Chen, Y., Chadderton, L.T., Gerald, J.F. and Williams, J. (1999) A solid-state process for formation. *Applied Physics Letters*, **74**, 2960–2.

58 Fu, J.J., Lu, Y.N., Xu, H., Huo, K.F., Wang, X.Z., Li, L., Hu, Z. and Chen, Y. (2004) The synthesis of boron nitride nanotubes by an extended vapor-liquid-solid method. *Nanotechnology*, **15**, 727–30.

59 Yu, J., Chen, Y., Wuhrer, R., Liu, Z. and Ringer, S.P. (2005) In situ formation of BN nanotubes during nitriding reactions. *Chemistry of Materials*, **17**, 5172–6.

60 Yu, J., Cheng, Y., Elliman, R.G. and Petravic, M. (2006) Isotopically enriched ^{10}BN nanotubes. *Advanced Materials*, **18**, 2157–60.

61 Cao, L.M., Zhang, X.Y., Tian, H., Zhang, Z. and Wang, W.K. (2007) Boron nitride nanotube branched nanojunctions. *Nanotechnology*, **18**, 1–4.

62 Gan, Z., Ding, Z., Huang, Z., Huang, X., Cheng, C., Tang, C. and Qi, S. (2005) Growth of boron nitride nanotube film in situ. *Applied Physics A*, **81**, 527–9.

63 Oku, T., Koi, N., Suganuma, K., Belosludov, R.V. and Kawazoe, Y. (2007) Formation and atomic structure of boron nitride nanotubes with a cup-stacked structure. *Solid State Communications*, **143**, 331–6.

64 Koi, N., Oku, T., Inoue, M. and Suganuma, K. (2008) Structures and purification of boron nitride nanotubes synthesized from boron-based powders with iron particles. *Journal of Materials Science*, **43**, 2955–61.

65 Dai, J., Xu, L., Fang, Z., Sheng, D., Guo, Q., Ren, Z., Wang, K. and Qian, Y. (2007) A convenient catalytic approach to synthesize straight boron nitride nanotubes using synergic nitrogen source. *Chemical Physics Letters*, **440**, 253–8.

66 Chen, X., Wang, X., Liu, J., Wang, Z. and Qian, Y. (2005) A reduction-nitridation route to boron nitride nanotubes. *Applied Physics A*, **81**, 1035–7.

67 Dibandjo, P.F., Chassagneux, F., Bois, L., Sigala, C. and Miele, P. (2006) Synthesis of boron nitride with a cubic mesostructure. *Microporous and Mesoporous Materials*, **92**, 286–91.

68 Lindquist, D.A., Borek, T.T., Kramer, S.J., Narula, C.K., Johnston, G., Schaeffer, S., Smith, D.M. and Paine, R.T. (1990) Formational and pore structure of boron-nitride aerogels. *Journal of the American Ceramic Society*, **73**, 757–60.

69 Paine, R.T. and Narula, C.K. (1990) Synthesis routes to boron nitride. *Chemical Reviews*, **90**, 73–91.

70 Fazen, P.J., Beck, J.S., Lynch, A.T., Remsen, E.E. and Sneddon, L.G. (1990) Thermally induced borazine dehydropolymerization reactions synthesis and ceramic conversion reaction of a new high-yield polymeric precursor to boron nitride. *Chemistry of Materials*, **2**, 96–7.

71 Wang, Y.T., Shimada, S., Yamamoto, Y. and Miyaura, N. (2008) Preparation of h-BN nano-tubes, -bamboos, and -fibers from borazine oligomer with alumina porous template. *Materials Research Bulletin*, **43**, 251–6.

72 Shelimov, K.B. and Moskovits, M. (2000) Composite nanostructures based on template-crown boron nitride nanotubules. *Chemistry of Materials*, **12**, 250–4.

73 Wang, X.Z., Wu, Q., Hu, Z. and Chen, Y. (2007) Template-directed synthesis of boron nitride nanotubes arrays by microwave plasma chemical reaction. *Electrochimica Acta*, **52**, 2841–4.

74 Han, W.Q., Redlich, P., Ernst, F. and Rühle, M. (1999) Synthesizing boron nitride nanotubes filled with SiC nanowires by using carbon nanotubes as templates. *Applied Physics Letters*, **75**, 1875–7.

75 Han, W.Q., Redlich, P., Ernst, F. and Rühle, M. (1999) Formation of $(BN)_xC_y$ and BN nanotubes filled with boron carbide nanowires. *Chemistry of Materials*, **11**, 3620–3.

76 Xu, F.F., Bando, Y., Golberg, D., Hasegawa, M. and Mitome, M. (2004) Phase and crystallization of encapsulated cobalt nanorods inside BN nanotubes. *Acta Materialia*, **52**, 601–3.

77 Golberg, D., Bando, Y., Fushimi, K., Mitome, M., Bourgeois, L. and Tang, C. (2003) Nanoscale oxygen generators: MgO_2-based fillings of BN nanotubes. *The Journal of Physical Chemistry B*, **107**, 8726–9.

78 Chen, Z.G., Zou, J., Li, F., Liu, G., Tang, D.M., Li, D., Liu, C., Ma, X., Cheng, H.M., Liu, G.Q. and Zhang, Z. (2007) Growth of magnetic yard-glass shaped boron nitride nanotubes with periodic iron nanoparticles. *Advanced Functional Materials*, **17**, 3371–6.

79 Yin, L., Bando, Y., Zhu, Y., Golberg, D. and Li, M. (2004) A two-stage route to coaxial cubic-aluminum-nitride-boron nitride composite nanotubes. *Advanced Materials*, **16**, 929–33.

80 Han, W.Q. and Zettl, A. (2002) GaN nanorods coated with pure BN. *Applied Physics Letters*, **81**, 5051–3.

81 Zhang, J., Zhang, L., Jiang, F. and Dai, Z. (2004) Intensive blue-light emission from semiconductor GaN nanowires sheathed with BN layers. *Chemical Physics Letters*, **383**, 423–7.

82 Seo, H., Bae, S., Park, J., Yang, H. and Kim, B. (2003) Direct synthesis of gallium nitride nanowires coated with boron carbon nitride layers. *The Journal of Physical Chemistry B*, **107**, 6739–42.

83 Tang, C., Bando, Y., Sato, T. and Kurashima, K. (2002) Comparative studies on BN-coating on SiC and Si_3N_4 nanowires. *Journal of Materials Chemistry*, **12**, 1910–13.

84 Tang, C., Bando, Y., Golberg, D., Mitome, M., Ding, X. and Qi, S. (2004) Facile nanocoating method: from B-doped to BN coated one-dimensional nanostructures. *Applied Physics Letters*, **85**, 106–8.

85 Zhu, Y., Bando, Y., Xue, D., Xu, F. and Golberg, D. (2003) Insulating tubular BN sheeting on semiconducting nanowires. *Journal of the American Chemical Society*, **125**, 14226–7.

86 Zhu, Y., Bando, Y. and Yin, L. (2004) Design and fabrication of BN-sheathed ZnS. *Nanoarchitectures. Advanced Materials*, **16**, 331–4.

87 Zhu, Y., Bando, Y. and Ma, R. (2003) Aluminum borate-boron nitride nanocables. *Advanced Materials*, **15**, 1377–9.

88 Li, Y., Dorozhkin, P., Bando, Y. and Golberg, D. (2005) Controllable modification of SiC nanowires encapsulated in BN nanotubes. *Advanced Materials*, **17**, 545–9.

89 Tang, C., Bando, Y., Sato, T., Kurashima, K., Ding, X., Gan, Z. and Qi, S. (2002) SiC and its bicrystalline nanowires with uniform BN coatings. *Applied Physics Letters*, **80**, 4641–3.

90 Shen, Z., He, L., Wu, E., Fan, Y., He, H., Cheng, H., Li, D. and Ye, H. (2002) Boron nitride filled with zirconium oxide. *Journal of Materials Research*, **17**, 2761–4.

91 Han, W.Q., Chang, C.W. and Zettl, A. (2004) Encapsulation of one-dimensional potassium halides crystals within BN nanotubes. *Nano Letters*, **4**, 1355–7.

92 Han, W.Q. and Zettl, A. (2004) Nanocrystal cleaving. *Applied Physics Letters*, **84**, 2644–5.

93 Mickelson, W., Aloni, S., Han, W.Q., Cumings, J. and Zettl, A. (2003) Packing C_{60} in boron nitride nanotubes. *Science*, **300**, 467–9.

94 Sun, Y.P., Fu, K., Lin, Y. and Hunag, W. (2002) Functionalized carbon nanotubes: properties and applications. *Accounts of Chemical Research*, **35**, 1095–104.

95 Chen, J., Hamon, M.A., Hui, H., Chen, Y., Rao, A.M., Eklund, P.C. and Haddon, R.C. (1998) Solution properties of single-walled carbon nanotubes. *Science*, **282**, 95–8.

96 Fu, K., Huang, W., Lin, Y., Riddle, L.A., Carroll, D.L. and Sun, Y.P. (2001) Defunctionalization of functionalized carbon nanotubes. *Nano Letters*, **1**, 439–41.

97 Khabashesku, V.N., Billups, W.E. and Margrave, J.L. (2002) Fluorination of single-wall carbon nanotubes and subsequent derivatization reaction. *Accounts of Chemical Research*, **35**, 188–94.

98 Han, W.Q. and Zettl, A. (2003) Functionalized boron nitride nanotubes with a stannic oxide coating: a novel chemical route to full coverage. *Journal of the American Chemical Society*, **125**, 2062–3.

99 Xie, S.Y., Wang, W., Fernando, K.A.S., Wang, X., Lin, Y. and Sun, Y.P. (2005) Solubilization of boron nitride nanotubes. *Chemical Communications*, 3670–2.

100 Zhi, C.Y., Bando, Y., Tang, C.C., Honda, S., Sato, K., Kuwahara, H. and Golberg, D. (2005) Covalent Functionalization: Towards soluble multiwalled boron nitride nanotubes. *Angewandte Chemie – International Edition*, **44**, 7932–5.

101 Wu, X.J., An, W. and Zheng, X.C. (2006) Chemical functionalization of boron-nitride nanotubes with NH_3 and amino functional groups. *Journal of the American Chemical Society*, **128**, 12001–6.

102 Pal, S., Vivekchand, S.R.C., Govindaraj, A. and Rao, C.N.R. (2007) Functionalization and solubilization of BN nanotubes by interaction with Lewis bases. *Journal of Materials Chemistry*, **17**, 450–2.

103 Ikuno, T., Sainsbury, T., Okawa, D., Frechet, J.M.J. and Zettl, A. (2007) Amine-functionalized boron nitride nanotubes. *Solid State Communications*, **142**, 643–6.

104 Zhi, C.Y., Bando, Y., Tang, C., Xie, R., Sekiguchi, T. and Golberg, D. (2005) Perfectly dissolved boron nitride nanotubes due to polymer wrapping. *Journal of the American Chemical Society*, **127**, 15996–7.

105 Zhi, C.Y., Bando, Y., Tang, C. and Golberg, D. (2006) Purification of boron nitride nanotubes through polymer wrapping. *The Journal of Physical Chemistry B*, **110**, 1525.

106 Zhi, C.Y., Bando, Y., Tang, C. and Golberg, D. (2006) Engineering of electronic structure of boron-nitride nanotubes by covalent functionalization. *Physical Review B*, **74**, 153–413.

107 Zhi, C., Bando, Y., Tang, C. and Golberg, D. (2005) Immobilization of proteins on boron nitride nanotubes. *Journal of the American Chemical Society*, **127**, 17144–5.

108 Joo, S.H., Choi, S.J., Oh, L., Kwak, J., Liu, Z., Terasaki, O. and Ryoo, R. (2001) Ordered nanoporous arrays of carbon supporting high dispersion of platinum nanoparticles. *Nature*, **412**, 169–72.

109 Bansal, R.C., Donnet, J. and Stoeckli, F. (1988) *Active Carbons*, Marcel Dekker, Inc., New York, Basel.

110 Narula, C.K., Schaeffer, R., Paine, R.T., Datye, A. and Hammetter, W.F. (1987) Synthesis of boron-nitride ceramics from poly(borazinylamine) precursors. *Journal of the American Chemical Society*, **109**, 5556–7.

111 Janik, J.F., Ackerman, W.C., Paine, R.T., Hua, D.W., Maskara, A. and Smith, D.M.

(1994) Boron nitride as a selective gas adsorbent. *Langmuir*, **10**, 514–18.
112 Narula, C.K., Schaeffer, R., Datye, A.K., Borek, T.T., Rapko, B.M. and Paine, R.T. (1990) Synthesis of boron-nitride ceramics from oligomeric precursors derived from 2-(dimethylamino)-4,6-dichloroborazine. *Chemistry of Materials*, **2**, 384–9.
113 Narula, C.K., Lindquist, D.A., Fan, M.M., Borek, T.T., Duesler, E.N., Datye, A.K., Schaeffer, R. and Paine, R.T. (1990) Models and polyborazine precursors for boron-nitride ceramics. *Chemistry of Materials*, **2**, 377–84.
114 Dibandjo, P., Bois, L., Chassagneux, F., Cornu, D., Toury, B., Babonneau, F. and Miele, P. (2005) Synthesis of boron nitride with ordered mesostructures. *Advanced Materials*, **17**, 571–3.
115 Dibandjo, P., Chassagneux, F., Bois, L., Sigala, C. and Miele, P. (2005) Comparison between SBA-15 silica and CMK-3 carbon nanocasting for mesoporous boron nitride synthesis. *Journal of Materials Chemistry*, **15**, 1917–23.
116 Han, W.Q., Brutchey, R., Tilley, T.D. and Zettl, A. (2004) Activated boron nitride derived from activated carbon. *Nano Letters*, **4**, 173–6.
117 Terrones, M., Charlier, J.C., Gloter, A., Cruz-Silva, E., Terres, E., Li, Y.B., Vinu, A., Zanolli, Z., Dominguez, J.M., Terrones, H., Bando, Y. and Golberg, D. (2008) Experimental and theoretical studies suggesting the possibility of metallic boron nitride edges in porous nanourchins. *Nano Letters*, **8**, 1026–32.
118 Corso, M., Auwärter, W., Muntwiler, M., Tamai, A., Greber, T. and Osterwalder, J. (2004) Boron nitride nanomesh. *Science*, **303**, 217–20.
119 Novoselov, K.S., Geim, A.K., Morozov, S.V., Dubonos, S.V., Zhang, Y. and Jiang, D. (2004) Electric field effect in atomically thin carbon films. *Science*, **306**, 666–9.
120 Novoselov, K.S., Geim, A.K., Morozov, S.V., Dubonos, S.V., Zhang, Y. and Jiang, D. (2005) Two-dimensional gas of massless Dirac fermions in graphene. *Nature*, **438**, 197–200.
121 Zhang, Y.B., Tan, Y.W., Stormer, H.L. and Kim, P. (2005) Experimental observation of the quantum Hall effect and Berry's phase in graphene. *Nature*, **438**, 201–4.
122 Son, Y.W., Cohen, M.L. and Louie, S. (2006) Half-metallic graphene nanoribbons. *Nature*, **444**, 347–9.
123 Nagashima, A., Tejima, N., Gamou, Y., Kawai, T. and Oshima, C. (1995) Electronic-structure of monolayer hexagonal boron-nitride physisorbed on metal surfaces. *Physical Review Letters*, **75**, 3918–21.
124 Rokuta, E., Hasegawa, Y., Suzuki, K., Gamou, Y., Oshima, C. and Nagashima, A. (1997) Phonon dispersion of an epitaxial monolayer film of hexagonal boron nitride on Ni(111). *Physical Review Letters*, **79**, 4609–12.
125 He, J.W. and Goodman, D.W. (1990) Interaction of borazine with a Re (0001) surface study by LEED, TDS, AES and ELS. *Surface Science*, **232**, 138–48.
126 Paffett, M.T., Simonson, R.J., Papin, P. and Paine, R.T. (1990) Borazine adsorption and decomposition at Pt (111) and Ru (001) surface. *Surface Science*, **232**, 286–96.
127 Desrosiers, R.M., Greve, D.W. and Gellman, A.J. (1997) Nucleation of boron nitride thin films on Ni (100). *Surface Science*, **382**, 35–48.
128 Nagashima, A., Tejima, N., Gamou, Y., Kawai, T., Terai, M. and Oshima, C. (1995) Electronic dispersion-relations of monolayer hexagonal boron-nitride formed on the Ni (111) surface. *Physical Review B*, **51**, 4606–13.
129 Nagashima, A., Tejima, N., Gamou, Y., Kawai, T. and Oshima, C. (1996) Electronic states of monolayer hexagonal boron nitride formed on the metal surfaces. *Surface Science*, **358**, 307–11.
130 Auwärter, W., Kreutz, T.J. and Greber, T. (1999) XPD and STM investigation of hexagonal boron nitride on Ni (111). *Surface Science*, **429**, 229–36.
131 Novoselov, K.S., Jiang, D., Schedin, F., Booth, T.J., Khotkevich, V.V., Morozov, S.V. and Geim, A.K. (2005) Two-dimensional atomic crystals. *Proceedings of the National Academy of Sciences of the United States of America*, **102**, 10451–3.

132 Pacilie, D., Meyer, J.C., Girit, C.O. and Zettl, A. (2008) The two-dimensional phase of boron nitride: few-atomic-layer sheets and suspended membranes. *Applied Physics Letters*, **92**, 133107.

133 Terrones, M., Romo-Herrera, J.M., Cruz-Silva, E., Lopez-Urias, F., Munoz-Sandoval, E., Velazquez, J.J., Terrones, H., Bando, Y. and Golberg, D. (2007) Pure and doped boron nitride nanotubes. *Materials Today*, **10**, 30.

134 Radosavljevic, M., Appenzeller, J., Derycke, V., Martel, R. and Avouris, P. (2003) Electrical properties and transport in boron nitride nanotubes. *Applied Physics Letters*, **82**, 4131–3.

135 Bai, X., Golberg, D., Bando, Y., Zhi, C., Tang, C., Mitome, M. and Kurashima, K. (2007) Deformation-driven electrical transport of individual boron nitride nanotubes. *Nano Letters*, **7**, 632–7.

136 Wu, J.Q., Han, W.Q., Walukiewicz, W., Ager, J.W., III, Shan, W., Haller, E.E. and Zettl, A. (2004) Raman spectroscopy and time-resolved photoluminescence of BN and $B_xC_yN_z$ nanotubes. *Nano Letters*, **4**, 467–71.

137 Zhi, C., Bando, Y., Tang, C., Golberg, D., Xie, R. and Sekigushi, T. (2005) Phonon characteristics and cathodoluminescence of boron nitride nanotubes. *Applied Physics Letters*, **86**, 213100.

138 Morelli, D.T., Heremans, J.P. and Slack, G.A. (2002) Estimation of the isotope effect on the lattice thermal conductivity of group IV and group III-V semiconductors. *Physical Review B*, **66**, 195304.

139 Chang, C.W., Han, W.Q. and Zettl, A. (2005) Thermal conductivity of B-C-N and BN nanotubes. *Applied Physics Letters*, **86**, 173102.

140 Chang, C.W., Han, W.Q. and Zettl, A. (2005) Thermal conductivity of B-C-N and BN nanotubes. *Journal of Vacuum Science Technology B*, **23**, 1883–6.

141 Chang, C.W., Okawa, D., Garcia, H., Majundar, A. and Zettl, A. (2007) Nanotube phonon waveguide, A. *Zettl. Physical Review Letters*, **97**, 045901.

142 Zettl, A., Chang, C.W. and Begtrup, G. (2007) A new look at thermal properties of nanotubes. *Physica Status Solidi*, **244**, 4181–3.

143 Chopra, N.G. and Zettl, A. (1998) Measurement of the elastic modulus of a multi-wall boron nitride nanotube. *Solid State Communications*, **105**, 297–300.

144 Golberg, D., Bai, X.D., Mitome, M., Tang, C.C., Zhi, C.Y. and Bando, Y. (2007) Structural peculiarities of in situ deformation of a multi-walled BN nanotube inside a high-resolution analytical transmission electron microscope. *Acta Materialia*, **55**, 1293–8.

145 Dumitrica, T., Bettinger, H.F., Scuseria, G. and Yakobson, B.I. (2003) Thermodynamics of yield in boron nitride nanotubes. *Physical Review B*, **68**, 085412.

146 Baraton, M.I., Merle, T., Quintard, P. and Lorenzelli, V. (1993) Surface activity of a boron nitride powder: a vibrational study. *Langmuir*, **9**, 1486–91.

147 Aoshima, H., Miyagisnima, A., Nozawa, Y., Sadzuka, Y. and Sonobe, T. (2005) Glycerin fatty acid esters as a new lubricant of tablets. *International Journal of Pharmaceutics*, **293**, 25–34.

148 Miller, T.A. and York, P. (1988) Pharmaceutical tablet lubrication. *International Journal of Pharmaceutics*, **41**, 1–19.

149 Turkoglu, M., Sahin, I. and San, T. (2005) Evaluation of hexagonal boron nitride as a new tablet lubricant. *Pharmaceutical Development and Technology*, **10**, 381–8.

150 Uğurlu, T. and Turkğlu, M. (2008) Hexagonal boron nitride as a tablet lubricant and a comparison with conventional lubricants. *International Journal of Pharmaceutics*, **353**, 45–51.

151 Arraudeau, J.P., Mellul, M. and Candau, D. (2003) Cosmetic composition capable of blurring skin defects. US Patent No. 5,223,559.

152 Butts, M., Sinha, M., Genovese, S.E. and Yamada, M. Cosmetic compositions comprising sub-micron boron nitride particles. US Patent Application #: 20070207101.

153 Buzatu, D.A., Wilkes, J.G., Miller, D., Darsey, J.A., Heinze, T., Biris, A., Berger, R. and Diggs, M. Nanotubes for cancer therapy and diagnostics. US Patent Application #: 20060067939.

154 Bansal, N.P., Hurst, J.B. and Choi, S.R. (2006) Boron nitride nanotubes-reinforced glass composites. *Journal of the American Ceramic Society*, **89**, 388–90.

155 Golberg, D., Bando, Y., Tang, C. and Zhi, C. (2007) Boron nitride nanotubes. *Advanced Materials*, **19**, 2413–32.

156 Zhi, C.Y., Bando, Y., Tang, C., Hond, S., Sato, K., Kuwahara, H. and Golberg, D. (2005) Characteristics of boron nitride nanotube-polyaniline composites. *Angewandte Chemie–International Edition*, **44**, 7929–32.

157 Zhi, C.Y., Bando, Y., Tang, C., Honda, S., Kuwahara, H. and Golberg, D. (2006) Boron nitride nanotubes/polystyrene. *Journal of Materials Research*, **21**, 2794–800.

158 Department of the Environment (2005) Roadmap on manufacturing for the hydrogen economy.

159 Schlapbach, L. and Züttel, A. (2001) Hydrogen-storage materials for mobile applications. *Nature*, **414**, 353–8.

160 Dillon, A.C., Jones, K.M., Bekkedahl, T.A., Klang, C.H., Bethune, D.S. and Heben, M.J. (1997) *Nature*, **386**, 377–9.

161 Hirscher, M., Becher, M., Haluska, M., Dettlaff-Weglikowska, U., Quintel, A., Duesberg, G.S., Choi, Y.M., Downes, P., Hulman, M., Roth, S., Stepanek, I. and Bernier, P. (2001) Hydrogen storage in sonicated carbon materials. *Applied Physics A*, **72**, 129–32.

162 Catellani, A., Posternak, M., Baldereschi, A. and Freeman, A.J. (1987) Bulk and surface electronic-structure of hexagonal boron-nitride. *Physical Review B*, **36**, 6105–11.

163 Wang, P., Orimo, S., Matsushima, T., Fujii, H. and Majer, G. (2002) Hydrogen in mechanically prepared nanostructured h-BN: a critical comparison with that in nanostructured graphite. *Applied Physics Letters*, **80**, 318–20.

164 Ma, R.Z., Bando, Y., Zhu, H.W., Sato, T., Xu, C.L. and Wu, D.H. (2002) Hydrogen uptake in boron nitride nanotubes at room temperature. *Journal of the American Chemical Society*, **124**, 7672–3.

165 Ma, R., Bando, Y., Sato, T., Golberg, D., Zhu, H., Xu, C. and Wu, D. (2002) Synthesis of boron nitride nanofibers and measurement of their hydrogen uptake capacity. *Applied Physics Letters*, **81**, 5225–7.

166 Hji, S. and Kwon, Y. (2004) Hydrogen adsorption on boron nitride nanotubes: a path to room temperature hydrogen storage. *Physical Review B*, **69**, 245407.

167 Wu, X., Yang, J., Hou, J. and Zhu, Q. (2004) Deformation-induced site selectivity for hydrogen adsorption on boron nitride nanotubes. *Physical Review B*, **69**, 153411.

168 Chen, X., Gao, X.P., Zhang, H., Zhou, Z., Hu, W.K., Pan, G.L., Zhu, H.Y., Yan, T.Y. and Song, D.Y. (2005) preparation and electrochemical hydrogen storage of boron nitride nanotubes. *The Journal of Physical Chemistry B*, **109**, 11525–9.

169 Nakamura, S. and Fasol, G. (1997) *The Blue Laser Diode*, Springer, New York.

170 Pankove, J. and Moustakas, T. (1998) *Gallium Nitride (GaN), Semiconductors and Semimetals*, Vol. **50**, Academic Press, San Diego.

171 Taniyasu, T., Kasu, M. and Makimoto, T. (2006) An aluminum nitride light-emitting diode with a wavelength of 210 nanometers. *Nature*, **441**, 325–8.

172 Watanaba, K., Taniguchi, T. and Kanda, H. (2004) Direct-bandgap properties and evidence for ultraviolet lasing of hexagonal boron nitride single crystal. *Nature Materials*, **3**, 404–9.

173 Reynolds, D.C., Look, D.C. and Jogai, B. (1996) Optically pumped ultraviolet lasing from ZnO. *Solid State Communications*, **99**, 873–5.

174 Kubota, Y., Watanaba, K., Tsuda, O. and Taniguchi, T. (2007) Deep ultraviolet light-emitting hexagonal boron nitride synthesized at atmospheric pressure. *Science*, **317**, 932–4.

175 Wu, J.C.S. and Chen, W.C. (2005) A novel BN supported bi-metal catalyst for selective hydrogenation of crotonaldehyde. *Applied Catalysis A: General*, **289**, 179–85.

176 Postole, G., Caldararu, M., Ionescu, N.I., Bonnetot, B., Auroux, A. and Guimon, C. (2005) Boron nitride: a high potential support for combustion catalysts. *Thermochimica Acta*, **434**, 150–7.

Keywords

boron nitride; nanotubes; porous; monolayer; growth mechanism; functionalization; filling; applications.

13
Spherical and Anisotropic Boron Nitride Nanomaterials: Synthesis and Characterization

Chengchun Tang and Yangxian Li

13.1
Introduction

Boron nitride (BN), a well-known and widely used nonoxide ceramic material, is known to exist as hexagonal (h-), rhombohedral (r-) and cubic (c-) crystalline structures, although some reports have also been made of other polymorphs [1]. h-BN has a graphite-type structure in which the planar networks are stacked regularly as a ABABAB double-layer sequence, while r-BN is arranged as a ABCABC three-layer ordering. The increasing number of technological applications of BN generally utilize the materials' excellent properties, that include chemical inertness, a high melting point, low density, a high thermal conductivity, high electrical insulation, high oxidation resistance at high temperatures and optical transparency [2]. When applied to the life sciences, h-BN powder has been used in the cosmetic industry, mainly because it does not absorb moisture from the skin and so can maintain the skin surface in a natural condition.

Recent studies in our laboratory have focused on the development of new morphologies, structures, properties and applications for BN materials with dimensions down to the nanometer scale, mainly because nanomaterials have become a focal point of a growing scientific community, on the basis of their interesting properties and potential applications. The initial interest in BN nanomaterials was stimulated by the discovery of C_{60} and fullerenes during the mid 1980s, and of carbon nanotubes (CNTs) in 1991 [3, 4]. Indeed, many investigations of BN nanomaterials followed the discovery of carbon nanomaterials. In view of the structural similarity of graphite and bulk h-BN, it is normal to discuss the formation mechanisms, properties and applications of BN nanomaterials in terms of carbon nanomaterial models. However, BN nanomaterials exhibit physical and chemical properties that are clearly different to those of their carbon counterparts. For example, the electronic structure of a pure CNT is known to be either metallic or semiconducting, depending on the tube diameter, wrapping angle, twisting and topological defects [5]. In contrast, BN nanotubes exhibit a wide band gap of about 5 eV that is insensitive to tube diameter and chirality, but can be controlled by the

Nanomaterials for the Life Sciences Vol. 3: Mixed Metal Nanomaterials. Edited by Challa S. S. R. Kumar

ISBN: 978-3-527-32153-7

chemical composition [6]. Such differences between these materials have formed the basis for the intensive studies conducted with BN nanomaterials over the past two decades.

In this chapter we provide a state-of-the-art review on the preparation, characterization, properties and prospective applications of BN nanomaterials. It should be noted that information relating to areas such as doped and functionalized BN nanomaterials can be found elsewhere [7].

13.2
BN Nanomaterials Synthesis

13.2.1
Spherical BN Particles

BN particles with a spherical morphology were observed microscopically for the first time by Paine and coworkers in 1991 [8], although the formation of spherical BN particles by a low-temperature chemical vapor deposition (CVD) reaction of BCl_3 and ammonia had been claimed earlier in a patent in 1990 [9]. Paine *et al.* were the first to synthesize a micrometer-sized aerosol droplet of a liquid ammonia solution of poly(borazinylamine) by using an aerosol generator [10]. When the droplet was then thermally decomposed in a flow reactor at 1000 °C, the powder obtained was white in color and consisted of submicrometer spherical particles and a small proportion of irregular fragments. These spherical particles were shown to be amorphous on X-ray diffraction (XRD) analysis and also isotropic, with sizes on the order of 500 nm. A small fraction of the larger spheres were hollow with a brittle shell. Further crystallization by calcination up to 1700 °C resulted in the isotropic particles being damaged, but the spherical particles retained their morphology, with the initially smooth surface becoming gradually more coarse. This spherical morphology had not been found in any previous studies using the same polymer precursor of BN reported by the same group, when 'normal' CVD or chemical reduction processes were adopted [11]. It was considered, therefore, that the aerosol treatment strategy was responsible for such special morphology formation.

h-BN, in its most common hexagonal structure, possesses a strong anisotropic characterization, not only in terms of its physical properties but also in its crystal growth. The most common synthetic route normally results in anisotropic growth, and so cannot be used to form the isotropic spherical morphology. Although the latter morphology should have a direct influence on the anisotropic physical properties of the typical BN crystal, very few studies have been reported on the preparation and characterization of these spherical aggregations since the first discovery of the spherical particles. A spherical morphology has been found occasionally, however, among various reports, when clearly attention had not been paid to the subject of morphology control. Sato and coworkers [12] carried out a microstructural study to evaluate the relationship between BN crystalline structure and its

morphology. For this, they synthesized columnar BN particles (that possessed no three-dimensional order) at 900 °C by using melamine diborate as a pyrolysis precursor. When heat-treated at a temperature in excess of 1700 °C, the BN could be converted to a well-crystallized h-BN or r-BN, with plate-like morphologies. Surprisingly, during the crystallographic transformation a spherical morphology was observed at the intermediate heat-treatment temperature of 1600 °C, which led the authors to speculate that a partially ordered structure was responsible for formation of the spherical BN powder.

A number of specially designed methods have also been investigated for the control of morphology. Paine and coworkers further described an aerosol-assisted vapor synthetic route for spherical particle formation, but using the different reaction precursors [13–15]. Here, the vapor was generated with a piezoelectric transducer, which imparts energy to overcome the surface tension of the liquid reagent or its solution. When swept rapidly over a high-temperature reaction area in the presence of ammonia, the vapor very quickly solidified and retained a spherical morphology within the reactant droplets.

The reaction of boric acid droplets generated from a H_3BO_3/water solution with ammonia first produced smooth, featureless spherical BN particles with amorphous or turbostratic structures [13]. (here, the term turbostratic was used to describe an imperfect BN structure without three-dimensional ordering [16]). The following equation represents a conceptual description of the reaction in the presence of water:

$$B(OH)_3\,(\text{droplet}) + NH_3 \rightarrow BN\,(\text{solidified sphere}) + 3\ H_2O$$

While the reaction was conducted at temperatures ranging from 600 to 1200 °C, the product could not be crystallized. Rather, the crystallization of hexagonal BN typically requires a temperature in excess of 1600 °C. The crystallized BN spheres can be obtained by further annealing the as-prepared product in an ammonia atmosphere at >1000 °C. It should be noted that the chemical composition analyses showed a notable abundance of oxygen, in both amorphous and crystallized structures, up to 27 at% even at a reaction temperature of 1000 °C. This was consistent with the growth mechanism proposed by the authors, in which spherical particles resulted from the surface reaction of ammonia on initially generated BO-containing particles. Clearly, the BO particles initially generated via the mechanical method struggled to form a uniform diameter, it having been observed that the BN spheres had a relatively wide distribution of diameter, ranging from 0.5 to 500 μm. The surface area was also disappointingly low, with values of approximately $1\,m^2g^{-1}$ for the as-prepared spheres and $5.4\,m^2g^{-1}$ after annealing at 1700 °C.

Wood and Paine [14] also examined the aerosol-assisted thermal decomposition of guanidinium tetraborate, pentaborate and nonaborate in the presence of ammonia. These pyrolyses produced micrometer- or submicrometer-sized spherical particles with a high oxygen content, although the subsequent ammonothermal reaction reduced the oxygen contents to <1% [15]. The diameter of the spherical

BN particles should depend on the precursor chemistry; for example, the pyrolysis of guanidinium tetraborate led to the formation of submicrometer-sized, but nonuniform, spheres.

Two years later, following the reporting of an aerosol-assisted synthesis using boric acid droplets, we described an alternative route for the synthesis of spherical BN particles with uniform diameters ranging from 50 to 400 nm, by using a two-step synthetic process [17]. The spherical B—N—O precursor was first synthesized at 700 °C via a CVD reaction of trimethoxyborane ($B(OMe)_3$) dissolved in methanol solution and ammonia, after which the oxygen was removed from the pyrolysis precursor by heating under an ammonia atmosphere at 1100 °C.

The vapor pressure was the initial consideration for a precursor choice. As $B(OMe)_3$ is a colorless volatile liquid with a slightly lower density than water, it could easily be transported (in vapor form) by an nitrogen flow to a quartz tube heated to 700 °C under an argon flow. Gaseous ammonia was then fed simultaneously into the tube to initialize the CVD reaction, without using the mechanical aerosol method. The XRD pattern of the CVD product (Figure 13.1) showed two broad diffraction peaks located at the (002) and (100) reflection positions of h-BN and/or at the (003) and (101) reflection positions of r-BN, thus verifying the occurrence of the BN phase in the low-temperature CVD product. However, a chemical composition analysis indicated that the product contained B, N, O and a small amount of carbon and hydrogen. The average B/N/O ratio was approximately 1.5/1/0.3, showing an abundant O impurity in the as-made samples.

The poor crystallization can be improved by pyrolysis under ammonia at 1100 °C. The XRD pattern showed the presence of a mixed-phase structure of h-BN and r-BN, despite exhibiting broad reflections especially for the strongest (002) diffraction peak of h-BN and (003) of r-BN. The broad diffraction peaks and smaller intensity ratio of (002)/(100) should result from the presence of impurities such as oxygen or carbon, or from the very small crystallite size. A scanning electron microscopy (SEM) examination indicated that both products consisted of spherical particles of fairly uniform diameter, with most BN particles 50–100 nm in diameter and of average size approximately 70 nm. Further pyrolysis under ammonia slightly increased the particle size to between 50 and 400 nm, and the surface area from ~17 $m^2 g^{-1}$ to ~20 $m^2 g^{-1}$.

The chemical composite measurement for the annealed bulk sample showed average impurity concentrations of 11% for O and 3% for C. The composition analysis using microscopic electron energy loss (EEL) spectroscopy indicated a nonuniform impurity distribution. High-resolution transmission electron microscopy (TEM) images after pyrolysis are shown in Figure 13.1, where only B and N characteristic K-edges could be clearly observed for the sphere edges. Hence, the core part of the sphere should contain more C and O impurities. Based on the EEL pattern, it is also worth noting that the fine structure of the B K-edge displayed a weaker π^* peak than σ^*, while well-crystallized h-BN and BN nanotubes possessed stronger π^*-bonding peaks [18, 19]. This implied a weakened inter-layered bonding and/or a partially disordered arrangement of the BN layers, as shown in the high-resolution TEM image shown in Figure 13.1. Although the basic layered

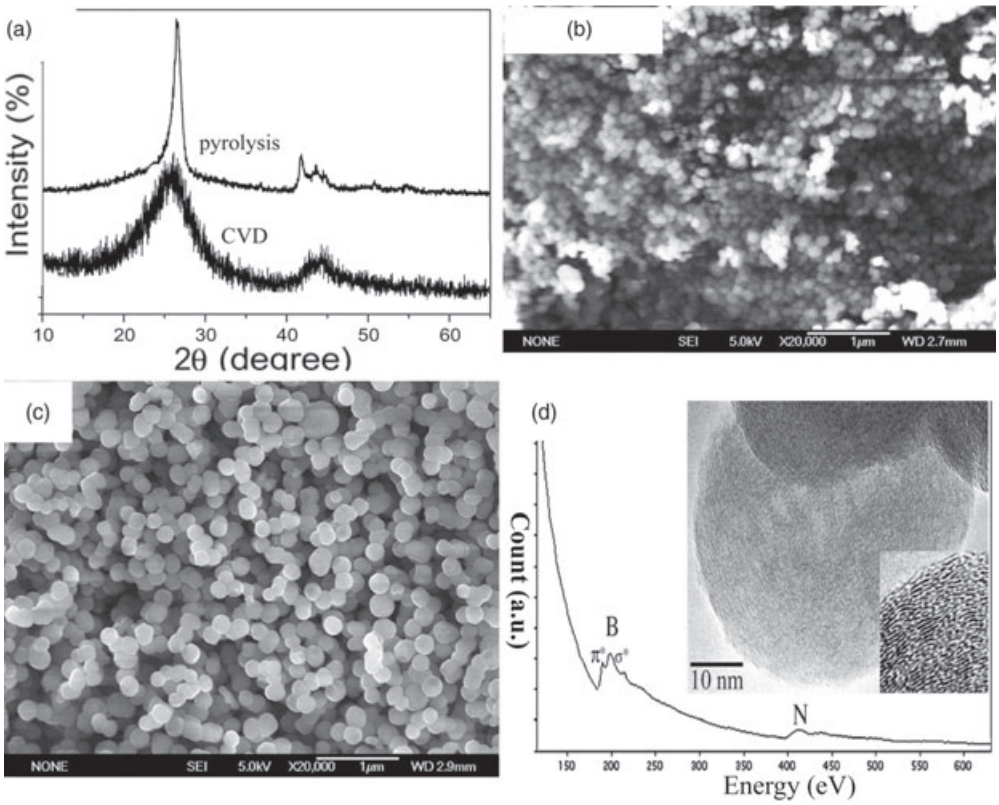

Figure 13.1 Spherical BN nanoparticles synthesized by a CVD reaction deposition of the pyrolysis of trimethoxyborane under ammonia atmosphere, and subsequent annealing at 1100 °C. (a) XRD characterization for the as-prepared CVD product (upper curve) and the annealed sample (lower curve); (b) SEM image showing the discharged BN with an abundant O impurity; (c) Pure BN nanoparticles after annealing; (d) Electron energy loss spectrum obtained from the final spherical BN particles (inset) and high-resolution TEM image with an enlarged surface area. [17] © The Royal Society of Chemistry 2002.

structure was retained, the stacking of the spherical BN particle showed a considerably strong distortion normal to the BN shell direction.

With regards to growth mechanisms, it is believed that the partial disorderings should be responsible for the spherical morphology. However, another factor relating to the spherical BO particles initially formed by the aerosol method (as proposed by Paine and coworkers [13]) more likely took effect in the sphere formation using $B(OMe)_3$ as precursor. The results of recent studies have indicated that the spherical structure would collapse when an extremely high annealing temperature was used, which fully removed the oxygen from the core. Therefore, it is now believed that spherical morphology of a BN layered crystal is a metastable intermediate phase, and its occurrence depends heavily on the morphology of the precursors and temperature.

The detailed chemical reaction between ammonia and trimethoxyborane vapor can be simply expressed as:

$$B(OMe)_3 + NH_3 \rightarrow BN + 3\ MeOH$$

This simple equation is consistent with the experimental observation that no water is formed. Nonetheless, detail of the reaction process have remained unclear, despite Wood and coworkers [20] having recently re-examined the reaction and demonstrating the existence of a weak molecular complex $(MeO)_3B \cdot NH_3$ crystal. With this aerosol result in mind, the stepped elimination of MeOH appears to be most consistent with the BN crystal formation. Thus, the more plausible reaction process should be:

$$B(OMe)_3 + NH_3 \rightarrow B(OMe)_3 \cdot H_3N \rightarrow B(OMe)_{3-x} \cdot H_{3-x}N + x\ MeOH \rightarrow BN + 3\ MeOH$$

The formation process is shown schematically in Figure 13.2. Here, the trimethoxyborane is required for the formation of spherical BN crystals, because the

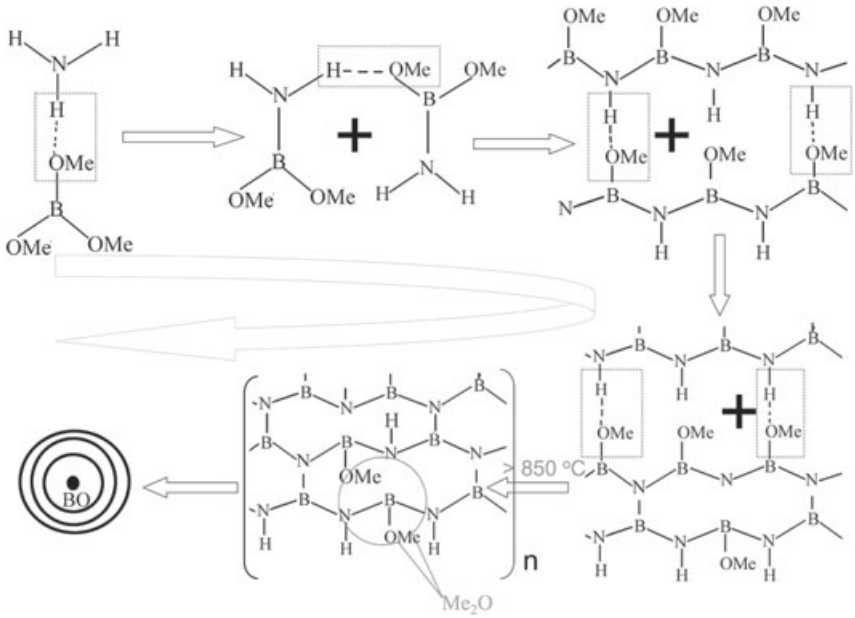

Figure 13.2 Schematic representation of the formation of the intermediate phases and the polymerization of $B(OMe)_3$-NH_3 system at the different CVD temperatures, and possible mechanism of the spherical morphology.

oxygen (boron–oxygen clusters) formed by decomposition of the trimethoxyborane must be key in the formation of a spherical morphology.

The technique described here represents a continuous process with a low-cost, high-purity and high-yield product, and is particularly useful for future commercial applications. It is difficult, however, to control the diameter distribution using both CVD and aerosol methods. In particular, when attention is focused on applications in the nanoscale field, reports on the preparation of spherical BN nanoparticles with a uniform diameter distribution have been very few in number, largely because of this relatively difficult synthesis. Bearing in mind the structural similarities of hexagonal BN and graphite, fullerene-type geometries prepared from BN were proposed as early in 1993, and the $B_{12}N_{12}$ configuration should be the BN analogue of C_{60}, based on *ab initio* calculations [21]. The synthesis of a spherical BN structure was renewed and attention focused on size (diameter) control. Boulanger *et al.* [22] found that the concentric-shelled BN nanoparticles could be synthesized by rapidly heating a reactant gas stream which consisted of ammonia and BCl_3 by using a high-powered continuous-wave CO_2 laser, although the product contained a large fraction of plate- or nanotube-like impurities. When examined using microscopy, sets of roughly parallel BN shell were visible, separated by approximately 0.34 nm, with a typical plane distance of (003) in hexagonal BN crystals. The layered planes were seen to bend from one facet to another; that is, the concentric shell was a strictly closed polyhedral rather than spherical, although the size of the concentric structure was at nanometer scale, ranging from 20 to 100 nm. Nonetheless, Banhart *et al.* [23] showed that under intense electron irradiation via TEM, the BN tended to form curling and forming concentric-shell, onion-like structures, while the spherical basal planes were not completely closed.

Wang *et al.* [24] prepared near-spherical BN nanoparticles using a laser-assisted liquid/solid interfacial reaction between acetone and BN crystal, although the product was found to consist of a mixture of hexagonal, cubic and explosion phases. Oku *et al.* [25] obtained BN nanoparticles by using two methods: (i) by mixing boric acid, urea and Ag salt to form a precursor and then reducing this in hydrogen flowing; and (ii) by arc melting the B/Fe/Au target. The synthesized product contained a nanocapsule structure, with some metal nanoparticles encapsulated in fine BN shells. The authors also observed BN nanocages which had a sharp inner angular and peculiar structure for the tip, possibly with four-membered ring defects (Figure 13.3).

Spherical BN nanoparticles with smaller diameter have not been obtained, although the size actually falls into the nanometer scale. Zhu *et al.* [26] synthesized hollow BN nanocages and GaN-encapsulated BN nanocages by using a home-made B—N—O precursor. The spherical morphologies had a crystallized structure with diameters ranging from 30 to 200 nm. These authors also observed a peanut-like structure with double walls, where the internal space was divided into separated compartments by the inner walls. The basic chemical reaction was defined as:

$$B_2O_3 + 3\,C + 2\,NH_3 \rightarrow 2\,BN + 3\,CO + 3\,H_2O$$

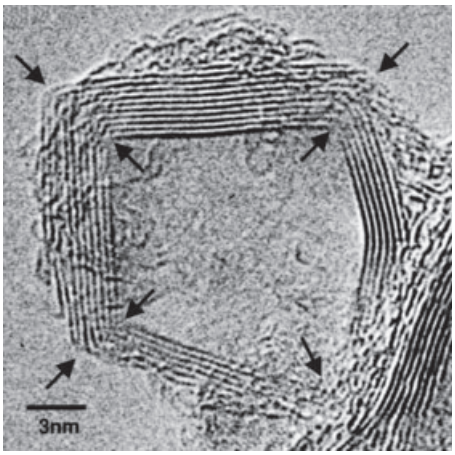

Figure 13.3 High-resolution TEM images of a BN nanocage. Reproduced with permission from Ref. [25]; © 2000, Elsevier.

Hollow spherical BN were also observed by Shi *et al.* [27], who reacted MgB_2 with NH_4Cl/NaN_3 in a stainless autoclave up to 500 °C. They described the complicated reaction as:

$$2\ NH_4Cl + MgB_2 \rightarrow 2\ BN + MgCl_2 + 4\ H_2$$

$$5\ NH_4Cl + 2\ MgB_2 + NaN_3 \rightarrow 4\ BN + 2\ MgCl_2 + 10\ H_2 + NaCl + 2\ N_2$$

The amount of NaN_3 used in the reactant had an influence on the diameter of the hollow spheres. Although this dangerous synthetic route is not recommended, hollow spheres made from BN have normally been observed when the pressure system was employed. Another example of production is from the reaction between Zn and KBH_4/NH_4BF_4, reported by the same group [28].

13.2.2 Anisotropic BN Nanostructures

13.2.2.1 Multiwalled Nanotubes

The discovery of CNTs was followed by extensive research into BN nanotubes [4], in view of the structural similarities of graphite and bulk BN. In 1994, for the first time Cohen and coworkers [29, 30] studied the structure and electronic properties of BN nanotubes from a theoretical standpoint, and emphasized that BN nanotubes should exhibit unique physical and chemical properties that are obviously different to those of CNTs. The electronic structure of a pure CNT is known to be either metallic or semiconducting, depending on the tube diameter, wrapping angle, twisting and topological defects [31], whereas BN nanotubes exhibit a wide band gap of about 5 eV that is insensitive to tube diameter and chirality, but could

be controlled by chemical composition [30] because of the ionic origin of the band gap in the nanotube-structured BN.

Strong ionic B—N bonding should also have an influence on the formation of BN nanotubes. Indeed, BN nanotubes have been synthesized using methods similar to those used to form CNTs, including arc-discharge [32, 33], laser ablation [34] and CVD [35]. Other novel synthesis processes have also been proposed, such as CNT- and template-confined methods [36, 37].

Historically, the first observation of a BN tube-like structure was of bamboo-like appearance. Early in 1981, Ishii and Sato [12] heated a precursor of h-BN with a considerable amount of oxygen at an extremely high temperature, and observed various morphologies such as 'horsetail' or 'jellyfish'. Detailed microscopic observations subsequently indicated that these curious structures consisted of a bamboo-like filament in which the hollow area was approximately 500 nm in diameter. Such bamboo-like hollow structures have also been observed during the ammonothermal reaction of ZrB_2 compound [38].

Hamilton and colleagues [39] were the first to claim the formation of a tubular morphology via a chemical reaction of B-trihaloborazines with alkali metals in the absence of any solvent. However, perhaps due to a low reaction temperature, the tubular materials were amorphous and of a poorly structured morphology. Consequently, the theoretically predicted nanotubes were identified and characterized microscopically as the product of a plasma arc discharge of h-BN rods, for the first time by Zettl and coworkers in 1995 [32]. By using an arc-discharged hafnium–diboride electrode, Loiseau *et al.* [40] also obtained BN nanotubes with single- or very few layers, and were the first to confirm the characteristic end closure of flat or triangular facets, which differs considerably from CNTs. Saito and Maida [41] further obtained other end morphologies by using an arc discharge between ZrB_2 electrodes in an N_2 atmosphere, and emphasized the existence of square, pentagonal and heptagonal rings at the BN nanotube tips. While Golberg *et al.* [42] reported BN nanotube formation by laser heating under a high nitrogen pressure, albeit with a very low yield, Han *et al.* [36] subsequently proposed a novel synthetic route, namely a CNT-substituted reaction method to form BN nanotubes. The proposed reaction was considered to be

$$B_2O_3\,(g) + 3\,C\,(\text{nanotubes}) + N_2 \rightarrow 2\,BN\,(\text{nanotubes}) + 3\,CO$$

where the carbon atoms in the starting CNTs were expected to be fully substituted by boron and nitrogen atoms.

Hu and coworkers [43] further studied the synthetic route by using different types of CNTs as starting reactants, and showed that the structures of the BN products depended weakly on the topology of the CNTs used. An intrinsic energy-modulated growth was then proposed that favorable sp^3 growth of the final BN product played a crucial role during formation of the hollow BN nanotubes (Figure 13.4).

The product yield of the CNT-substituted reaction can be further improved by using oxide-promoted assistance [44]. Golberg *et al.* [45] analyzed in detail the

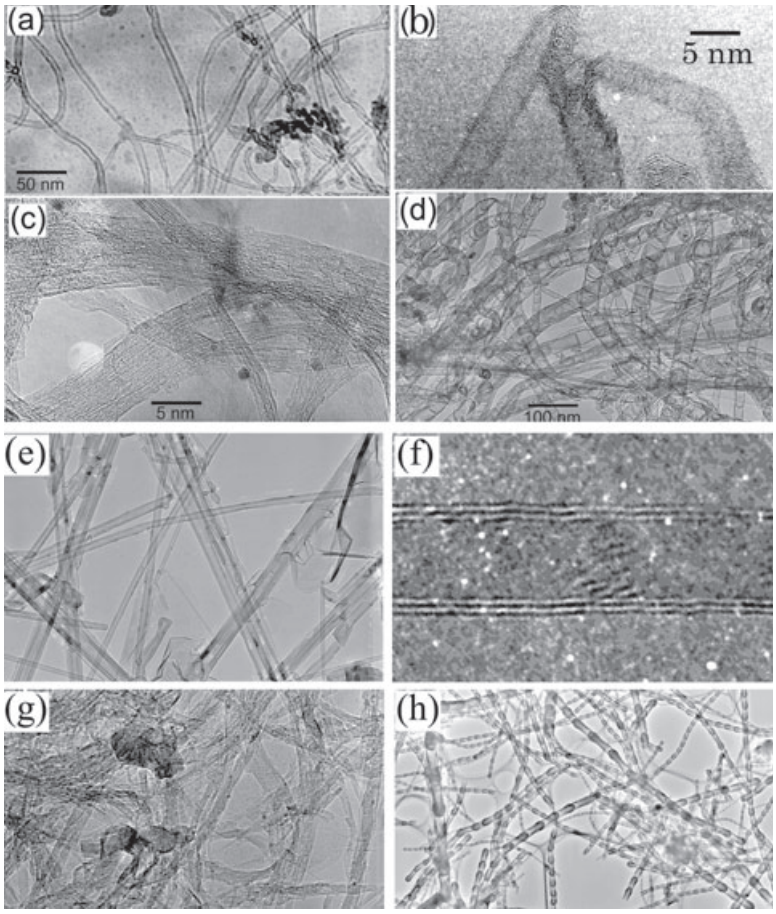

Figure 13.4 BN one-dimensional nanomaterials synthesized by carbon nanomaterials-substituted reaction by using the different carbon with (a) multiwalled, (b) double-walled, (c) single-walled and (d) nanobambooed structures. After the reaction, BN nanomaterials with (e) multiwall, (f) double-layered, (g) multiwalled + single-walled and (h) bambooed structures, respectively, can be observed. Reproduced with permission from Ref. [43]; © 2004, Elsevier.

microstructure using high-resolution TEM and EEL spectroscopy, and identified perfectly straight shapes, a limited number of shells and a remarkable ordering of the graphene-like sheets in zigzag fashion, instinct with the BN nanotubes. With the same product, further microscopy studies [46, 47] displayed another type of BN nanotube, namely the nanocone. This consisted of an ordered stacking of seamless conical shells, and resulted from the line defects necessary to curve BN sheets. Although all experimental observations confirmed the growth mechanism proposed by Hu *et al.* [43], the method has been one of the few routes shown capable of synthesizing BN nanotubes in relatively high yields. Chen *et al.* [48], however, subsequently described a ball-milled ammonothermal reaction capable

of producing nanotubes in high yield. The latter product exhibited a clear bamboo structure and contained a considerable proportion of irregular bulk BN, as indicated from TEM images.

CVD has been used widely, both to grow CNTs and also in investigations of the synthesis of BN nanotubes, although several efforts have yielded BN nanostructures with a bamboo morphology or poorly crystallized walls [49–51]. The catalyst or reaction substrate is key to controlling the tubular morphology. For example, Lourie and coworkers first observed hollow BN nanotubes on a nickel boride catalyst by pyrolysis of $B_3N_3H_6$ [52]. However, because the catalyst particle size was in the micrometer range – far beyond the size of the nanoparticles used to prepare nanotube materials – the diameters of the tubes produced exhibited a relatively wide distribution. In another study, Ma *et al.* [53] reported BN nanotube formation by using a B—N—O precursor generated from melamine diborate, without using any metal catalyst. The BN nanotubes formed showed a remarkable ordering of the concentric atomic layers and the bulbous tips, with B—N—O amorphous clusters encapsulated within BN cages and perhaps playing a catalytic role in the nanotube growth. The self-generated catalytic effect was further investigated and confirmed by incorporating silicon, aluminum and calcium into the B—N—O clusters [54].

Previously, arc-discharge routes have been reported normally to produce multiwalled BN nanotubes with a relatively high crystallization degree but with limited yields, possibly because the BN target is electrically insulating and forms an unsuitable arcing electrode. In order to circumvent this problem, various metals and/or metal borides have been explored, aiming to improve the yield. Unfortunately, however, the introduction of metals usually produced metal encapsulation or depressed tube growth [32, 55]. The main drawback of laser-ablation or high-pressure processes also results in a relatively low yield of BN nanotubes, coupled with a high cost for the extreme experimental conditions required. Although, in principle, CNT-substituted reaction methods can be used to produce large yields of BN nanotubes, it is extremely difficult to fully remove any carbon impurities, such that the final product invariably incorporates a significant proportion of ternary B—C—N nanotubes containing significant amounts (2–10 at%) of residual carbon at the expense of pure BN nanotubes [56].

Although CVD of the catalytic decomposition of carbonaceous vapors has been confirmed as an effective method for the large-scale synthesis of pure CNTs, the synthesis of BN nanotubes is hindered by carbon contamination when CVD is used, mainly because carbon is the first solid phase to appear when cooling the vapors that contain B, N and C [57]. The key to the synthesis of pure BN nanotubes is, therefore, to design a carbon-free precursor and catalyst, and the successful synthesis of BN nanotubes on a nickel boride catalyst from the hazardous carbon-free precursor, borazine, has confirmed this suggestion [52].

Based on these considerations, we proposed the use of a novel route – a removable catalyst CVD method – to produce pure and large-scale BN nanotubes, without introducing transition metals as catalysts [58]. Here, the BN nanotubes were the sole resultant phase in the reaction area; the other reactants (mainly metallic

magnesium) were evaporated and transported far from the product area. In detail, the reaction vapor precursors of the mixture B_2O_2 and Mg were first generated by the following reaction of boron with MgO at 1300 °C [59]:

$$2\,B\,(s) + 2\,MgO\,(s) \rightarrow B_2O_2\,(g) + 2\,Mg\,(g)$$

The vapors were argon-transported into a reaction chamber and reacted with ammonia to form BN at 1100 °C:

$$B_2O_2\,(g) + 2\,NH_3\,(g) \rightarrow 2\,BN\,(s) + 2\,H_2O\,(g) + H_2\,(g)$$

The liquid-phase magnesium which formed (by vapor cohesion) was deposited first, acted as a catalyst, and then evaporated after the reaction; consequently, there were no impurities in the final product. Subsequent examinations using XRD, TEM and EEL indicated that the product contained only a mixed phase of h-BN and r-BN of high purity and crystallinity (Figure 13.5), and exhibited a one-

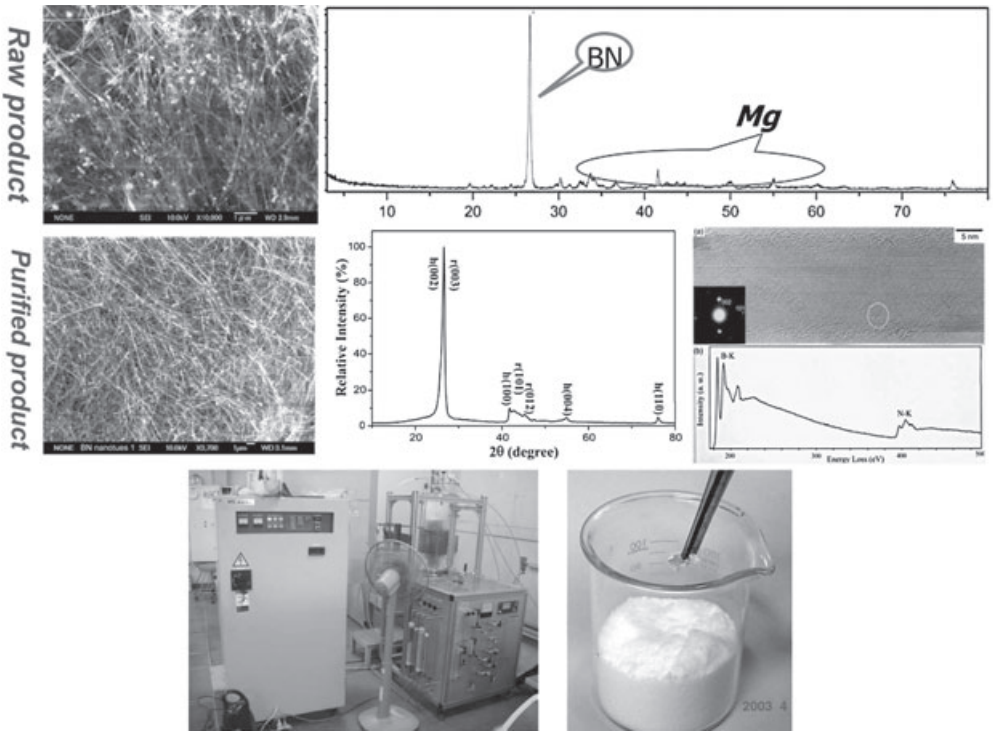

Figure 13.5 Multiwalled BN nanotubes synthesized by removable catalyst CVD method using B and MgO as the precursors. The only possible contamination from Mg is easily removed by simple evaporation. The laboratory-scale set-up was installed in our laboratory; the pure BN nanotubes, after further acid-washing, can provide sufficient sample to perform property and application research.

dimensional nanostructure with the diameter ranging from several nanometers to about 70 nm, and a length of up to 10 μm. The structure and defects in the BN nanotubes were also investigated [60]. Very recently, a system has been set up in our laboratory to produce BN nanotubes in gram quantities and high purity, sufficient for use in extensive scientific explorations.

The proposed growth mechanism of Mg catalysis remains the subject of much speculation, however, as solidified Mg particles have not (yet) been found at the tube tip, a situation partly confirmed by other investigations. During early 2001, we showed that BN nanotubes could be synthesized by heating a mixture of boron and iron oxide in flowing ammonia. Transition metal impurities were seen to play an important role in determining nanotube diameter and morphology, while growth could be clearly defined to a catalyst growth mechanism within the framework of a vapor–liquid–solid (VLS) process [61] (Figure 13.6). Similar routes, using the ammonia reaction of B and SiO_2 in the presence of Fe [62]; of B and NiB/Al_2O_3 [63]; of $Ba(BO_3)_2$ in the presence of Ga [64]; of Fe—B nanoparticles [65]; of B and Ga_2O_3 [66]; and of B and $LaNi_5$ [67] have also been examined, although to date only the reaction of B and MgO has been shown capable of obtaining high-purity, high-yield BN nanotubes.

Recently, remarkably extensive explorations for the synthesis of BN nanotubes by other routes have been undertaken. For example, Terauchi *et al.* [68] noted the presence of several short, pure multiwalled BN nanotubes in a resultant powder

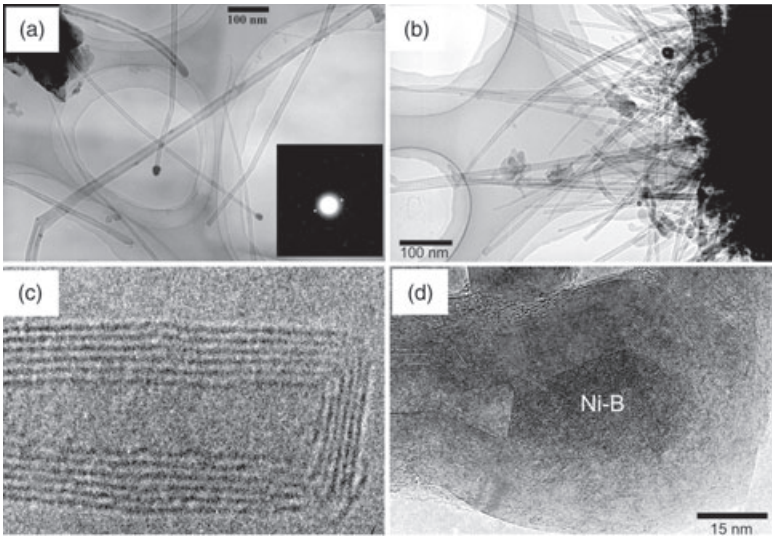

Figure 13.6 BN nanotubes (b) synthesized by the reaction of B and NH_3 in the presence of a transition metal, which behaves as the 1-D catalyst within the framework of the VLS mechanism. The metal particles can be found from the tip (a) or the encapsulated tube (d). Another end is usually closed in a flat tip (c), which is different from carbon nanotubes. Reproduced with permission from Ref. [62]; © 2002, Elsevier.

synthesized by the reaction of B and Li powders in a BN crucible at 1200 °C in a N_2 atmosphere. Likewise, Shelimov and Moskivits [69] employed trichloroborazine to yield submicrometer BN tubular fibers in an alumina filter membrane, while Xu *et al.* [70] produced BN nanotubes by copyrolyzing NH_4BF_4, KBH_4 and NaN_3 at temperatures ranging from 450 to 600 °C. Chen *et al.* [71] presented a simple reduction–nitridation route to prepare boron nitride nanotubes in the presence of Fe—Ni powder as catalyst at 600 °C, in which boron trifluoride etherate and sodium azide were used as the reactants. Ma *et al.* [72] synthesized BN nanotubes from the reaction of $NaBH_4$ with NH_4Cl, and proposed a layer-by-layer growth scenario. The low-temperature CVD synthesis of multiwalled BN nanotube-patterned aligned bundles in the presence of Fe nanoparticles at a temperature as low as 600 °C has also recently been reported [73]. Straight BN nanotubes with pure hexagonal phase were prepared by heating the mixture of $Mg(BO_2)_2$, NH_4Cl, NaN_3 and Mg powder in an autoclave at 600 °C [74].

13.2.2.2 **Single-Walled Nanotubes**

Single-walled BN nanotubes are of scientific importance because their structure permits the study of intrinsic physical properties to become both clearer and easier, although no clear theoretical evidence has yet been provided detailing any correlation between layer number and physical properties. Both, laser ablation and arc-discharge methods have been identified as powerful tools for the synthesis of single-walled nanotubes made from either carbon or BN [75]. The first report of BN nanotubes synthesized via plasma arc discharge with a pure BN electrode yielded seven to nine layers of the BN sheet, while a double-layered tube was identified in the product obtained by HfB_2 discharge. Yu *et al.* [76] used excimer laser ablation at 1200 °C to produce single-layered or few-layered BN nanotubes, this being the first occasion where the formation of single-walled BN nanotubes was claimed. An arc discharge between ZrB_2 electrodes in an N_2 atmosphere was also used to produce single-walled BN nanotubes, as reported by Saito *et al.* [77] in 1999. That double-walled nanotubes should be more energetically favorable than single-walled nanotubes was supported by the first claim of mass-production of BN nanotubes by Cumings and Zettl, who noted that the double-walled structure was obtained more easily when using plasma arcing [55]. The structural stability of the double-walled BN nanotubes was further confirmed by Golberg *et al.* [78], who identified the occasional double-walled structures among the product synthesized via a CNT-substituted reaction. These authors also observed a change in the chirality of tubular layers, from armchair to zigzag arrangement in a 30° double-walled nanotube kink, this being the first occasion that any defect structure of a double-walled BN nanotube had been structurally characterized. Demczyk *et al.* [79] also suggested that, in nanotube production, the armchair would be formed first, followed by the zigzag.

Although only limited evidence is available confirming the presence of single-walled BN nanotubes, Bengu and Marks [80] used a low-energy, electron–cyclotron resonance plasma to deposit single-layer BN nanostructures, and noted the dominance of kinks and bends involving four- and eightfold ring structures as against

five or sevenfold, in accord with the theoretical predictions [81]. Lee *et al.* [82] adopted a continuous CO_2 laser ablation reactor without the benefit of a metal catalyst, and claimed the successful formation of single-walled BN nanotubes in gram quantities. The synthesized samples were composed of single-walled BN nanotubes organized in long and well-crystallized bundles. However, based on the reported TEM images, there was considerable impurity among the final product. A very recent report from the same group [83] described a systematic and detailed microscopy study on various types of nanotube (Figure 13.7) and byproducts, placing particular emphasis on the effects of temperature with regards to:

- The formation of liquid boron droplets from the decomposition of different boron compounds that exist in the hexagonal boron nitride target.
- The reaction of the boron droplets with nitrogen gas present in the vaporization chamber, and recombination of these elements to form boron nitride.
- The incorporation of nitrogen atoms at the root of the boron particle at active reaction sites for growth of the tube.

A root-growth model was proposed, therefore, that involved the presence of a droplet of boron, in addition to the solubility, solidification and segregation of target elements within this boron droplet.

Other than laser-assisted and arc-discharge methods, no other reliable method has yet been devised for the production of single-walled and/or double-walled BN

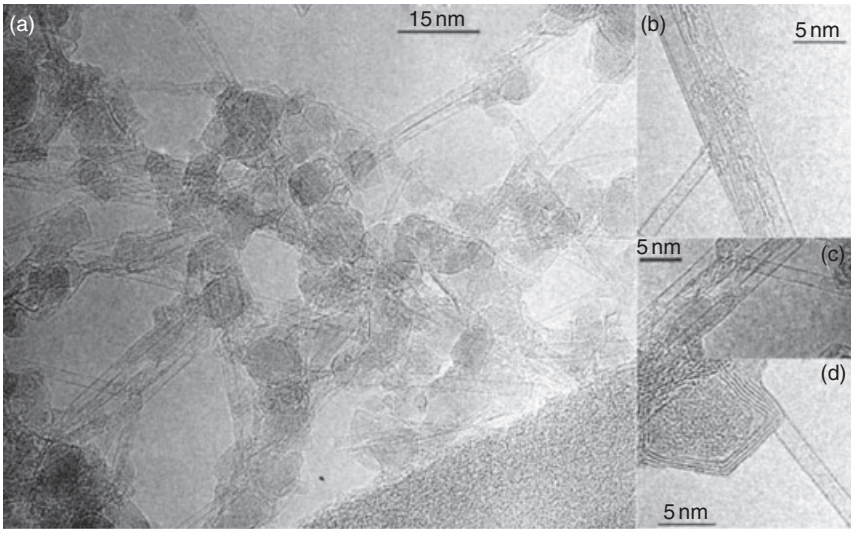

Figure 13.7 (a–d) High-resolution TEM images of the different objects present in the samples: individuals or organized BN nanotubes (single-walled in small bundles) and multiwalled (mostly double-walled), cages and other types of nanoparticle. Reproduced with permission from Ref. [83]; © 2007, The American Chemical Society.

nanotubes, especially in bulk amounts and with high purity. Hence, these novel experimental approaches aimed at the efficient and controllable production of few-layered BN nanotubes, notably to improve both yield and purity, require further development.

13.2.2.3 **Collapsed BN Nanotubes**

Another type of BN nanotube, which has a highly disordered arrangement of BN sheets, was first proposed in 2002 and subsequently named the 'collapsed nanotubes' [84]. This structure was first observed during investigations into the effect of high temperatures on multiwalled BN nanotubes, when it was found that their morphology could be strongly modified by a post-production treatment of heating the pure BN nanotubes in the presence of platinum. This resulted in a near-total collapse of the BN nanotube walls, with the consequent formation of crystalline and disordered hair-like BN nanotube fragments. A typical TEM image, showing maintenance of the one-dimensional nanotubular morphology of the starting BN nanotubes is shown in Figure 13.8, where the inner areas of the collapsed nanotubes appear in bright contrast. On examination, all of the wall layers were seen to be fractured and protruding outwards, forming a hair-like structure. A further examination with high-resolution TEM showed the disordered BN layers to be composed of highly crystallized BN fragments. Both, energy-dispersion X-ray (EDX) and EEL spectroscopic analyses further confirmed a stoichiometric BN composition, without any traces of carbon, platinum and oxygen in the collapsed BN nanotubes.

A metal-catalyzed growth mechanism was also proposed to explain the growth mechanism, although to date this has remained somewhat speculative. Whilst BN nanostructures, which are known for their high defect density, numerous dangling bonds and high surface area, may demonstrate many interesting functional properties (including a very high gas uptake capacity), it is their product yield that limits their commercial application, due mainly to the extremely high treatment tem-

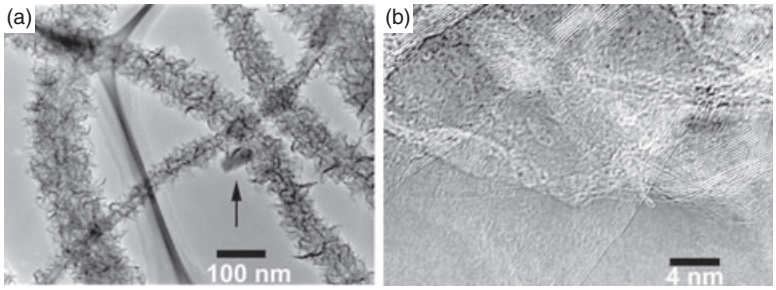

Figure 13.8 (a) TEM image of BN nanotubes after heating at 1500 °C for 6 h in the presence of platinum; the arrow points to a platinum nanoparticle; (b) High-resolution TEM image of the collapsed BN nanotubes. Reproduced with permission from Ref. [84]; © 2002, The American Chemical Society.

peratures required, and the high cost. Hence, an alternative CVD procedure was recently explored for the high-yield growth of collapsed BN nanotubes, using a cheap and easily available chemical, namely ammonium tetrafluoroborate (NH_4BF_4), as the single-source precursor of BN [85].

Following a systematic investigation of the thermodynamics of NH_4BF_4 under inert (N_2, Ar) and reactive conditions (NH_3) [86], it transpired that no BN phases could be produced via routine CVD of the precursor. Hence, a novel chemistry for BN formation was proposed, based on the experimental fact that a similar compound containing isolated molecules of NH_3-BF_3 has a high thermal stability and functions well in CVD-based BN formation [86]. It was assumed that the excess HF generated by the decomposition of NH_4BF_4 must be responsible for the absence of BN during normal CVD. For the first time, it was suggested that a BN phase could be obtained if the F content in the precursor were to be depressed by the formation of a stable fluoride. A possible CVD reaction could now be proposed as follows:

$$2\ NH_4BF_4 + MgCl_2 \rightarrow 2\ NH_3\text{-}BF_3 + MgF_2\ (s) + 2\ HCl(g)$$

$$2\ NH_3\text{-}BF_3 + 3\ MgCl_2 \rightarrow 2\ BN\ (s)\ +\ 3\ MgF_2\ (s) + 6\ HCl(g)$$

Other than HF stabilization, the introduction of $MgCl_2$ offers the benefit of one-dimensional (1-D) growth, which has indeed been proven during the formation of BN-based 1-D materials [58]. In order to put this idea in motion, we first obtained an intermediate product, namely MgF_2 nanowires that were fully coated with a chemically stable BN shield. A detail characterization of the coated BN composite nanowires (see Figure 13.9) proved that the BN coatings actually form the collapsed structure. Finally, it was found that the MgF_2 core could be totally removed using a high-temperature evaporation route, taking into consideration the relative instability of MgF_2 as opposed to BN in a high-temperature treatment. Subsequent treatment in a flow of argon at 1600 °C caused sole collapse of the BN nanotubes, the typical morphology of which is shown in Figure 13.10. The length and width of the collapsed nanotubes were larger than 1 μm and 20–50 nm, respectively, and similar to those of the initial BN-coated MgF_2 nanowires. This indicated that a high-temperature evaporation might not affect the BN structure of the initial coatings. The thickness of collapsed nanotubes synthesized at low temperature was normally more than 10 nm, with a high degree of disordering. In addition, almost all of the collapsed BN nanotubes synthesized at high temperature displayed outer diameters that peaked at approximately 100 nm, as well as very thin walls that generally ranged from a few nanometers to more than 10 nm. The tube diameter was not strictly uniform along the tube length, with some layers being broken and protruding outwards, forming a typical collapsed morphology.

Thus, the use of NH_4BF_4 as a simple and cheap precursor for the BN CVD reaction in the formation of collapsed BN nanotubes, via the above-described two-step reaction process was highly successful, and will undoubtedly prove to be valuable in the future commercial development of novel BN nanostructures.

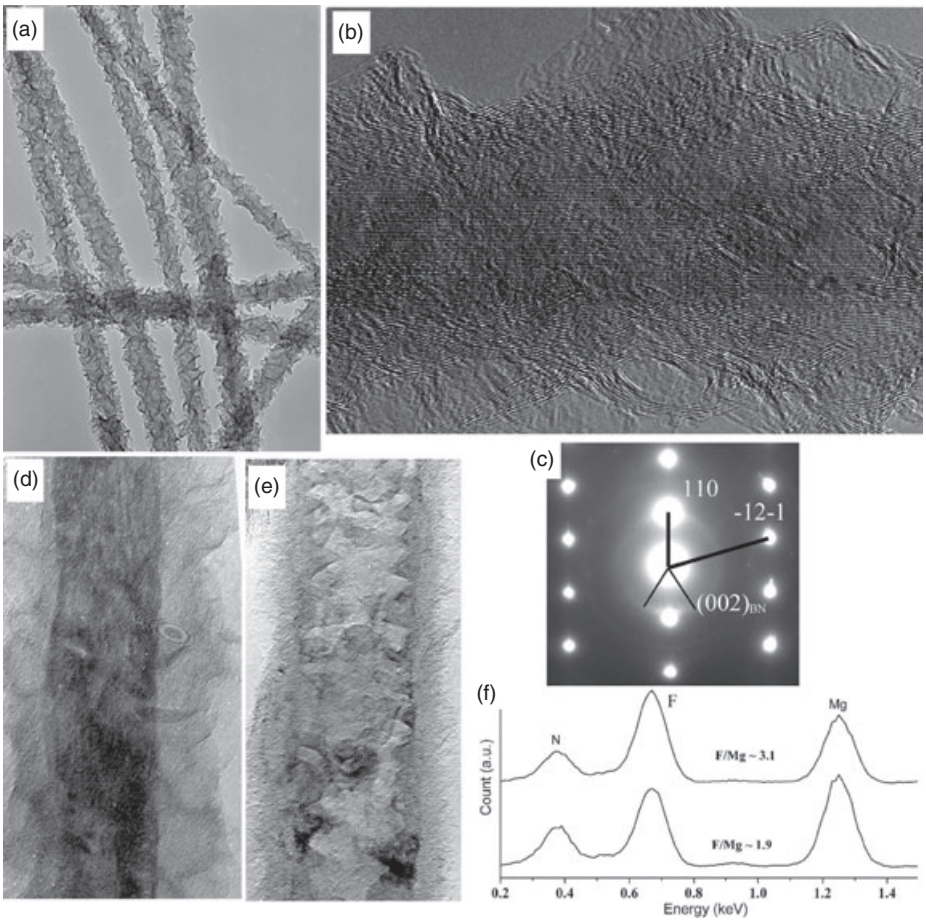

Figure 13.9 (a) Low-magnification TEM image of the nanowires, showing a flocky structure; (b) High-resolution TEM image of a single flocky nanowire clearly displaying an inner MgF_2 nanowire with a diameter of ~10 nm coated with the disordered BN layers; (c) The corresponding selected-area electron diffraction pattern taken from the [–113] zone axis of tetragonal MgF_2; the (002) diffraction ring originating from an outer BN shield implies random orientations; (d) High-magnification TEM image of a starting BN-coated MgF_2 nanowire with a well-crystallized structure; (e) The same nanowire in (d) but electron-beam-irradiated for 3 min; (f) EDS spectra showing a change in chemical composition of flocky BN-coated MgF_2 nanowires before and after electron-beam irradiation. From Ref. [85], © 2006 IOP Publishing Ltd).

13.2.2.4 **Nanowires**

Solid-whisker (fiber) structures were widely discussed and synthesized long before the conceptual proposal of nanotube structure. During the early 1970s, Economy and Anderson [87] fabricated BN fiber by the nitridation of boron-oxide fibers in an ammonia atmosphere. although the quality of the precursor fiber and the nitridation process were notoriously difficult to control [88]. Previous important

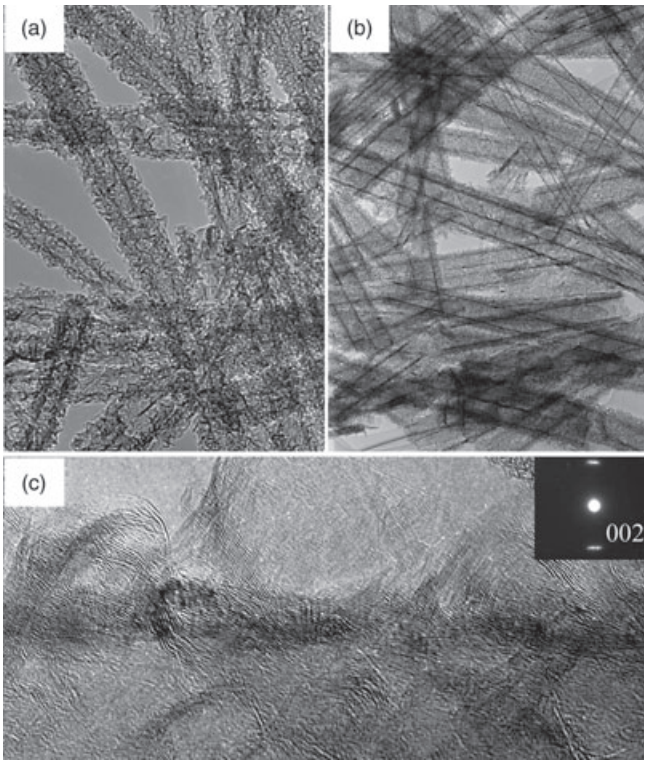

Figure 13.10 Low-magnification TEM images of the purified products synthesized at (a) 700 °C and at (b) 900 °C, and the corresponding high-resolution TEM image (c) clearly displaying a collapsed morphology after the treatment. From Ref. [85], © 2006 IOP Publishing Ltd).

studies [12] conducted by Ishii and Sato reported on not only bamboo-like hollow-fiber but also solid-whisker structures. Paine and coworkers obtained oriented BN fibers with microstructures similar to graphite fibers by using a die extrusion fiber-spinning technique with poly(borazinylamine) solutions [89]. Although the oxidation resistance at high temperatures and dielectric properties of BN whiskers might offer some applications showing certain advantages over carbon fibers, BN fibers have been comparatively less studied than their carbon counterparts, due partly to the difficult synthesis of BN crystals. Consequently, although a large number of investigations have been undertaken on nanotube-like BN since 1995, fewer have involved studies of BN fibers. Although a polymer precursor, poly(aminoborazinyl) has long been confirmed for the formation of BN fibers [90], these investigations are clearly ongoing [91]. Today, the spinnable polymers based on borazine, which already overshadow the hexagonal structure of h-BN and its B : N stoichiometry, are recognized as appropriate for the formation of BN fibers, due not only to the presence of alkyl groups in the pendent borazine units but also

to the type of linkage between the borazine rings in the polymer structure, with both being prerequisites for the preparation of BN fibers [92].

Huo *et al.* [93] conducted the reaction of a mixture gas of nitrogen (N_2) and ammonia (NH_3) over nanoscale FeB particles at 1100 °C, and noted the formation of solid-whisker structures, except for the nanotubes. Examinations using microscopy indicated that the abundant quantity of BN whiskers possessed diameters down to the nanometer scale, and this allowed the claim for a first successful formation of BN nanowires. In the meantime, Rao *et al.* [94] heated boric acid with activated carbon, multiwalled CNTs, catalytic iron particles and/or a mixture of activated carbon and iron particles, in the presence of ammonia, and also obtained the BN nanowires. The basic chemical reaction was the traditional carbon-thermal process, which can be written as:

$$2\ H_3BO_3 + 3\ C\ + 2\ NH_3 \rightarrow 2\ BN + 3\ CO + 3\ H_2 + 3\ H_2O$$

Here, the catalytic iron played a vital role in diameter control, as the plate- or whisker-structured BN particles were converted to BN nanowires. Thus, it was reasonable to assume that the presence of iron during the BN chemical formation was responsible for the solid nanowire structure. However, it was also obvious that the metal particles could simultaneously catalyze nanotube growth. This relationship between catalyst and morphology, as well as the actual growth mechanism, requires further investigation. The proposed growth mechanism normally involved common chemical reactions rather than a detailed catalytic growth process. In fact, the catalytic effect of metal iron should be amphibolous, because the high melting point of iron nitride rather than metallic iron appeared in the BN formation when the reaction was carried out in the presence of ammonia. This catalytic role of iron, which usually takes effect for the fiber and 1-D growth within the framework of the well-known VLS growth mechanism [95, 96], should be invalid. Hence, with the catalyst activity in mind, further consideration for a CVD or chemical reaction synthesis of BN nanowires should seek out those catalysts that are stable or easily form liquid droplets at the intermediate CVD temperature (800–1200 °C). Zhang *et al.* [97] obtained conical BN nanowires on Si substrates via a ball-milling and annealing route for the nitridation of boron carbide in the presence of Fe impurity, while the ammonothermal reaction between B and ZnO at 1100 °C in the presence of a stainless-steel foil ($Cr_{0.19}Fe_{0.70}Ni_{0.11}$) also led to the formation of BN nanowires [98]. Alternatively, a prismatic structure of BN nanowires was found with the mechanical ball-milling of B_4C powder and a Fe/Si alloy and subsequent nitridation in a nitrogen-containing atmosphere [99]. The conical, cylindrical and prismatic morphologies that appeared for the different precursor cases with a similar catalyst should also reflect a sensitive dependence of the precursor effect on structure control. This conclusion may be confirmed by a recent study conducted by Tang *et al.* [100], who systematically examined precursor dependence by using a floating catalyst CVD method. The method involved tuning experimental parameters such as growth temperature, floating catalyst concentration and boron precursor, while BN nanostructures including

nanotubes, nanobamboos and nanowires were selectively produced. By using $B+B_2O_3$ as the BN precursor, nanotubes, nanobamboos and platelet nanowires were synthesized in the presence of ferrocene at 1450 °C, ferrocene at 1350 °C, and nickelocene at 1350 °C, respectively.

The formation of pure BN nanowires was recently claimed by Chen *et al.* [101], who adopted a CVD process with boron triiodide as precursor in the absence of any catalyst particle, but using a Si substrate. The formed BN exhibited a nanowire structure with a uniform diameter of 20 nm, while some BN nanowires self-assembled into thick threads up to several hundred micrometers in length, on top of the nanowire layer. The crystal structure was of the turbostratic type and, because no catalytic particles existed at the tips of nanowires, the growth mechanism was attributed to a vapor–solid (VS) growth process. Another experiment reported by Komatsu *et al.* [102] indicated that the BN fibers could also be synthesized on polycrystalline nickel and Si substrates using a plasma-assisted laser CVD of $B_2H_6+NH_3$, with an excimer laser. Although metals were used in these experiments, the investigators maintained that the growth involved the surface diffusion of precursor species, assisted by laser light rather than the VLS mechanism. Therefore, BN nanowires might also be prepared by other routes, including certain specially designed chemical reactions or techniques.

At this point, some peculiar routes for the preparation of BN nanowires should perhaps be noted. As an example, Lin *et al.* [103] synthesized BN nanowires with a polyhedral morphology by the nitridation of an intermediate prepared by the reaction of KBH_4 and NH_4Cl [103]. A nanowire-structured BN was also synthesized by the reaction of sodium borohydride with sodium azide in an autoclave at 600 °C [104]. Although the yield and purity of the formed BN nanowires might be further improved, the concepts proposed by these authors were of considerable interest.

13.3
Remarks on Properties and Applications

An intrinsic impetus for the synthesis and characterization of BN nanomaterials is to pursue the potential for improving traditional BN-based materials, taking advantage of the expected excellent properties that result from nanoscale effects. However, the number of methods available to produce BN nanomaterials in sufficient quantities and – more importantly – impurity-free, is limited to say the least. Although the basic synthetic procedures for BN nanomaterials (whether high-yield, high-purity multiwalled nanotubes or spherical nanoparticles) have reported in detail, the use of a relatively complicated route and a toxic atmosphere (ammonia, B-containing organics) limit their extensive use, even on the laboratory scale. Moreover, the commercial development of these materials will require major efforts to be made over a long period of time, and consequently much of research involving the physical and chemical properties of BN nanomaterials has been – and will continue to be – carried out by very few groups. Nonetheless, numerous results have been acquired over the past few years, with notable breakthroughs being

achieved in the synthesis, atomic structure determination and property predictions, within both theoretical and experimental groups.

13.3.1 High-Temperature Chemical Inertness

We first compared the effects of BN coatings on the anti-oxidation ability of SiC nanowires by studying the chemical inertness of multiwalled BN nanotubes. Under oxidizing condition, SiC nanowires without BN coatings were cracked into nanoparticles or almost fully converted into SiO_2 nanowires at a temperature above 800 °C, depending on the crystallization degree of SiC nanowires. However, it was found that, at a temperature in excess of 1000 °C, the BN coatings effectively improved the anti-oxidation ability of SiC nanowires and exhibited strong oxidation resistance. These results confirmed the excellent chemical stability of BN nanotubes at high temperatures [105].

13.3.2 Electrical Properties

Both, bulk and nanoscale BN with high purity and complete structures are basically electrical insulators with a bandgap of >5 eV, almost independent of tube diameter, helicity, and whether the nanotube is single- or multiwalled within the nanotube system [29]. The first study to evaluate, on a practical basis, the transport current voltage (I–V) for an individual pure multiwalled BN nanotube, was reported by Cumings and Zettl [106]. The *I–V* characteristic of an individual pure, single BN nanotube synthesized in our laboratory were also measured, using a four-probe technique [107], and indicated the resistance and resistivity to be ~$2 \times 10^9\,\Omega$ and ~$300\,\Omega \cdot$ cm, respectively. The relative uniformity of the electronic properties in BN nanotubes, combined with their chemical inertness, may serve as a key advantage in nanoelectronic applications. In fact, there is no need to control the diameter and helicity of BN-based nanoelectronic devices, which in the past has been extremely difficult to achieve in the case of CNTs [5].

The electronic structure of nanoscale BN – especially BN nanotubes – can be modulated by doping the BN, as such structure relies heavily on the chemical composition. In this context, uniformly doped BN nanotubes obtained via chemical modification would serve as prospective objects for tailoring the electronic properties. Based on these consideration, we first described an original route towards the synthesis of F-doped BN nanotubes by introducing F atoms at the stage of tube growth, and obtained a relatively uniform doping in pure BN nanotubes with a doping concentration of 5%. The fluorination of BN nanotubes resulted in highly curled tubular BN sheets, and transformed the insulating BN nanotubes into semiconductors. The resistance of the individual F—BN nanotube was approximately $(2\text{–}4) \times 10^6\,\Omega$, and the resistivity 0.2–0.6 $\Omega \cdot$ cm, indicating a typical heavily doped semiconductor. Xiang *et al.* [108] preformed a first-principles calculation and suggested that such electrical enhancement was induced by the

adsorption of F atoms. Liu *et al.* [109] also studied, on a theoretical basis, the structural and electronic properties of fluorinated, double-walled BN nanotubes, and emphasized that an interstitial F doping could provide more effective conducting channels than could F adsorption on the outmost shell. Even so, the detailed electronic structure change induced by F doping remains the subject of much debate [110]. Both, theoretical and experimental investigations for the doping of BN nanotubes are especially important with regards to the future application of nanoscale electronic devices with tunable properties.

Other techniques which have also been considered to modulate the electronic properties of BN nanotubes include flattening deformation [111] or the application of a transverse electric field (Stark effect) [112], which may cause a dramatic reduction in the bandgap of BN nanotubes. Kral *et al.* [113] showed that an electrical current should appear when a BN nanotube was exposed to polarized light. In addition, Mele and Kral [114] predicted a piezoelectric behavior, while Bai and coworkers [115] verified, experimentally, a deformation-driven electrical transport and the first signs of a piezoelectric behavior in multiwalled BN nanotubes. Polarization under tube deformation and related piezoelectric phenomena represent important factors in the electrical behavior of BN nanotubes. The general feeling is that many research investigations have demonstrated the possibility of creating ultrafast optoelectronic and optomechanical devices by using BN nanotubes.

13.3.3
High Thermal Conductivity

As predicted, in theoretical terms, by molecular dynamics simulations, CNTs most likely possess an extremely high thermal conductivity of 6600 $W\,mK^{-1}$ [116, 117], although values measured experimentally are generally much lower when compared to matched deviations [118–122]. A high thermal conductivity suggests that CNTs would serve as effective fillers for thermal interface materials that have been fabricated by adding CNTs into polymer matrices [123]. The enhancement of thermal conductivity has been observed in CNT-incorporated epoxy and silicon elastomer matrixes [124]. It should be noted that a CNT incorporation of only 0.2 wt% led to a sharp increase in electrical conductivity, by a factor of nearly 10000, most likely due to the easy formation of a percolated nanotube network [125]. Unfortunately, this is not a positive sign for thermal interface materials, as a high electrical resistivity is required in applications where the materials come into contact with working electrical components. In this context, the quest for new thermally conducting, yet electrically insulating, materials with superb rheological properties would be a vital issue where problems of heat dissipation may be encountered. It is very likely that, in future, BN will serve as an appropriate choice for highly insulating, high thermally conductive materials.

The measurement of thermal conductivity for BN nanotubes generally results in a value on the order of 350 $W\,mK^{-1}$ for tubes with an outer diameter of 30–40 nm [126]. The nanotubes also display the room-temperature enhancement of 50% with the isotopic disorder effect, which is the largest for any material known. Zettl's

group [127] have shown that BN nanotubes with an impurity loading, possess asymmetric axial thermal conductance properties, with a greater heat flow in the direction of decreasing mass density. The group proposed that solitons were responsible for this observation, and suggested substantial implications for diverse nanoscale calorimeters, microelectronic processors, macroscopic refrigerators and energy-saving buildings. We also have measured the thermal conductivity of bulky pellets made from various BN-based nanomaterials [128], including spherical nanoparticles, perfectly structured, bamboo-like nanotubes and collapsed nanotubes, and showed thermal conductivity to depend heavily on the morphology of the BN nanomaterials, and especially on the surface structure. Hence, a thermal conductivity of ~14 $W\,mK^{-1}$ was estimated for nanospheres, ~18 $W\,mK^{-1}$ for nanotubes, ~17 $W\,mK^{-1}$ for nanobamboo, and ~46 $W\,mK^{-1}$ for the collapsed nanotubes. Spherical BN particles were shown to have the lowest thermal conductivity, while collapsed BN nanotubes possessed the best thermoconductive properties. Such dependence of conductivity in relation to the BN nanomaterial structure might be explained on the basis of heat percolation.

The predicted high thermal conductivity of >5000 $W\,mK^{-1}$ has not yet been achieved experimentally, largely because such measurement involves strategies that are used for individual nanomaterials, notably for single-walled and pure BN nanotubes, which serve as characteristic points for identifying the high conductivity of BN nanotubes. Yet, based on obtained values, it is perhaps more beneficial to use nanotube- or spherical BN nanomaterials as a polymer filler since, for traditional thermal interface materials, this will improve the thermal conductivity while retaining the electrical insulation. The results of a recent study on the morphology-dependence of thermal conductivity in various BN nanomaterials indicated clearly that a predicted high thermal conductivity of a BN nanotube could be achieved only when the interface thermal resistance could be effectively suppressed. This would pave the way for the smart integration of BN nanomaterials into thermal conductor technology. When facing the challenge of synthetic exploration, however, single-walled and effectively arranged BN nanotubes would be much preferred.

13.3.4 Mechanical Properties

The theoretical estimate of the elastic modulus of BN nanotubes reaches ~850 GPa, slightly lower than that of CNTs [129, 130]. Despite the slightly lower elastic modulus, Dumitrica *et al.* [131] noted that the resistance to yield and thermal degradation of BN nanotubes may surpass that of CNTs. Chopra and Zettl [132] measured the yield stress of BN nanotubes as ~1.1 TPa. Using the high-purity BN nanotubes developed in our laboratory, the effective elastic modulus of BN nanotubes was measured using an electric-field-induced resonance system, fitted inside a TEM unit [133]. The average value was determined as 722 GPa, comparable to the theoretical estimate of 850 GPa, and no major variation in the elastic modulus with BN nanotube diameter was observed. When elastic and plastic deformation

experiments related to the peculiarities of individual BN nanotubes were conducted [134], individual multiwalled BN nanotubes were shown to be very flexible and elastic while being deformed between the two gold leads inside the high-resolution TEM unit. In spite of the significant corrugation and buckling of BN tubular shells under severe bending deformation, the perfect BN nanotube shape was remarkably restored when the load was released, demonstrating a superb flexibility which had not been expected for a layered tubular BN compound.

The introduction of nanotube-shaped BN into polymer or ceramic matrices represents a promising approach to obtaining ultra-strong, extra-tough materials for inclusion into multifunctional composites, especially when taking into account the mechanical behavior of such composites at elevated temperatures. Huang *et al.* [135] showed that the addition of a small amount of BN nanotubes could dramatically enhance the high-temperature superplastic deformation of engineering ceramics. The addition of BN nanotubes (0.5 wt%) led to an inspiring brittle-to-ductile transition in Al_2O_3 ceramics, even at a temperature of 1300 °C. For Si_3N_4 ceramics, a similar addition (0.5 wt%) also decreased the true stress by 75%, under the same deformation conditions. Such data suggest that BN nanotubes should show great promise as components in cost-effective complex ceramics with good compressive mechanical properties.

13.3.5
Hydrogen Storage

Ma *et al.* [136] first showed that BN nanostructures might absorb hydrogen at a level equivalent to 1.8–2.6 wt% under 10 MPa at room temperature, while Tang *et al.* [84] later showed, experimentally, that a significant hydrogen uptake (up to ca. 4.2 wt%) might occur in collapsed BN nanotubes. It was subsequently demonstrated that the modification of a BN nanotube surface with certain metals and/or intermetallic compounds might significantly improve the electrochemical hydrogen storage capacity of BN nanotubes [67, 137]. This issue requires further experimental and theoretical input with regards to the mechanism details and concept, notably how to improve the dynamic properties of hydrogen absorption [138].

13.3.6
Life Sciences

To date, few reports have been made on the properties and applications of BN-based nanomaterials, mainly because of the minimal investigations conducted into the toxicity of BN materials. Nonetheless, considerations have been made regarding possible applications in the life sciences, the main basis being the intrinsic electronic structure of BN-based nanomaterials. Based on the structure of nanotubes, an individual BN layer will become buckled such that the B atoms protrude inwards and the N atoms outwards, to form a dipolar, double-cylinder shell structure [29]. This results in an intrinsic ionic characteristic of the electronic

structure and, more importantly, an almost free-electron-like state at the bottom of the conduction band [139]. The consequent noncovalent interactions in such chemical systems are primarily electrostatic in nature. A comparative analysis [140] of the surface electrostatic potentials of CNTs and BN nanotubes indicated that, unlike the relatively weak and bland potentials in CNTs, the outer electrostatic potential distribution of a BN nanotube possessed alternating positive and negative regions, with the inside region being strongly positive. Such theoretical prediction might be confirmed by carefully performing experiments, and this was made possible within our group when a catalyst-removal CVD method was developed to synthesize high-purity BN nanotubes with a large yield [58]. These BN nanotubes were strongly attracted to glass, metal and even human skin, due to their pronounced electrostatic interactions (see Figure 13.11). It was also found that, when

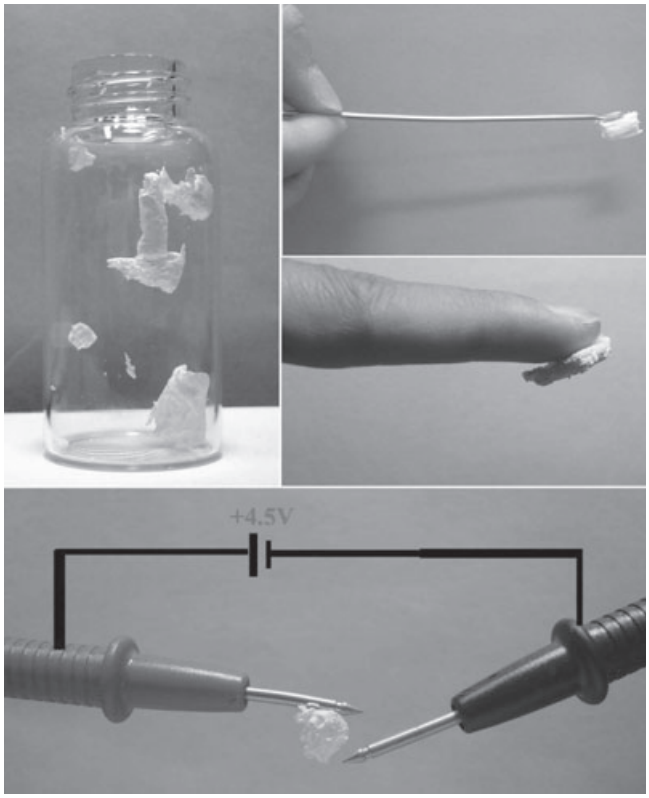

Figure 13.11 Electrostatic interactions in high-purity, multi-walled BNNTs synthesized by the developed CVD method: BNNTs can be attracted to glass, metal and even human skin and can also move to positive pole when subjected to an electric field. This implies a specific surface charge distribution in an ordered nanomaterials systems.

subjected to an electric field, the BN nanotubes moved towards a positive pole, implying a predominant electron distribution. The intrinsic electrostatic field at the BN nanotube surface should lead to the expected absorption and transfer; an example would be drug adsorption at the surface of nanotubes, followed by desorption from the surface to the cell, if the drug molecule/ion could be transferred electronically due to the difference in potential between the BN matrix and the cell.

Zhi studied the interaction between multiwalled BN nanotubes and DNA. As a natural biological polymer, the specific structure of DNA has inspired many biological applications. Aromatic nucleotide bases in single-stranded DNA (ssDNA) may be exposed to allow p-stacking interactions with the BN nanotube side-walls. This also may allow the dispersion of BN nanotubes in water. In fact, the covalent modification of multiwalled BN nanotubes and the dispersion in organic solvents was obtained [141]; more interestingly, the noncovalent functionalization in water due to the electrostatic interaction was also demonstrated [142]. A simple route, which is shown schematically in Figure 13.12, involves the sonication of BN nanotubes in solutions of denatured DNA, and led to the effective functionalization and strong interaction of DNA with the surface of BN nanotubes. These effects were identified by notable variations in color, as well as by microscopy and spectroscopy measurements [142]. The strong interactions between DNA and BN nanotubes allowed a nematic ordering of the BN nanotubes, as observed in this experiment, and implied a possible method for localizing BN nanotubes at specific areas, for example in cells undergoing pathological change (i.e., cancer cells).

As with the immobilization and conjugation of proteins with CNTs [143], the immobilization of ferritin proteins on BNNT surfaces has also been investigated, and targeted for various prospective medical and nanobiological applications [144]. The immobilization was thought to be due to carboxylation of the BN nanotube-bound amino groups, or to prominent tube–protein electrostatic interactions. The noncovalently functionalized BN nanotubes improved the efficiency of protein immobilization, while the electrical properties of the BN nanotubes were seen to be much more consistent and reproducible compared to CNTs.

The excellent results of these initial studies should stimulate the possible investigation of BN nanomaterials in the life sciences, based on their electronic noncovalent interactions. Further investigations will require the integration of BN nanotubes into medicines, together with the requisite chemical and biological analyses to assess any safety issues related not only to the human body but also to the environment.

13.4 Concluding Remarks

In this chapter we have presented – in historical sequence – details of the synthesis and characterization of spherical and 1-D BN nanomaterials. Despite the

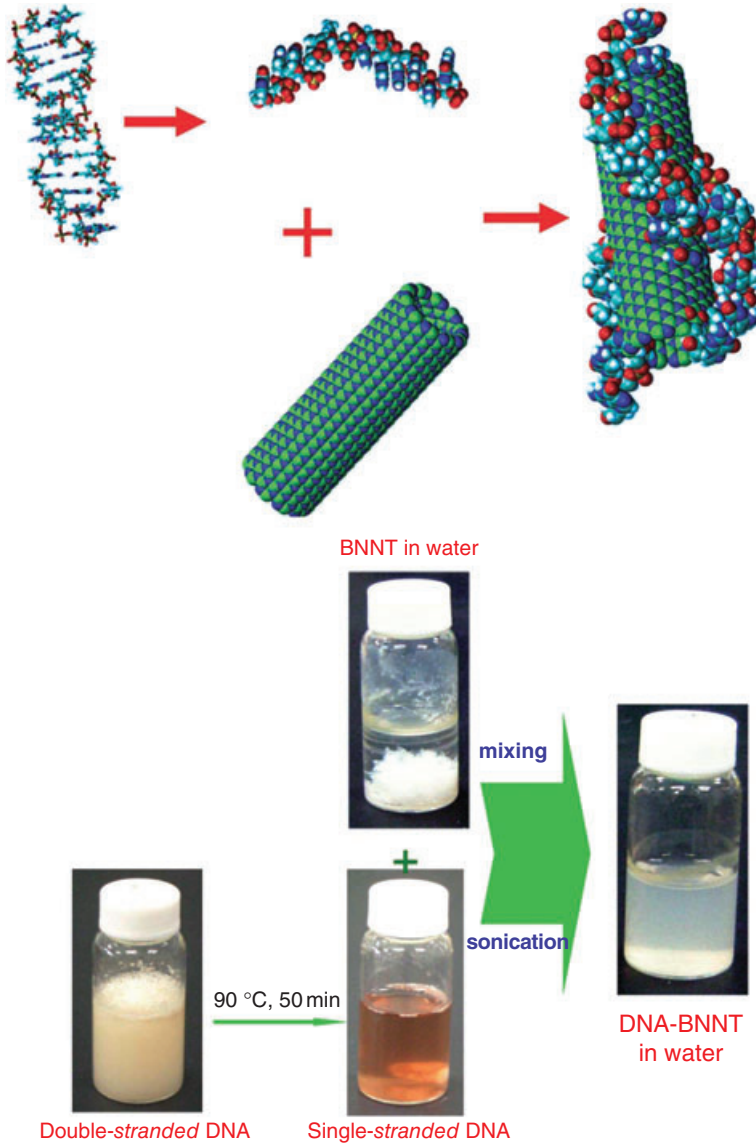

Figure 13.12 The process of fabrication of the DNA–BNNT hybrid. Reproduced with permission from Ref. [142]; © 2007, Wiley-VCH.

significant difficulties involved in the preparation and characterization of these materials, certain notable breakthroughs have been achieved. For a high-yield synthesis a CVD-modified procedure, using trimethoxyborane as a nontoxic and effective precursor, proved to be extremely effective. Investigations were also con-

ducted into the mechanism of formation of BN nanotubes, culminating in the laboratory-scale preparation of the multiwalled BN nanotubes that are vital in investigations of the properties and applications of these anisotropic nanomaterials. Collapsed BN nanotubes, with their large surface area and abundant 'dangling' bonds, have also be synthesized in a high-yield, while many intriguing areas have also been explored with regards to the mechanical, thermal, electronic and optical properties of these materials, as well as their future roles in gas absorption and in the life sciences.

Despite such progress, the challenge remains to create enhanced methods for the synthesis and characterization of BN nanomaterials, whether by developing new methods or by optimizing those already in existence. Additional problems to overcome will include an improved control of the synthesis of single-walled BN nanotubes, and the identification of new applications not only in the world of chemistry but also in the life sciences, such as cosmetics and drug transfer and release.

Acknowledgments

The authors are grateful to Drs Y. Bando, D. Golberg, Y. Uemura, R.Z. Ma, C.Y. Zhi, Q. Huang, J. Zhang, Y. Huang, T. Sato and F.F. Xu for their guidance, experimental contributions, stimulating discussions and technical support in the preparation of this chapter.

References

1 Palatnik, L.S., Gladkikh, L.I., Kolupaeva, Z.I. and Gabarak, M.N. (1985) Polymorphism of boron-nitride. *Inorganic Materials*, **21**, 1306–9.
2 Yoon, S.J. and Jha, J. (1995) Vapor-phase reduction and the synthesis of boron-based ceramics phase. 1. The phase-equilibria in the B-C-N-O system. *Journal of Materials Science*, **30**, 607–14.
3 Kroto, H.W., Heath, J.R., O'Brien, S.C., Curl, R.F. and Smalley, R.E. (1985) C_{60} buckminsterfullerene. *Nature*, **318**, 162–3.
4 Iijima, S. (1991) Helical microtubules of graphitic carbon. *Nature*, **354**, 56–8.
5 Crespi, V.H., Cohen, M.L. and Rubio, A. (1997) In situ band gap engineering of carbon nanotubes. *Physical Review Letters*, **79**, 2093–6.
6 Blase, X., Charlier, J.-C., De Vita, A. and Car, A. (1997) Theory of composite $B_xC_yN_z$ nanotube heterojunctions. *Applied Physics Letters*, **70**, 197–9.
7 Golberg, D., Bando, Y., Tang, C.C. and Zhi, C.Y. (2007) Boron nitride nanotubes. *Advanced Materials*, **19**, 2413–32.
8 Lindquist, D.A., Kodas, T.T., Smith, D.M., Xiu, X.M., Hietala, S.L. and Paine, R.T. (1991) Boron nitride powders formed by aerosol decomposition of poly(borazinylamine) solutions. *Journal of the American Ceramic Society*, **74**, 3126–8.
9 Iltis, A. and Maguier, C. (1990) European Patent 396448, 11 July.
10 Narula, C.K., Schaeffer, R. and Paine, R.T. (1987) Synthesis of boron-nitride ceramics from poly(borazinylamine) precursors. *Journal of the American Chemical Society*, **109**, 5556–7.
11 Narula, C.K., Schaeffer, R., Datye, A.K., Borek, T.T., Ropko, B.M. and Paine, R.T. (1990) Synthesis of boron-nitride

ceramics from oligomeric precursors derived from 2-(dimethylamino)-4,6-dichloroborazine. *Chemistry of Materials*, **2**, 384–9.

12 Ishii, T., Sato, T., Sekikawa, Y. and Iwata, M. (1981) Growth of whiskers of hexagonal boron-nitride. *Journal of Crystal Growth*, **52**, 285–9.

13 Pruss, E.A., Wood, G.L., Kroenke, W.J. and Paine, R.T. (2000) Aerosol assisted vapor synthesis of spherical boron nitride powders. *Chemistry of Materials*, **12**, 19–21.

14 Wood, G.L. and Paine, R.T. (2006) Aerosol synthesis of hollow spherical morphology boron nitride particles. *Chemistry of Materials*, **18**, 4716–18.

15 Wood, G.L., Janik, J.F., Visi, M.Z., Schubert, D.M. and Paine, R.T. (2005) New borate precursors for boron nitride powder synthesis. *Chemistry of Materials*, **17**, 1855–9.

16 Brozek, V. and Hubacek, M. (1992) A contribution to the crystallochemistry of boron-nitride. *Journal of Solid State Chemistry*, **100**, 120–9.

17 Tang, C., Bando, Y. and Golberg, D. (2002) Large-scale synthesis and structure of boron nitride sub-micron spherical particles. *Chemical Communications*, 2826–7.

18 Thomas, J., Weston, N.E. and O'Connor, T.E. (1962) Turbostratic boron nitride, thermal transformation to ordered-layer-lattice boron nitride. *Journal of the American Chemical Society*, **84**, 4619.

19 Choi, H.C., Bae, S.Y., Jang, W.S., Park, J., Song, H.J. and Shin, H.J. (2005) X-ray absorption near edge structure study of BN nanotubes and nanothorns. *The Journal of Physical Chemistry B*, **109**, 7007–11.

20 Wood, G.L., Janik, J.F., Pruss, E.A., Dreissig, D., Kroenke, W.J., Habereder, T., Noth, H. and Paine, R.T. (2006) Aerosol synthesis of spherical morphology boron nitride powders from organoborate precursors. *Chemistry of Materials*, **18**, 1434–42.

21 Jensen, F. and Toftlund, H. (1993) Structure and stability of C_{24} and $B_{12}N_{12}$ isomers. *Chemical Physics Letters*, **201**, 89–96.

22 Boulanger, L., Andriot, B., Cauchetier, M. and Willaime, F. (1995) Concentric shelled and plate-like graphitic boron-nitride nanoparticles produced by CO_2-laser pyrolysis. *Chemical Physics Letters*, **234**, 227–32.

23 Banhart, F., Zwanger, M. and Muhr, H.-J. (1994) The formation of curled concentric-shell clusters in boron-nitride under electron-irradiation. *Chemical Physics Letters*, **231**, 98–104.

24 Wang, J.B., Zhong, X.L., Zhang, C.Y., Huang, B.Q. and Yang, G.W. (2003) Explosion phase formation of nanocrystalline boron nitrides upon pulsed-laser-induced liquid/solid interfacial reaction. *Journal of Materials Research*, **18**, 2774–8.

25 Oku, T., Hirano, T., Kuno, M., Kusunose, T., Niihara, K. and Suganuma, K. (2000) Synthesis, atomic structures and properties of carbon and boron nitride fullerene materials. *Materials Science and Engineering B*, **74**, 206–17.

26 Zhu, Y.C., Bando, Y., Yin, L.W. and Golberg, D. (2004) Hollow boron nitride (BN) nanocages and BN-nanocage-encapsulated nanocrystals. *Chemistry – A European Journal*, **10**, 3667–72.

27 Shi, L., Gu, Y.L., Chen, L.Y., Qian, Y.T., Yang, Z.H. and Ma, J.H. (2004) Synthesis and morphology control of nanocrystalline boron nitride. *Journal of Solid State Chemistry*, **177**, 721–4.

28 Xu, L.Q., Peng, Y.Y., Meng, Z.Y., Wang, D.B., Zhang, W.Q. and Qian, Y.T. (2003) Fabrication and characterization of hollow spherical boron nitride powders. *Chemical Physics Letters*, **381**, 74–9.

29 Blasé, X., Rubio, A., Louie, S.G. and Cohen, M.L. (1994) Stability and band-gap constancy of boron-nitride nanotubes. *Europhysics Letters*, **28**, 335–40.

30 Rubio, A., Corkill, J. and Cohen, M.L. (1994) Theory of graphitic boron-nitride nanotubes. *Physical Review B*, **49**, 5081–4.

31 Saito, R., Fujita, M., Dresselhaus, G. and Dresselhaus, M.S. (1992) Electronic-structure of graphene tubules based on C_{60}. *Physical Review B*, **46**, 1804–11.

32 Chopra, N.G., Luyken, R.J., Cherrey, K., Crespi, V.H., Cohen, M.L., Louie, S.G. and Zettl, A. (1995) Boron-nitride nanotubes. *Science*, **269**, 966–7.

33 Terrones, M., Hsu, W.K., Terrones, H., Zhang, J.P., Ramos, S., Hare, J.P., Castillo, R., Prassides, K., Cheetham, A.K., Kroto, H.W. and Walton, D.R.M. (1996) Metal particle catalysed production of nanoscale BN structures. *Chemical Physics Letters*, **259**, 568–73.

34 Laude, T., Matsui, Y., Marraud, A. and Jouffrey, B. (2000) Long ropes of boron nitride nanotubes grown by a continuous laser heating. *Applied Physics Letters*, **76**, 3239–41.

35 Ma, R.Z., Bando, Y., Sato, T. and Kurashima, K. (2001) Thin boron nitride nanotubes with unusual large inner diameters. *Chemical Physics Letters*, **350**, 434–40.

36 Han, W., Bando, Y., Kurashima, K. and Sato, T. (1998) Synthesis of boron nitride nanotubes from carbon nanotubes by a substitution reaction. *Applied Physics Letters*, **73**, 3085–7.

37 Shelimov, K.B., Davydov, D.N. and Moskovits, M. (2000) Template-grown high-density nanocapacitor arrays. *Applied Physics Letters*, **77**, 1722–4.

38 Gleize, P., Herreyre, S., Gadelle, P., Mermoux, M., Cheynet, M.C. and Abello, L. (1994) Characterization of tubular boron-nitride filaments. *Journal of Materials Science Letters*, **13**, 1413–15.

39 Hamilton, E.J.M., Dolan, S.E., Mann, C. E., Colijin, H.O., McDonald, C.A. and Shore, S.G. (1993) Preparation of amorphous boron-nitride and its conversion to a turbostratic, tubular form. *Science*, **260**, 659–61.

40 Loiseau, A., Willaime, F., Demoncy, N., Hug, G. and Pascard, H. (1996) Boron nitride nanotubes with reduced numbers of layers synthesized by arc discharge. *Physical Review Letters*, **76**, 4737–40.

41 Saito, Y. and Maida, M. (1999) Square, pentagon, and heptagon rings at BN nanotube tips. *The Journal of Physical Chemistry A*, **103**, 1291–3.

42 Golberg, D., Bando, Y., Eremets, M., Takemura, K., Kurashima, K. and Yusa, H. (1996) Nanotubes in boron nitride laser heated at high pressure. *Applied Physics Letters*, **69**, 2045–7.

43 Hu, L., Li, Y.X., Ding, X.X., Tang, C. and Qi, S.R. (2004) Insight into carbon nanotubes-template reaction at high temperature. *Chemical Physics Letters*, **397**, 271–6.

44 Golberg, D., Bando, Y., Kurashima, K. and Sato, T. (2000) MoO_3-promoted synthesis of multi-walled BN nanotubes from C nanotube templates. *Chemical Physics Letters*, **323**, 185–91.

45 Golberg, D., Han, W., Bando, Y., Bourgeois, L., Kurashima, K. and Sato, T. (1999) Fine structure of boron nitride nanotubes produced from carbon nanotubes by a substitution reaction. *Journal of Applied Physics*, **86**, 2364–6.

46 Han, W.Q., Bourgeois, L., Bando, Y., Kurashima, K. and Sato, T. (2000) Formation and structure of boron nitride conical nanotubes. *Applied Physics A*, **71**, 83–5.

47 Bourgeois, L., Bando, Y., Han, W.Q. and Sato, T. (2000) Structure of boron nitride nanoscale cones: ordered stacking of 240 degrees and 300 degrees disclinations. *Physical Review B*, **61**, 7686–91.

48 Chen, Y., Gerald, J.F., Williams, J.S. and Bulcock, S. (1999) Synthesis of boron nitride nanotubes at low temperatures using reactive ball milling. *Chemical Physics Letters*, **299**, 260–4.

49 Gleize, P., Schouler, M.C., Gadelle, P. and Caillet, M. (1994) Growth of tubular boron-nitride filaments. *Journal of Materials Science*, **29**, 1575–80.

50 Sen, R., Satishkumar, B.C., Govindaraj, A., Harikumar, K.R., Raina, G., Zhang, J.P., Cheetham, A.K. and Rao, C.N.R. (1998) B-C-N, C-N and B-N nanotubes produced by the pyrolysis of precursor molecules over Co catalysts. *Chemical Physics Letters*, **287**, 671–6.

51 Bourgeois, L., Bando, Y. and Sato, T. (2000) Tubes of rhombohedral boron nitride. *Journal of Physics D: Applied Physics*, **22**, 1902–8.

52 Lourie, O.R., Jones, C.R., Bartlett, B.M., Gibbons, P.C., Ruoff, R.S. and Buhro, W.E. (2000) CVD growth of boron nitride nanotubes. *Chemistry of Materials*, **12**, 1808–10.

53 Ma, R., Bando, Y. and Sato, T. (2001) CVD synthesis of boron nitride nanotubes without metal catalysts. *Chemical Physics Letters*, **337**, 61–4.

54 Ma, R., Bando, Y., Sato, T. and Kurashima, K. (2001) Growth, morphology, and structure of boron nitride nanotubes. *Chemistry of Materials*, **13**, 2965–71.

55 Cumings, J. and Zettl, A. (2000) Mass-production of boron nitride double-wall nanotubes and nanococoons. *Chemical Physics Letters*, **316**, 211–16.

56 Han, W.Q., Mickelson, W., Cumings, J. and Zettl, A. (2002) Transformation of $B_xC_yN_z$ nanotubes to pure BN nanotubes. *Applied Physics Letters*, **81**, 1110–12.

57 Suenaga, K., Willaime, F., Loiseau, A. and Colliex, C. (1999) Organisation of carbon and boron nitride layers in mixed nanoparticles and nanotubes synthesised by arc discharge. *Applied Physics A*, **68**, 301–8.

58 Tang, C., Bando, Y., Sato, T. and Kurashima, K. (2002) A novel precursor for synthesis of pure boron nitride nanotubes. *Chemical Communications*, 1290–1.

59 Searcy, A.W. and Myers, C.E. (1957) The heat of sublimation of boron and the gaseous species of the boron-boric oxide system. *The Journal of Physical Chemistry*, **61**, 957–60.

60 Tang, C.C., Bando, Y. and Golberg, D. (2004) Multiwalled BN nanotubes synthesized by carbon-free method. *Journal of Solid State Chemistry*, **177**, 2670–4.

61 Tang, C.C., de la Chapelle, M.L., Li, P., Liu, Y.M., Dang, H.Y. and Fan, S.S. (2001) Catalytic growth of nanotube and nanobamboo structures of boron nitride. *Chemical Physics Letters*, **342**, 492–6.

62 Tang, C.C., Ding, X.X., Huang, X.T., Gan, Z.W., Qi, S.R., Liu, W. and Fan, S. S. (2002) Effective growth of boron nitride nanotubes. *Chemical Physics Letters*, **356**, 254–8.

63 Tang, C.C., Bando, Y. and Sato, T. (2002) Catalytic growth of boron nitride nanotubes. *Chemical Physics Letters*, **362**, 185–9.

64 Yuan, S.D., Ding, X.X., Huang, Z.X., Huang, X.T., Gan, Z.W., Tang, C. and Qi, S.R. (2003) Synthesis of BN nanobamboos and nanotubes from barium metaborate. *Journal of Crystal Growth*, **256**, 67–72.

65 Huo, K.F., Hu, Z., Fu, J.J., Xu, H., Wang, X.Z., Chen, Y. and Lv, Y.N. (2003) Microstructure and growth model of periodic spindle-unit BN nanotubes by nitriding Fe-B nanoparticles with nitrogen/ammonia mixture. *The Journal of Physical Chemistry B*, **107**, 11316–20.

66 Tang, C.C., Bando, Y. and Sato, T. (2002) Synthesis and morphology of boron nitride nanotubes and nanohorns. *Applied Physics A*, **75**, 681–5.

67 Chen, X., Gao, X.P., Zhang, H., Zhou, Z., Hu, W.K., Pan, G.L., Zhu, H.Y., Yan, T. Y. and Song, D.Y. (2005) Preparation and electrochemical hydrogen storage of boron nitride nanotubes. *The Journal of Physical Chemistry B*, **109**, 11525–9.

68 Terauchi, M., Tanaka, M., Suzuki, K., Ogino, A. and Kimura, K. (2000) Production of zigzag-type BN nanotubes and BN cones by thermal annealing. *Chemical Physics Letters*, **324**, 359–64.

69 Shelimov, K.B. and Moskivits, M. (2000) Composite nanostructures based on template-crown boron nitride nanotubules. *Chemistry of Materials*, **12**, 250–4.

70 Xu, L.Q., Peng, Y.Y., Meng, Z.Y., Yu, W.C., Zhang, S.Y., Liu, X.M. and Qian, Y. T. (2003) A co-pyrolysis method to boron nitride nanotubes at relative low temperature. *Chemistry of Materials*, **15**, 2675–80.

71 Chen, X., Wang, X., Liu, J., Wang, Z. and Qian, Y. (2005) A reduction-nitridation route to boron nitride nanotubes. *Applied Physics A*, **81**, 1035–7.

72 Ma, R.Z., Goldberg, D., Bando, Y. and Sasaki, T. (2004) Syntheses and properties of B-C-N and BN nanostructures. *Philosophical Transactions of the Royal Society of London. Series A*, **362**, 2161–86.

73 Wang, J.S., Kayastha, V.K., Yap, Y.K., Fan, Z.Y., Lu, J.G., Pan, Z.W., Ivanov, I. N., Puretzky, A.A. and Geohegan, D.B. (2005) Low temperature growth of boron nitride nanotubes on substrates. *Nano Letters*, **5**, 2528–32.

74 Dai, J., Xu, L.Q., Fang, Z., Sheng, D., Guo, Q., Ren, Z., Wang, K. and Qian, Y. (2007) A convenient catalytic approach to synthesize straight boron nitride nanotubes using synergic nitrogen

source. *Chemical Physics Letters*, **440**, 253–8.

75 Thess, A., Lee, R., Nikolaev, P., Dai, H., Petii, P., Robert, J., Xu, C., Lee, Y.H., Kim, S.G., Rinzler, A.G., Colbert, D.T., Scuseria, G.E., Tomanek, D., Fischer, J.E. and Smalley, R.E. (1996) Crystalline ropes of metallic carbon nanotubes. *Science*, **273**, 483–7.

76 Yu, D.P., Sun, X.S., Lee, C.S., Bello, I., Lee, S.T., Gu, H.D., Leung, K.M., Zhou, G.W., Dong, Z.F. and Zhang, Z. (1998) Synthesis of boron nitride nanotubes by means of excimer laser ablation at high temperature. *Applied Physics Letters*, **72**, 1966–8.

77 Saito, Y., Maida, M. and Matsumoto, T. (1999) Structures of boron nitride nanotubes with single-layer and multilayers produced by arc discharge. *Japanese Journal of Applied Physics*, **38**, 159–63.

78 Golberg, D., Bando, Y., Bourgeois, L., Kurashima, K. and Sato, T. (2000) Insights into the structure of BN nanotubes. *Applied Physics Letters*, **77**, 1979–81.

79 Demczyk, B.G., Cumings, J., Zettl, A. and Ritchie, R.O. (2001) Structure of boron nitride nanotubules. *Applied Physics Letters*, **78**, 2772–4.

80 Bengu, E. and Marks, L.D. (2001) Single-walled BN nanostructures. *Physical Review Letters*, **86**, 2386–9.

81 Alexandre, S.S., Chacham, H. and Nunes, R.W. (2001) Structure and energetics of boron nitride fullerenes: the role of stoichiometry. *Physical Review B*, **63**, 045402.

82 Lee, R.S., Gavillet, J., Lamy de la Chapelle, M., Loiseau, A., Cochon, J.L., Pigache, D., Thibault, J. and Willaime, F. (2001) Catalyst-free synthesis of boron nitride single-wall nanotubes with a preferred zig-zag configuration. *Physical Review B*, **64**, 121405.

83 Arenal, R., Stephan, O., Cochon, J. and Loiseau, A. (2007) Root-growth mechanism for single-walled boron nitride nanotubes in laser vaporization technique. *Journal of the American Chemical Society*, **129**, 16183–9.

84 Tang, C.C., Bando, Y., Ding, X.X., Qi, S.R. and Golberg, D. (2002) Catalyzed collapse and enhanced hydrogen storage of BN nanotubes. *Journal of the American Chemical Society*, **124**, 14550–1.

85 Tang, C.C., Bando, Y., Shen, G.Z., Zhi, C.Y. and Golberg, D. (2006) Single-source precursor for chemical vapour deposition of collapsed boron nitride nanotubes. *Nanotechnology*, **17**, 5882–8.

86 Gobbels, D. and Meyer, G. (2002) Production and decomposition of $(NH_4)[BF_4]$ and H_3N-BF3. *Zeitschrift für Anorganische und Allgemeine*, **628**, 1799–805.

87 Economy, J. and Anderson, R.V. (1967) Boron nitride fibers. *Journal of Polymer Science, C*, **19**, 283.

88 Highsmit, R.E., Mason, J.H. and Economy, J. (1971) BN Fiberboard – New form of boron nitride. *American Ceramic Society Bulletin*, **50**, 452.

89 Lindquist, D.A., Janik, J.F., Datye, A.K. and Paine, R.T. (1992) Boron-nitride fibers processed from poly(borazinylamine) solutions. *Chemistry of Materials*, **4**, 17–19.

90 Kimura, Y., Kubo, Y. and Hayashi, N. (1994) High-performance boron-nitride fibers from poly(borazine) preceramics. *Composites Science and Technology*, **51**, 173–9.

91 Toury, B., Bernard, S., Cornu, D., Chassagneux, F., L'étoffe, J.-M. and Miele, P. (2003) High-performance boron nitride fibers obtained from asymmetric alkylaminoborazine. *Journal of Materials Chemistry*, **13**, 274–9.

92 Toutois, P., Miele, P., Jacques, S., Cornu, D. and Bernard, S. (2006) Structural and mechanical behavior of boron nitride fibers derived from poly [(methylamino) borazine] precursors: optimization of the curing and pyrolysis procedures. *Journal of the American Ceramic Society*, **89**, 42–9.

93 Huo, K.F., Hu, Z., Chen, F., Fu, J.J., Chen, Y., Liu, B.H., Ding, J., Dong, Z.L. and White, T. (2002) Synthesis of boron nitride nanowires. *Applied Physics Letters*, **80**, 3611–13.

94 Deepak, F.L., Vinod, C.P., Mukhopadhyay, K., Govindaraj, A. and Rao, C.N.R. (2002) Boron nitride nanotubes and nanowires. *Chemical Physics Letters*, **353**, 345–52.

95 Wagner, R.S. and Ellis, W.C. (1964) Vapor-liquid-solid mechanism of single crystal growth. *Applied Physics Letters*, **4**, 89.

96 Morales, A.M. and Lieber, C.M. (1998) A laser ablation method for the synthesis of crystalline semiconductor nanowires. *Science*, **279**, 208–11.

97 Zhang, H.Z., Yu, J., Chen, Y. and Gerald, J.F. (2006) Conical boron nitride nanorods synthesized via the ball-milling and annealing method. *Journal of the American Ceramic Society*, **89**, 675–9.

98 Chen, Y.J., Chi, B., Mahon, D.C. and Chen, Y. (2006) An effective approach to grow boron nitride nanowires directly on stainless-steel substrates. *Nanotechnology*, **17**, 2942–6.

99 Zhang, H.Z., FitzGerald, J.D., Chadderton, L.T., Yu, J. and Chen, Y. (2006) Growth and structure of prismatic boron nitride nanorods. *Physical Review B*, **74**, 045407.

100 Tang, D.M., Liu, C. and Cheng, H.M. (2007) Controlled synthesis of quasi-one-dimensional boron nitride nanostructures. *Journal of Materials Research*, **22**, 2809–16.

101 Chen, Y.J., Zhang, H.Z. and Chen, Y. (2006) Pure boron nitride nanowires produced from boron triiodide. *Nanotechnology*, **17**, 786–9.

102 Komatsu, S., Kazami, D., Tanaka, H., Shimizu, Y., Moriyoshi, Y., Shiratani, M. and Okada, K. (2006) *Applied Physics Letters*, **88**, 151914.

103 Lin, L.X., Zheng, Y., Li, Z.H., Shen, X.N. and Wei, K.M. (2007) A simple method to synthesize polyhedral hexagonal boron nitride nanofibers. *Solid State Sciences*, **9**, 1099–104.

104 Ma, J.H., Li, J., Li, G.X., Tian, Y.G., Zhang, J., Wu, J.F., Zheng, J.Y., Zhuang, H.M. and Pan, T.H. (2007) One simple synthesis route to whisker-like nanocrystalline boron nitride by the reaction of $NaBH_4$ and NaN_3. *Materials Research Bulletin*, **42**, 982–8.

105 Tang, C.C. and Bando, Y. (2003) Effect of BN coatings on oxidation resistance and field emission of SiC nanowires. *Applied Physics Letters*, **83**, 659–61.

106 Cumings, J. and Zettl, A. (2001) *Electronic Properties of Molecular Nanostructures*, AIP Conference Proceedings Series, American Institute of Physics, New York, p. 577.

107 Tang, C.C., Bando, Y., Huang, Y., Yue, S.L., Gu, C.Z., Xu, F.F. and Golberg, D. (2005) Fluorination and electrical conductivity of BN nanotubes. *Journal of the American Chemical Society*, **127**, 6552–3.

108 Xiang, H.J., Yang, J.L., Hou, J.G. and Zhu, Q.S. (2005) Are fluorinated boron nitride nanotubes n-type semiconductors? *Applied Physics Letters*, **87**, 243113.

109 Liu, H.T., Zhou, G., Yan, Q.M., Wu, J., Gu, B.L. and Duan, W.H. (2007) Structural and electronic properties of fluorinated double-walled boron nitride nanotubes: effect of interwall interaction. *Physical Review B*, **75**, 125410.

110 Lai, L., Song, W., Lu, J., Gao, Z.X., Nagase, S., Ni, M., Mei, W.N., Liu, J.J., Yu, D.P. and Ye, H.Q. (2006) Structural and electronic properties of fluorinated boron nitride nanotubes. *The Journal of Physical Chemistry B*, **110**, 14092–7.

111 Kim, Y.-H., Chang, K.J. and Louie, S.G. (2001) Electronic structure of radially deformed BN and BC3 nanotubes. *Physical Review B*, **63**, 205408.

112 Ishigami, M., Sau, J.D., Aloni, S., Cohen, M.L. and Zettl, A. (2005) Observation of the giant stark effect in boron-nitride nanotubes. *Physical Review Letters*, **94**, 056804.

113 Kral, P., Mele, E.J. and Tomanek, D. (2000) Photogalvanic effects in heteropolar nanotubes. *Physical Review Letters*, **85**, 1512–15.

114 Mele, E.J. and Kral, P. (2002) Electric polarization of heteropolar nanotubes as a geometric phase. *Physical Review Letters*, **88**, 056803.

115 Bai, X.D., Golberg, D., Bando, Y., Zhi, C.Y., Tang, C. and Mitome, M. (2007) Deformation-driven electrical transport of individual boron nitride nanotubes. *Nano Letters*, **7**, 632–7.

116 Berber, S., Kwon, Y.K. and Tomanek, D. (2000) Unusually high thermal conductivity of carbon nanotubes. *Physical Review Letters*, **84**, 4613–16.

117 Che, J.W., Cagin, T. and Goddard, W.A. (2000) Unusually high thermal

conductivity of carbon nanotubes. *Nanotechnology*, **11**, 65–9.

118 Hone, J., Whitney, M., Piskoti, C. and Zettl, A. (1999) Thermal conductivity of single-walled carbon nanotubes. *Physical Review B*, **59**, R2514.

119 Yi, W., Lu, L., Zhang, D.L., Pan, Z.W. and Xie, S.S. (1999) Linear specific heat of carbon nanotubes. *Physical Review B*, **59**, R9015.

120 Hone, J., Liaguno, M.C., Nemes, N.M., Johnson, A.T., Fischer, J.E., Walters, D. A., Casavant, M.J., Schmidt, J. and Smalley, R.E. (2000) Electrical and thermal transport properties of magnetically aligned single wall carbon nanotube films. *Applied Physics Letters*, **77**, 666–8.

121 Kim, P., Shi, L., Majumdar, A. and McEuen, P.L. (2001) Thermal transport measurements of individual multiwalled nanotubes. *Physical Review Letters*, **87**, 215502.

122 Yang, D.J., Zhang, Q., Chen, G., Yoon, S.F., Ahn, J., Wang, S.G., Zhou, Q., Wang, Q. and Li, J.Q. (2002) Thermal conductivity of multiwalled carbon nanotubes. *Physical Review B*, **66**, 165440.

123 Gao, X.Q., Liu, L., Guo, Q.G., Shi, J.L. and Zhai, G.T. (2005) Fabrication and mechanical/conductive properties of multi-walled carbon nanotube (MVNT) reinforced carbon matrix composites. *Material Letters*, **59**, 3062–5.

124 Liu, C.H., Huang, H., Wu, Y. and Fan, S.S. (2004) Thermal conductivity improvement of silicone elastomer with carbon nanotube loading. *Applied Physics Letters*, **84**, 4248–50.

125 Biercuk, M.J., Liaguno, M.C., Radosavijevic, M., Hyun, J.K., Johnson, A.T. and Fischer, J.E. (2002) Carbon nanotube composites for thermal management. *Applied Physics Letters*, **80**, 2767–9.

126 Yum, K. and Yu, M.-F. (2006) Measurement of wetting properties of individual boron nitride nanotubes with the Wilhelmy method using a nanotube-based force sensor. *Nano Letters*, **6**, 329–33.

127 Chang, C.W., Okawa, D., Majumdar, A. and Zettl, A. (2006) Solid-state thermal rectifier. *Science*, **314**, 1121–3.

128 Tang, C.C., Bando, Y., Liu, C.H., Fan, S. S., Zhang, J., Ding, X.X. and Golberg, D. (2006) Thermal conductivity of nanostructured boron nitride materials. *The Journal of Physical Chemistry B*, **110**, 10354–7.

129 Hernandez, E., Goze, C., Bernier, P. and Rubio, A. (1998) Elastic properties of C and $B_xC_yN_z$ composite nanotubes. *Physical Review Letters*, **80**, 4502–5.

130 Kudin, K.N., Scuseria, G.E. and Yakobson, B.I. (2001) C_2F, BN, and C nanoshell elasticity from ab initio computations. *Physical Review B*, **64**, 235406.

131 Dumitrica, T., Bettinger, H.F., Scuseria, G. and Yakobson, B.I. (2003) Thermodynamics of yield in boron nitride nanotubes. *Physical Review B*, **68**, 085412.

132 Chopra, N.G. and Zettl, A. (1998) Measurement of the elastic modulus of a multi-wall boron nitride nanotube. *Solid State Communications*, **105**, 297–300.

133 Suryavanshi, A.P., Yu, M.-F., Wen, J.G., Tang, C.C. and Bando, Y. (2004) Elastic modulus and resonance behavior of boron nitride nanotubes. *Applied Physics Letters*, **84**, 2527–9.

134 Golberg, D., Bai, X.D., Mitome, M., Tang, C., Zhi, C.Y. and Bando, Y. (2007) Structural peculiarities of in situ deformation of a multi-walled BN nanotube inside a high-resolution analytical transmission electron microscope. *Acta Materialia*, **55**, 1293–8.

135 Huang, Q., Bando, Y., Xu, X., Nishimura, T., Zhi, C.Y., Tang, C.C., Xu, F.F., Gao, L. and Golberg, D. (2007) Enhancing superplasticity of engineering ceramics by introducing BN nanotubes. *Nanotechnology*, **18**, 485706.

136 Ma, R.Z., Bando, Y., Zhu, H.W., Sato, T., Xu, C.L. and Wu, D.H. (2002) Hydrogen uptake in boron nitride nanotubes at room temperature. *Journal of the American Chemical Society*, **124**, 7672–3.

137 Wu, X.J., Yang, J.L. and Zeng, X.C. (2006) Adsorption of hydrogen molecules on the platinum-doped boron nitride nanotubes. *The Journal of Chemical Physics*, **125**, 044704.

138 Shevlin, S.A. and Guo, Z.X. (2006) Transition-metal-doping-enhanced

hydrogen storage in boron nitride systems. *Applied Physics Letters*, **89**, 153104.

139 Zettl, A. (1996) Non-carbon nanotubes. *Advanced Materials*, **8**, 443.

140 Politzer, P., Lane, P., Murray, J.S. and Concha, M.C. (2005) Comparative analysis of surface electrostatic potentials of carbon, boron/nitrogen and carbon/boron/nitrogen model nanotubes. *Journal of Molecular Modeling*, **11**, 1–7.

141 Zhi, C.Y., Bando, Y., Tang, C., Honda, S., Sato, K., Kuwahara, H. and Golberg, D. (2005) Characteristics of Boron nitride nanotube-polyaniline composites. *Angewandte Chemie–International Edition*, **44**, 7929–32.

142 Zhi, C.Y., Bando, Y., Wang, W.L., Tang, C.C., Kuwahara, H. and Golberg, D. (2007) DNA-mediated assembly of boron nitride nanotubes. *Chemistry–An Asian Journal*, **2**, 1581–5.

143 Pantarotto, D., Partidos, C.D., Graff, R., Briand, J., Oebeke, J., Prato, M. and Bianco, A. (2003) Synthesis, structural characterization, and immunological properties of carbon nanotubes functionalized with peptides. *Journal of the American Chemical Society*, **125**, 6160–1.

144 Zhi, C.Y., Bando, Y., Tang, C. and Golberg, D. (2005) Immobilization of proteins on boron nitride nanotubes. *Journal of the American Chemical Society*, **127**, 17144–5.

Abstract

In this chapter we describe the recent achievements in the synthesis and characterization of boron nitride (BN) nanomaterials with spherical and anisotropic (nanotube and nanowire) structures, and pay special attention to the methods of their preparation and mechanisms of formation. In particular, the latest breakthroughs in the investigation of spherical structures and the synthetic difficulties are highlighted. A wide range of potential uses for these materials, involving their mechanical, thermal, chemical, electric and gas absorption properties are also outlined, together with details of applications in the life sciences, based on recent pioneering studies of the interaction of BN nanotubes with biomolecules.

Keywords

boron nitride; nanomaterials; nanotube; nanowire; structures; synthesis; biomolecules.

Index

1-D bimetallic heteronanostructures 174–179
3-D mesoscale bimetallic patterning 185–188

a
absorbance-based biosensing 37–38
absorption coefficients, Mie theorie 5
Ag-core/Au-shell nanoparticles 198–201
Ag-shell nanoparticles 201–204
agents, therapy 29–31
alloy metal nanoparticles, silica-coated 354–355
alloy nanomaterials
– and drug delivery 382
– aspect ratio 378
– bioimaging (magnetic resonance imaging) 381–382
– characterization using X-ray absorption spectroscopy 377–400
– EXAFS 380, 392–393, 396–397
– particle size, shape and aspect ratio measurements 387–388
– TEM 379–380
– XAS methods 389–390
– XRD 379
alloy nanostructures 179–185
alloys, profunctional bimetallic 224–229
amperometric immunosensor 202
anisotropic bimetallic nanomaterials, biofunctionalization 197–240
anisotropic bimetallic nanoparticles, synthesis and functionalization 45–48
anisotropic boron nitride nanomaterials 463–489
– collapsed nanotubes 478–479
– electrical properties 484
– high-temperature chemical inertness 484
– high thermal conductivity 485
– hydrogen storage 487
– life science applications 487–488
– mechanical properties 486
– multiwalled nanotubes 470–475
– nanowires 480–482
– properties and applications 483–488
– single-walled nanotubes 476–477
– spherical particles 464–469
– synthesis 464–482
anisotropic metallic NSET biosensors 103–139
anisotropic oxide nanomaterials, life sciences 45–56
anisotropically shaped nanoparticles, nanorods and nanowires 209–224
anode catalysts, biofuel cells 90–91
antibody conjugation 204
aqueous-phase synthesis 248–255
aspect ratio, core-shell nanomaterials 378
Au–Ag nanocomposites, TEM images 249
Au–Ag nanoparticles, TEM images 46
Au_{core}/Ag_{shell} nanoparticles 201–204
Au nanoparticles, in hollow silica spherical structures 363–366
Au_{shell} nanoparticles 198–201
Au@Pd nanocubes 174
Au–Pt nanomaterials
– biofuel cell applications 79–91
– electrocatalytic oxidation of D-(+)-glucose 73–76
– glucose oxidation 70–84

Nanomaterials for the Life Sciences Vol. 3: Mixed Metal Nanomaterials. Edited by Challa S. S. R. Kumar

ISBN: 978-3-527-32153-7

– oxygen reduction reaction 58–63
– synthesis and structural properties 71–72
Au-silica core-shell nanoparticles, tem images 164

b
bacteria, detection by nanorods 271
bilirubin oxidase, oxygen reduction 66–70
bimetallic alloys
– nanostructures 179–185
– *see also* profunctional bimetallic alloys
bimetallic core-shell nanostructures 164–174
bimetallic heteronanostructures 174–179
bimetallic nanomaterials
– anisotropic 45–54, 209–223
– biofunctionalization 197–240
– biosensing 48
– encapsulated 225–228
– functionalization 45–47
– gene delivery 49–51
– imaging 49
– life sciences 48–54
– spherical 198–208
– synthesis 45–47
– vaccine applications 52–53
bimetallic nanoparticles
– dendrimer-encapsulated 225–228
– spherical core-shell bimetallic 198–209
– surface and core composition analysis 391
– synthesis and functionalization 45–48
bimetallic nanorods 45–46, 243–245, 248–250
– aqueous-phase synthesis 248–249
– organic-phase synthesis 243–244
bimetallic nanostructures 164–185
– biofunctionalization 206–209
– core-shell 164–174
– life sciences 161–196
bimetallic nanowires 47
bimetallic patterning, mesoscale 185–188
bimetallic/trimetallic oxide nanorods, aqueous-phase synthesis 252–253
biofuel cells
– Au–Pt nanomaterials 79–91
– glucose/oxygen 85–91
bioimaging, core-shell nanomaterials 381–382
biological detection, nanotechnology promises 105
biomolecular delivery vehicles, core-shell nanomaterials 319
biomolecule (protein) core–polymer shell core-shell nanoparticles 304
biosensors 48–49, 103–139
– absorbance-based 37
– gold nanoshell-based 35–37, 129–130
– SERS 37
BNN, hexagonal *see* hexagonal boron nitride nanomaterials
borazinic precursors, direct pyrolyzing 439
boron nitride nanomaterials (BNN)
– anisotropic *see* anisotropic boron nitride nanomaterials
– hexagonal *see* hexagonal boron nitride nanomaterials

c
cancer cells
– detection by NSET 128–129
– prostatic 30
cancer detection
– in vitro 26–27
– in vivo 28, 31–33
cancer imaging 29–31
– and therapy agents 29
cancer therapy, BNN application 449
carbon-containing core-shell nanomaterials 313–315
carbon nanotubes-substitution reaction, nanotube synthesis 420–425
carbon template-substitution reaction 441–442
catalysis
– core-shell nanomaterials 319
– heterogeneous photo- 141–150
catalysts
– biofuel cell applications 57–103
– efficiency 75–76
– electrocatalytic oxidation 73–77
– surface characterization 74–75
catalyzation
– bilirubin oxidase 66–70
– glucose oxidation 78–85
– laccase 64–66
CD8 responses, ovalbumin-specific 53
cell detection, NSET 128–129
chaperonin templates, engineered 233
charge separation principle, photocatalysts 154
chemical vapor deposition (CVD), nanotube synthesis 426–428
collapsed nanotubes 478–479
composites, BNN application 449

core-dissolution, controlled 298–299
core-shell bimetallic nanoparticles 198–209
core-shell bimetallic nanostructures, biofunctionalization for the construction of 206–209
core-shell nanomaterials 281–286
– and drug delivery 382
– applications 316–319
– aspect ratio 378
– bioimaging (magnetic resonance imaging) 381–382
– bioimaging applications 318
– biological/medical applications 317–319
– biomolecular delivery vehicles 319
– biomolecule (protein) core–polymer shell 304
– carbon-containing 313–315
– catalysis applications 319
– characterization using X-ray absorption spectroscopy 377–400
– deposition of shells over 290
– drug delivery vehicles 319
– dye-doped silica–metal oxide 305
– EXAFS 380, 392–393, 396–397
– immunoassay applications 318
– insulator–insulator 302–306
– insulator–metal 301, 313
– insulator–semiconductor 309
– metal 288
– metal core–dendrimer 300
– metal core–semiconducting metal oxide 300
– metal-dense metal oxide 292–293
– metal-functionalized metal oxide 294
– metal–insulator 291–300
– metal–metal 310–312
– metal–metal oxide 298–299
– metal oxide 289, 305
– metal oxide–carbon 313
– metal oxide–dye-doped silica 305
– metal oxide–metal 301
– metal oxide–metal oxide 305
– metal oxide–polymer 305
– metal–polymer 295–297
– metal–porous metal oxide 294
– nonmagnetic 287
– particle size, shape and aspect ratio measurements 387–388
– polymer–metal 301
– polymer–metal oxide 302
– polymer–polymer 303
– polymeric 290
– semiconductor 290
– semiconductor–insulator 307
– semiconductor–semiconductor 308
– semiconductor–semiconductor–dendrimer 308
– spherical and anisotropic nonmagnetic 281–321
– synthesis of cores 288–290
– synthetic methods 316
– TEM 379–380
– types of 291–316
– XAS methods 389–390
– XRD 379
core-shell nanoparticles, DNA-assisted synthesis 205–206
core-shell nanostructures
– bimetallic 164–174
– biofunctionalization 206–209
– building strategy 162–163
– characterized by XAS 389–390
– metal-oxide 163–164
– polymer–metal 301
cosmetic materials, BNN application 448
CVD *see* chemical vapor deposition

d

D-(+)-glucose, electrocatalytic oxidation 73–76
dendrimer-encapsulated bimetal nanoparticles 225–228
dendrite nanostructures 186
distance-dependent NSET 115–119
DNA
– fluorescence intensity 115
– functionalization of nanorods 218–219
– NW/NR functionalization 218–220
DNA-assisted synthesis 205–206
DNA cleavage detection, NSET 125–127
DNA detection
– by nanorods 269–270
– multiplex NSET 119–120
DNA metallization 228–229
DNA plasmids, selective binding 219
DNA/RNA hybridization detection, NSET probes for 112–114
doped TiO_2 mixed-metal oxides
– UV-light-sensitive photocatalysts 141–146
– visible-light-sensitive photocatalysts 146–150
drug delivery vehicles, core-shell nanomaterials 319
dye-doped silica–metal oxide core-shell nanostructures 305

e

EGFR *see* epidermal growth factor receptor
electrical nanoinsulators, BNN application 452
electrodes, oxidation process 70–77
endothelial gap 24
enhanced green fluorescence protein (EGFP), gene delivery 50–51
environmental remediation
– mixed-metal oxide nanomaterials for 139–156
– TiO_2 heterogeneous photocatalysis for 141–150
enzymatic catalysts
– biofuel cell applications 57–103
– enzymatic reduction of oxygen to water 63–69
– enzyme immobilization 61–62
– ORR 61–69
epidermal growth factor receptor (EGFR) 230–231
extended X-ray absorption fine structure (EXAFS), core-shell nanomaterials 380, 392–393

f

FePt nanoparticles, TEM images 246
Förster resonance energy transfer (FRET) 109
fuel cells 85–91
– performances 88, 91

g

gap, endothelial 24
gas adsorption, BNN application 450–451
gaseous molecules, detection by nanorods 265
GDH, glucose oxidation 78–79
gene delivery, oxide nanomaterial application 49–52
glucose
– electrocatalytic oxidation 73–77
glucose biofuel cells 85–90
glucose electro-oxidation 59
glucose oxidase, direct electron transfer 80–82
glucose oxidation 70–85
– Au–Pt nanomaterials 70–84
– catalyst efficiency 75–76
– catalyzation by GDH 78–79
– catalyzation by Gox 79–85
– via enzymes 77–84
glucose/oxygen biofuel cells 85–91
gold, dielectric function 6–7
gold nanoparticles
– Ag_{Core}/Au_{shell} 198–200
– Au_{Core}/Ag_{shell} 201–203
– hyperefficient quenching 107
– quenching efficiency variation 117, 121
– silver enhancement 204–205
gold nanorods, coating of 344
gold nanoshells 1–44
– absorption efficencies 3
– bioconjugation 18–19
– biodistribution 20–21
– biomedical applications 26–37
– biosensors 35–37, 129–131
– drug delivery 34
– extinction efficencies 3
– extinction spectra 12
– in vitro cancer detection 26–27, 29–30
– in vivo cancer detection 28
– in vivo photothermal therapy 31–33
– integrated cancer imaging and therapy agents 29
– near-field enhancement 13–14
– optical properties 2–5
– physical properties 2–16
– plasmon resonance hybridization picture 13
– scattering efficencies 3
– synthesis 16–19
– TEM picture 2
– tissue welding 35
– toxicity 25
– transport mechanisms 19–26
gold-platinum catalysts 73–77
gold-platinum nanoparticles
– diffraction patterns 72
– lattice constant parameter 73
– structural properties 71
– synthesis 71–73
GOx, glucose oxidation 79–85

h

heterogeneous photocatalysis, environmental remediation 141–150
heteronanostructures, 1-D bimetallic 174–179
hexagonal boron nitride nanomaterials (BNN)
– applications 447–452
– as support for catalysts 452
– carbon template-substitution reaction 441–442
– composites 449
– cosmetic materials 448

– direct pyrolyzing borazinic precursors 439
– electrical nanoinsulators 452
– for cancer therapy and diagnostics 449
– gas adsorption 450–451
– meshes 439–442
– mesoporous molds 440
– mono- or few-layer sheets 443–445
– nano-objects 433–438
– pharmaceutical table lubricants 447
– physical properties of 446
– porous 439–442
– synthesis and applications 411–453
– ultraviolet lasers and LEDs 452
– *see also* nanotube synthesis
high-temperature chemical inertness, anisotropic boron nitride nanomaterials 484
hollow metal–metal oxide shells 298–299
hybrid materials, silica-encapsulated magnetic nanoparticles 359–362
hybridization detection, NSET probe 112–115
hybridization picture, plasmon resonance 13
hydrogels, nanoshell–polymer 35
hydrogen storage, anisotropic boron nitride nanomaterials 487
hyperefficient quenching, gold nanoparticles 107

i

imaging 49
– cancer 26–28
– in vivo 28–29
immunoassays, core-shell nanomaterials for 318
immunosensors, amperometric 202
insulator–insulator core-shell nanoparticles 302–306
insulator–metal core-shell nanomaterials 301
insulator–metal core-shell nanoparticles 313
insulator–semiconductor core-shell nanomaterials 309
integrated cancer imaging 29–31

l

laccase, oxygen reduction 64–70
laser ablation, nanotube synthesis 416–419
laser irradiation, destruction of nanoshells 15
LEDs, BNN application 452
life sciences 45–56
– anisotropic boron nitride nanomaterials 487–488
– nanoparticle applications 48–54
– nonmagnetic metal-oxide and bimetallic nanostructures 161–191
ligand exchange, profunctional bimetallic alloys 228–229
light-sensitive photocatalysts, metal-doped TiO_2 mixed-metal oxides 141–146
liposomes, migrating 24
low-temperature autoclaving, nanotube synthesis 430
luminescence intensity, enhanced by silica-coated metal nanoparticles 342–344

m

magnetic metal oxide nanoparticles, silica-coated 356–358
magnetic resonance imaging, core-shell nanomaterials 381–382
material characteristics, photothermal 14–16
mediated electron transfer, glucose oxidase 82
mercaptoalkyl oligonucleotide modified Ag/Au core-shell particles 200
metal catalysts, oxygen reduction reaction (ORR) 60
metal core–dendrimer core-shell nanoparticles 300
metal core–semiconducting metal oxide shell nanoparticles 300
metal cores, synthesis 288
metal-dense metal oxide core-shell nanomaterials 292–293
metal-doped TiO_2 mixed-metal oxides
– UV-light-sensitive photocatalysts 141–146
– visible-light-sensitive photocatalysts 146–150
metal electrodes, oxidation process 70–77
metal-functionalized metal oxide core-shell nanoparticles 294
metal–insulator core-shell nanomaterials 291–300
metal ions, detection by nanorods 265–266
metal–metal core-shell 310–312
metal–metal oxide shells, hollow 298–299
metal nanoparticle stabilization, PAMAM dendrimers 226
metal oxide–carbon core-shell nanoparticles 313
metal-oxide core-shell nanostructures 163–164

metal oxide cores, synthesis 289
metal oxide–dye-doped silica core-shell nanostructures, core-shell nanostructures 305
metal oxide–metal core-shell nanostructures 301
metal oxide–metal oxide core-shell nanomaterials 305
metal oxide nanomaterials, mixed *see* mixed-metal oxide nanomaterials
metal oxide nanoparticles, silica-coated 356–358
metal oxide nanostructures, nonmagnetic 161–163
metal oxide–polymer core-shell nanoparticles 305
metal oxide shells 305
– metal–metal oxide 298–299
– metal oxide–metal 301
– polymer–metal oxide 302
metal–polymer core-shell nanoparticles 295–297
metal–porous metal oxide core-shell 294
metallic NSET biosensors 103–139
Mg^{2+}-dependent RNA folding, NSET 121–124
Mie theory
– absorption coefficients 5
– gold nanoshells 13–14
migrating liposomes 24
mixed-metal oxide nanomaterials
– environmental remediation 139–156
– metal-doped TiO_2 141–150
– TiO_2 heterogeneous photocatalysis 141–149
molecular oxygen reduction, kinetic model 60
multicopper oxidases, molecular oxygen reduction 63
multielemental nanorods
– absorption 256–257
– analytical applications 241–280
– aqueous-phase synthesis 248–254
– bimetallic 243–244, 248–249
– bimetallic/trimetallic oxide 252–253
– catalytic properties 262
– characterization 241–280
– detection of gaseous molecules 265
– detection of metal ions 265–266
– detection of pathogens and bacteria 271
– DNA detection 269–270
– emission 258–259
– magnetism 263
– multisegmented 250–251
– organic-phase synthesis 243
– properties 255–263
– semiconductor 245–247, 254
– separation and sensing of proteins 267–268
– surface-enhanced raman scattering 260–261
– synthesis 241–280
multiplex DNA detection 119–121
multisegmented nanorods, aqueous-phase synthesis 250–251
multisegmented NRS 250–252
multiwalled nanotubes (MWNT) 470–475

n

nanocubes 174
nanomaterial surface energy transfer (NSET) 109–129
– biosensors 103–139
– distance-dependent 115–118
– for cancer cell detection 128
– for DNA cleavage detection 125–127
– for monitoring Mg^{2+}-dependent RNA folding 121–124
– multiplex DNA detection 119–120
– portable probes 111
– probes for DNA/RNA hybridization detection 112–114
– problems and challenges 131
– size-dependence sensitivity 114
nanomaterials
– biofuel cell applications 57–103
– core-shell *see* core-shell nanomaterials
– for environmental remediation 139–161
– life sciences 45–56
– NSET biosensors based on 103–139
– quenching properties 106–109
– size- and shape-dependent super quenching properties 106–108
– *see also* bimetallic nanomaterials
nanoparticles
– Ag_{core}/Au_{shell} 198–201
– anisotropically shaped *see also* nanorods; nanowires 209–224
– Au_{core}/Ag_{shell} 201–204
– dendrimer-encapsulated 225–228
– DNA-assisted synthesis 205–206
– silver enhancement 204–205
– synthesis 71–73
– synthesis and functionalization 45–48
nanorods (NR) 209–224
– bimetallic 45–46
– coating of 344

– detection and sensing applications 220–224
– functionalization by DNA 218–219
– functionalization with protein molecules 212–217
– multielemental *see* multielemental nanorods
– surface modifications 210–211
– synthesis 241–280
– TEM picture 2
nanoshell destruction 15
nanoshell growth phases 17
nanoshell–polymer hydrogels 35
nanoshells, gold *see* gold nanoshells
nanostructures
– alloy 179–185
– bimetallic *see* bimetallic nanostructures
– biofunctionalization 206–209
– core-shell *see also* core-shell nanostructures, 162–163
– hetero- 174–179
– potential applications in the life sciences 161–196
nanotechnology, promises for biological detection 105–111
nanotube (NT) nano-objects
– filled 433–435
– functionalized 436–438
nanotube (NT) synthesis
– arc discharge 413–415
– arc-jet plasma 432
– carbon nanotubes-substitution reaction 420–425
– chemical vapor deposition 426–428
– hexagonal boron nitride 412–433
– laser ablation 416–419
– low-temperature autoclaving 430
– pore-template 430–431
– solid–gas reaction 429
nanotubes (NT), collapsed 478–479
nanowires (NW) 47–48, 209–224, 480–482
– bimetallic 47
– synthesis 241–280
– *see also* nanorods
neutral media, electro-oxidation of glucose 76
noble metal nanoparticles 332–337
nonmagnetic metal-oxidenanostructures, life sciences 161–196
NR *see* nanorods
NSET *see* nanomaterial surface energy transfer
NW *see* nanowires
NW/NR functionalization
– DNA 218–220
– protein molecules 212–218

o

oligonucleotides, for modifying silica shells 338
optic materials dopants, silica-encapsulated magnetic nanoparticles 359–362
organic-phase synthesis 243–245
ORR *see* oxygen reduction reaction
ovalbumin-specific CD8 responses 53
oxidation 73–77
– catalyzation by GDH 78–79
– catalyzation by Gox 79–85
– enzymes 77–85
– glucose 70–85
– metal electrodes 70–77
oxide nanomaterials
– anisotropic 45–54
– environmental remediation 139–161
– gene delivery 49–52
– life sciences 45–56
oxide NRS, bimetallic/trimetallic 252–254
oxide photocatalysts 150–156
oxides
– UV-light-sensitive photocatalysts 141–146
– visible-light-sensitive photocatalysts 146–150
oxygen, enzymatic reduction to water 63–70
oxygen biofuel cells 85–90
oxygen reduction
– catalyzed by laccase 64–70
– molecular 60
oxygen reduction reaction (ORR) 58–70
– enzymatic catalysts 61–69
– enzymatic reduction to water 63–69
– enzyme immobilization 61–62
– metal catalysts 60

p

PAMAM dendrimers 226
pathogens, detection by nanorods 271
Pd/Au nanostructures
– XAS methods 393–394, 398–399
pharmaceutical table lubricants, BNN application 447
photocatalysis, environmental remediation 141–150
photocatalysts 141–156
– charge separation principle 154
– mixed-metal oxide 150–156
– UV-light-sensitive 141–146
– visible-light-sensitive 146–150

photoluminescence, gold nanoshells 14–16
photothermal therapy 31–34
– in vivo 31–33
plasmon resonance, quasi-static approximation 7–13
plasmon resonance hybridization picture, gold nanoshells 13
platinum, silica-encapsulated 345
platinum catalysts 73–77
platinum nanomaterials, biofuel cell applications 57–103
platinum nanoparticles
– in hollow silica spherical structures 363–366
– synthesis 71–73
polymer–metal core-shell nanostructures 301
polymer–metal oxide core-shell nanomaterials 302
polymer–polymer core-shell nanomaterials 303
polymeric cores, synthesis 290
polypyrrole film, glucose oxidase 83–85
profunctional bimetallic alloys 224–233
– dendrimer-encapsulated bimetal nanoparticles 225–227
– DNA metallization 228
– engineered chaperonin templates 232–233
– epidermal growth factor receptor 230–231
– miscellaneous 229–233
– surface stabilization by ligand exchange 228
prostatic cancer cells 30
proteins
– functionalization of nanorods 212–217
– selective adsorption 216
– separation and sensing by nanorods 267–268
Pt *see* platinum

q

quantum dots (QDs) see silica-coated quantum dots
quenching, size- and shape-dependent 106–108

r

RNA folding, Mg^{2+}-dependent 121–124
RNA hybridization detection, NSET probe 112–115

s

scattering coefficients, Mie theory 5
self-assembly, orthogonal 213
semiconductor cores, synthesis 290
semiconductor–insulator core-shell nanomaterials 307
semiconductor nanorods 245–248, 254–255
– aqueous-phase synthesis 254
– organic-phase synthesis 245–247
semiconductor–semiconductor core-shell nanomaterials 308
semiconductor–semiconductor–dendrimer core-shell-shell nanoparticles, nanoparticles 308
SERS *see* surface-enhanced Raman scattering
shape-dependent super quenching, nanomaterials 106–109
silica-coated alloy metal nanoparticles 354–355
silica-coated magnetic metal oxide nanoparticles 356–358
silica-coated metal nanoparticles
– biofunctionalization 338
– enhanced luminescence intensity 342–344
– modified with oligonucleotides 338
– noble metals 332–337
– silica-encapsulated platinum 345
– silica gold nanorods 344
– sol–gel method for silica coating 334–337
– surface-enhanced Raman scattering effect 339–341
silica-coated quantum dots 345–350
– advantages 346
– hydrophilic 349–350
– hydrophobic 347–348
– types 347–350
silica core, nanoshell growth phases 17
silica-encapsulated magnetic nanoparticles 351–362
– alloy metal 354–355
– applications 359–362
– forming hybrid materials 359–362
– metal oxide 356–358
– optic materials dopants 359–362
silica-encapsulated platinum 345
silica gold nanorods, coating of 344
silica shell nanomaterials 331–367
– hollow silica spherical structures 363–366

– *see also* silica-coated metal nanoparticles; silica-coated quantum dots, silica-encapsulated magnetic nanoparticles
silica spherical structures, hollow 363–366
silver enhancement, gold nanoparticles 204–205
single-walled nanotubes (SWNT) 476–477
size-dependence sensitivity 114–115
size-dependent super quenching, nanomaterials 106–109
sol–gel method, for silica coating 334–337
solid–gas reaction, nanotube synthesis 429
spherical and anisotropic bimetallic nanomaterials, biofunctionalization 197–240
spherical bimetallic nanomaterials, biofunctionalization 197–240
spherical BN particles 464–469
spherical core-shell bimetallic nanoparticles 198–209
spherical metallic NSET biosensors 103–139
super quenching, nanomaterials 106–109
surface energy transfer *see* nanomaterial surface energy transfer (NSET)
surface-enhanced Raman scattering (SERS)
– biosensing 37
– silica-coated metal nanoparticles 339–341
surface plasmon resonance, quasi-static approximation 7–13
surface stabilization, ligand exchange 228–229

t

TEM *see* transmission electron microscopy
therapy, photothermal 31–34
therapy agents, and cancer imaging 29
thermal material characteristics 14–16
TiO_2 heterogeneous photocatalysis, environmental remediation 141–150
TiO_2 mixed-metal oxides
– UV-light-sensitive photocatalysts 141–146
– visible-light-sensitive photocatalysts 146–150
tissue welding, gold nanoshells 35–37
toxicity profile, gold nanoshells 19–26
transmission electron microscopy (TEM), core-shell nanomaterials 379–380
trimetallic oxide NRS 252–254

u

ultraviolet lasers, BNN application 452
UV-light-sensitive photocatalysts, metal-doped TiO_2 mixed-metal oxides 141–146

v

visible-light-sensitive photocatalysts, metal-doped TiO_2 mixed-metal oxides 146–150

w

water, enzymatic reduction of oxygen to 63–70
WAXS *see* wide-angle x-ray scattering
welding, tissue 35–37
wide-angle X-ray scattering (WAXS), gold-platinum nanoparticles 71–73

x

X-ray absorption spectroscopy (XAS)
– characterization of surface interactions 399–400
– core-shell nanomaterials 377–400
– core-shell structure analysis 389–390
– data collection and analysis 386
– fundamentals 384–385
– particle size, shape and aspect ratio measurements 387–388
– review of characterization methodologies 392–398
– surface and core composition analysis 391
X-ray diffraction (XRD), core-shell nanomaterials 379
XAS *see* X-ray absorption spectroscopy